Geophysik

Department für Geo- und Umweltwissenschaften

Fakultät für Geowissenschaften

Ludwig-Maximilians-Universität München

Zusammenfassung der
kumulativen Habilitationsschrift

"Entwicklung und Anwendung der Diskontinuierlichen Galerkin Finite Element Methode in der Numerischen Seismologie"

von

Dr. Martin Andreas Käser

München, den 30. November 2011

Simulation seismischer Wellenausbreitung

Das Thema der vorliegenden Habilitation ist die Entwicklung und Anwendung einer neuen Simulationstechnik für die Generierung seismischer Wellen und die numerische Berechnung deren Ausbreitung.

Eine in den vergangenen zwei Jahrzehnten immer wichtiger werdende Disziplin der Seismologie stellt die rechnergestützte Seismologie (*Computational Seismology*) dar, die sich vor allem durch die rapide Zunahme moderner Rechenressourcen zu einem äußerst aktiven und interdisziplinären Forschungszweig innerhalb der Geophysik entwickelt hat. Nur durch eine intensive Zusammenarbeit auf den Gebieten der Erdbeben-, Bohrloch- oder Explorationsseismologie, der Numerischen Mathematik und der Informatik wird es in Zukunft möglich sein, neue und wissenschaftlich weiterführende Erkenntnisse auf der Basis von rechentechnisch aufwendigen Simulationen zu gewinnen. Dies ist vor allem im Bereich der Erdbebenseismologie von besonderem Interesse, weil der klassische Versuchsaufbau und die durch gezielte Beobachtungen und aufgezeichnete Messwerte erhaltenen Ergebnisse schwierig zu erhalten und nicht zu reproduzieren ist.

Um zuverlässige Aussagen durch Simulationsergebnisse zu treffen, ist es entscheidend, dass diese sogenannten synthetischen Ergebnisse – in der Seismologie im speziellen die synthetischen Seismogramme – mit möglichst kleinen Fehlern behaftet sind. Dies setzt mehrere Punkte voraus:

- eine geeignete Beschreibung des physikalischen Vorgangs durch ein mathematisches Modell (z.B. partielle Differentialgleichungen)
- eine möglichst realistische Parametrisierung des Modells (z.B. Geometrie und geophysikalische Eigenschaften des Computermodells)
- eine ausreichend feine räumliche und zeitliche Auflösung des physikalischen Phänomens der seismischen Wellenausbreitung und die damit verbundenen Rechenressourcen
- ein numerisches Simulationsverfahren, das geometrisch flexibel ist, hohe Approximationsgenauigkeit liefert und in der Lage ist, verschiedene Eigenschaften der realen Untergrundstruktur und der seismischen Quelle abzubilden

Die Habilitation beschäftigt sich dabei vor allem mit dem letzten Punkt und umfasst die Entwicklung und Anwendung einer speziellen Art von Finite-Elemente Methode im Bereich der Computational Seismology.

Diskontinuierliches Galerkin Finite-Elemente Verfahren

Es handelt sich dabei um ein numerisches Verfahren – ursprünglich entwickelt im Bereich der Simulation von Neutronentransport – , bei dem der dreidimensionale Raum in sogenannte Elemente unterteilt wird, innerhalb derer jeweils die Materialeigenschaften, der Zustand des Drucks, die Schwinggeschwindigkeit eines Partikels oder dessen Spannungszustand durch eine numerische Approximation in Form eines Polynoms angenähert wird. Das Verfahren verfügt über eine enorme geometrische Flexibilität des Rechengitters, eine Eigenschaft, die schon seit Jahrzehnten vor allem in den Ingenieurwissenschaften sehr erfolgreich verwendet wird.

Des Weiteren kann durch die Verwendung höherer Polynomgrade eine bessere und vor allem lokale Approximation erreicht werden. Im Gegensatz zu anderen numerischen Verfahren (z.B. Finite Differenzen, Finite Volumen) erhöht sich dadurch nur die Anzahl der Polynomkoeffizienten – oft auch als Freiheitsgrade bezeichnet – innerhalb eines Elements, ohne dass eine steigende Zahl von Nachbarelementen und deren Eigenschaften mit einbezogen werden müssen. Das Konzept des sogenannten *stencil* ist dadurch unnötig und die Implementierung auf großen parallelen Rechnern wird erheblich erleichtert.

Eine zusätzliche Besonderheit des Verfahrens besteht in der Diskontinuität der Polynome an den Elementgrenzen, d.h. innerhalb eines Elements liegt eine glatte Polynomapproximation vor, die jedoch am Übergang zu den Nachbarelementen Sprünge aufweisen kann. Diese Diskontinuitäten werden bei besserer räumlicher Auflösung zwar infinitesimal klein, sind aber einer der entscheidendsten Bestandteile des Verfahrens, weil dadurch ein sogenanntes Riemann-Problem definiert wird. Ein Riemann-Problem setzt sich aus zwei Zustandswerten auf den jeweiligen Seiten einer Diskontinuität und einer hyperbolischen Differentialgleichung zusammen, die die räumliche und zeitliche Entwicklung dieser Zustände an der Diskontinuität beschreibt. Die Lösung des Riemann-Problems definiert schließlich den Zustand an den Elementgrenzen. Das Konzept und die Behandlung von Riemann-Problemen mit Riemann-Lösern ist ein eigenes Forschungsfeld der angewandten, numerischen Mathematik und wurde im Verlaufe der letzten 50 Jahre vor allem durch die Entwicklung der Finite-Volumen Methode vorangetrieben. Nach der Einführung der ADER-Methode (Arbitrarily high-order DERivatives) im Rahmen der Riemann-Löser für Finite-Volumen konnte dieser Ansatz auch für die Diskontinuierlichen Galerkin Finite-Elemente (DG) übernommen werden, was dem Verfahren nicht nur eine beliebig hohe Approximationsordnung im Raum, sondern auch in der Zeit verschafft, eine Eigenschaft, die vor allem für die hochgenaue Berechnung der Ausbreitung von Wellen über lange Distanzen von großer Bedeutung ist. Nicht nur die numerische Diffusion wird dadurch reduziert, um Amplitudeninformationen zu erhalten, sondern auch die numerische Dispersion, um Phaseninformationen korrekt zu transportieren.

Komplexe Geometrie und realistische Medien

Ein Simulationsmodell erfordert immer eine Simplifikation der realen Gegebenheiten, da das Kontinuum diskret, d.h. in Form eines Gitters, dargestellt wird. Das Rechengitter kann beim DG-Verfahren aus verzerrten Hexaedern, Tetraedern, Prismen oder Pyramiden bestehen, wobei die Tetraedergitter bei der Anwendung klar im Vordergrund stehen. Zum einen bieten Tetraedergitter die größte geometrische Flexibilität und zum anderen stehen für diese Art von Diskretisierungsgitter mehrere leistungsfähige Software-Packete zur Gittererzeugung zur Verfügung. Komplexe geometrische Eigenschaften des geologischen Untergrunds, wie sie etwa in Lagerstätten (Falten, diskordante Schichtung, Einschlüsse, etc.) in Verwerfungs- und Subduktionszonen (diskordante Schichtung, Versatz von Gesteinseinheiten, Verschneidung von Bruch- und Schichtungsflächen) oder in Vulkanen (Sills, Dykes) stellen eine große Herausforderung bei der Berücksichtigung der Materialgrenzen im Prozess der Gittergenerierung dar. Insbesondere bei Anwendungen in der hochauflösenden Ingenieursseismik (Untersuchung Bauwerken, Baugrund, Deponien, etc.) spielt die genau Repräsentation dieser klein-skaligen geometrischen Gegebenheiten eine außerordentlich wichtige Rolle. Ähnlich schwierig ist die Einbeziehung der Topographie mit bewegtem Relief, wie es bei Gebirgsregionen oder tiefen Taleinschnitten (Canyons) vorliegt. Da seismische Wellen von den steilen Flanken und dem extremen Materialkontrast zwischen Gestein und Luft quasi totalreflektiert werden, finden starke Streuungs- bzw. Fokussierungseffekte statt, die die Bodenbewegung an der Oberfläche in hohem Maße beeinflussen.

Des Weiteren müssen bei der Simulation seismischer Wellenausbreitung die Materialeigenschaften der Medien, die von den Wellen durchdrungen werden, so gut wie möglich durch die zugrundeliegenden physikalischen Modelle und deren mathematischer Formulierung in Form von Differentialgleichungen beschrieben werden. In erster Näherung verhalten sich viele Gesteinsarten elastisch, d.h. die Deformation des Gesteins beim Durchgang einer seismischen Welle ist reversibel und die Struktur des Gesteins geht in ihre Ausgangslage zurück und die Energie der seismischen Welle bleibt erhalten.
Bei genauerer Betrachtung treten aber inelastische Eigenschaften auf, wodurch ein Teil der kinetischen Energie in Wärme umgewandelt wird. Dadurch nimmt die Wellenamplitude stärker ab und auch die Ausbreitungsgeschwindigkeit der Wellen wird stark frequenzabhängig. Die Beschreibung dieser inelastischen Eigenschaften konnte durch das Konzept der generalisierten Maxwell-Körper in das DG-Verfahren aufgenommen werden und lieferte ausgezeichnete Ergebnisse. Die Approximationsgenauigkeit der kann dabei nicht nur von der Wahl des Polynomgrades, sondern auch von der Anzahl der parallel geschalteten Maxwell-Körper gesteuert werden, wobei sich eine Anzahl von drei bis fünf als guter Kompromiss zwischen Genauigkeit und Rechenaufwand herausgestellt hat.

Eine ebenso wichtige Eigenschaft ist die Anisotropie des Gesteins, die für die Richtungsabhängigkeit der Ausbreitungsgeschwindigkeit der Wellen verantwortlich ist. Durch die Einbeziehung aller 21 Koeffizienten der Hooke's matrix im DG-Ansatz kann die Anisotropie aller kristallinen Symmetrieklassen (triklin, monoklin, orthorhombisch, tetragonal, hexagonal, rhombisch, kubisch) definiert und in die Berechnung der Wellenausbreitung integriert werden.
Besonders für die Anwendung in Lagerstätten (z.B. Erdölexploration) oder oberflächennahen, flüssigkeitsgesättigten Medien (z.B. in der Hydrologie) spielen auch poroelastische Eigenschaften eine wichtige Rolle und sind im DG-Verfahren durch die theoretische Beschreibung von Biot implementiert. Da die Gesteinsmatrix und die Porenflüssigkeit unterschiedliche seismische Geschwindigkeiten aufweisen entsteht in poroelastischen Medien ein neuer Wellentyp, die langsame P-Welle, die sich bei niedrigen Frequenzen nur als Diffusionswelle äußert. Der theoretisch-technische Rahmen ist also im Simulationsverfahren gegeben, allerdings ist es oft schwierig, die nötigen Parameter (z.B. Porosität, Permeabilität, Tortuosität und Viskosität) des Materials zu kennen.
Eine für die Zukunft noch wichtige Materialeigenschaft, vor allem im Hinblick auf Effekte im Nahfeld von Erdbebenquellen, ist die Nichtlinearität bzw. Plastizität des Gesteins. Die Berücksichtigung nichtlinearer Effekte ist speziell bei der Berechnung von dynamischen Bruchprozessen von großem Interesse, da der Einfluss nichtlinearen Materialverhaltens in unmittelbarer Umgebung des Bruches auf die Bruchausbreitung Gegenstand aktueller Forschungsaktivitäten ist.
Mit Bezug auf die Approximation der Materialeigenschaften innerhalb eines Elements, wurden beim diskontinuierlichen Galerkin Finite-Elemente Verfahren standardmäßig oft nur die Eigenschaften am Elementmittelpunkt verwendet und dann als repräsentativ und konstant für die Region des Elements angenommen. Diese Methodik konnte ersetzt werden durch die Approximation der Materialschwankungen innerhalb eines Elements durch Polynome (sub-cell resolution). Dabei handelt es sich um die gleiche Polynombasis wie bei der Approximation der physikalischen Zustandsvariablen, die die Wellenausbreitung beschreiben. Vor allem bei der Verwendung grober Gitter liefert diese neue Methodik einen deutlichen Genauigkeitsgewinn, der sich jedoch im Falle stark verfeinerter Gitter immer weniger auszahlt, wenn man das Verhältnis von *Genauigkeit / Rechenzeit* berücksichtigt.

Regelmäßige, unstrukturierte, hybride, nicht-konforme und adaptive Gitter

Auf dem Gebiet der numerischen Simulation stellt, wie oben erwähnt, die Gittererzeugung eine große Herausforderung dar. Zum einen muss der zu untersuchende, physikalische Raum mit allen geometrischen und geophysikalischen Parametern und deren Grenzschichten möglichst genau durch die Diskretisierung erfasst werden, zum anderen muss aber auch der Rechenaufwand in einem

vertretbaren Rahmen bleiben. Regelmäßige Gitter, die einer einfachen Logik bei der Nummerierung der Gitterelemente folgen, haben große Vorteile bei der Implementierung des numerischen Lösungsverfahrens. Im Hinblick auf Speicherbedarf muss nur ein einziger Index zur Identifikation des Elements im Speicher gehalten werden. Aufgrund der Regelmäßigkeit des Gitters können daraus Position und Geometrie einfach angeleitet werden. Außerdem liegt Information benachbarter Elemente in der Regel auch im Speicher an benachbarten Registern, sodass extrem schnell auf diese Information zugegriffen und zu Rechenoperationen benutzt werden kann. Einen entscheidenden Nachteil stellt jedoch die geringe geometrische Flexibilität dar, da regelmäßige Gitter kaum, oder nur unter erheblichem Verlust der Rechengenauigkeit an komplizierte Geometrien angepasst werden können.

Es wurde eine Studie durchgeführt, um zu klären, welche Auflösung bei regelmäßigen Gittern mindestens nötig ist, um noch Ergebnisse einer bestimmten Genauigkeit zu erhalten, wenn seismische Wellen klar definierte Materialgrenzen durchlaufen und dadurch Wellenreflexion, -transmission und -konversion auftritt. Die Untersuchung zeigt, wie die Wahl der regelmäßigen Gitterweite von der Frequenz der propagierten Wellen und der Stärke des Materialkontrasts abhängt, wenn das numerische Gitter nicht den geometrisch komplizierten Materialgrenzen angepasst werden kann.

Vor allem aus diesem Grund wurden Verfahren entwickelt, die auch unstrukturierte Gitter – vor allem Dreiecksgitter in 2D oder Tetraedergitter in 3D – zur Modeldiskretisierung nutzen können. In der Regel handelt es sich dabei um Finite Elemente oder Finite Volumen Verfahren. Gekrümmte Linien oder Flächen können dabei durch stückweise lineare Linien oder Flächenelemente repräsentiert werden, wobei die Approximationsgüte durch die räumliche Auflösung Δx gesteuert werden kann. Außerdem lässt sich die räumliche Auflösung Δx graduell variieren, sodass die Gitterweite adaptiv, also z.B. proportional zur seismischen Ausbreitungs-geschwindigkeit c_s gewählt werden kann. Dadurch wird die durch ein Stabilitätskriterium vorgegebene Zeitschrittlänge Δt optimal ausgenutzt, da $\Delta t \sim \Delta x/c_s$. Diese Gitteradaptivität kann auch benutzt werden, um den Rechenaufwand auf Modelregionen von besonderem Interesse zu konzentrieren, während andere Bereiche (z.B. Modelränder) gröber aufgelöst und damit rechentechnisch weniger aufwendig werden. Der Rechen- und Speicheraufwand pro Element bei unstrukturierten Gittern ist oft deutlich höher als bei regelmäßigen Gittern, da Koordinaten und Konnektivitätseigenschaften jedes Elements als Matrizen im Speicher gehalten werden müssen und der Zugriff auf Nachbarelemente nicht einfach durch die Erhöhung oder Erniedrigung eines Index möglich ist.

Ein vielversprechender Kompromiss ist daher die Kombination beider Gittertypen zu hybriden Gittern, um die Vorteile beider Ansätze zu nutzen und Bereiche mit unstrukturierten Gittern begrenzt zu halten, dafür aber möglichst hohe Genauigkeit

bei möglichst geringem Rechenaufwand zu erhalten. Um die Ankopplung verschiedener Gittertypen (z.B. Dreiecks- und Rechtecksgitter oder Tetraeder- und Hexaedergitter) im DG-Verfahren zu ermöglichen, ist eine Methodik für nicht-konforme Gitter entwickelt worden. Dabei müssen sich benachbarte Elemente keine gemeinsame Elementgrenze und Eckpunkte mehr teilen, sondern können entlang ihrer Begrenzung verschoben aneinander liegen. Nur so kann im dreidimensionalen Raum die Einführung von Übergangselementen wie Pyramiden oder Prismen vermieden werden. Das DG-Verfahren auf hybriden, nicht-konformen Gittern erhält auch seine Approximationsordnung, sodass die numerische Genauigkeit auch bei mehrmaligem Übergang von einem zu anderen Gittertyp erhalten bleibt.

Quantitativer Vergleich verschiedener numerischer Methoden

Bei der Entwicklung neuer numerischer Methoden zur Simulation der seismischen Wellenausbreitung kommt dem Vergleich mit analytischen Lösungen und der Gegenüberstellung der numerischen Ergebnisse mit denen anderer Verfahren eine überaus große Bedeutung zu. Im Rahmen des SPICE-Projektes wurde dazu eine Reihe von Testszenarien erstellt, die für verschiedene Entwicklungsstufen einer neu entwickelten Methodik, zum *benchmarking* frei verfügbar sind. Die Ergebnisse können dann mit anderen, bereits publizierten Lösungen verglichen werden und die Unterschiede analysiert werden. Dazu werden klar definierte Fehlernormen verwendet, die den numerischen Fehler sowohl in Amplituden- und Phasenfehler des synthetischen Seismogramms aufspalten und eine zeit-, distanz- und frequenzabhängige Analyse des Fehlers zulassen. Durch die Fehleranalysen des DG-Verfahrens konnte – in enger Zusammenarbeit mit anderen Gruppen innerhalb der SPICE-Projektes – die Wichtigkeit und die Gesamtheit einer gründlichen Fehler- und Genauigkeitsanalyse im Bereich der Computational Seismology deutlich stärker in den Vordergrund gestellt werden, als dies vorher oft der Fall war.

Ein allerdings weiterhin bestehendes Problem ist die Anwendung verschiedener Rechenverfahren auf unterschiedlichen Rechenarchitekturen. Vor allem durch den starken Trend der Parallelisierung der Verfahren auf verschiedenen Supercomputern und der damit einhergehenden Optimierung erweist es sich oft als schwierig einen fairen Vergleich im Hinblick auf das Verhältnis von *Genauigkeit / Rechenzeit* anzustellen.

Software-Entwicklung, Optimierung und Hochleistungsrechnen

Aktuell in der Seismologie verwendete Simulationsverfahren, wie auch das DG-Verfahren, müssen in der Lage sein, unterschiedlichste Problemstellungen von seismologischem Interesse zu behandeln. Um auch die ausreichende Genauigkeit der erzeugten Ergebnisse und die dafür erforderliche Auflösung zu erhalten müssen Simulationsverfahren an die Hardware und Infrastruktur der modernen Hochleistungsrechenzentren angepasst werden, um diese Rechenressourcen effizient zu nutzen.
Ein Problem, das in vielen Bereichen der Naturwissenschaften auftritt, ist die Vorgehensweise bei der Entwicklung neuer Simulationssoftware, da in der Regel problemorientiert vorgegangen wird, ohne allzu viel Zeit in das Design und die Strukturierung bei der eigentlichen Code-Entwicklung zu investieren. Bei der Entwicklung der DG-basierten Simulationssoftware „SeisSol“, der zum Teil bis zu fünf Entwickler gleichzeitig angehörten, wurden durch die Einführung eines Systems zur Code-Verwaltung und Versionskontrolle enorme Vorteile erzielt. Unabhängig voneinander weiterentwickelte Software-Teile konnten so immer zu einer neues Version des Simulationscodes ohne Mehraufwand zusammengeführt werden. Des Weiteren wurde durch die Erstellung einer neuen Version automatisch die Berechnung einer Reihe von Testszenarien ausgelöst, um die Korrektheit der erweiterten Software zu kontrollieren und so evtl. auftretende Fehler sofort zu identifizieren und zu beheben.
Im weiteren Verlauf des Projekts sind auf Experten aus dem Bereich des Software-design einbezogen worden, um die Strukturierung und Modularisierung der Software zu verbessern und die zukünftige Entwicklung bzw. Instandhaltung des codes zu erleichtern. Methodiken aus dem Software-design, wie *requirement analysis* und *re-factoring*, wurden damit auch im Computational Seismology eingeführt und umgesetzt, um eine verbesserte Struktur ohne den Verlust der operativen Funktionalitäten zu erreichen.
Da jedoch in vielen Fällen die Anwendung der Simulationssoftware auf dringende Fragen der Seismologie im Vordergrund steht, kommt der Effizienz eine außerordentlich hohe Bedeutung zu. Die Algorithmen müssen daher nicht nur verfahrenstechnisch sondern auch implementationstechnisch hochoptimiert sein, was in der Regel nur durch die Unterstützung aus der numerischen Mathematik und der Informatik zu bewerkstelligen ist. Da die Verwendung der Software im Poduktionsmodus nur auf Hochleistungsrechnern an großen Rechenzentren stattfindet, muss auch auf die Spezifika der verschiedenen Rechnerarchitekturen bei der Entwicklung – vor allem bei der Kompilierung – eingegangen werden. Außerdem stellen die neuesten Höchstleistungsrechner mit mehreren hunderttausend Rechenkernen eine enorme Herausforderung an eine effiziente Parallelisierungsstrategie dar. Die Rechenlast muss dabei möglichst gleichmäßig auf die einzelnen Rechenkerne verteilt werden (load-balancing), und der Austausch von

Information zwischen den Recheneinheiten muss minimiert werden, um die Rechenkapazität eines solchen Systems im Sinne von *Rechenoperationen / Zeit* auszunutzen. Des Weiteren müssen alle Teile des Simulationscodes skalierbar sein, d.h. auf einer zunehmenden Anzahl von Rechenkernen sollte die benötigte Rechenzeit möglichst proportional abnehmen. Durch mehrere Initiativen (z.B. mit dem LRZ oder DEISA) zwischen den Bereichen Computational Seismology und High Performance Computing (HPC) konnten enge Verbindungen und Kooperationen aufgebaut werden, die sich nicht nur positiv auf die Code-Entwicklung und Optimierung von „SeisSol“ auswirken sondern sich auch bei der Finanzierung von weiteren Forschungsvorhaben durch Fördermittel verschiedener Organisationen für den Bereich *Supercomputing Applications* als entscheidend erwiesen haben. Selbst direkte und andauernde Kooperationen mit Herstellern massiv-paralleler Rechnerarchitekturen (z.B. IBM) konnten dadurch realisiert werden. Hervorzuheben ist dabei, dass immer spezielle Anwendungen in diesen Projekten im Vordergrund stehen, um nicht nur theoretische Aspekte der Parallelisierung oder algorithmische Verfahren zu verbessern, sondern auch einen klaren Nutzen für die Anwender – in diesem Fall die Seismologie – zu erzielen.

Anwendungen in der Seismologie

Aufgrund der vielseitigen Anwendungsmöglichkeiten des DG-Verfahrens zur Simulation seismischer Wellen sind im Folgenden exemplarisch einige Beispiele aus der Explorations- und Erdbebenseismologie herausgegriffen und zusammenfassend erläutert. Detaillierte Informationen finden sich in den publizierten Arbeiten im Anschluss an diese Zusammenfassung.

Ground motions considering non-planar rupture models and topography

Die Untersuchung deterministisch modellierter starker Bodenbewegungen bis zu 1Hz basierend auf dem Bruchmodel des M6 Parkfield-Bebens 2004 zeigt, dass theoretisch die vertikale und strike-parallele Bewegungskomponente bei perfekt-planarer Bruchfläche jeweils Null sein sollte. Da dies jedoch in der Realität nicht beobachtet wurde, sind die Auswirkungen dreier Effekte – nämlich eine nicht-planare Bruchfläche, eine 3D Geschwindigkeitsverteilung und die Topographie – analysiert worden, um die in etwa gleichstarken Amplituden auf den einzelnen Komponenten zu erklären. Dabei ergab sich, dass die Berücksichtigung komplexer Bruchflächengeometrie oder Topographie nicht ausreichen, sondern die Einbeziehung eines möglichst genauen 3D Geschwindigkeitsfeldes in der Region um Parkfield von entscheidender Bedeutung ist, um realistischere Bodenbewegungen zu erhalten. Für eine umfassende Studie sollten aber noch die Eigenschaften der

Störungszone, site-effects, Anisotropie sowie nicht-lineares Bodenverhalten berücksichtigt werden.

Simulation Dynamischer Bruchausbreitung

Die Beantwortung fundamentaler Fragen der Erdbebendynamik verlangt einen genauen und effizienten Simulationscode, der nicht nur die Wellenausbreitung, sondern auch den Ablauf des Bruchvorgangs modellieren kann. Aufbauend auf einer Formulierung des DG-Verfahrens in 2D konnte auch eine Erweiterung auf 3D erreicht werden. Die Vorteile der diskontinuierlichen Approximation an Elementgrenzen und der damit verbundenen Lösung des Riemann-Problems (siehe oben) unter Einbeziehung der nicht-linearen Reibungsgesetze ergeben sich dabei vor allem in der Glattheit der simulierten, zeitabhängigen Lösungen. Die bei anderen numerischen Verfahren auftretenden starken Oszillationen in den Scherspannungen und den Verschiebungsraten werden im DG-Verfahren vermieden und erfordern deshalb keine künstliche Dämpfung. Durch die Verwendung unstrukturierter Dreiecksgitter kann der Rechenaufwand mithilfe von Gitteradaptivität auf die Region nahe und an der Bruchfläche konzentriert und das Simulationsgitter an komplexe Bruchgeometrien (z.B. Krümmungen, Verzweigungen, Neigung zur Oberfläche, …) angepasst werden.

Bohrloch- und Explorationsseismologie

Seismische und akustische Messungen spielen in der Erdöl- und Erdgasexploration eine wichtige Rolle, um ein besseres Verständnis der geophysikalischen Bedingungen, der Struktur und den Veränderungen im Porenraum der Lagerstätten zu erhalten. Die Anwendung des DG-Verfahrens auf HPC-Architekturen erlaubt es, auch in komplexen Lagerstättenmodellen hochgenaue synthetische Seismogramme zu berechnen, die mit Observationsdaten aus dem Feld oder aus einem Bohrloch verglichen werden können. Welleneffekte von Salzdomen, oder zerscherten Sedimentschichten, Ausbrüchen an der Bohrlochwand oder der Einfluss des Bohrloch-casings können damit untersucht werden. Unter anderem wurden auch die Unterschiede der akustischen Wellenausbreitung im Bohrloch bei der Verwendung verschiedener Anregungsmethoden analysiert. Die Fragestellung war, welche akustische Quelle bzw. welche Anordnung der Geophone zur Bestimmung der S-Wellengeschwindigkeit im umgebenden Gestein am besten geeignet ist. Die Konfiguration der akustischen Quellen wurde dabei zwischen Monopol, Dipol und Quadrupol variiert. Auch die nötige Auflösung der Bohrlochgeometrie durch Tetraeder-Elemente war von Interesse, um bei möglichst geringem Rechenaufwand, d.h. bei möglichst groben Elementen, die Ergebnisse nicht in einer inakzeptablen Weise zu beeinflussen.

Komponenten Seismischer Rotationsbewegungen

Die Rotationsbewegungen, die an Gesteinspartikeln durch die Propagation seismischer Wellen erzeugt werden, fanden in der Vergangenheit im Gegensatz zu den Translationskomponenten der Bewegungsgeschwindigkeit oder -beschleunigung entlang der drei Raumrichtungen wenig Beachtung. Mit der Installation von Ring-Lasern und anderen Instrumenten zur genauen Messung der Rotation kommt seit wenigen Jahren auch diesen Bewegungskomponenten eine immer wichtigere Bedeutung zu. Das DG-Verfahren wurde in diesem Zusammenhang zur Untersuchung von registrierten und simulierten Rotationen in der P-Wellencoda teleseismischer Wellen herangezogen. Dabei konnte gezeigt werden, dass Rotationsbewegungen durch die Streuung von P in SH Wellen in heterogenem Material – wie etwa der Erdkruste – erklärt werden können. Aus dem Verhältnis der Energien der vertikalen Rotations- und Translationskomponenten konnte sogar auf die Stärke der Geschwindigkeitsperturbation geschlossen werden. Außerdem konnte ausgeschlossen werden, dass bei teleseismischen Events die Anisotropie des Mediums signifikante Rotationsbewegungen verursachen. Bei großen, lokalen Erdbebenevents oder unter stark anisotropen Lagerstättenbedingungen können aber durchaus Rotationskomponenten gemessen werden, die als zusätzliche Nebenbedingungen zur Lösung von Inversionsproblemen verwendet werden könnten.

Inhalt der kumulativen Habilitationsschrift

[1] De la Puente, Josep, Jean-Paul Ampuero, and Martin Käser (2009), Dynamic Rupture Modeling on Unstructured Meshes Using a Discontinuous Galerkin Method, J. Geophys. Res., 114, B10302.

eigener Beitrag: ursprüngliche Idee, Konzeption der numerischen Experimente, Interpretation der Konvergenztests, Wahl des Anwendungsbeispiels, Verfassen und Revidieren des Artikels

[2] Gallovic, Frantisek, Martin Käser, Jan Burjanek, and Ch. Papaioannou (2010), Three-dimensional modeling of near-fault ground motions with nonplanar rupture models and topography: Case of the 2004 Parkfield earthquake, J. Geophys. Res., 115, B03308.

eigener Beitrag: Erstellung des Simulationsgitters und Geschwindigkeitsmodels, Erstellung der Bruchflächegeometrie und Implementierung der Bruchmodelle, Durchführung der numerischen Experimente, Erstellung der Graphiken, Verfassen und Revidieren des Artikels

[3] Pham, D. N., H. Igel, J. de la Puente, M. Käser, and M. A. Schoenberg (2010), Rotational motions in homogeneous anisotropic elastic media, Geophysics, 75(5), D47–D56.

eigener Beitrag: Bereitstellung der Simulationssoftware, Unterstützung bei der Gittergenerierung und der Erstellung der anisotropen Materialparameter, Unterstützung der theoretischen Herleitungen und der Durchführung der numerischen Experimente, Revidieren des Artikels

[4] Pelties, Christian, Martin Käser, Verena Hermann, and Cristobal E. Castro (2010), Regular versus irregular meshing for complicated models and their effect on synthetic seismograms, Geophysical Journal International, 183(2), 1031–1051.

eigener Beitrag: Konzeption der numerischen Experimente, Bereitstellung der Software und Hardware, Idee zur Aufbereitung der graphischen Darstellung der Ergebnisse, Auswahl der Anwendungsbeispiele, Verfassen und Revidieren des Artikels

[5] Käser, Martin, Christian Pelties, E. Cristobal Castro, Hugues Djikpesse, and Michael Prange (2010), Wave Field Modeling in Exploration Seismology Using the Discontinuous Galerkin Finite Element Method on HPC-infrastructure, The Leading Edge, 29, 76-85.

eigener Beitrag: Initiieren der Kooperation, Auswahl der Anwendungsbeispiele, Gittergenerierung, graphische Darstellung, Durchführung und Analyse der Tests zur Skalierbarkeit, Verfassen und Revidieren des Artikels

[6] Chaljub, Emmanuel, Peter Moczo, Seiji Tsuno, Pierre-Yves Bard, Jozef Kristek, Martin Käser, Marco Stupazzini, and Miriam Kristekova (2010), Quantitative Comparison of Four Numerical Predictions of 3D Ground Motion in the Grenoble Valley, France, Bull. Seis. Soc. Am., 100(4), 1427–1455.

eigener Beitrag: Mitinitiieren der Kooperation, Gittergenerierung, Durchführung der Simulationen, graphische Darstellung, komplette Erstellung des DG-Kapitels, Verfassen und Revidieren des Artikels

[7] Castro, Cristóbal E., Martin Käser, and Gilbert B. Brietzke (2010), Seismic Waves in Heterogeneous Material: Sub-cell Resolution of the Discontinuous Galerkin Method, Geophys. J. Int., 182(1), 250-264.

eigener Beitrag: ursprüngliche Idee, Initiieren der Kooperation, Unterstützung der theoretischen Herleitungen, Konzeption der Konvergenzstudie, Erstellung der heterogenen Geschwindigkeitsmodelle, graphische Darstellung, Verfassen und Revidieren des Artikels

[8] Kremers, Simon, Andreas Fichtner, Gilbert B. Brietzke, Heiner Igel, Carene Larmat, Lianjie Huang, and Martin Käser (2011), Exploring the potentials and limitations of the time-reversal imaging of finite seismic sources, Solid Earth, 95-105.

eigener Beitrag: Erstellung des Setups und Implementation des Bruchmodels, Durchführung der numerischen Simulationen, Unterstützung bei der Interpretation der Ergebnisse, Revidieren des Artikels

[9] Hermann, Verena, Martin Käser, and E. Cristobal Castro (2011), Non-conforming hybrid meshes for efficient 2D wave propagation using the Discontinuous Galerkin method, Geophys. J. Int., 184(2), 746-758. (*best student paper award*)

eigener Beitrag: ursprüngliche Idee, Unterstützung der theoretischen Herleitung, Gittererzeugung, Unterstützung bei der Erstellung der Konvergenztests, graphische Darstellungen, Aufbau der numerischen Anwendungsbeispiele, Interpretation der Ergebnisse, Verfassen und Revidieren des Artikels

[10] Pelties, Christian, J. de la Puente, J.-P. Ampuero, and Martin Käser (2011), Three-dimensional dynamic rupture simulation with a high-order discontinuous Galerkin method on unstructured tetrahedral meshes, J. Geophys. Res., submitted

eigener Beitrag: ursprüngliche Idee, Initiieren der Kooperation, Unterstützung der theoretischen Herleitung, Unterstützung bei der Gittererzeugung, Ideen zur graphischen Darstellung, Auswahl des numerischen Anwendungsbeispiels, Interpretation der Konvergenzergebnisse, Verfassen und Revidieren des Artikels

JOURNAL OF GEOPHYSICAL RESEARCH, VOL. 114, B10302, doi:10.1029/2008JB006271, 2009

Dynamic rupture modeling on unstructured meshes using a discontinuous Galerkin method

J. de la Puente,[1,2] J.-P. Ampuero,[3] and M. Käser[1]

Received 23 December 2008; revised 23 June 2009; accepted 6 July 2009; published 1 October 2009.

[1] We introduce the application of an arbitrary high-order derivative (ADER) discontinuous Galerkin (DG) method to simulate earthquake rupture dynamics. The ADER-DG method uses triangles as computational cells which simplifies the process of discretization of very complex surfaces and volumes by using external automated tools. Discontinuous Galerkin methods are well suited for solving dynamic rupture problems in the velocity-stress formulation as the variables are naturally discontinuous at the interface between two elements. Therefore, the fault has to be honored by the computational mesh. The so-called Riemann problem can be solved to obtain well defined values of the variables at the discontinuity itself. Fault geometries of high complexity can be modeled thanks to the flexibility of unstructured meshes, which solves a major bottleneck of other high-order numerical methods. Additionally, element refinement and coarsening are easily controlled in the meshing process to better resolve the near-fault area of the model. The fundamental properties of the method are shown, as well as a series of validating exercises with reference solutions and a comparison with the well-established finite difference, boundary integral, and spectral element methods, in order to test the accuracy of our formulation. An example of dynamic rupture on a nonplanar fault based upon the Landers 1992 earthquake fault system is presented to illustrate the main potentials of the new method.

Citation: de la Puente, J., J.-P. Ampuero, and M. Käser (2009), Dynamic rupture modeling on unstructured meshes using a discontinuous Galerkin method, *J. Geophys. Res.*, *114*, B10302, doi:10.1029/2008JB006271.

1. Introduction

[2] Computational earthquake dynamics is emerging as a key component in physics-based approaches to strong motion prediction for seismic hazard assessment, and in physically constrained inversion approaches to earthquake source imaging from seismological and geodetic observations. Typical applications in both areas require the ability to deal with rupture surfaces of complicated, realistic geometries with high computational efficiency. A variety of numerical methods have been used in the past decades to simulate the dynamics of earthquake rupture, as finite differences (FD) [e.g., *Andrews*, 1973; *Day*, 1982; *Madariaga et al.*, 1998; *Andrews*, 1999; *Dalguer and Day*, 2007; *Moczo et al.*, 2007; *Ely et al.*, 2009], finite elements (FE) [e.g., *Oglesby et al.*, 1998, 2000; *Aagaard et al.*, 2001], boundary integral (BI) [e.g., *Das*, 1980; *Andrews*, 1985; *Cochard and Madariaga*, 1994; *Geubelle and Rice*, 1995; *Lapusta et al.*, 2000], spectral element (SE) [*Ampuero*, 2002; *Vilotte et al.*, 2006; *Kaneko et al.*, 2008], or finite volume (FV) [*Benjemaa et al.*, 2007] methods.

[3] These techniques offer different advantages and drawbacks. The BI method offers very high accuracy and efficiency, but is not well suited for handling heterogeneous media and nonlinear materials. The FD method is very accurate but is difficult to apply to nonplanar faults, with some remarkable exceptions [e.g., *Cruz-Atienza and Virieux*, 2004]. The FE and FV methods are very flexible geometrically but are often implemented as first- to second-order operators that are very dispersive for wave propagation problems. The hexahedra-based SE method is both accurate and flexible, but designing good quality hexahedral meshes for complicated geometries in three dimensions, such as faults with branching, and adapting smoothly the element sizes to different material properties are still very challenging tasks [*Igel et al.*, 2008] and a major bottleneck.

[4] Here, we present an alternative for the computation of the dynamics of two-dimensional in-plane rupture phenomena, based upon a discontinuous Galerkin (DG) method combined with an arbitrary high-order derivatives (ADER) time integration. The DG methods can be thought of as a high-order version of FV methods, where a polynomial basis is used inside each element to represent the unknowns. In our implementation, triangular elements are used which allows for a better fit of the geometrical constraints of the problem, i.e., the fault shape, and for an easy control of the

[1]Department of Earth and Environmental Sciences, Ludwig-Maximilians-University, Munich, Germany.
[2]Now at Institut de Ciències del Mar, CSIC, Barcelona, Spain.
[3]Seismological Laboratory, California Institute of Technology, Pasadena, USA.

0148-0227/09/2008JB006271$09.00

variation of element sizes using smooth refining and coarsening strategies.

[5] The ADER-DG method has been applied to continuous wave propagation problems [*Käser and Dumbser*, 2006; *Dumbser and Käser*, 2006], including viscoelastic [*Käser et al.*, 2007a], anisotropic [*de la Puente et al.*, 2007] and poroelastic [*de la Puente et al.*, 2008] rheologies. Also the kinematic description of nonplanar irregular faults has been successfully implemented [*Käser et al.*, 2007b].

[6] A particular feature of DG methods, inherited from FV methods, is the usage of numerical fluxes at element interfaces. Between any two elements the variables of the elastic equations are allowed to be discontinuous, even when no faults are present. This is enabled by the availability of the exact solution to the elastic wave equation at a discontinuity, obtained by the solution of the well-known Riemann problem [*Toro*, 1999; *LeVeque*, 2002]. In the case of faults, the solution of the Riemann problem has to be modified to incorporate frictional boundary conditions. Once the Riemann problem is solved, numerical fluxes are used to exchange information between elements.

2. Dynamics of Fault Rupture

[7] Faults are classically described as surfaces (or curves in two dimensions) of tangential displacement discontinuity (slip) on which traction and slip are related by friction [e.g., *Andrews*, 1976a, 1976b]. In our description of the rupture process, the material surrounding the fault is assumed elastic, so all nonlinearities of the problem are contained in the fault boundary conditions. We confine the presentation to the 2-D in-plane case. Following usual conventions, we call the sides of the fault the positive and negative sides, and define the fault normal vector pointing from the positive toward the negative side. The kinematics of the sliding process can be described by the slip rate $\Delta v = v_t^+ - v_t^-$, where where v_t is the velocity parallel to the fault, and the slip Δd, so that $\Delta v = \dot{\Delta d}$. We denote τ and σ the absolute shear and normal stresses on the fault, respectively.

[8] Slip starts when the shear stress on the fault overcomes a certain threshold, the fault strength. In the Coulomb friction model adopted here the strength is proportional to the normal stress. During active slip, the slip rate and the shear traction have opposite directions. These three phenomena are accounted for in the following expressions:

$$\begin{gathered} |\tau| \le \mu_f \sigma, \\ (|\tau| - \mu_f \sigma)\Delta v = 0, \\ \Delta v |\tau| + |\Delta v| \tau = 0, \end{gathered} \tag{1}$$

where μ_f is the friction coefficient, which generally depends on slip, slip rate and fault state variables. We adopt the linear slip weakening (LSW) friction law [*Ida*, 1972; *Palmer and Rice*, 1973]

$$\mu_f = \begin{cases} \mu_s - \dfrac{\mu_s - \mu_d}{D_c} \Delta d & \text{if } \Delta d < D_c, \\ \mu_d & \text{if } \Delta d \ge D_c. \end{cases} \tag{2}$$

In this expression μ_s, μ_d and D_c are all friction parameters, namely the static friction coefficient, dynamic friction coefficient and critical slip distance, respectively. This friction law, although simple, is sufficient to describe the initial rupture, arrest of sliding and reactivation of slip. Because of its simplicity, it is commonly used in numerical modeling of earthquake dynamics and in related validation problems. Notice that this friction law has discontinuous derivatives with respect to slip. As a consequence, numerical methods which achieve high-order accuracy using smooth polynomial expansions of the variables might fail to describe with sufficient accuracy those rupture phenomena described with the aforementioned LSW friction.

3. The Riemann Problem for Elastodynamics

[9] Considering two-dimensional elasticity for an isotropic medium in velocity-stress formulation and omitting external sources (e.g., moments or body forces) leads to the elastic wave equation, a linear hyperbolic system of the form

$$\begin{aligned} \frac{\partial}{\partial t}\sigma_{xx} - (\lambda + 2\mu)\frac{\partial}{\partial x}u - \lambda \frac{\partial}{\partial y} v &= 0, \\ \frac{\partial}{\partial t}\sigma_{yy} - \lambda \frac{\partial}{\partial x}u - (\lambda + 2\mu)\frac{\partial}{\partial y} v &= 0, \\ \frac{\partial}{\partial t}\sigma_{xy} - \mu\left(\frac{\partial}{\partial x} v + \frac{\partial}{\partial y} u\right) &= 0, \\ \rho \frac{\partial}{\partial t} u - \frac{\partial}{\partial x}\sigma_{xx} - \frac{\partial}{\partial y}\sigma_{xy} &= 0, \\ \rho \frac{\partial}{\partial t} v - \frac{\partial}{\partial x}\sigma_{xy} - \frac{\partial}{\partial y}\sigma_{yy} &= 0, \end{aligned} \tag{3}$$

where λ is the first Lamé constant, μ is the shear modulus, not to be confused with the friction coefficient μ_f mentioned earlier, and ρ is the mass density of the material. The components of the stress tensor are σ_{xx}, σ_{yy} and σ_{xy}. The components of the particle velocities in x and y direction are denoted by u and v, respectively.

[10] The elastic wave equation requires continuity of the involved variables, i.e., particle velocities and stresses. However, the partial differential equations of (3) can be solved also at variable discontinuities and material discontinuities. An evolution problem with initial values that are piecewise constant, discontinuous across an interface, is called a Riemann problem [*Toro*, 1999; *LeVeque*, 2002]. Riemann problems are local, involving only the points immediately contiguous to the discontinuity interface.

[11] Following *LeVeque* [2002], we group the stress and velocity variables into a vector $\boldsymbol{Q} = (\sigma_{xx}, \sigma_{yy}, \sigma_{xy}, u, v)^T$ and write the equations (3) in matrix form as

$$\frac{\partial Q_p}{\partial t} + A_{pq}\frac{\partial Q_q}{\partial x} + B_{pq}\frac{\partial Q_q}{\partial y} = 0. \tag{4}$$

The classical tensor notation is adopted, which implies summation over repeated indices. The matrices A_{pq} and B_{pq} are the space-dependent Jacobian matrices, which are given explicitly by *Käser and Dumbser* [2006].

[12] To illustrate the solution of the Riemann problem for the system (4), we consider an element interface S with a normal that is aligned with the x axis. The corresponding

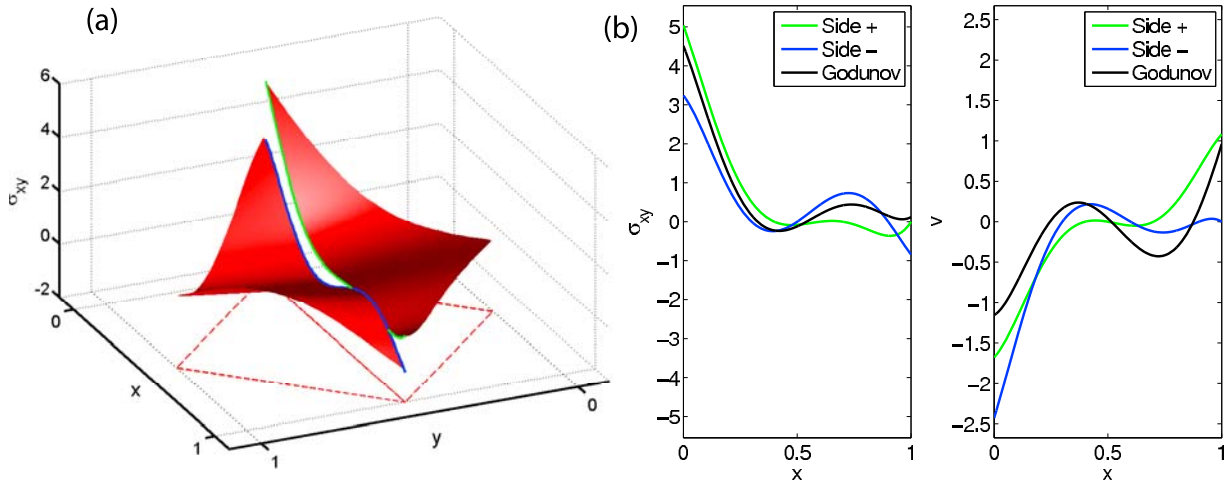

Figure 1. (a) Two triangle-based polynomial representations of the σ_{xy} variable which are discontinuous at their interface situated at $y = 0.5$. (b) The Godunov state of variables σ_{xy} and v at that same interface.

Riemann problem is purely one-dimensional and depends exclusively on the Jacobian matrix A. We suppose two discontinuous initial states at both sides of the interface, $\boldsymbol{Q}^+$ and $\boldsymbol{Q}^-$, and assume that the material properties are the same on both sides of the interface. The Jacobian matrix A is diagonalized as

$$A_{pq} = R_{pm}\Lambda_{ml}R^{-1}_{lq}, \tag{5}$$

where Λ is a diagonal matrix containing the eigenvalues $\{\lambda_i\}_{i=1,\ldots,5}$ of A and R a matrix containing the corresponding right eigenvectors of A. The boundary values on the positive side, $\boldsymbol{Q}(S^+)$, are obtained as a linear combination of the right eigenvectors associated to the positive eigenvalues, λ_1 and λ_2, corresponding to P and S waves traveling from the negative side to the positive side:

$$Q_p(S^+) = Q_p^+ + \sum_{i=1}^{2} \alpha_i R_{pi}. \tag{6}$$

The so-called wave strengths α_i are given by

$$\alpha_i = R^{-1}_{ij}\left(Q_j^- - Q_j^+\right). \tag{7}$$

Similarly, the boundary values on the negative side, $\boldsymbol{Q}(S^-)$, are obtained from the eigenvectors associated to the negative eigenvalues, λ_4 and λ_5:

$$Q_p(S^-) = Q_p^- - \sum_{i=4}^{5} \alpha_i R_{pi}. \tag{8}$$

In the absence of additional forces both expressions (6) and (8) give the same value, coined the Godunov state:

$$Q_p^G = Q_p(S^-) = Q_p(S^+). \tag{9}$$

The explicit values of all variables in the Godunov state are

$$\begin{aligned}
2\sigma_{xx}^G &= \left(\sigma_{xx}^- + \sigma_{xx}^+\right) + \frac{\lambda+2\mu}{c_p}(u^- - u^+),\\
2\sigma_{yy}^G &= \frac{\lambda}{c_p}(u^- - u^+) + \frac{\lambda}{\lambda+2\mu}\left(\sigma_{xx}^- + \sigma_{xx}^+\right) + 2\sigma_{yy}^+,\\
2\sigma_{xy}^G &= \left(\sigma_{xy}^- + \sigma_{xy}^+\right) + \frac{\mu}{c_s}(v^- - v^+),\\
2u^G &= (u^- + u^+) + \frac{c_p}{\lambda+2\mu}\left(\sigma_{xx}^- - \sigma_{xx}^+\right),\\
2v^G &= (v^- + v^+) + \frac{c_s}{\mu}\left(\sigma_{xy}^- - \sigma_{xy}^+\right),
\end{aligned} \tag{10}$$

where c_p and c_s are the P and S wave velocities, respectively. Equations (10) show that the Godunov state is the result of applying a bilinear operator to $\boldsymbol{Q}^+$ and $\boldsymbol{Q}^-$, so we define

$$\boldsymbol{Q}^G \equiv \|\boldsymbol{Q}^+, \boldsymbol{Q}^-\|\,. \tag{11}$$

The computation of the Godunov state makes it possible to use discontinuous approximations of the unknowns to solve accurately a physically continuous problem, such as the linear elastic wave equation. This is in fact the main ingredient of FV and DG methods. As an example, we can compute the Godunov state at a boundary for the one-dimensional boundary of length unity that connects two triangular cells. Figure 1 shows a polynomial representation of the shear stress σ_{xy} which is continuous inside each of the triangular domains but discontinuous at the interface. Assuming also a discontinuous state of the perpendicular velocity v, we can compute the Godunov state along the interface by applying the third and fifth equations in (10). The result is shown in Figure 1, where we have assumed $\rho = 1$, $\mu = 1$. The two interface values of the discontinuous variables produce one single Godunov state which is pointwise a linear combination of the values at both sides. As a consequence, the Godunov state is smooth if the values of the variables at both sides of the interface are smooth as well.

[13] In order to impose boundary conditions we must perturb the boundary variables out of their Godunov state. Obtaining the perturbed wave strengths in (6) and (8) that enforce a perturbed boundary variable is referred by *Käser and Dumbser* [2006] as solving the inverse Riemann problem. In our case, in order to impose a perturbed value of fault traction, $\tilde{\sigma}_{xy} = \sigma^G_{xy} + \delta\sigma_{xy}$, that satisfies a certain friction law, we need to apply

$$Q_3(S^-) = Q_3(S^+) = \tilde{\sigma}_{xy}. \tag{12}$$

We find that the perturbed values of the wave strengths that ensure (12) are

$$\begin{aligned} \alpha_2' &= \alpha_2 + \frac{\delta\sigma_{xy}}{\mu}, \\ \alpha_4' &= \alpha_4 - \frac{\delta\sigma_{xy}}{\mu}. \end{aligned} \tag{13}$$

Substituting these values into (6) and (8) leads to

$$\begin{aligned} \tilde{\boldsymbol{Q}}(S^+) &= \boldsymbol{Q}^G + \left(0, 0, \delta\sigma_{xy}, 0, \frac{c_s}{\mu}\,\delta\sigma_{xy}\right)^T, \\ \tilde{\boldsymbol{Q}}(S^-) &= \boldsymbol{Q}^G + \left(0, 0, \delta\sigma_{xy}, 0, -\frac{c_s}{\mu}\,\delta\sigma_{xy}\right)^T. \end{aligned} \tag{14}$$

Notice that (12) is fulfilled by (14) by design, but a side effect of the perturbation is that $\tilde{Q}_5(S^+) \neq \tilde{Q}_5(S^-)$, hence two different values for the boundary velocity are obtained:

$$\begin{aligned} \tilde{v}^+ &= v^G + \frac{c_s}{\mu}\left(\tilde{\sigma}_{xy} - \sigma^G_{xy}\right), \\ \tilde{v}^- &= v^G - \frac{c_s}{\mu}\left(\tilde{\sigma}_{xy} - \sigma^G_{xy}\right). \end{aligned} \tag{15}$$

Making use of the definitions of the Godunov variables σ^G_{xy} and v^G given in (10), we infer

$$\tilde{v}^+ = v^+ + \frac{c_s}{\mu}\left(\tilde{\sigma}_{xy} - \sigma^+_{xy}\right) \tag{16}$$

and

$$\tilde{v}^- = v^- - \frac{c_s}{\mu}\left(\tilde{\sigma}_{xy} - \sigma^-_{xy}\right). \tag{17}$$

These expressions are crucial for the understanding of fault dynamics using fluxes, as they state that a certain imposed traction value instantly and locally generates an imposed velocity parallel to the fault. Further, subtracting the equations in (15), we find the slip rate as

$$\Delta\tilde{v} = \frac{2c_s}{\mu}\left(\tilde{\sigma}_{xy} - \sigma^G_{xy}\right). \tag{18}$$

This shows that slip ($\Delta\tilde{v} \neq 0$) occurs only if $\tilde{\sigma}_{xy} \neq \sigma^G_{xy}$.

[14] Expression (18) is clearly different from the $\Delta v = v^+ - v^-$ commonly used in continuous methods such as FD or FE. Discontinuous methods as FV or DG display in general discontinuities between stresses and velocities at any interface, but this does not represent a discontinuity of the physical variables themselves, which are uniquely determined by the Godunov state. The classical slip rate definition $\Delta v = v^+ - v^-$ is recovered if $\sigma^+_{xy} = \sigma^-_{xy} = \tilde{\sigma}_{xy}$; that is, prescribing the traction states at both sides and at the interface to be identical. Only in this context do the classic and the discontinuous expressions for the slip rate fully agree.

[15] The rest of Godunov's variables, normal velocity and bulk stresses, can be all computed using (10) as they are independent of $\tilde{\sigma}_{xy}$, thus resulting in a physically continuous problem, although still with a discontinuous mathematical representation.

4. The Numerical Method

[16] In the ADER-DG approach a two-dimensional computational domain Ω is divided into conforming triangular elements $\mathcal{T}^{(m)}$ addressed by a unique index (m). The numerical solution of equation (4) is approximated inside each element $\mathcal{T}^{(m)}$ by a linear combination of space-dependent polynomial basis functions $\Phi_l(\boldsymbol{\xi})$ of degree N, where $\boldsymbol{\xi} = (\xi, \eta)$ are the coordinates in a canonical reference element $\mathcal{T}_E$ [*Käser and Dumbser*, 2006], and time-dependent degrees of freedom $\hat{Q}^{(m)}_{pl}(t)$

$$Q^{(m)}_p(\boldsymbol{\xi}, t) = \hat{Q}^{(m)}_{pl}(t)\Phi_l(\boldsymbol{\xi}). \tag{19}$$

The index p is associated with the unknowns in the vector $\boldsymbol{Q}$. The index l indicates the lth basis function and ranges from 0 to $L - 1$, where $L = (N + 1)(N + 2)/2$ is the number of required basis functions in two dimensions for a polynomial degree N, leading to a numerical approximation of order $\mathcal{O} = N + 1$.

[17] Let us assume that the state of the variables Q_p is known at a certain time level t. Then, multiplying (4) by a test function Φ_k and integrating over an element $\mathcal{T}^{(m)}$ and over a time interval of size Δt gives

$$\begin{aligned} &\int_t^{t+\Delta t}\int_{\mathcal{T}^{(m)}} \Phi_k \frac{\partial Q_p}{\partial t}\,dV dt \\ &\quad + \int_t^{t+\Delta t}\int_{\mathcal{T}^{(m)}} \Phi_k\left(A_{pq}\frac{\partial Q_q}{\partial x} + B_{pq}\frac{\partial Q_q}{\partial y}\right)dV dt = 0. \end{aligned} \tag{20}$$

Integration of equation (20) by parts yields

$$\begin{aligned} &\int_t^{t+\Delta t}\int_{\mathcal{T}^{(m)}} \Phi_k \frac{\partial Q_p}{\partial t}\,dV dt + \sum_{j=1}^{3}\mathcal{F}^j_{pk} \\ &\quad - \int_t^{t+\Delta t}\int_{\mathcal{T}^{(m)}} \left(\frac{\partial\Phi_k}{\partial x}A_{pq} + \frac{\partial\Phi_k}{\partial y}B_{pq}\right)Q_q\,dV dt = 0. \end{aligned} \tag{21}$$

Equation (21) can then be used to obtain the values of Q_p at the following time level $t + \Delta t$, as explained in the introductory papers by *Käser and Dumbser* [2006] and *Dumbser and Käser* [2006]. In these seminal studies the

integration of the first and third terms in (21) are fully detailed. The second term is the sum of numerical fluxes $\mathcal{F}^j_{pk}$ across the three edges, $j = 1, 2, 3$, of the triangular element, accounting for the possible discontinuity of $\boldsymbol{Q}$. Although its resolution for interfaces with no faults is described in the aforementioned papers, for the case of faults we require a different strategy, explained in section 4.1.

4.1. Fluxes at Faults

[18] We consider for simplicity a single edge of a triangular element with its normal aligned with the x axis and drop the j indices. The flux term in (21) can be expressed as

$$\mathcal{F}_{pk} = A_{pr} \int_t^{t+\Delta t} \int_S \Phi_k \tilde{Q}_r dS dt. \tag{22}$$

The integral covers the whole edge S and a time interval of size Δt. For standard interfaces without faults we have $\tilde{\boldsymbol{Q}} = \boldsymbol{Q}^G = \|\boldsymbol{Q}^+, \boldsymbol{Q}^-\|$, where $\boldsymbol{Q}^G$ is the Godunov state created from the variable states $\boldsymbol{Q}^+$ and $\boldsymbol{Q}^-$ at both sides of the fault. When faults are present, however, some of the values of $\tilde{\boldsymbol{Q}}$ must be imposed using, for example, the expressions derived in section 3 for LSW friction. In this particular case, for $Q_1 = \sigma_{xx}$, $Q_2 = \sigma_{yy}$ and $Q_4 = u$, expression (22) is exactly the same as that described in the flux formulation of *Käser and Dumbser* [2006]. In contrast, for $Q_3 = \sigma_{xy}$ and $Q_5 = v$ a different approach must be followed.

[19] A suitable temporal expansion of the variables at both sides is obtained via a Taylor expansion near the time instant t. At time $t + \tau$, with $\tau \leq \Delta t$, the expansion reads

$$Q_p(\boldsymbol{\xi}, t+\tau) = \sum_{k=0}^{N} \frac{\tau^k}{k!} \frac{\partial^k Q_q(\boldsymbol{\xi}, t)}{\partial t^k}. \tag{23}$$

The high-order time derivatives in (23) are substituted by spatial derivatives using the expression (4) in an iterative way

$$\frac{\partial^k Q_p(\boldsymbol{\xi}, t)}{\partial t^k} = (-1)^k \left(A_{pq} \frac{\partial}{\partial x} + B_{pq} \frac{\partial}{\partial y} \right)^k Q_q(\boldsymbol{\xi}, t). \tag{24}$$

This yields

$$Q_p(\boldsymbol{\xi}, t+\tau) = \sum_{k=0}^{N} \frac{\tau^k}{k!} (-1)^k \left(A_{pq} \frac{\partial}{\partial x} + B_{pq} \frac{\partial}{\partial y} \right)^k Q_q(\boldsymbol{\xi}, t). \tag{25}$$

The expansion (25) is performed separately for the unknown states $\boldsymbol{Q}^+(\boldsymbol{\xi}, t)$ and $\boldsymbol{Q}^-(\boldsymbol{\xi}, t)$ and then linearly combined according to (10) to obtain the temporal polynomial expansion of the Godunov state $\boldsymbol{Q}^G(\boldsymbol{\xi}, t) = \|\boldsymbol{Q}^+(\boldsymbol{\xi}, t), \boldsymbol{Q}^-(\boldsymbol{\xi}, t)\|$.

[20] In preparation for the numerical integration of the flux (22), we evaluate $\boldsymbol{Q}^G(\boldsymbol{\xi}, t)$ at a set of space-time Gaussian integration points along the triangle's edge at space locations $\boldsymbol{\xi}_i = (\xi_i, \eta_i)$, with $i = 1, \ldots, 2N + 1$, and along the time axis at time levels $\tau_l \in [t, t + \Delta t]$, with $l = 1, \ldots, N + 1$. We write

$$Q^G_{p,il} = Q^G_p(\boldsymbol{\xi}_i, \tau_l) = \hat{Q}^G_{ps}(\tau_l) \Phi_s(\boldsymbol{\xi}_i). \tag{26}$$

Notice that we are using more integration points than are sufficient for exact Gauss integration given the polynomial degree of the integrand in (22). Such large number of integration points can allow future, more general formulations where, for example, the material properties are variable inside one element.

[21] We solve for the fault physics locally, at each space-time integration point, in three steps. First, we evaluate the failure criterion (1) so that

$$\tilde{\sigma}_{xy,il} = \min\left\{ \sigma^G_{xy,il}, \mu_{f,il} \left(\sigma^G_{xx,il} + \sigma^0_{xx} \right) - \sigma^0_{xy} \right\}, \tag{27}$$

where $\mu_{f,il}$ is the local value of the dynamic friction coefficient and σ^0_{xx} and σ^0_{xy} are the initial normal and shear stress values, respectively. Once we have solved (27) for the point $(\boldsymbol{\xi}_i, \tau_l)$ we can compute the slip rate using (18) locally such that

$$\Delta\tilde{v}_{il} = \frac{2c_s}{\mu} \left(\tilde{\sigma}_{xy,il} - \sigma^G_{xy,il} \right). \tag{28}$$

The slip $\Delta\tilde{d}_{il}$ is obtained by integrating (28). Finally, we apply the LSW friction law (2) to obtain the time-updated value of $\mu_{f,il+1}$ as

$$\mu_{f,il+1} = \max\left\{ \mu_d, \mu_s - \frac{\mu_s - \mu_d}{D_c} \Delta\tilde{d}_{il} \right\}. \tag{29}$$

Equations (27), (28), and (29) are solved for each space-time integration point while ensuring causality by updating the time levels in a sequential way, i.e., from $l = 1$ to $l = N + 1$.

[22] The values of the velocities at each side of the fault can be retrieved from (16) and (17) as

$$\begin{aligned} \tilde{v}^+_{il} &= v^+_{il} + \frac{c_s}{\mu} \left(\tilde{\sigma}_{xy,il} - \sigma^+_{xy,il} \right), \\ \tilde{v}^-_{il} &= v^-_{il} - \frac{c_s}{\mu} \left(\tilde{\sigma}_{xy,il} - \sigma^-_{xy,il} \right). \end{aligned} \tag{30}$$

Using the shear stress from (27) and the velocities from (27), all values of $\tilde{\boldsymbol{Q}}$ at the interface are then known and the flux (22) can be integrated numerically as

$$\mathcal{F}_{pk} = A_{pr} \sum_{i=1}^{2N+1} \sum_{l=1}^{N+1} \omega^S_i \omega^T_l \Phi_k(\boldsymbol{\xi}_i) \tilde{Q}_{r,il}. \tag{31}$$

where ω^S_i and ω^T_l are the weights of the spatial and temporal Gaussian integration, respectively. The appropriate value of the fault-parallel velocity, $\tilde{v}^+$ or $\tilde{v}^-$ from equation (27), is employed depending on which side of the fault the element under consideration lies on.

[23] Although so far we have considered an edge that has its normal vector aligned with the x axis, we can generalize (31) to an arbitrary orientation of the normal vector $\boldsymbol{n}$ as

$$\mathcal{F}_{pk} = T_{pq} A_{qr} \sum_{i=1}^{2N+1} \sum_{l=1}^{N+1} \omega^S_i \omega^T_l \Phi_k(\boldsymbol{\xi}_i) \tilde{q}_{r,il}, \tag{32}$$

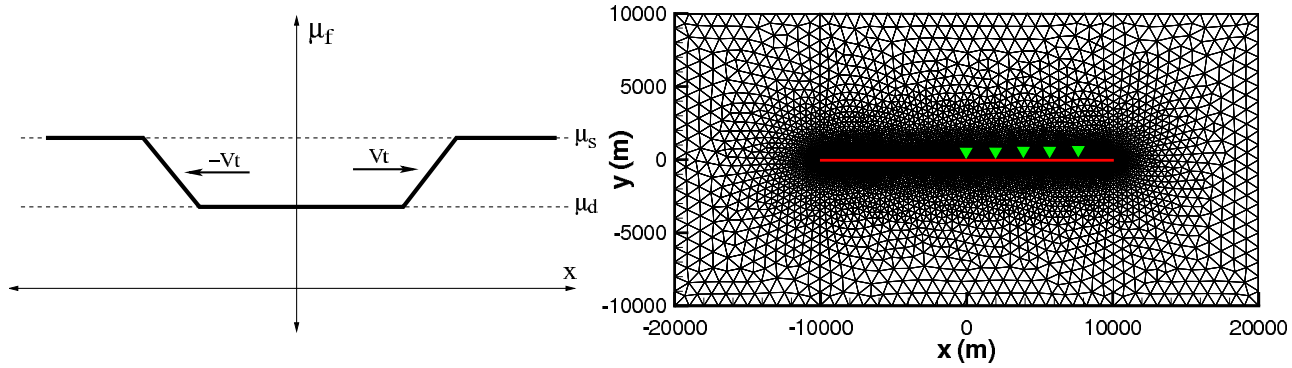

Figure 2. (left) Assumed friction along the fault in the self-similar crack case. The low-friction patch expands at constant velocity V. (right) Mesh used for this case. The red line depicts the fault and the triangles receiver locations.

where T is a rotation matrix, given explicitly by *Käser and Dumbser* [2006] and *Dumbser and Käser* [2006], and $\tilde{\boldsymbol{q}}$ are the variables transformed to the local edge coordinate system from the global xy-aligned one by

$$\tilde{q}_p = T^{-1}_{pq} \tilde{Q}_q. \tag{33}$$

The fault equations (27) to (27) are readily applied to $\tilde{\boldsymbol{q}}$.

4.2. Stability Criterion

[24] In order to guarantee the numerical stability of our explicit time advancement scheme, we constrain the size of the time step following the Courant-Friedrichs-Lewy (CFL) criterion of *Courant et al.* [1928], thus having

$$\Delta t \leq \frac{C}{2N+1} \min\left(\frac{2r_{\text{in}}}{c_p}\right), \tag{34}$$

where C is an empirically determined constant (in the following we will use $C = 0.5$) and r_{in} is the radius of the in circle of the triangle. The minimum is taken among all elements in the domain. Note that this is the same stability criterion as that used for the ADER-DG method in the absence of faults.

5. Self-Similar Crack Validation Problem

[25] We test the performance of the ADER-DG scheme for the case of a self-similar crack. In this case the traction at the fault is imposed beforehand as a function of space and time, similarly to the case proposed by *Kostrov* [1964]. This problem and variations of it have been used in previous works on dynamic rupture modeling [e.g., *Andrews*, 1985; *Cruz-Atienza and Virieux*, 2004; *Rojas et al.*, 2008; *Benjemaa et al.*, 2007]. We remark that the problem is not really reproducing the dynamic behavior of a fault because the traction is imposed externally. However, in our case it is advantageous because it allows us to validate the relation between traction and slip rate (18) without having to solve any friction laws or failure criteria, which would add further errors in the final solutions. Furthermore it is easy to model it with the spectral boundary integral equation (SBIE) method in its BIMAT implementation [*Cochard and Rice*, 2000; *Rubin and Ampuero*, 2007]. The acknowledged accuracy of this last method makes it usable as a reference solution for our purposes. In our case, the friction coefficient follows the expression

$$\mu_f(x,t) = \max\{\mu_d, \mu_s - (\mu_s - \mu_d)(Vt - |x|)/L\}, \tag{35}$$

where we choose to take the values $L = 250$ m, $V = 2000$ m/s, $\mu_s = 0.5$ and $\mu_d = 0.25$. The value of μ_f is depicted in Figure 2. The problem is further characterized by an initial normal stress of 40.0 MPa and shear stress of 20.0 MPa. We represent a straight fault 20 km long centered at the coordinates origin and surrounded by a homogeneous material with density $\rho = 2500$ kg/m^3, P wave velocity $c_p = 4000$ m/s and S wave velocity $c_s = c_p/\sqrt{3}$, so the same material properties as those used by *Benjemaa et al.* [2007]. The simulation is performed on a rectangular domain of 40 km per 20 km, meshed with elements of 100 m edge length at the fault itself, as shown in Figure 2. The mesh is then smoothly coarsened toward the boundaries of the domain, thus having elements of a maximum of 1000 m edge length. In total the mesh contains 11850 elements. As a comparison, a regular triangular mesh containing equilateral triangles with resolution of 100 m everywhere would contain 13 times more elements. Figure 3 shows the solution obtained with a sixth-order ADER-DG scheme (ADER-DG $\mathcal{O}6$) recorded at five different receivers, separated 2000 m from each other, and compared to the reference solution. No large differences between the numerical and the reference solutions can be observed in the slip, slip rate or traction. Furthermore, we have plotted the root-mean-square (RMS) of the time histories of slip rate for the same receivers for the whole 5 s of simulation obtained with schemes $\mathcal{O}3$ to $\mathcal{O}6$. For distances 2000 m to 8000 m the high-order schemes produce both smaller errors and a slower decrease of accuracy at longer distances. At 2000 m, the schemes $\mathcal{O}4$ to $\mathcal{O}6$ produce roughly identical results. At longer distances the usage of the highest orders produces more precise results. It is worth noticing that no significant effects from the artificial absorbing boundaries or spurious oscillations are observed. We remark that no artificial damping has been used in any of the simulations.

6. Spontaneous Rupture Validation Problem

[26] We test the performance of the ADER-DG method on a 2-D version of the benchmark problem for spontaneous

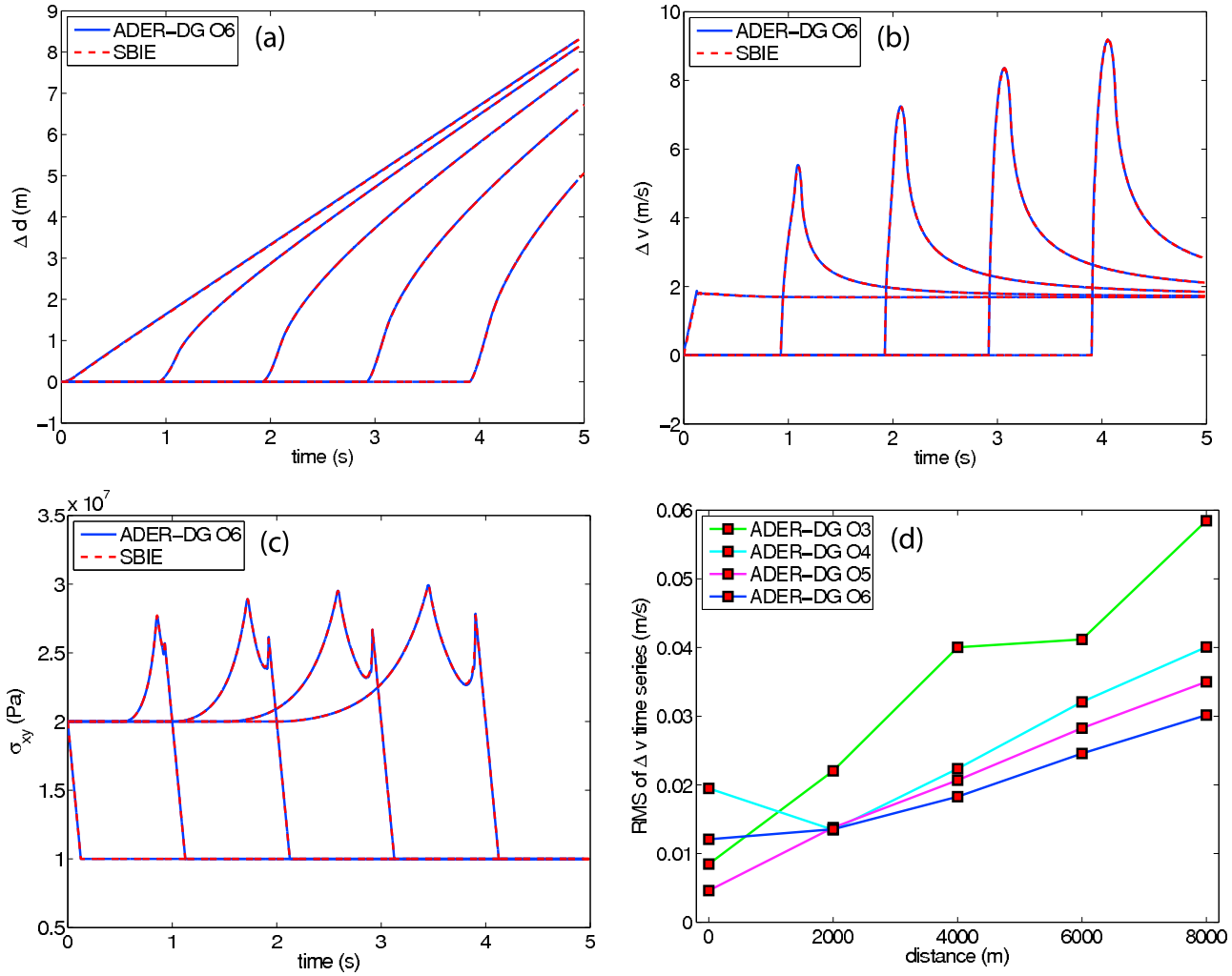

Figure 3. Results of the self-similar crack test obtained with the ADER-DG $\mathcal{O}6$ method (blue) and the SBIE method (red). (a) Slip, (b) slip rate, and (c) traction errors are measured on the fault at five points with hypocentral distance 0, 2, 4, 6 and 8 km. (d) RMS difference of the slip rate time histories as a function of hypocentral distance for orders $\mathcal{O}3$ to $\mathcal{O}6$.

rupture propagation of the Southern California Earthquake Center (SCEC). The original 3-D SCEC test (Version 3) is detailed by *Harris et al.* [2004]. The 2-D analog of this benchmark problem, considered here, was presented by *Rojas et al.* [2008] and used in further publications in order to asses the accuracy of numerical methods [e.g., *Kaneko et al.*, 2008]. The setup is a straight fault, represented by a 2-D line, embedded in a homogeneous elastic body. The fault is 30 km long, and the medium has a density of $\rho = 2670$ kg/m^3, P wave velocity c_p = 6000 m/s, and S wave velocity c_s = 3464 m/s. A nucleation zone of 3 km is defined at the center of the fault. The fault is governed by a LSW friction law with the parameters given in Table 1.

[27] The problem has been tested in eight different meshes, comprising computational domains of size 72 × 72 km, with edge lengths h ranging from 100 m to 1500 m. All meshes are completely unstructured, with regular mesh spacing forced along the fault plane. The mesh is gradually coarsened toward the external boundaries, up to an edge spacing 10 times larger than that at the fault. We have employed different orders, from $\mathcal{O}2$ to $\mathcal{O}6$. The equivalent mesh spacing, accounting for the polynomial subcell resolution, is $\Delta x = h/(N + 1)$.

6.1. Comparison to Other Methods

[28] We first study the similarities between existing numerical methods and the ADER-DG method developed here. We solved the 2-D analog of the SCEC test problem with the following methods: (1) the ADER-DG $\mathcal{O}6$ method using an edge length h = 150 m, which leads to an equivalent mesh spacing of Δx = 25 m, (2) the spectral boundary integral equation (SBIE) method of *Geubelle and*

Table 1. Parameters Describing the Fault for the SCEC Test Case

Parameter	Nucleation Zone	Outside Nucleation Zone
Initial shear traction (MPa)	81.6	70.0
Initial normal traction (MPa)	120.0	120.0
Static friction coefficient	0.677	0.677
Dynamic friction coefficient	0.525	0.525
Critical slip distance (m)	0.4	0.4

Rice [1995] in the multidimensional spectral boundary integral (MDSBI) implementation (E. Dunham, MDSBI: Multidimensional spectral boundary integral, version 3.9.10, 2008, available at http://pangea.stanford.edu/~edunham/codes/codes.html) and a node spacing of Δx = 12.5 m, (3) the traction-at-split-node (TSN) FD method described by *Andrews* [1973], (4) the staggered-grid split node (SGSN) FD method developed by *Dalguer and Day* [2007], in particular, the 2-D second-order implementation of *Brietzke et al.* [2009]. Both FD methods use similar representations of the fault zone and a node spacing of Δx = 12.5 m with no artificial damping, (5) the spectral element (SE) method (J.-P. Ampuero, SEM2DPACK: A spectral element method for 2-D wave propagation and earthquake source dynamics, version 2.3.3, 2008, available at http://sourceforge.net/projects/sem2d/), with a much finer resolution Δx = 6.25 m and with no artificial damping, and (6) the same SE method but with Kelvin-Voigt damping (SE-KV) as described by *Day and Ely* [2002], restricted here to a two-element wide layer around the fault, with artificial viscosity $\gamma = 0.1\Delta t$.

[29] Figure 4 shows slip rate and shear stress for all methods on the fault point located at x = 12.5 km. All computed solutions agree in their main features. A first issue apparent from the slip rate plots in Figures 4a and 4b is that both FD and SE undamped simulations produce high-frequency oscillations of amplitudes around 3% of the peak slip rate value. These oscillations are strongly reduced by adding artificial damping terms to the governing equations, as illustrated in Figure 4c by the SE-KV simulation, although the oscillations do not vanish completely with our choice of γ. Increasing further the artificial viscosity can eliminate the oscillations but has also negative side effects such as a decrease in the peak slip rate and a delay in the rupture times [see, e.g., *Dalguer and Day*, 2007]. The ADER-DG solutions are remarkably smooth, similar to SBIE solutions, despite containing no additional damping. In fact, the ADER-DG and the SBIE solutions in Figures 4b and 4e are virtually identical, except for a small oscillation of frequency around 30 Hz.

[30] To further explore the frequency dependence of all solutions, we plot in Figure 5 the slip rate spectra, evaluated over a Gaussian-tapered time window containing the rupture front but not the healing fronts, thus avoiding further high-frequency contributions not coming from the rupture front itself. Good agreement between all methods is obtained at low and intermediate frequencies, up to 20 or 30 Hz. Moreover, the spectral decay exponents are consistent with theoretical expectations. Recall that if slip rate behaves as t^{α}, where t is time after the rupture front, then its spectrum behaves as $f^{-1-\alpha}$. At low frequencies (below 10 Hz in this example) slip rate spectra decay as $f^{-1/2}$, consistent with the $1/\sqrt{t}$ behavior of singular crack models. At intermediate frequencies (above 10 Hz in this example) the $f^{-3/2}$ decay is consistent with the $\sqrt{t}$ onset predicted analytically for slip-weakening crack models under the assumption of a steady state process zone [*Ida*, 1973]. At very high frequencies the FD and SE methods develop numerical artifacts due to the dispersion relation of the discrete lattice. Artificial damping reduces significantly the amplitude of these artifacts. Comparing the undamped and damped SE simulations reveals that numerical artifacts (spectral peaks) are excited beyond 100 Hz in this example. In contrast, the ADER-DG results have a smooth spectral decay without sign of spuriously amplified modes.

6.2. Convergence of the ADER-DG Method

[31] Since analytical solutions do not exist for the spontaneous rupture problem, one cannot determine with absolute certainty which numerical solutions solve the proposed test better. We measure the error of the ADER-DG method by the RMS difference of rupture time, peak slip rate and final slip between our finest grid solution ($\mathcal{O}6$, 100 m edge length) and the solutions for coarser grids. This particular error norm choice will further allow us to compare the accuracy of our method with other numerical solutions. For a justification of the usage of fine-grid solutions for convergence analysis we refer the reader to the appendix of *Goto and Bielak* [2008]. The RMS are evaluated on fault points spaced every 62.5 m from the nucleation point, and are expressed as a percentage of the RMS value along the whole fault obtained with our finest solution. The RMS values for the rupture time, peak slip rate and final slip are 2.92 s, 6.78 m/s and 5.90 m, respectively. Receivers located at vertices of triangles are ignored, as they show unrepresentative errors due to the undefined Riemann problem solution at points that are common to more than two elements. The amount of points involved in the RMS computation range from 144 to 207. The difference in rupture time is measured as the first time sample at which the slip rate exceeds the value of 1 mm/s. The peak slip rate value has been obtained by finding the maximum of an interpolating cubic polynomial around the maximum of the slip rate time histories.

[32] The results of the simulations are compiled in Table 2 and plotted in Figure 6. We observe that lower-order schemes can only achieve equivalent errors as higher-order schemes when using a smaller equivalent mesh spacing. Similarly, a better accuracy is obtained for higher-order schemes for the same equivalent node spacing. From Figure 6a it is clear that, when reaching rupture time difference values close to Δt, the accuracy of all solutions collapse to values on the order of the transit time of the rupture front across a nodal spacing Δx, which is proportional to Δt, as has been previously observed for other numerical methods [*Day et al.*, 2005; *Dalguer and Day*, 2007]. Considering only simulations with RMS above this $\propto \Delta t$ asymptote, the rupture time differences as a function of average grid size Δx behave as a power law with convergence exponents (the slopes of the log-log convergence plots) ranging from 1.54 to 2.26, as shown in Table 3. On the other hand, taking only those points obtained with $\mathcal{O}6$ simulations which lie at Δt accuracy we obtain a slope of 1.15, similar to the theoretical power law exponent 1 followed by the time step, as in general the time step (34) is linearly proportional to the minimum mesh spacing. For all cases the scattering around the least squares values is noticeable, due to the use of completely unstructured meshes.

[33] An indicator of the resolution required to model the rupture process with sufficient accuracy is the number of points per median cohesive zone size, $\overline{N_c} = \overline{\Lambda}/\Delta x$. The value of the median cohesive zone size $\overline{\Lambda}$ = 258 m was obtained by *Rojas et al.* [2008] for the 2-D analog of the SCEC test. Figure 6a shows that ADER-DG $\mathcal{O}6$ yields RMS errors in

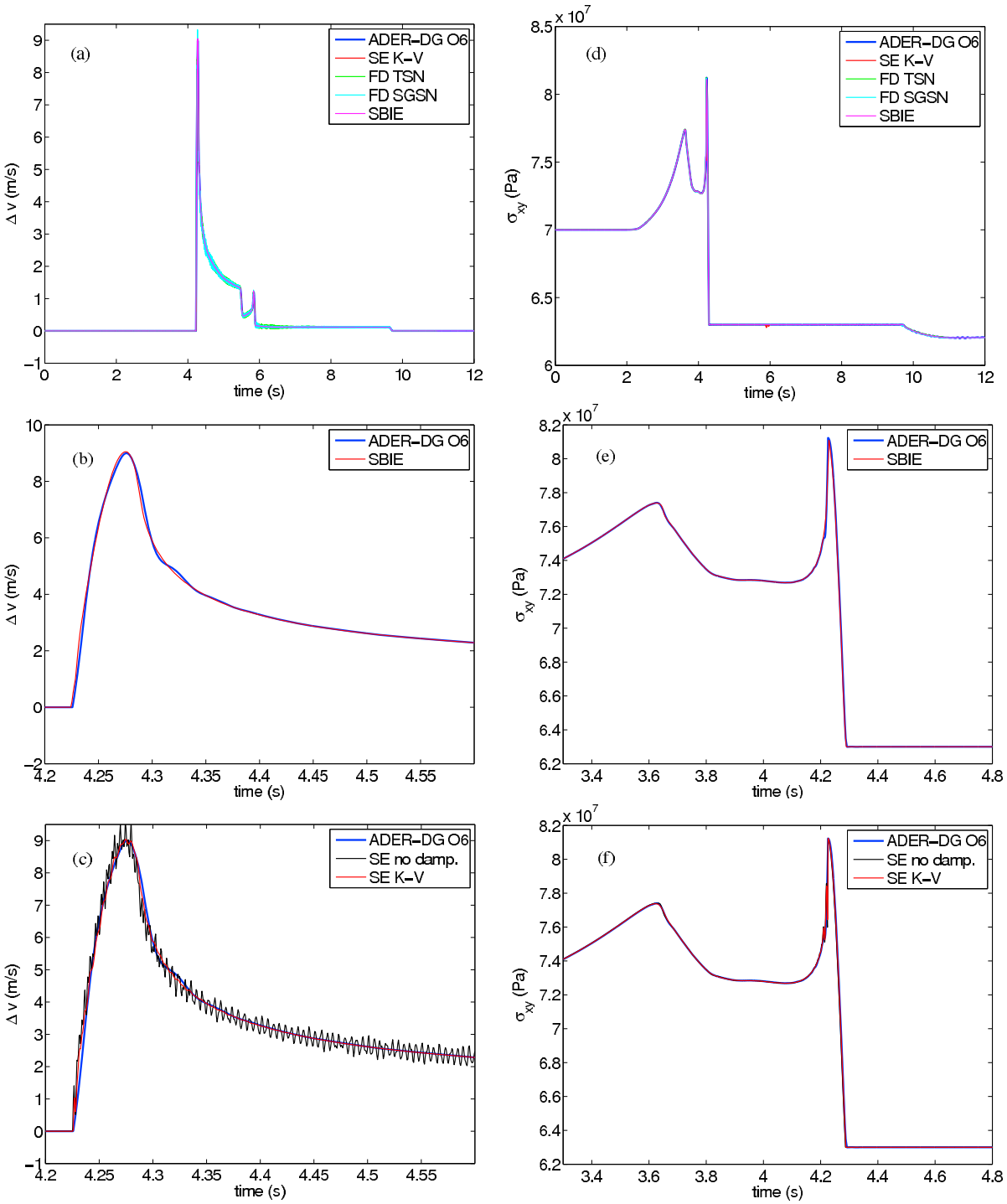

Figure 4. (a) Slip rate and (d) traction recorded at a receiver situated at $x = 12.5$ km. One SE, two FD, and a SBIE implementations are compared to the ADER-DG solution. Zoom of (b) the slip rate and (e) traction for SBIE close to the rupture front. (c) Slip rate and (f) traction compared to the SE method solution with and without Kelvin-Voigt damping.

rupture times below 0.3% with $\overline{N_c} \approx 1.5$, corresponding to a mesh spacing $h \approx 1000$ m. This performance is superior to that of the mimetic operator split node (MOSN) scheme and the DFM studied by *Rojas et al.* [2008], which achieved 0.3% RMS rupture time error at $\overline{N_c} \approx 3.2$ and $\overline{N_c} \approx 4.3$, respectively. We note though that these convergence studies must be compared with caution because their respective error norms are based on different reference solutions.

[34] The computational time was measured in all simulations, performed on a single Pentium 4 2.8 GHz processor. Figure 6b shows cost efficiency curves for the ADER-DG method of different orders, defined as the computational

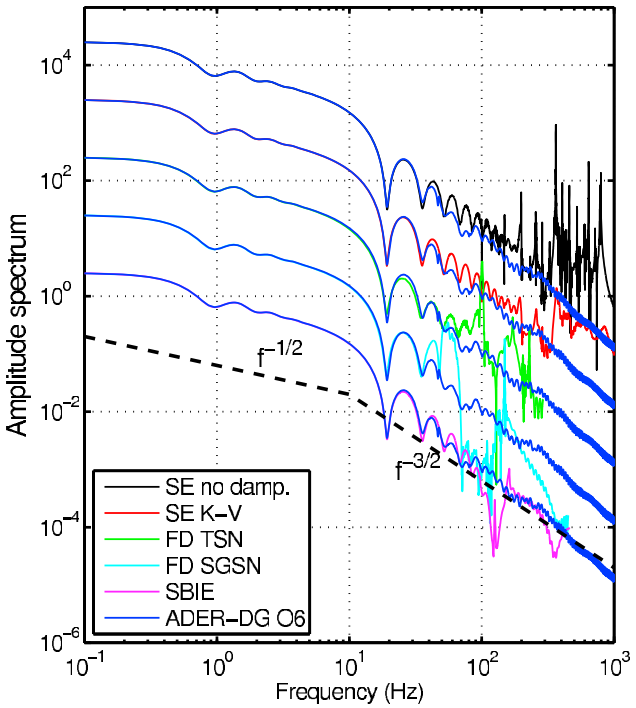

Figure 5. Spectra of the a window of slip rate at x = 12.5 km tapered near the rupture front for the SCEC test problem solved with several methods. Dashed lines indicate theoretical expectations, $f^{-1/2}$ at frequencies lower than 10 Hz and $f^{-3/2}$ at higher frequencies. The SBIE line has the correct offset, whereas all others have been shifted by a factor 10 in amplitude.

time required to achieve a given accuracy. The schemes of orders $\mathcal{O}4$ to $\mathcal{O}6$ have a similar efficiency which is superior to orders $\mathcal{O}2$ and $\mathcal{O}3$, for coarser meshes. After the Δt limit is reached, the trade-off rate drops to a smaller value.

[35] The final slip error, shown in Figure 6c, has a behavior similar to the rupture time error, although with smaller convergence exponents ranging from 0.87 to 1.27, as shown in Table 3. The RMS slip error is however not representative of the whole fault: the maximum slip misfits accumulate on elements containing the fault tips. The fraction of the total RMS accumulated on fault tip elements is higher than 60% in all but three simulations of order higher than $\mathcal{O}2$, averaging a value of 70.8% through all simulations performed. These errors most likely reflect problems capturing sudden, and probably unrealistic, rupture stopping conditions and can be reduced by smoother transitions to larger strength excess or larger fracture energy. These errors do not visibly propagate across the fault, as the stopping phases are accurately captured in our slip rate time histories elsewhere (see, e.g., Figure 4a). The errors in slip ignoring the fault tip elements are around two thirds of the values shown in Figure 6c.

[36] The peak slip rate differences are plotted in Figure 6d. For the coarser Δx values, the order of the ADER-DG scheme has little impact on the peak slip error. However, for resolutions finer than Δx = 100 m the different convergence exponents produce significant differences in the RMS obtained with different schemes for the same spatial sampling.

7. Mesh Coarsening and Absorbing Boundaries

[37] Throughout sections 4 and 5 we have used meshes with high ratios of coarsening toward the exterior domain boundaries. No strong reflecting phase appears to affect our results on the fault. However we wish to explore the effect of the coarsening on the propagating waves generated by the fault rupture.

[38] We record the fault-parallel velocity, u, at 35 receivers located at coordinates (0, i) km with i = 1, . . ., 35. We perform two new simulations with an $\mathcal{O}4$ scheme, using a mesh spacing at the fault of h = 375 m, which corresponds to Δx = 93.75 m. The first simulation is performed in the coarsened mesh used in section 6, with 5862 elements of size up to h = 3750 m. The second simulation uses a uniform mesh with constant element size h = 375 m, with 83,220 elements, roughly 14 times more elements than in the coarsened mesh.

Table 2. Results of the Simulations Realized for the SCEC Test

h (m)	$\mathcal{O}$	Δx (m)	RMS Rupture Time (%)	RMS Final Slip (%)	RMS Peak Slip Rate (%)	CPU (s)
1500	4	375	2.20×10^{0}	2.85×10^{0}	4.11×10^{1}	68
	5	300	1.16×10^{0}	1.88×10^{0}	3.52×10^{1}	122
	6	250	5.97×10^{-1}	1.30×10^{0}	3.00×10^{1}	216
750	2	375	4.81×10^{0}	7.95×10^{0}	5.06×10^{1}	74
	3	250	2.11×10^{0}	2.15×10^{0}	3.82×10^{1}	133
	4	187.5	6.09×10^{-1}	1.23×10^{0}	2.74×10^{1}	286
	5	150	2.30×10^{-1}	7.74×10^{-1}	2.10×10^{1}	589
	6	125	1.25×10^{-1}	5.25×10^{-1}	1.51×10^{1}	1,051
500	2	250	2.04×10^{0}	6.12×10^{0}	4.56×10^{1}	129
	3	166.6	6.14×10^{-1}	1.52×10^{0}	3.06×10^{1}	272
	4	125	1.86×10^{-1}	8.73×10^{-1}	1.98×10^{1}	535
	5	100	1.03×10^{-1}	5.48×10^{-1}	1.29×10^{1}	1,080
	6	83.3	8.46×10^{-2}	3.70×10^{-1}	7.55×10^{0}	2,082
375	2	187.5	1.39×10^{0}	4.42×10^{0}	4.12×10^{1}	388
	3	125	3.63×10^{-1}	1.15×10^{0}	2.35×10^{1}	805
	4	93.7	1.11×10^{-1}	6.40×10^{-1}	1.25×10^{1}	1,561
	5	75	8.10×10^{-2}	3.91×10^{-1}	6.99×10^{0}	3,056
	6	62.5	5.88×10^{-2}	2.52×10^{-1}	3.75×10^{0}	6,021
300	2	150	1.24×10^{0}	3.62×10^{0}	3.58×10^{1}	538
	3	100	2.49×10^{-1}	8.39×10^{-1}	1.90×10^{1}	1,298
	4	75	8.60×10^{-2}	4.78×10^{-1}	9.41×10^{0}	2,685
	5	60	6.11×10^{-2}	2.89×10^{-1}	4.45×10^{0}	5,669
	6	50	4.47×10^{-2}	1.72×10^{-1}	2.65×10^{0}	11,822
250	2	125	7.83×10^{-1}	2.59×10^{0}	3.38×10^{1}	821
	3	83.3	1.41×10^{-1}	7.87×10^{-1}	1.68×10^{1}	1,851
	4	62.5	6.27×10^{-2}	4.18×10^{-1}	6.80×10^{0}	4,116
	5	50	6.51×10^{-2}	2.33×10^{-1}	3.24×10^{0}	8,432
	6	41.7	3.87×10^{-2}	1.89×10^{-1}	2.33×10^{0}	17,296
187.5	2	93.5	6.57×10^{-1}	1.96×10^{0}	2.57×10^{1}	1,287
	3	62.3	1.40×10^{-1}	5.89×10^{-1}	9.20×10^{0}	3,072
	4	46.7	8.12×10^{-2}	2.82×10^{-1}	3.72×10^{0}	6,638
	5	37.4	5.48×10^{-2}	1.79×10^{-1}	3.62×10^{0}	14,078
	6	31.7	3.66×10^{-2}	1.41×10^{-1}	2.21×10^{0}	28,110
150	2	75	3.84×10^{-1}	1.97×10^{0}	2.30×10^{1}	1,948
	3	50	7.89×10^{-2}	5.05×10^{-1}	8.31×10^{0}	4,067
	4	37.5	3.96×10^{-2}	3.15×10^{-1}	2.68×10^{0}	8,249
	5	30	2.79×10^{-2}	9.23×10^{-2}	2.23×10^{0}	16,604
	6	25	1.70×10^{-2}	6.32×10^{-2}	1.33×10^{0}	33,110
100	2	50	1.75×10^{-1}	1.58×10^{0}	1.67×10^{1}	4,598
	3	33.3	3.79×10^{-2}	2.79×10^{-1}	3.98×10^{0}	9,596
	4	25	1.81×10^{-2}	1.27×10^{-1}	1.98×10^{0}	19,578
	5	20	7.07×10^{-3}	5.54×10^{-2}	5.50×10^{-1}	39,593
	6	16.7	0	0	0	80,000

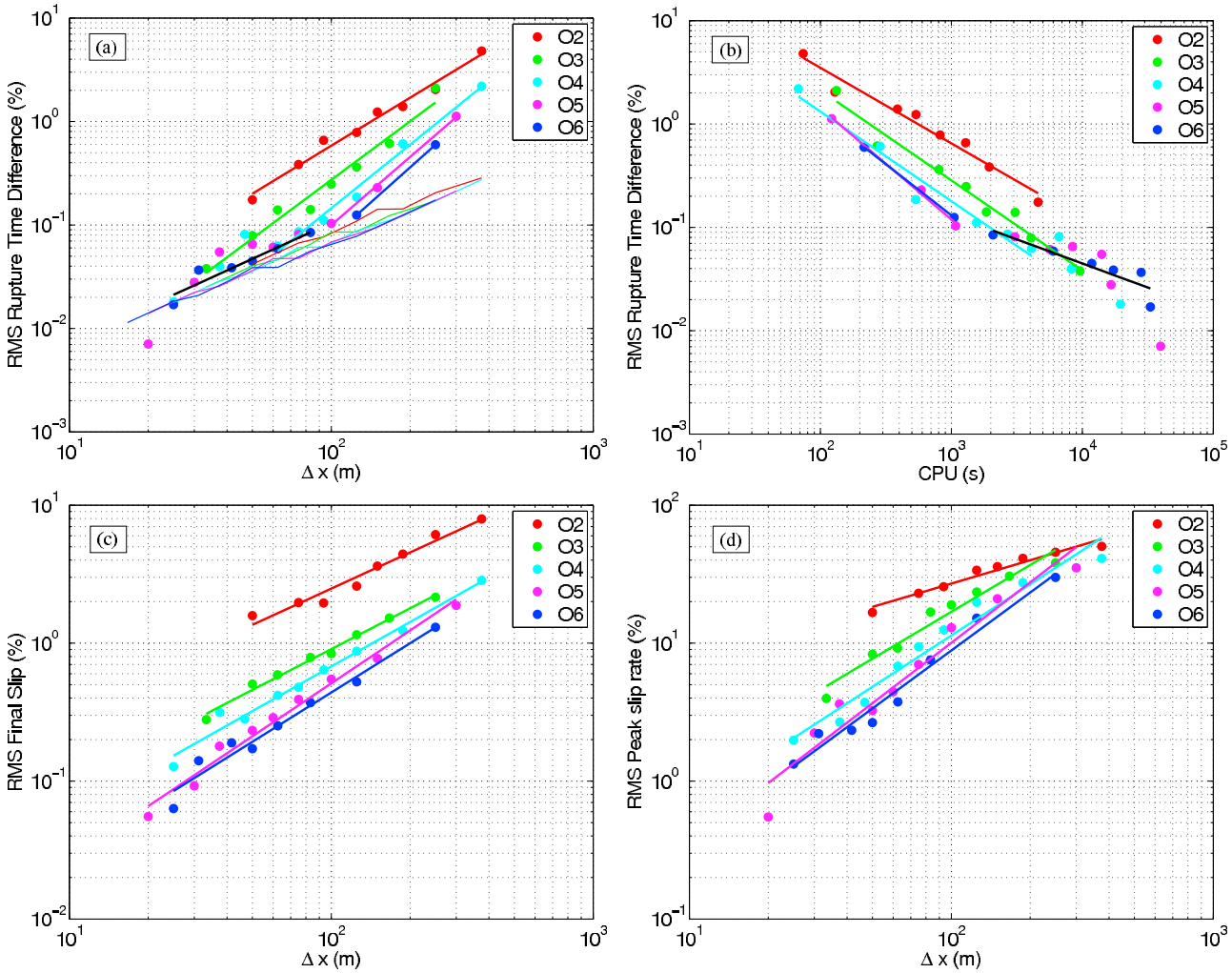

Figure 6. Convergence results for the 2-D analog SCEC test. Dots are simulation results. Colored thick lines of different steep slopes show least squares fits of these dots obtained by different orders of accuracy. To this end, we used only dots which have not reached the Δt uncertainty levels, whereas the thick black line has been obtained by fitting the remaining points. The thin lines of smaller slope represent the uncertainty levels determined by the Δt values. Misfits are shown for (a) rupture time, (c) final slip, and (d) peak slip rate. (c) The convergence of the rupture time misfit as a function of its computational cost.

[39] The results obtained with both meshes, plotted in Figure 7, show two clear behaviors. First, no main reflection phase is observed in any of the seismograms. This is to be expected because, on the receiver line, the main reflected energy has normal incidence to our absorbing boundaries (see *Käser and Dumbser* [2006] for details on the absorbing boundary condition) which have a much better performance for this case than for incidence at grazing angles. In addition, we observe that the seismograms lose high-frequency content as we move away from the fault toward larger elements.

[40] To quantify the latter effect, we study some receivers situated at elements of known size and analyze their velocity amplitude spectra (Figure 8). The low frequencies are identical for both meshes. The high frequencies begin to differ from a certain corner frequency which becomes lower as the size of the elements increases. This frequency is found to be approximately $f_m = 0.69 c_s/h$ Hz in the present case. Figure 8 shows seismograms obtained with the coarsened mesh, unfiltered, and seismograms obtained with the uniform mesh, low-pass filtered with corner frequencies $f_m^{h=500} = 5$ Hz, $f_m^{h=1000} = 2.5$ Hz and $f_m^{h=1300} = 1.9$ Hz. The minimum wavelength resolvable with our scheme is $\lambda_{\min} = 1.45h$, so that we can resolve wavelengths down to approximately 1.45 times the size of our elements.

Table 3. Error Convergence Exponents for Schemes of Different Order

Error Metric	$\mathcal{O}2$	$\mathcal{O}3$	$\mathcal{O}4$	$\mathcal{O}5$	$\mathcal{O}6$
Rupture time	1.54	1.88	2.04	2.19	2.26
Final slip	0.87	0.98	1.07	1.27	1.19
Peak slip rate	0.56	1.13	1.23	1.45	1.40

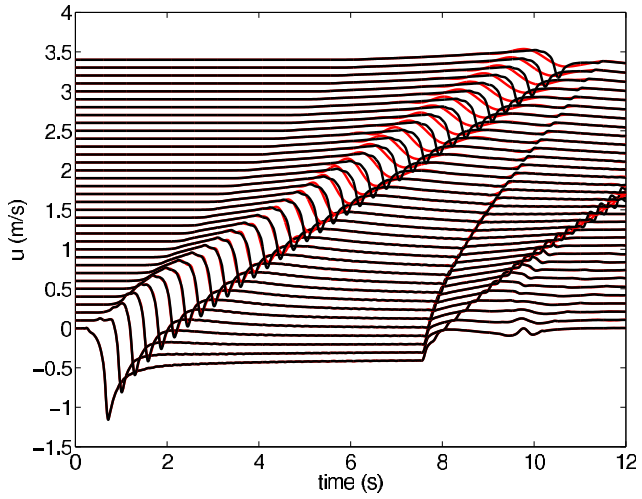

Figure 7. Fault-parallel velocity seismograms registered with 1 km spacing from the hypocenter, along the $x = 0$ axis, obtained with (black) a homogeneous mesh and (red) a graded mesh with a factor 10 coarsening toward the domain boundaries.

For a more thorough study on numerical accuracy of the ADER-DG scheme related to mesh size and propagated wavelengths, see *Käser et al.* [2008].

8. Dynamic Rupture on a Branched Fault System

[41] To show the potential of unstructured triangular meshes to represent complex fault systems, we simulate an earthquake occurring on the fault system that ruptured during the 28 June 1992 Landers earthquake (M_w = 7.3). This earthquake has been previously studied through 3-D dynamic rupture modeling using the boundary integral equation (BIE) method [*Aochi and Fukuyama*, 2002; *Aochi et al.*, 2002]. The fault system consists of six subfaults. The hypocenter is situated on its southernmost segment, the Johnson Valley fault, at a point which is the coordinate origin of our model.

[42] We assume a homogeneous initial stress field with principal stresses σ_1 = 300 MPa and σ_3 = 100 MPa and principal direction N22°E. This creates a heterogeneous stress state along the fault due to the orientation of the strike relative to the principal stresses. The fault has the homogeneous frictional parameters given in Table 4. The nucleation is forced by imposing a lower principal stress value of σ_3 = 70 MPa over a radius of 1.5 km around the hypocenter. The fault is allowed to rupture spontaneously for 10 s.

[43] We have used a circular domain of 120 km radius, using a mesh spacing of h = 600 m at the fault and coarsened up to h = 6 km for a total of 9605 elements. The mesh details can be seen in Figure 9. The simulation has been performed using an ADER-DG $\mathcal{O}5$ scheme, reaching the desired simulation time in 2.3 h in a single Pentium 4 2.8 GHz processor.

[44] Figure 10 shows snapshots of particle velocity generated by the earthquake. The rupture initially propagates bilaterally (Figure 10a). After approximately 2 s the northern rupture front faces the choice of following the Johnson Valley fault or breaking the eastern Kickapoo fault (Figure 10b). This second option seems to be favored as the energy concentrates on the eastern side of the Kickapoo fault. Later on the rupture propagates all along the Kickapoo fault and extends to the Homestead Valley fault. The rupture reaches a relatively sudden end at a kink situated approximately at (−2, 17) km and radiates a circular wavefront (Figure 10c). After 6 s most of the rupture has already stopped (Figure 10d).

[45] *Aochi et al.* [2002] showed that using a homogeneous initial stress the Kickapoo fault does not break, and rupture is confined to the Johnson Valley fault. In order to successfully reproduce the rupture pattern of the Landers earthquake, the authors used heterogeneous initial stress fields. In our 2-D simulation, in order to keep the setup as simple as possible, we kept the initial stress field homogeneous. However, this requires a large nucleation strength excess to break the Kickapoo and Homestead Valley faults, and produces unrealistically large slip at the Johnson Valley fault, of up to 12.3 m. Moreover, the northern branch of the Johnson Valley fault breaks with slip values of around 4 m, compared to the up to 6 m of slip recorded at the Kickapoo fault, and certain locations of the northernmost segments also break eventually with final slip values of up to 1 m in very small patches. These differences between our 2-D results and previous 3-D results are expected, and the only purpose of this exercise is to illustrate the potential of our new method.

9. Discussion

[46] The convergence test quantifies the accuracy of the ADER-DG method for the 2-D analog of the SCEC benchmark problem. To put these results in context, we compare them to the performance of the following four methods for the same problem: an FV method developed by *Benjemaa et al.* [2007], the SE method described by *Kaneko et al.* [2008], and two FD implementations (MOSN and DFM) presented by *Rojas et al.* [2008]. For the first two methods there is published information only on rupture time errors, whereas for the other two there is also information on peak slip rate and final slip errors. For each method, the reported errors are relative to the highest resolution simulation computed with that given method. Two attributes are summarized in Table 5: the convergence order before Δt saturation and the error obtained with average grid spacing Δx = 100 m.

[47] The second attribute has some bias due to the use of different reference solutions for each method. Whereas *Rojas et al.* [2008] noted that convergence rates and misfit at Δx = 100 m for the original 3-D version of the SCEC problem are systematically better than for the 2-D version, we expect the overall differences in accuracy between methods to be independent of the dimensionality of the problem.

[48] In terms of rupture time, ADER-DG $\mathcal{O}6$ compares favorably to all other 2-D methods studied. In terms of final slip DFM has better convergence rate than both ADER-DG and MOSN, but ADER-DG has lower error at Δx = 100 m. For peak slip rates the situation reverts: ADER-DG shows a

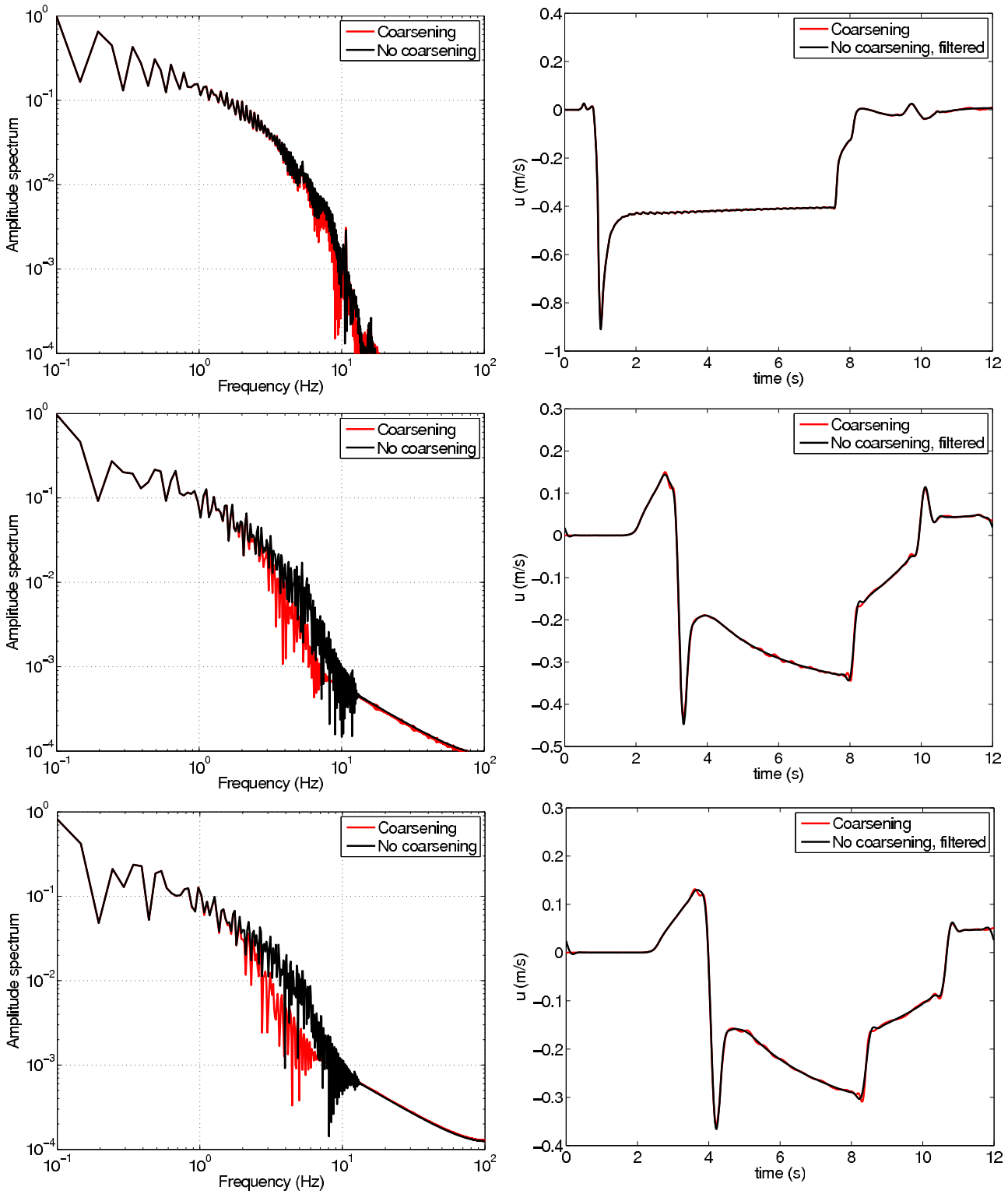

Figure 8. (left) Amplitude spectra for the uniform (black) and the coarsened mesh (red), for receivers situated at 2, 10, and 13 km, respectively. For the coarse mesh this corresponds to element sizes of 500, 750, and 1300 m, respectively. (right) Seismograms obtained with the coarsened mesh (red) and uniform mesh (black), low-passed filtered below 5, 2.5, and 1.9 Hz, respectively.

better convergence rate whereas both MOSN and DFM are more accurate at Δx = 100 m. Overall, ADER-DG yields results of similar or better accuracy than other existing methods for the 2-D analog of the SCEC test.

[49] The most remarkable outcome of the code comparison exercise in section 6.1 is the relative smoothness of the ADER-DG solution, which is free of spurious high-frequency oscillations. One possible reason for this feature

Table 4. Frictional Parameters for the Landers Fault System

Parameter	Nucleation Zone	Outside Nucleation Zone
Principal stress σ_1 (MPa)	300.0	300.0
Principal stress σ_3 (MPa)	70.0	100.0
Static friction coefficient	0.6	0.6
Dynamic friction coefficient	0.4	0.4
Critical slip distance (m)	0.8	0.8

is that ADER-DG captures the analytical form of the fault stress response at very high frequencies. In fact, (18) can be rewritten as

$$\tilde{\sigma}_{xy} = \frac{\mu}{2c_s}\Delta\tilde{v} + \sigma^G_{xy}. \tag{36}$$

This is analogous to the analytical formulation of the problem as a boundary integral equation problem, the basis of the BI method [e.g., *Cochard and Madariaga*, 1994], in which the fault tractions are expressed as the sum of a radiation damping term ($\mu\Delta v/2c_s$) and tractions induced by the previous slip history. The radiation damping term is the instantaneous (high frequency) response of the fault stress to slip rate fluctuations. In contrast, FD, FE and SE methods implemented with the natural TSN approach lead to a discrete equation of the form

$$\sigma_{xy} = M\Delta a + \sigma^t_{xy}. \tag{37}$$

where M is an effective mass, Δa is slip acceleration and σ^t_{xy} is a trial stress evaluated from previous values under the assumption of no further slip [see, e.g., *Andrews*, 1999, equation 3]. We refer here to a primordial relation between traction and slip that depends on the spatial discretization but not on the time discretization scheme. At high frequencies the fault stress fluctuations in both equations (36) and (37) are dominated by the first term of their right hand side, the second term fluctuates more slowly. In FD, FE and SE the second-order, inertial term of equation (37) naturally leads to oscillatory behavior, whereas in ADER-DG and BI the first-order nature of this term in equation (36) leads to the expected radiation-damped behavior.

[50] The practical implication of the absence of amplification of spurious modes is that ADER-DG simulations do not require artificial handling of high frequencies, such as artificial viscous damping or postprocessing filtering. Spurious oscillations pose no serious problem for linear systems, as they can be eliminated by low-pass filtering in a postprocessing stage without compromising the low frequencies. However, for strongly nonlinear problems the spurious oscillations can lead to instabilities or inaccurate results, and are typically damped by artificial viscous terms, like the Kelvin-Voigt mechanism described by *Day and Ely* [2002]. Artificial viscosity introduces additional dissipation that can affect the solution; for instance, it tends to reduce the rupture speed. Not requiring artificial viscosity in ADER-DG clearly poses a benefit in terms of not introducing accuracy losses due to additional dissipation. Moreover, a proper control on numerical dissipation is particularly important in ill-posed dynamic rupture problems that require regularization, for instance, in some bimaterial rupture problems [e.g., *Cochard and Rice*, 2000]. As the nonlinearities in dynamic rupture problems are strictly related to the choice of the friction law, one might expect instabilities to show up more strongly for certain laws. In LSW simulations the oscillations do not lead to propagating instabilities, but a stronger feedback would be expected with velocity-dependent friction laws. Fortunately, usual regularizations of velocity-weakening friction by a state variable reduce the order of the rupture front singularity and the amplitude of the associated spurious oscillations, which in practice yields accurate results without artificial damping [*Kaneko et al.*, 2008].

[51] Some aspects of the current formulation of the ADER-DG method for dynamic rupture can be further improved. The first and perhaps more obvious is the linearization approximation assumed when adopting expression (25). Basically, for the time sub levels between two time steps we use predictions of the elastic unknowns obtained with continuous elastic theory, i.e., without faults, based on the so-called Cauchy-Kovalewski procedure [*Käser and Dumbser*, 2006]. This is clearly inappropriate and a correct study should use a Taylor expansion of the variables which already includes the rupture criterion (27) to recover better convergence rates, for example following what is shown by *Castro and Toro* [2008] for other nonlinear systems. Nevertheless, using the linearized version of the problem is already producing results which we consider satisfactory.

[52] The ADER-DG scheme, for linear seismic wave propagation problems, is a relatively expensive method in terms of computing time required per element. The addition of fault dynamics in the simulations has little impact on its performance. For the 2-D analog of the SCEC test case, we observe an increase of the CPU time of about 4.5% in the worst case with respect to a simulation on the continuous elastic case with the same mesh and with an identical order and number of iterations. We regard this percentage as negligible.

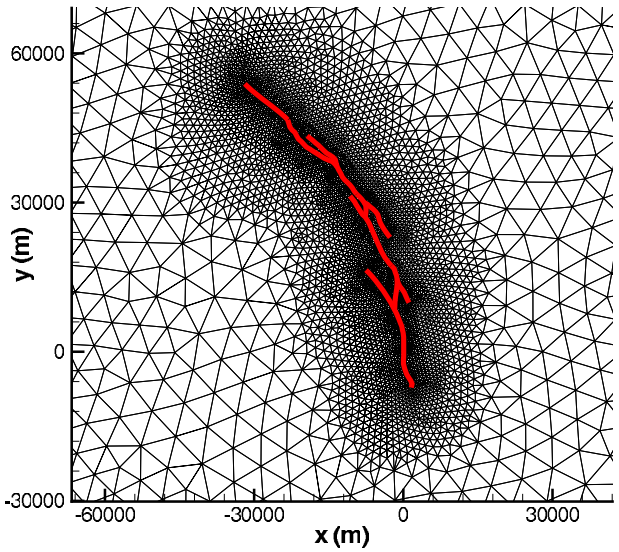

Figure 9. Mesh used for simulation of the dynamic rupture of the Landers fault system. The red line depicts the fault traces.

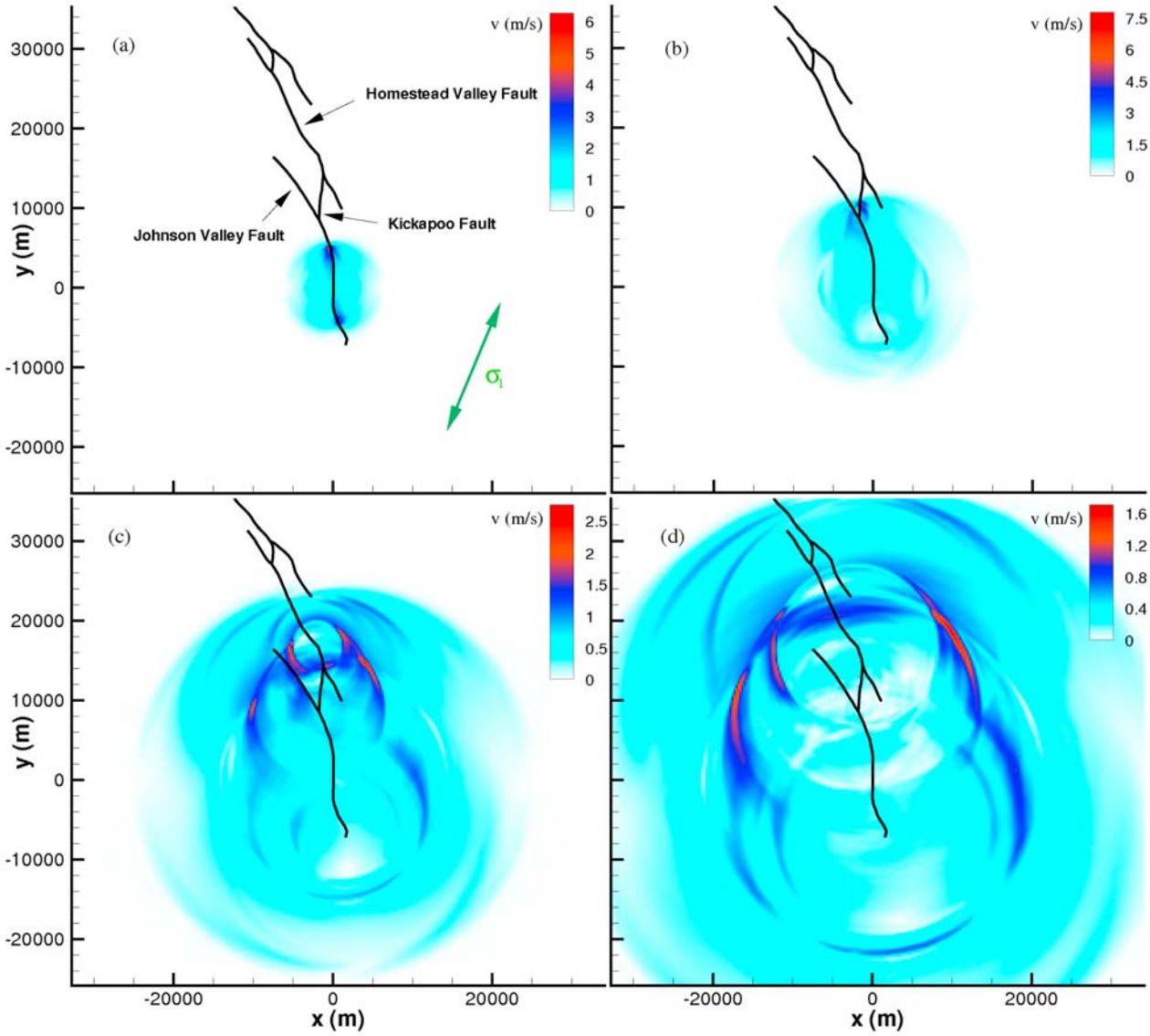

Figure 10. Snapshots of absolute particle velocity for the Landers fault system taken at (a) 1, (b) 2, (c) 4, and (d) 6 s. The direction of the principal stress σ_1, N22°E, is shown as a green arrow.

[53] The method is currently limited to linear element boundaries, so curved faults can be represented only by piecewise linear segments, and to constant material properties within each element. On the other hand, the ADER-DG method, unlike the SBIE approach, models the whole wavefield and each element can be considered viscoelastic, anisotropic and/or poroelastic (see *de la Puente* [2008] for a review of these cases). Using unstructured meshes can further help to reduce the amount of elements required to mesh very complex structures while its high accuracy could allow the use of coarser spatial samplings than that of other methods and therefore could help ADER-DG to become a competitive tool for dynamic rupture simulations in complicated setups.

[54] The potential of mesh coarsening is twofold. First of all, as has been shown in all cases studied in this paper, coarsening can work as a very effective way to mimic unbounded problems as the domains can be largely extended at the cost of adding a relatively small amount of elements. This is however largely irrelevant, as other approaches can be used for a similar effect (e.g., perfectly matched layers [*Collino and Tsogka*, 2001; *Komatitsch and Martin*, 2007]). The other potential use, far more unique and

Table 5. Summary of Error Metrics in the 2-D SCEC Benchmark Problem for Different Methods[a]

	Rupture Time		Peak Slip Rate		Final Slip	
Method	Order	RMS	Order	RMS	Order	RMS
ADER-DG $\mathcal{O}6$	2.26	0.1%	1.40	9.0%	1.19	0.4%
FV	1.78	5.0%	NA	NA	NA	NA
SE	1.88	1.0%	NA	NA	NA	NA
DFM	1.53	0.8%	0.68	6.5%	1.28	1.3%
MOSN	0.97	0.4%	0.85	7.0%	1.14	1.2%

[a]All RMS values correspond to resolutions of Δx = 100 m. The FV convergence value has been inferred from Figure 11 of *Benjemaa et al.* [2007] and is lower than their reported value (1.8 to 2.1). The SE values have been obtained in a subset of integration points and not along the whole fault line. NA, not applicable.

interesting, is the adaptation of the mesh size to the resolution required by the problem locally. Dynamic rupture simulations require a fine sampling of the fault in order to capture the cohesive zone. Applying this fine sampling to the whole wave propagation medium would imply to resolve frequencies much higher than what is typically regarded as useful in strong ground motion records. This warrants a different mesh resolution for the rupture process and for the propagation of the waves. Most mesh-based methods (FD, FE and SE) provide some kind of mesh coarsening strategy. However, a smooth or abrupt transition from a fine to a coarser mesh has to be implemented with care in order to avoid spurious numerical noise or reflections due to the transition [e.g., *Moczo et al.*, 2007]. In contrast, in the presented ADER-DG method using unstructured triangular meshes the mesh coarsening is a pure mesh generation issue and no particular implementation is necessary. The coarsening of the mesh then acts as a filter on the outward propagating wave which leaves the lower frequencies unaffected and does not produce noticeable spurious reflections. We believe this is a remarkable property which rounds up the great potential of the ADER-DG method as a tool to simulate earthquake scenarios with a correct representation of the fault and accurate propagation of the waves through very heterogeneous media.

[55] The obvious next step in the development of the method is to extend the implementation to three dimensions, where the simplicity of tetrahedral meshing will prove more useful for many scenarios and realistic applications. This is especially promising if combined with the so-called local time stepping (LTS) algorithm, that relaxes the CFL stability condition to make it local instead of global [*Dumbser et al.*, 2007]. The reduction of iterations required can considerably speed up the simulations, especially in meshes including elements of very dissimilar sizes. Further improvements will aim at introducing more complex friction laws as well as the heterogeneous Riemann problem, in order to simulate bimaterial ruptures.

10. Conclusion

[56] The ADER-DG method has been successfully adapted to the simulation of dynamic rupture under linear slip weakening friction. We have solved the Riemann problem for elastodynamics to find a linear relation between slip rate and traction at any fault point. This relation is not dependent on the actual choice of the friction law and might be the reason for the remarkably smooth solutions obtained, similar to those obtained with the SBIE method. Such smoothness makes it unnecessary to apply any sort of viscous damping mechanisms in the model. The results obtained for a simple test case show that a scheme of sixth order, i.e., using polynomials of degree five in space and time to represent the unknowns, reaches an error smaller than 0.3% with 1.5 equivalent nodes per cohesive zone size. All orders investigated produce converging solutions for all error measures used: RMS of rupture time, peak slip rate and final slip. The ADER-DG $\mathcal{O}6$ method displays power law exponent on the convergence experiment for the 2-D analog of the SCEC test of 2.26 for rupture time, 1.40 for peak slip rate and 1.19 for final slip. Additionally we have shown with an application example that the method is very well suited for the simulation of earthquake scenarios involving fault systems which include variations in strike and multiple branches. The method has also been proved to have a very good behavior for meshes with varying element size. The overall effect of a mesh coarsening is the reduction of the amplitude spectra at high frequencies while the low frequencies are preserved. No increase of amplitude in the form of spikes in the spectra is observed for any frequency when comparing results obtained with a coarsened mesh to those obtained on meshes with regular element size. For the 2-D analog of the SCEC test case and for $\mathcal{O}4$ we find the relation between minimum wavelength resolved and element spacing to be $\lambda_{\min} = 1.45\ h$. We conclude that the combination of meshing flexibility and high-order accuracy of the ADER-DG method makes it a very interesting tool to study earthquake dynamics on complex fault systems.

[57] **Acknowledgments.** The authors thank the Deutsche Forschungsgemeinschaft (DFG), as the work was supported through the Emmy Noether-program (KA 2281/2-1). We thank Gilbert Brietzke for providing us with the FD and SBIE solutions shown for the 2-D analog of the SCEC test case in section 6 and Cristóbal Castro for some fruitful discussions on the treatment of nonlinear Riemann problems. Steve M. Day and Peter Moczo are also acknowledged for their useful reviews which have helped to clarify and improve the original manuscript.

References

Aagaard, B. T., T. H. Heaton, and J. F. Hall (2001), Dynamic earthquake rupture in the presence of lithostatic normal stresses: Implications for friction models and heat production, *Bull. Seismol. Soc. Am.*, *91*, 1765–1796, doi:10.1785/0120000257.

Ampuero, J.-P. (2002), Etude physique et numérique de la nucléation des séismes, Ph.D. thesis, Univ. Denis Diderot Paris 7, Paris.

Andrews, D. J. (1973), A numerical study of tectonic stress release by underground explosions, *Bull. Seismol. Soc. Am.*, *63*, 1375–1391.

Andrews, D. J. (1976a), Rupture propagation with finite stress in antiplane strain, *J. Geophys. Res.*, *81*, 3575–3582, doi:10.1029/JB081i020p03575.

Andrews, D. J. (1976b), Rupture velocity of plane-strain shear cracks, *J. Geophys. Res.*, *81*, 5679–5687, doi:10.1029/JB081i032p05679.

Andrews, D. J. (1985), Dynamic plane-strain shear rupture with a slip-weakening friction law calculated by a boundary integral method, *Bull. Seismol. Soc. Am.*, *75*, 1–21.

Andrews, D. J. (1999), Test of two methods for faulting in finite-difference calculations, *Bull. Seismol. Soc. Am.*, *89*, 931–937.

Aochi, H., and E. Fukuyama (2002), Three-dimensional nonplanar simulation of the 1992 Landers earthquake, *J. Geophys. Res.*, *107*(B2), 2035, doi:10.1029/2000JB000061.

Aochi, H., R. Madariaga, and E. Fukuyama (2002), Effect of normal stress during rupture propagation along nonplanar fault, *J. Geophys. Res.*, *107*(B2), 2038, doi:10.1029/2001JB000500.

Benjemaa, M., N. Glinsky-Olivier, V. M. Cruz-Atienza, J. Virieux, and S. Piperno (2007), Dynamic non-planar crack rupture by a finite volume method, *Geophys. J. Int.*, *171*(1), 271–285, doi:10.1111/j.1365-246X.2006.03500.x.

Brietzke, G. B., A. Cochard, and H. Igel (2009), Importance of bimaterial interfaces for earthquake dynamics and strong ground motion, *Geophys. J. Int.*, *178*(2), 921–938, doi:10.1111/j.1365-246X.2009.04209.x.

Castro, C. E., and E. F. Toro (2008), Solvers for the high-order Riemann problem for hyperbolic balance laws, *J. Comput. Phys.*, *227*(4), 2481–2513, doi:10.1016/j.jcp.2007.11.013.

Cochard, A., and R. Madariaga (1994), Dynamic faulting under rate-dependent friction, *Pure Appl. Geophys.*, *142*, 419–445, doi:10.1007/BF00876049.

Cochard, A., and J. R. Rice (2000), Fault rupture between dissimilar materials: Ill-posedness, regularization, and slip-pulse response, *J. Geophys. Res.*, *105*, 25,891–25,907, doi:10.1029/2000JB900230.

Collino, F., and C. Tsogka (2001), Application of the PML absorbing layer model to the linear elastodynamic problem in anisotropic heterogeneous media, *Geophysics*, *66*, 294–307, doi:10.1190/1.1444908.

Courant, R., K. Friedrichs, and H. Lewy (1928), Über die partiellen Differenzialgleichungen der mathematischen Physik, *Math. Ann.*, *100*, 32–74, doi:10.1007/BF01448839.

Cruz-Atienza, V. M., and J. Virieux (2004), Dynamic rupture simulation of non-planar faults with a finite-difference approach, *Geophys. J. Int.*, *158*(3), 939–954, doi:10.1111/j.1365-246X.2004.02291.x.

Dalguer, L. A., and S. M. Day (2007), Staggered-grid split-node method for spontaneous rupture simulation, *J. Geophys. Res.*, *112*, B02302, doi:10.1029/2006JB004467.

Das, S. (1980), A numerical method for determination of source time functions for general three-dimensional rupture propagation, *Geophys. J. R. Astron. Soc.*, *62*, 591–604, doi:10.1111/j.1365-246X.1980.tb02593.x.

Day, S. M. (1982), Three-dimensional finite-difference simulation of fault dynamics: Rectangular faults with fixed rupture velocity, *Bull. Seismol. Soc. Am.*, *72*, 705–727.

Day, S. M., and G. P. Ely (2002), Effect of a shallow weak zone on fault rupture: numerical simulation of scale-model experiments, *Bull. Seismol. Soc. Am.*, *92*, 3022–3041, doi:10.1785/0120010273.

Day, S. M., L. A. Dalguer, N. Lapusta, and Y. Liu (2005), Comparison of finite difference and boundary integral solutions to three-dimensional spontaneous rupture, *J. Geophys. Res.*, *110*, B12307, doi:10.1029/2005JB003813.

de la Puente, J. (2008), *Seismic Wave Propagation for Complex Rheologies*, VDM, Saarbrücken, Germany.

de la Puente, J., M. Käser, M. Dumbser, and H. Igel (2007), An arbitrary high order discontinuous Galerkin method for elastic waves on unstructured meshes IV: Anisotropy, *Geophys. J. Int.*, *169*(3), 1210–1228, doi:10.1111/j.1365-246X.2007.03381.x.

de la Puente, J., M. Dumbser, M. Käser, and H. Igel (2008), Discontinuous Galerkin methods for wave propagation in poroelastic media, *Geophysics*, *73*(5), T77–T97, doi:10.1190/1.2965027.

Dumbser, M., and M. Käser (2006), An arbitrary high order discontinuous Galerkin method for elastic waves on unstructured meshes II: The three-dimensional case, *Geophys. J. Int.*, *167*(1), 319–336, doi:10.1111/j.1365-246X.2006.03120.x.

Dumbser, M., M. Käser, and E. F. Toro (2007), An arbitrary high order discontinuous Galerkin method for elastic waves on unstructured meshes V: Local time stepping and p-adaptivity, *Geophys. J. Int.*, *171*(2), 695–717, doi:10.1111/j.1365-246X.2007.03427.x.

Ely, G., S. M. Day, and J.-B. Minster (2009), A support-operator method for 3D rupture dynamics, *Geophys. J. Int.*, *177*(3), 1140–1150, doi:10.1111/j.1365-246X.2009.04117.x.

Geubelle, P. H., and J. R. Rice (1995), A spectral method for three-dimensional elastodynamic fracture problems, *J. Mech. Phys. Solids*, *43*, 1791–1824, doi:10.1016/0022-5096(95)00043-I.

Goto, H., and J. Bielak (2008), Galerkin boundary integral equation method for spontaneous rupture propagation problems: SH-case, *Geophys. J. Int.*, *172*(3), 1083–1103, doi:10.1111/j.1365-246X.2007.03694.x.

Harris, R. A., et al. (2004), The source physics of large earthquakes: Validating spontaneous rupture methods, *Eos Trans. AGU*, *85*(47), Fall Meet. Suppl., Abstract S12A-05.

Ida, Y. (1972), Cohesive force across the tip of a longitudinal-shear crack and Griffith's specific surface energy, *J. Geophys. Res.*, *77*, 3796–3805, doi:10.1029/JB077i020p03796.

Ida, Y. (1973), The maximum acceleration of seismic ground motion, *Bull. Seismol. Soc. Am.*, *63*, 959–968.

Igel, H., M. Käser, and M. Stuppazini (2008), Simulation of seismic wave propagation in media with complex geometries, in *Encyclopedia of Complexity and System Science*, Springer, New York, in press.

Kaneko, Y., N. Lapusta, and J.-P. Ampuero (2008), Spectral element modeling of spontaneous earthquake rupture on rate and state faults: Effect of velocity-strengthening friction at shallow depths, *J. Geophys. Res.*, *113*, B09317, doi:10.1029/2007JB005553.

Käser, M., and M. Dumbser (2006), An arbitrary high order discontinuous Galerkin method for elastic waves on unstructured meshes I: The two-dimensional isotropic case with external source terms, *Geophys. J. Int.*, *166*(2), 855–877, doi:10.1111/j.1365-246X.2006.03051.x.

Käser, M., M. Dumbser, J. de la Puente, and H. Igel (2007a), An arbitrary high order discontinuous Galerkin method for elastic waves on unstructured meshes III: Viscoelastic attenuation, *Geophys. J. Int.*, *168*(1), 224–242, doi:10.1111/j.1365-246X.2006.03193.x.

Käser, M., P. Mai, and M. Dumbser (2007b), On the accurate treatment of finite source rupture models using ADER-DG on tetrahedral meshes, *Bull. Seismol. Soc. Am.*, *97*, 1570–1586, doi:10.1785/0120060253.

Käser, M., V. Hermann, and J. de la Puente (2008), Quantitative accuracy analysis of the discontinuous Galerkin method for seismic wave propagation, *Geophys. J. Int.*, *173*(3), 990–999, doi:10.1111/j.1365-246X.2008.03781.x.

Komatitsch, D., and R. Martin (2007), An unsplit convolutional perfectly matched layer improved at grazing incidence for the seismic wave equation, *Geophysics*, *72*(5), SM155–SM167, doi:10.1190/1.2757586.

Kostrov, B. V. (1964), Self-similar problem of propagation of shear crack, *J. Appl. Math. Mech.*, *28*, 1077–1087, doi:10.1016/0021-8928(64)90010-3.

Lapusta, N., J. R. Rice, Y. Ben-Zion, and G. Zheng (2000), Elastodynamic analysis for slow tectonic loading with spontaneous rupture episodes on faults with rate- and state dependent friction, *J. Geophys. Res.*, *105*, 23,765–23,789, doi:10.1029/2000JB900250.

LeVeque, R. (2002), *Finite Volume Methods for Hyperbolic Problems*, Cambridge Univ. Press, Cambridge, U. K.

Madariaga, R., K. B. Olsen, and R. Archuleta (1998), Modeling dynamic rupture in a 3D earthquake fault model, *Bull. Seismol. Soc. Am.*, *88*, 1182–1197.

Moczo, P., J. Kristek, M. Galis, P. Pazak, and M. Balazovjech (2007), The finite-difference and finite-element modeling of seismic wave propagation and earthquake motion, *Acta Phys. Slovaca*, *57*(2), 177–406.

Oglesby, D. D., R. J. Archuleta, and S. B. Nielsen (1998), Earthquakes on dipping faults: the effects of broken symmetry, *Science*, *280*, 1055–1059, doi:10.1126/science.280.5366.1055.

Oglesby, D. D., R. J. Archuleta, and S. B. Nielsen (2000), The three-dimensional dynamics of dipping faults, *Bull. Seismol. Soc. Am.*, *90*, 616–628, doi:10.1785/0119990113.

Palmer, A. C., and J. R. Rice (1973), The growth of slip surfaces in the progressive failure of overconsolidated clay slopes, *Proc. R. Soc. London, Ser. A*, *332*, 527–548, doi:10.1098/rspa.1973.0040.

Rojas, O., S. M. Day, J. Castillo, and L. A. Dalguer (2008), Modelling of rupture propagation using high-order mimetic finite differences, *Geophys. J. Int.*, *172*(2), 631–650, doi:10.1111/j.1365-246X.2007.03651.x.

Rubin, A., and J.-P. Ampuero (2007), Aftershock asymmetry on a bimaterial interface, *J. Geophys. Res.*, *112*, B05307, doi:10.1029/2006JB004337.

Toro, E. F. (1999), *Riemann Solvers and Numerical Methods for Fluid Dynamics*, Springer, Berlin.

Vilotte, J.-P., G. Festa, and J.-P. Ampuero (2006), Dynamic fault rupture propagation using nonsmooth spectral element method, *Eos Trans. AGU*, *87*(52), Fall Meet. Suppl., Abstract S52B-05.

J.-P. Ampuero, Division of Geological and Planetary Sciences, California Institute of Technology, 1200 E. California Boulevard, MC 252-21, Pasadena, CA 91125, USA.

J. de la Puente, Barcelona Center for Subsurface Imaging, Institut de Ciències del Mar, CSIC, Passeig Marítim de la Barceloneta 37-49, Barcelona, Spain. (jdelapuente@cmima.csic.es)

M. Käser, Department of Earth and Environmental Sciences, Section Geophysics Ludwig-Maximilians-University, Theresienstrasse 41, D-80333 Munich, Germany.

JOURNAL OF GEOPHYSICAL RESEARCH, VOL. 115, B03308, doi:10.1029/2008JB006171, 2010

Three-dimensional modeling of near-fault ground motions with nonplanar rupture models and topography: Case of the 2004 Parkfield earthquake

F. Gallovič,[1] M. Käser,[2] J. Burjánek,[3] and C. Papaioannou[4]

Received 27 October 2008; revised 25 September 2009; accepted 15 October 2009; published 24 March 2010.

[1] We study the applicability of deterministic strong ground motion simulations at very near fault distances for a subvertical strike-slip fault model corresponding to the 2004 *M*6 Parkfield, California, earthquake in the frequency range up to 1 Hz. Theoretical modeling under the assumptions of a planar rupture and 1-D medium shows that as a consequence of the *S* wave radiation pattern, the particle motion for such close stations should be almost linear in the fault-normal (FN) direction, having fault-parallel (FP) and vertical (V) components of almost zero. However, as shown on the Parkfield earthquake recordings, observed particle motions are rather circular with peak velocities at FP and V components comparable to those at FN components. We investigate several realistic features that could explain this controversy, namely, nonplanar fault, realistic three-dimensional (3-D) medium, and the topography of the area. We test and quantify these hypotheses using discrete wave number and discontinuous Galerkin modeling methods applying 1-D and 3-D velocity structures, respectively, and two nonplanar rupture models. We compare the synthetic and observed particle motions and peak velocity ratios and conclude that deviations from a planar rupture geometry in reasonable bounds for the Parkfield fault and the influence of topography only partially explain the behavior of the observed seismograms. On the contrary, the heterogeneous 3-D velocity structure significantly reduces the synthetic peak ratios to values closer to 1 and provides rather circular particle motions. Therefore, the 3-D velocity model is crucial to obtain realistic estimates of ground motions at near-fault distances and is more important than the detailed fault geometry or topography in the Parkfield area.

Citation: Gallovič, F., M. Käser, J. Burjánek, and C. Papaioannou (2010), Three-dimensional modeling of near-fault ground motions with nonplanar rupture models and topography: Case of the 2004 Parkfield earthquake, *J. Geophys. Res.*, *115*, B03308, doi:10.1029/2008JB006171.

1. Introduction

[2] Studies concerned with the potential earthquake hazard and damage need realistic estimates of ground motion in a broad frequency band and in a broad range of distances at all three components. In particular, for the low-frequency band (<1−2 Hz) very close to the earthquake rupture, deterministic models [*Pitarka et al.*, 2000; *Mai and Beroza*, 2003; *Hartzell et al.*, 2005; *Gallovič and Brokešová*, 2007; *Wang et al.*, 2008] are preferable to stochastic methods [*Boore*, 1983] because they can capture near-fault effects. These models, being usually based on simple assumptions (planar fault, 1-D or relatively smoothly varying 3-D medium with no topography) are able to explain three component ground motions observed during real earthquakes at stations lying typically at distances larger than several kilometers from the fault. Nevertheless, as we demonstrate in this paper, problems may arise when simulating ground motions for stations lying very close to the earthquake fault. In particular, we take advantage of the well-studied 2004 *M*6 Parkfield, California, earthquake, which was recorded at stations lying basically above the fault rupture. On the basis of these recording, we show to what extent the deterministic methods are able to explain amplitudes at all the three ground motion components for such station locations in a low-frequency band. We discuss the ability of several modeling features to improve near-fault ground motion estimates.

[3] The earthquake of *M*6 struck the central coast of California at 1015:24 LT (Pacific Standard Time) (1715:24 UTC) on 28 September 2004. The hypocenter was 11 km southeast of Parkfield at a depth of approximately 8 km; the earthquake had a strike-slip mechanism on an almost vertical fault. The analysis of the aftershocks and the proposed rupture models indicate that the rupture occurred along the

[1]Department of Geophysics, Faculty of Mathematics and Physics, Charles University, Prague, Czech Republic.
[2]Department of Earth and Environmental Sciences, Ludwig Maximilians University, Munich, Germany.
[3]Swiss Seismological Service, Institute of Geophysics, ETH Zurich, Zurich, Switzerland.
[4]ITSAK, Thessaloniki, Greece.

0148-0227/10/2008JB006171

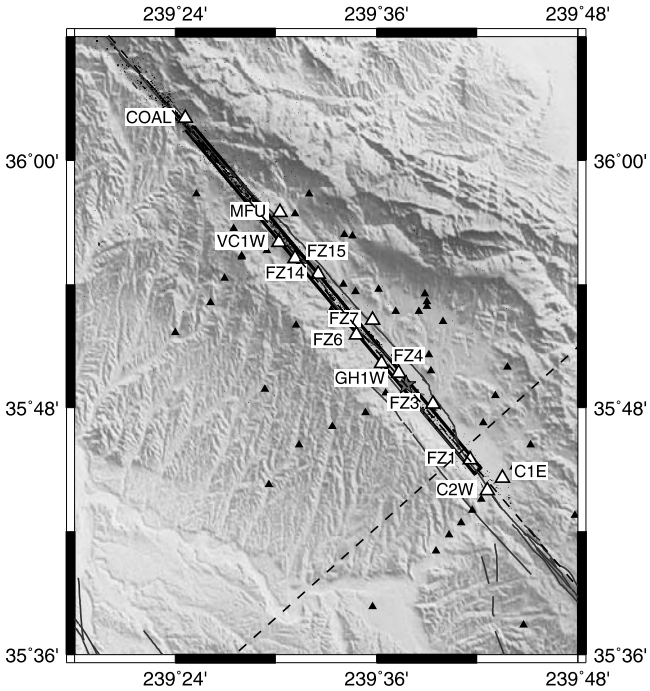

Figure 1. Map of the Parkfield area. Stations (small and large triangles), aftershocks (points), faults (thin lines), projection of the Parkfield rupture (bold line rectangle), projection of the cross sections of Figure 3 (dashed lines), and the main shock epicenter (star) are shown. In this paper we consider only stations displayed by large triangles together with their names. The elevation of the area under consideration ranges from 138 to 1335 m height.

same section of the San Andreas fault as those of the similar magnitude Parkfield earthquake series in 1881, 1901, 1922, 1934, and 1966 [*Nadeau et al.*, 1995; *Bakun and McEvilly*, 1979; *Toppozada et al.*, 2002]. The earthquake and its rupture propagation have been studied by many authors and even led to a special issue of the Bulletin of the Seismological Society of America [*Harris and Arrowsmith*, 2006], where most of the work was collected. A consensus was reached suggesting a rupture direction predominantly toward the northwest, opposite to the rupture propagation direction of the previous 1966 Parkfield earthquake. To date, the 2004 Parkfield earthquake has been a subject of a number of slip inversion studies using various kinds of data [*Hartzell et al.*, 2007; *Liu et al.*, 2006; *Dreger et al.*, 2005; *Kim and Dreger*, 2008].

[4] In particular, *Liu et al.* [2006] performed a slip inversion using strong motion data in the frequency band 0.16–1 Hz assuming a planar fault geometry and two different one-dimensional (1-D) velocity models separated by the fault plane to take into account different crustal properties northeast (NE) and southwest (SW) of the fault. This slip inversion suggested two main asperities located northwest (NW) and southeast (SE) of the epicenter. However, in their inversion, *Liu et al.* [2006] down-weighted vertical (V) components for all stations and deliberately omitted fault parallel (FP) components of three stations located almost above the earthquake fault plane or its prolongation in the strike direction. For these two components forward modeling produces synthetics with almost zero amplitudes, while the faut normal (FN) component show a strong signal, having linear particle motion perpendicular to the fault strike. This is due to the radiation pattern of a predominantly strike-slip rupture along a perfectly planar fault in a 1-D medium. On the contrary, the observed data are characterized by peak amplitudes of similar magnitude for all three components and rather circular particle motions. We claim that this inconsistency between modeled and observed particle motions (and FN/FP and FN/V peak velocity ratios) can be attributed to the simplifying assumptions usually made in the modeling process, namely, a fault model that is perfectly planar, a 1-D medium with no lateral variations of the material properties and the negligence of relevant free-surface topography.

[5] Note that the small peak velocity ratios represent a more general issue as they are observed in similar settings. For example, relatively large ratio was observed during the Kobe earthquake. *Irikura* [1996] shows that one of the near-fault stations was characterized by large ratio between FN and V components of 8.5, while the ratio between FN and FP components was lower, 2.5.

[6] There could be many explanations for the inconsistency described above, such as presence of the fault zone, anisotropy, nonlinear soil effect, etc. In our study, which is not intended to cover a complete set of possible physical models, we rather propose and quantitatively test only three hypotheses. In particular, the first one is based on nonplanar faults. *Käser and Gallovič* [2008] performed a numerical study on the radiation of seismic waves from kinematic nonplanar rupture models. They showed that an increasing geometrical complexity of a rupture surface can introduce relatively strong signals at FP and V components for stations lying above a vertical strike-slip fault, which would be of zero amplitude for a perfectly planar model. As mentioned above, this is mainly a consequence of the properties of the S wave radiation pattern. In the case of the nonplanar fault, both local strike and dip angles vary along the fault and thus the seismic radiation pattern is more distorted. Let us emphasize that the 2004 *M*6 Parkfield earthquake represents a unique opportunity to test such effects of nonplanar ruptures to explain the observed FP and V components because of a large amount of very near fault (<1–2 km) strong motion records (see Figure 1).

[7] The second hypothesis is that in the real Earth the seismic waves propagate in a complex 3-D medium that distorts the source radiation pattern. We do not attribute such effects to scattering due to stochastic properties of the medium since the study is performed in a relatively low frequency band up to 1 Hz in which the seismic waves are rather affected by deterministic larger-scale 3-D variations in the crustal structure. A number of 3-D tomographical crustal models exist for the Parkfield area [*Michelini and McEvilly*, 1991; *Eberhart-Phillips and Michael*, 1993; *Thurber et al.*, 2006], which further favors this region for this kind of study.

[8] As a third hypothesis the free surface topography in the Parkfield area could cause signals on the theoretically zero FP and V components. The influence of free surface topography has been studied by many authors, [e.g., *Bouchon*, 1973; *Zahradník and Urban*, 1984; *Geli et al.*, 1988; *Bouchon et al.*, 1996]. Typically, its effect has to be analyzed for each region separately and, moreover, usually depends strongly on

the frequency band of interest. Therefore, we will compare our results for the 3-D heterogeneous material including or omitting the free surface topography.

[9] To summarize, assuming frequency range up to 1 Hz we quantitatively study the effects of rupture nonplanarity, 3-D heterogeneous material and topography in terms of their ability to decrease synthetic FN/FP and FN/V peak amplitude ratios at stations lying above a vertical strike-slip fault closer to unity as observed in the Parkfield earthquake data. We start with the planar source model inverted by *Liu et al.* [2006]. Then, two speculative nonplanar rupture models are introduced. The slip distribution and rupture propagation of *Liu et al.* [2006] is transcribed on these nonplanar faults in order to have all rupture models consistent. The ground motions generated by these nonplanar earthquake source models are computed in both the 1-D medium adopted by *Liu et al.* [2006] and 3-D medium obtained by *Thurber et al.* [2006]. Finally, we show the influence of real surface topography.

[10] We compare the changes of the particle motions, synthetic seismograms, their Fourier spectra and peak velocity ratios with the real data observed during the 2004 Parkfield earthquake as a reference. We point out that we are not particularly interested in improving the fit with the observed waveforms. We rather study to what extent nonplanar fault geometries, the 3-D medium and the topography effects can distort the linear particle motions and improve FN/FP and FN/V amplitude ratios in terms of reducing them close to unity as observed in real data. In this respect, we discuss which of the model features are advisable to be taken into account in the slip inversions and strong ground motion simulations to provide realistic estimates for similar problems.

2. Stations and Recorded Data

[11] The 2004 *M*6 Parkfield earthquake was recorded by analog recorders operated by the California Geological Survey (CGS) network and digital recorders maintained by the U.S. Geological Survey (USGS) (Figure 1). In our study we consider only stations in a very close vicinity (<1.5 km) of the fault, which were also used in the slip inversion by *Liu et al.* [2006]. Thus the results are presented for 13 stations which exhibit typical features as described in the introduction and later in the text. *Liu et al.* [2006] used their recordings in the slip inversions after determining approximative correction to the site effects. The exceptions are stations MFU, FZ14 and COAL for which the site effect correction was not determined. Nevertheless, they were successfully used in the slip inversion. Note that some of the station components were not used in the inversion or not fitted. In particular, although FP and V components of COAL station were used in the inversion, the synthetic amplitudes are more than 20 times lower than the observed ones. FP components for stations C2W, GH1W, and FZ1 were completely omitted in the inversion for questionable polarities [*Liu et al.*, 2006]. We note that the fit is also poor due to the station position with respect to the rupture as explained in the introduction.

[12] Processed data (velocity records) were downloaded from the US National Center for Engineering Strong Motion Data (http://www.strongmotioncenter.org/). We applied a band-pass filter in the frequency band from 0.16 to 1 Hz following the work of *Liu et al.* [2006]. The lower and upper limits of the filter are dictated by inaccurate instrument performance below 0.16 Hz and the inability to model deterministically the Green's functions at high frequencies, respectively.

3. Crustal Models and Wave Propagation Codes

[13] The Parkfield area is geologically very complex. One of its most evident features is the substantial change of material properties across the San Andreas Fault (SAF) separating different geological units, namely, sedimentary Franciscan terrain in the NE and granitic Salinian block in the SW [*Brocher*, 2005]. This is not surprising as the SAF has undergone several hundreds of kilometers of cumulative slip, which brings together geological units originally developed far away from each other. The SAF has been subject to intensive research. For example, the studies of the fault zone head waves treated the fault as an abrupt material interface [*Ben-Zion and Malin*, 1991; *Ben-Zion*, 1990], while others considered the fault as a narrow (100–150 m) transition zone capable of producing fault zone trapped waves [*Li et al.*, 1990]. This damaged core layer (or fault zone) surrounding the fault is a low-velocity zone characterized by velocity reductions up to 40% and low Q values of ~30 [*Li et al.*, 2004]. Other investigations revealed that the structure at the SAF area is characterized by a wider (~1 km) damaged zone [*Unsworth et al.*, 1997] containing different fault branches that are visible on the surface. This zone spreads from the main fault trace in the northeast to the southwestern fracture zone.

[14] The crustal model of the Parkfield area has been subject to a number of 3-D tomographic studies [*Michelini and McEvilly*, 1991; *Eberhart-Phillips and Michael*, 1993]. In the present paper we use the most recent model by *Thurber et al.* [2006]. Starting from the model of *Eberhart-Phillips and Michael* [1993], *Thurber et al.* [2006] include a large number of earthquake events and active shots and present a new compressional wave speed (v_p) model with a locally increased resolution along the SAF (up to 1–2 km in the Parkfield area), particularly imaging the strong material contrast and its depth variation. As such, the model does not include the observed fault zone [*Li et al.*, 2004] as a distinct waveguide feature which is supposedly only 100–200 m wide. The 3-D velocity model by *Thurber et al.* [2006] only perhaps partly images the wider damaged zone as pointed out by *Lewis et al.* [2007]. Nevertheless, as the lowest S wave velocity in the damaged zone can by as low as 500 m s^{-1}, which corresponds to wavelengths of 500 m for our largest frequency of 1 Hz, such details are a few times below the resolution of *Thurber et al.*'s [2006] model (see section 3.2). With this respect, we emphasize that our study does not intend to cover an exhaustive set of all features possibly influencing the ground motions. Rather, it concentrates on distinct effects of nonplanar source models and 3-D velocity medium typically used in the ground motion modeling studies on the simulated three-component ground motions. Nevertheless, other features of the Parkfield area are presumably important and will be subject of our further study.

Table 1. Parameters of NE and SW Crustal Models Describing the Bimaterial Character of the Parkfield Area[a]

Depth (km)	v_p (km s^{-1})	v_s (km s^{-1})	ρ (g cm^{-3})	Q_P	Q_S
		NE Crustal Model			
0.0	2.0	1.1	2.0	70	35
0.7	3.8	2.2	2.3	300	180
1.4	4.3	2.4	2.3	340	190
2.0	4.8	2.7	2.3	450	250
3.6	5.3	3.1	2.5	500	300
7.6	5.8	3.3	2.7	550	300
14.3	6.2	3.8	2.8	600	350
20.5	6.8	3.8	2.8	650	350
24.6	7.0	4.0	2.8	700	400
		SW Crustal Model			
0.0	1.9	1.0	2.0	70	35
1.0	3.4	1.7	2.3	270	160
2.0	4.6	2.4	2.3	450	260
3.0	5.1	3.1	2.7	500	300
4.0	5.6	3.6	2.7	550	350
5.4	6.3	3.6	2.8	600	350
18.7	6.8	3.6	2.8	680	360

[a]After *Liu et al.* [2006].

[15] For comparison purposes, in accordance with *Liu et al.* [2006], we use also two 1-D velocity models approximating the bimaterial structure NE and SW of the fault separately. More details on the modeling are explained below.

3.1. One-Dimensional Crustal Models

[16] We adopt the two 1-D crustal models from *Liu et al.* [2006] shown in Table 1 to take into account the presence of different materials on the two sides of the fault. The models are derived from the 3-D models of *Eberhart-Phillips and Michael* [1993] and *Thurber et al.* [2006].

[17] The kinematic fault model is numerically approximated by 128 × 64 rectangular elements represented by double-couple point sources. For each source-receiver pair the Green's functions are calculated using the DWN method of *Bouchon* [1981]. The ground motion at a given station is then obtained by summing up contributions from all the point sources taking into account the prescribed slip history, which corresponds to the numerical evaluation of the fault surface integral in the representation theorem [*Aki and Richards*, 2002]. For details on the source model properties, see section 4. Note that we downsample the source model provided by *Liu et al.* [2006] in the electronic supplement with 260 × 95 samples. We have tested that our resolution is sufficient and results in decreased numerical expense due to a lower number of needed Green's functions.

[18] *Liu et al.* [2006] determined correction amplitude factors at the Parkfield array from the 1983 *M*6.5 Coalinga earthquake spectra in the frequency range of 0.16–1 Hz to approximate the site effects. Their corrected values are presented in the erratum. In order to validate our 1-D media simulations against their synthetic data we apply the same amplification factors.

3.2. Three-Dimensional Crustal Model

[19] For the simulations based on a 3-D velocity structure we use the model proposed by *Thurber et al.* [2006]. It is defined by values at nodes with spacing ranging from 2 to 5 km in the vicinity of the SAF. We interpolate this v_p model using cubic splines and derive the shear wave speeds (v_s) and densities (ρ) using the empirical relations of *Brocher* [2005] as suggested by *Thurber et al.* [2006]. Explicitly, we use

$$v_s = 0.7858 - 1.2344\,v_p + 0.7949\,v_p^2 - 0.1238\,v_p^3 + 0.0064\,v_p^4 \quad (1)$$

$$\rho = 1.6612\,v_p - 0.4721\,v_p^2 + 0.0671\,v_p^3 - 0.0043\,v_p^4 + 0.000106\,v_p^5, \quad (2)$$

where the unit of v_p, v_s and ρ are given in km s^{-1} and g cm^{-3}, respectively. We have near-surface minimum wave speeds of v_p = 1.224 km s^{-1} and v_s = 0.253 km s^{-1} at very localized parts of the model. Note that the rules given by *Brocher* [2005] have been derived only for $v_p > 1.5$ km s^{-1} so we simply extrapolate the rules to lower velocities obtaining a reasonable decrease of v_s velocities. Assuming our highest frequency of 1 Hz, the corresponding wavelength is of about 0.25 km. This is several times smaller than the resolution of the model by *Thurber et al.* [2006]. Nevertheless, we point out that this is a typical situation in the ground motion estimations. Assuming that we can at least partially approximate the site effects by using the interpolated 3-D model, we do not use the amplification factors determined by *Liu et al.* [2006]. Let us emphasize that the accurate knowledge of near-surface material properties is only crucial for the absolute amplitude values [*Olsen et al.*, 2003]. This means that this effect would influence all components rather equally, so it is not a critical point for the peak amplitude ratios we are mainly interested in.

[20] The simulation of the seismic wavefield in the 3-D crustal model was carried out by the ADER-DG method [*Käser and Dumbser*, 2006; *Dumbser and Käser*, 2006]. To this end, the computational domain of the Parkfield area was discretized by an unstructured tetrahedral mesh using roughly 1.5 million elements. The computational domain is bounded by absorbing boundaries along a prolate ellipsoid of length 100 km, width 60 km in the lateral extend and a depth of 28 km as shown in Figure 2.

[21] In the calculations when the topography is taken into account, the top of the mesh is bounded by the free surface given by the digital elevation model of the Parkfield area. The mesh spacing is variable and ranges from 300 m at the surface in the vicinity of the source projection to the surface and the receivers locations to 4000 m toward the remaining boundaries of the computational domain. The elastic parameters inside each element are determined by the velocity model described above. Cross sections through the 3-D heterogeneous v_p and v_s velocity model are shown in Figure 3. In particular, the cross sections in Figures 3a and 3c have the same along-strike location and fault-normal orientation as the one shown in Figure 3f of *Thurber et al.* [2006]. Similarly, the cross sections in Figures 3b and 3d have the same fault-normal location and along-strike orientation as the one shown in Figure 4b of *Thurber et al.* [2006]. This way, the body of high P wave velocity, as reported by *Eberhart-Phillips and Michael* [1993] and analyzed with respect to its importance for fault behavior by *Michael and Eberhart-Phillips* [1991], is nicely visible.

[22] The approximation order of the applied ADER-DG scheme is set to 5 in time and space providing sufficient

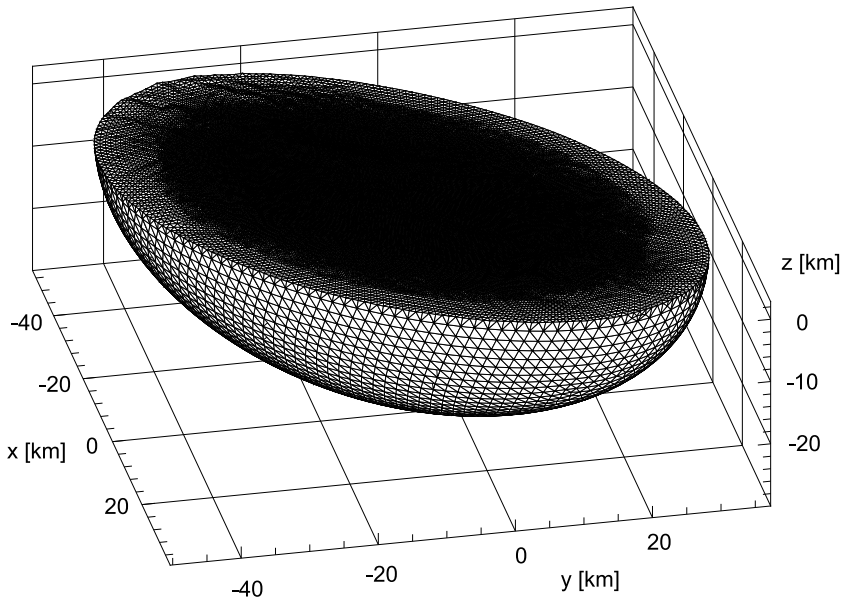

Figure 2. Discretization of the computational domain with an unstructured tetrahedral mesh with variable mesh spacing and smooth elliptic model boundaries to optimize the resolution of the simulation and avoid boundary effects.

accuracy of the numerical scheme as validated by the DWN method for a simplified, layered 1-D medium (not presented here [see, e.g., *Käser and Gallovič*, 2008]).

4. Source Models

[23] Here we introduce the geometrical fault models of the 2004 Parkfield earthquake considered in this paper. They are all based on the relocated aftershock distribution [*Thurber et al.*, 2006]. In a first-order approximation the aftershocks delineate a planar fault as used by *Liu et al.* [2006] that we denote as the *planar fault* (PF) model. However, when looking at the cross sections of the aftershock distribution in SW–NE direction apparent trends can be seen, such as the opposite dipping directions of the NW and SE part of the fault [see *Thurber et al.*, 2006, Figure 6b]. Moreover, an apparent variability of the aftershock distribution, especially in the upper part of the 2004 Parkfield rupture associated with the southwest fraction (SWF) zone [*Harris and Arrowsmith*, 2006; *Simpson et al.*, 2006], might suggest possibly even more complicated geometrical properties. Therefore, we introduce two nonplanar models, referred to as the *aftershock-constrained nonplanar fault* (ACNF) and the *aftershock-constrained nonplanar fault with stochastic component* (ACNFS), as shown in Figure 4. In order to emphasize the effects of rupture nonplanarity on the ground motion, especially the ACNFS model is considered as maybe an *extreme* case just allowed by the maximum lateral extent of the aftershock distribution. We keep all three models easily comparable by keeping their kinematic properties and scalar seismic moments the same as those for the inverted PF model (see further).

4.1. Planar Fault Model

[24] In accordance with the work of *Liu et al.* [2006], the geometry of the PF model is determined by fitting a plane through the Parkfield earthquake aftershocks [*Thurber et al.*, 2006], obtaining strike $\varphi = 140^\circ$ and dip $\delta = 87^\circ$. The hypocenter is located at 35.8185 N, 120.3706 W, and at a depth of 8.26 km. The fault has a length of $L = 40$ km and a width of $W = 15$ km and is buried 500 m below the surface as the surface breaks observed in the Parkfield area are considered to be secondary cracks, not direct coseismic surface rupture [*Rymer et al.*, 2006; *Simpson et al.*, 2006]. The RMS distance of the relocated aftershocks from this planar fault is 343 m.

[25] All the kinematic source parameters come from the inversion of strong motion records done for the same fault geometry by *Liu et al.* [2006], namely, the slip values, rake angles, rise times and rupture time distributions. Figure 4a shows the PF model geometry together with the distribution of scalar seismic moment. The scalar moment distribution is determined by the inverted slip values and a depth-dependent effective rigidity μ given by the formula for a source lying within a bimaterial interface [*Wu and Chen*, 2003]

$$\mu(z) = 2\mu^{NE}(z)\mu^{SW}(z)/\left(\mu^{NE}(z) + \mu^{SW}(z)\right), \qquad (3)$$

where $\mu^{NE}(z)$ and $\mu^{SW}(z)$ are the rigidities of the NE and SW crustal models at depth z, respectively (see Table 1). Note that the same scalar seismic moment distribution including the effective rigidity factors for the two separate 1-D models is used even when the 3-D model is considered. Consequently, all the models in our paper are characterized by the same scalar moment distribution. The total scalar seismic moment for the planar rupture model is 1.20×10^{18} N m as shown in Table 2. This table also shows source moment tensor parameters obtained by waveform inversions of teleseismic recordings carried out in Berkeley (0.98×10^{18} N m) and Harvard (1.13×10^{18} N m), which are in good agreement with the value used in this paper.

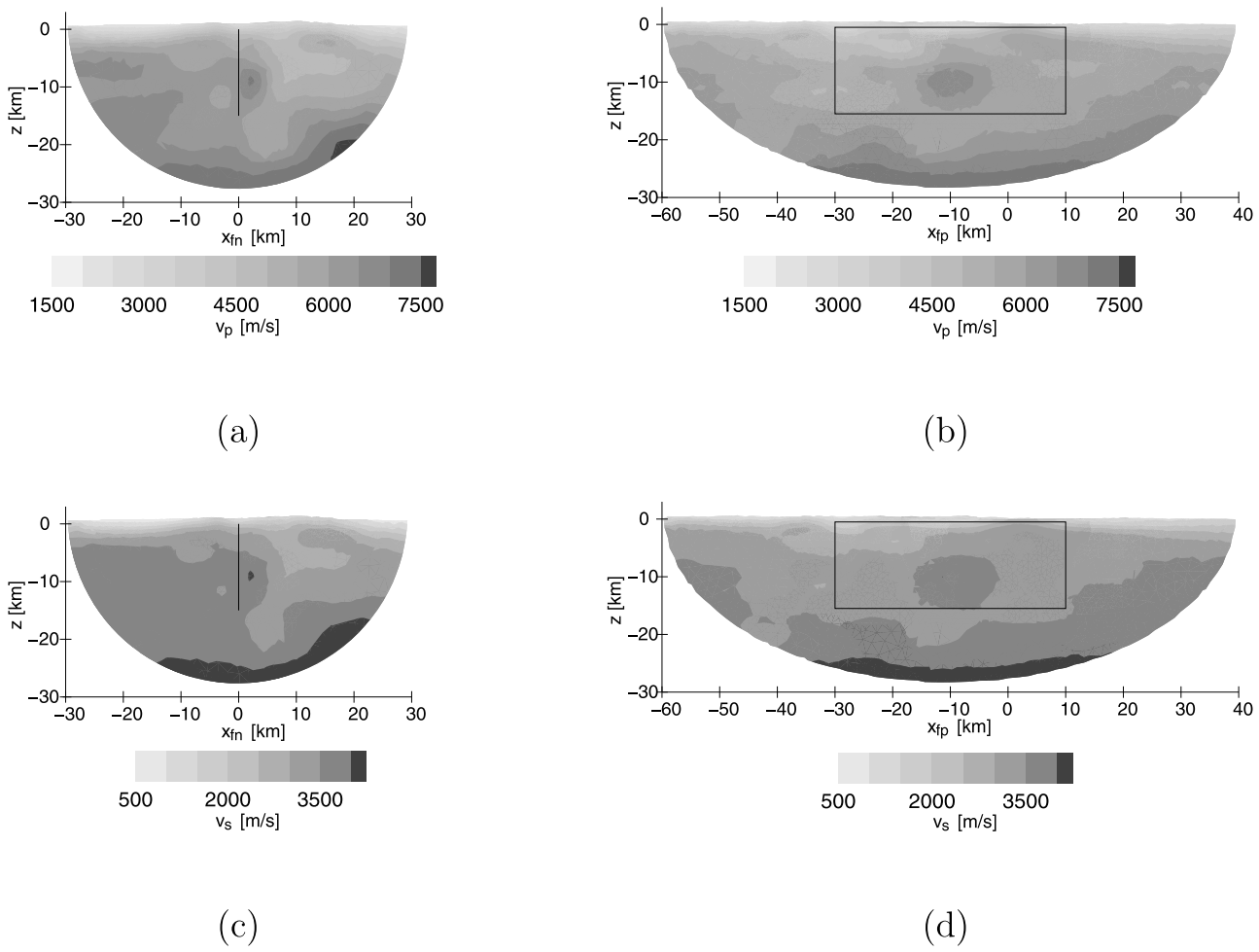

Figure 3. Cross sections of the 3-D velocity model. (a) and (c) Cuts through the v_p and v_s structure from SW to NE in the fault normal direction (x_{fn}) seen from the SE. (b) and (d) Cuts from NW to SE in the fault parallel direction (x_{fp}) seen from the SW. We also show the projection of the rupture surface dimension as a black line in Figures 3a and 3c or a rectangle in Figures 3b and 3d. Locations of the cross sections are shown in Figure 1.

4.2. Aftershock-Constrained Nonplanar Fault Model

[26] We group the aftershocks into 10 bins along the 40 km distance in the strike direction. Then we represent the local fault geometry by subplanes using a linear least squares approximation that leads to 10 subfaults of 4 km length and 15 km depth. We then connect the midpoints in strike direction of all subfaults at five equidistant depth levels together to a 10 × 5 grid. On the basis of this coarse mesh of the fault geometry, we construct a fine mesh of 128 × 64 point sources by cubic spline interpolation. The resulting fault model is shown in Figure 4b. The ACNF model accounts for the apparent trend in the aftershock locations; that is, the NW part seems to be characterized by an opposite dipping direction than the SE part. The RMS distance between the fault and the aftershocks is 282 m, which is lower with respect to the PF model. The strike and dip variations are determined by the fault geometry.

[27] The other kinematic parameters of the rupture process are kept the same as in the PF case. However, since the complex fault geometrical properties determine variations of strike and dip along the fault, the final seismic moment tensor of the whole ACNF model is not the same as that of the PF model. We analyze it in Table 2, showing that it is characterized by 1.4% of a compensated linear vector dipole (CLVD) component as described by *Frohlich* [1994]. Also we obtain a slightly lower seismic moment. In order to keep the scalar seismic moment of the planar and nonplanar model the same, we simply multiply the results obtained for the ACNF model by the ratio of scalar seismic moments for planar and ACNF models.

4.3. Aftershock-Constrained Nonplanar Fault With Stochastic Component Model

[28] As already mentioned above, the perhaps highly damaged shallow (<5 km depth) zone at the SAF area between the San Andreas Fault trace in the east and the southwest fracture zone is only poorly known [*Unsworth et al.*, 1997]. It presumably contains fault branches that extent to the surface, but the upper 5 km of the fault surface are very poorly constrained by aftershock distribution [see, e.g., *Thurber et al.*, 2006]. As the aim is to investigate whether variation of strike and dip angles is able to explain the observed peak velocity ratios, we introduce another speculative model that is even more nonplanar in its upper part

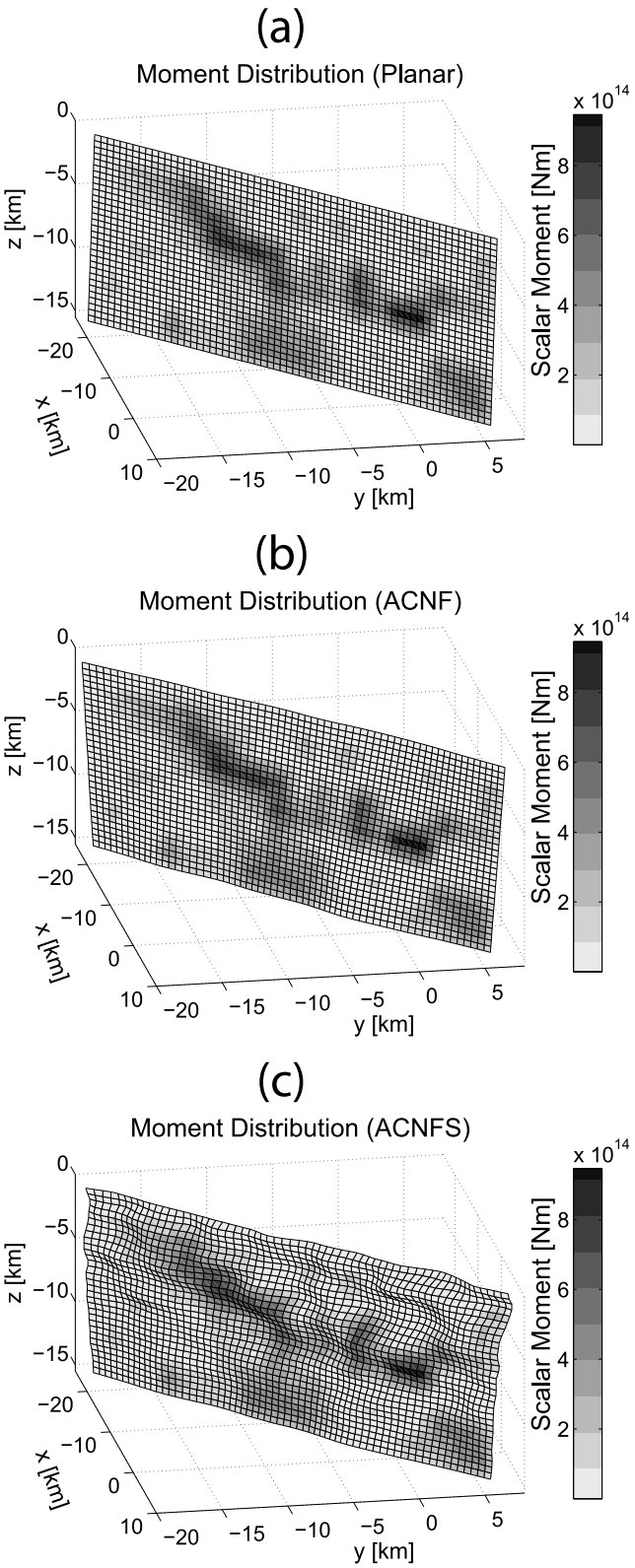

Figure 4. Scalar seismic moment distribution and geometries of the Parkfield source models considered in this work: (a) planar fault, (b) aftershock-constrained nonplanar fault (ACNF), and (c) aftershock-constrained nonplanar fault with stochastic component (ACNFS).

than the ACNF model. The ACNFS fault surface model has to be considered only as "exploratory and suggestive," representing the uncertainty at shallow depth where strike and dip of SAF are poorly constrained. Note that the larger the variations of strike and dip, the more pronounced effect on ground motions.

[29] Following the work by *Käser and Gallovič* [2008], we generate random geometrical deflections of the rupture surface from the ACNF model. The deflections, i.e., distances from the ACNF rupture surface, are created using a random field generator: First, random numbers are prescribed to each of the rupture elements. Then, this white noise is transformed to the spatial Fourier domain. Here the amplitude spectrum is modified by a k^{-3} function

$$P(k_x, k_z) = \left[1 + \left((k_x L_x)^2 + (k_z L_z)^2\right)^{3/2}\right]^{-1} \quad (4)$$

where k_x and k_z are wave numbers in the strike and dip directions, respectively, and L_x and L_z are correlation lengths in the corresponding directions. The modified spectrum is then high-cut filtered just below the Nyquist wave number and Fourier transformed back to the spatial domain. Finally, the random field root mean square (RMS) responsible for the strength of the deflections is imposed.

[30] We set L_x = 10 km and L_z = 3.5 km and the RMS values equal to 350 m. These stochastic deflections are modified by a linear function 1-z/W, where z goes from 0 (top of the fault) to W = 15 km (bottom of the fault). In this way, the variations are less severe in the lower part of the fault, where the aftershocks tend to delineate a smoother rupture surface. The spatial variations of strike and dip due to the source geometry are computed for each rupture element by the spatial derivative of the deflection field in the strike and dip directions, respectively.

[31] Figure 4c shows the generated ACNFS model used in our modeling. Its RMS deflections, i.e., RMS of distances of the ACNFS model from the PF model, is 382 m, which roughly corresponds to RMS distance between the PF model and the relocated aftershock distribution (343 m). This means that in a loose statistical sense the deflections of ACNFS model reflect the variability of aftershock locations with respect to a mean plane. As in the previous case of the ACNF model, we keep all the remaining kinematic parameters the same as for the PF case.

[32] Table 2 shows parameters of the moment tensor of this rupture model, being again different from those of the PF and ACNF models. The CLVD component represents about 2.9% of the seismic moment and the scalar seismic moment is again slightly lower than that for the PF model. We again multiply all the synthetics obtained by this source model by the moment correction factor given by the ratio between scalar moments of the ACNFS and the PF model in order to have all three fault models consistent.

5. Modeling Results

[33] We simulate ground velocities with both 1-D and 3-D subsurface velocity structures and all the fault surface models. Figure 5 shows observed and synthetic horizontal

Table 2. Observed and Modeled Moment Tensor Parameters of the 2004 Parkfield Earthquake[a]

Parameter	Moment Inversion		PF Model	ACNF Model	ACNFS Model
	Berkeley	Harvard			
Source composition					
Scalar moment (N m)	0.98×10^{18}	1.13×10^{18}	1.20×10^{18}	1.19×10^{18}	1.08×10^{18}
DC	98.8%	82.6%	100.0%	98.6%	97.1%
CLVD	1.2%	17.4%	0.0%	1.4%	2.9%
Iso	0.0%	0.0%	0.0%	0.0%	0.0%
Best DC parameters					
Strike	147.0°	321.0°	140.0°	139.7°	138.9°
Dip	83.0°	72.0°	87.0°	86.9°	87.4°
Rake	−175.0°	−177.9°	150.6°	150.6°	150.6°
Moment correction factors	–	–	1.00	1.01	1.11

[a]Note that in order to have all the models the same, we introduce the moment correction factor (ratio between the scalar moment of the planar and nonplanar rupture).

particle motions for all the models considered. Figures 6 and 7 show the synthetic seismograms in the time domain for the 1-D and 3-D models, respectively. Examples of corresponding Fourier amplitude spectra are shown in Figures 8 and 9. Note that the considered stations are ordered in Figures 8 and 9 according to their fault distance, the first and the last station lying at approximately 1.5 km to the NE and SW, respectively.

[34] We emphasize that our aim is not obtaining better fit with the observed data. The observed data, when compared to the inverted model (1-D medium, PF model), serves only for illustration of the best fit that can be obtained in the current setting. This "reference misfit" helps when evaluating the strong or weak influence of the individual model complexities (fault nonplanarity, 3-D medium, and topography), i.e., whether the change in particle motions, waveforms, and Fourier spectra when introducing, for example, a nonplanar fault is comparable to the misfit between the observed data and the synthetics for the best fitting model or not.

5.1. Effect of the Rupture Geometry in 1-D Media

[35] Figures 5 and 6 show the modeling results in the 1-D crustal models characterizing the bimaterial Parkfield area for all the three source models in terms of the horizontal particle motion and waveforms. Note that the results for the PF model, in fact, replicate the calculations of *Liu et al.* [2006] for their best fitting Parkfield model that we use in this study. Therefore, the fit to the observed data is the best achievable with our actual setup.

[36] The particle motions of the observed data (Figure 5) exhibit complex behavior at all distances, even very close to

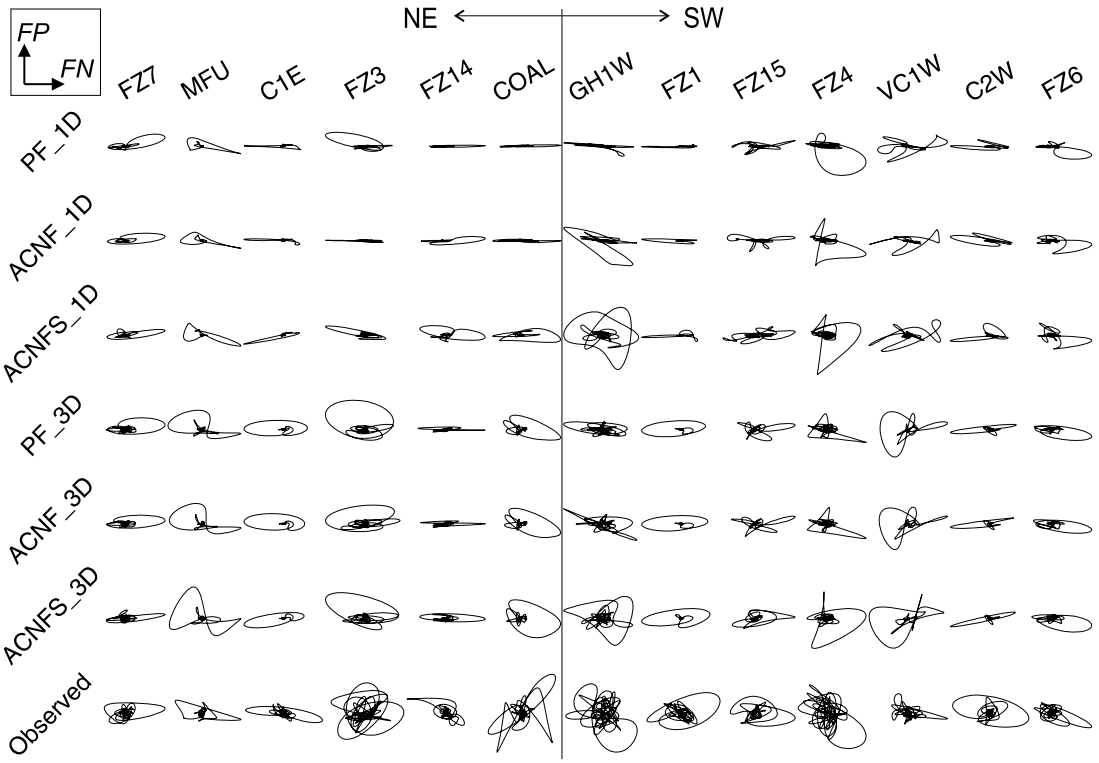

Figure 5. Horizontal particle motions for 13 stations closest to the rupture for all the models taken into account in this study and for the observed data. The vertical line illustrates the relative position of the fault.

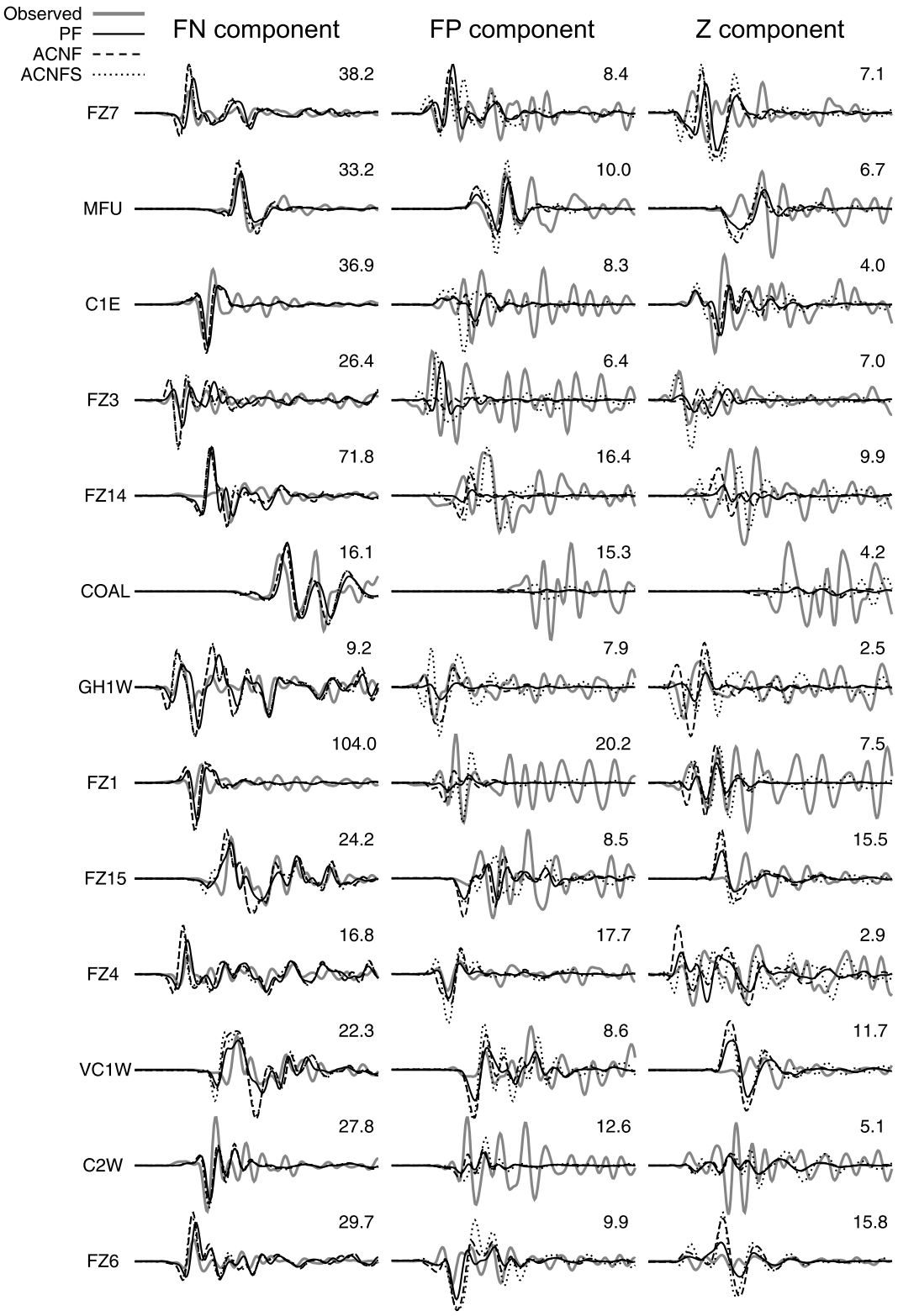

Figure 6. Synthetic velocity seismograms obtained for the three source models for the 1-D bimaterial medium. The values are the maxima from all the waveforms under comparison. The time axis corresponds to 18 s.

the earthquake rupture. On the contrary, the synthetic particle motions have strongly linear character (perpendicular to the fault strike) especially for the very close stations. Figure 5 further shows particle motions for both the nonplanar models ACNF and ACNFS. Generally, the most geometrically complex model ACNFS provides the most nonlinear polarization, for example, at stations FZ14, COAL, GH1W or FZ15. More distant stations do not

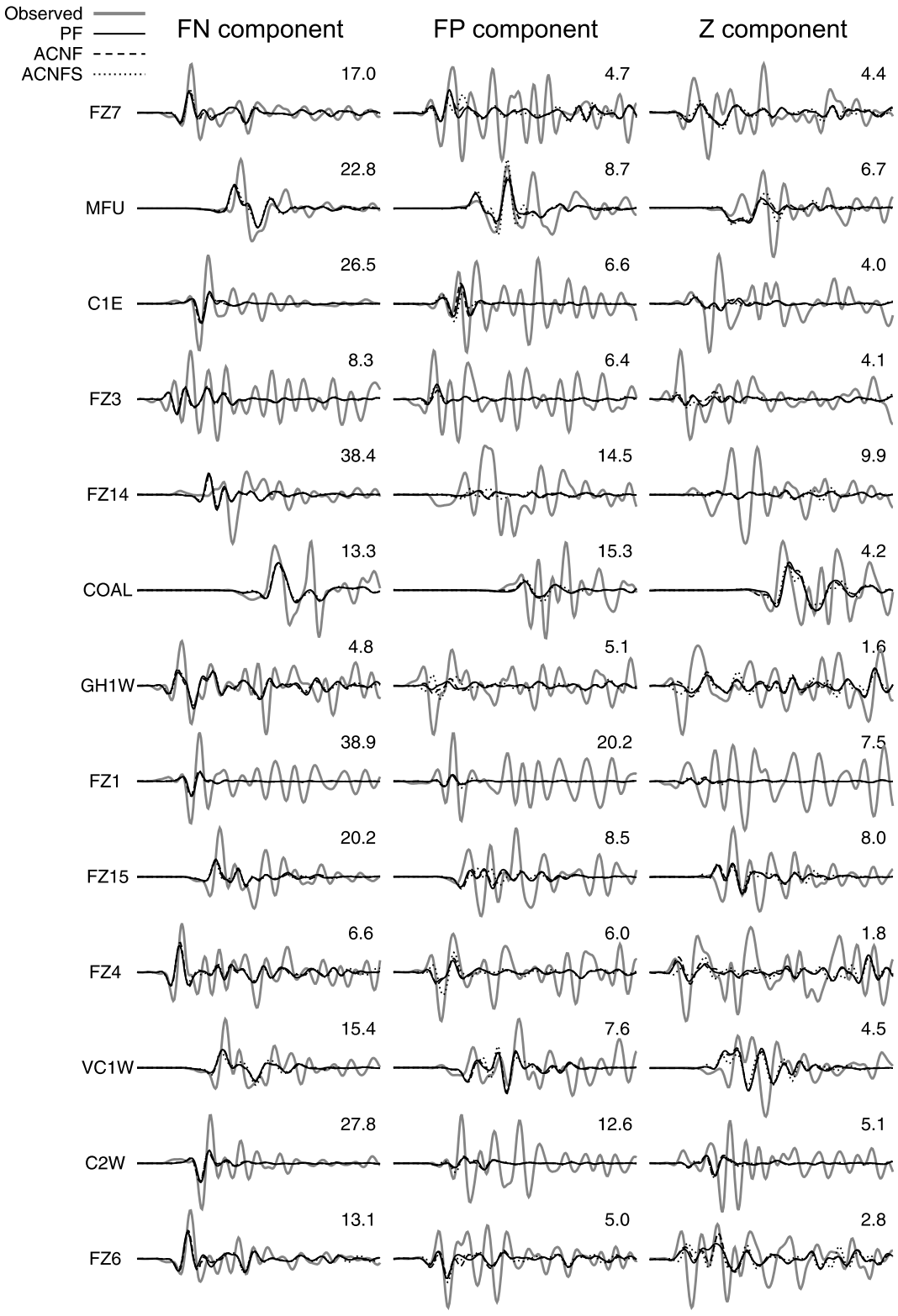

Figure 7. Synthetic velocity seismograms obtained for the three source models for the 3-D heterogeneous medium. The values are the maxima from all the waveforms under comparison. The time axis corresponds to 18 s.

change their particle motions much when adding the fault geometrical complexity. Interestingly, only for station FZ3 the ACNF model provides more linear particle motion than the PF model. Note that only in the case of the station GH1W the nonplanar rupture causes the particle motion to have similar complex shape as what is observed in real data.

[37] Regarding the waveform comparison for the PF model (Figure 6), the fit is better for the FN components

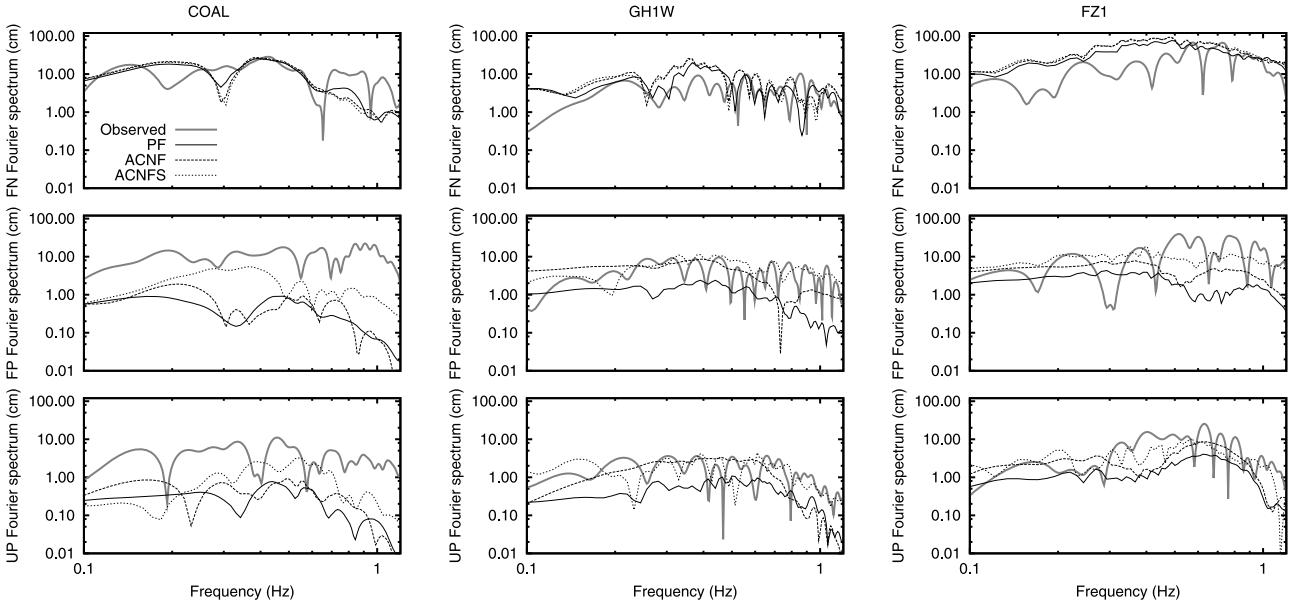

Figure 8. Fourier amplitude spectra of three selected seismograms shown in Figure 6 for the 1-D bimaterial medium.

than for the other two. In fact, some of the FP components of particular stations (FZ1, C2W and GH1W) were not used in the slip inversion by *Liu et al.* [2006]. The synthetics for the stations closest to the fault, e.g., FZ14, COAL, GH1W, and FZ1 are systematically characterized by very low amplitudes at FP and V components with respect to the FN components and, especially, to the observed data. The strong amplitude differences are related to the linear polarization explained above as a consequence of radiation pattern of a planar strike-slip rupture in a 1-D medium.

[38] Figure 6 also shows the synthetics for the nonplanar source models ACNF (dashed) and ACNFS (dotted). The FN components are almost insensitive to the variations of the fault geometry, which is in agreement with the results found by *Käser and Gallovič* [2008]. Note that this is due to the moment correction factor that scales the synthetics to the same scalar seismic moment. On the contrary, the FP and V components are generally more sensitive to the variations of the fault geometry, however, the variations need to be relatively strong as those associated with the ACNFS model. In general, the amplitudes of the FP and V components tend to increase with an increasing complexity of the fault geometry [*Käser and Gallovič*, 2008]. For example, while at COAL station the synthetics for the PF and the ACNF model are almost the same, those for the ACNFS model deviate much more. Only the stations FZ14, GH1W

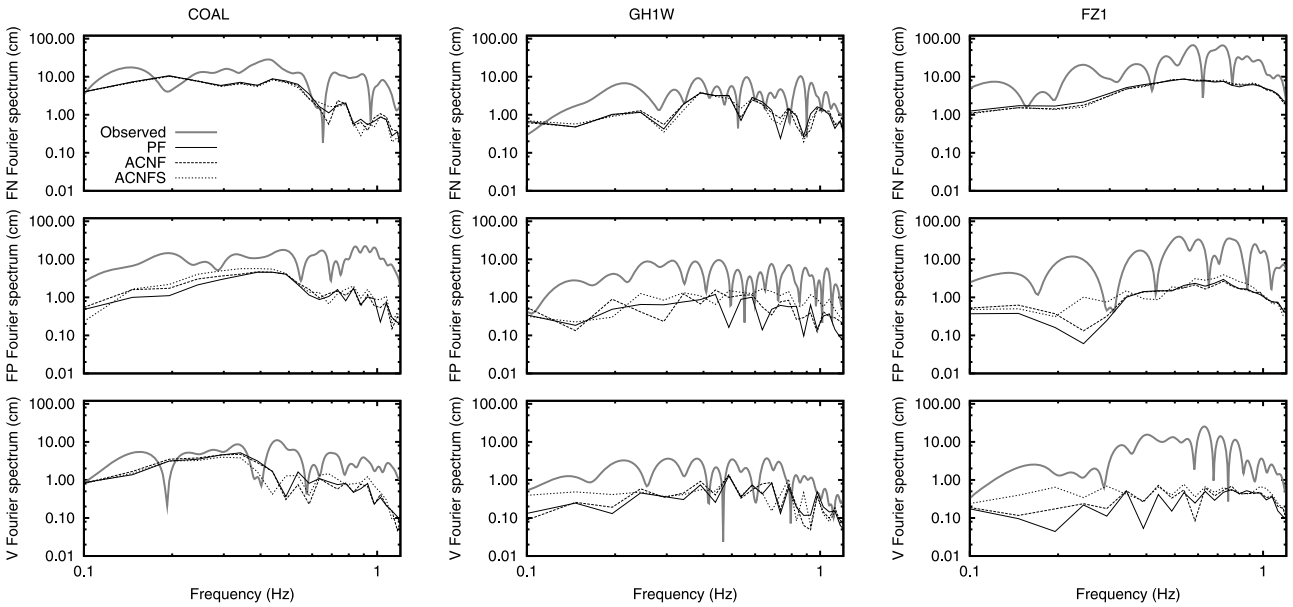

Figure 9. Fourier amplitude spectra of three selected seismograms shown in Figure 7 for the 3-D heterogeneous medium.

and FZ15 are characterized by a strong sensitivity even to the relatively small geometrical variations of the ACNF model. Nevertheless, the peak amplitude values still do not reach the observed ones.

[39] We point out that, generally, the nonplanar source models do not provide a better fit with the observed data on the FP and Z components. Station GH1W is the only exception, for which the nonplanar models, especially ACNF, lead to a better fit of the observed data at FP and V components. Nevertheless, the sensitivity of the stations to the geometrical variations of the fault is predominantly determined by the proximity of the station to strong local changes in the fault geometry. Let us emphasize that our aim was not to optimize the fault geometry to obtain a better fit of the observed waveforms. We rather recognize that at most of the stations the geometrical variations are not even strong enough to increase the synthesized amplitudes in such a way that their peaks would be more balanced among all station components as it is seen in observed data (see further). This is due to the fact that the particle motions are still too linear (see Figure 5).

[40] Figure 8 displays examples of the amplitude Fourier spectra for three closest stations for the 1-D velocity structure and the three source models. As before, the fit for the PF model (solid black) with observed data (solid gray) is the same as obtained by *Liu et al.* [2006]. The fit of the FN components is relatively good, while for the other components the synthetic amplitudes are much lower than the observed ones. Regarding the effect of fault nonplanarity on the spectra, we can see almost no difference at FN component with respect to the PF model, which is in agreement with our observation in the time domain. On the contrary, the other components are affected in the whole frequency range, which agrees with the finding by *Käser and Gallovič* [2008].

[41] Generally speaking, larger geometrical variations, i.e., the ACNFS (dotted line) with respect to the ACNF (dashed line) model, produce higher amplitudes in the Fourier domain. Nevertheless, the fault nonplanarity does not amplify the amplitudes sufficiently to fit the observed ones.

5.2. Effect of the Rupture Geometry in the 3-D Heterogeneous Medium

[42] Figure 5 shows the resulting particle motions for all the three source models computed assuming a heterogeneous 3-D velocity model. Only for stations FZ14 and C2W the PF model provides a linear particle motion. For the other stations (especially when compared with the results for the 1-D medium), the particle motions are relatively complex, being more similar to the observed ones. When adding the geometrical complexity by assuming source models ACNF and ACNFS, one can see that, contrarily to the modeling in the 1-D media, the basic character of the particle motions does not change much. Only at stations MFU, COAL, GH1W and FZ4 the particle motions become more elliptical.

[43] Figure 7 shows, similar to Figure 6, the synthetics for all the source models in the 3-D medium and the recorded data as a reference. As already observed for the particle motions, the synthetics are less sensitive to the variations of the fault geometry. Perhaps the only exception are the FP components at stations MFU, GH1W and FZ4. Therefore, in the following we will discuss mainly the results for the PF model since the statements also (or even more) hold for the nonplanar models ACNF and ACNFS.

[44] One can see that the fit between the simulated data and the observed data for the 3-D medium is generally worse than in Figure 6 for the 1-D media. Almost all the synthetics are characterized by smaller amplitudes and similar duration on the FN components. However, the amplitudes at the FP and V components are generally larger, which results in a better balance between the three components. The fact that the 3-D medium provides smaller amplitudes than the 1-D model can be surprising because typically including a 3-D crustal structure with low velocities under the surface results in amplified synthetic ground motion [e.g., *Frankel*, 1993; *Yomogida and Etgen*, 1993]. However, such crustal models contain basin-like structures, in which the ground motions are amplified by soft sediments and by constructive interference of waves trapped inside the basin. Our 3-D velocity model does not represent a basin-like structure but is characterized by strong velocity gradients in both vertical and horizontal directions. There are also near-surface low-velocity zones that can trap the energy and enhance the ground shaking. Our 3-D structural model also does not contain any discontinuities in wave velocities so that there are only weak refractions from the velocity gradients. Nevertheless, the 3-D structure seems to distribute the radiated energy more equally among the three components of motion, not preserving the linear polarization at the near-fault stations.

[45] Although the peak amplitudes at the FN components are smaller than those obtained for the 1-D medium, the waveforms themselves are similar to the observed ones. This amplitude difference cannot be simply explained by the small seismic moment of our source model (being linearly related to the synthetics), because it is already very close to that published by world agencies (see Table 2). The slip model would be quite different if the slip inversion was done assuming a more realistic 3-D velocity structure.

[46] As an example, Figure 9 shows for three stations the Fourier spectra corresponding to the time histories displayed in Figure 7. Generally, all the velocity components are not affected much by the fault nonplanarity. If we compare the overall shape of these spectra with respect to the spectra obtained for the 1-D media (Figure 8), they are characterized by very similar shapes especially for the FN component. However, the absolute level is smaller for the 3-D case.

5.3. Effect of Surface Topography

[47] Similar to the 3-D medium, the surface topography could produce the strong signals on the FP and V components which are not obtained by simplified models that do not incorporate the surface topography. Therefore, we compute synthetic ground motion taking into account the surface topography as given by a high-resolution digital elevation model [*Farr et al.*, 2007]. Because of the tetrahedral discretization of the computational domain, the mesh can be adapted to the topography using a surface triangulation with linear triangular element faces. We use again the velocity structure of *Thurber et al.* [2006]. However, as it is given only for a flat model surface we modify it in a way that the depth does not refer to an absolute depth but to a depth below the surface. Different approaches to combine

heterogeneous 3-D velocity models with real topography have been studied by *Ma et al.* [2007] or *Aagaard et al.* [2008].

[48] The results including the topography show only very small differences compared to the flat model, suggesting that the topography in the Parkfield area has little influence on the signals, at least in the frequency band 0.16–1 Hz used in our study. The most obvious effects are phase shifts due to the differences in station elevations when using the topographic model. However, the waveforms, amplitudes and spectra remain almost unchanged (not shown here). Therefore, in the following, we discuss only the influence of the topography on the peak amplitudes and its effects on the ratio between the FN, FP and V components.

5.4. Ratios of Peak Velocity Amplitudes

[49] As stated before, modeling in 1-D media with the PF model provides reasonable good fits at the FN components, while for some stations we are not able to explain the large amplitudes in the observed data at the FP and V components (C1E, FZ14, COAL, GH1W and FZ1).

[50] Peak velocity ratios of FN to FP and FN to V components are shown in Figure 10 for all the selected 13 stations. Note that these amplitude ratios correspond to the ratios between maximum heights and widths of the horizontal or vertical particle motions. Note that the observed data give typically ratios around 1–2 for the FN/FP ratio and about 4 for the FN/V ratio. Table 3 shows mean root-mean-square (RMS) errors between the observed and synthetic peak velocity ratios (computed from the logarithmic values) over all 13 selected stations for all the considered models.

[51] As already discussed above, there is a clearly visible large discrepancy between observed and synthetic ratios for the combination of the 1-D medium and the PF model (Figure 10, top). For example, at FZ14, COAL and FZ1 stations the FN/FP or FN/V ratio values are close to 30 or 40, respectively. For other stations this discrepancy is less but typically exceeds by far the observed ratios. The mean RMS error (from logarithmic values) is 1.54 and 1.29 for FN/FP and FN/V ratios, respectively (see Table 3).

[52] Figure 10 (top) further shows results for both the nonplanar faults in the 1-D medium. In general, introducing a larger degree of geometrical complexity of the source decreases the ratios and brings them closer to the observed values. This can be also seen from the decreased RMS values for the nonplanar models with respect to the PF model (Table 3). This general tendency is violated for station FZ3, for which the use of nonplanar models results in even larger ratio than the PF model. Although the ratios decrease for the nonplanar models, for stations such as COAL and FZ1 even the strongly deformed ACNFS model does not provide ratios as low as the observed ones.

[53] In the case of the 3-D medium (Figure 10, middle), synthetic ratios hold generally lower values than for the 1-D medium for all stations. This is manifested also by lower mean RMS values in Table 3, 0.88 and 0.82 for FN/FP and FN/V ratios, respectively. Nevertheless, stations FZ14 and FZ1 are still characterized by a strong discrepancy with the observed ratios.

[54] The increasing complexity of the fault geometry in the 3-D medium has only a minor influence on the peak ratios with respect to the PF model (see also velocity seismograms in Figure 7). Only for the above mentioned stations FZ14 and FZ1 the ratios considerably decrease when considering nonplanar faults. Thus the mean RMS decreases also even more with respect to the PF model for the 3-D medium.

[55] Let us recall that the results for the 3-D medium provide generally a worse fit with the observed data than that for the 1-D medium for which the source model with its particular slip distribution was originally determined. In particular, the FN component waveforms obtained for the 3-D medium are characterized by smaller absolute amplitudes with respect to those obtained for 1-D medium (compare Figures 6 and 7). On the other hand, the FP and V components are larger or at least similar, which causes that the FN/FP and FN/V ratios are reduced to values closer to the observed peak ratios, and the particle motions are more circular as observed for the real data (Figure 5).

[56] Finally, the introduction of the free surface topography and its effect on the peak velocity ratios is shown in Figure 10 (bottom). It leads to only little change of the FN/FP and FN/V ratios as can be seen also from the mean RMS values in Table 3. In particular, the topography effect slightly reduces ratios of the problematic stations FZ14 and FZ1. However, it is clear from Figure 10 (bottom) that the topography has a much weaker effect on the amplitudes than the variation of the fault surface geometry or especially the choice of velocity structure (see also Table 3).

6. Discussion

[57] Observed near-fault ground motions are characterized by features, which can hardly be explained by simplified models. Here, we study in particular the distribution of ground motions on horizontal and vertical components in a relatively low-frequency range (<1 Hz) for stations lying basically above the earthquake rupture. As we show on the example of the 2004 Parkfield earthquake recordings, the amplitudes observed at fault-normal (FN), fault-parallel (FP), and vertical (V) components are almost the same with complex (nonlinear) particle motions. On the other hand, simulations utilizing a planar source model (although with complex rupture evolution) and 1-D medium result in synthetics having typically a linear polarization perpendicular to the fault. Theoretically, this can be explained as a consequence of the properties of the radiation pattern. As simulations of near-fault ground motions are of interest for seismic engineers, we study certain model features that have to be considered in the modeling to provide more realistic ground motion estimates. In particular, we pay attention to the use of nonplanar rupture geometry, 3-D crustal model and free surface topography. Amongst others, as mentioned later, these three factors are capable of generating signals at the FP and V components but with different significance.

[58] We introduce three speculative fault models of increasing geometrical complexity, approximating the relocated aftershock distribution [*Thurber et al.*, 2006]: one is a perfectly planar fault (PF) as proposed by *Liu et al.* [2006], whereas the others are obtained by a piecewise interpolation of aftershock hypocenter locations; the aftershock-constrained nonplanar fault (ACNF) and the aftershock-constrained nonplanar fault with stochastic component (ACNFS). As

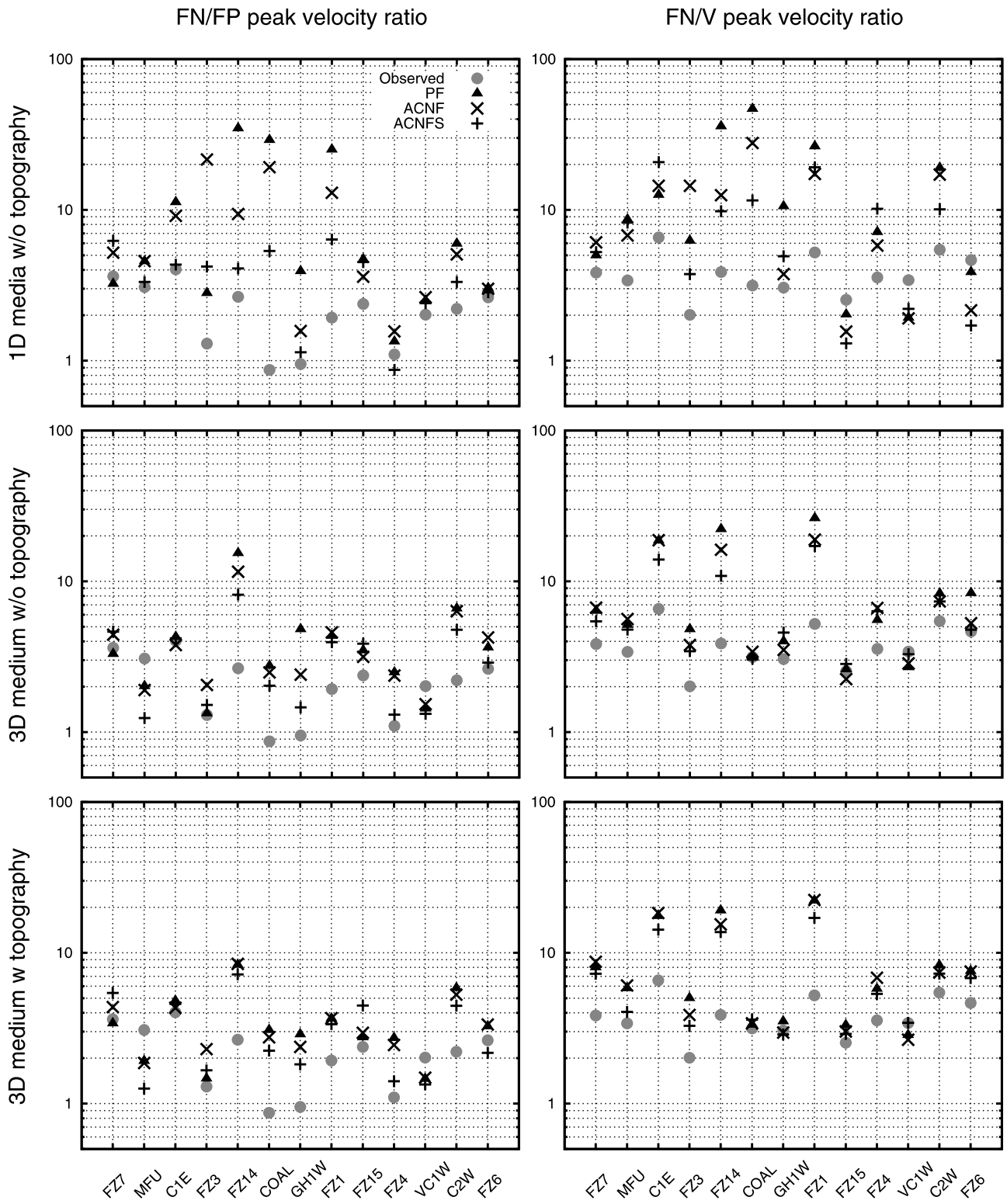

Figure 10. Results in terms of peak ground velocity (PGV) ratios for (top) the 1-D medium without topography, (middle) the 3-D medium excluding topography, and (bottom) the 3-D medium including topography.

regards the crustal model, we use both 1-D models and a 3-D velocity structure based on the model proposed by *Thurber et al.* [2006]. In both velocity structures we apply the different rupture models that all obey the same kinematic properties obtained from the slip inversion by *Liu et al.* [2006]. Finally, we incorporate the surface topography of the Parkfield region given by a digital elevation model.

[59] The effect of the kinematic nonplanar faults on the seismograms is rather small compared to the influence of the different velocity models. Interestingly, the effect of the

Table 3. RMS Errors of Peak Velocity Ratios for All the Models Considered in This Study

	FN/FP			FN/V		
Crustal model	PF	ACNF	ACNFS	PF	ACNF	ACNFS
1-D media without topography	1.54	1.39	0.75	1.29	1.09	0.88
3-D medium without topography	0.88	0.76	0.60	0.82	0.70	0.57
3-D medium with topography	0.72	0.69	0.61	0.79	0.75	0.60

rupture plane geometry is even smaller for the 3-D structure than for the 1-D one. The generally small effect of the rupture nonplanarity is due to the fact that the geometrical complexity of the fault models stays in reasonable limits given by the relatively small diffusion of the aftershocks that are assumed to delineate the rupture surface. The Parkfield area is a part of the San Andreas Fault, which, being seismically active for perhaps millions of years, has accommodated very long slip and is, therefore, relatively smooth especially in the strike direction. If a geometrically more complex rupture plane was taken into account, its sole geometry effect on the ground motion could be more severe [*Käser and Gallovič*, 2008]. However, in our opinion this would not be justifiable for the Parkfield fault.

[60] In general, mainly the fault parallel (FP) and vertical (V) components are affected by the nonplanarity of the fault. This supports the possibility to use only the FN components of stations lying almost above the fault in a slip inversion since they are less affected by the fault geometry.

[61] Figure 10 shows that for the 2004 Parkfield earthquake the 3-D velocity structure reduces the large amplitude differences obtained for a perfectly planar fault in a 1-D medium more than the increase of the fault nonplanarity. Therefore, we claim that highly accurate 3-D velocity structures are always crucial when modeling the ground motions close to the fault, especially on the FP and V components. In particular, local low-velocity structures near the surface and right below a station as well as local fault zone properties can strongly influence the wave amplitudes [see, e.g., *Jahnke et al.*, 2002; *Olsen et al.*, 2003; *Peng et al.*, 2000; *Li et al.*, 2004].

[62] Finally, we find that the effect of the free surface topography for the 2004 Parkfield earthquake is insignificant, regarding the stations of interest right above the fault and a frequency band of 0.16–1 Hz.

[63] Note that none of the models is successful in explaining the long duration of the observed records. This suggests that the *Thurber et al.*'s [2006] 3-D velocity model is missing a distinct fault zone that might generate resonant oscillation giving rise to the late arrivals [see, e.g., *Igel et al.*, 1997; *Hough et al.*, 1994; *Ben-Zion*, 1998]. However, the fault zones are usually associated with a very low Q factor that might suppress large amplitudes in coda of the synthetics. Another possible interpretation for the high amplitudes of late arrivals in some of the observed seismograms could be a strong back-scattering from other heterogeneities that are not resolved in Thurber et al.'s 3-D model. Therefore, we emphasize the importance of an additional study that will include a refined 3D model including the fault zone effects and/or the scatterers in detail to resolve this issue. Note also that such a model has to be very inhomogeneous since not all stations exhibit the strong late arrivals.

7. Conclusions

[64] In summary, our results show that a more realistic balance of the peak velocity amplitudes in the FN, FP and V components for near-fault stations are obtained when a 3-D heterogeneous velocity structure is taken into account although the 3-D model is still relatively smooth and does not include the fault zone. The effect of an increasing geometrical complexity of the rupture geometry is less important in our setting. However, its use can still lead to more realistic peak velocity ratios especially when considered together with a simple 1-D medium. The influence of the topography (in addition to a 3-D structural model) is of less significance, for the considered low-frequency band (up to 1 Hz).

[65] Our study suggests the FN components would be used in the slip inversion as they show stable features. Generally, amplitudes of our synthetic FN components in 3-D velocity structure are smaller than the other components, but their waveforms (in time and frequency domain) remain similar in the case of the 3-D or 1-D velocity model. The FP and V components seem to be more affected by the 3-D model, and, therefore, show a higher sensitivity to the quality of the 3-D model. Thus, features in the FP and V components are less robust when used in the inversion process where the velocity structure is uncertain. Furthermore, all components show a higher sensitivity to the velocity structure than to the fault geometry variations. Therefore, we support the suggestion by *Kim and Dreger* [2008] to exclude at least the FP and V components of the closest stations in the slip inversion due to their strong sensitivity to the quality of the Green's functions. To avoid the unrealistic linear polarization of the particle motions obtained from 1-D velocity models in combination with the planar fault, we strongly suggest using a well-constrained 3-D velocity model if available as it seems to be more important than the fault geometry.

[66] We emphasize that we used only a limited frequency range (up to 1 Hz). Some of the conclusions could also be true for high-frequency motion but they would have to be appropriately tested. Moreover, this is also not a complete study of all possible effects that could influence the ground motions. The existence of a fault zone structure is one of the most important effects to consider in further investigations. Furthermore, directional site effects [*Bonamassa and Vidale*, 1991], medium anisotropy [*Cochran et al.*, 2006], or nonlinear behavior [*Bataille and Calisto*, 2008; *Karabulut and Bouchon*, 2007; *Wu and Chen*, 2009] might also contribute to better explain the observed data.

[67] **Acknowledgments.** The work has been supported by EU project ITSAK-GR (MTKD-CT-2005-029627), the Grant Agency of Charles University (279/2006/B-GEO/MFF), MSM0021620800, Grant Agency of the Czech Republic (205/08/P013 and 205/07/0502), and Deutsche Forschungsgemeinschaft (Emmy Noether-Program KA 2281/2-1). We also thank the Leibniz Rechenzentrum in Garching for their support to compute the numerical results of the ADER-DG method presented in this work.

References

Aagaard, B. T., T. M. Brocher, D. Dolenc, D. Dreger, R. W. Graves, S. Harmsen, S. Hartzell, S. Larsen, and M. L. Zoback (2008), Ground motion modeling of the 1906 San Francisco earthquake I: Validation using the 1989 Loma Prieta earthquake, *Bull. Seismol. Soc. Am.*, *98*, 989–1011, doi:10.1785/0120060409.

Aki, K., and P. G. Richards (2002), *Quantitative Seismology*, Univ. Sci. Books, Sausalito, Calif.

Bakun, W. H., and T. V. McEvilly (1979), Earthquakes near Parkfield, California: Comparing the 1934 and 1966 sequences, *Science*, *205*, 1375–1377, doi:10.1126/science.205.4413.1375.

Bataille, K., and I. Calisto (2008), Seismic coda due to non-linear elasticity, *Geophys. J. Int.*, *172*(2), 572–580, doi:10.1111/j.1365-246X.2007.03639.x.

Ben-Zion, Y. (1990), The response of two half spaces to point dislocations at the material interface, *Geophys. J. Int.*, *101*, 507–528, doi:10.1111/j.1365-246X.1990.tb05567.x., (Corrigendum to "the response of two half spaces to point dislocations at the material interface," *Geophys. J. Int.*, *137*, 580–582, doi:10.1046/j.1365-246X.1999.1372001.x, 1999.).

Ben-Zion, Y. (1998), Properties of seismic fault zone waves and their utility for imaging low-velocity structures, *J. Geophys. Res.*, *103*(B6), 12,567–12,585, doi:10.1029/98JB00768.

Ben-Zion, Y., and P. Malin (1991), San Andreas Fault zone head waves near Parkfield, California, *Science*, *251*, 1592–1594, doi:10.1126/science.251.5001.1592.

Bonamassa, O., and J. E. Vidale (1991), Directional site resonances observed from aftershocks of the 18th October 1989 Loma Prieta earthquake, *Bull. Seismol. Soc. Am.*, *81*, 1945–1957.

Boore, D. M. (1983), Stochastic simulation of high-frequency ground motions based on seismological models of the radiated spectra, *Bull. Seismol. Soc. Am.*, *73*, 1865–1894.

Bouchon, M. (1973), Effect of topography on surface motions, *Bull. Seismol. Soc. Am.*, *63*(3), 615–632.

Bouchon, M. (1981), A simple method to calculate Green's functions for elastic layered media, *Bull. Seismol. Soc. Am.*, *71*, 959–971.

Bouchon, M., C. A. Schultz, and M. N. Toksoz (1996), Effect of 3D topography on seismic motion, *J. Geophys. Res.*, *101*(B3), 5835–5846, doi:10.1029/95JB02629.

Brocher, T. (2005), Empirical relations between elastic wavespeeds and density in the Earth's crust, *Bull. Seismol. Soc. Am.*, *95*, 2081–2092, doi:10.1785/0120050077.

Cochran, E. S., Y.-G. Li, and J. E. Vidale (2006), Anisotropy in the shallow crust observed around the San Andreas Fault before and after the 2004 *M* 6.0 Parkfield earthquake, *Bull. Seismol. Soc. Am.*, *96*(4b), S364–S375, doi:10.1785/0120050804.

Dreger, D. S., L. Gee, P. Lombard, M. H. Murray, and B. Romanowicz (2005), Rapid finite-source analysis and near-fault strong ground motions: Application to the 2003 M_w 6.5 San Simeon and 2004 M_w 6.0 Parkfield earthquakes, *Seismol. Res. Lett.*, *76*, 40–48, doi:10.1785/gssrl.76.1.40.

Dumbser, M., and M. Käser (2006), An arbitrary high order discontinuous Galerkin method for elastic waves on unstructured meshes II: The three-dimensional case, *Geophys. J. Int.*, *167*(1), 319–336, doi:10.1111/j.1365-246X.2006.03120.x.

Eberhart-Phillips, D., and A. J. Michael (1993), Three-dimensional velocity structure, seismicity, and fault structure in the Parkfield region, central California, *J. Geophys. Res.*, *98*(B9), 15,737–15,758, doi:10.1029/93JB01029.

Farr, T. G., et al. (2007), The Shuttle Radar Topography Mission, *Rev. Geophys.*, *45*, RG2004, doi:10.1029/2005RG000183.

Frankel, A. (1993), Three-dimensional simulations of ground motions in the San Benardino valley, California, for hypothetical earthquakes on the San Andreas Fault, *Bull. Seismol. Soc. Am.*, *83*, 1020–1041.

Frohlich, C. (1994), Earthquakes with non-double-couple mechanisms, *Science*, *264*, 804–809, doi:10.1126/science.264.5160.804.

Gallovic, F., and J. Brokešová (2007), Hybrid k-squared source model for strong ground motion simulations: Introduction, *Phys. Earth Planet. Inter.*, *160*, 34–50, doi:10.1016/j.pepi.2006.09.002.

Geli, L., P. Y. Bard, and B. Jullien (1988), The effect of topography on earthquake ground motion: A review and new results, *Bull. Seismol. Soc. Am.*, *78*(1), 42–63.

Harris, R. A., and J. R. Arrowsmith (2006), Introduction to the special issue on the 2004 Parkfield earthquake and the Parkfield earthquake prediction experiment, *Bull. Seismol. Soc. Am.*, *96*(4b), S1–S10, doi:10.1785/0120050831.

Hartzell, S., M. Guatteri, P. M. Mai, P. Liu, and M. Fisk (2005), Calculation of broadband time histories of ground motion, part II: Kinematic and dynamic modeling using theoretical Green's functions and comparison with the 1994 Northridge earthquake, *Bull. Seismol. Soc. Am.*, *95*(2), 614–645, doi:10.1785/0120040136.

Hartzell, S., P. Liu, C. Mendoza, C. Ji, and K. M. Larson (2007), Stability and uncertainty of finite-fault slip inversions: Applications to the 2004 Parkfield, California, earthquake, *Bull. Seismol. Soc. Am.*, *97*(6), 1911–1934, doi:10.1785/0120070080.

Hough, S. E., Y. Ben-Zion, and P. Leary (1994), Fault-zone waves observed at the southern Joshua Tree earthquake rupture zone, *Bull. Seismol. Soc. Am.*, *84*, 761–767.

Igel, H., Y. Ben-Zion, and P. C. Leary (1997), Simulation of SH- and P-SV-wave propagation in fault zones, *Geophys. J. Int.*, *128*(3), 533–546, doi:10.1111/j.1365-246X.1997.tb05316.x.

Irikura, K. (1996), Near-fault ground motions causing the great Hanshin Earthquake disaster (in Japanese), *Annu. Disas. Prev. Res. Inst. Kyoto Univ.*, *39*(A), 17–33.

Jahnke, G., H. Igel, and Y. Ben-Zion (2002), Three-dimensional calculations of fault-zone-guided waves in various irregular structures, *Geophys. J. Int.*, *151*(2), 416–426, doi:10.1046/j.1365-246X.2002.01784.x.

Karabulut, H., and M. Bouchon (2007), Spatial variability and non-linearity of strong ground motion near a fault, *Geophys. J. Int.*, *170*, 262–274, doi:10.1111/j.1365-246X.2007.03406.x.

Käser, M., and M. Dumbser (2006), An arbitrary high order discontinuous Galerkin method for elastic waves on unstructured meshes I: The two-dimensional isotropic case with external source terms, *Geophys. J. Int.*, *166*(2), 855–877, doi:10.1111/j.1365-246X.2006.03051.x.

Käser, M., and F. Gallovič (2008), Effects of complicated 3D rupture geometries on earthquake ground motion and their implications: A numerical study, *Geophys. J. Int.*, *172*(1), 276–292, doi:10.1111/j.1365-246X.2007.03627.x.

Kim, A., and D. S. Dreger (2008), Rupture process of the 2004 Parkfield earthquake from near-fault seismic waveform and geodetic records, *J. Geophys. Res.*, *113*, B07308, doi:10.1029/2007JB005115.

Lewis, M. A., Y. Ben-Zion, and J. J. McGuire (2007), Imaging the deep structure of the San Andreas Fault south of Hollister with joint analysis of fault zone head and direct P arrivals, *Geophys. J. Int.*, *169*, 1028–1042, doi:10.1111/j.1365-246X.2006.03319.x.

Li, Y.-G., P. Leary, K. Aki, and P. Malin (1990), Seismic trapped modes in the Oroville and San Andreas Fault zones, *Science*, *249*, 763–766, doi:10.1126/science.249.4970.763.

Li, Y.-G., J. H. Vidale, and E. S. Cochran (2004), Low-velocity damaged structure of the San Andreas Fault at Parkfield from fault zone trapped waves, *Geophys. Res. Lett.*, *31*, L12S06, doi:10.1029/2003GL019044.

Liu, P., S. Custodio, and R. J. Archuleta (2006), Kinematic inversion of the 2004 *M* 6.0 Parkfield earthquake including an approximation to site effects, *Bull. Seismol. Soc. Am.*, *96*(4b), S143–S158, doi:10.1785/0120050826, (Erratum to kinematic inversion of the 2004 M 6.0 Parkfield earthquake including an approximation to site effects, *Bull. Seismol. Soc. Am.*, *98*, 2101, doi:10.1785/0120080959, 2008.).

Ma, S., R. J. Archuleta, and M. T. Page (2007), Effects of large-scale surface topography on ground motions, as demonstrated by a study of the San Gabriel Mountains, Los Angeles, California, *Bull. Seismol. Soc. Am.*, *97*(6), 2066–2079, doi:10.1785/0120070040.

Mai, P. M., and G. C. Beroza (2003), A hybrid method for calculating near-source, broadband seismograms from an extended source, *Phys. Earth Planet. Inter.*, *137*, 183–199, doi:10.1016/S0031-9201(03)00014-1.

Michael, A. J., and D. Eberhart-Phillips (1991), Relations among fault behaviour, subsurface geology, and three-dimensional velocity models, *Science*, *253*, 651–654, doi:10.1126/science.253.5020.651.

Michelini, A., and T. V. McEvilly (1991), Seismological studies at Parkfield, part I: Simultaneous inversion for velocity structure and hypocenters using cubic B-splines parameterization, *Bull. Seismol. Soc. Am.*, *81*, 524–552.

Nadeau, R., W. Foxall, and T. V. McEvilly (1995), Clustering and periodic recurrence of microearthquakes on the San Andreas Fault at Parkfield, California, *Science*, *267*, 503–507, doi:10.1126/science.267.5197.503.

Olsen, K. B., S. M. Day, and C. R. Bradley (2003), Estimation of *Q* for long-period (>2 sec) waves in the Los Angeles basin, *Bull. Seismol. Soc. Am.*, *93*(2), 627–638, doi:10.1785/0120020135.

Peng, Z., Y. Ben-Zion, A. J. Michael, and L. Zhu (2003), Quantitative analysis of seismic fault zone waves in the rupture zone of the 1992 Landers, California, earthquake: Evidence for a shallow trapping structure, *Geophys. J. Int.*, *155*(3), 1021–1041, doi:10.1111/j.1365-246X.2003.02109.x.

Pitarka, A., P. Somerville, Y. Fukushima, T. Uetake, and K. Irikura (2000), Simulation of near-fault strong-ground motion using hybrid Green's functions, *Bull. Seismol. Soc. Am.*, *90*, 566–586, doi:10.1785/0119990108.

Rymer, M. J., et al. (2006), Surface fault slip associated with the 2004 Parkfield, California, earthquake, *Bull. Seismol. Soc. Am.*, *17*, 211–220.

Simpson, R. W., M. Barall, J. Langbein, J. R. Murray, and M. J. Rymer (2006), San Andreas Fault geometry in the Parkfield, California, region, *Bull. Seismol. Soc. Am.*, *96*(4b), S28–S37, doi:10.1785/0120050824.

Thurber, C., H. Zhang, F. Waldhauser, J. Hardebeck, A. Michael, and D. Eberhart-Phillips (2006), Three-dimensional compressional wavespeed model, earthquake relocations, and focal mechanisms for the Parkfield, California, region, *Bull. Seismol. Soc. Am.*, *96*(4b), S38–S49, doi:10.1785/0120050825.

Toppozada, T. R., D. M. Branum, M. S. Reichle, and C. L. Hallstrom (2002), San Andreas Fault zone, California; M $\geq$ 5.5 earthquake history, *Bull. Seismol. Soc. Am.*, *92*, 2555–2601, doi:10.1785/0120000614.

Unsworth, M. J., P. E. Malin, G. D. Egbert, and J. R. Booker (1997), Internal structure of the San Andreas Fault at Parkfield, *Calif. Geol.*, *25*(4), 359–362.

Wang, H., H. Igel, F. Gallovič, A. Cochard, and M. Ewald (2008), Source-related variations of ground motions in 3-D media: Application to the Newport-Inglewood fault, Los Angeles basin, *Geophys. J. Int.*, *175*, 202–214, doi:10.1111/j.1365-246X.2008.03878.x.

Wu, Z. L., and Y. T. Chen (2003), Definition of seismic moment at a discontinuity interface, *Bull. Seismol. Soc. Am.*, *93*, 1832–1834, doi:10.1785/0120020234.

Wu, Z. L., and Y. T. Chen (2009), Non-linearity and temporal changes of fault zone site response associated with strong ground motion, *Geophys. J. Int.*, *176*(1), 265–278, doi:10.1111/j.1365-246X.2008.04005.x.

Yomogida, K., and J. T. Etgen (1993), 3-D wave propagation in the Los Angeles basin for the Whittier-Narrows earthquake, *Bull. Seismol. Soc. Am.*, *83*, 1325–1344.

Zahradník, J., and L. Urban (1984), Effect of a simple mountain range on underground seismic motion, *Geophys. J. R. Astron. Soc.*, *79*, 167–183.

J. Burjánek, Swiss Seismological Service, Institute of Geophysics, ETH Zurich, No. 69.4, Soneggstrasse 5, CH-8092 Zürich, Switzerland.

F. Gallovič, Department of Geophysics, Faculty of Mathematics and Physics, Charles University, V Holešovičkách 2, Prague 8, 180 00, Czech Republic. (gallovic@karel.troja.mff.cuni.cz)

M. Käser, Department of Earth and Environmental Sciences, Ludwig Maximilians University, Theresienstrasse 41, D-80333 Munich, Germany.

C. Papaioannou, ITSAK, PO Box 53 Foinikas, Thessaloniki GR-55102, Greece.

GEOPHYSICS, VOL. 75, NO. 5 (SEPTEMBER-OCTOBER 2010); P. D47–D56, 7 FIGS., 3 TABLES.
10.1190/1.3479489

Rotational motions in homogeneous anisotropic elastic media

Nguyen Dinh Pham[1], Heiner Igel[2], Josep de la Puente[3], Martin Käser[2], and Michael A. Schoenberg[4]

ABSTRACT

Rotational motions in homogeneous anisotropic elastic media are studied under the assumption of plane wave propagation. The main goal is to investigate the influences of anisotropy in the behavior of the rotational wavefield. The focus is on P-waves that theoretically do not generate rotational motion in isotropic media. By using the Kelvin–Christoffel equation, expressions are obtained of the rotational motions of body waves as a function of the propagation direction and the coefficients of the elastic modulus matrix. As a result, the amplitudes of the rotation rates and their radiation patterns are quantified and it is concluded that (1) for strong local earthquakes and typical reservoir situations quasi P-rotation rates induced by anisotropy are significant, recordable, and can be used for inverse problems; and (2) for teleseismic wavefields, anisotropic effects are unlikely to be responsible for the observed rotational energy in the P coda.

INTRODUCTION

Seismological studies are traditionally based on the observation, processing, and inversion of three orthogonal components of translational ground motions (displacement, velocity, or acceleration). In theory, to fully describe the motion of the solid volume around a point, one needs to consider not only three components of translation but also six components of strain and three components of rotations (see Aki and Richards, 2002; Stein and Wysession, 2003; Cochard et al., 2006). Although geophysical studies associated with translational motions and strain have attained a large success, the full benefits of rotational motions are still under investigation, and this type of signal has been ignored for a long time. This is mainly because sensors for rotational motions with sufficient resolution were not available until recently. After advances in laser technology, instruments that consistently record rotational ground motions around one axis or all three orthogonal axes have already been developed and tested (McLeod et al., 1998; Pancha et al., 2000; Schreiber et al., 2006, 2009; Wassermann et al., 2009). As a consequence, studies that aim to exploit the additional information given by collocated measurements of translational and rotational ground motion are growing rapidly (e.g., Igel et al., 2005, 2007; Cochard et al., 2006; Suryanto et al., 2006; Pham et al., 2009a, 2009b; Ferreira and Igel, 2009; Fichtner and Igel, 2009; Bernauer et al., 2009). For example, several recent studies covering many aspects of rotational ground motions have been presented in a special issue on Rotational Seismology and Engineering Applications of the *Bulletin of the Seismological Society of America* in May 2009 (Lee et al., 2009b). In particular, a review by Lee et al. (2009a) envisions the emergence of a new branch in the fields of observational seismology and earthquake engineering.

Once the technology for its measurement has become available, the key question is: What kind of information do we expect to retrieve from carrying out joint measurements of translations and rotations — compared with just translational observations? Early studies (Takeo and Ito, 1997) indicate that earthquake rupture histories can be better constrained with measurements of rotational motions. Furthermore, the multicomponent point measurements of rotational and translational motions allow the estimation of wavefield properties (e.g., phase velocities, propagation direction; Igel et al., 2007, Cochard et al., 2006) and allow the recovery of shear-wave structure without traveltime information (Fichtner and Igel, 2009; Bernauer et al., 2009) as well as constraining the scattering properties of the near-receiver crustal structure (Pham et al., 2009b).

An aspect that has been missing in previous studies is the role that the elastic anisotropy might play in the rotational measurements. It is well known that anisotropy is a ubiquitous phenomenon in the

Manuscript received by the Editor 16 July 2009; revised manuscript received 14 April 2010; published online 5 October 2010.
[1]Formerly Ludwig-Maximilians-Universität, Department of Earth and Enviornmental Sciences, Geophysics Section, Munich, Germany; presently Vietnam Academy of Science and Technology, Institute of Geophysics, Hanoi, Vietnam.
[2]Ludwig-Maximilians-Universität, Department of Earth and Environmental Sciences, Geophysics Section, Munich, Germany. E-mail: nguyendp@igp-vast.vn; ndpseis@googlemail.com.
[3]Institut de Ciències del Mar, Barcelona Center for Subsurface Imaging, Department of Marine Geology, Barcelona, Spain.
[4]Earth Sciences Division, Lawrence Berkeley National Laboratory, Berkeley, CA (Michael A. Schoenberg passed away on 29 August 2008).

earth's crust and upper mantle. Many authors (e.g., Crampin, 1981, 1984; Crampin et al., 1982, 1984; Sams et al., 1993; Larner, 1993) report the influence of anisotropic effects on seismic processing and interpretation. Tsvankin (1996) emphasized that progress in seismic inversion and processing in anisotropic media depend on our ability to relate different seismic signatures to the anisotropy parameters. In reservoir and drilling engineering, the simultaneous determination of the elastic coefficients and anisotropy parameters helps in predicting flow paths for improved oil recovery, designing a hydraulic fracturing scheme, determining mud weight and selecting drill bit, and preventing hole collapse during and after drilling (Wang, 2002). At present, the anisotropy parameters can only be retrieved using laboratory measurements or arrays of standard translational seismometers deployed, at least, along a line.

At the onset of this study, there are several open questions: (1) How does anisotropy affect rotational ground motions? (2) Can rotational motions help to constrain anisotropic properties? (3) What instrument configurations are necessary to extract the relevant information? We will attempt to give preliminary answers to these questions in the following sections.

The main goal of this study is to estimate the amplitudes of the rotational motions that we can expect in various geophysical problems and their dependence on the anisotropic properties of the medium and the propagation direction. We first approach the problem in an analytical way, focusing on the solution for plane waves in linear elastic anisotropic media. Moreover, we provide estimates of the expected amplitudes of rotational motions induced by P-waves as a function of the degree of anisotropy. Last but not least, this study confirms the fact that anisotropy alone cannot account for the P coda vertical rotational motions observed on a ring laser at the Fundamental station in Wettzell, Germany, as reported by Igel et al. (2007) and Pham et al. (2009b).

FUNDAMENTAL THEORY

In the framework of classical elasticity, a general plane-harmonic-wave solution for the displacement vector **u** of body waves is

$$\mathbf{u} = A\mathbf{n}\exp[i(\omega t - \boldsymbol{\kappa}\cdot\mathbf{x})], \tag{1}$$

where A is the ground displacement peak amplitude; $\mathbf{n} = n_1\mathbf{e}_1 + n_2\mathbf{e}_2 + n_3\mathbf{e}_3$ is the unit vector denoting the direction of the particle displacement (i.e., the wavefield polarization; $\mathbf{e}_i$ ($i = 1,2,3$) are the unit vectors along the coordinate axes); $n_i = u_i/\sqrt{u_1u_1^* + u_2u_2^* + u_3u_3^*} = \|u_i\|/A$ are the direction cosines of **n** and i is the imaginary unit; superscript * represents complex conjugate; and $\|z\|$ stands for magnitude of the complex number z. Furthermore, the wavenumber vector is $\boldsymbol{\kappa} = \omega/v(\ell_1\mathbf{e}_1 + \ell_2\mathbf{e}_2 + \ell_3\mathbf{e}_3) = \omega/v\mathbf{l}$ and the quantities ω, v, and $\mathbf{l} = \ell_1\mathbf{e}_1 + \ell_2\mathbf{e}_2 + \ell_3\mathbf{e}_3$ are, respectively, the angular frequency, the phase velocity, and the unit vector denoting the propagation direction of the plane wave. Finally, the direction cosines of **l** are denoted ℓ_i.

The rotational motions $\boldsymbol{\Omega}$ generated by the plane wave expressed by equation 1 can be calculated by taking half of the curl of the displacement field (Igel et al., 2005, Cochard et al., 2006)

$$\boldsymbol{\Omega} = \frac{1}{2}(\nabla\times\mathbf{u}) = -\frac{A}{2}i\boldsymbol{\kappa}\times\mathbf{n}\exp[i(\omega t - \boldsymbol{\kappa}\cdot\mathbf{x})]$$
$$= -\frac{A}{2}\frac{i\omega}{v}\begin{pmatrix}\ell_2n_3 - \ell_3n_2\\ \ell_3n_1 - \ell_1n_3\\ \ell_1n_2 - \ell_2n_1\end{pmatrix}\exp\left[i\omega\left(t - \frac{1}{v}\mathbf{l}\cdot\mathbf{x}\right)\right]. \tag{2}$$

The corresponding rotation rates $\dot{\boldsymbol{\Omega}}$ are then

$$\dot{\boldsymbol{\Omega}} = \partial_t\boldsymbol{\Omega} = \frac{A}{2}\frac{\omega^2}{v}\begin{pmatrix}\ell_2n_3 - \ell_3n_2\\ \ell_3n_1 - \ell_1n_3\\ \ell_1n_2 - \ell_2n_1\end{pmatrix}\exp\left[i\omega\left(t - \frac{1}{v}\mathbf{l}\cdot\mathbf{x}\right)\right]. \tag{3}$$

Looking at equation 3, one can recognize that, in homogeneous unbounded isotropic media, P-waves do not generate any rotational motion. This is because, for P-waves, the vectors **l** and **n** are identical, in opposition to S-waves, which have perpendicular **l** and **n** and hence produce rotation motion. Hence, in unbounded isotropic media, rotations can only be the consequence of an S-wave. However, this is no longer the case in anisotropic elastic media in which the phase velocity v and the direction cosines n_i depend on the wave propagation direction ℓ_i. Hence, P-waves in anisotropic media can, in general, produce rotational motions. As a consequence, the measurement of significant rotational signals during the passage of a P-wave can be regarded as an indicator of anisotropy.

To understand the behavior of the rotational motions in anisotropic elastic media, we must first realize that the phase velocity v, the polarization n_i, and the material properties are bound by the Kelvin–Christoffel equation (see e.g., Musgarve, 1970; Carcione, 2001, p. 11)

$$(\boldsymbol{\Gamma} - \rho v^2\mathbf{I}_3)\cdot\mathbf{u} = 0, \tag{4}$$

where ρ is the material density — a constant isotropic parameter; $\mathbf{I}_3$ is the 3×3 identity matrix; $\boldsymbol{\Gamma}$ is the symmetric Kelvin–Christoffel matrix

$$\boldsymbol{\Gamma} = \mathbf{L}\cdot\mathbf{C}\cdot\mathbf{L}^{\mathrm{T}}, \tag{5}$$

$$\mathbf{L} = \begin{pmatrix}\ell_1 & 0 & 0 & 0 & \ell_3 & \ell_2\\ 0 & \ell_2 & 0 & \ell_3 & 0 & \ell_1\\ 0 & 0 & \ell_3 & \ell_2 & \ell_1 & 0\end{pmatrix}, \tag{6}$$

and **C** is the elastic modulus matrix and is given by

$$\mathbf{C} = \begin{pmatrix}c_{11} & c_{12} & c_{13} & c_{14} & c_{15} & c_{16}\\ c_{12} & c_{22} & c_{23} & c_{24} & c_{25} & c_{26}\\ c_{13} & c_{23} & c_{33} & c_{34} & c_{35} & c_{36}\\ c_{14} & c_{24} & c_{34} & c_{44} & c_{45} & c_{46}\\ c_{15} & c_{25} & c_{35} & c_{45} & c_{55} & c_{56}\\ c_{16} & c_{26} & c_{36} & c_{46} & c_{56} & c_{66}\end{pmatrix}. \tag{7}$$

Whenever a material possesses more than two independent parameters defining the entries of **C**, the seismic wave velocities differ depending on the propagation direction and the material is called "anisotropic." A material that has all 21 coefficients in **C** independent is called a material of the triclinic symmetry class, or simply tri-

clinic material. This is the most general case of anisotropy and includes as special cases all of the other crystalline symmetry classes (i.e., monoclinic, trigonal, tetragonal, orthorhombic, hexagonal, cubic, and isotropic). One of the most important anisotropy symmetry classes for seismological purposes is transverse isotropy. When the symmetry axis coincides with $\mathbf{e}_3$ the elastic modulus matrix $\mathbf{C}_{\mathrm{TI}}$ of a transversely isotropic material is (see e.g., Thomsen, 1986; Carcione, 2001, p. 6)

$$\mathbf{C}_{\mathrm{TI}} = \begin{pmatrix} c_{11} & c_{12} & c_{13} & 0 & 0 & 0 \\ c_{12} & c_{11} & c_{13} & 0 & 0 & 0 \\ c_{13} & c_{13} & c_{33} & 0 & 0 & 0 \\ 0 & 0 & 0 & c_{55} & 0 & 0 \\ 0 & 0 & 0 & 0 & c_{55} & 0 \\ 0 & 0 & 0 & 0 & 0 & c_{66} \end{pmatrix}, \quad 2c_{66} = c_{11} - c_{12}. \tag{8}$$

The isotropic case can be considered as a special case of anisotropy in which $c_{11} = c_{22} = c_{33} = \lambda + 2\mu$, $c_{12} = c_{13} = c_{23} = \lambda$, $c_{44} = c_{55} = c_{66} = \mu$ and all of the other coefficients are equal to zero. Here λ and μ are the Lamé coefficients of the material.

Explicitly, the components of the Kelvin–Christoffel matrix are

$$\begin{aligned}
\Gamma_{11} &= c_{11}\ell_1^2 + c_{66}\ell_2^2 + c_{55}\ell_3^2 + 2c_{56}\ell_2\ell_3 + 2c_{15}\ell_3\ell_1 \\
&\quad + 2c_{16}\ell_1\ell_2 \\
\Gamma_{22} &= c_{66}\ell_1^2 + c_{22}\ell_2^2 + c_{44}\ell_3^2 + 2c_{24}\ell_2\ell_3 + 2c_{46}\ell_3\ell_1 \\
&\quad + 2c_{26}\ell_1\ell_2 \\
\Gamma_{33} &= c_{55}\ell_1^2 + c_{44}\ell_2^2 + c_{33}\ell_3^2 + 2c_{34}\ell_2\ell_3 + 2c_{35}\ell_3\ell_1 \\
&\quad + 2c_{45}\ell_1\ell_2 \\
\Gamma_{12} &= c_{16}\ell_1^2 + c_{26}\ell_2^2 + c_{45}\ell_3^2 + (c_{46} + c_{25})\ell_2\ell_3 \\
&\quad + (c_{14} + c_{56})\ell_3\ell_1 + (c_{12} + c_{66})\ell_1\ell_2 \\
\Gamma_{13} &= c_{15}\ell_1^2 + c_{46}\ell_2^2 + c_{35}\ell_3^2 + (c_{45} + c_{36})\ell_2\ell_3 \\
&\quad + (c_{13} + c_{55})\ell_3\ell_1 + (c_{14} + c_{56})\ell_1\ell_2 \\
\Gamma_{23} &= c_{56}\ell_1^2 + c_{24}\ell_2^2 + c_{34}\ell_3^2 + (c_{44} + c_{23})\ell_2\ell_3 \\
&\quad + (c_{36} + c_{45})\ell_3\ell_1 + (c_{25} + c_{46})\ell_1\ell_2.
\end{aligned} \tag{9}$$

It is clear that equation 4 is an eigenequation for the eigenvalues $(\rho v^2)_{\mathrm{m}}$ and eigenvectors $(\mathbf{u})_{\mathrm{m}}$, $m = 1,2,3$. The dispersion relation is expressed by

$$\det(\mathbf{\Gamma} - \rho v^2 \mathbf{I}_3) = 0, \tag{10}$$

from which we can obtain the three phase velocities v_{m} $(m = 1,2,3)$ as a function of the direction cosines ℓ_{i} and the independent coefficients of the elastic modulus matrix $\mathbf{C}$. These velocities correspond to the three body wave modes propagating in an unbounded homogeneous medium: the highest value of v_{m} corresponds to a quasi-P-wave (qP), whereas the other two correspond to quasi-S-waves qS1 and qS2, usually ordered in descending v_{m} value. For each solution v, we obtain from equation 4 an associated eigenvector $\mathbf{u}$; hence, the polarizations n_{i} are fully determined. As a consequence, finding the rotation rates produced by any plane wave is possible for a given anisotropic material. First, we set a propagation direction and wave mode, so that we can find the values v and n_{i} using equations 10 and 4. Substituting these values into equation 3 and setting a value for the wave's peak displacement A and frequency ω, one finally obtains the three components of the rotation rate $\dot{\mathbf{\Omega}}$.

We can now use the aforementioned process in an effort to visualize the influence that anisotropy has in the behavior of the rotational wavefield. In Figure 1, we use a plotting similar to that used by de la Puente (2008) to depict the variability of the phase velocities and peak rotation rates depending on the propagation direction. In particular, we show the values of peak rotation rates around two axes $\boldsymbol{\theta}$ and $\boldsymbol{\phi}$ generated by plane waves in a transversely isotropic (TI) medium. The three axes $\mathbf{l}$ (corresponding to the propagation direction), $\boldsymbol{\theta}$, and $\boldsymbol{\phi}$ of an orthogonal Cartesian coordinate system are defined in Appendix A. For the particular case of a wave propagating in the x direction, we have $\mathbf{l} = \mathbf{e}_1$, $\boldsymbol{\theta} = \mathbf{e}_3$ and $\boldsymbol{\phi} = \mathbf{e}_3$, so that the three directions coincide with the Cartesian axes x, y, and z. The rotation rates in all cases are obtained by rotating the three components of the rotation rates that we obtained using equation 3, as shown in Appendix B. We assume plane harmonic waves of peak displacement $A = 10^{-5}$ m and period $T = 1$ s propagating in Mesaverde clay shale. The elastic parameters of the material are taken from Thomsen (1986) and are presented in Table 1. The plots show the highest values (phase velocity or rotation rates around $\boldsymbol{\theta}$ and $\boldsymbol{\phi}$ components) for each propagation direction. Our calculations for this particular material reveal that, for all qP-, qS1-, and qS2-waves, no rotational motion around the wave-propagation direction $\mathbf{l}$ is generated. The same result (i.e., the component of the rotation rate vector in the propagation direction $\mathbf{l}$ is zero) is also obtained for the monoclinic, orthorhombic, and tri-

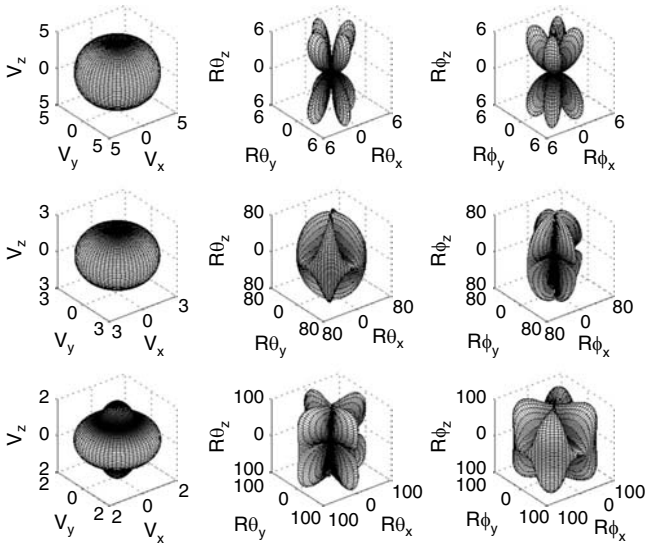

Figure 1. Example of isosurfaces of the peak phase velocity in km/s (left column) and peak rotation rate around two axes $\boldsymbol{\theta}$ and $\boldsymbol{\phi}$ (middle and right columns) in nrad/s as a function of the wave propagation direction. The plots shown correspond to qP- (top row), qS1- (middle row), and qS2- (bottom row) waves. A plane harmonic wave of peak displacement 10^{-5} m and period $T = 1$ s propagating in a TI material (Mesaverde clay-shale) was assumed. The propagation direction $\mathbf{l}$ of the plane wave together with the $\boldsymbol{\theta}$ and $\boldsymbol{\phi}$ axes create an orthogonal Cartesian axis system. The vertical propagation direction in this example coincides with the symmetry axis of the TI material. For all three wave types, no rotational motion around the propagation direction $\mathbf{l}$ is generated.

clinic materials for which the elastic coefficients were mentioned in de la Puente (2008). In fact, this result follows directly from equation 3 if we project the value of the rotation rate on the $\mathbf{l}$ direction, which results in $\mathbf{l}\cdot\dot{\boldsymbol{\Omega}}=0$, regardless of the material's properties.

Figure 1 shows us that the phase velocity and rotation rates strongly depend on the wave's propagation direction. The anisotropic behavior is clearly revealed by the apparition of rotational motions caused by qP-waves, which should be zero for all directions in homogeneous isotropic materials, as we mentioned previously. This again suggests that qP rotational motions contain information on anisotropic properties of the medium. It should be noted that there is more than one order of magnitude difference between the rotational amplitude of qP-waves and that of qS-waves in this example. Thus, to know if qP rotational motions can be used for inversion, it is fundamental to investigate the magnitude of the rotation rates associated with qP for different levels of anisotropy.

Although there are several symmetry classes in anisotropy, the elastic anisotropy of rocks is usually moderate and, in most cases, a TI symmetry is sufficient to describe its effects in the wavefield (e.g., Tsvankin, 1996; Guéguen and Sarout, 2009). Moreover, transverse isotropy is also acknowledged as the anisotropic case of broadest geophysical applicability (Thomsen, 1986). Thus, hereafter in this study our investigations focus only on the rotational motions caused by qP-waves in the particular case of a $(\mathbf{e}_1,\mathbf{e}_3)$ plane of a TI medium with $\mathbf{e}_3$ as the axis of symmetry.

Before going further, we attempt to verify the analytical equations that we have. We will compare in the following section the peak rotation rates of qP-waves obtained using this analytical solution with the results obtained from numerical simulations using the ADER-DG method (the combination of a Discontinuous Galerkin finite element method and an Arbitrary high-order DERivative time integration approach developed by Dumbser and Käser, 2006 and extended to anisotropic materials by de la Puente et al., 2007).

qP ROTATIONAL MOTIONS IN TI MEDIA

When considering plane P-waves propagating in the $(\mathbf{e}_1,\mathbf{e}_3)$ plane ($\ell_2=0, n_2=0$) of a TI medium whose symmetry axis is $\mathbf{e}_3$, equation 3 can be rewritten as

$$\dot{\boldsymbol{\Omega}}=\frac{A}{2}\frac{\omega^2}{v}\begin{pmatrix}0\\ \ell_3 n_1-\ell_1 n_3\\ 0\end{pmatrix}\exp\left[i\omega\left(t-\frac{1}{v}\mathbf{l}\cdot\mathbf{x}\right)\right], \quad (11)$$

and the Kelvin-Christoffel equation 4 can be simplified as

$$\begin{pmatrix} c_{11}\ell_1^2+c_{55}\ell_3^2-\rho v^2 & 0 & (c_{13}+c_{55})\ell_1\ell_3\\ 0 & c_{66}\ell_1^2+c_{55}\ell_3^2-\rho v^2 & 0\\ (c_{13}+c_{55})\ell_1\ell_3 & 0 & c_{55}\ell_1^2+c_{33}\ell_3^2-\rho v^2\end{pmatrix}\cdot\begin{pmatrix}u_1\\ u_2\\ u_3\end{pmatrix}=0. \quad (12)$$

Equation 12 shows the dispersion relation for coupled waves (qP and qSV)

$$(c_{11}\ell_1^2+c_{55}\ell_3^2-\rho v^2)(c_{55}\ell_1^2+c_{33}\ell_3^2-\rho v^2)-(c_{13}+c_{55})^2\ell_1^2\ell_3^2=0, \quad (13)$$

that allows estimating the phase velocities v of qP-waves as (see e.g., Tsvankin, 1995a; Carcione, 2001)

$$v=(2\rho)^{-1/2}\sqrt{c_{11}\ell_1^2+c_{33}\ell_3^2+c_{55}+D}, \quad (14a)$$

$$D=\sqrt{[(c_{11}-c_{55})\ell_1^2+(c_{55}-c_{33})\ell_3^2]^2+4[(c_{13}+c_{55})\ell_1\ell_3]^2}. \quad (14b)$$

The polarization of qP can be inferred from equations 12 and 13

$$\frac{n_1}{n_3}=\frac{u_1}{u_3}=s\sqrt{\frac{c_{55}\ell_1^2+c_{33}\ell_3^2-\rho v^2}{c_{11}\ell_1^2+c_{55}\ell_3^2-\rho v^2}}, \quad (15)$$

where $s=-1$ if $\ell_1\ell_3(c_{11}\ell_1^2+c_{55}\ell_3^2-\rho v^2)\geq 0$; $s=1$ if $\ell_1\ell_3(c_{11}\ell_1^2+c_{55}\ell_3^2-\rho v^2)<0$.

In the $(\mathbf{e}_1,\mathbf{e}_3)$ plane $u_2=0$, using $n_1^2+n_3^2=1$ and equation 15 we obtain

$$n_1=s\sqrt{\frac{c_{55}\ell_1^2+c_{33}\ell_3^2-\rho v^2}{c_{11}\ell_1^2+c_{33}\ell_3^2+c_{55}-2\rho v^2}}, \quad (16)$$

$$n_3=\sqrt{\frac{c_{11}\ell_1^2+c_{55}\ell_3^2-\rho v^2}{c_{11}\ell_1^2+c_{33}\ell_3^2+c_{55}-2\rho v^2}}. \quad (17)$$

Substituting equations 14a, 16, and 17 into equation 11, the rotation rates induced by plane P-waves propagating in the $(\mathbf{e}_1,\mathbf{e}_3)$ plane of a TI material with $\mathbf{e}_3$ as the axis of symmetry can be expressed as a function of the propagation direction as

$$\dot{\boldsymbol{\Omega}}=A\omega^2\sqrt{\frac{\rho}{2(c_{11}\ell_1^2+c_{33}\ell_3^2+c_{55}+D)}}\begin{pmatrix}0\\ \ell_3 n_1-\ell_1 n_3\\ 0\end{pmatrix}\times\exp\left[i\omega\left(t-\frac{1}{v}\mathbf{l}\cdot\mathbf{x}\right)\right], \quad (18a)$$

$$n_1=s\sqrt{\frac{D-(c_{55}-c_{11})\ell_1^2-(c_{33}-c_{55})\ell_3^2}{2D}}, \quad (18b)$$

$$n_3=\sqrt{\frac{D+(c_{55}-c_{11})\ell_1^2+(c_{33}-c_{55})\ell_3^2}{2D}}, \quad (18c)$$

$$s=-1 \quad \text{if} \quad \ell_1\ell_3[(c_{11}-c_{55})\ell_1^2+(c_{55}-c_{33})\ell_3^2-D]\geq 0, \quad (18d)$$

Table 1. Elastic coefficients for the TI material (Mesaverde clay shale), given in $[10^9\ \mathrm{N\cdot m^{-2}}]$.

ρ	c_{11}	c_{12}	c_{13}	c_{22}	c_{23}	c_{33}	c_{44}	c_{55}	c_{66}
2590	66.6	19.7	39.4	66.6	39.4	39.9	10.9	10.9	23.45

The material density ρ is given in $[\mathrm{kg\cdot m^{-3}}]$. All of the other coefficients are zero.

$$s = 1 \quad \text{if} \quad \ell_1\ell_3[(c_{11} - c_{55})\ell_1^2 + (c_{55} - c_{33})\ell_3^2 - D] < 0. \tag{18e}$$

Assuming that ψ is the angle between the wave propagation direction **l** and the symmetry axis $\mathbf{e}_3$ of the TI medium, we have

$$\ell_1 = \sin\psi \tag{19a}$$

$$\ell_3 = \cos\psi. \tag{19b}$$

This substitution allows us to calculate the rotation rates induced by plane P-waves propagating in the ($\mathbf{e}_1$,$\mathbf{e}_3$) plane of a TI material as a function of ψ.

To evaluate the correctness of the analytical solution, we model the synthetic seismograms created by a plane P-wave of dominant period of 1 s propagating upward through a TI medium that the symmetry axis belongs to the ($\mathbf{e}_1$,$\mathbf{e}_3$) plane. A model of 30,000 m length, 30,000 m width, and 20,000 m depth is used. The material chosen is Mesaverde clay shale (Table 1). To check the effect of different incidence angles, we rotate the symmetry axis of the material a full circle inside the ($\mathbf{e}_1$,$\mathbf{e}_3$) plane with steps of 5°. Such rotation of the material, having fixed the propagation direction of the plane wave, is equivalent to a test in which the material is fixed and the wave propagation direction **l** is rotated. In total, we investigate 72 different cases characterized by the angle between the material's symmetry axis and the vertical axis, ranging from 0° to 360°.

Six-component seismograms (three components of rotation rates and three components of translational velocities) are calculated using the ADER-DG method. The modeling parameters are detailed in Table 2.

The simulation results show that there is only rotational signal around the $\mathbf{e}_2$ axis, as we expected from theory (see equation 18). We superimpose the normalized peak rotation rates around the $\mathbf{e}_2$ axis obtained from the simulations and the analytic approach as a function of the angle ψ between the wave propagation direction and the symmetry axis of the material in a polar coordinate system. The excellent fit between both results presented in Figure 2 indicates the consistency of the analytical and numerical solutions.

We summarize that, for homogeneous anisotropic elastic media, we can estimate the rotational motions caused by a certain plane wave as a function of propagation direction and elastic coefficients. The anisotropic behavior is clearly revealed by the appearance of qP rotational motions. In the following, we extend the analytical equations to be able to infer the magnitude of the rotation rates associated with qP depending on the degree of anisotropy of the material.

Table 2. The modeling parameters used in this study.

Mesh type	Hexahedral
Element edge length	1000 m
Total number of elements	18,000
Polynomial degree inside elements	3
Number of processors	64
Length of seismograms	5 s
Boundary conditions	Absorbing (top), inflow (bottom), periodic (sides)
Average time step	1.4085×10^{-2} s
Run time per simulation	~50 s

MAGNITUDE OF qP ROTATIONS IN TERMS OF THOMSEN PARAMETERS

As reported by Thomsen (1986), for the case of transverse isotropy, an alternative and more descriptive set of parameters can be used to fully describe the medium's properties in substitution of the five elastic coefficients presented in equation 8. These parameters are the two elastic equivalent quantities α_0 and β_0 and three coefficients γ, ε, and δ^* (usually called Thomsen parameters) expressed as follows

$$\alpha_0 = \sqrt{\frac{c_{33}}{\rho}}, \tag{20}$$

$$\beta_0 = \sqrt{\frac{c_{55}}{\rho}}, \tag{21}$$

$$\varepsilon = \frac{c_{11} - c_{33}}{2c_{33}}, \tag{22}$$

$$\gamma = \frac{c_{66} - c_{55}}{2c_{55}}, \tag{23}$$

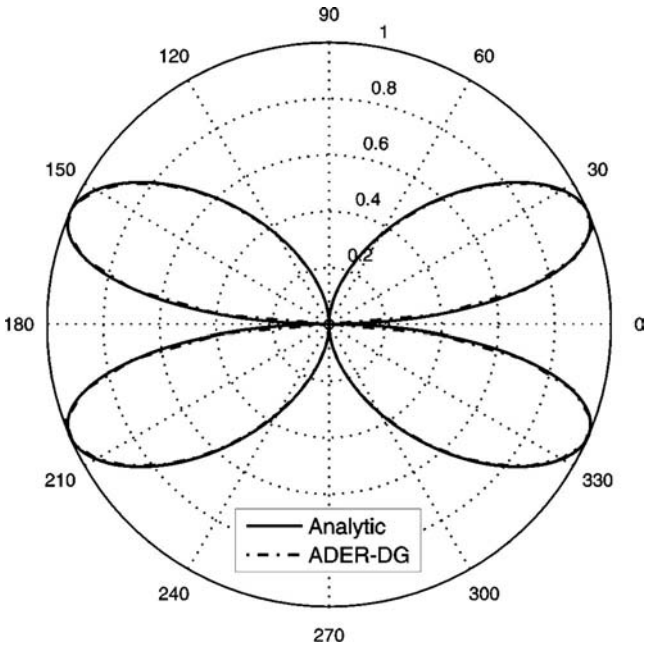

Figure 2. Variations of the normalized peak rotation rate induced by a qP-wave of period $T = 1$ s propagating in a vertical plane of a TI medium (Mesaverde clay shale) as a function of the angle ψ between the wave propagation direction and the symmetry axis of the medium. The results are presented in a polar coordinate system. Solid line = analytic results, dash-dot line = numerical simulation results using the ADER-DG method.

$$\delta^* = \frac{1}{2c_{33}^2}[2(c_{13}+c_{55})^2 - (c_{33}-c_{55})(c_{11}+c_{33}-2c_{55})]. \quad (24)$$

The coefficients γ, ε, and δ^* are dimensionless anisotropy parameters that fully characterize the strength of the anisotropy. Thus, to quantify the magnitude of qP rotations in anisotropic elastic media, in this section we investigate the dependence of the peak rotation rate values of qP-waves on these Thomsen parameters.

As mentioned by Tsvankin and Thomsen, 1994 and Tsvankin, 1995b, the parameter γ does not affect the propagation of the qP- or the qSV-waves in TI media. Only the SH mode depends on this parameter. This can also be recognized from equation 13. For the coupled waves, neither the phase velocities nor the Kelvin–Christoffel equations depend on c_{66}. As a consequence, the rotation rates induced by qP-waves are also independent of c_{66} (see equation 18). This means that, in a certain TI medium with a constant value of β_0 (or equivalently c_{55}), the qP rotation rates are independent of γ (see equations 21 and 23). Hence, we consequently skip the parameter γ in the following. We quantify the peak rotation rates of the qP-waves generated in TI materials with different levels of anisotropy only as a function of the two parameters ε and δ^*.

We define a set of elastic modulus matrices **C** by assuming fixed values of α_0, β_0, ρ, and γ and letting ε and δ^* take different values. For each (ε, δ^*) couple, we aim to obtain the peak rotation rates produced by a qP-wave traveling in any direction. To this goal, for each elastic modulus matrix **C** and for each propagation direction, we first extract the phase velocity and the polarization of the considered qP-wave by solving equation 10. The corresponding rotation rates are calculated using equation 3. The corresponding peak rotation rate can be then obtained trivially from the full rotation rate vector. In this way, we obtain the peak qP rotation rate that can be generated by a certain plane wave in the considered materials, each characterized by its ε and δ^* values, in all propagation directions **l**. We consider values of ε ranging from 0 to 0.35 and those of δ^* from -0.3 to 1. These values cover most TI cases observed (Thomsen, 1986). Four case studies are investigated: (1) a plane wave of peak ground displacement (PGD) 355.78 nm and period $T = 1$ s (caused by a distant earthquake) propagating through bedrock; (2) a plane wave of PGD $= 48 \times 10^{-4}$ m and period $T = 0.8$ s (can be caused by a local earthquake M7.0, epicenter distance 100 km) propagating through bedrock; (3) a plane wave of PGD $= 10^{-6}$ m and frequency $f = 150$ Hz (can originate from a microseismic event of $M_w = 0$ at hypocenter distance of approximately 1 km) propagating through reservoir rock; and (4) a plane wave of PGD $= 180.35 \times 10^{-6}$ m and $f = 5$ Hz (can be caused by an air-gun experiment) propagating though reservoir rock (see Chen et al., 2008). For each case study, reasonable values of α_0, β_0, and mass density ρ are used and are detailed in Table 3. Because of the independence of the qP rotation rates on γ, any arbitrary value of this Thomsen parameter can be taken. Here we note that the first case study is based on measurements of the 25 September 2003 M8.1 Tokachi-oki earthquake at the Wettzell station in southeast Germany (see Pham et al., 2009a) except for the anisotropy, which has been solely added for the purpose of the research presented here.

We compute for each of the four study cases the peak rotation rates of qP-waves generated in different TI materials for a set of ε and δ^* values. The results are given in Figures 3–6. Every point in the plot depicts the maximum qP rotation rate among all propagation directions for a given couple of values of (ε, δ^*). A general trend that can be observed is that peak qP rotation rates are higher with increasing values of ε and δ^*. In particular, if we look at the results obtained for the case of the distant earthquake (Figure 3), we can safely conclude that, if we consider weakly anisotropic bedrock under Wettzell (Lee et al., 2009b), we should measure qP rotation rates of at most 5×10^{-11} rad/s. This value is much smaller than the amplitude (6.3×10^{-10} rad/s) observed in P coda rotations, as reported by Pham et al. (2009a). However, for the other three study cases, significant amplitudes of qP rotation rates are expected (Figures 4–6). With peak qP rotation rates in the order of μrad/s, even in weakly anisotropic materials the signals can be recorded with current instrument technology (Nigbor et al., 2009; Wassermann et al., 2009).

DISCUSSION

The rotational motion of qP-waves studied in this paper is another expression of the polarization deviation of the P-waves in anisotropic media studied in earlier papers (e.g., Pšenčík and Gajewski, 1998; Zheng and Pšenčík, 2002). However, at the beginning of this study it was not clear how anisotropy affects rotational ground motions and if rotational motions can help putting constraints on anisotropic properties. The results obtained in this paper under the assumption of plane wave propagation show that (1) anisotropic behavior in elastic media can be recognized from rotational motion records, especially by the appearance of qP rotations; (2) for typical reservoir situations and strong local earthquakes qP rotation signals are significant, recordable, and can be used for inverse problems.

It should be noted that our original motivation to study the relation between anisotropy and rotational motions comes from efforts to explain the observed P coda rotations reported by Igel et al. (2007) and Pham et al. (2009b). At the beginning of this study, it was unclear whether rotational motions induced by qP-waves in anisotropic media contribute to the observed rotational signals in the P coda. Relat-

Table 3. Parameters used for quantifying peak rotation rates of qP-waves in terms of the Thomsen parameters for four case studies.

Case study	Peak ground displacement (m)	Considered period (s)	α_0 (m/s)	β_0 (m/s)	ρ (kg/m^3)
1. Bedrock/distant earthquake	355.78×10^{-9}	1	6600	3700	2900
2. Bedrock/local earthquake	48×10^{-4}	0.8	6600	3700	2900
3. Reservoir/microseismic event	10^{-6}	1/150	3928	2055	2590
4. Reservoir/air-gun experiment	180.35×10^{-6}	0.2	3928	2055	2590

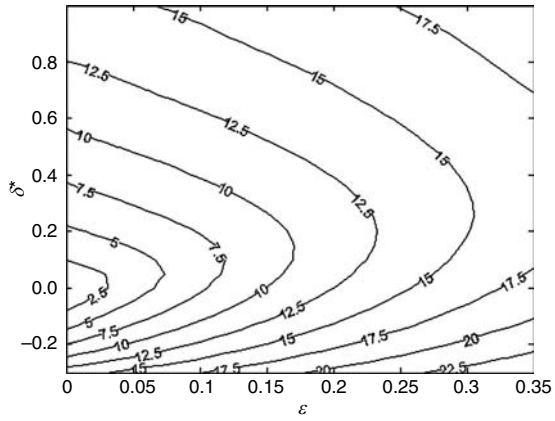

Figure 3. The maximum peak rotation rates (in 10^{-11} rad/s) caused by plane P-waves in a full space TI medium as a function of the Thomsen parameters ε and δ^*, as expected for a distant earthquake with PGD of 355.78 nm and period $T = 1$ s. A vertical P velocity $\alpha_0 = 6600$ m/s, vertical S velocity $\beta_0 = 3700$ m/s, and $\rho = 2900$ kg/m^3 were assumed. Every point in the plot depicts the maximum qP rotation rate among all propagation directions for a given couple of values of (ε, δ^*).

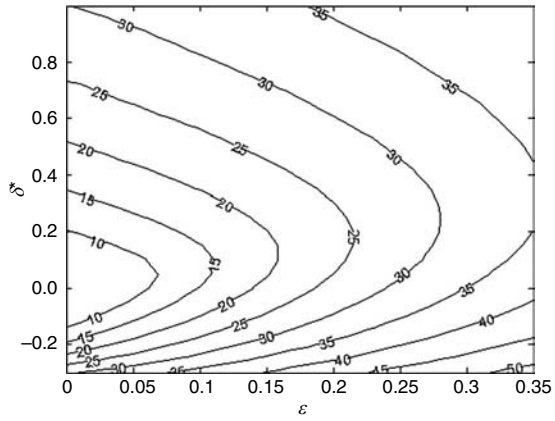

Figure 4. The maximum peak rotation rate (in 10^{-7} rad/s) caused by qP-waves in a full space TI medium as a function of the Thomsen parameters ε and δ^*, as expected for a local earthquake with PGD 48 $\times 10^{-4}$ m and period $T = 0.8$ s. A vertical P velocity $\alpha_0 = 6600$ m/s, vertical S velocity $\beta_0 = 3700$ m/s, and $\rho = 2900$ kg/m^3 were assumed. Every point in the plot depicts the maximum qP rotation rate among all propagation directions for a given couple of values of (ε, δ^*).

ed to this, several results obtained in the study presented here need to be mentioned. First, although anisotropy does generate qP rotations, for teleseismic wavefields the rotational energy induced by anisotropic effects is expected to be much smaller than the observed one in the P coda. Second, it is evident from equation 3 that translational acceleration and the resulting qP rotation rates would have the same waveforms coinciding in time. However, as reported by Pham et al. (2009b), the P coda rotations observed at the Wettzell station come later than the appearance of direct P-waves. These results demonstrate that anisotropic qP rotational signals cannot be the main cause of the observed P coda rotations. The difference in the arrival time of anisotropic qP rotational motions and scattering P coda rotations can be used to separate these two cases for specific purposes when a heterogeneous medium is present.

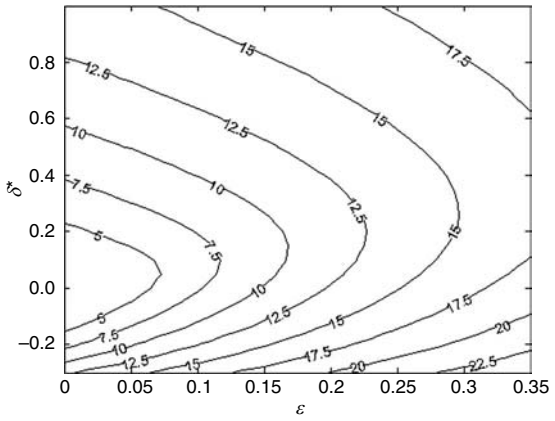

Figure 5. The maximum peak rotation rate (in 10^{-6} rad/s) caused by qP-waves in a full space TI medium as a function of the Thomsen parameters ε and δ^* as expected for a reservoir microseismic event with PGD of 10^{-6} m and frequency $f = 150$ Hz. A vertical P velocity $\alpha_0 = 3928$ m/s, vertical S velocity $\beta_0 = 2055$ m/s, and $\rho = 2590$ kg/m^3 were assumed. Every point in the plot depicts the maximum qP rotation rate among all propagation directions for a given couple of values of (ε, δ^*).

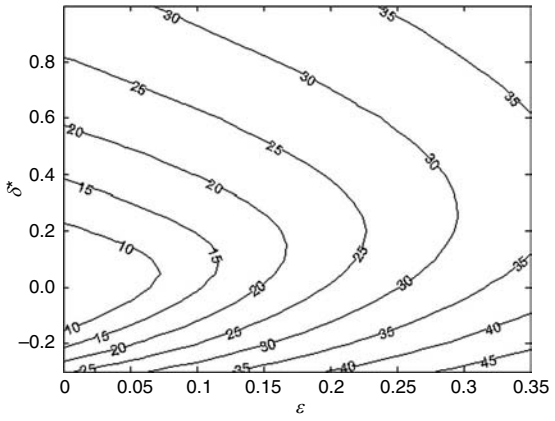

Figure 6. The maximum peak rotation rate (in 10^{-7} rad/s) caused by qP-waves in a full space TI medium as a function of the Thomsen parameters ε and δ^* as expected for an air-gun experiment in a reservoir area with PGD 180.35×10^{-6} m and frequency $f = 5$ Hz. A vertical P velocity $\alpha_0 = 3928$ m/s, vertical S velocity $\beta_0 = 2055$ m/s, and $\rho = 2590$ kg/m^3 were assumed. Every point in the plot depicts the maximum qP rotation rate among all propagation directions for a given couple of values of (ε, δ^*).

CONCLUSIONS

In summary, we conclude that rotational motions contain additional information about the material's anisotropic properties and that joint measurements of translational and rotational motions of qP-waves in anisotropic media might allow one to constrain anisotropic parameters. Our results not only demonstrate the potential benefit of measurements of rotational ground motions but also pose several issues that need to be addressed in the future.

1) Because we have shown that the amplitudes of the qP rotational motions generated in anisotropic materials are high enough to be observed and recorded, one of the key questions is: Can we extract additional information about the material's properties using qP rotations?

2) In the study presented here, we focus mainly on qP-waves, the rotational motions of which are completely independent of the Thomsen parameter γ. Thus, the consideration of this measure of S anisotropy (i.e., γ) is out of the framework of this paper. Theoretically, qS motions also contain additional information. Can we constrain the Thomsen parameter γ using measurements of rotational motions of qS-waves? What additional information can be extracted if these motions are used?
3) The well-known result for isotropic media that the rotation vector is orthogonal to the propagation direction (i.e., the component of the rotation rate vector in the propagation direction is zero) is theoretically and numerically demonstrated to also hold for anisotropic media. This opens an opportunity to investigate scattering properties of heterogeneous media on the basis of variations of rotational motions around the wave propagation direction.

Finally, the applicability of the presented theory to real data will rest on the ability to develop reliable sensors (borehole- and surface-based) for rotational motions with a broad enough frequency bandwidth and dynamic range.

ACKNOWLEDGMENTS

This research was supported by the Geophysics Section of Ludwig-Maximilians-Universität Munich, the Vietnamese government (project 322 and Vietnam's National Foundation for Science and Technology Development), and the German Academic Exchange Service (DAAD). We thank the KONWIHR project and the Munich Leibniz Supercomputing Centre for computational resources and the European Human Resources Mobility Program (SPICE Project). We thank Mirko van der Baan and four anonymous reviewers for their suggestions and comments that helped to improve the manuscript. J. de la Puente acknowledges the funding of the Kaleidoscope project, supported by Repsol-YPF. H. Igel thanks Mike Schoenberg, who passed away in 2008, for his early thoughts on the problem, the discussions they had a few days before his death, and above all for his friendship and support.

APPENDIX A

ORTHOGONAL CARTESIAN COORDINATE SYSTEM ℓ, Θ, Φ

For the purpose of visualization of the influence that anisotropy has in the behavior of the rotational wavefield, an orthogonal Cartesian coordinate system $\mathbf{l}$, $\boldsymbol{\theta}$, $\boldsymbol{\phi}$ is used in the paper (see Figure A-1). The system is defined as follows. We first build the unit vector $\mathbf{l} = (\ell_1,\ell_2,\ell_3)$ so that its axis coincides with the wave propagation direction. Furthermore, we generate a set of three auxiliary vectors $\mathbf{p}$, $\mathbf{q}$, and $\mathbf{r}$ that will help us define the two remaining axes of our Cartesian coordinate system. These are defined as

$$\mathbf{p} = (\ell_1, -\ell_2, 0), \tag{A-1}$$

$$\mathbf{q} = (0, -\ell_3, \ell_2), \tag{A-2}$$

$$\mathbf{r} = (\ell_3, 0, -\ell_1). \tag{A-3}$$

The definition of the two remaining Cartesian axes will depend on whether the auxiliary vectors are collinear or not and whether one of them is the vector $\mathbf{0}$. The three distinct cases are described as follows. If $|\mathbf{l}\times\mathbf{p}| > 0$, then $\boldsymbol{\theta}$ is defined as

$$\boldsymbol{\theta} = \mathbf{l}\times\mathbf{p} = (\ell_2\ell_3, \ell_1\ell_3, -2\ell_1\ell_2). \tag{A-4}$$

If $|\mathbf{l}\times\mathbf{p}| = 0$ and $|\mathbf{l}\times\mathbf{q}| > 0$, then $\boldsymbol{\theta}$ is defined as

$$\boldsymbol{\theta} = \mathbf{l}\times\mathbf{q} = (\ell_2^2 + \ell_3^2, -\ell_1\ell_2, -\ell_1\ell_3). \tag{A-5}$$

If $|\mathbf{l}\times\mathbf{p}| = 0$ and $|\mathbf{l}\times\mathbf{q}| = 0$, then $\boldsymbol{\theta}$ is defined as

$$\boldsymbol{\theta} = \mathbf{l}\times\mathbf{r} = (-\ell_1\ell_2, \ell_3^2 + \ell_1^2, -\ell_2\ell_3). \tag{A-6}$$

The vector $\boldsymbol{\phi}$ is always obtained by cross product of $\mathbf{l}$ and $\boldsymbol{\theta}$,

$$\boldsymbol{\phi} = \mathbf{l}\times\boldsymbol{\theta}. \tag{A-7}$$

APPENDIX B

AXIS TRANSFORMATIONS OF ROTATIONS

To set up the relationship between components of a rotational motion in two orthogonal Cartesian coordinate systems (x,y,z) and (x^*,y^*,z^*), we start by recalling the definition of the rotation rate

$$\begin{pmatrix}\dot{\Omega}_x\\ \dot{\Omega}_y\\ \dot{\Omega}_z\end{pmatrix} = \frac{1}{2}\nabla\times\mathbf{V} = \frac{1}{2}\begin{pmatrix}\partial_y V_z - \partial_z V_y\\ \partial_z V_x - \partial_x V_z\\ \partial_x V_y - \partial_y V_x\end{pmatrix}, \tag{B-1}$$

where $\mathbf{V}$ is the ground translational velocity and $\dot{\Omega}$ is the rotation rate.

In the (x^*,y^*,z^*) system, we can similarly find that

$$\dot{\Omega}_x{}^* = \frac{1}{2}(\partial_{y^*}V_z{}^* - \partial_{z^*}V_y{}^*). \tag{B-2}$$

The relationship between the components of the translational motion in the two systems can be expressed as

$$\mathbf{V}^* = A\mathbf{V}, \tag{B-3}$$

which explicitly can be written as

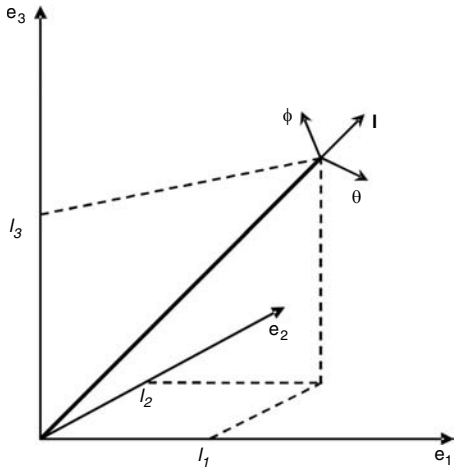

Figure A-1. Illustration of the orthogonal Cartesian coordinate system $\mathbf{l}$, $\boldsymbol{\theta}$, $\boldsymbol{\phi}$ used in this study.

$$\begin{pmatrix} V_x^* \\ V_y^* \\ V_z^* \end{pmatrix} = \begin{pmatrix} a_{11} & a_{12} & a_{13} \\ a_{21} & a_{22} & a_{23} \\ a_{31} & a_{32} & a_{33} \end{pmatrix} \begin{pmatrix} V_x \\ V_y \\ V_z \end{pmatrix}, \tag{B-4}$$

where $a_{ij} = \mathbf{e}_i^* . \mathbf{e}_j = \cos \alpha_{ij}$ ($i = 1, 2, 3$; $j = 1, 2, 3$) are the so-called direction cosines; α_{ij} are angles between two sets of axes; and ($\mathbf{e}_1^*$,$\mathbf{e}_2^*$,$\mathbf{e}_3^*$) and ($\mathbf{e}_1$,$\mathbf{e}_2$,$\mathbf{e}_3$) denote the unit basis vectors of the axes of the two systems.

Using B-4, equation B-2 can be rewritten as

$$\dot{\Omega}_x^* = \frac{1}{2}[(a_{31}\partial_{y*}V_x + a_{32}\partial_{y*}V_y + a_{33}\partial_{y*}V_z) - (a_{21}\partial_{z*}V_x + a_{22}\partial_{z*}V_y + a_{23}\partial_{z*}V_z)]. \tag{B-5}$$

Now we use the Jacobian of the transformation to obtain the derivatives in the new coordinate system.

$$\partial_{x*} = \frac{\partial x}{\partial x^*}\partial_x + \frac{\partial y}{\partial x^*}\partial_y + \frac{\partial z}{\partial x^*}\partial_z = a_{11}\partial_x + a_{12}\partial_y + a_{13}\partial_z, \tag{B-6}$$

$$\partial_{y*} = \frac{\partial x}{\partial y^*}\partial_x + \frac{\partial y}{\partial y^*}\partial_y + \frac{\partial z}{\partial y^*}\partial_z = a_{21}\partial_x + a_{22}\partial_y + a_{23}\partial_z, \tag{B-7}$$

$$\partial_{z*} = \frac{\partial x}{\partial z^*}\partial_x + \frac{\partial y}{\partial z^*}\partial_y + \frac{\partial z}{\partial z^*}\partial_z = a_{31}\partial_x + a_{32}\partial_y + a_{33}\partial_z. \tag{B-8}$$

Substituting B-6–B-8 and B-5, we find that

$$\dot{\Omega}_x^* = \frac{1}{2}\left[(a_{33}a_{22} - a_{32}a_{23})\left(\frac{\partial V_z}{\partial y} - \frac{\partial V_y}{\partial z}\right) + (a_{31}a_{23} - a_{33}a_{21})\left(\frac{\partial V_x}{\partial z} - \frac{\partial V_z}{\partial x}\right) + (a_{32}a_{21} - a_{31}a_{22})\left(\frac{\partial V_y}{\partial x} - \frac{\partial V_x}{\partial y}\right)\right] \tag{B-9}$$

which leads to the final form

$$\dot{\Omega}_x^* = (a_{33}a_{22} - a_{32}a_{23})\dot{\Omega}_x + (a_{31}a_{23} - a_{33}a_{21})\dot{\Omega}_y + (a_{32}a_{21} - a_{31}a_{22})\dot{\Omega}_z. \tag{B-10}$$

Similarly, we also obtain

$$\dot{\Omega}_y^* = (a_{13}a_{32} - a_{33}a_{12})\dot{\Omega}_x + (a_{11}a_{33} - a_{31}a_{13})\dot{\Omega}_y + (a_{12}a_{31} - a_{32}a_{11})\dot{\Omega}_z, \tag{B-11}$$

$$\dot{\Omega}_z^* = (a_{23}a_{12} - a_{13}a_{22})\dot{\Omega}_x + (a_{21}a_{13} - a_{11}a_{23})\dot{\Omega}_y + (a_{11}a_{22} - a_{12}a_{21})\dot{\Omega}_z. \tag{B-12}$$

The last three equations can be written in the compact form

$$\dot{\mathbf{\Omega}}^* = (\mathrm{A}^{-1})^{\mathrm{T}}\dot{\mathbf{\Omega}}, \tag{B-13}$$

which we can compare to B-3 to see how the rotation-rate vector can be transformed into a rotated Cartesian system once we know the expression of the unitary vectors ($\mathbf{e}_1^*$,$\mathbf{e}_2^*$,$\mathbf{e}_3^*$) that form the basis of the new system.

REFERENCES

Aki, K., and P. G. Richards, 2002, Quantitative seismology, 2nd ed.: University Science Books.

Bernauer, M., A. Fichtner, and H. Igel, 2009, Inferring earth structure from combined measurements of rotational and translational ground motions: Geophysics, **74**, no. 6, WCD41–WCD47.

Carcione, J. M., 2001, Wave fields in real media: wave propagation in anisotropic, anelastic and porous media, 31: Pergamon.

Chen, Y., L. Liu, H. Ge, B. Liu, and X. Qiu, 2008, Using an airgun array in a land reservoir as the seismic source for seismotectonic studies in northern China: experiments and preliminary results: Geophysical Prospecting, **56**, no. 4, 601–612.

Cochard, A., H. Igel, B. Schuberth, W. Suryanto, A. Velikoseltsev, U. Schreiber, J. Wassermann, F. Scherbaum, and D. Vollmer, 2006, Rotational motions in seismology: theory, observations, simulation, *in* R. Teisseyre, M. Takeo, and E. Majewski, eds., Earthquake source asymmetry, structural media and rotation effects: Springer-Verlag, 391–412.

Crampin, S., 1981, A review of wave motion in anisotropic and cracked elastic-media: Wave Motion, **3**, no. 4, 343–391.

Crampin, S., 1984, Effective anisotropic elastic-constants for wave propagation through cracked solids: Geophysical Journal of the Royal Astronomical Society, **76**, 135–145.

Crampin, S., E. M. Chesnokov, and R. G. Hipkin, 1984, Seismic anisotropy — the state of the art II: Geophysical Journal of the Royal Astronomical Society, **76**, 1–16.

Crampin, S., R. A. Stephen, and R. McGonigle, 1982, The polarization of P-waves in anisotropic media: Geophysical Journal of the Royal Astronomical Society, **68**, 477–485.

de la Puente, J., 2008, Seismic wave propagation for complex rheologies: VDM Verlag.

de la Puente, J., M. Käser, M. Dumbser, and H. Igel, 2007, An arbitrary high order discontinuous Galerkin method for elastic waves on unstructured meshes IV: Anisotropy: Geophysical Journal International, **169**, no. 3, 1210–1228.

Dumbser, M., and M. Käser, 2006, An arbitrary high order discontinuous Galerkin method for elastic waves on unstructured meshes II: the three-dimensional isotropic case: Geophysical Journal International, **167**, no. 1, 319–336.

Ferreira, A., and H. Igel, 2009, Rotational motions of seismic surface waves in a laterally heterogeneous earth: Bulletin of the Seismological Society of America, **99**, 2B, 1429–1436.

Fichtner, A., and H. Igel, 2009, Sensitivity densities for rotational ground motion measurements: Bulletin of the Seismological Society of America, **99**, 2B, 1302–1314.

Guéguen, Y., and J. Sarout, 2009, Crack-induced anisotropy in crustal rocks: predicted dry and fluid-saturated Thomsen's parameters: Physics of the Earth and Planetary Interiors, **172**, no. 1–2, 116–124.

Igel, H., A. Cochard, J. Wassermann, A. Flaws, U. Schreiber, A. Velikoseltsev, and N. D. Pham, 2007, Broadband observations of earthquake induced rotational ground motions: Geophysical Journal International, **168**, no. 1, 182–196.

Igel, H., U. Schreiber, A. Flaws, B. Schuberth, A. Velikoseltsev, and A. Cochard, 2005, Rotational motions induced by the M8.1 Tokachi-oki earthquake, September 25, 2003: Geophysical Research Letters, **32**, L08309.

Larner, K., 1993, Dip-moveout error in transversely isotropic media with linear velocity variation in depth: Geophysics, **58**, 1442–1453.

Lee, H. K. W., H. Igel, and M. D. Trifunac, 2009a, Recent advances in rotational seismology: Seismological Research Letters, **80**, no. 3, 479–490.

Lee, H. K. W., M. Çelebi, M. I. Todorovska, and H. Igel, 2009b, Introduction to the special issue on rotational seismology and engineering applications: Bulletin of the Seismological Society of America, **99**, 2B, 945–957.

McLeod, D. P., G. E. Stedman, T. H. Webb, and U. Schreiber, 1998, Comparison of standard and ring laser rotational seismograms: Bulletin of the Seismological Society of America, **88**, 1495–1503.

Musgarve, M. J. P., 1970, Crystal acoustics: Holden-Day.

Nigbor, R. L., J. R. Evans, and C. R. Hutt, 2009, Laboratory and field testing of commercial rotational seismometers: Bulletin of the Seismological Society of America, **99**, 2B, 1215–1227.

Pancha, A., T. H. Webb, G. E. Stedman, D. P. McLeod, and U. Schreiber, 2000, Ring laser detection of rotations from teleseismic waves: Geophysical Research Letters, **27**, no. 21, 3553–3556.
Pšenčík, I., and D. Gajewski, 1998, Polarization, phase velocity and NMO velocity of qP-waves in arbitrary weakly anisotropic media: Geophysics, **63**, 1754–1766.
Pham, D. N., H. Igel, J. Wassermann, A. Cochard, and U. Schreiber, 2009a, The effects of tilt on interferometric rotation sensors: Bulletin of the Seismological Society of America, **99**, 2B, 1352–1365.
Pham, D. N., H. Igel, J. Wassermann, M. Käser, J. de la Puente, and U. Schreiber, 2009b, Observations and modelling of rotational signals in the P-coda: constraints on crustal scattering: Bulletin of the Seismological Society of America, **99**, 2B, 1315–1332.
Sams, M. S., M. H. Worthington, M. S. King, and M. S. Khanshir, 1993, A comparison of laboratory and field measurements of P-wave anisotropy: Geophysical Prospecting, **41**, no. 2, 189–206.
Schreiber, U., G. E. Stedman, H. Igel, and A. Flaws, 2006, Ring laser gyroscopes as rotation sensors for seismic wave studies, *in* R. Teisseyre, M. Takeo, and E. Majewski, eds., Earthquake source asymmetry, structural media and rotation effects: Springer-Verlag, 377–390.
Schreiber, K. U., J. N. Hautmann, A. Velikoseltsev, J. Wassermann, H. Igel, J. Otero, F. Vernon, and J. P. R. Wells, 2009, Ring laser measurements of ground rotations for seismology: Bulletin of the Seismological Society of America, **99**, 2B, 1190–1198.
Stein, S., and M. Wysession, 2003, An introduction to seismology, earthquake, and earth structure: Blackwell Press.
Suryanto, W., H. Igel, J. Wassermann, A. Cochard, B. Schuberth, D. Vollmer, F. Scherbaum, U. Schreiber, and A. Velikoseltsev, 2006, First comparison of array-derived rotational ground motions with direct ring laser measurements: Bulletin of the Seismological Society of America, **96**, no. 6, 2059–2071.
Takeo, M., and H. M. Ito, 1997, What can be learned from rotational motions excited by earthquakes?: Geophysical Journal International, **129**, no. 2, 319–329.
Thomsen, L., 1986, Weak elastic anisotropy: Geophysics, **51**, 1954–1966.
Tsvankin, I., 1995a, Seismic wavefields in layered isotropic media: Samizdat Press.
Tsvankin, I., 1995b, Body-wave radiation patterns and AVO in transversely isotropic media: Geophysics, **60**, 1409–1425.
Tsvankin, I., 1996, P-wave signatures and notation for transversely isotropic media: an overview: Geophysics, **61**, 467–483.
Tsvankin, I., and L. Thomsen, 1994, Nonhyperbolic reflection moveout in anisotropic media: Geophysics, **59**, 1290–1304.
Wang, Z., 2002, Seismic anisotropy in sedimentary rocks. Part 2: laboratory data: Geophysics, **67**, 1423–1440.
Wassermann, J., S. Lehndorfer, H. Igel, and U. Schreiber, 2009, Performance test of a commercial rotational motion sensor: Bulletin of the Seismological Society of America, **99**, 2B, 1449–1456.
Zheng, X., and I. Pšenčík, 2002, Local determination of weak anisotropy parameters from qP-wave slowness and particle motion measurements: Pure and Applied Geophysics, **159**, no. 7–8, 1881–1905.

Geophysical Journal International

Geophys. J. Int. (2010) **183,** 1031–1051 doi: 10.1111/j.1365-246X.2010.04777.x

Regular versus irregular meshing for complicated models and their effect on synthetic seismograms

Christian Pelties, Martin Käser, Verena Hermann and Cristóbal E. Castro*

Department of Earth and Environmental Sciences, Geophysics Section, Ludwig-Maximilians-Universität, München, Germany.
E-mail: pelties@geophysik.uni-muenchen.de

Accepted 2010 August 14. Received 2010 August 13; in original form 2010 June 26

SUMMARY

We present a detailed study on the numerical effects due to staircase approximations of non-planar material interfaces and the importance of mesh alignment to such material boundaries using the discontinuous Galerkin finite element method. Our aim is to define clear rules that have to be adhered to guarantee acceptable synthetic data in seismic forward modelling for the cases where material contrasts occurring along curved interfaces are discretized with regular meshes. To this end, we compare results of structured staircase approximations with reference results obtained by unstructured triangular meshes that can be aligned to non-planar interfaces. We investigate different mesh spacings, wave frequencies, and material contrasts to cover various parameter ranges that allow us to measure their influence on the accuracy of the resulting waveforms. Our results show that acceptable synthetic results strongly depend on the material contrast and we give a quantitative estimate of the required mesh resolution in the sense of numbers of elements per shortest dominant wavelength to obtain satisfying seismograms even if the material interfaces are not respected by the mesh. We apply our rules to two different test cases including a multilayered model and a basin structure, both with non-planar interfaces of small and large material contrasts to confirm the validity of our study. We finally conclude that for moderate material contrasts regular meshing can be beneficial due to its simple mesh generation process and typically superior computational efficiency compared to unstructured meshes, however, the correct frequency- and material-dependent mesh resolution has to be chosen.

Key words: Numerical approximations and analysis; Computational seismology; Wave scattering and diffraction; Wave propagation.

1 INTRODUCTION

Recently, the development of seismic forward modelling tools seem to increasingly consider the use of unstructured meshes (Bao *et al.* 1998; Gao & Zhang 2006; Stupazzini *et al.* 2008; Ichimura *et al.* 2009; Etienne *et al.* 2009; Wilcox *et al.* 2010). The main motivation for this discretization approach is the alignment of the mesh to geometrically complex material discontinuities or topographic features. The accurate representation of the real geometry of a physical problem is generally assumed to be important to achieve high-quality simulation results avoiding numerical artefacts due to inappropriate model discretization. However, unstructured meshes typically require more computational memory than regular, structured grids as the connectivity between element vertices has to be stored explicitly. Furthermore, they often are computationally more expensive to obtain a numerical solution. Nevertheless, unstructured meshes tend to become a popular choice for wave propagation applications, as the mesh spacing h can be changed locally (h-adaptation) to adjust the element size to the material properties or to improve the resolution of particular areas of interest. Alternatively, a solution can be approximated within each element using polynomials of various degree p leading to locally increased accuracy (p-adaptation). In addition, local time stepping might be used (Dumbser *et al.* 2007) to reduce the computational cost. Unfortunately, these advanced methods can be difficult to implement, maintain, or extend to further functionalities due to the underlying data structures and sophisticated algorithms.

Within the topic of unstructured 3-D meshes there is a further distinction, mainly between meshes of hexahedral or tetrahedral elements, as other element types like pyramids or prisms are rarely used. Methods like the spectral element method (SEM) show particular advantages for hexahedral meshes, while their efficient formulation even for 2-D triangular meshes seems to be problematic (Pasquetti & Rapetti 2006; Mercerat *et al.* 2006). On the other hand, the discontinuous Galerkin (DG) method is well suited for

*Now at: University of Hamburg, KlimaCampus, Hamburg, Germany.

tetrahedral or triangular meshes but in general computationally more expensive. In both cases, however, the creation of the computational meshes for geometrically complex domains requires advanced mesh generators, for example, CUBIT, ANSYS ICEM-CFD, Fluent Gambit or TetGen. Most of this meshing software is developed and used for engineering problems such as structural mechanics, fluid dynamics, etc. and can handle geometries that typically represent combinations and modifications of simple geometrical shapes. In contrast, many problems in geoscience consists of more complicated structures and geological units with irregular internal material interfaces, non-planar earthquake faults or complex domain boundaries due to topography. Furthermore, the geometrical information is given as a large data set of discrete points of regular or irregular distributions, which have to be interpolated to obtain surface splines that can then be processed by the mesh generators. The step of building this geometry typically is a time consuming task requiring a large amount of manual interaction. Finally, not all geoscientists, or computational seismologists in particular, have access to the appropriate, often commercial software, which hinders the distribution of codes based on specific mesh generators within the community of seismology or geoscience in general.

On the other hand, methods based on regular, structured grids like finite differences (FD), for example, Moczo *et al.* (2007) or Olsen *et al.* (2006), helped tremendously to answer many scientific questions in the past and are widely spread in the seismological community. However, the assignment of material properties to nodes located at the interface can be problematic and staircase approximations of material discontinuities usually occur. For internal material interfaces the accuracy often relies on sufficiently fine grid spacing and special treatments to avoid spurious diffractions (Zahradník *et al.* 1993; Collino *et al.* 1997). The misalignment of the regular grid to material discontinuities leads to first-order errors proportional to the grid spacing or time step that are insensitive to the approximation order of the numerical scheme (Gustafsson & Wahlund 2004; Symes *et al.* 2008). Therefore, work has been done to represent such interfaces through an appropriate usage of effective material using harmonic and arithmetic averaging of elastic moduli and densities, for example, by Graves (1996) or Moczo *et al.* (2002). Zhang & LeVeque (1997) developed a second-order accurate method for the acoustic wave equations in heterogeneous media using high resolution multidimensional flux-limiters on a Cartesian grid. Near the material interface special formulas are developed using the immersed interface method that incorporate the jump conditions and give pointwise second order accuracy even when the interface is not aligned with the grid. This approach was then extended to fourth-order accuracy and for elastic waves (Zhang & Symes 1998). A major disadvantage of regular grid methods occurs when dealing with complex free-surface topography. It is well known that standard FD schemes require a high grid resolution at free-surface boundaries to avoid numerical artefacts, in particular, if non-planar free-surface topography has to be included (Robertsson 1996; Bohlen & Saenger 2006). Moczo *et al.* (2007) summarize and analyse existing FD schemes for this topic in detail and suggest an alternative approach to model free-surface topography. However, standard FD schemes rely on dense meshes which could result in an enormous computational effort. An interesting estimation of the computational requirements needed for a large-scale FD simulation is given by Bao *et al.* (1998). Nevertheless, the use of regular grids allows in general for highly efficient codes both in terms of memory and computational cost.

In this paper, we analyse quantitatively numerical errors of synthetic seismograms due to staircase approximations of material discontinuities using the DG method, as its implementation on regular meshes is computationally also much more efficient. To this end, we focus on the systematic dependence of the errors on mesh spacing, material contrast, and frequency content of the seismic signal. To our knowledge only few quantitative studies exist for this topic and mainly consider the FD approach, for example, van Vossen *et al.* (2002) or Bohlen & Saenger (2006). There, FD schemes are investigated by modelling free-surface conditions and solid-fluid contrasts using variable grid spacings and different angles between the orientation of the grid and the interface. However, they perform their studies for material properties typically occurring in geosciences but do not focus explicitly on error dependencies on the wave speed ratio. In our study, we simulate the reflection and transmission of a 2-D plane wave at a semi-circular interface between two materials and also investigate the effects at a non-planar free-surface boundary condition using regular, quadrilateral meshes. The reference solution for all tests is produced with the same, well-tested high-order DG method on unstructured triangular meshes to fully account for the geometrical features of the test cases. This way, differences due to the usage of different numerical methods are excluded. Hence, we can compare synthetic seismograms whose misfits can only originate from the different discretization approaches. Our goal is to define proper discretization rules that should be considered in forward modelling of seismic wave propagation in order to guarantee a desired accuracy. Finally, we show that these rules also hold for more realistic applications with complicated geometrical properties and material distributions typically encountered in layered or sedimentary basin environments.

The paper is structured as follows. Section 2 defines the model setup and studies the results of the different staircase discretization approaches. We analyse in detail the errors of the synthetic seismograms and their spatial distribution to set up discretization rules which should help modellers to choose a sufficient geometry sampling. In a second step, we verify these rules in Section 3 with a more complicated layered model with two arbitrary shaped interfaces. Finally, we apply and test our rules in a realistic scenario of a basin structure in Section 4 and finally draw our conclusions in Section 5.

2 IMPORTANCE OF INTERFACE APPROXIMATION

To quantify the dependency of the numerical errors on the approximation quality of the discretization, the material contrast, and the frequency content of the seismic waves, we set up a test case which allows us to perform a systematic analysis by the variation of the respective parameters. This will then lead to the definition of some fundamental rules concerning the discretization of complex geometries with regular meshes and the importance of the interface approximation by mesh alignment.

2.1 Model setup

Similar to previous work (Kawase 1988; Ohminato & Chouet 1997) we simulate the incidence of a plane P wave with a Ricker-type source time function onto a semi-circular material interface separating a basin-like structure from a homogeneous half-space (see Fig. 1). Material 1 located in the half-circle of radius $r = 100$ m is surrounded by material 2 of higher wave velocities. In addition to five different material contrasts of elastic media, we also consider two special cases, where the material 1 in the basin is an acoustic

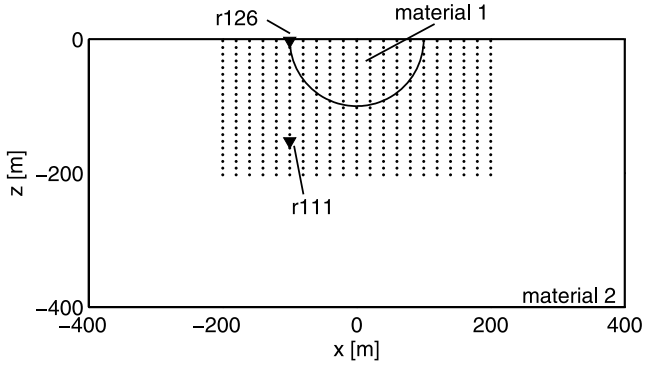

Figure 1. Model setup of the accuracy study with a basin-like structure (material 1) in a homogeneous half-space (material 2). We show a zoomed section of the area of the material interface with receiver locations denoted by dots. Seismograms at positions of highlighted geophones (downward-pointing triangle) are discussed in detail in Section 2.2.

fluid, or where the material interface represents a free-surface boundary such that material 1 vanishes. We will focus on the computational domain $(x, z) \in \Omega = [-400, 400] \times [-400, 0]\,\mathrm{m} \in \mathbb{R}^2$ with the top boundary ($z = 0$ m) being a free surface. In fact, the other boundaries of the model are extended sufficiently to avoid any interference of possible reflections from non-perfectly absorbing boundaries with the waves of interest that are reflected, transmitted, or converted at the material interface or the free surface. Tests, which are not shown here, indicated that, in principle, similar results are obtained for plane *S*-wave incidence or waves from single-force sources generating *P* and *S* waves as well as for different interface geometries, for example, a notch (Godinho *et al.* 2009). The dots in Fig. 1 denote the locations of 21 × 21 receivers allowing for a dense sampling of the wavefield to obtain an overview of the spatial error distribution.

In Fig. 2, we show the two different discretization approaches used. On the left-hand side a regular, structured grid with a mesh spacing of $h = 20$ m is sketched. In our study we assign constant material properties within each element determined by the location of the element's barycentre. With the displayed coarse resolution of only a fifth of the semi-circle's radius the discretized shape of the material interface hardly represents the true geometry. On the right side of Fig. 2 we show an unstructured, triangular mesh with an average triangular edge length of $h = 10$ m. This discretization is used to produce a reference solution for the problem and provides a sufficiently accurate discretization, as further mesh refinement to $h = 5$ m generates quasi-identical seismograms. Therefore, we also remark that the unstructured triangular mesh with its piecewise linear edge-alignment of $h = 10$ m represents the material interface sufficiently accurate.

For our tests concerning the sensitivity of numerical seismograms to the discretization of complex geometry, we use a series of regular square-shaped meshes with $h = 20$, 10 and 5 m providing an improved discretization of the curved material interface by an increasingly fine staircase approximation. Furthermore, we vary the material contrast to investigate its importance with respect to the discretization approach. The material contrast between two materials 1 and 2 is given through the ratio of the *S*-wave speeds $v_{S,1}/v_{S,2}$, with $v_{S,1} \leq v_{S,2}$. In this way, small numbers represent strong material contrasts. Table 1 gives an overview of the applied material contrasts and wavelengths. Finally, we use plane, Ricker-type *P* waves of different dominant frequency contents, $f15 = 15$ Hz, $f20 = 20$ Hz and $f25 = 25$ Hz to analyse the dependence of the discretization effects on the seismic wavelengths. We mention, that the Ricker wavelet of a dominant frequency f contains significant energy up to a maximum frequency of around $2.5f$.

The used simulation code is based on a DG method and is well tested and verified against analytical solutions and other numerical schemes (Dumbser & Käser 2006; Käser *et al.* 2008). Its accuracy and applicability to strong material heterogeneities was also confirmed in previous work (Castro *et al.* 2010; Chaljub *et al.* 2010). Using the same numerical solver for structured and unstructured meshes ensures that differences in the seismograms originate only from diverse geometry representations and not from numerical biases like diffusion, dispersion, underresolution, or different ways of incorporating material properties. We remark, that all simulations are performed with order 7 in space and time and use enough elements per wavelength to resolve the wavefield sufficiently accurate. This is confirmed by running the simulations of highest frequency content and coarsest discretization with a decreased order of accuracy, which basically does not change the resulting seismograms and therefore proves numerical convergence of the solution. The remaining small differences are much smaller than the effects obtained by varying the parameters of our accuracy analysis.

2.2 Accuracy analysis

In the following we analyse the results of the 63 test cases obtained by seven different material contrasts, three mesh spacings and three frequencies. First, we study the spatial error distribution to identify areas of particularly high errors. Then we investigate and display the misfits of selected seismograms to define some basic rules. These rules should guarantee a desired level of accuracy for curved

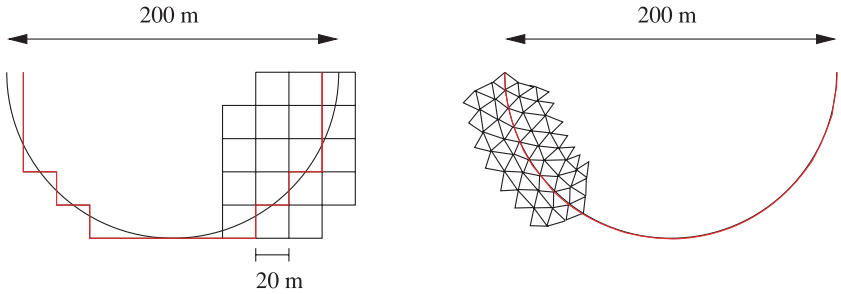

Figure 2. Sketch of the two different discretization approaches. Material properties for the DG method are set element-wise determined by the barycenter of each element. Hence, the discrete material interface (red line) is dislocated from the exact position (black semi-circle) and depends on the mesh. Left: an example of a regular mesh with 20 m spacing is shown which is not able to represent the interface properly leading to a coarse and jagged approximation. Right: an example of a triangular mesh with 10 m spacing (triangular edge lengths) used to compute the reference solution. In this case, the shape of semi-circle is approximated with piecewise linear edges of triangular elements.

Table 1. Material properties for the seven test cases with different contrasts across the interface. Furthermore, the dimensionless values of the shortest wavelength per mesh spacing λ_S/h are given for the dominant frequencies f. Please, note that a P wave represents the shortest wavelength in the Solid–Fluid test case.

				λ_s/h for f25			λ_s/h for f20			λ_s/h for f15		
Test case	ρ (kg m^{-3})	v_P (m s^{-1})	v_S (m s^{-1})	h20	h10	h5	h20	h10	h5	h20	h10	h5
Solid–Solid 1												
Material 1	1000	1732	1000	2	4	8	2.5	5	10	3.3	6.7	13.3
Material 2	1299	2249	1299	2.6	5.2	10.4	3.2	6.5	13	4.3	8.7	17.3
Contrast		0.77	0.77									
Solid–Solid 2												
Material 1	1000	1732	1000	2	4	8	2.5	5	10	3.3	6.7	13.3
Material 2	1538	2665	1538	3.1	6.2	12.3	3.8	7.7	15.4	5.1	10.2	20.5
Contrast		0.65	0.65									
Solid–Solid 3												
Material 1	1000	1732	1000	2	4	8	2.5	5	10	3.3	6.7	13.3
Material 2	2000	3464	2000	4	8	16	5	10	20	6.7	13.3	26.7
Contrast		0.5	0.5									
Solid–Solid 4												
Material 1	1000	1732	1000	2	4	8	2.5	5	10	3.3	6.7	13.3
Material 2	2500	4503	2600	5.2	10.4	20.8	6.5	13	26	8.7	17.3	34.7
Contrast		0.38	0.38									
Solid–Solid 5												
Material 1	1000	1732	1000	2	4	8	2.5	5	10	3.3	6.7	13.3
Material 2	5000	8660	5000	10	20	40	12.5	25	50	16.7	33.3	66.7
Contrast		0.2	0.2									
Solid–Free Surface												
Material 1	–	–	–	–	–	–	–	–	–	–	–	–
Material 2	2000	3464	2000	4	8	16	5	10	20	6.7	13.3	26.7
Contrast		–	–									
Solid–Fluid												
Material 1	1020	1500	0	3	6	12	3.8	7.5	15	5	10	20
Material 2	2000	3464	2000	4	8	16	5	10	20	6.7	13.3	26.7
Contrast		0.43	–									

interface approximations, that have to be obeyed when using structured meshes.

2.2.1 *Spatial error distribution*

We compare the quality of the obtained seismograms at all 441 receivers indicated in Fig. 1. To measure the misfit between the simulated test seismogram $S_{h,i}(t)$ and the reference solutions $S_{\mathrm{ref},i}(t)$ we use the root mean square (rms) error

$$E_i = \sqrt{\frac{\int |S_{h,i}(t) - S_{\mathrm{ref},i}(t)|^2 \mathrm{d}t}{\int |S_{\mathrm{ref},i}(t)|^2 \mathrm{d}t}}, \tag{1}$$

where i is the index of the receiver, h the mesh spacing of the numerical computation, and t is time. We emphasize that the rms error is not always suitable to compare seismograms quantitatively.

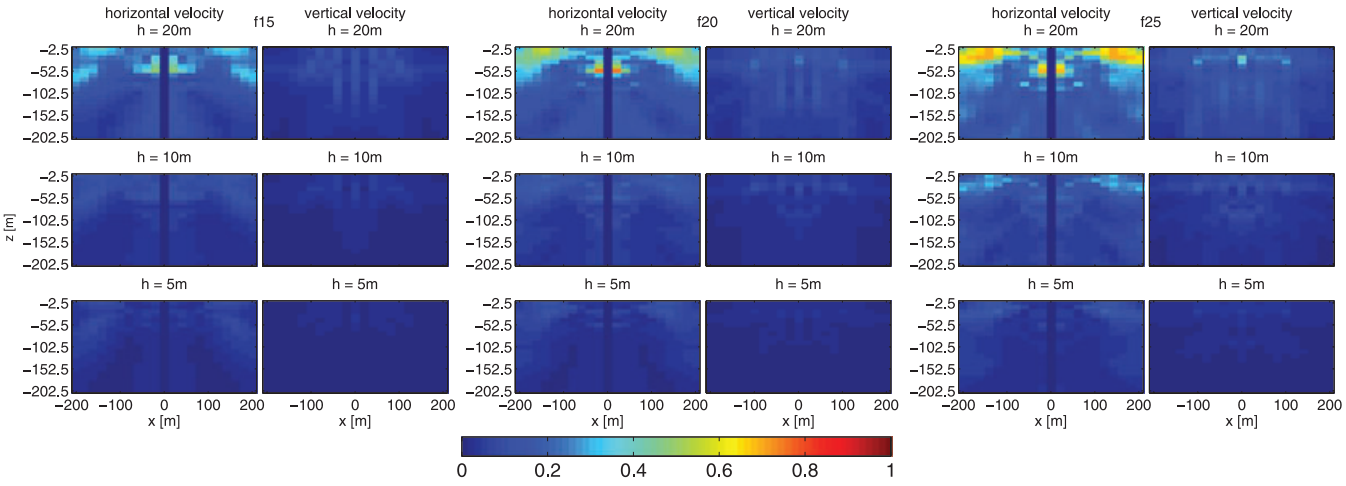

Figure 3. Error maps of the rms error E for the test case Solid–Solid 1 with the material contrast 0.77.

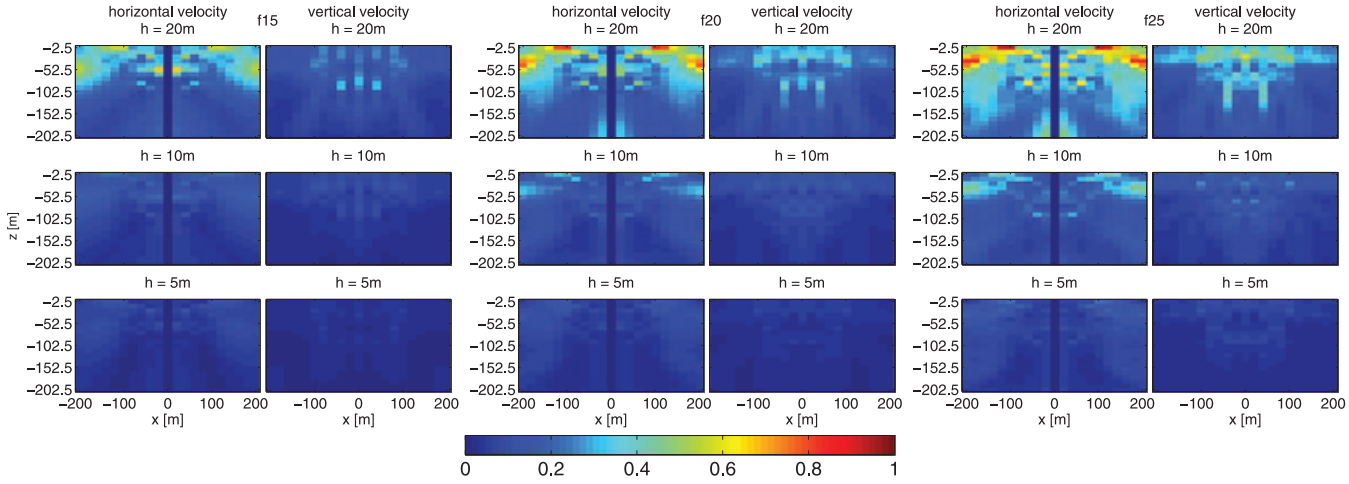

Figure 4. Error maps of the rms error E for the test case Solid–Solid 2 with the material contrast 0.65.

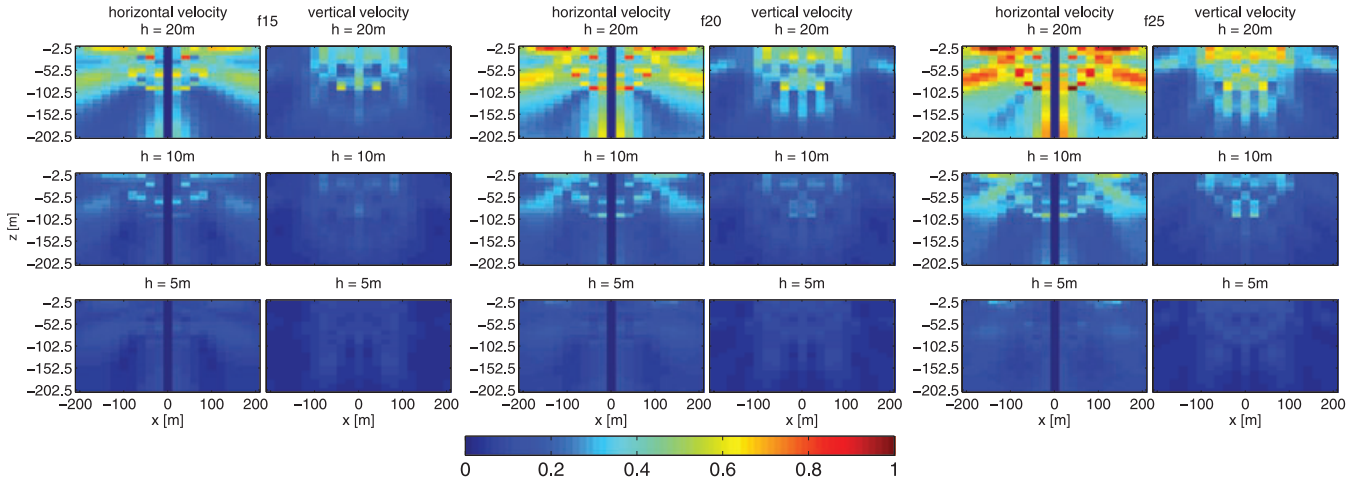

Figure 5. Error maps of the rms error E for the test case Solid–Solid 3 with the material contrast 0.5.

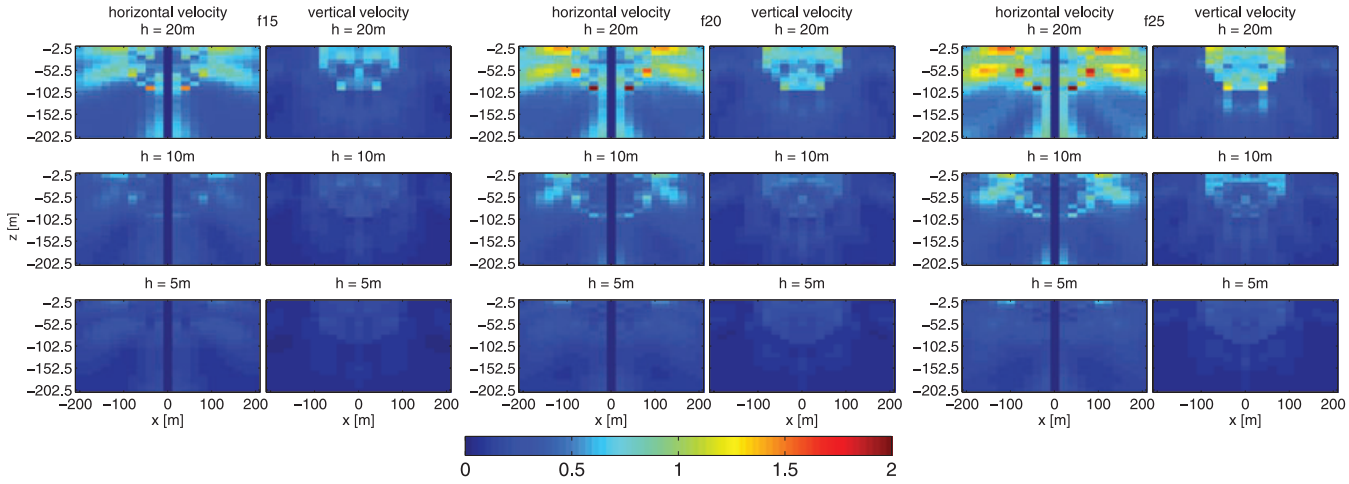

Figure 6. Error maps of the rms error E for the test case Solid–Solid 4 with the material contrast 0.38.

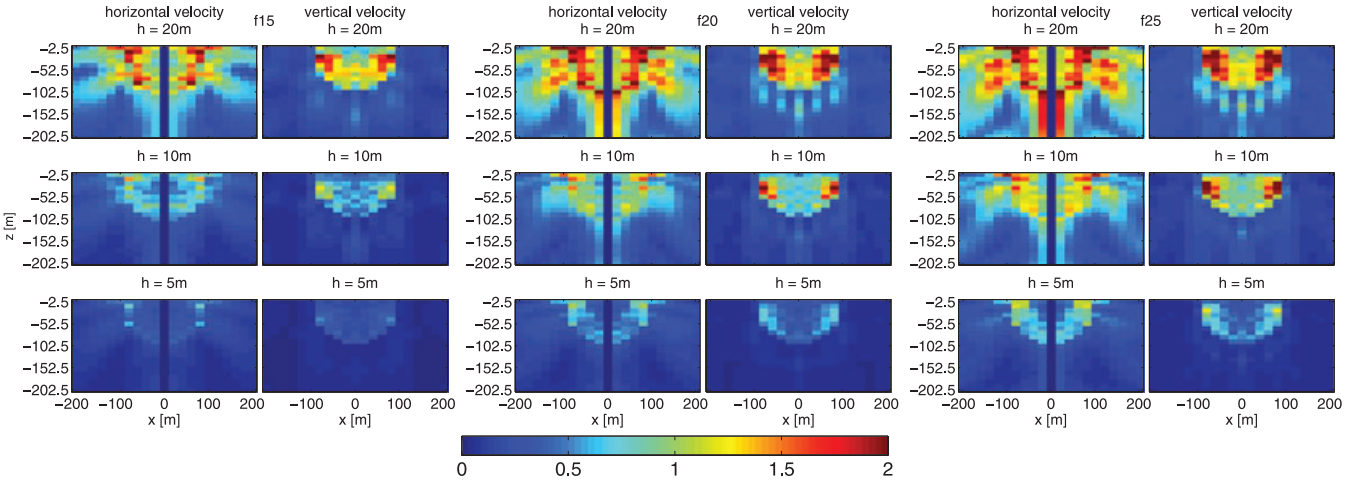

Figure 7. Error maps of the rms error E for the test case Solid–Solid 5 with the material contrast 0.2.

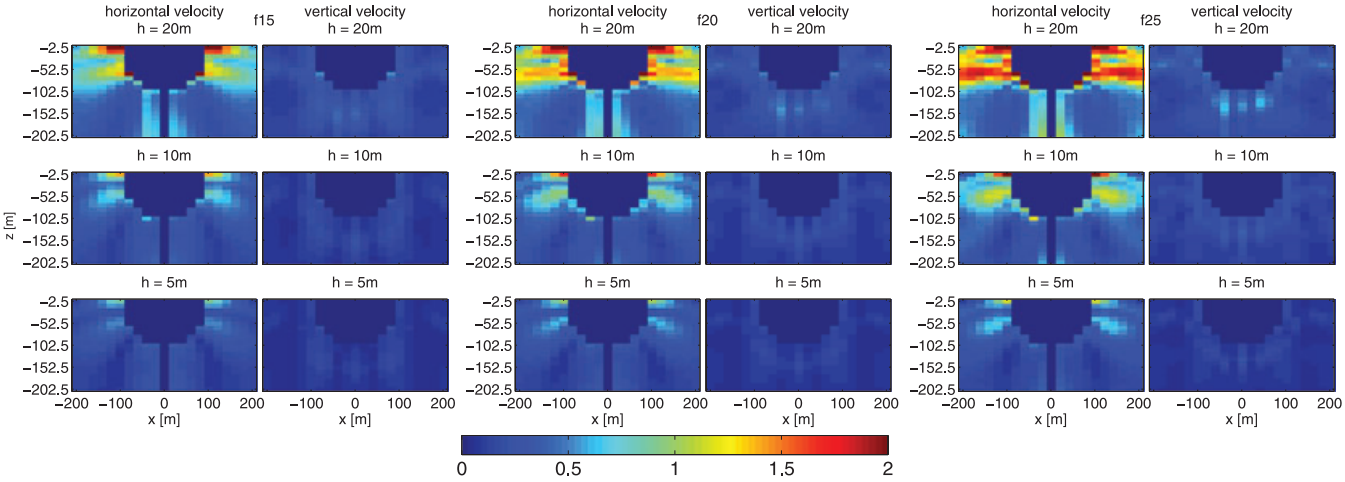

Figure 8. Error maps of the rms error E for the test case Solid–Free Surface.

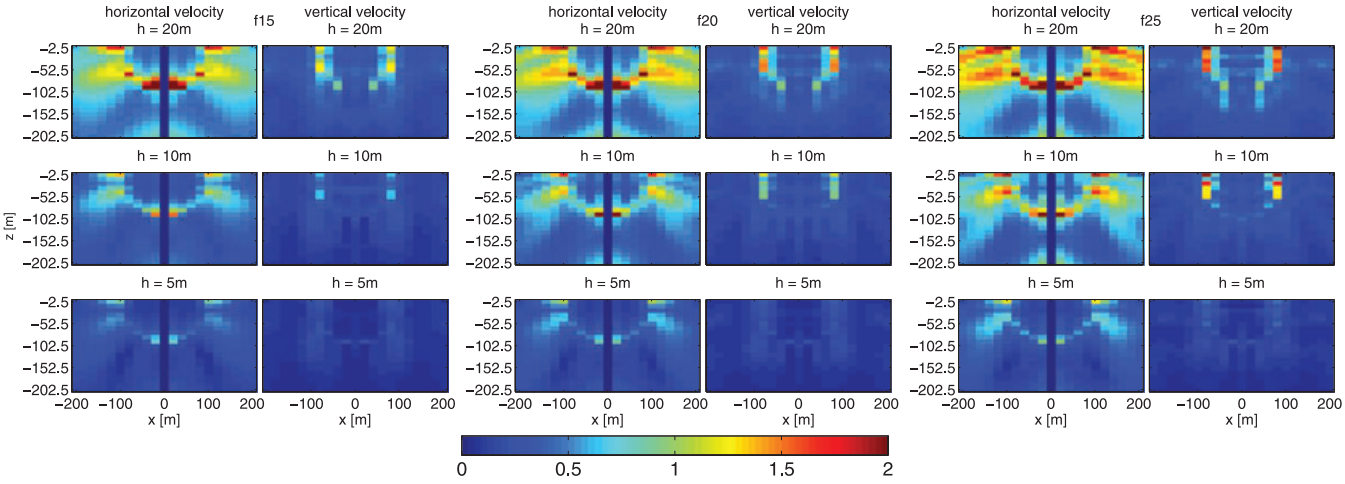

Figure 9. Error maps of the rms error E for the test case Solid–Fluid.

Instead, time-frequency (TF) misfit criteria as suggested by Kristeková *et al.* (2006, 2009) represent a more appropriate approach for the comparison of two signals. The main advantage of the TF-misfit is to obtain separate information about phase and envelope errors. We also determined the envelope and phase misfits individually, however, it turned out that the combined analysis of these envelope and phase misfits at each receiver gives at least a similar pattern as the rms error. Even though we, in general, strongly recommend the use of the TF-misfit analysis we prefer the single-valued rms error in this case to provide an overview of the spatial error distribution without splitting all our results considering envelope and phase misfits separately. Furthermore, the rms error typically tends to overestimate the errors compared to separate envelope and phase misfits and therefore serves as an upper limit estimation.

To present the errors we assign a coloured pixel to each receiver depending on the single valued rms misfit of its seismograms distinguishing horizontal and vertical components.

In Figs 3–9, we show the spatial error maps representing the single valued rms misfit E_i between reference solutions and seismograms obtained with the structured grid. Each figure belongs to one material contrast and contains the results of the three dominant frequencies $f15$, $f20$ and $f25$ (ordered from left- to right-hand side) obtained from the three refined mesh spacings $h = 20, 10, 5$ m (ordered from top to bottom). For each frequency and mesh size we display the horizontal and vertical velocity components. For better visualization and comparison the colour bars are normalized ranging between 0 and 1 for the minor material contrasts Solid–Solid 1 (Fig. 3) to Solid–Solid 3 (Fig. 5) and between 0 and 2 for the stronger contrasts

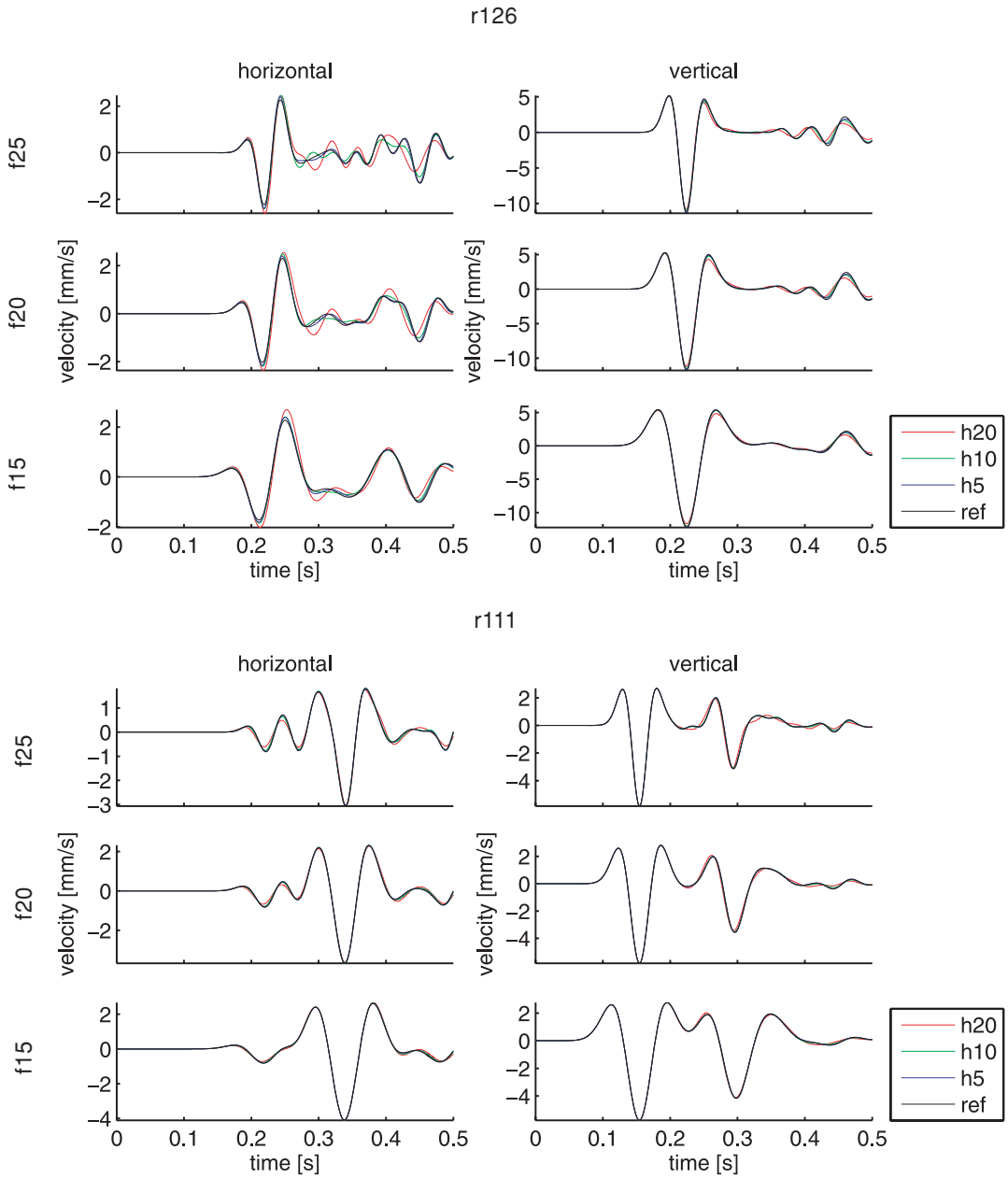

Figure 10. Example seismograms of the accuracy study test case Solid–Solid 1 with the material contrast 0.77. Shown are the horizontal and vertical velocity components of r126 (top panel) and r111 (bottom panel).

Solid–Solid 4 (Fig. 6) to Solid–Fluid (Fig. 9) where the errors are larger.

A first and obvious observation is that the misfit of the horizontal velocity components in the centre of the model ($x = 0$ m) is always zero, as no energy appears on this component caused by the plane vertical P wave incident from below. However, higher error levels appear, in general, for the horizontal component. This is also due to the fact that all energy in the system is primarily in the vertical component and only by reflections, refractions and transmissions energy is transferred into the horizontal component. Therefore, the horizontal component seems to be especially sensitive to the geometry approximations of the semi-circular interface. A further observation is the higher error level close to the material interface, at the free-surface, and at two areas leading away from the semi-circular basin at approximately 30° downward. The shape of the semi-circle is easily identifiable by warmer colours for the stronger material contrasts. Besides higher errors occur at the inside of the semi-circle close to the material contact. Furthermore, a general increase of the error level with increasing mesh spacing, higher frequency content and stronger material contrast is visible.

Particularly high errors appear in the case of the Solid–Free Surface (Fig. 8) and Solid–Fluid (Fig. 9) contrasts where the staircase approximation of the curved interface obviously creates large misfits compared to the reference solution obtained with the rather smooth approximation via aligned triangular edges. In these two cases even for the finest mesh spacing $h = 5$ m and lowest frequency f15 the horizontal component already shows an error level clearly above $E_i = 0.5$. However, for the Solid–Solid material interfaces in Figs 3–7 the finest mesh spacing $h = 5$ m seems to work surprisingly well.

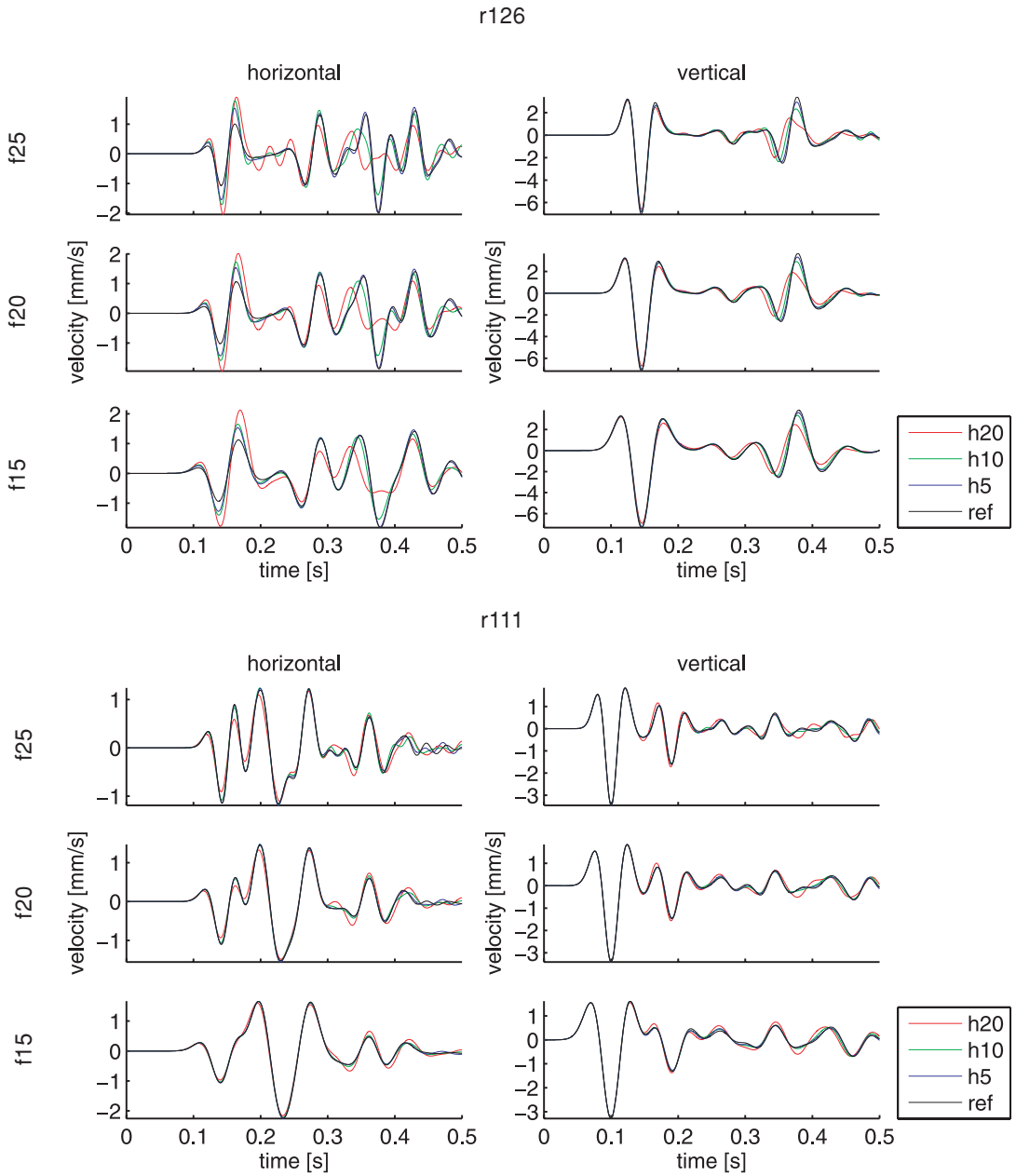

Figure 11. Example seismograms of the accuracy study test case Solid–Solid 3 with the material contrast 0.5. Shown are the horizontal and vertical velocity components of r126 (top panel) and r111 (bottom panel).

Based on this investigation of the spatial error distribution we can now focus on the seismogram misfits and the effects of the staircase approximation of a curved interface on the seismic signature in more detail.

2.2.2 Seismogram misfits

After the analysis of the overall distribution of rms errors, we study the seismic waveforms at two receivers in different areas of the computational domain. To this end, we show the variation of the seismograms for the test cases Solid–Solid 1 (Fig. 10), Solid–Solid 3 (Fig. 11), Solid–Free Surface (Fig. 12) and Solid–Fluid (Fig. 13) with respect to their dependence on the mesh spacing (different colours) and frequency (ordered from top to bottom) for both horizontal (left) and vertical (right) components. In each figure we display the results obtained for receivers r111 and r126 at the locations indicated by the downward-pointing triangles in Fig. 1. While receiver r111 $(x, z) = (-100.0, -152.5)$ m lies in an area of a generally low rms error, receiver r126 $(x, z) = (-100.0, -2.5)$ m has a crucial position close to the free-surface boundary at the top of the computational domain and directly at the material interface. If we compare the behaviour of the seismogram misfit in Figs 10–13 with each other, the growing misfits with increasing material contrast is clearly observable again. The seismograms of the test case Solid–Solid 1 (Fig. 10) are examples of a remarkably good fit, which is due to the small material contrast. Only at the crucial position of r126 for a coarse mesh spacing of $h = 20$ m we obtain larger amplitude errors and phase shifts for the horizontal velocity component. The seismograms of receiver r126 for the test case Solid–Solid 3

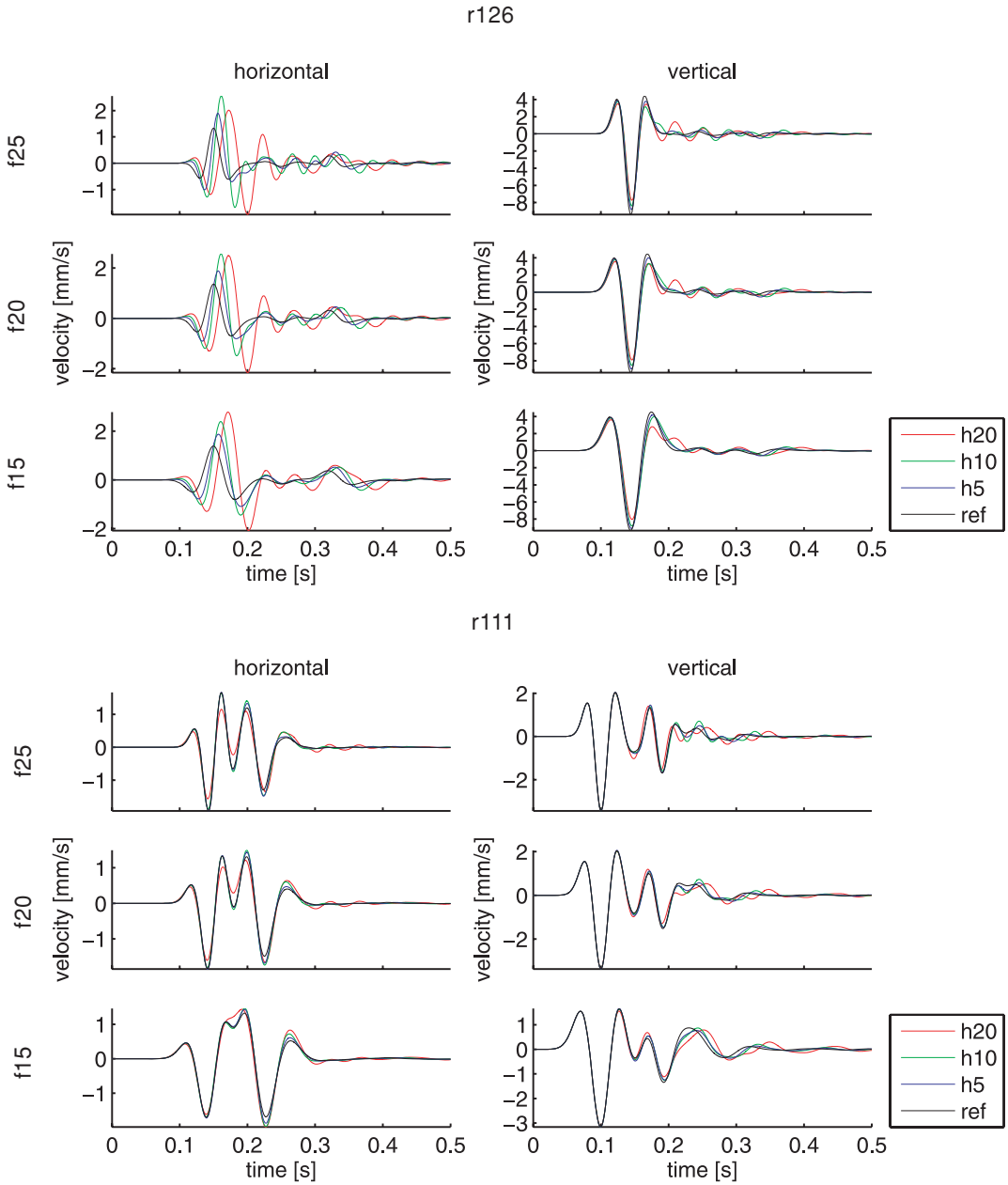

Figure 12. Example seismograms of the accuracy study test case Solid–Free Surface. Shown are the horizontal and vertical velocity components of r126 (top panel) and r111 (bottom panel).

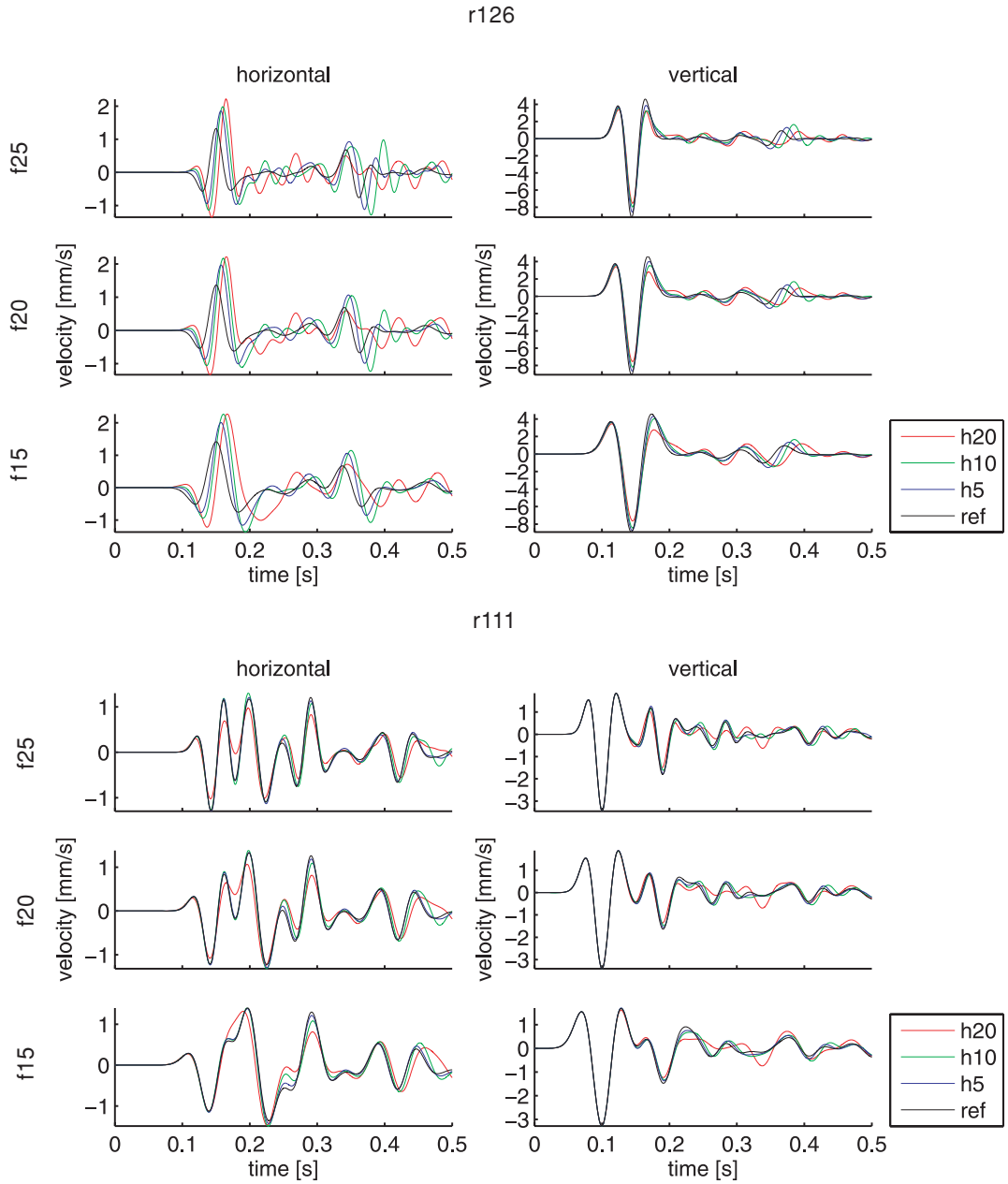

Figure 13. Example seismograms of the accuracy study test case Solid–Fluid. Shown are the horizontal and vertical velocity components of r126 (top panel) and r111 (bottom panel).

(Fig. 11) show nicely how the error decreases with decreasing mesh spacing. However, we can observe only a small decrease of the misfit at lower frequencies. In contrast, receiver r111 seems to be much less affected. As expected, the quality of seismograms at receiver r126 depends strongly on the combination of the three different simulation parameters due to its worst case position identified in Section 2.2.1

Furthermore, the seismograms of the test cases Solid–Free Surface (Fig. 12) and Solid–Fluid (Fig. 13) clearly demonstrate that the waveforms are strongly affected by the staircase approximation of the semi-circular interface. While the misfits at receiver r111 again are much smaller and decrease even more with reduced mesh spacing and frequency, the seismograms at receiver r126, especially the horizontal components, are not acceptable even for the finest mesh h5 and lowest frequency f15.

2.3 Discretization rules

To facilitate the definition of useful discretization rules that have to be considered when approximating curved material interfaces we introduce the total error

$$E_{\text{tot}} = \frac{1}{N}\sum_{i}(E_{i,\text{horizontal}} + E_{i,\text{vertical}}) \tag{2}$$

over all receivers i that occur in an error map of Figs 3–9, where N is the number of receivers. Note, that N changes for the test case Solid–Free Surface depending on how many receivers are still below the free-surface boundary, while $N = 441$ for all other test cases. The error E_{tot} allows us to measure the overall seismogram misfit of a simulation depending on different mesh spacings, frequencies, and material contrasts. A threshold of the error E_{tot} is shown as a dashed

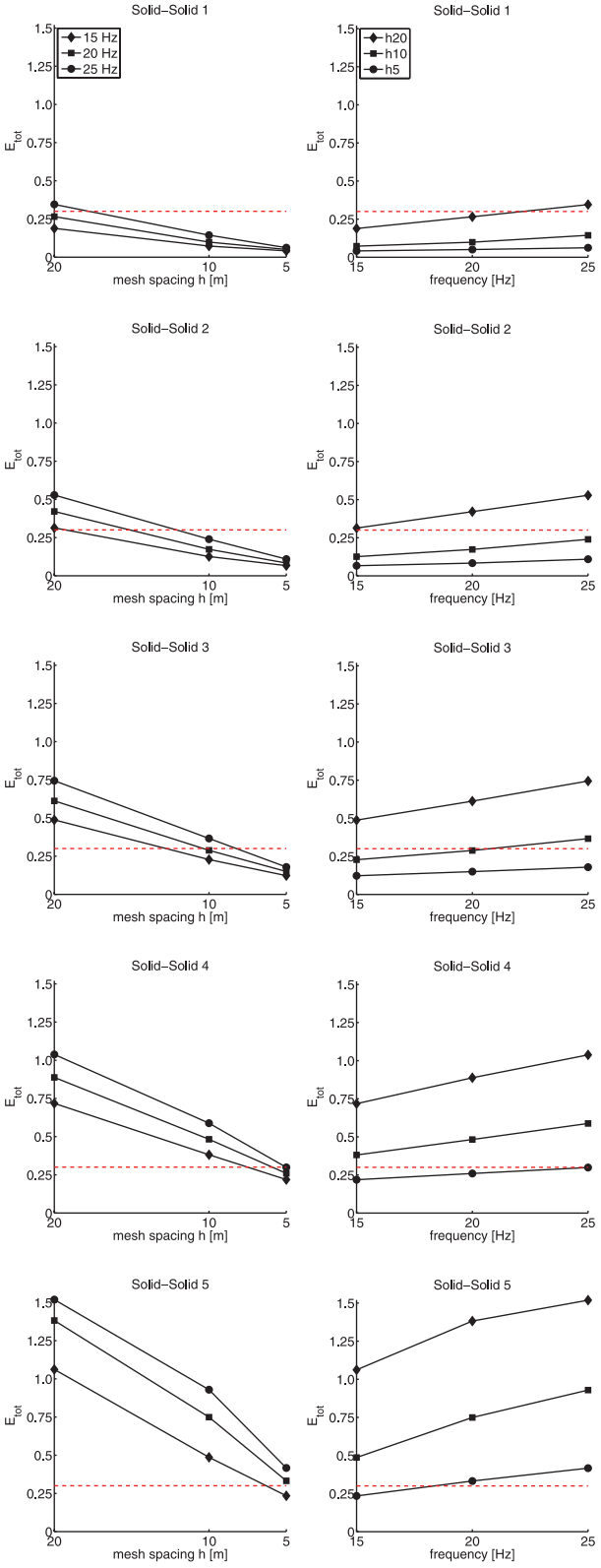

Figure 14. Left: error E_{tot} versus mesh spacing h with varying frequencies f for the different material contrasts. Right: error E_{tot} versus frequency f with varying mesh spacing h. The threshold of acceptance is shown as a dashed red line.

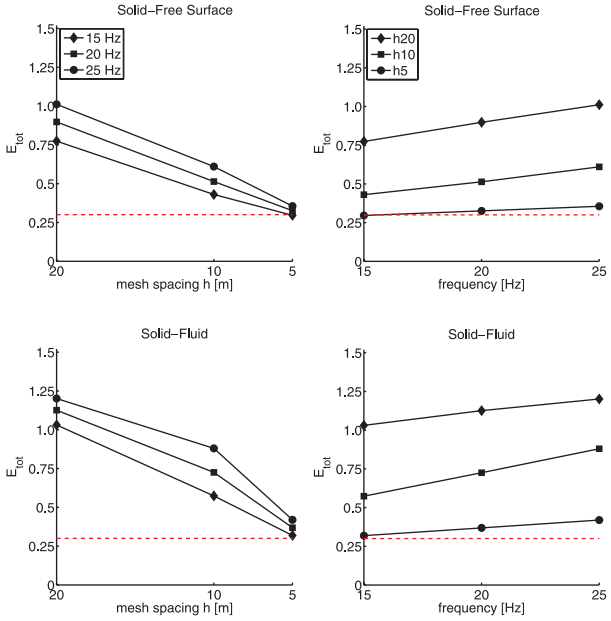

Figure 15. Left: error E_{tot} versus mesh spacing h with varying frequencies f for the different material contrasts. Right: error E_{tot} versus frequency f with varying mesh spacing h. The threshold of acceptance is shown as a dashed red line.

red line in all plots of Figs 14–16. The results of the systematic error analysis are shown in Figs 14 and 15 on the left displaying the behaviour of the error E_{tot} with respect to mesh refinement for each of the seven different material contrasts. The three lines of different symbols represent the frequencies. Clearly, the errors are consistently smaller for lower frequencies and decrease almost linearly with mesh refinement for all seven test cases. Therefore, our DG approach confirms the first-order error behaviour due to the simple staircase approximation as predicted by studies on the immersed interface method (Zhang & LeVeque 1997; Zhang & Symes 1998) even though the approximation of the solution using our DG scheme is of order 7 in space and time. We mention that the basic idea in immersed interface methods is to take into account the jump conditions for the discontinuous solution or its derivatives at an interface and to find linear combinations of these discontinuous values that give more accurate numerical approximations at or near the interface.

Presenting the results in a different way in Figs 14 and 15 on the right, where the error is plotted against frequency, shows that systematically finer meshes provide smaller errors that increase with higher frequency content. In a third presentation of our results in Fig. 16 we show the behaviour of the error for all seven material contrasts (different line symbols) in one plot. In the top row the frequency is fixed in each plot and the error decreases with decreasing mesh spacing h. In the bottom row the mesh spacing is fixed and the error behaviour depending on frequency is shown. Obviously, the errors are generally smaller for smaller material contrasts, however, the test case Solid–Fluid seems to be even more sensitive to the staircase approximation than the Solid–Free Surface. We point out that it is important to consider interface waves such as Rayleigh waves at the free surface and Scholte waves at an elastic–acoustic interface when signals are recorded directly at or in the vicinity of the interface. Even though such interface waves propagate slower than the S wave inside the elastic material their phase velocities are usually close to the S-wave velocity. Therefore the suggested mesh

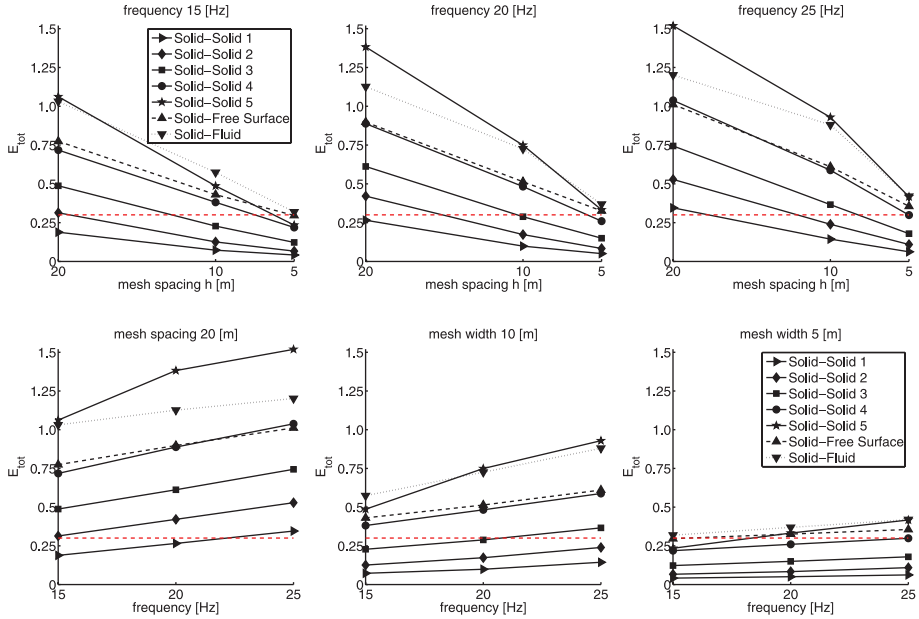

Figure 16. Error E_{tot} versus mesh spacing h and frequency f, respectively with varying material contrasts. The threshold of acceptance is shown as a dashed red line.

spacing of the following discretization rules would have to be adjusted by using a correspondingly smaller mesh spacing. Furthermore, the velocities of the interface waves show significant frequency-dependence (dispersion) and their energy content compared to the body waves is difficult to estimate. Therefore, a systematic study of their influence would go beyond the scope of this work. However, our results agree, in general, with the studies of Bohlen & Saenger (2006) concerning staircase approximations of free-surface boundaries in numerical modelling of seismic wave propagation, as accurate simulations including topography or bathymetry (van Vossen *et al.* 2002) require a much higher mesh resolution than those treating internal elastic interfaces. They show that surface waves are particularly sensitive to non-smooth topography. In contrast, for the Solid–Solid test cases a regular mesh with staircase approximation of material interfaces can generate acceptable results depending on the combination of mesh spacing, frequency and material contrast. For seismic wave speed contrasts across a material discontinuity of 0.77 (Solid–Solid 1) only small differences in the seismograms are obtained even for relatively high frequencies and coarse meshes (see Fig. 3). An increase of the material contrast requires in turn an adjustment of either a higher mesh resolution or a reduction of the frequency.

Finally, we can establish rules, which should be adhered when modelling complex geological interfaces, especially with the DG approach using regular, structured meshes and which should also be considered in wave propagation modelling using other methods. First we define a threshold for classifying a seismogram to be acceptable. In our case, this threshold is defined as $E_{\text{tot}} = 0.3$ above which seismograms are degenerated too much due to the geometrical representation of the interface. This threshold is shown as a dashed red line in all plots of Figs 14 and 16. As examples to clarify the meaning of this threshold with respect to the seismic waveforms and their misfits we refer to the seismograms shown in Section 2.2.2 In Fig. 11 the horizontal component obtained at receiver r126 with frequency content $f15$ and mesh spacing h10 (green) has an error level $E_i = 0.285$ and is therefore classified as just acceptable. A non-acceptable example is given in the same graphic for frequency $f25$ obtained with h10 (green) with $E_i = 0.500$. In contrast, a clearly acceptable horizontal seismogram is shown in Fig. 11 for receiver r111, frequency $f25$ and h10 (green), with $E_i = 0.135$.

If we now use the results shown, for example in Fig. 15, none of our simulations of the Solid–Free Surface or Solid–Fluid cases produced acceptable seismograms. Therefore, we will focus on the different Solid–Solid test cases in the following. However, we point out that our tests consider a v_p/v_s-ratio of $\sqrt{3}$ of a Poisson material. As shown recently by Moczo *et al.* (2010) the accuracy of most of the used numerical schemes decreases with increasing v_p/v_s-ratio and values of 5 and larger can occur in near-surface sedimentary structures. From each of the plots of Fig. 14 we use the acceptable data point with the highest error value but still below the red threshold line. Also, we use the non-acceptable data point with the lowest error level but larger than the error threshold. Using the information of the shortest dominant wavelength per mesh spacing for each test case given in Table 1 we can plot these data into the graph in Fig. 17 to determine a transition zone that separates two regions. Above the transition zone (grey shaded), bounded by the solid black line from above, the sampling in the sense of elements per wavelength is good enough for the particular material contrast to produce acceptable seismograms. Below the transition zone, bounded by the dashed red line from below, the sampling is insufficient and non-acceptable seismograms according to our threshold are obtained. Considering this result is extremely important for high-order accurate numerical schemes, like the DG or SEM methods, as such methods usually allow for large mesh spacings due to their high-order approximation properties within an element. In cases, where geometrically complicated material interfaces cannot be honoured by mesh alignment or regular meshes are used for computational efficiency, it is crucial to respect the results represented in Fig. 17 to reduce numerical artefacts due to the staircase approximation. From Fig. 17 we also can conclude that low-order schemes using the staircase approximation naturally seem to overcome the problem of complex geometry as the number of gridpoints or elements per wavelength is typically chosen high enough (e.g. 8 gridpoints per wavelength) to obtain satisfying results. Furthermore, our results confirm the

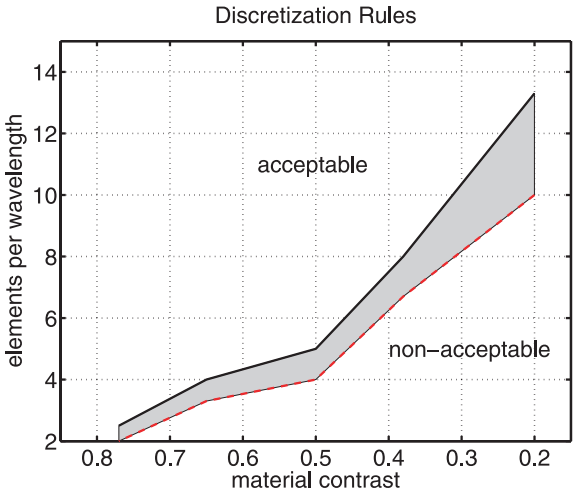

Figure 17. Diagram representing the discretization rules by displaying what mesh spacing (measured in elements per shortest dominant wavelength) is required for a given material contrast to obtain acceptable seismograms above the black solid line. The material contrast between two materials 1 and 2 is given through the ratio of S-wave speeds $v_{S,1}/v_{S,2}$, with $v_{S,1} \leq v_{S,2}$. Values below the red dashed line produce non-acceptable results, while the grey shaded area denotes a transition zone.

exceptionally fine mesh spacing required to model Solid–Fluid or Solid–Free Surface contacts with methods which cannot align the mesh to such non-planar interfaces typically occurring for strong bathymetry or topography. For further details on this topic for FD schemes we refer to the work of Robertsson (1996) and Bohlen & Saenger (2006).

3 MULTIPLE LAYERS WITH UNDULATING INTERFACES

Since our previous study consist of a rather simple geometry with only one interface, we here construct a more complex situation representing a more realistic application. This test case contains three layers separated by two undulating interfaces with a material contrast of 0.5 each. The regular grid spacing of the quadrilateral mesh is constructed by respecting the rules of Section 2.3. Representative seismograms of selected receivers are analysed and discussed in detail.

Table 2. Material properties used for the multiple layer application.

	ρ (kg m^{-3})	v_P (m s^{-1})	v_S (m s^{-1})
Material 1	1000.0	1732.1	1000.0
Material 2	2000.0	3464.1	2000.0
Material 3	4000.0	6928.2	4000.0

3.1 Test case description

An overview of the layered model is given in Fig. 18 with material properties given in Table 2. The top boundary at $z = 0$ m is a free surface, the bottom at $z = -8000$ m is absorbing and the lateral boundaries are set periodic. The source is a point source at $(x, z) = (10, -1990)$ m using a force pair on the two velocity components with a Ricker-type source time function of dominant frequency $f = 8$ Hz. The total simulation time is 10 s.

Considering Fig. 17, we should be able to use a mesh spacing of five elements per dominant wavelength to represent an interface with material contrast 0.5 sufficiently accurate with a structured discretization. Like in Section 2, we cover a large part of the domain with a dense receiver array of 31 × 31 receivers distributed within a rectangular area of $(x, z) \in [-3000, 3000] \times [-6000, 0]$ m. The shortest dominant wavelengths for material 1 and 2 are 125 and 250 m, respectively, leading to mesh spacings of $h = 25$ and $h = 50$ m at the interfaces. The employment of a regular but non-conforming mesh (Hermann *et al.* 2010) enables us to test both interfaces with their specific resolutions. In more specific terms, this means that we use a regular mesh spacing of $h = 25$ m above $z = -3000$ m and $h = 50$ m below this depth. An example of the interface discretization by the structured grid is given in Fig. 18(b). To ensure a correct resolution of the wavefield we choose the approximation order 6 in space and time. Again, a reliable reference solution is produced using the same numerical method and order of accuracy on an unstructured edge-aligned triangular mesh with a resolution of 2.5 elements per shortest dominant wavelength.

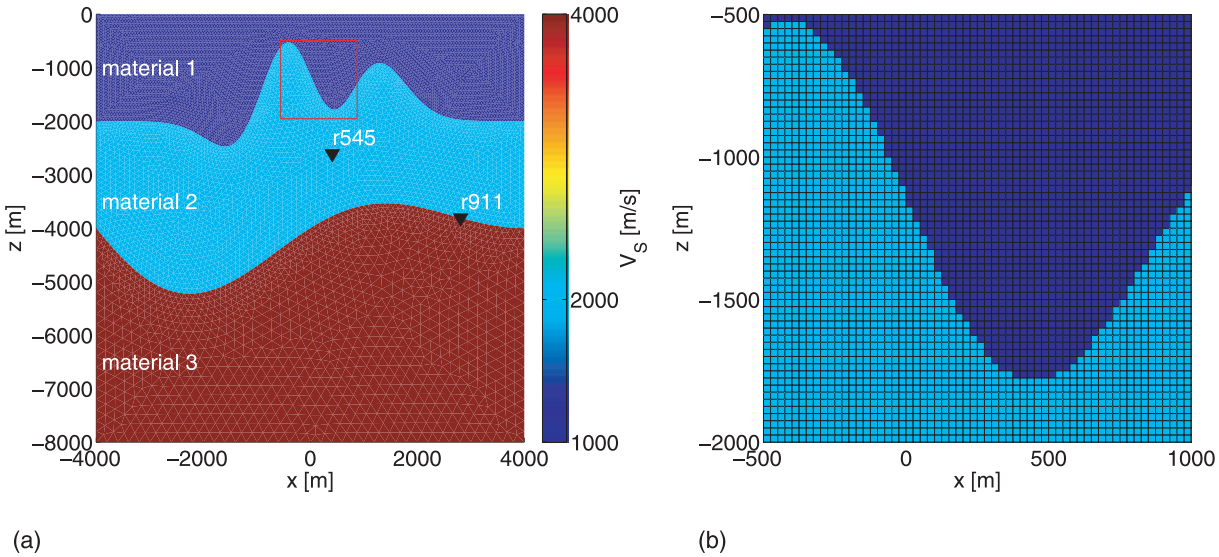

Figure 18. (a) S-wave velocity distribution of the multiple layer application. The area within the red rectangular is zoomed in (b) together with an overlay of the quadrilateral mesh.

3.2 Results and discussion

The overall rms error distribution is shown in Fig. 19 and its level is very small as expected. A clear error pattern with error concentrations at the material interfaces is much harder to recognize than in the test cases of Section 2.2.1. However, a trace of higher errors along the lower interface still can be identified. Our interpretation is that due to the complicated wavefield, interface waves, multiple reflections, and transmissions the errors might locally sum up close to the interfaces. Therefore, the seismogram with the largest misfit is obtained by receiver r911 and one with a very small misfit by r545. The locations of these stations are denoted in the overview Fig. 18(a)

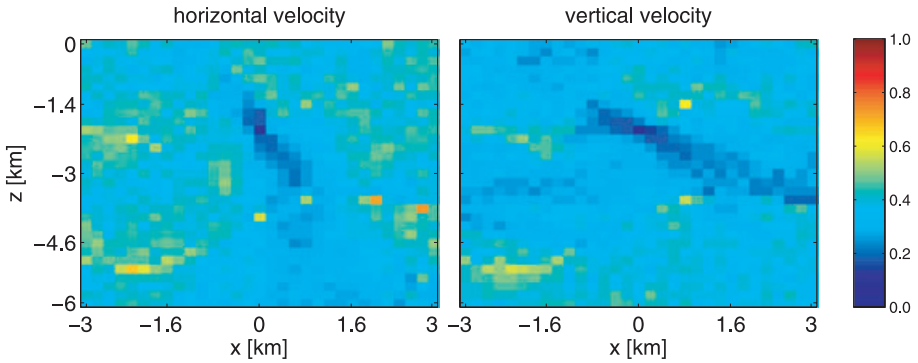

Figure 19. Error maps of the rms error E_i for the multiple layer test case.

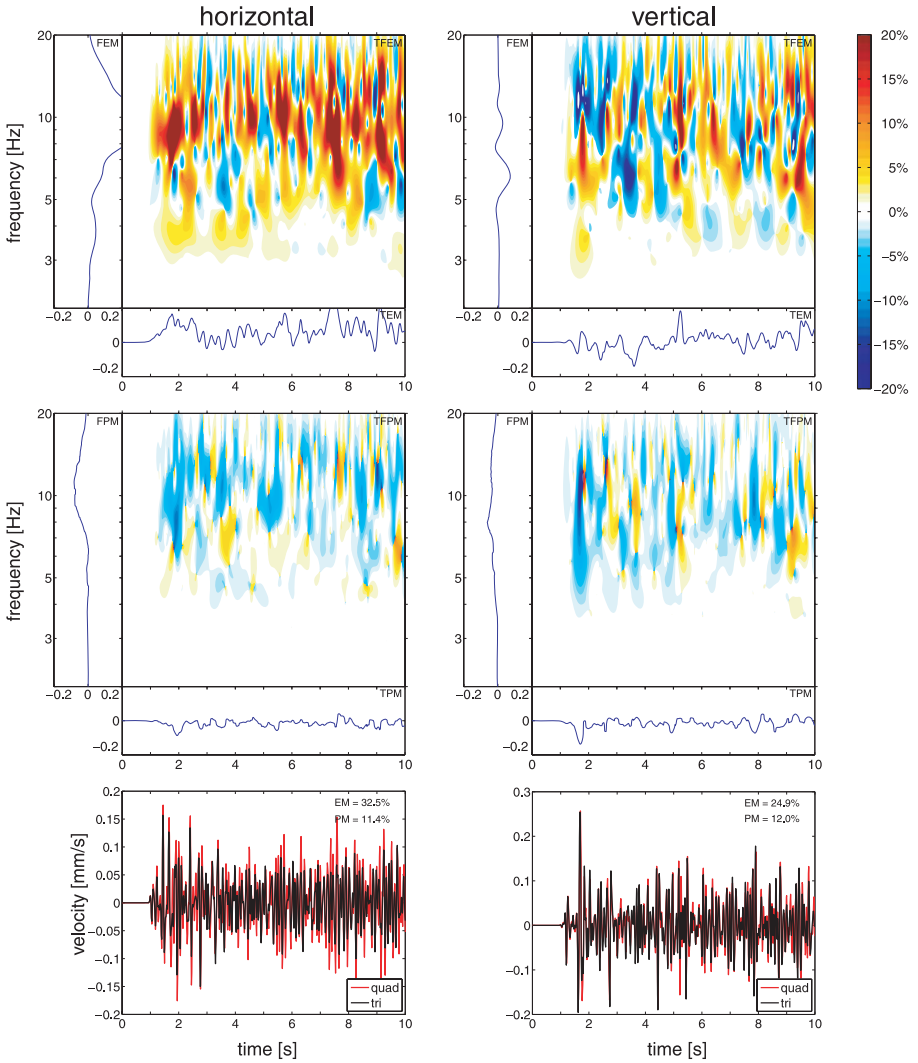

Figure 20. Time–frequency misfits of the horizontal and vertical velocity components of the worst receiver r911. We also show the seismograms comparison between the reference solution obtained on the triangular mesh (black) and the solution obtained on the quadrilateral mesh (red) together with their single-valued EM and PM of Table 3.

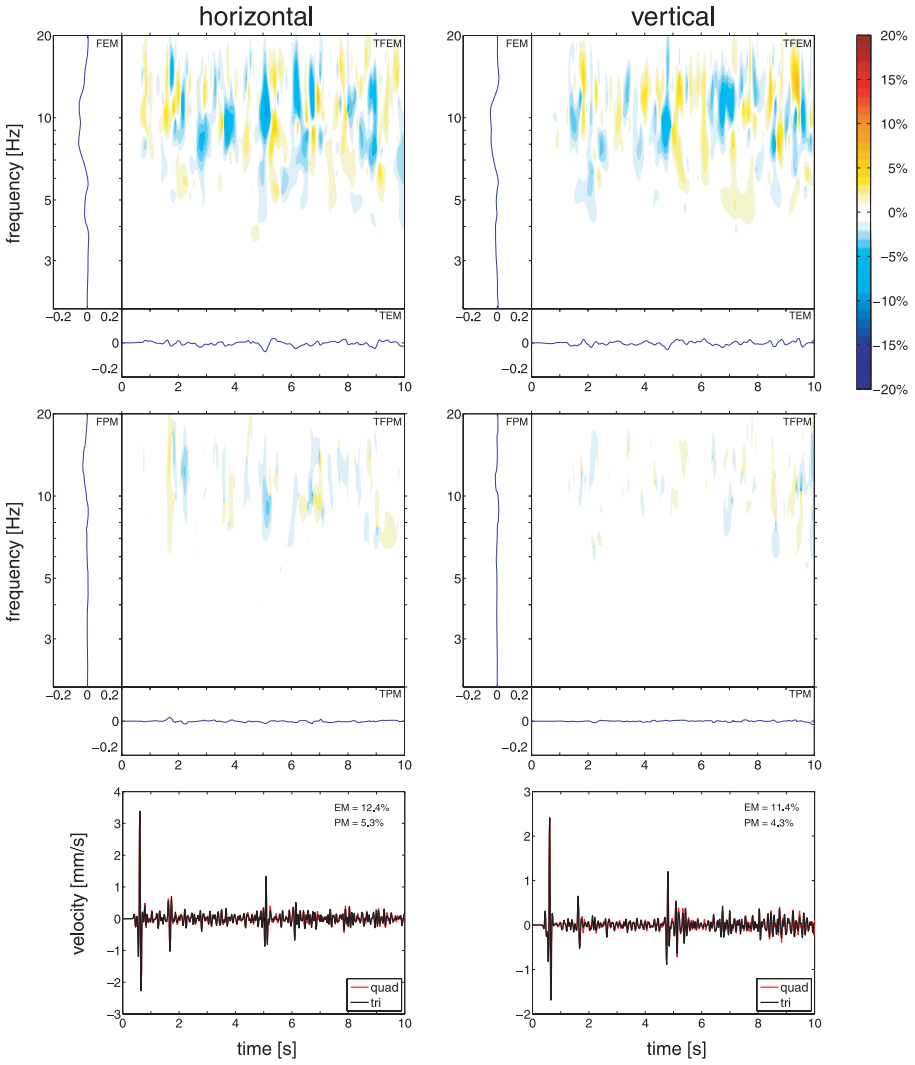

Figure 21. Time–frequency misfits of the horizontal and vertical velocity components of the receiver r545. We also show the seismograms comparison between the reference solution obtained on the triangular mesh (black) and the solution obtained on the quadrilateral mesh (red) together with their single-valued EM and PM of Table 3.

and the seismograms together with their time-frequency envelope (TFEM) and phase (TFPM) misfits (Kristeková *et al.* 2006, 2009) are shown in Figs 20 and 21, respectively, using Kristeková's signal analysis code from www.nuquake.eu/Computer_Codes/index.html.

Obviously, the envelope misfits of both components at r911 are relatively large compared to the much smaller phase misfits. Furthermore, the misfits dominate in the frequency range from $f = 8$ Hz to $2.5f = 20$ Hz as expected due to the dominant and maximum frequency content of the Ricker wavelet. However, most features of the waveforms can be found in both seismograms and the goodness-of-fit values (Kristeková *et al.* 2009) are still equal or better than 7.2, which in the verbal classification is a 'good' result (Table 3). We point out that Anderson (2004), introducing this classification, used the empirical earthquake-engineering characteristics of earthquake ground motion and adjusted his scale to the fact that differences between synthetics and real records are in most cases large. Therefore, for comparisons of numerical solutions the chosen scale of the time-frequency goodness-of-fit might be too robust, as the comparison of numerical solutions typically has differences much less than those between synthetics and real records. Nevertheless, the seismograms at receiver r545 shown in Fig. 21 are in our opinion in a perfect agreement as underscored by the goodness-of-fit values equal or better than 8.8.

Table 3. Table of envelope misfit (EM), phase-misfit (PM) and corresponding goodness-of-fit values of envelope (EG) and phase (PG) for selected receivers r545 and r911.

	Horizontal				Vertical			
	EM (per cent)	EG	PM (per cent)	PG	EM (per cent)	EG	PM (per cent)	PG
r545	12.4	8.8	5.3	9.5	11.4	8.9	4.3	9.6
r911	32.5	7.2	11.4	8.9	24.9	7.8	12.0	8.8

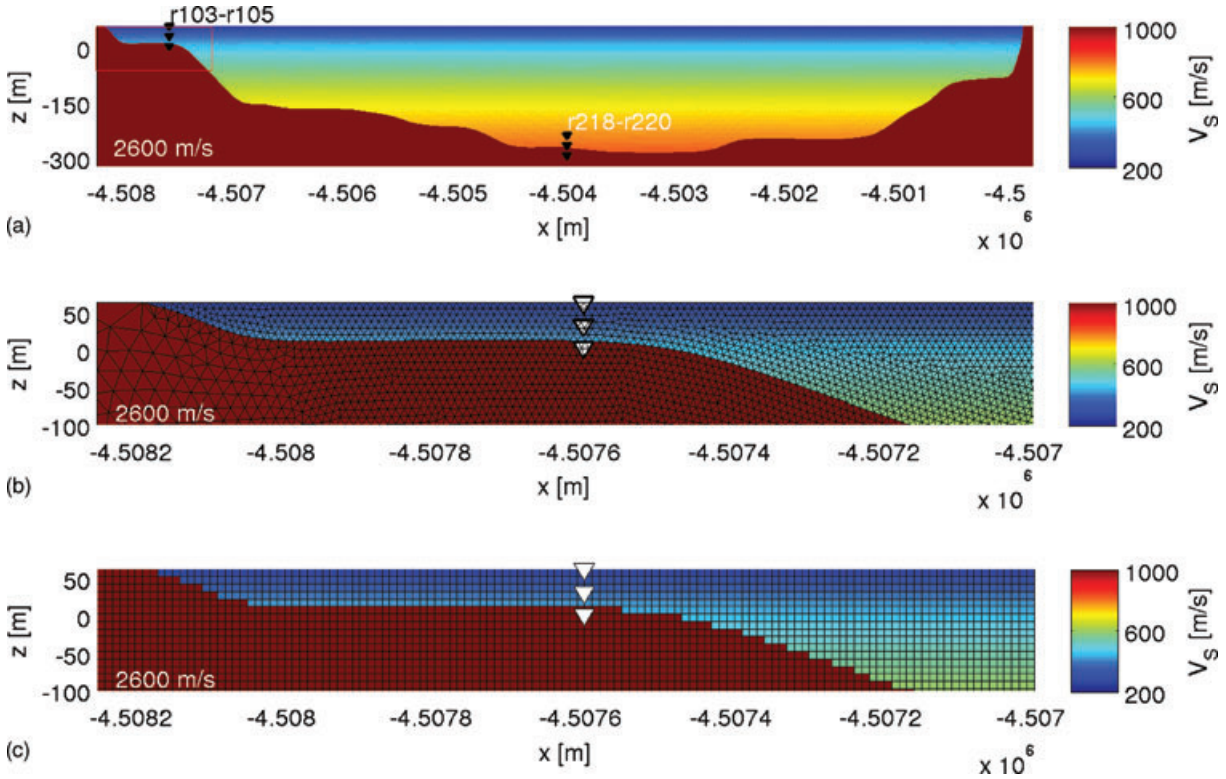

Figure 22. (a) *S*-wave velocity structure of the basin model stretched in vertical direction by a factor of 3. (b) Zoomed section of the left border of the basin with an overlay of the triangular mesh which respects the interface of the bedrock. White triangles mark the positions of the three geophone positions r103–r105. (c) Same area as (b) but with an overlay of the quadrilateral mesh with staircase approximation of the interface.

Note that this test case includes two non-planar interfaces and that the 10 s simulation time allows for the arrival of waves that crossed these interfaces several times. Furthermore, waves can travel through the model in the horizontal direction due to the periodic boundaries and could be strongly affected by the material interfaces. Nevertheless, our rules of Section 2.3 still hold. The structured mesh with 5 elements per shortest dominant wavelength seems to represent an arbitrarily shaped interface of material contrast 0.5 with satisfying accuracy.

4 SEDIMENTARY BASIN

The accuracy and reliability of synthetic seismograms is of fundamental importance for the investigation of realistic modelling scenarios. Therefore, we use our previous study on the sensitivity of numerical seismograms on geometrically complex material interfaces and apply our resulting discretization rules on a realistic example of a sedimentary basin derived from the EuroseisTest Verification and Validation Project (Chaljub *et al.* 2009). The aim is to test if the numerical effects of staircase approximations of curved boundaries are acceptable under the consideration of our proposed rules, as this would justify simple and fast regular mesh generation in contrast to a more involved mesh alignment procedure to well-defined material interfaces. Our simplified EuroseisTest model contains a strong discontinuity that separates the bedrock of constant seismic wave velocities from the basin with depth-dependent wave speeds producing moderate material contrasts from 0.32 at the deepest part of the basin to extreme contrasts of 0.1 close to the surface as shown in Fig. 22. In this section, we check, if our rules hold also in a real world case, where a sedimentary basin with extremely low wave velocities is embedded in a high-velocity bedrock.

4.1 Test case description

The model setup is a simplified 2-D version of the 'EuroseisTest Verification and Validation Project' model (Chaljub *et al.* 2009) describing the geological setting of the Mygdonian sedimentary basin near the city of Thessaloniki in northern Greece as shown in Fig. 22(a). The vertical direction of the *S*-wave velocity structure is stretched by a factor of 3 for better visualization of the thin basin. The complete extension of the physical domain has 28.32 km width and 15 km depth. So only the part of the computational domain around the basin is shown. The free surface elevation is at $z = 63$ m and the deepest point of the basin is at $z = -319.6$ m. Within the basin the wave speeds depend on depth d from the surface and are constant for the bedrock as given in Table 4.

Thus, high *S*-wave velocity contrasts of 0.1 exist at the top left and right borders of the basin. With increasing depth the *S*-wave ratio continuously changes to 0.32 in $d = -382.6$ m depth. In the following we select two positions, one with high and one with low material contrast, which will be discussed on the basis of recorded

Table 4. Material properties used for the sedimentary basin application.

	ρ (kg m^{-3})	v_P (m s^{-1})	v_S (m s^{-1})
Basin	2100.0	$1000.0 + 100.0\sqrt{d}$	$200.0 + 32.0\sqrt{d}$
Bedrock	2600.0	4500.0	2600.0

seismograms. Again, we use a 21 × 21 receiver array to cover the basin and the adjacent bedrock but focus on two sets of receivers to illustrate representative results. These receiver stations are marked by six black triangles in Fig. 22(a). The two highlighted receiver sets cross the material discontinuity, which means that the lowest receiver is based in the bedrock (r218, r103), the middle close to the interface but already in the basin (r219, r104), and the topmost clearly inside the basin (r220, r105). As a source we choose again the force pair with a 5 Hz Ricker pulse of Section 3.1 located at $(x, z) = (-4.5075 \times 10^6, -1000)$ m. The total simulation time is 10 s.

Like in the previous experiments material properties are assigned elementwise, but to achieve a better representation of the velocity gradient in the basin we first assign the material properties to the vertices of an element and average them in a second step. A reference solution is produced with a fine triangular mesh respecting the material discontinuities by element edges and using a DG scheme of accuracy order 5.

Figs 22(b) and (c) show a zoomed view of the left part of the basin with an overlay of the triangular and quadrilateral meshes, respectively. The triangles of the reference model have a mean edge size of 10 m in the basin and for the bedrock we allow a smooth increase to 100 m, enough to resolve the propagating waves properly. The mesh spacing for the regular mesh is 10 m in a box including the basin and 100 m around this box using the non-conforming mesh approach introduced by Hermann *et al.* (2010). An edge size of 100 m in the bedrock corresponds to 3.7 elements per shortest dominant wavelength, while the higher resolution of 10 m in the basin area leads to depth-dependent sampling of 2.8–11.7 elements per shortest dominant wavelength. Since large parts of the basin-bedrock interface lie in larger depth with material contrast of 0.32 an interface approximation using 10 elements per shortest dominant wavelength should be sufficient, as suggested by the graph in Fig. 17. We admit that this value represents a lower limit regarding our rules, however, we remark that even the regular mesh aligns well to the predominantly flat and smoothly varying basin-bedrock interface. At smaller depth the stronger material contrasts cause an undersampling of the interface geometry with 2.8 elements per shortest dominant wavelength, which is clearly less than what is required by our rules of Section 2.3. However, these cases appear only in very small areas near the borders of the basin at the surface. As computational efficiency is also an issue in real applications we deliberately avoid the very fine mesh spacing close to the surface to prohibit heavy oversampling of the interface in the deeper parts of the model and to keep the computational cost low. In the following we will show that even in such extreme cases where compromises have to be found we still obtain satisfactory results.

4.2 Results and discussion

As expected from Section 2.2 both discretization approaches produce similar seismograms except for small differences, since we are using less elements per wavelength than required by Section 2.3 in areas of extremely high material contrasts. Thus, we focus on two representative areas.

One of the best matching seismograms are recorded at receivers r218–r220 although they are located directly at the basin-bedrock interface and are shown in Fig. 23. While the arrival times fit almost perfectly, differences in amplitude can be observed in r219 and r220. A quantitative determination of the single-valued EM and PM criteria of Kristeková *et al.* (2009) shows a decrease of the misfit with increasing depth (Table 5). This means that seismograms in the bedrock are less affected by the geometry approximation than the ones in the basin. As numerous reflections are typical for low velocity basins embedded in high-velocity bedrock, it is expected that amplitude and phase errors are accumulating. However, the resulting goodness-of-fit values of around 9 confirm the excellent agreement. A time-frequency misfit analysis for the best matching receiver r218 is given in Fig. 24. Occurring errors are smaller than 10 per cent and provide acceptable numerical seismograms obtained by the chosen staircase approximation. Furthermore, all receivers located in the bedrock and most of the stations in the basin show similar well matching seismograms.

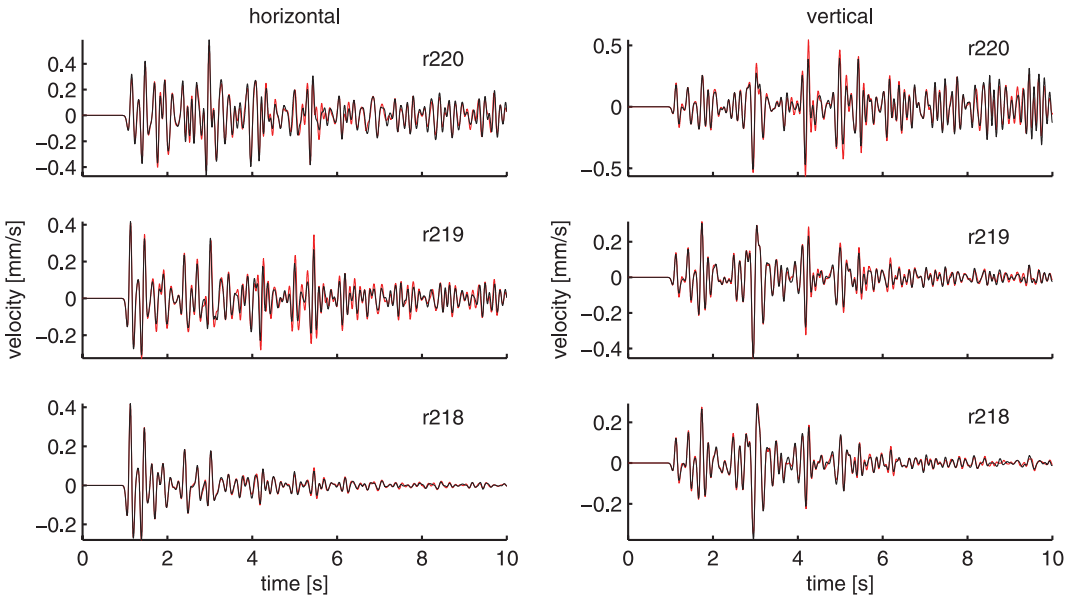

Figure 23. Seismograms of the receiver set r218–r220 located in the middle of the basin. The seismogram in the lowermost plot (r218) is recorded in the bedrock, the other two are 30 and 60 m above already in the basin. The black line denotes the reference solution, the red line the seismogram obtained using the quadrilateral mesh.

Table 5. Table of envelope misfit (EM), phase-misfit (PM) and corresponding goodness-of-fit values of envelope (EG) and phase (PG) for selected receivers.

	Horizontal				Vertical			
	EM (per cent)	EG	PM (per cent)	PG	EM (per cent)	EG	PM (per cent)	PG
r220	14.3	8.7	5.5	9.5	18.0	8.4	6.2	9.4
r219	20.4	8.2	8.1	9.2	10.8	9.0	3.2	9.7
r218	5.4	9.5	2.2	9.8	9.1	9.1	3.9	9.6
r105	23.7	7.9	29.0	7.1	12.6	8.8	15.1	8.5
r104	20.3	8.1	15.7	8.4	12.5	8.8	15.8	8.4
r103	3.7	9.6	3.7	9.6	6.0	9.4	4.2	9.6

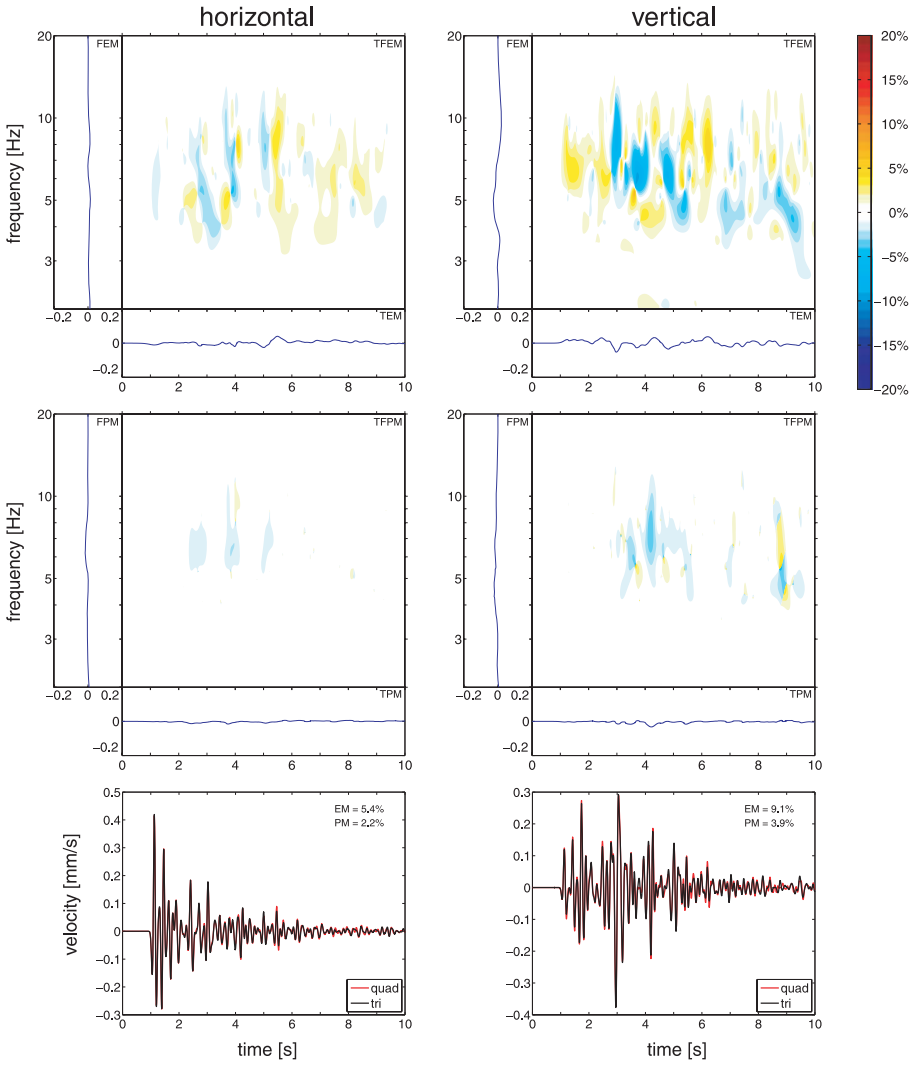

Figure 24. Time–frequency misfits of the horizontal and vertical velocity components of receiver r218. We also show the seismograms comparison between the reference solution obtained on the triangular mesh (black) and the solution obtained on the quadrilateral mesh (red) together with their single-valued EM and PM of Table 5.

In contrast, receivers r103–r105 located in a very shallow region of the basin and close to the basin–bedrock interface show the largest differences of all receivers. In this area the basin has a depth of only 50 m. Hence, the resulting *S*-wave speed ratio is 0.16. Due to the high material contrast and the vicinity to the left boundary numerical effects due to insufficient geometry approximation are most prevalent here. The corresponding seismograms are shown in Fig. 25. Although still satisfactory a regress to a goodness-of-fit value of 8 or even 7 is observable for receivers r104 and r105 (Table 5). r103 is located in the bedrock and as mentioned above is less affected by the geometry approximation effects, which results in a significantly smaller misfit. Actually, seismograms of r103 are among the best matching seismograms of all, while the largest misfits appear only 30 or 60 m above at receivers r104 and r105. Most obvious are the strong phase misfits at receivers r104 and r105 starting after 3 s as shown in the time-frequency analysis for receiver r105 in Fig. 26. Here, strong envelope misfits are also observed directly after the first arrival on the horizontal component and after

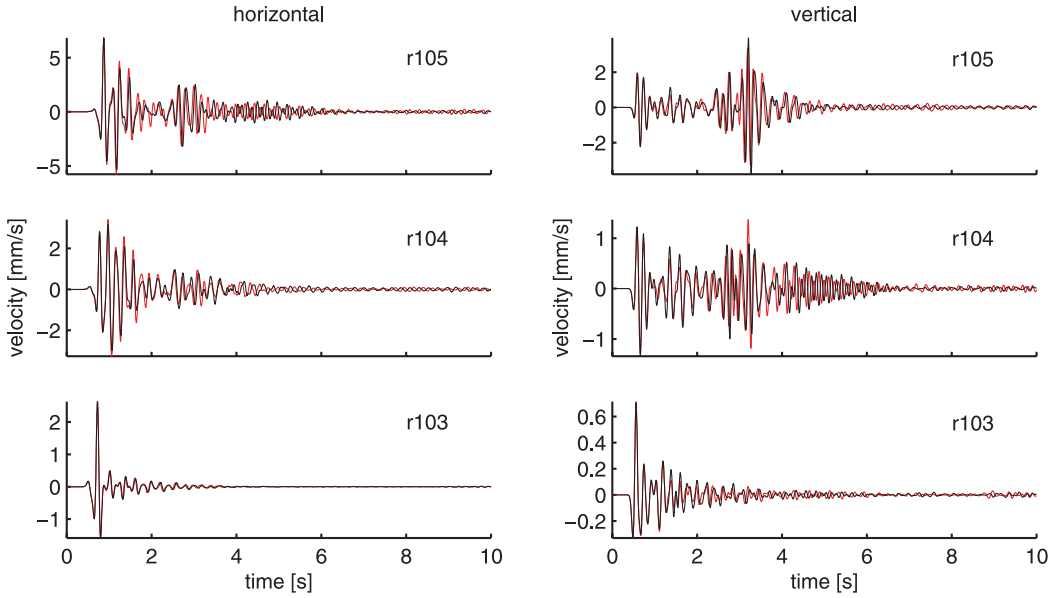

Figure 25. Seismograms of the receiver set r103–r105 located in the middle of the basin. The seismogram in the lowermost plot (r103) is recorded in the bedrock, the other two are 30 and 60 m above already in the basin. The black line denotes the reference solution, the red line the seismogram obtained using the quadrilateral mesh.

3 s on the vertical component. These critical misfit levels can be explained by the lower number of elements per wavelength for the interface approximation in this area than suggested in Section 2.3.

However, with respect to the different discretization approaches and the compromise between computational effort and approximation accuracy of the material interface, the agreement between the seismograms is still remarkably good. Furthermore, we mention that the obtained results still provide goodness-of-fit values of 'good' or 'excellent', which are reasonable for comparisons of synthetics in benchmarks of seismic wave propagation scenarios.

5 CONCLUSIONS

In this work, we investigated the effect of staircase approximations of material discontinuities along curved interfaces using a DG Finite Element method trying to clarify under which conditions such geometry approximations, typically used by regular grid schemes like FD, provide acceptable results. We produced reference solutions using a high-order accurate DG scheme on triangular meshes which can be aligned to the geometry of curved interfaces. We then solved the wave equations on regular square-shaped meshes leading to jagged material contacts. We studied the misfits of seismograms depending on the signal frequency, the mesh spacing, and the material contrast. In fact, the misfits increase with a decreasing number of elements per wavelength and with increasing material contrast. The systematic parameter study of Section 2 enabled us to define rules that should be adhered to ensure accurate synthetic data, if regular meshing is applied. A general finding was that up to a material contrast, in the sense of a S-wave speed ratio, of 0.5 a discretization of five elements per shortest dominant wavelength generates acceptable seismograms in spite of complex material interfaces. Furthermore, high-order accurate numerical methods can reduce this resolution on structured grids for weaker material contrasts. However, in the case of stronger material contrasts than 0.5 the number of elements per wavelength has to be increased significantly to avoid numerical artefacts due to the staircase approximation. Special cases of a free-surface boundary or an acoustic–elastic coupling should be treated by mesh alignment to the interface as we were not able to produce acceptable seismograms within the range of tested frequencies and mesh spacings with the staircase approximation of such boundaries.

In Section 3, we considered a more complicated test case to verify our discretization rules containing a three layer problem separated by two undulating interfaces with material contrasts of 0.5 each and using a minimum number of elements for geometry approximation. In summary, all seismograms show the expected minor misfits compared to the reference solution.

Finally, we applied our results to a realistic scenario of a basin structure. The main issue was to find a compromise between a correct resolution of the material interface and computational efficiency. At the shallow basin boundaries where extremely high material contrasts occur we used less elements per wavelength than suggested by our rules to keep the computational cost low and still obtain good matching seismograms. As expected, the largest but surprisingly moderate misfits can be found in these areas. However, these critical areas are very localized and therefore do not seem to influence the overall error or the accuracy in other areas dramatically. Nevertheless, the surprising result is that even for such untypically high material contrasts over a basin-bedrock interface close to the surface we still obtained a satisfying accuracy of the synthetic seismograms although a structured mesh is applied, which does not respect the material interface.

We conclude that taking into account our approximation rules defined in this study ensures reliable modelling results when using structured discretizations including non-planar material interfaces. Furthermore, adhering these rules can help to minimize the mesh generation effort and computational cost. Conclusions for high-order methods, like SEM and DG, applied on structured meshes can also be drawn. If the material properties allow for large elements these coarse meshes can violate the interface geometry to a certain degree and do not have to be aligned exactly with them in order to produce acceptable results. On the other hand, we remark that fine

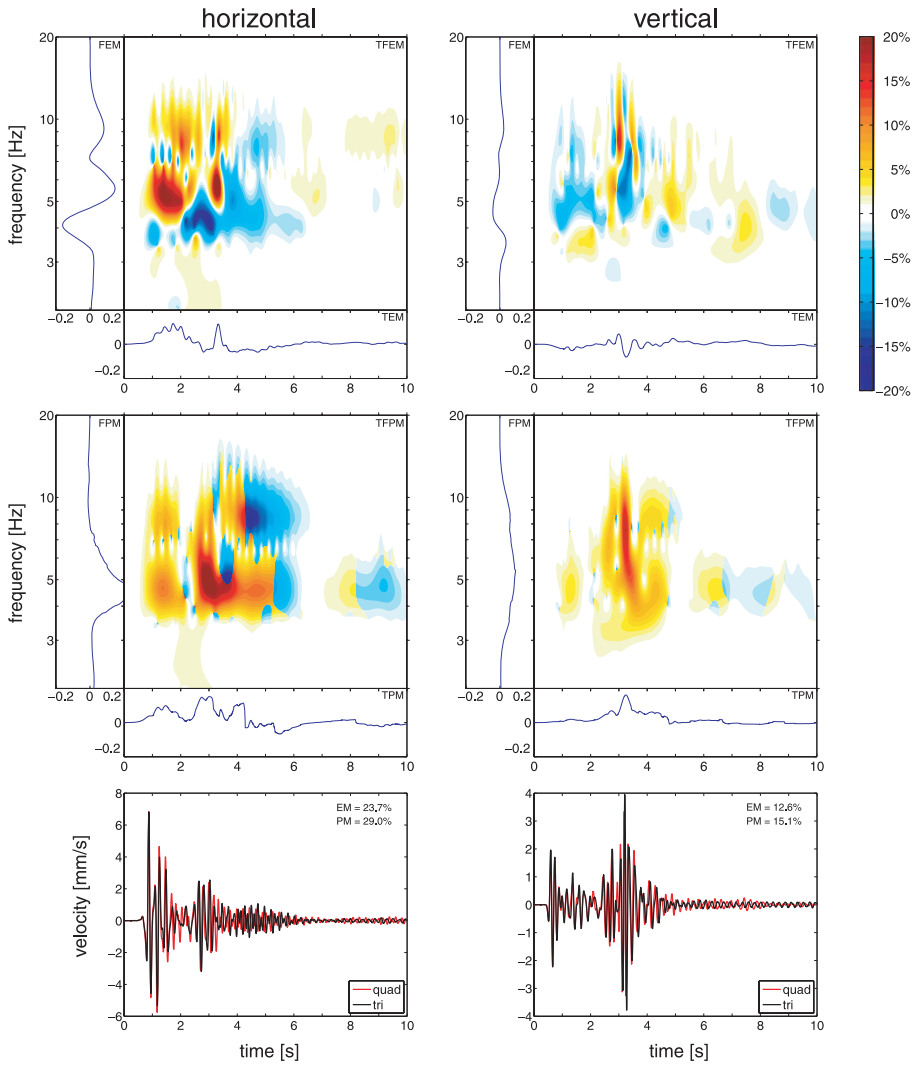

Figure 26. Time–frequency misfits of the horizontal and vertical velocity components of receiver r105. We also show the seismograms comparison between the reference solution obtained on the triangular mesh (black) and the solution obtained on the quadrilateral mesh (red) together with their single-valued EM and PM of Table 5.

discretizations often required by low-order methods often account for the geometry with sufficient accuracy automatically.

ACKNOWLEDGMENTS

The authors thank the Deutsche Forschungsgemeinschaft (DFG), as the work was supported through the *Emmy Noether-Programm* (KA 2281/2-1). Furthermore, we thank our system administrator Jens Oeser for the support when using the local cluster (Oeser *et al.* 2006). Access to the HPC facilities of the Leibniz-Rechenzentrum was provided through the SeBaSim DEISA-project, where the simulations of Section 4 have been computed. Peter Moczo and an anonymous referee are also acknowledged for their useful reviews, which have helped to improve the original manuscript.

REFERENCES

Anderson, J.G., 2004. Quantitative measure of the goodness-of-fit of synthetic seismograms, in *13th World Conf. on Earthquake Engineering Conference Proc.,* Paper 243, International Association for Earthquake Engineering, Vancouver, BC.

Bao, H., Bielak, J., Ghattas, O., Kallivokas, L.F., O'Hallaron, D.R., Shewchuk, J.R. & Xu, J., 1998. Large-scale simulation of elastic wave propagation in heterogeneous media on parallel computers, *Computer Methods in Applied Mechanics and Engineering,* **152**(1-2), 85–102, Containing papers presented at the Symposium on Advances in Computational Mechanics.

Bohlen, T. & Saenger, E., 2006. Accuracy of heterogeneous staggered-grid finite-difference modeling of rayleigh waves, *Geophysics,* **71**(4), 109–115.

Castro, C.E., Käser, M. & Brietzke, G.B., 2010. Seismic waves in heterogeneous material: subcell resolution of the discontinuous galerkin method, *Geophys. J. Int.,* **182,** 250–264.

Chaljub, E. *et al.*, 2009. Assessing the capability of numerical methods to predict earthquake ground motion: the EuroseisTest Verification and Validation Project, *EOS, Trans. Am. geophys. Un.*, Poster S43A-1968, Am. geophys. Union.

Chaljub, E., Moczo, P., Tsuno, S., Bard, P.-Y., Kristek, J., Käser, M., Stupazzini, M. & Kristekova, M., 2010. Quantitative comparison of four numerical predictions of 3D ground motion in the Grenoble valley, france, *Bull. seism. Soc. Am.,* **100**(4), 1427–1455.

Collino, F., Joly, P. & Millot, F., 1997. Fictitious domain method for unsteady problems, *J. Comput. Phys.,* **138**(2), 907–938.

Dumbser, M. & Käser, M., 2006. An arbitrary high order discontinuous Galerkin method for elastic waves on unstructured meshes II: the three-dimensional case, *Geophys. J. Int.,* **167**(1), 319–336.

Dumbser, M., Käser, M. & Toro, E., 2007. An arbitrary high order discontinuous Galerkin method for elastic waves on unstructured meshes V: local time stepping and p-adaptivity, *Geophys. J. Int.,* **171**(2), 695–717.

Etienne, V., Virieux, J. & Operto, S., 2009. A massively parallel time-domain discontinuous galerkin method for 3D elastic wave modeling, *SEG Expanded Abstracts,* **28,** 2657–2661.

Gao, H. & Zhang, J., 2006. Parallel 3-D simulation of seismic wave propagation in heterogeneous anisotropic media: a grid method approach, *Geophys. J. Int.,* **165,** 875–888.

Godinho, L., Mendes, P.A., Tadeu, A., Cadena-Isaza, A., Smerzini, C., Sánchez-Sesma, F.J., Madec, R. & Komatitsch, D., 2009. Numerical simulation of ground rotations along 2D topographical profiles under the incidence of elastic plane waves, *Bull. seism. Soc. Am.,* **99**(2B), 1147–1161.

Graves, R., 1996. Simulating seismic wave propagation in 3D elastic media using staggered-grid finite differences., *Bull. seism. Soc. Am.,* **86**(4), 1091–1106.

Gustafsson, B. & Wahlund, P., 2004. Time compact difference methods for wave propagation in discontinuous media, *SIAM J. Sci. Comput.,* **26**(1), 272–293.

Hermann, V., Käser, M. & Castro, C.E., 2010. Improved flexibility and efficiency of seismic wave propagation modeling using the discontinuous Galerkin scheme on non-conforming hybrid meshes, submitted.

Ichimura, T., Hori, M. & Bielak, J., 2009. A hybrid multiresolution meshing technique for finite element three-dimensional earthquake ground motion modelling in basins including topography, *Geophys. J. Int.,* **177,** 1221–1232.

Käser, M., Hermann, V. & de la Puente, J., 2008. Quantitative accuracy analysis of the discontinuous Galerkin method for seismic wave propagation, *Geophys. J. Int.,* **173**(3), 990–999.

Kawase, H., 1988. Time-domain response of a semi-circular canyon for incident SV, P, and Rayleigh waves calculated by the discrete wavenumber boundary element method, *Bull. seism. Soc. Am.,* **78**(4), 1415–1437.

Kristeková, M., Kristek, J. & Moczo, P., 2009. Time-frequency misfit and goodness-of-fit criteria for quantitative comparison of time signals, *Geophys. J. Int.,* **178,** 813–825.

Kristeková, M., Kristek, J., Moczo, P. & Day, S., 2006. Misfit criteria for quantitative comparison of seismograms, *Bull. seism. Soc. Am.,* **96**(5), 1836–1850.

Mercerat, E., Vilotte, J.-P. & Sánchez-Sesma, F., 2006. Triangular spectral element simulation of two-dimensional elastic wave propagation using unstructured triangular grids, *Geophys. J. Int.,* **166,** 679–698.

Moczo, P., Kristek, J., Vavrycuk, V., Archuleta, R. & Halada, L., 2002. 3D heterogeneous staggered-grid finite-difference modeling of seismic motion with volume harmonic and arithmetic averaging of elastic moduli and densities, *Bull. seism. Soc. Am.,* **92**(8), 3042–3066.

Moczo, P., Kristek, J., Galis, M., Pazak, P. & Balazovjech, M., 2007. The finite-difference and finite-element modeling of seismic wave propagation and earthquake motion, *Acta Physica Slovaca,* **57**(2), 177–406.

Moczo, P., Robertsson, J.O.A. & Eisner, L., 2007. The finite-difference time domain method for modeling of seismic wave propagation, *Adv. Geophysics,* **48,** 421–516.

Moczo, P., Kristek, J., Galis, M. & Pazak, P., 2010. On accuracy of the finite-difference and finite-element schemes with respect to P-wave to S-wave speed ratio, *Geophys. J. Int.,* **182,** 493–510.

Oeser, J., Bunge, H.-P. & Mohr, M., 2006. Cluster design in the earth sciences: TETHYS, in *Lecture Notes in Comp. Sci.,* **4208,** 31–40.

Ohminato, T. & Chouet, B.A., 1997. A free-surface boundary condition for including 3D topography in the finite-difference method, *Bull. seism. Soc. Am.,* **87**(2), 494–515.

Olsen, K. *et al.*, 2006. Strong shaking in Los Angeles expected from Southern San Andreas earthquake., *Geophys. Res. Lett.,* **33**(7), 575–596.

Pasquetti, R. & Rapetti, F., 2006. Spectral element methods on unstructured meshes: comparisons and recent advances, *J. Sci. Comput.,* **27,** 377–387.

Robertsson, J., 1996. A numerical free-surface condition for elastic/viscoelastic finite-difference modeling in the presence of topography, *Geophysics,* **96**(4B), S11–S27.

Stupazzini, E.C.M., Lee, S.J., Komatitsch, D., Piersanti, A. & Tromp, J., 2008. CUBIT and seismic wave propagation based upon the spectral-element method: an advanced unstructured mesher for complex 3D geological media, in *Proceedings of the 16th International Meshing Roundtable,* pp. 579–597, Springer, Berlin.

Symes, W.W., Terentyev, I.S. & Vdovina, T.W., 2008. Gridding requirements for accurate finite difference simulation, *SEG Expanded Abstracts,* **27,** 2077–2081.

van Vossen, R., Robertsson, J. & Chapman, C., 2002. Finite-difference modeling of wave propagation in a fluid-solid configuration, *Geophysics,* **67**(2), 618–624.

Wilcox, L.C., Stadler, G., Burstedde, C. & Ghattas, O., 2010. A high-order discontinuous galerkin method for wave propagation through coupled elastic-acoustic media, *J. Comput. Phys.,* submitted.

Zahradník, J., Moczo, P. & Hron, F., 1993. Testing four elastic finite-difference schemes for behaviour at discontinuities, *Bull. seism. Soc. Am.,* **83,** 107–129.

Zhang, C. & LeVeque, R.J., 1997. The immersed interface method for acoustic wave equations with discontinuous coefficients, *Wave Motion,* **25,** 237–263.

Zhang, C. & Symes, W.W., 1998. Fourth order, full-stencil immersed interface method for elastic waves with discontinuous coeffcients, *SEG Expanded Abstracts,* **17,** 1929–1932.

Wavefield modeling in exploration seismology using the discontinuous Galerkin finite-element method on HPC infrastructure

Martin Käser, Christian Pelties, and Cristobal E. Castro, Geophysics LMU Munich
Hugues Djikpesse and Michael Prange, Schlumberger-Doll Research

Seismic and acoustic measurements in a broad sense, including surface seismic, borehole seismic and sonic waveforms, play an important role in improving our knowledge of hydrocarbon reservoirs in both exploration and production phases. In that context, accurate modeling of wave propagation, in particular when considering irregular free-surface effects, complicated subsurface geological structures, or the physics of a sonic tool deployed downhole, is one of the major challenges geophysicists are facing.

We present a discontinuous Galerkin (DG) finite-element method recently developed in computational seismology for application on high-performance computing (HPC) facilities, and illustrate its potential for seismic and sonic modeling in oil and gas exploration.

The exploration industry has developed a broad spectrum of techniques to initially detect, accurately survey, and constantly monitor these reservoirs to supply our still increasing demand for fossil fuels. Typically, surface seismic acquisitions are characterized with sources at or near the free surface and 3D multicomponent data recorded either at the free surface or eventually at the seafloor using ocean-bottom cables (OBC). With a typical frequency bandwidth of about 5–250 Hz, the flexibility and density of source and receiver distributions provide a wide lateral coverage of the prospected area that ranges on a scale of several square kilometers. Borehole seismic surveys are characterized with sources either at the surface (e.g., 3D VSP) or downhole (cross-well imaging, localization of microseismic events) with receivers in the borehole close to the targeted reservoir. They provide complementary information, as compared to surface seismic interpretation, by shedding more light onto particular structures of the reservoir that are up to several hundred meters away from the wellbore. For imaging with much higher depth-resolution (typically 0.5 ft) along the wellbore sonic measurements with frequencies of 1–5 kHz are used to derive, for instance, lithology propertiesand rock textures at diff erent depths. They are also used to analyze borehole stability, borehole mud invasion, and any formation damage within a few meters from the wellbore.

For instance, independent of the scale of the problem, seismic and sonic waves within this broad frequency range are used to extract the reservoir's structural characteristics and compositional properties. The underlying inversion and migration techniques often rely on accurate synthetic data produced via special forward modeling tools. Solving the forward problem, in this case, means solving the full 3D seismic wave equations. This involves generation of synthetic data sets of seismograms recorded at desired locations for a given velocity model and source characteristics. Another application of wave-propagation simulations is in the design of survey geometries and parameters to save valuable resources. The generation of highly accurate and reliable synthetic data incorporating all important model features can be challenging, but represents an absolutely crucial prerequisite. The importance as well as the difficulties to produce such data sets are emphasized by the foundation of the SEG Advanced Modeling (SEAM) project (Fehler, 2009), which is dedicated to large-scale geophysical modeling in industry. New numerical methods can provide such synthetics, even though they might still be computationally more involved than standard techniques like finite differences (FD) due to their better approximation capabilities. Thus, future developments aim for strong interconnections between flexible and accurate numerical simulation methods and powerful computational resources such as those provided by current HPC facilities.

In this article, we present the discontinuous Galerkin finite-element method to emphasize its advantages and future potential, especially for seismic modeling in the exploration industry. In the following, the principles of this numerical scheme are explained and its promising properties with respect to HPC hardware are discussed. Two examples occurring in seismic exploration demonstrate the method's applicability and flexibility and cover 3D problems of a marine survey on the kilometer scale to sonic logging on the centimeter-to-meter depth scale.

Discontinuous Galerkin method

An approach for the simulation of seismic wave propagation, introduced by Käser and Dumbser (2006), is the discontinuous Galerkin (DG) finite-element method. In particular, its combination with the explicit time integration method of Titarev and Toro (2002) using *arbitrary high-order derivatives* (ADER) leads to a high-order accuracy in both space and time. The extension of the method to 3D unstructured tetrahedral meshes enables automatic mesh generation for complex model geometries. Furthermore, different material properties can be considered, such as acoustic fluids and elastic, anisotropic, viscoelastic or poroelastic solids (de la Puente et al., 2008). Therefore, the ADER-DG scheme provides extremely high flexibility with respect to a wide range of wave-propagation problems. The numerical method belongs to the class of finite-element (FE) methods, but uses the discontinuous Galerkin approach (e.g., Cockburn et al., 2000; Hesthaven and Warburton, 2008). Here, in contrast to typical FE schemes, the approximating 3D polynomials inside each element are allowed to be discontinuous along interfaces between neighboring elements. These discontinuities are then treated as in high-order finite-volume (FV) methods using the well-established theory of Riemann problems and Riemann solvers (e.g., Toro, 1999). While the degree of the approximating polynomials determines the spatial order of

accuracy, the ADER time integration approach provides the same time accuracy. Thereby, the time extrapolation of the solution to future time levels uses a Taylor expansion where higher-order time derivatives are replaced by space derivatives via a recursive use of the velocity-stress wave equation. A further advantage is that the polynomial basis functions are orthogonal which leads to a diagonal mass matrix. In fact, such basis functions exist for many different element types (e.g., triangles, quadrilaterals, tetrahedrons, hexahedrons, pyramids, and prisms). Furthermore, the scheme's extension to higher approximation orders does not require an increased stencil as typically necessary for FV or FD schemes. Instead, only the number of degrees of freedom (i.e., the polynomial coefficients) inside an element increases. Therefore, the numerical algorithm keeps a spatially local character as each time update of the solution inside one element only depends on the minimum number of direct neighbors sharing a common interface (Figure 1). At these interfaces the concept of numerical fluxes is a key ingredient and strength of ADER-DG as it allows a variety of physical effects to be accommodated: boundary conditions, friction laws for dynamic rupture processes, or the combination of different element types and nonconforming mesh transitions.

Approximation order	1	2	3	4	5	6	7	8
m (DOF per element)	1	4	10	20	35	56	84	120
M_e (memory per element [bytes])	2664	2880	3312	4032	5112	6624	8640	11232
Elements per core M_c = 0.5GB	200,000	180,000	160,000	130,000	100,000	80,000	60,000	45,000

Table 1. *Number m of degrees of freedom (DOF), memory consumption M_e per element, and an estimate of the element number per core of M_c=0.5 GB memory in dependence of approximation order.*

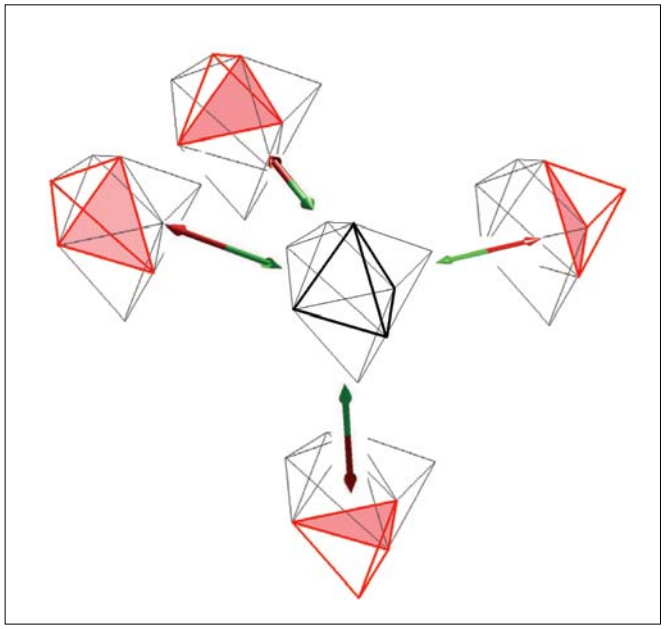

Figure 1. *Tetrahedral element with its direct neighbor elements for minimal communication across their common interfaces (red).*

In order to focus the computational effort on particular areas of interest, local adaptation of the approximation order and local time stepping is possible. In particular, the local time-stepping approach allows each element to use its own optimal time-step length according to the local stability condition. Hence, these features increase the performance and efficiency in models with strongly varying element sizes without losing accuracy.

Suitability for HPC infrastructure

A major advantage of ADER-DG is its locality as an element updated in time only requires information from the direct neighbors in the form of polynomial coefficients. This property does not change with increasing approximation order as only the number of coefficients grows. Therefore, the scheme is well suited for parallelization. In fact, communication between elements takes place only once per time step and represents much less than 1% of the CPU time. The results of a strong-scaling test for the borehole application, where the model size (i.e. the total number of elements) remains constant (~1.3e6) but the number of cores increases, are shown in Figure 2. The CPU time reduction remains still close to the ideal case and the speedup is satisfactory up to 1024 cores with an efficiency of 76%. The crucial issue for the scaling properties of the algorithm is the load bal-

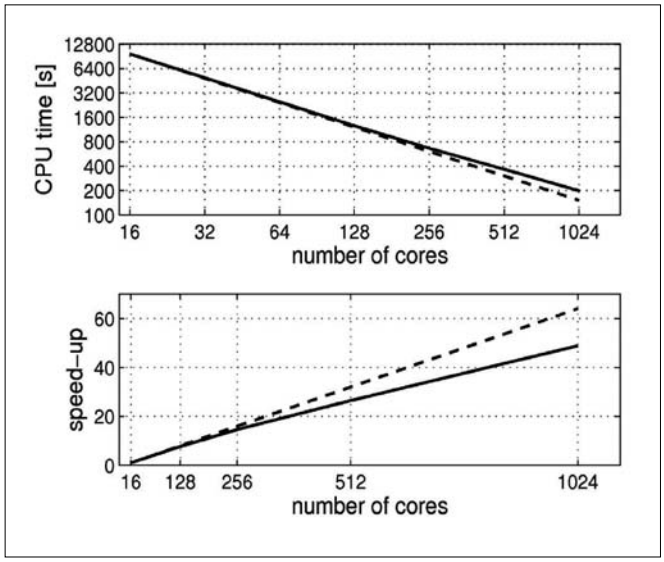

Figure 2. *CPU time decrease (top) and speedup (bottom) for an increasing number of cores for the strong-scaling test (solid line) in comparison to the theoretically ideal case (dashed line).*

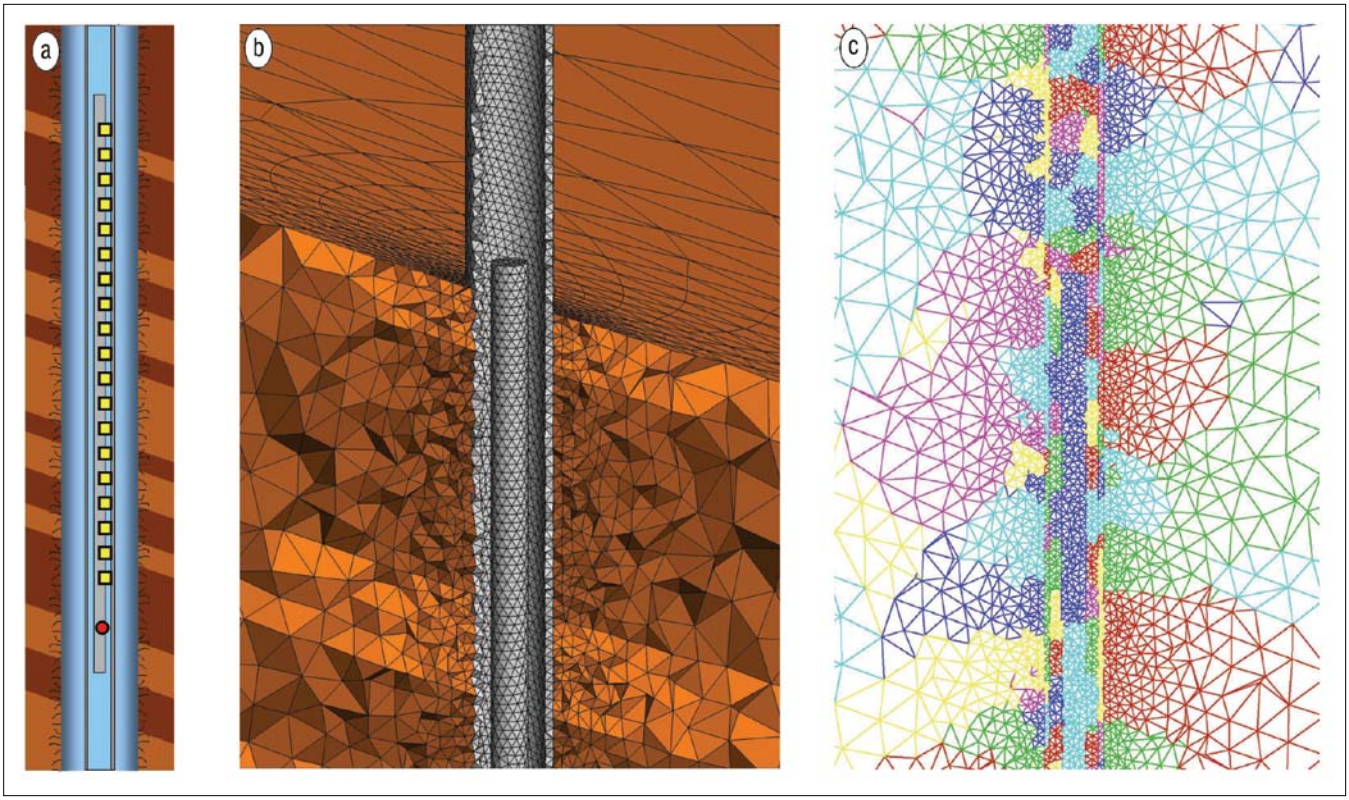

Figure 3. *Problem setup for sonic logging. (a) Sonic logging tool in a cased, fluid-filled borehole penetrating a formation of tilted layers with an invasive zone of mud in the vicinity of the well. (b) Sketch of the sliced 3D model discretized by a problem-adapted tetrahedral mesh. (c) 2D projection of a cut through the 3D mesh showing the zonal partitioning approach for multiprocessor computations, where different colors represent the subdomains processed on different cores.*

ance which depends on the mesh partitioning strategy. For a standard, global time-stepping scheme, where all elements are updated to the next time level, optimal load balance is achieved by dividing the computational domain into subdomains with the same number of elements. However, the local time-stepping approach yields more difficulties as each element runs its own time step. Therefore, element updates happen asynchronously as smaller elements update more often than larger ones. The resulting load imbalances are currently overcome by grouping elements into zones, partitioning each zone separately as shown in Figure 3c, and spreading the parts equally to different cores.

Therefore, significant improvements of the algorithm should be achieved by run-time optimization of the serial part of the code. In fact, each tetrahedral element update requires the computation of three volume integrals and eight flux integrals (two per element face). Each integral computation consists of local matrix multiplications where three matrices of dimensions 9×9, $9 \times m$, and $m \times m$ are related to the nine velocity-stress variables and the number (m) of degrees of freedom (DOF), which depends on the degree (N) of the approximation polynomial as $m = (N + 1)(N + 2)(N + 3) / 6$.

Memory consumption is not an issue as all data can be kept in arrays for each core. For every element, there are $9 \times m$ degrees of freedom and 9×9 entries of the Jacobian matrices as double-precision real numbers to store in memory. In contrast, volume and flux integral matrices of size $m \times m$ are element-independent and have to be kept in memory only once. Table 1 shows the memory requirement and the estimated maximum number of elements on an IBM Bluegene architecture with $M_c = 0.5$ GB of memory per core with respect to the approximation order.

The 3D wave equations in velocity-stress formulation contain nine unknowns (six stresses and three velocities), each of which is approximated by the DOF inside an element leading to a $9 \times m$ matrix. Furthermore, each element side has its own 9×9 matrix of flux-orientation and material information. Therefore, the total memory per tetrahedral element is given by $M_e = (9m + 4*92)*8$ bytes (Table 1). Note that the estimate of elements per core considers the memory requirement of a few MB for additional data (e.g., volume and flux matrices, basis functions, mesh coordinates, etc.). Other architectures like the SGI Altix system or the IBM Power 6 often have 2 GB or 4 GB of memory per core and therefore can accommodate correspondingly more elements.

The applicability and geometrical flexibility of ADER-DG using 3D unstructured tetrahedral meshes is demonstrated in the following two examples which are relevant in hydrocarbon reservoir exploration. The examples show the wide range of applications from borehole sonic measurements on the centimeter scale up to fully 3D salt reservoir models on the kilometer scale. Both problems are solved on the HPC facilities of SGI and IBM.

Borehole-scale modeling

Sonic logging can estimate geophysical and petrophysical

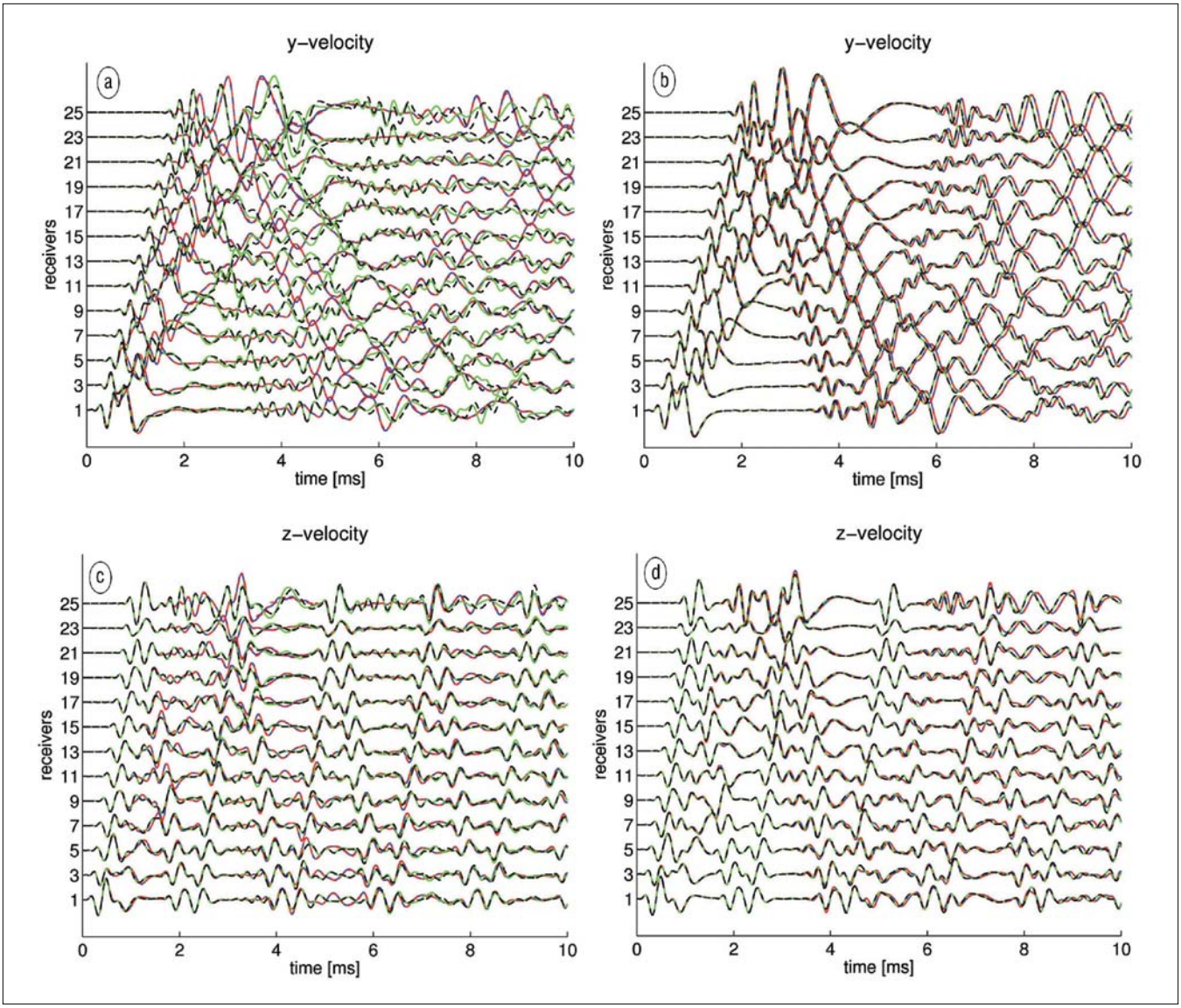

Figure 4. *Synthetic waveforms of velocity components for the sonic logging experiment. (a) Damage zone (material gradient) of 2-m radius is assumed. Results are shown for four experiments: small (blue solid line) and large (red dashed line) material contrast with casing, and small (green solid line) and large (black dashed line) material contrast without casing. (b) Same as (a), however, without damage zone. (c), (d) Same as (a), (b) for the z-velocity component instead of the y velocity.*

properties (especially velocities and porosity) of a penetrated formation with a depth resolution of ~0.5 ft. To validate sonic measurements via modeling of acoustic-wave propagation modeling, it turns out to be fundamental to consider the model geometry and heterogeneous material distribution in and around the well. In Figure 3a, we sketch a setup of a sonic logging experiment, where a logging tool is inside a fluid-filled well that penetrates an interbedded formation of two different materials. It is assumed that a steel casing separates the borehole fluid from a damaged formation zone. Due to the damage of the formation around the wellbore, the drilling fluid (mud) typically causes an invasive zone leading to a nearly radial material gradient of a few meters away from the well. In our study, we investigate the effect of the steel casing on sonic measurements and the importance of the material gradient with respect to the recorded signals. To this end, we use an explosive source at the lower end of the tool and 25 equally

	ρ [kg/m³]	λ [10⁹Pa]	μ [10⁹ Pa]	V_p [m/s]	V_s [m/s]
Tool/casing	**7800**	**65.0000**	**65.0000**	**5000**	**2887**
Bore fluid	**1020**	**2.2950**	**0.0000**	**1500**	**0**
Material 1	**2700**	**14.5480**	**14.5480**	**4020**	**2321**
Material 2	**2700**	**13.5480**	**13.5480**	**3880**	**2240**
Material 3	**2500**	**10.5480**	**10.5480**	**3423**	**1977**

Table 2. *Material properties of the modeling setup for sonic measurements in the borehole considering the logging tool, the bore fluid, the casing, and the heterogeneous formation.*

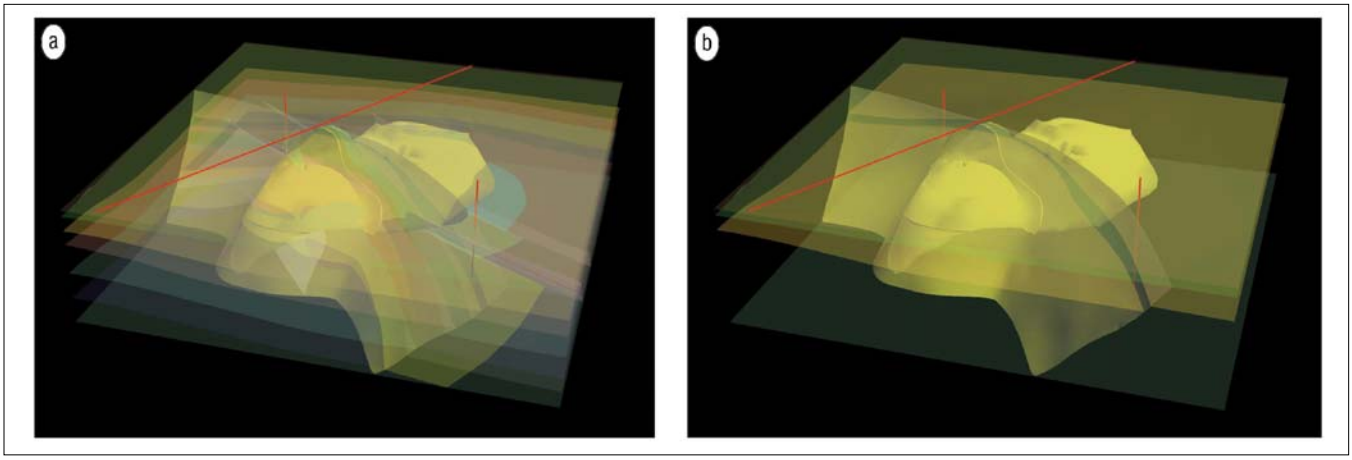

Figure 5. *SEG/EAGE salt model. (a) Complete and (b) simplified model including the fundamental features of intersections of layers, faults, and the salt body. The horizontal red line indicates the cross section along A-A'; the vertical red lines indicate the two boreholes.*

spaced receivers along the tool (Figure 3a). In Figure 3b, we show a cut through the 3D mesh where the ratio between smallest and largest elements (here ~50) is visible. The mesh of the fluid and the uppermost layers is omitted for better visualization of the geometry. In this case, the local time-step algorithm particularly pays off, as the steel tool and casing force the use of extremely small elements (~1 inch edge length), but yield a P-wave speed of 5000 m/s. These parameters lead to a time-step length of ~1 μs in these elements. Figure 3c shows the mesh partition strategy, where each color represents a different subdomain. Note that the tool, fluid, casing, and formation are partitioned individually via the separation into zones. Then subdomains of each zone are collected and put to one core to achieve an acceptable load balance as in the local time-stepping approach smaller elements are computationally more expensive than larger ones. Comparisons show, that the local time-step approach is about three times faster than a global time-step algorithm for this application.

Table 2 gives the material properties of the steel tool and casing, the fluid, and the geological formation for our tests. First we consider a cased well and a material gradient around the well of 2-m radius where

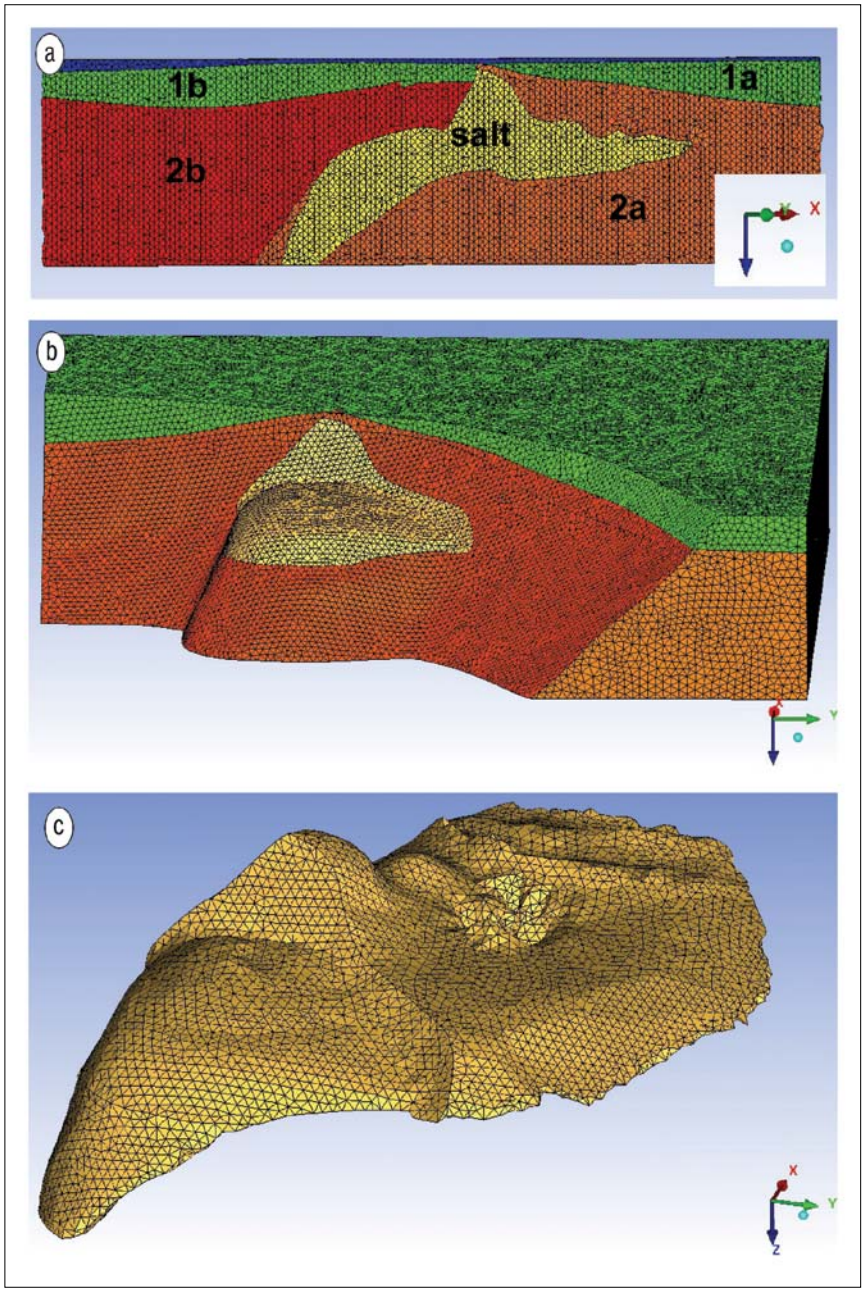

Figure 6. *(a) Cut through the tetrahedral mesh produced with ICEM-CFD (ANSYS) along the A-A' profile showing the geometry of the salt body of the SEG/EAGE salt model. (b) 3D perspective of the salt (yellow) exhibiting complex features due to its intersection with a fault. (c) 3D geometry of the discretized salt body.*

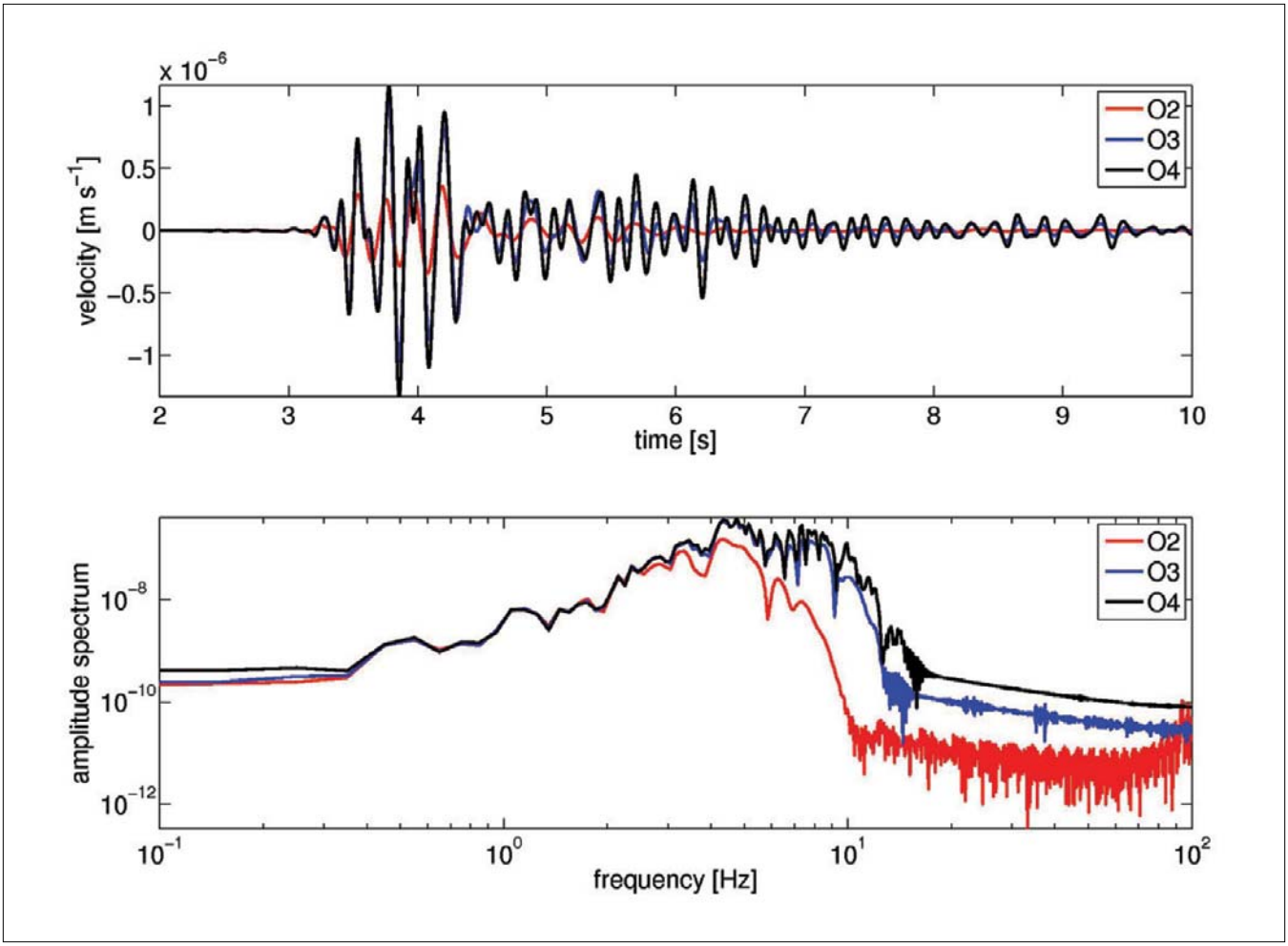

Figure 7. *Reduced numerical diffusion and extended frequency content of synthetic seismograms due to higher approximation orders on the same mesh spacing.*

the properties change linearly from the bore fluid to the unperturbed formation values. The interbedded layers consist of material 1 and 2, producing a synthetic data set shown in blue in Figure 4a. Enhancing the material contrast by replacing material 2 by material 3 results in virtually the same data set (shown in red). However, we obtain clear differences by removing the casing and repeating the experiments as shown by the green and black data in Figure 4a. Obviously, the casing strongly obscures the effect of different material properties on the seismogram. In a second series of tests, we omit the gradient and use the unaltered material properties of the formation directly adjacent to the wellbore. In this case, the casing again has a larger effect on the seismograms than the material contrasts in the formation. In fact, the removal of the casing leads to increasing phase shifts of later arrivals in the seismograms.

Consideration of the z-velocity components in Figure 4c and Figure 4d shows slightly different results with less pronounced phase shifts. However, the effect of the tool's geometry on the P-wave bouncing up and down the tool due to the strong impedance contrast between the steel and the surrounding fluid (Kaser and Dumber, 2008) is clearly visible. Furthermore, a systematic analysis of the rotational motion (not shown) could provide additional information and promote the construction and design of rotational borehole sensors.

Reservoir-scale modeling

Surface seismic data generally provide a large-scale picture of the geological subsurface and the geometrical features of a reservoir. Seismic simulations are used for model validation or survey design. In particular, time-lapse seismic measurements allow assessment of changes in the subsurface with time, such as fluid movement or effects of secondary oil recovery. Such data are examined for variations in seismic attributes related to pore-fluid content. Therefore, reservoirs are described by dynamically changing properties and reduced turnaround times for model updates through efficient model-building technologies are becoming increasingly important.

ADER-DG is capable of using unstructured tetrahedral meshes for the accurate simulation of seismic-wave propagation phenomena. For geometrically complex models, such as the SEG/EAGE salt model (Figure 5a), the mesh generation process for tetrahedral meshes can be highly automatized once the model geometry is defined. The mesh can be aligned

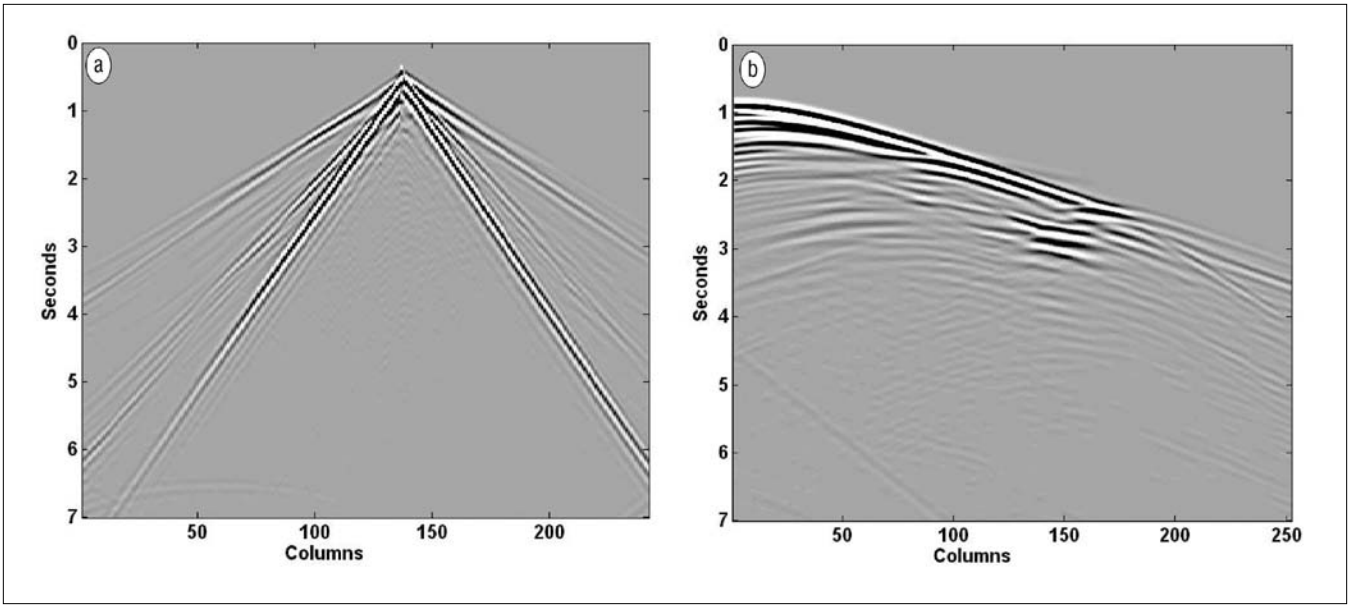

Figure 8. *Synthetic raw shots of two surface receiver lines across the salt model. (a) The source position is at the surface close to the center of receiver line A-A'. (b) The source is inside a borehole with a receiver line connecting the two wells at the surface.*

to complex shapes of free surface topography, structural interfaces, or faults in order to approximate correctly such structural features. This is particularly important when these features represent sharp material discontinuities that should not be smoothed out by strong gradients. To demonstrate the capability of the methodology, we apply our software to a simplified salt model (Figure 5b) that contains the main features (like the complex salt body, the major fault, and some sedimentary layers) of the SEG/EAGE model. The problem of the original complete model is that it requires a tedious, manual correction of the geometry definition, as some interfaces and surfaces forming the geological units are intersecting in a nonphysical manner. Different sections and parts of our simplified salt model are shown in Figure 6 and the according material properties are given in Table 3. A 2D cut along profile A-A' (red surface line in Figure 5) is shown in Figure 6a together with the notation of the material distribution. In Figure 6b, we display a 3D perspective view of the model, where the water layer and geological units 1b and 2b are removed in order to see the deformation of the fault due to the salt body intrusion. A separate view of the complex 3D geometrical structure of the salt body is shown in Figure 6c. Note that holes in the original definition of the enclosing salt body surface are closed according to the geometry of the intersecting faults. Here, we emphasize that a crucial precondition of the automatic mesh generation process is the exact definition of the model's geometry. Once this is done, the appropriate mesh spacing has to be chosen such that the geometrical features are accounted for with sufficient resolution and that the propagated seismic waves are approximated with the desired accuracy.

	ρ [kg/m^3]	λ [10^9]	M [Pa 10^9]	V_P [m/s]	V_S [m/s]
Water	1020	2.2950	00000	1500	0
Layer 1a	2000	4.5067	4.5067	2600	1501
Layer 1b	2050	5.0000	5.0000	2705	1562
Layer 2a	2500	7.5000	7.5000	3000	1732
Layer 2b	2600	9.0000	9.0000	3223	1861
Salt	2160	20.8000	14.4570	5094	3103

Table 3. *Material properties of the modeling example of the simplified 3D salt model problem.*

It is important to remember that the accuracy of the numerical seismograms depends on three factors: (1) the mesh spacing, (2) the approximation order, and (3) the propagation distance of the waves. A detailed study of the influence of these parameters on the accuracy of synthetic seismograms obtained by ADER-DG has been carried out by Käser et al. (2008).

An example of the effect of different approximation orders for the SEG/EAGE salt model is shown in Figure 7. The seismogram is obtained by using a tetrahedral mesh of 3.1e6 elements of ~200-m edge length and is recorded by a receiver inside one of the boreholes indicated as vertical red lines in Figure 5. An explosive source producing a Ricker wavelet with dominant frequency of 5 Hz is in the other well. Using an ADER-DG scheme of second-order (O2) in time and space generates a smooth seismogram, where much of the amplitude information is essentially lost due to numerical diffusion. Therefore, the problem is under-resolved, but gives a first rough estimate of the solution without producing numerical artifacts. Increasing the order to O3 or O4

preserves more amplitude information, while the change between two consecutive orders indicates how close the solution has already converged towards a quasi-analytic solution. The frequency spectra in Figure 7 clearly show the extended frequency content of the synthetic signal of higher approximation quality while preventing spurious high-frequency noise.

We finally apply the ADER-DG O4 scheme to the simplified salt model to produce synthetic raw shots, similar to acquired data in surface surveys, running a computation on 512 cores. Examples of resulting data sets are shown in Figure 8 for two different shot locations recorded along surface receiver lines (a) on cross section A-A' and (b) connecting the two boreholes. The strong direct water wave is clearly visible in Figure 8a while effects due to the structural features of the salt body are visible in Figure 8b. Data processing can now be applied as for real data. Besides, the synthetics allow for systematic studies of source signature effects and structural or compositional subsurface properties on the seismic response.

Concluding remarks

We presented the new discontinuous Galerkin finite-element method for modeling seismic wave propagation using HPC infrastructures and applied to relevant problems in oil and gas exploration. The geometrical flexibility of unstructured tetrahedral meshes combined with the method's high-order approximation properties in space and time, due to a novel time-integration technique for explicit schemes, demonstrates the potential of the proposed simulation technology to produce accurate and reliable synthetic data sets for challenging modeling problems. The applicability of the software using different hardware architectures of modern HPC-infrastructure, its scaling properties, and memory usage allow the solution of large-scale wave-propagation problems to support model validation by comparing synthetics with field data. Further technical improvements with respect to run time and cache optimization are necessary to enhance the method's performance on HPC facilities. Developments covering a broader field of geophysical applications should be motivated by specific needs of the users. TLE

References

Cockburn, B., G. E. Karniadakis, and C. W. Shu, 2000, *Discontinuous Galerkin Methods, Theory, Computation and Applications*. LNCSE, 11, Springer.

de la Puente, J., M. Dumbser, M. Käser, and H. Igel, 2008, Discontinuous Galerkin methods for wave propagation in poroelastic media. Geophysics, 73, 5, T77–T97.

Dumbser, M. and M. Käser, 2006, An arbitrary high order discontinuous Galerkin method for elastic waves on unstructured meshes II: The three-dimensional case. *Geophysical Journal International,* 167, 319–336.

Fehler, M., 2009, SEAM Phase I, Progress report: Numerical simulation verification. *The Leading Edge*, 28, 270–271.

Hesthaven, J. and T. Warburton, (2008). *Nodal Discontinuous Galerkin Methods: Algorithms, Analysis, and Applications.* Springer.

Käser, M. and M. Dumbser, 2006, An arbitrary high order discontinuous Galerkin method for elastic waves on unstructured meshes I: The two-dimensional isotropic case with external source terms. *Geophysical Journal International*, 166, 855–877.

Käser, M. and M. Dumbser, M., 2008, A highly accurate discontinuous Galerkin method for complex interfaces between solids and moving fluids. Geophysics, 73, 3, T23–T35.

Käser, M., V. Hermann, and J. de la Puente, 2008, Quantitative accuracy analysis of the discontinuous Galerkin method for seismic wave propagation. *Geophysical Journal International*, 173, 990–999.

Titarev, V. and E. Toro, 2002, ADER: Arbitrary high order Godunov approach. *Journal of Scientific Computing*, 17, 609–618.

Toro, E.F., 1999. *Riemann Solvers and Numerical Methods for Fluid Dynamics*. Springer.

Acknowledgments: The authors thank the Deutsche Forschungsgemeinschaft (DFG) as the work was supported through the Emmy Noether-program (KA 2281/2-1). Furthermore, the technical advice of the user-support team for Distributed European Infrastructure for Supercomputing Applications (DEISA) of the Leibniz-Rechenzentrum (LRZ) is gratefully acknowledged.

Corresponding author: martin.kaeser@geophysik.uni-muenchen.de

Bulletin of the Seismological Society of America, Vol. 100, No. 4, pp. 1427–1455, August 2010, doi: 10.1785/0120090052

Quantitative Comparison of Four Numerical Predictions of 3D Ground Motion in the Grenoble Valley, France

by Emmanuel Chaljub, Peter Moczo, Seiji Tsuno, Pierre-Yves Bard,* Jozef Kristek, Martin Käser, Marco Stupazzini, and Miriam Kristekova

Abstract This article documents a comparative exercise for numerical simulation of ground motion, addressing the seismic response of the Grenoble site, a typical Alpine valley with complex 3D geometry and large velocity contrasts. Predictions up to 2 Hz were asked for four different structure wave-field configurations (point source and extended source, with and without surface topography). This effort is part of a larger exercise organized for the third international symposium on the effects of surface geology (ESG 2006), the complete results of which are reported elsewhere (Tsuno *et al.*, 2009).

While initial, blind computations significantly differed from one another, a remarkable fit was obtained after correcting for some nonmethodological errors for four 3D methods: the arbitrary high-order derivative discontinuous Galerkin method (ADER-DGM), the velocity-stress finite-difference scheme on an arbitrary discontinuous staggered grid (FDM), and two implementations of the spectral-element method (SEM1 and SEM2). Their basic formulation is briefly recalled, and their implementation for the Grenoble Valley and the corresponding requirements in terms of computer resources are detailed.

Besides a visual inspection of PGV maps, more refined, quantitative comparisons based on time-frequency analysis greatly help in understanding the origin of differences, with a special emphasis on phase misfit. The match is found excellent below 1 Hz, and gradually deteriorates for increasing frequency, reflecting differences in meshing strategy, numerical dispersion, and implementation of damping properties.

While the numerical prediction of ground motion cannot yet be considered a mature, push-button approach, the good agreement reached by four participants indicates that, when used properly, numerical simulation is actually able to handle correctly wave radiation from extended sources in complex 3D media. The main recommendation to obtain reliable numerical predictions of earthquake ground motion is to use at least two different but comparably accurate methods, for instance the present formulations and implementations of the FDM, SEM, and ADER-DGM.

Introduction

The very fact that a large part of the world's populations lives in earthquake-prone areas implies that seismologists must predict earthquake ground motion during potential future earthquakes, no matter whether they can or cannot timely predict earthquake occurrence. Prediction of the earthquake motion at a site of interest is extremely important for designing new buildings and reinforcing existing ones, as well as for undertaking actions that could help mitigate losses during future earthquakes.

Theory and numerical simulation are irreplaceable tools in the earthquake ground-motion research, mainly for two reasons. Considering the present-day limitations of direct controlled physical experiments in seismology, it is extremely difficult to scale laboratory experiments to real structures. Moreover, in most cases, there is a drastic lack of earthquake recordings at the sites of interest.

Given the present state of our knowledge of the processes and structures that form earthquake ground motion, and, at the same time, capabilities of modern seismic arrays, realistic 3D computational models have to include nonplanar interfaces between layers, gradients in velocity, density, and quality

*Also at Laboratoire Central des Ponts-et-Chaussées, 58 Bd Lefebvre, 75732, Paris Cedex 15, France.

factors inside layers, and often free-surface topography. In particular, the rheology of the medium has to allow for realistic broadband attenuation. Realistic strong ground-motion simulations should also account for nonlinear behavior in soft soils, which will, however, be neglected here for the sake of simplicity.

Only approximate computational methods are able to account for the structural complexity of the realistic models. The most important aspects of each method are accuracy and computational efficiency (in terms of computer memory and time). These two aspects are in most cases contradictory. A reasonable balance between the accuracy and computational efficiency in case of complex realistic structures made the numerical modeling methods dominant among all approximate methods.

A number of different numerical modeling methods have been developed within the last few decades. Each method has its advantages and disadvantages that often depend on the particular application. Therefore, it is very unlikely that one of the existing or recently developed numerical modeling methods can be systematically and simultaneously the most accurate and the most efficient for all important medium wave-field configurations.

In general, a sufficiently high level of agreement or sufficiently small level of misfit between data and theoretical prediction can be considered a confirmation of a theoretical model of an investigated process. In particular, the agreement between recorded and numerically predicted earthquake motion can be considered an ultimate criterion for capability of seismologists to simulate earthquake ground motion. A procedure of evaluating the capability of the theoretical model to describe the reality can be called validation. Clearly, in the validation it is necessary to understand what is a reasonable level of agreement. Given the complexity and inevitable uncertainty of realistic models (earthquake source and material structure), this is not a simple problem. Certainly, first we have to be sure that the numerical simulation method and its implementation in the computer code are correct. A procedure of evaluating the capability of the method to solve the elastodynamic equations with initial and boundary conditions can be called verification. Without the method verification, it is impossible to properly evaluate the level of agreement between recorded and simulated motions. Consequently, verification of the recent numerical modeling methods for complex realistic models is an important task.

The importance of the objective comparison, verification, and validation of the numerical modeling methods is evidenced by different initiatives. On one hand, the Southern California Earthquake Center (SCEC) has recently organized 3D numerical simulation code validation projects for wave propagation (Day *et al.*, 2003) and dynamic rupture simulations (Harris *et al.*, 2009). The goal was to validate and compare 3D earthquake simulation methods, and foster their application by the engineering community. On the other hand the EU FP6 SPICE project (Seismic Wave Propagation and Imaging in Complex Media: A European Network, www.spice-rtn.org, 2004–2007) aimed at development of computational tools for seismic wave propagation, earthquake motion, and seismic imaging. SPICE has established an open Internet-based digital library (Gallovic *et al.*, 2007; www.spice-rtn.org/library), which comprises computer codes, training materials, simulation exercises, and an interactive web interface for code validation (Moczo *et al.*, 2006; www.nuquake.eu/SPICECVal/). The main goal of the SPICE Code Validation is to provide an open long-term basis for possible tests and comparisons of the numerical methods and codes for the seismic wave propagation and earthquake motion simulations. The objective evaluation of accuracy and comparison is facilitated using the time-frequency misfit criteria (Kristekova *et al.*, 2006) interactively applicable to a solution one wants to compare with any of the previously uploaded solutions.

In parallel, real sites and realistic models were prime targets of the blind prediction tests in framework of three international symposia on the effects of surface geology (ESG) in Odawara, Japan (1992), Yokohama, Japan (1998), and Grenoble, France (2006). The ESG 2006 symposium provided an excellent opportunity to focus on numerical modeling of earthquake motion in the Grenoble Valley for local weak and moderate earthquakes. The Grenoble Valley is a very interesting and typical deep Alpine sediment-filled structure. The Grenoble urban area, mostly built over the sedimentary area, gathers a significant population (around 500,000), a number of high-tech and/or sensitive industrial facilities, and educational and research institutions. Therefore, despite an only moderate regional seismic hazard (with known historical events hardly reaching magnitude 6) and considerable broadband site effects, Lebrun *et al.* (2001) raised the concern about the seismic risk in such Alpine valley configurations, which are also met in different other areas within the European Alps, and in other mountainous areas with embanked valleys filled with young, postglacial lacustrine sediments.

Our article presents results of a multi-institution project and an unprecedented comparison of very different and important methods applied to a structurally complex model of a real site. The scope of our article is not to benchmark computer codes that solve a well-referenced problem with a known analytical solution. Rather, our article considers a realistic 3D problem for which we do not have a reference solution. There is no objective way of defining an absolute level of accuracy for the different predictions of the seismic response of the Grenoble Valley.

The applied methods have been developed by various teams in different institutions using different computer facilities. It was not technically feasible to perform presented simulations on the same computer. It is important to realize that the use of the same computer is of marginal importance compared with the main aspect of the article.

The scope and goal of our article match those of the SCEC code validation project that targeted the Los Angeles basin to demonstrate the reachable level of agreement among

the leading U.S. modeling teams. Our article has a similar goal; in addition, it considers a wider set of numerical methods and a significantly higher maximum frequency.

Compared with the Los Angeles basin, the modeling of the Grenoble Valley is complicated by the relatively large velocity contrast and the complex interface geometry. The level of the reached agreement was not possible to anticipate and thus is not trivial.

Structurally complex models of real sedimentary valleys pose great challenges. Even though there have been a number of attempts at validation, the agreement between synthetics and data remains far from satisfactory, except for very low frequencies, say < 0.1 Hz. This is because one cannot isolate the validity of the simulation from that of other factors, such as the material model, including possible nonlinearities, and the source description. One common way to reduce the influence of these factors is to use small earthquakes, whose rupture can be modeled as a point source.

Given the model complexity and methodological differences among the applied methods, we found a surprisingly good level of agreement for four of the submitted predictions obtained by different teams: Käser *et al.* (2006) used the arbitrary high-order derivative discontinuous Galerkin method (ADER-DGM), Chaljub (2009) used the spectral-element method (SEM), Kristek *et al.* (2009) used the finite-difference method (FDM), and Stupazzini (2009) and Stupazzini *et al.* (2009) used another implementation of the SEM. The ADER-DGM, FDM, and SEM differ both in the basic formulations of the equations of motion and boundary conditions, and the way they construct discrete models and the resulting systems of algebraic equations. They also differ in the required computer memory and time. At the same time these three methods, together with the finite-element method (FEM), are at present the most powerful numerical modeling methods for earthquake ground motion. Whereas the FDM and FEM have a relatively long tradition, the SEM has been used since the early 1990s; ADER-DGM has been elaborated and applied to seismology rather recently. Despite this relatively long tradition of the FDM and FEM, they are still being developed in terms of accuracy and efficiency, and it is reasonable to expect considerable improvements.

In this article we first present the structural model of the Grenoble Valley and definition of the numerical simulations. In the next section we briefly introduce the ADER-DGM, FDM, and SEM. Computational aspects of the simulations for the Grenoble Valley are then discussed. The main part of the article presents comparison of the numerical results obtained with the ADER-DGM, FDM, and two implementations of the SEM. We conclude with main lessons learned and recommendations for future blind predictions and benchmark tests.

Structural Model of the Grenoble Valley

Grenoble is settled on Quaternary fluvial and postglacial deposits at the junction of three large valleys of the French external Alps (Fig. 1), surrounded by three mountain ranges. This junction mimics the letter Y (the so-called Grenoble Y), with three legs:

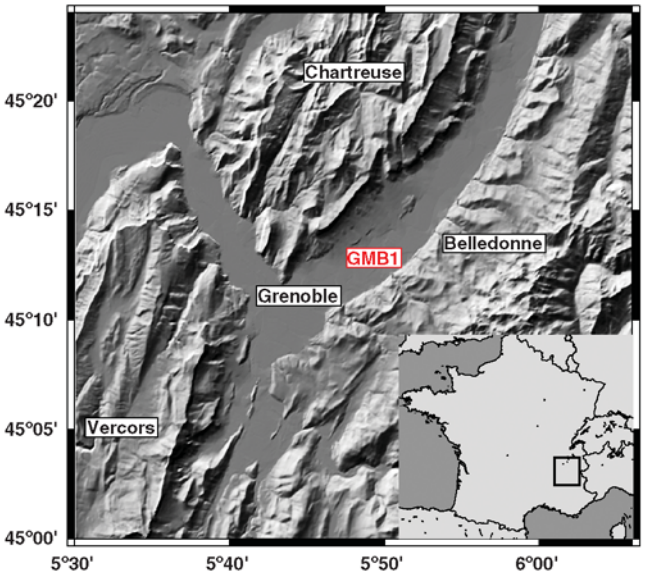

Figure 1. Situation map of the Grenoble area in the French Alps, showing the Y-shaped Grenoble Valley surrounded by the Vercors and Chartreuse limestone massifs with maximal elevation of 2000 m, and the crystalline Belledonne chain where elevation reaches 3000 m. GMB1 indicates the location of the Montbonnot borehole (see text).

1. The northeastern branch of the Y is the N30°–40° trending Grésivaudan Valley, extending about 60 km upstream along the Isère River.
2. The northwestern branch is the N150° trending, Cluse-de-l'Isère Valley, extending from Grenoble to Moirans (about 20 km), where the Isère River flows to the northwest.
3. The southern branch follows the Drac River, flowing from the south and arriving in a small plain about 15 km upstream of Grenoble.

The three massifs delineated by these valleys are the Belledonne crystalline massif to the east and two subalpine foothills consisting of sedimentary rocks (limestone) to the north (Chartreuse) and the southwest (Vercors). These foothills were formed when the Alpine shortening displaced the sedimentary cover to the northwest, forming folds and related thrusts (7 to 5 m.y. B.P.) and uplifted the crystalline basement (5 m.y. B.P.) to the east of the study area (Belledonne massif).

The IsèreValley (from upper Grésivaudan to downstream Cluse-de-l'Isère) therefore extends for about 110 km from Albertville in the northwest to Rovon west of the Vercors massif; it is 3 to 5 km wide and quasi-flat, with slowly decreasing altitudes (330 m in Albertville, 211 m in Grenoble, 180 m in Rovon). The surrounding mountains exhibit, however, a pronounced topography with maximum elevations slightly above 2000 m in Vercors and Chartreuse and above 3000 m in the Belledonne massif. As explained by Gamond *et al.*

(2009), this course runs along several hundred meters deep paleovalley carved in the Mesozoic sedimentary cover of the Alpine foothills. The northeast-southwest Grésivaudan Valley was dug by erosion around 5 m.y. B.P. through the tributaries of the paleo-Isère River, while the northwest-southeast Cluse-de-l'Isère was carved by epigenesis between 5 and 2 m.y. B.P. when the foothills were uplifted.

Its present morphology presents asymmetrical inclined sides and longitudinal moraines typical of glacial valleys. During the last glacial-interglacial cycles, as all valleys in the western Alps, it was successively eroded and overdeepened by thick Alpine glaciers (Isère glacier, local glaciers of the Belledonne massif, Drac-Romanche glacier) feeding large ice lobes at the piedmont and then filled essentially by lake sediments as glaciers were melting and retreating higher up in the catchments during warm phases. In the IsèreValley, both proglacial and deltaic lacustrine sediments completely filled an up to 900 m deep and 100 km long fjordlike basin during the last deglaciation, while only a thin, fluvial sequence formed during our interglacial period (Chapron *et al.*, 2009).

Despite the relatively good mechanical characteristics of these quaternary deposits, the large impedance contrast with the embedding rocks, together with the large embankment ratio, cause huge amplifications as observed by Lebrun *et al.* (2001), Cornou *et al.* (2003a, 2003b), and Cornou *et al.* (2009). A series of geotechnical and geophysical investigations has thus been carried out in the Grenoble area to improve the knowledge of the underground structure. A summary of these investigations can be found in the series of dedicated articles included in Volume 2 of the ESG 2006 proceedings (Chapron *et al.*, 2009; Cornou *et al.*, 2009; Dietrich *et al.*, 2009; Gamond *et al.*, 2009; Guéguen *et al.*, 2009; Jerram *et al.*, 2009; Ménard, Blein, Fournier *et al.*, 2009; Ménard, Dietrich, Vallon *et al.* 2009) and in Guéguen *et al.* (2007). Their primary focus was to constrain the deep structure responsible for the low-frequency effects; once this objective was met, a secondary objective was assigned to better understand the shallow structure controlling the higher-frequency amplification and its short-wavelength lateral variations. Because the ESG 2006 numerical simulations were limited to a 2 Hz maximum frequency, only the deep underground structure and large-scale geometry and topography are presented here.

The first deep investigations consisted in several hundreds of gravimetric measurements that allowed constraining the geometry of the sediment/bedrock interface and indicating a large thickness close to 1 km in the deepest part (Vallon, 1999). This information was checked and calibrated through the drilling of one deep borehole in the Grésivaudan Valley (the Montbonnot GMB1 site in Fig. 1, now instrumented with three accelerometers at the surface, GL-42 m, and GL-550 m), which reached the bedrock at a depth of 535 m, very close to the expectations from the gravimetric survey. Above a thin (4 m thick) glacial till, the post-Würm filling sequence consists in 520 meters of monotonous lacustrine sandy-silty formations corresponding to the postglacial lake, and ends with 15 meters of sandy-pebbly alluvium deposited when the presently working Isère fluviatile regime started again (Nicoud *et al.*, 2002).

As described by Chapron *et al.* (2009), Dietrich *et al.* (2009) and Ménard, Dietrich, Vallon *et al.* (2009), the nature of this postglacial sedimentary infill has also been documented by a set of seismic reflection profiles acquired both on land in the Isère Valley and in large valley lakes, such as the Le Bourget Lake 50 km to the north of Grenoble. All highlight very thick, rather homogeneous quaternary deposits with nonnegligible *P*- and *S*-wave velocity gradients. All these measurements have been complemented by several hundreds of microtremor measurements processed with the H/V technique (Guéguen *et al.*, 2007, 2009), which consistently exhibit a low-frequency peak (usually between 0.3 and 0.5 Hz) associated with the thick lacustrine filling, and in some parts, a second higher frequency peak (ranging from 2 to 5–6 Hz).

In summary, the main conclusions of all these deep investigations are:

- 20 km of seismic reflection profiles at different cross sections along the Isère Valley, together with the information collected in the borehole drilled near Grenoble and reaching the sediment-bedrock, allowed us to calibrate or confirm the information provided by gravimetric surveys and background noise H/V measurements on distribution of the sediment thickness in the valley.
- The bottom of the valley is marked by an irregular topography. The bottom of the Isère Valley shows a great variety of shapes: flat bottom, wide open V-shape, V-shape interlocked in a larger U-shaped valley. At some places, there exist underground substratum highs, such as a hillock (probably of tithonic age) that could be identified just south of the Grenoble downtown (see Fig. 2).
- The depth of the substratum increases downstream the Isère River from about 200 m in the upper Grésivaudan, 500 m in the lower Grésivaudan, and more than 800 m in the Cluse of Grenoble.
- The seismic velocities are roughly laterally homogeneous at depths larger than 20–40 m, in line with the filling of the valley by the postglacial lacustrine deposits.
- The *P*- and *S*-wave velocity distributions within the sediments are characterized by moderate to strong vertical gradients, with the V_P/V_S ratio varying between 6 near the surface and 2.7 at several hundred meters depth.

Given the limitation of our numerical simulation exercise to an upper frequency of 2 Hz, we thus considered a simple depth-varying sediment velocity model derived from the deep borehole measurements. The valley model is thus described by two main components:

- A 3D geometry consisting of a free-surface topography and a sediment-basement interface.
- Sediment and bedrock velocity models exhibiting only a 1D depth dependence.

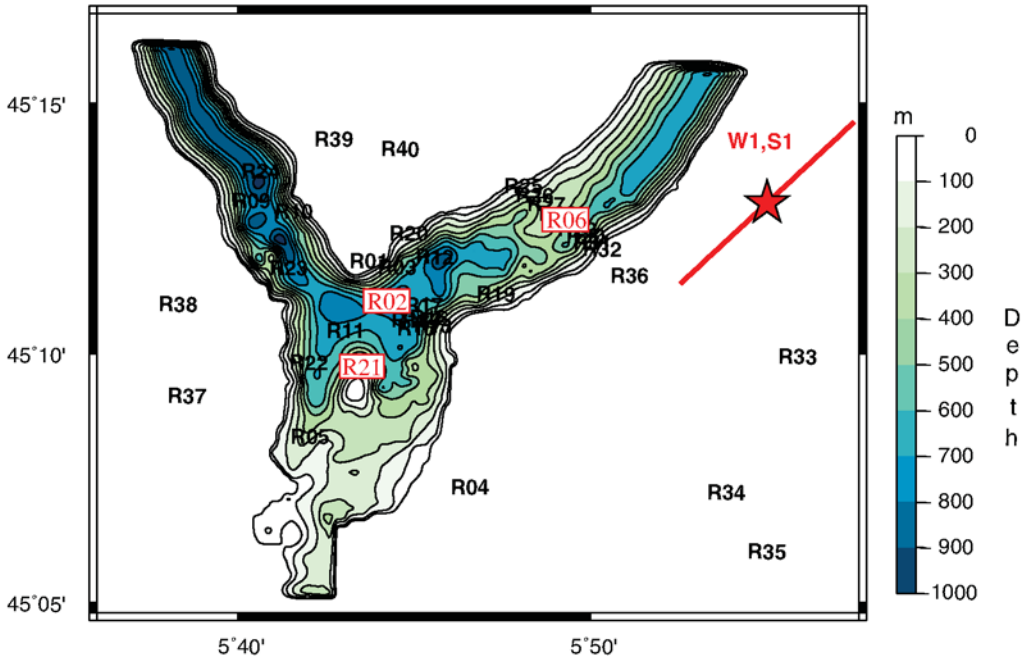

Figure 2. Map of sediment thickness in the Grenoble Valley showing 40 receivers (R01 to R40) used in the simulations. Contour lines every 100 m are shown; the bold black line indicates the points where the sediment thickness equals 50 m. The positions of the point source W1 and extended source S1 are shown in red. Red boxes indicate particular receivers for which a detailed comparison is shown further in the article. Receiver R06 corresponds to the GMB1 location in Figure 1.

The geometry of the surface topography is shown in Figure 1, and the underground topography is depicted in Figure 2. The velocity model is detailed in Table 1. This model is still distant from the reality, especially for the shallow part. It constitutes, however, a good starting model that is able to reproduce the main features of the low-frequency response, and it is complex enough to enable a meaningful comparison between different numerical methods.

The quality factor values were chosen infinite in the underlying bedrock. The bedrock is very stiff and the computations are performed only for local, shallow sources, so that crustal damping effects may be thought negligible in a first step. The quality factor was taken slightly larger than that actually measured in the Montbonnot borehole ($Q_P = 35$, see Cornou, 2002), but these measurements were obtained at higher frequencies (several tens of Hertz); higher Q values are needed to reproduce the observed low-frequency duration within the valley (Chaljub, 2009).

Selected Earthquakes

Various active tectonic features such as basement thrusts and strike-slip faults have been described in this part of the Alps (Thouvenot *et al.*, 2003, 2009). However, the known history reports only moderate earthquakes with intensities reaching VIII on the Medvedev, Sponheuer, and Karnik (MSK) scale, and estimated magnitudes between M 5 and M 6. The last significant earthquake in the Grenoble immediate surroundings was an M 5.3 earthquake that occurred in Corrençon (Vercors, about 30 km to the southwest of Grenoble) in 1962, which caused some chimney falls in the city.

The densification of the seismic monitoring networks undertaken in the late 1980s revealed some clear, previously unsuspected seismic alignments. In particular, the Belledonne Border Fault (BBF) has been identified as the most active of these new features: it consists of a 50 to 70 km long, northeast-southwest trending segment, characterized by

Table 1
Mechanical Parameters for the Grenoble Valley Model

Unit	Thickness	Unit Mass (kg/m^3)	S-Wave Velocity β (m/sec)	P-Wave Velocity α (m/sec)	Quality Factor Q_S	Quality Factor Q_P
Sediments	Up to 1000 m	$2140 + 0.125z$*	$300 + 19\sqrt{z}$	$1450 + 1.2z$	50	$37.5\ \alpha^2/\beta^2$
Bedrock	0–3 km	2720	3200	5600	∞	∞
	3–27 km	2720	3430	5920	∞	∞
	27–35 km	2920	3810	6600	∞	∞
	>35 m	3320	4450	8000	∞	∞

*z refers to depth expressed in meters.

many small earthquakes exhibiting a right-lateral strike-slip motion consistent with an east–west compressive tectonic environment. Such a segment could therefore easily accommodate an M 6 event, with recurrence rates, however, well beyond the 500- to 1000-year historic period. This fault runs indeed east of and parallel to the northeast branch of the Y, with a distance of approximately 5–7 km from the eastern edge of the Isère–Grésivaudan Valley.

Because several recordings could be obtained at different sites from a small magnitude event on this fault near the village of Lancey in 2003, it was decided to simulate the ground motion for two earthquakes (Chaljub *et al.*, 2009):

- A real, weak one, called W1, corresponding to this 2003 event. This event had a moment magnitude M 2.9, and was assumed to be a point source with a 45° strike angle and a 90° dip angle, located at a 3 km depth. (There is, however, a significant uncertainty on the depth estimate, which could be up to 8 km).
- A hypothetical, stronger event (S1), corresponding to an M 6 event rupturing the Belledonne Border Fault along a segment centered at the W1 hypocenter. The fault length and width were assumed to be 9 and 4.5 km, respectively. A very simple (and, indeed, somewhat pessimistic and unrealistic) kinematics was assumed. The rupture nucleates at the fault center, propagates circularly with a rupture velocity equal to 2.8 km/sec, and stops abruptly when it reaches the boundary of the rectangular fault area. In addition, the slip distribution is flat (i.e., constant slip over the whole ruptured area). Such a fault mechanism generates very strong stopping phases, especially as the rupture is very shallow: the resulting ground-motion values are thus unrealistically high, and should be taken with much caution if applied to hazard estimates. Such a scenario nevertheless constitutes a good case for a comparison between different numerical methods, because it includes very strong pulses with high directivity.

For both cases, the source function was defined as

$$s(t) = 0.5(1 + \mathrm{erf}[4(t - 2\tau)/\tau]), \qquad (1)$$

where τ is the rise time chosen to provide an average slip velocity on the fault plane equal to 1 m/sec. It was thus taken equal to 0.03 sec for the weak event (W1) case, and to 1.16 sec for the strong event case (S1).

The ground motion from each of these events was computed at a series of 40 receivers displayed in Figure 2 (some of them corresponding to the location of a few seismological or accelerometric stations that recorded the M 2.9, 2003 Lancey earthquake). Most of these receivers are located at the surface, but two are located at depth and correspond to the Montbonnot downhole sensors (receiver R06 corresponds to the GMB1 location in Fig. 1). Receivers R01, R04, and R33 to R40 are located on rock outcrops, whereas all the others are located within the valley.

The simulation exercise proposed for the ESG 2006 symposium also included another set of twin events (W2, S2), located 20 km to the south of Grenoble, corresponding to a conjugate strike-slip fault with a west-northwest–east-southeast strike. A more complete description of the simulation exercise can be found in Chaljub *et al.* (2009) and Tsuno *et al.* (2009). In the present article, however, only the (W1, S1) set of events is considered.

Fourteen different groups from eight countries contributed to the ESG 2006 comparison, providing a total of 18 prediction sets; three groups used the empirical Green's function technique for the few receivers collocated with strong motion stations, two used a 1D (horizontal layering) approach for the borehole site, three modeled the response of a 2D cross section, and seven addressed the 3D problem, out of which three could account for the effects of both underground and surface topography. The numerical schemes used for 3D contributions belong to the finite-difference, spectral-element and discontinuous-Galerkin finite-element methods. Four participants whose 3D predictions were surprisingly close updated their results after the ESG meeting, after correcting some nonmethodological errors (evidenced by comparing to other predictions) in preparation of the numerical simulations. Only the results from the corrected predictions are considered here. Further details on all other methods and results can be found in Tsuno *et al.* (2009).

Computational Methods

3D Fourth-Order Velocity-Stress Finite-Difference Scheme on an Arbitrary Discontinuous Staggered Grid

Although the FDM has been used in seismology since the late 1960s, its elaboration for the structurally complex media is certainly far from being completed. Recent elaboration of the staggered-grid schemes for viscoelastic media with material interfaces as well as the development of the optimally accurate schemes are two examples soundly indicating that the best times of the finite-difference modeling are still ahead of us. Because we do not have space here for more details, we refer to the recent comprehensive review (Moczo, Robertsson, Eisner, 2007) and monograph (Moczo *et al.*, 2007).

For the numerical simulations we used a 3D fourth-order velocity-stress finite-difference scheme on an arbitrary discontinuous staggered grid. A complete theory can be found in articles by Moczo *et al.* (2002, 2004), Kristek *et al.* (2002), Kristek and Moczo (2003), and Moczo and Kristek (2005). Here we restrict our focus to the essential aspects of the simulation method.

The scheme solves the equation of motion and Hooke's law for viscoelastic medium with rheology of the generalized Maxwell body,

$$\rho \dot{v}_i = \sigma_{ij,j} + f_i, \qquad (2)$$

and

$$\dot{\sigma}_{i,j} = \kappa\dot{\varepsilon}_{kk}\delta_{ij} + 2\mu\left(\dot{\varepsilon}_{ij} - \frac{1}{3}\dot{\varepsilon}_{kk}\delta_{ij}\right) - \sum_{l}^{4}\left[\kappa Y_l^{\kappa}\xi_l^{kk}\delta_{ij} + 2\mu Y_l^{\mu}\left(\xi_l^{ij} - \frac{1}{3}\xi_l^{kk}\delta_{ij}\right)\right], \quad (3)$$

$$\dot{\xi}_l^{ij} + \omega_l\xi_l^{ij} = \omega_l\dot{\varepsilon}_{ij}; \qquad l = 1, \ldots, 4. \quad (4)$$

Here, in a Cartesian coordinate system (x_1, x_2, x_3), $\rho(x_i)$; $i\in\{1, 2, 3\}$, is density; $\kappa(x_i)$ and $\mu(x_i)$ unrelaxed (elastic) bulk and shear moduli; Y_l^{κ} and Y_l^{μ} anelastic coefficients; $\vec{u}(x_i, t)$ displacement vector; t time; $\vec{f}(x_i, t)$ body force per unit volume; $\sigma_{ij}(x_k, t)$, $\varepsilon_{ij}(x_k, t)$, i, j, and $k\in\{1, 2, 3\}$ stress and strain tensors; ξ_l^{ij} material-independent anelastic functions; and ω_l relaxation angular frequencies. Summation convention does not apply to index l. The anelastic coefficients are obtained from

$$Y_l^{\kappa} = \left(\alpha^2 Y_l^{\alpha} - \frac{4}{3}\beta^2 Y_l^{\beta}\right)\Big/\left(\alpha^2 - \frac{4}{3}\beta^2\right), \qquad Y_l^{\mu} = Y_l^{\beta}; \qquad l = 1, \ldots, 4, \quad (5)$$

where α and β are elastic (corresponding to the unrelaxed moduli) P- and S-wave velocities, and anelastic coefficients Y_l^{α} and Y_l^{β} are obtained from the desired/measured quality factor values

$$Q_{\nu}^{-1}(\tilde{\omega}_k) = \sum_{l=1}^{n}\frac{\omega_l\tilde{\omega}_k + \omega_l^2 Q_{\nu}^{-1}(\tilde{\omega}_k)}{\omega_l^2 + \tilde{\omega}_k^2}Y_l^{\nu}; \qquad k = 1, \ldots, 7, \qquad \nu\in\{\alpha, \beta\}. \quad (6)$$

The schemes for solving the equation of motion and time derivative of Hooke's law have the same structure as standard fourth-order velocity staggered-grid schemes. The accuracy of our scheme is determined by how we treat smooth material heterogeneity and material discontinuity. The effective grid density for a corresponding particle velocity component is evaluated as an integral volume arithmetic average of density inside a grid cell centered at the grid position of the corresponding particle velocity component; for example

$$\rho^A_{I,J+1/2,K+1/2} = \frac{1}{h^3}\int_{x_{I-1/2}}^{x_{I+1/2}}\int_{y_J}^{y_{J+1}}\int_{z_K}^{z_{K+1}}\rho\,\mathrm{d}x\mathrm{d}y\mathrm{d}z. \quad (7)$$

The effective grid, unrelaxed bulk, and shear moduli are evaluated as integral volume harmonic averages of moduli in respective grid cells centered at grid positions of the stress-tensor components; for example

$$\kappa^H_{I+1/2,J+1/2,K+1/2} = \left[\frac{1}{h^3}\int_{x_I}^{x_{I+1}}\int_{y_J}^{y_{J+1}}\int_{z_K}^{z_{K+1}}\frac{1}{\kappa}\mathrm{d}x\mathrm{d}y\mathrm{d}z\right]^{-1}. \quad (8)$$

The integrals are evaluated numerically, and the grid cell can contain a material discontinuity. The anelastic coefficients Y_l^{κ} and Y_l^{μ} are determined as follows: An average viscoelastic modulus in the frequency domain is numerically determined for a cell as an integral harmonic average. A corresponding quality factor is then determined from the averaged viscoelastic modulus at specified frequencies. Equation (6) for the bulk and shear moduli is then used to determine average anelastic functions. A coarse spatial distribution of the anelastic functions is applied in order to reduce the memory requirements.

The free surface is simulated using the AFDA technique (Kristek *et al.*, 2002; Moczo *et al.*, 2004).

If the near-surface sedimentary body with lower seismic wave velocities is covered by a fine spatial grid and underlying stiffer bedrock with larger velocities is covered by a coarser spatial grid, the number of grid points and, consequently, the computer memory and time requirements are significantly reduced compared with the uniform grid. In order to make such a combined (or discontinuous) spatial grid efficient, the ratio of the size of the spatial grid spacing in the coarser grid and that in the finer grid should correspond to the ratio of the shear-wave velocities in the stiffer bedrock and softer sediments. Therefore, Kristek *et al.* (2009) and Moczo *et al.* (2007) developed an algorithm that enables us to adjust a discontinuous spatial grid accordingly except that, due to the structure of the staggered grid, the ratio of the spatial grid spacings in the coarser and finer grids has to be an odd number. In other words, depending on the model of medium, we can choose a 1:1 (uniform) grid, or 1:3, 1:5, … discontinuous grid. The grid is illustrated in Figure 3. A Fortran 95 computer code 3DFD_VS has been developed for performing the finite-difference scheme. PML absorbing boundary conditions are implemented. The code is MPI parallelized (see the Data and Resources section for details).

3D Spectral-Element Method

The spectral-element method (SEM) has been introduced quite recently for seismological applications (Seriani and Priolo, 1991, 1994; Faccioli *et al.*, 1997; Komatitsch and Vilotte, 1998). The SEM is a special kind of the finite-element method (FEM) that relies on the use of a high-order spectral polynomial basis. Like the FEM, the SEM can naturally handle media with complex geometries, including surface topography and nonplanar interfaces, and it allows local mesh refinement to account for variations in seismic wavelengths. Moreover, compared with the traditional low-order FEM, the high-order spectral basis yields very accurate results by minimizing numerical dispersion and numerical anisotropy (Seriani and Oliveira, 2007; de Basabe and Sen, 2007). In practice, polynomial orders $N = 4$ to $N = 8$ are used and provide sufficiently accurate results for both body and surface waves, as soon as 5 to 6 points are used to sample the seismic wavelengths.

In the classical SEM, as in the two implementations presented hereafter, the choice of the element shapes, polynomial basis, and numerical integration rule relies on tensorization, that is, on separation of variables. The advantage is the possibility to increase significantly the computational

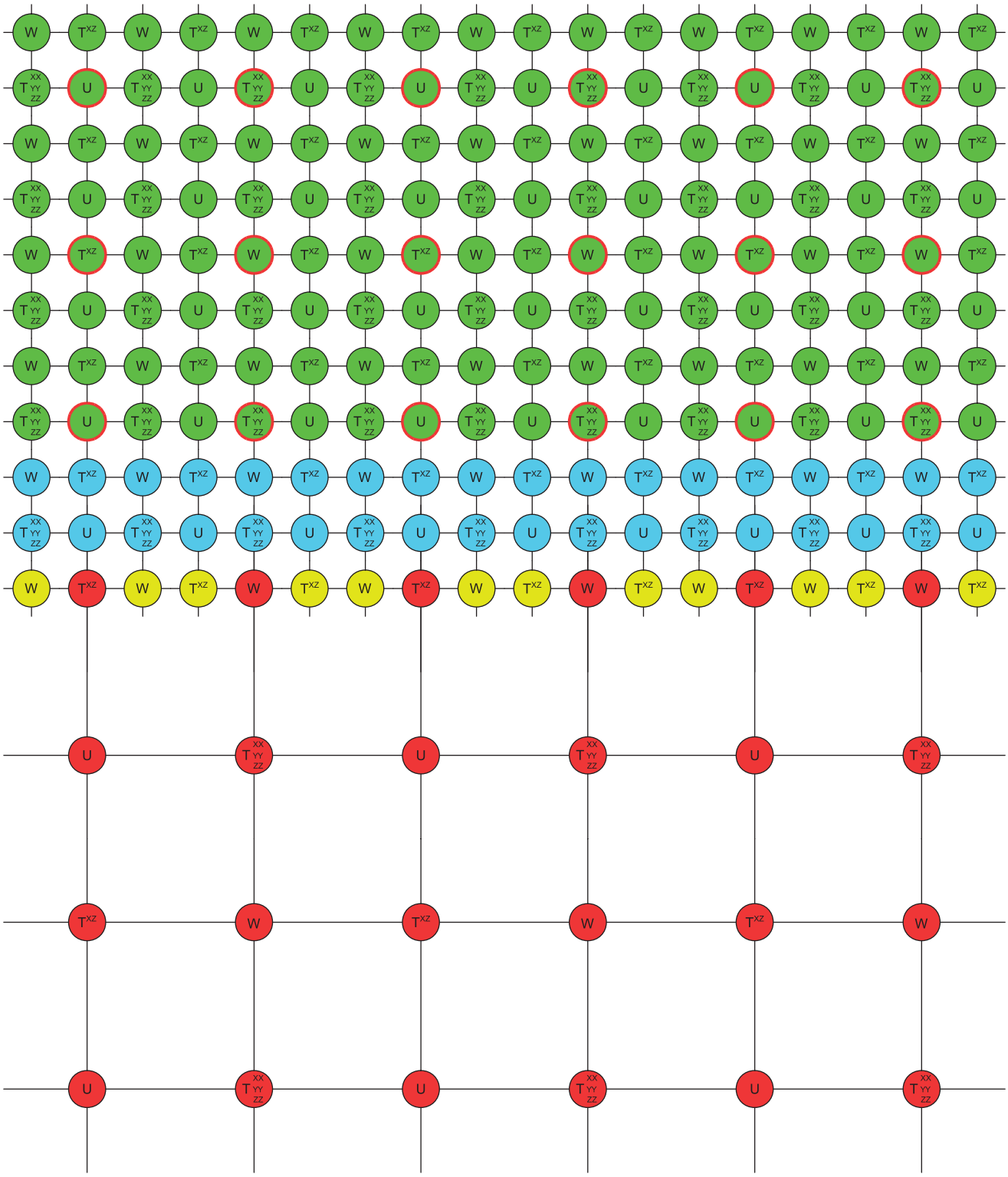

Figure 3. A vertical grid plane in the arbitrary discontinuous spatial staggered grid in the case of the coarser-to-finer spatial grid spacing equal to 3. The interior grid positions of the finer grid: green, 4th-order FD scheme; blue, 2nd-order FD scheme; yellow, bicubic interpolation. The interior grid positions of the coarser grid: red, 4th-order FD scheme. The red-circumscribed green positions define the boundary of the coarser grid.

efficiency by (1) leading to a diagonal mass matrix, allowing fully explicit schemes to be used for time evolution; and (2) decreasing the computational cost of the internal forces. The drawback is the restriction of the geometry of spectral elements to quadrangles in 2D and to hexahedra in 3D. Recall indeed that in order to account properly for discontinuities in elastic parameters, the spectral elements must not intersect the physical interfaces. This condition is not always easy to account for in a hexahedra-based SEM, for example, near valley or basin edges. Extensions of the SEM to 2D meshes of triangular elements have been proposed recently at the price of either losing the diagonal character of the mass matrix (Mercerat *et al.*, 2005) or decreasing the spectral accuracy (Komatitsch *et al.*, 2001).

Review papers presenting the numerous developments of the SEM for global or regional seismology applications can be found in Komatitsch *et al.* (2005) and Chaljub *et al.* (2007). Here, we briefly recall the key features of the SEM discretization.

Through the principle of virtual work, the dynamic equilibrium problem for the medium Ω can be stated in the following weak or variational form: find $\boldsymbol{u} = \boldsymbol{u}(\boldsymbol{x}, t)$, displacement vector, such that $\forall t \in (0, T)$

$$\frac{\partial^2}{\partial t^2}\int_\Omega \rho \boldsymbol{u}\cdot\boldsymbol{v}d\Omega + \int_\Omega \sigma_{ij}(\boldsymbol{u})\varepsilon_{ij}(\boldsymbol{v})d\Omega = \int_{\Gamma_N}\boldsymbol{t}\cdot\boldsymbol{v}d\Gamma + \int_\Omega \boldsymbol{f}\cdot\boldsymbol{v}d\Omega,$$
$$i, j = 1\ldots d \quad \text{for all } \boldsymbol{v}, \tag{9}$$

where t is time, $\rho = \rho(\boldsymbol{x})$ the material density, σ_{ij} the stress-tensor, ε_{ij} the infinitesimal strain tensor, $\boldsymbol{f} = \boldsymbol{f}(\boldsymbol{x}, t)$ the known body force distribution, $\boldsymbol{t} = \boldsymbol{t}(\boldsymbol{x}, t)$ the vector of external traction prescribed on Γ_N, and $\boldsymbol{v} = \boldsymbol{v}(x)$ is the generic function (candidate to represent admissible displacements). Note that the free-surface condition is obtained implicitly, or naturally, in the weak formulation. The stress and strain tensors in (9) are related to the displacement by Hooke's law (3).

An appropriate numerical solution of (9) can be achieved through discretization in the space and time domain. Herein, the latter is done via finite differences; the best trade-off in terms of accuracy, stability, and computational complexity is obtained using the explicit second-order leapfrog scheme (LF2-LF2) (Maggio and Quarteroni, 1994) that must satisfy the well-known Courant-Friedrichs-Lewy (CFL) stability condition.

The spatial discretization is based upon the Galerkin approximation to equation (9). It starts with a decomposition of the computational domain Ω into a family of nonoverlapping, unstructured quadrilaterals Ω_k (or hexahedra in 3D). Each element Ω_k is obtained by a regular mapping of a reference element Ω_{ref} (the unit square $[-1, +1]^2$ in 2D and the unit cube $[-1, +1]^3$ in 3D). Then, admissible displacements are approximated by polynomials of degree N on each element. This writes formally

$$\sum_{k=1}^{K}\frac{\partial^2}{\partial t^2}\int_{\Omega_k}\rho u_N^{(i)}\cdot v^{(i)}d\Omega + \sum_{k=1}^{K}\int_{\Omega_k}\sigma_{lm}(\boldsymbol{u}_N^{(i)})\varepsilon_{lm}(\boldsymbol{v}_N^{(i)})d\Omega = \sum_{k=1}^{K}\int_{\Gamma_N^{(k)}} t^{(i)}v^{(i)}d\Gamma_N + \sum_{k=1}^{K}\int_{\Omega_k} f^{(i)}v^{(i)}d\Omega, \tag{10}$$

where $\boldsymbol{u}_N$ and $\boldsymbol{v}_N$ denote the approximations of $\boldsymbol{u}$ and $\boldsymbol{v}$, and $u_N^{(i)}$, $v_N^{(i)}$, $t_N^{(i)}$, $f^{(i)}$ the scalar components of the vectors $\boldsymbol{u}_N$, $\boldsymbol{v}_N$, $\boldsymbol{t}$ and $\boldsymbol{f}$. Note that equation (10) implicitly assumes that the displacements are globally continuous, but the material properties can be discontinuous across elements.

The integrals in (10) are evaluated numerically by a high-order quadrature formula based on the Gauss-Lobatto-Legendre (GLL) points (Davis and Rabinowitz, 1984; Canuto *et al.*, 1988). The polynomials used to approximate the displacements are then defined as the shape functions of the GLL points. Thanks to this particular choice, the SEM inherits the exponential accuracy of spectral methods in space: for problems with sufficiently smooth exact solution $\boldsymbol{u}$, the numerical solution $\boldsymbol{u}_N$ obtained in the SEM converges more rapidly than those based upon the classical FEM. This property is known as spectral accuracy in the literature, and the convergence of the spectral methods is referred to as exponential or geometrical, as opposed to the algebraic convergence of the classical FEM. Note that this does not hold for the numerical realization of the free-surface condition: the convergence of numerical traction toward the prescribed traction is only algebraical (Deville *et al.*, 2002). For the wave propagation applications, the numerical accuracy is more properly assessed by the analysis of numerical dispersion, which has been shown recently to be optimal for the SEM (Seriani and Oliveira, 2007; de Basabe and Sen, 2007).

Assembling the elementary contributions to account for the continuity of displacements, equation (10) can be written as a global system of ordinary differential equations in time,

$$[M]\ddot{\boldsymbol{U}}(t) + [K]\boldsymbol{U}(t) = \boldsymbol{F}(t) + \boldsymbol{T}(t), \tag{11}$$

where vectors $\boldsymbol{F}$ and $\boldsymbol{T}$ stem from the contributions of the external forces and applied tractions, $\boldsymbol{U}$ stores the displacement values $\boldsymbol{u}_N(x, t)$ at the GLL nodes, and $[M]$ and $[K]$ denote the mass and the stiffness matrices, respectively. An important consequence of the choice of the polynomial basis is that the mass matrix is diagonal, which, as stated previously, allows for the use of fully explicit finite-difference schemes for the time evolution.

In the following we will present two different implementations of the SEM. In the first SEM-based code, hereafter referred to as SEM1, viscoelasticity is accounted for using a superposition of the standard linear solids (SLS; Liu *et al.*, 1976), which are implemented via memory variables (see Chaljub *et al.*, 2007, and references therein). Note that a parallel superposition of the SLS is also called the generalized Zener body. Also note that the rheology of the generalized Zener body is equivalent to that of the generalized Maxwell body as shown by Moczo and Kristek (2005). Thus,

the rheology in the SEM1 is equivalent to that implemented in the FD and ADER-DGM methods described in the article. The Lysmer and Kuhlemeyer (1969) absorbing boundary conditions are applied. (See the Data and Resources section for details on the SEM1 software package.)

In the second implementation, hereafter referred to as SEM2, the viscoelastic behavior is implemented with a frequency linear dependent quality factor, implying that all frequency components are equally attenuated (Faccioli *et al.*, 1997). Kosloff and Kosloff (1986) showed that this can be easily obtained by replacing the inertia term into the wave equation with an *ad hoc* expression. The absorbing boundaries are implemented following Stacey's (1988) first-order P3 paraxial conditions. A more detailed description of the software package adopted for the SEM2 simulation can be found in Stupazzini *et al.* (2009) (also see the Data and Resources section for details on the SEM2 software).

3D Velocity-Stress Discontinuous Galerkin Scheme with ADER-Time Integration of Unstructured Tetrahedral Meshes

The proposed numerical method combines a discontinuous Galerkin (DG) finite-element scheme with a time-integration technique using Arbitrarily high-order DERivatives (ADER) in order to solve the governing PDE with arbitrarily high approximation order in time and space. The system of the 3D seismic wave equations formulated in velocity-stress leads to a hyperbolic system of the form

$$\frac{\partial Q_p}{\partial t} + A_{pq}\frac{\partial Q_q}{\partial \xi} + B_{pq}\frac{\partial Q_q}{\partial \eta} + C_{pq}\frac{\partial Q_q}{\partial \zeta} = E_{pq}Qq + S_p, \tag{12}$$

where the vector Q of unknowns contains the six stress and the three velocity components. The Jacobian matrices A, B, and C include the material values and can include anisotropic, viscoelastic, or poroelastic material properties as explained in detail in Dumbser and Käser (2006), Käser *et al.* (2007), de la Puente *et al.* (2007) and (2008). The viscoelastic medium and the attenuation is defined by rheology of the GMB-EK, the same as described in the section on the finite-difference method. Furthermore, the reactive source term E is necessary, if viscoelastic attenuation is considered, and S is an external source term accommodating force of moment tensor sources. In the discontinuous Galerkin approach, the solution is approximated inside each tetrahedral element by a linear combination of space-dependent polynomial basis functions and time-dependent degrees of freedom as expressed through

$$(Q_h)_p(\xi,\eta,\zeta,t) = \hat{Q}_{pl}(t)\Phi_l(\xi,\eta,\zeta), \tag{13}$$

where the basis functions Φ_l form an orthogonal modal basis and are defined on the canonical reference tetrahedron. Note that there are no integration points necessary, because the basis is a modal basis and not a nodal basis as typically used in the SEM.

As the fully detailed derivation of the numerical scheme would go beyond the scope of this article, we refer to the previous work of Käser and Dumbser (2006) and Dumbser and Käser (2006) for a detailed mathematical formulation of the discontinuous Galerkin method. The unique property of the ADER-DGM scheme is, that the time accuracy of the scheme is automatically coupled to the space accuracy determined by the degree of approximation polynomials used in equation (13). This is due to the ADER time-integration approach (Titarev and Toro, 2002), where the fundamental idea is to expand the solution of equation (12) via a Taylor series in time

$$Q_p(\xi,\eta,\zeta,t) = \sum_{k=0}^{N}\frac{t^k}{k!}\frac{\partial^k}{\partial t^k}Q_p(\xi,\eta,\zeta,0), \tag{14}$$

where we then replace all time derivatives in equation (14) by space derivatives using the governing PDE in equation (12). It can be shown that the k-th time derivative can be expressed recursively as

$$\frac{\partial^k}{\partial t^k}Q_p = (-1)^k\left(A_{pq}\frac{\partial}{\partial \xi} + B_{pq}\frac{\partial}{\partial \eta} + C_{pq}\frac{\partial}{\partial \zeta}\right)^k Q_q + E_{pq}\frac{\partial^{k-1}}{\partial t^{k-1}}Q_p + \frac{\partial^{k-1}}{\partial t^{k-1}}S_p. \tag{15}$$

Using equations (13) and (15) in (14), the Taylor series expansion only depends on space derivatives of the basis functions Φ_l and lower order time derivatives of the source terms. The resulting expression for the degrees of freedom can be integrated in time analytically as shown in detail by Dumbser and Käser (2006) or Käser *et al.* (2007). Therefore, this new approach, termed ADER-DG method, provides arbitrarily high-order approximation in space and time depends on the degree of the used basis polynomials Φ_l in equation (13) and the corresponding order of the time Taylor series chosen in equation (14).

Once the high-order time-integrated degrees of freedom are computed, the evolution of the numerical solution in time is calculated via local stiffness and flux terms (Dumbser and Käser, 2006). Especially, the flux computations contribute as the major part with more than 80% to the overall computational cost. A numerical flux out of the element and a numerical flux into the element have to be calculated for each element boundary, that is, triangular surface, for each tetrahedral element. Each flux computation requires a multiplication of two matrices F and Q of the sizes:

size of F: (number of degrees of freedom) × (number of degrees of freedom) and
size of Q: (number of degrees of freedom) × (number of variables in the system).

The stiffness terms, however, are relatively cheap as only one matrix-matrix-multiplication of the same computational complexity has to be carried out. Nevertheless, all

operations use only local data, that is, data from the element itself and its direct neighbor sharing a common element boundary. Due to this local character of the numerical scheme, a number of different optimization approaches have been developed (Dumbser *et al.*, 2007) to enhance computational efficiency, in particular for parallel computing.

p_τ-Adaptation. In most applications, the computational domain is larger than a particular zone of interest. Therefore, a large number of elements is needed to discretize the entire geometry of the model. However, high-order accuracy might only be required in a relatively small portion of the computational domain, which makes it desirable to choose the accuracy adaptively in space. With the ADER-DG approach, it is possible to vary the degree p of the approximation polynomials Φ_l in equation (13) from one element to the other. Due to the direct coupling of the time and space accuracy via the ADER approach, the scheme automatically becomes adaptive in time accuracy, which is referred to as p_τ-adaptation.

Local Timestepping. Geometrically complex computational domains or spatial resolution requirements often lead to meshes with small or possibly degenerate elements. The timestep for explicit numerical schemes is determined by the ratio of the mesh size h of the smallest element and the corresponding maximum wave speed in this element. For global timestepping schemes, all elements are updated with this extremely restrictive timestep length, leading to a large amount of iterations. With the ADER approach, time accurate local timestepping can be used, so that each element is updated by its own, optimal timestep. An element can be updated to the next time level if its actual time level and its local timestep Δt fulfill the condition with respect to all neighboring tetrahedrons n,

$$t + \Delta t \leq \min(t_n + \Delta t_n). \tag{16}$$

Information exchange between elements across interfaces appears when numerical fluxes are calculated. These fluxes depend on the length of the local time interval over which a flux is integrated and the corresponding element is evolved in time. Therefore, when the update criterion (16) is fulfilled for an element, the flux between the element itself and its neighbor n has to be computed over the local time interval:

$$\tau_n = [\max(t, t_n), \min(t + \Delta t, t_n + \Delta t_n)]. \tag{17}$$

This can reduce the overall amount of flux calculations dramatically because only the small elements have to be updated frequently according to their small timestep lengths. A full description of the p_τ-adaptation and local timestepping of the ADER-DG scheme is given by Dumbser *et al.* (2007).

Grouped Mesh Partitioning. For large-scale applications it is essential to design a parallel code for supercomputing facilities, where load balancing is an important issue. However, if p_τ-adaptivity and especially local timestepping are applied, the partitioning is sophisticated because a subdomain can have different polynomial orders and timestep lengths. We split the computational domain into zones that usually contain geometrical or geological entities that are meshed individually. Then, each of these zones is partitioned separately into subdomains of equal numbers of elements, which now include tetrahedral elements with roughly the same sizes and orders of accuracy. Finally, each processor receives a subdomain from each zone and therefore gets a similar computational load. In Figure 4a we show a partition of the full tetrahedral mesh used for the Grenoble model, where each subdomain is color-coded. In Figure 4b we show the grouped partitioning used to improve load balance.

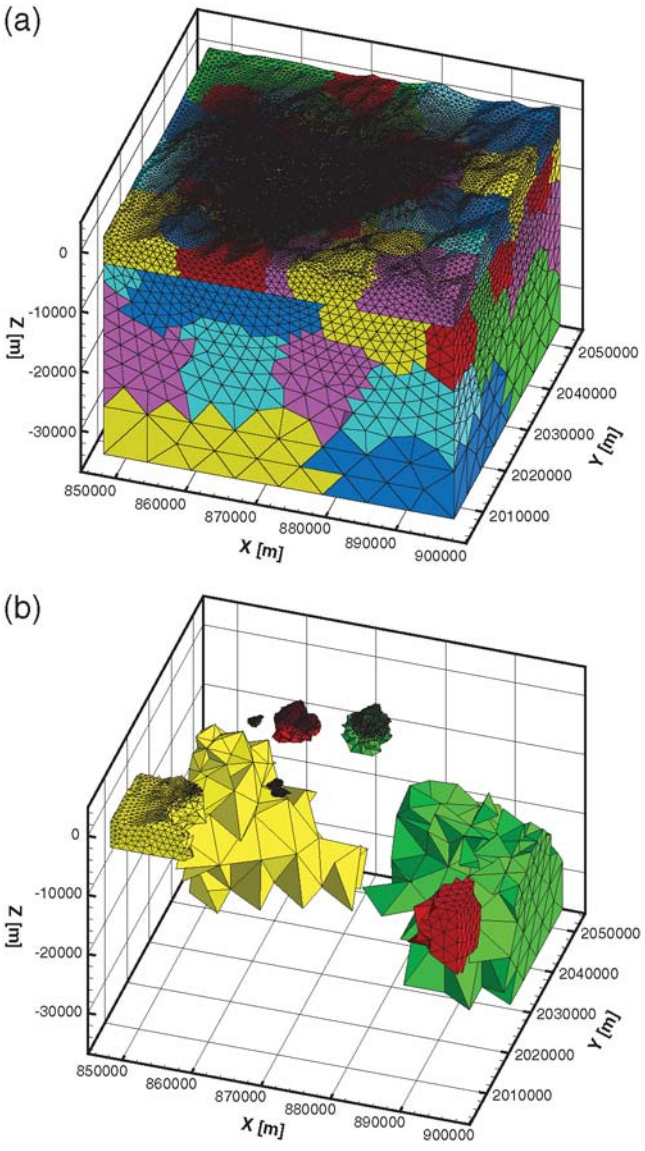

Figure 4. (a) Partitioning of an unstructured tetrahedral discretization of the Grenoble model. (b) Separate subdomains that contain a balanced number of small and large tetrahedrons from different zones are given to each processor, as indicated by the same color, to optimize the load balance.

Comparison of Computational Aspects in Modeling Earthquake Motion in Grenoble Basin

3D Fourth-Order Velocity-Stress Finite-Difference Scheme on an Arbitrary Discontinuous Staggered Grid

Space-Time Grid. The computational domain is a rectangular parallelepiped covered by a discontinuous staggered grid. The upper part of the model with a sedimentary body, 1125 m thick, is covered by a finer grid with a grid spacing of 25 m. The finer grid is made of $1321 \times 1431 \times 45$ grid cells. The lower part of the model, covering a major part of the bedrock, 8125 m thick, is covered by a coarser grid with a grid spacing of 125 m. The coarser grid is made of $265 \times 287 \times 65$ grid cells. The coarser grid is overlapping 187.5 m of the finer grid. The 1:5 discontinuous spatial grid means 87% reduction in the total number of grid cells compared to the uniform grid with a grid spacing of 25 m (approximately 90 mil. of grid cells in the discontinuous grid instead of 700 mil. of grid cells in the uniform grid). Fifty and ten grid spacings are grid thicknesses of the PML boundary regions in the finer and coarser grids, respectively. The timestep is 0.0022 sec. The used spatial grid means that the simulation should be sufficiently accurate up to 2.5 Hz.

Material Heterogeneity and Attenuation. The true model geometry of the material interfaces as well as the smooth material heterogeneity inside the sedimentary body are accounted for in the evaluation of the effective material elastic and anelastic grid parameters grid using relations (5)–(8) and the approach described therein. We can note that the scheme using the integral volume harmonic averages of the moduli and integral volume arithmetic average of density, evaluated for each cell centered at a relevant grid position, is capable to sense the true position of the material interfaces within the cell.

The constant $Q(\omega)$ law is simulated using the rheology of the generalized Maxwell body. The so-called coarse grid graining is applied in the spatial discretization of the anelastic coefficients and functions. The Q values are specified at four frequencies: 0.07 Hz, 0.225 Hz, 0.71 Hz, and 2.25 Hz. This should accurately cover the frequency range of 0.04 to 4 Hz. The P- and S-wave velocities are specified at a frequency of 1 Hz.

Treatment of the Kinematic Source. The finite kinematic model of the rupturing surface is simulated using 1836 regularly distributed point double-couple sources over a fault area 9 km × 4.5 km for the S1 event. Each point source is simulated using a discrete system of body forces acting at the grid positions centered at the grid position of the normal stress-tensor component. All point sources have the same focal parameters and source-time functions. The action of the individual point sources in time is prescribed and corresponds to the specified rupture velocity.

Accuracy versus Efficiency. All simulations were performed on a small cluster of the Opteron 2.2 machines (6 CPUs, 10 GB RAM in total). The computational parameters are given in Table 2.

3D Spectral-Element Method: The SEM1 Implementation

Model Geometry and Mesh Generation. In the first implementation of the SEM, SEM1, a simple meshing strategy, as proposed by Komatitsch *et al.* (2004), is adopted. The topology of the mesh is that of a layer-cake model in which the interfaces are deformed to follow, as much as possible, the physical interfaces. This strategy has the advantage of being easy to implement, but it also has some drawbacks. First, the size of the elements does not vary horizontally, which prevents the use of very large models as the ones that would be needed to propagate the seismic wave field from a distant earthquake to the Grenoble Valley. For the Grenoble simulation, which considers only local sources, this point is not critical; it has the nice consequence of providing a more accurate discretization of the free-surface topography, which is rather stiff in the Grenoble area (see Fig. 5). Second, the sediment-bedrock interface is not accounted for at depths shallower than about 350 m (see Fig. 6). The velocity

Table 2
Comparison of the Computational Parameters

Test Case	Number of Grid Cells or Elements	Order in Space/Time	Timestep	Number of Central Processing Units	Central Processing Unit Time	Memory
DSG Velocity-Stress FD						
W1 Flat	90,009,370	4/2	0.0022 sec	6	~33 hr	~10 GB
S1 Flat	90,009,370	4/2	0.0022 sec	6	~33 hr	~10 GB
SEM1						
W1 Flat	332,160	4/2	0.0005 sec	32	~9 hr	~10 GB
S1 Topography	332,160	4/2	0.0005 sec	32	~9 hr	~10 GB
SEM2						
S1 Topography	216,972	3/2	0.0003 sec	63	~10 hr	~18 GB
ADER-DG						
W1, S1 Flat	870,613	5/5	0.0001 sec	510	~32 hr	~50 GB
S1 Topography	1,259,721	5/5	0.0001 sec	510	~48 hr	~70 GB

contrasts near the valley edges are thus approximated by continuous variations using the polynomial basis within each spectral element. Although not quantified, the error due to this approximation is not expected to be too large because the size of the near-surface elements close to the valley edges is that of the smallest wavelength in the simulation (that is, about 150 m for a 2 Hz calculation). The mesh is coarsened with depth using the conforming strategy proposed by Komatitsch *et al.* (2004) as shown in Figure 6. We use a polynomial order $N = 4$ within each element. For calculations accurate for frequencies up to 2 Hz, the mesh contains 332,160 elements and 22,062,624 grid points.

Material Heterogeneity and Attenuation. For the attenuation model provided in the ESG exercise, the generalized Zener body with three relaxation mechanisms was used in order to mimic a constant shear quality factor in the sediments within the frequency band (0.2 Hz–10 Hz). The reference frequency, which was not imposed, is chosen to be the fundamental frequency of the Grenoble Valley, $f0 = 0.3$ Hz. Time extrapolation was handled by a second-order explicit Newmark finite-difference scheme, with an additional Runge-Kutta scheme being used to march in time the memory variables needed to model viscoelasticity (see details in Komatitsch and Tromp, 1999).

Treatment of the Kinematic Source. To model the strong motion case S1, we considered a set of 1250 point sources regularly distributed on the prescribed fault plane. Each point source was assigned a moment magnitude M 2.9 and an onset time consistent with the imposed rupture kinematics.

Accuracy versus Efficiency. All simulations were performed on a cluster of 42 SUN-V40Z nodes equipped with four AMD-Opteron 2.6 GHz processors, each having 8 GB RAM. The computational parameters are summarized in Table 2.

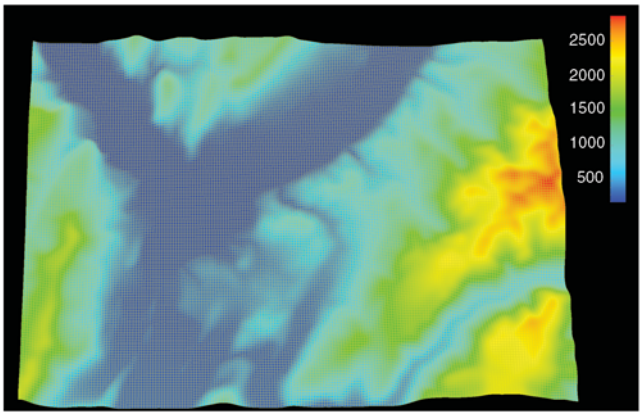

Figure 5. Surface view of the mesh of 192 × 160 elements used in the SEM1 calculations. The colors indicate surface elevation. The mesh contains 192 × 160 elements for 2 Hz calculations. The length of the elements does not vary horizontally and is kept smaller than 150 m. Each surface element contains 125 gridpoints (not shown here).

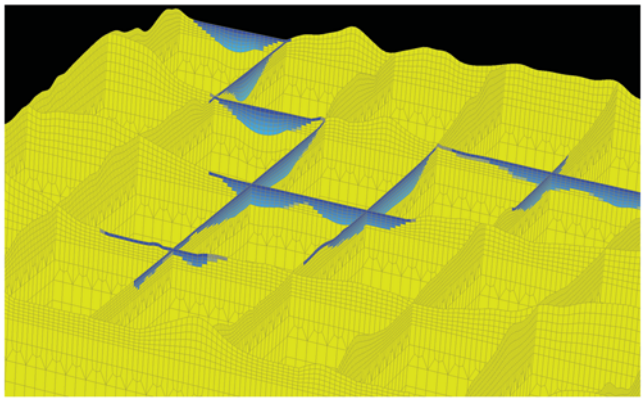

Figure 6. View of the 3D mesh of elements used in the SEM1 calculations. Golden colors indicate elements that are entirely within the bedrock, whereas blue colors stand for elements that intersect the sediments. The bedrock-sediment interface is not accounted for at depths shallower than 350 m, in particular for elements close to valley edges. The mesh is coarsened with depth following a simple conforming strategy proposed in (Komatitsch *et al.*, 2004).

3D Spectral-Element Method: The SEM2 Implementation

Model Geometry and Mesh Generation. In the second implementation of the SEM, SEM2, the meshing strategy adopted aims at accounting for true positions of material interfaces. This task was successfully solved thanks to the software CUBIT, which incorporates a set of powerful and advanced meshing schemes specifically developed to handle the hexahedral unstructured meshing problem (see the Data and Resources section for details). A thorough description of the meshing strategy adopted to strictly account for the geometry of the Grenoble Valley can be found in Stupazzini (2009). The final mesh is depicted in Figure 7 and consists of 216,972 elements, the size of which ranges from a minimum of about 20 m (inside the alluvial valley) up to 900 m. The mesh is designed to propagate frequencies up to 2 Hz with $N = 3$ (5,659,551 nodes) and up to around 3 Hz with $N = 4$ (13,300,892). A detailed zoom of a portion of the computational domain is presented in Figure 8, showing the strategy adopted to account for the discontinuity between the soft soil and bedrock. The computational domain is subdivided into small chunks; each of them is sequentially meshed starting from the alluvial basin down to the bedrock.

Material Heterogeneity and Attenuation. Inside the alluvial deposit the smooth vertical variation is taken into account assigning at each GLL point the mechanical properties evaluated according to the prescribed depth variation. The layer stratification is considered in the bedrock. The discontinuity between the soft soil and bedrock is strictly accounted for as previously mentioned. With respect to the constant quality factor model, frequencies smaller than 0.5 Hz will be overdamped, whereas higher frequencies will be enhanced in the alluvial deposits.

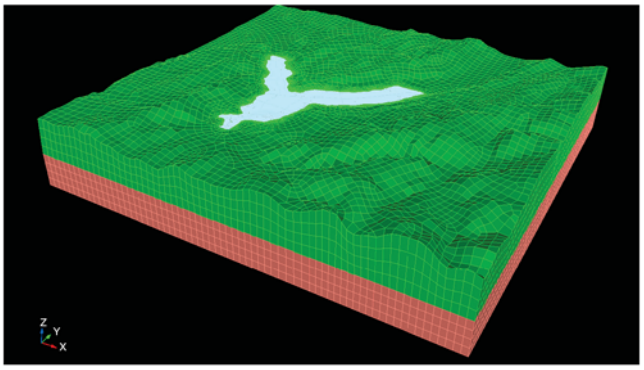

Figure 7. Three-dimensional view of the mesh used in the SEM2 calculations. The mesh contains 216,972 elements, ranging from 20 m (inside the alluvial basin) up to 900 m; for 2 Hz calculations $N = 3$ is sufficient. Different colors refer to different mechanical properties.

Treatment of the Kinematic Source. The seismic source is introduced through an appropriate distribution of the seismic moment tensor density (Aki and Richards, 2002). To model the strong motion case S1, we considered a set of 750 point sources regularly distributed on the prescribed fault plane.

Accuracy versus Efficiency. The simulations were performed on AMD Opteron 250 (64 bit single core 2.4 GHz) with 2 GB RAM and 1000T Ethernet (Oeser *et al.*, 2006). The computational parameters are summarized in Table 2.

3D Velocity-Stress Discontinuous Galerkin Scheme with ADER Time Integration of Unstructured Tetrahedral Meshes

Model Geometry and Mesh Generation. The ADER-DG method uses a tetrahedral mesh that accounts for the given geometry of the internal and external boundaries. Both the digital elevation model of the topography and the interface between the basin structure and the bedrock are provided on a regular grid with x-, y-, and z-coordinates, which is imported into a CAD tool to construct parameterized surfaces.

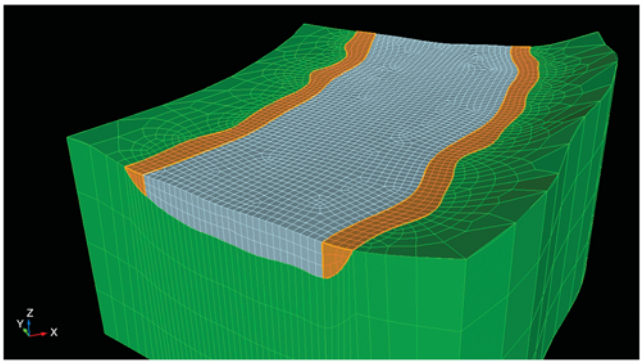

Figure 8. In order to account for the discontinuity between soft soil and bedrock the computational domain is subdivided into small chunks, each of them is sequentially meshed starting from the alluvial basin down to the bedrock.

These surfaces are then triangulated with an appropriate mesh size, and finally the volumes between the surfaces are filled with tetrahedral elements. Hereby the tetrahedral elements are conformingly connected to the surface triangulations. Furthermore, variable element sizes are chosen in order to account for the variable seismic velocity structure. Therefore, the edge lengths of the tetrahedral elements vary between 200 m inside the basin up to 5000 m at the bottom of the model, smoothly growing with increasing distance from the basin. Within the whole basin structure the mesh size increases vertically up to 500 m at the bottom of the basin.

In order to capture the topography sufficiently accurately the lateral growths factor along the free surface is chosen to result in a maximum edge length of 1000 m at the top lateral boundaries.

Material Heterogeneity and Attenuation. The smooth vertical heterogeneities inside the basin and in the surrounding bedrock are approximated in the ADER-DG approach by piecewise constant material; that is, the material parameters are evaluated at the barycenter of a tetrahedral element and are then assumed to be constant within the volume covered by the element. Similarly, the Q-factor for the viscoelastic material properties inside the basin is evaluated at the barycenter. The given wave velocities at that position are then assumed to be given for a central frequency of 1 Hz within the absorption band from 0.1 to 10 Hz. The frequency-independent constant Q-law is approximated with three relaxation mechanisms defined by a generalized Maxwell body.

Treatment of the Kinematic Source. The ADER-DG method treats the source term in both cases (W1 and S1) as a kinematic seismic source. Whereas the W1 case uses a single, double-couple point source with given location and source parameters, the S1 source is represented by 5000 aligned slip patches of a dimension of 90 m × 90 m to cover the specified 9 km × 4.5 km fault surface. Each slip patch is treated as a point source with the same parameters (strike, dip, rake) and the same shape of the source time function and possess different onset times as derived from the given rupture velocity. Therefore, the resulting seismic wave field is generated as a superposition of all individual slip patches.

Accuracy versus Efficiency. The simulations were performed on Intel Itanium2 Madison processors 1.6 GHz, 4 GB RAM per node. The computational parameters are summarized in Table 2.

Comparison of Numerical Predictions

Outline of the Comparison Method

Comparing numerical predictions of ground motion in a realistic 3D application is not straightforward because no reference solution is available, and each prediction may come with its own errors, either intrinsic (due to the limita-

tions of the numerical method used) or case-dependent (due to implementation and human errors). While it can be assumed that intrinsic errors can be identified by a proper knowledge of the numerical method being used, implementation errors need more user experience and often a complex iterative process to be tracked and hopefully minimized.

Here we present the results of such comparison process for the Grenoble Valley between four implementations of the numerical techniques presented before: DGM based on the discontinuous Galerkin method, FDM based on the finite-difference method, and SEM1 and SEM2, two implementations of the spectral-element method. We carefully checked that the presented numerical predictions are not affected by technical mistakes in individual implementations and simulations.

We compare the ground-motion predictions for the weak and strong motion cases W1-FLAT and S1-FLAT, respectively. The comparison includes a visual inspection of ground acceleration at selected receivers and global maps of peak ground velocity, as well as a quantitative analysis based on two different measures introduced recently: the goodness-of-fit score proposed by Anderson (2004), which consists of an average of ground-motion indicators of common use in engineering seismology, and the misfit measure proposed by Kristekova *et al.* (2006), which is based on the time-frequency representation of the seismograms.

Finally, we present the results obtained for the strong motion case S1-TOPO and compare the different predictions of the effects of surface topography.

Peak Velocities

Figure 9 shows the global maps of PGV (i.e., the peak values of the norm of the ground velocity vector) computed for the strong case motion case S1-FLAT by the four codes: DGM, FDM, SEM1, and SEM2.

Note the high level of ground motion for this M 6 event, especially in the eastern part of the valley. Lower values would be obtained by choosing a more physical source kinematics (instead of the Haskell model considered here, which produces a very strong directivity effect on the S wave) and depth (the top of the fault for the S1 event is located only 750 m below sea level, or about 1.5 km below surface). All maps show little correlation with the sediment thickness, except near the receiver R21, where the low values of ground velocity are consistent with the presence of steep bedrock uplift (see Fig. 2). The strongest amplitudes occur in the southeast part of the valley, with peak velocities exceeding 1.5 m/sec. These localized high values are caused by late interferences of surface waves diffracted off the eastern edge of the valley with surface waves backscattered off the bedrock uplift.

The PGV maps computed by the four codes look remarkably similar. Subtle differences can be seen, for example, in the source region where the patterns differ slightly. This could indicate small differences in the implementations of the extended source. Also, the level of the peak values displayed by the FDM code seems systematically larger than that of the other predictions. However, given the intrinsic difficulty of comparing peak values, the level of agreement shown in Figure 9 is found to be satisfactory.

Quantitative Comparison

Similarity Score and Misfit Measure. The issue of assessing the reliability of numerical predictions of ground motion has received renewed interest in recent years with the introduction of new tools to quantify the fit, either between synthetics and observations or between numerical predictions.

Anderson (2004) proposed a measure of the goodness-of-fit between two seismograms that is based on the comparison of 10 criteria that are commonly used in engineering applications: Arias duration (criterion1, or C1), energy duration (C2), Arias integral (C3), energy integral (C4), peak acceleration (C5), peak velocity (C6), peak displacement (C7), response spectrum (C8), Fourier spectrum (C9), and cross correlation (C10). These criteria are evaluated in narrow frequency bands and scaled between 0 and 10. A global average (between individual criteria and different frequency bands) is then applied to end up with one number, the so-called similarity score. Based on the systematic comparison of the horizontal components of recorded motions, Anderson (2004) introduced the following verbal scale for goodness-of-fit: a score below 4 is a poor fit, between 4 and 6 is a fair fit, between 6 and 8 is a good fit, and beyond 8 is an excellent fit.

Figure 10 shows an example of calculation of the similarity between the predictions of the north–south ground acceleration at the borehole receiver R06 for the S1-FLAT case. Solution SEM1-FLAT is used as a reference for all measurements, and only one frequency band, 0.1,2 Hz, is considered. Figure 10 confirms the impression of good fit from visual inspection of seismograms. It also shows that the differences between predictions obtained by different codes are smaller than the difference between predictions obtained by the same code with and without including the effect of surface topography (SEM1-FLAT and SEM1-TOPO).

Kristekova *et al.* (2006) proposed a measure of the misfit between two seismograms, which relies on the time-frequency representations of the signals. Their time-frequency misfit measure (hereafter referred to as TF misfit measure or simply TF misfit) allows separating amplitude (envelope) and phase differences both in the time and frequency domains.

Figure 11 shows an example of application of the TF misfit to the predictions of north–south ground acceleration at R06 for the S1-FLAT case by the FDM and SEM1 codes. The figure shows the time-frequency envelope (amplitude) and phase misfits, respectively, denoted by TFEM and TFPM. An average of the absolute values of TFEM and TFPM over time and frequency results in single-valued estimations of the envelope (EM) and of the phase (PM) misfits. A single,

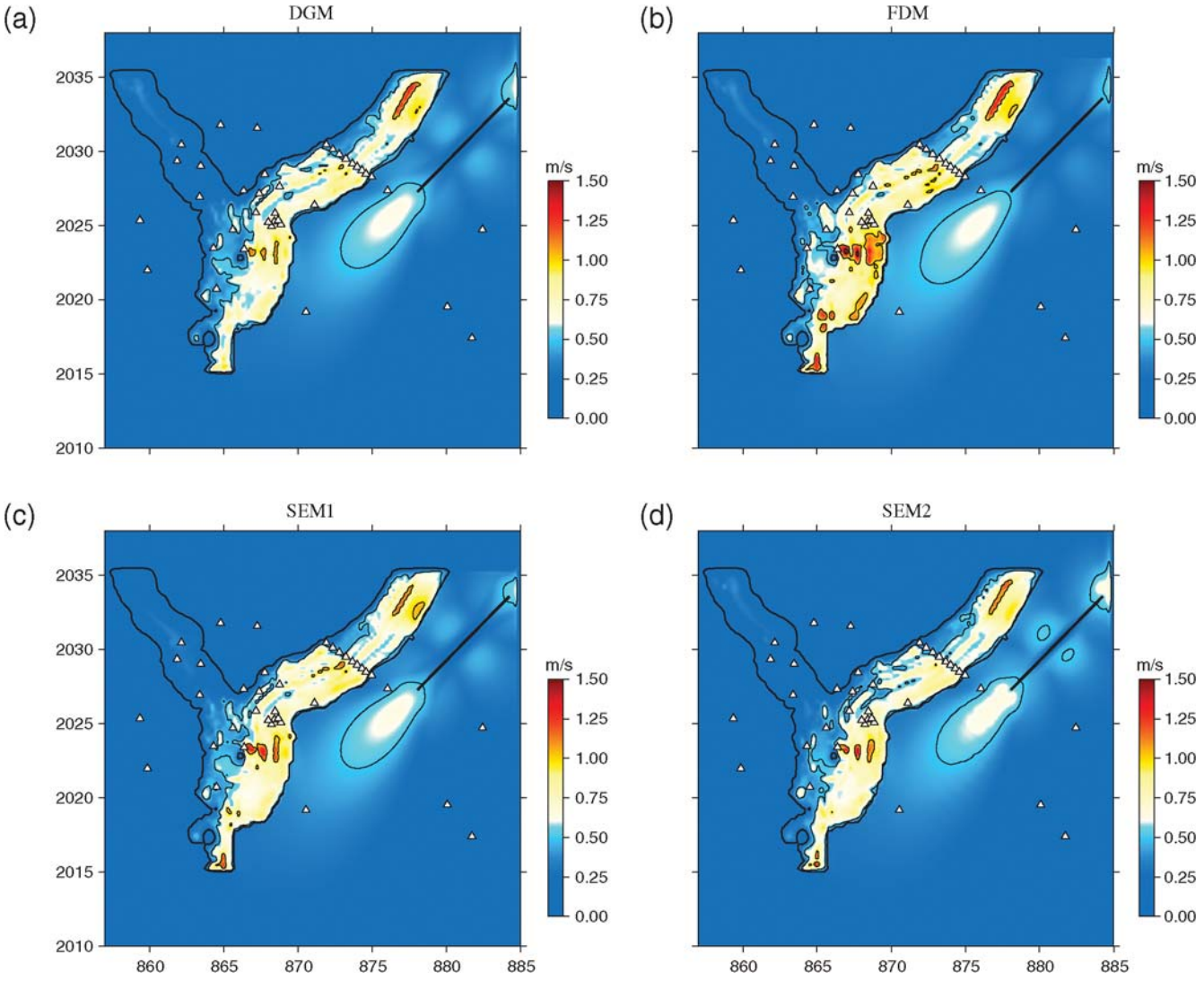

Figure 9. PGV maps obtained by the four codes (a) DGM, (b) FDM, (c) SEM1, (d) SEM2 for the strong motion case S1 without surface topography (S1-FLAT). Receiver locations are indicated by the triangles. The *X* and *Y* labels denote distances (in km) in the local Lambert coordinate system. The bold curve indicates the 50 m contour line in the sediment thickness map and the bold straight line shows the surface projection of the fault for the S1 event.

global score (denoted by EPM) is finally obtained by averaging EM and PM.

Application to the S1-FLAT and W1-FLAT Cases. We computed both the similarity score and the TF misfit for all 40 receivers and all predictions, taking the SEM1 result as a reference. We chose to use a single reference to alleviate the task of computing the misfits for each pair of predictions. Our analysis was performed for a time window 0,20.48 sec (2048 samples with timestep $\Delta t = 0.01$ sec) for each component of ground acceleration.

The correspondence between the similarity score and the TF misfit is summarized in Figure 12. Each dot represents a pair of measures evaluated at a single receiver, on a single component of ground acceleration for one of the cases S1-FLAT, S1-TOPO, or W1-FLAT. The figure shows a linear trend between the results of the two measures, which is particularly accurate for well-matching predictions. The level of the excellent fit, defined by Anderson (2004) as the similarity score above 8, corresponds to a TF misfit level below 0.4. The equation of the linear regression writes $(10\text{-}S) = 5M$, where S and M stand for the similarity score and TF misfit, respectively. Based on this equivalence, we will hereafter represent the results of the comparison of numerical predictions using the sole TF misfit measure.

We found no significant dependence of the TF misfit on the ground-motion component considered: the mean difference (averaged over the 40 receivers) between different single-component TF misfits does not exceed 0.04 (or 0.2 in terms of the similarity scores). We will therefore use a unique misfit value at each receiver, referred to as the total misfit, and defined as the arithmetic mean of the three individual TF misfits computed for the *X*, *Y*, and *Z* components.

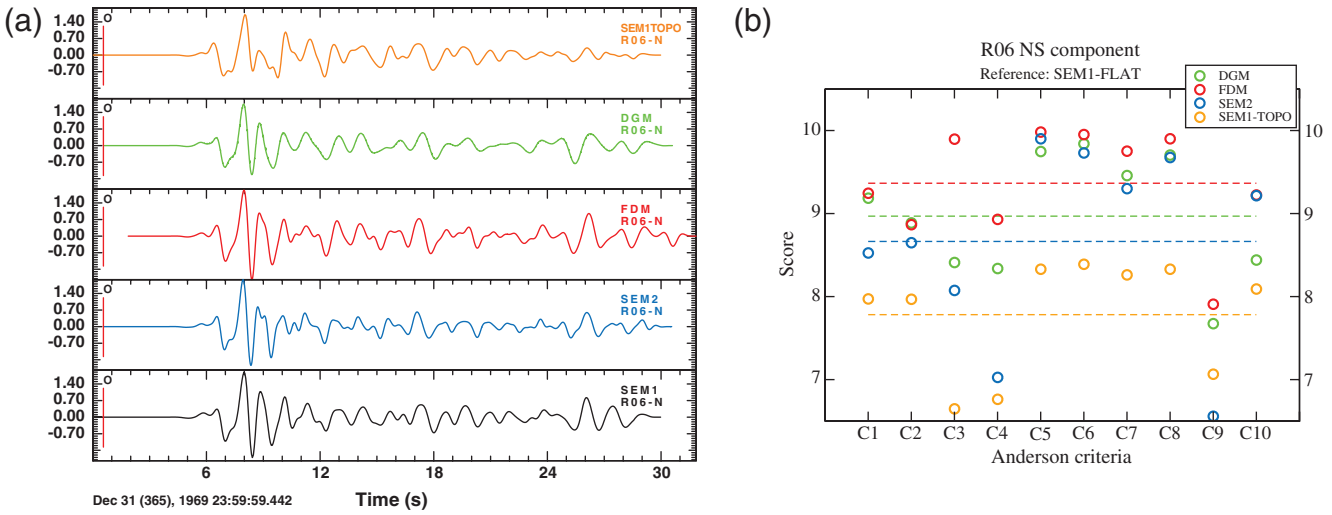

Figure 10. (a) Time series of the NS ground acceleration computed at receiver R06 by 4 different codes for the strong motion case S1-FLAT: DGM (green), FDM (red), SEM1 (black), and SEM2 (blue). The topmost trace (orange curve) was computed by the code SEM1 including surface topography (S1-TOPO). (b) Goodness-of-fit as measured by the 10 criteria proposed by Anderson (2004). The SEM1-FLAT prediction is used as reference in each case. The dashed lines indicate the levels of the global similarity scores for each prediction. Note that the fit between different predictions of the same simulation case (S1-FLAT) is better than the fit between predictions of different simulation cases (S1-TOPO and S1-FLAT) by the same code (SEM1).

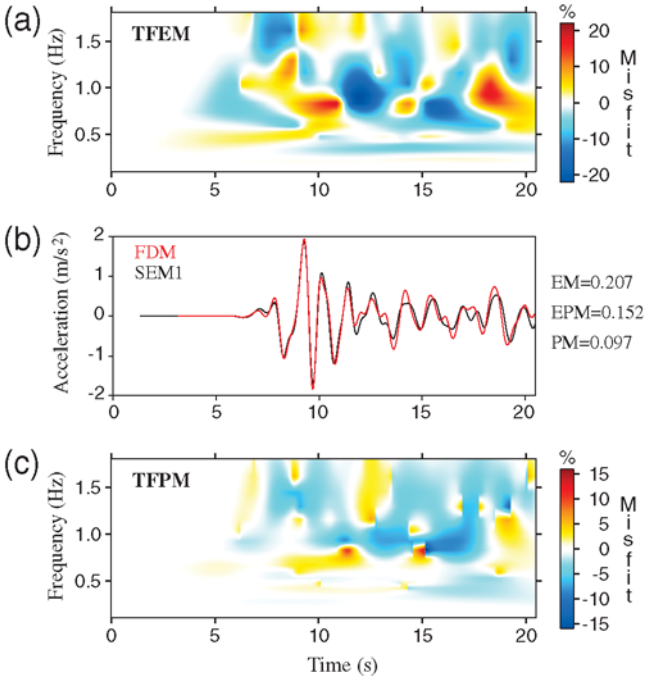

Figure 11. Example of application of the TF misfit analysis to the predictions of the NS ground acceleration at receiver R06 for the S1-FLAT case. (a),(c) Panels show the time-frequency envelope (TFEM) and phase (TFPM) misfits, respectively, taking the SEM1 prediction as a reference. (b) Time series of acceleration predicted by codes FDM (red) and SEM1 (black) are shown. Single-valued envelope (EM) and phase (PM) misfits are obtained by averaging the absolute values of TFEM and TFPM over time and frequency. The total TF misfit is obtained by averaging the envelope and phase misfits EM and PM.

Figure 13 shows the TF misfits between the different predictions of the S1-FLAT and W1-FLAT cases computed at the 40 receivers in the frequency band 0.1–2 Hz. Each dot corresponds to the total TF misfit averaged over the three components of ground acceleration.

For the S1-FLAT case, the misfit between the different predictions is almost everywhere lower than 0.4, which corresponds to the level of the excellent fit defined by Anderson (2004). Note the high similarity between the predictions of the FDM and SEM1 codes, despite the systematic amplitude shift observed in Figure 9. This illustrates the importance of

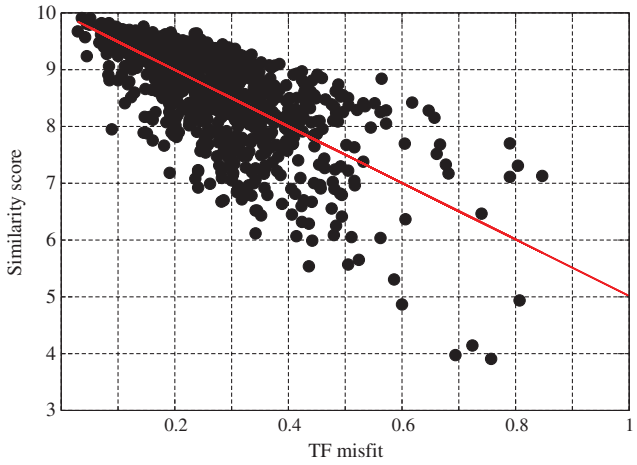

Figure 12. Comparison of results obtained with the TF misfit (M) plotted against those using the similarity score (S). Both measures have been applied to the 3 components of the 40 receivers for the benchmark cases S1-FLAT, S1-TOPO, and W1-FLAT. A global linear trend (red line) with equation ($10\text{-}S = 5M$) is found.

using a quantitative misfit measure instead of a single ground-motion parameter. Although the implementation of the point source is expected to be much simpler, the level of misfit is higher for the weak-motion case W1-FLAT than for the strong-motion case S1-FLAT. This is related to the larger high-frequency content of the W1 source, compared with the S1 source, which challenges the numerical methods at hand. Individual time series and amplitude spectra of the three components of ground acceleration at receiver R02, located in the center of the Grenoble Valley, are shown in Figure 14 and Figure 15 for the S1-FLAT case and W1-FLAT case, respectively.

Visual inspection of the traces and spectra confirms the high similarity between the different predictions of the S1-FLAT case, including at late arrival times, whereas larger differences in amplitude and phase arise for the predictions of the W1-FLAT case. Note in particular in Figure 15 the differences in timing and amplitude between the predictions of the diffracted Rayleigh wave arriving around 8 sec. Because of the wider frequency content of the source, the weak motion case also tends to highlight the differences in the implementation of intrinsic attenuation as described in the previous section (see, for example, the larger high-frequency content of the SEM2 prediction compared with the others).

Figure 16 and Figure 17 show the results obtained for the S1-FLAT case at two other locations: R06 (Montbonnot borehole ground-level station) in the middle of the 2D profile across the Grésivaudan Valley and R21 close to the steep bedrock uplift (see Fig. 2). Note the high similarity between all predictions at receiver R06 and the differences in amplitude and phase that lead to the large misfit between SEM1 and DGM at R21. This last example (R21) is one of the only cases where the level of misfit is surprisingly high in one component only (Z).

The global TF misfit distributions displayed in Figure 13 do not show any particular dependence on either the soil condition or the receiver location within the valley. The main trend is a systematic increase of the misfit with increasing distance to the source. This is expected because intrinsic errors (e.g., numerical dispersion) or differences in physical modeling (e.g., intrinsic attenuation) tend to accumulate with time and with the distance propagated. In the remainder of this section, we will therefore represent the misfit as a function of the source-receiver distance. The detail of the TF misfits in terms of amplitude and phase is shown for the S1-FLAT case in Figure 18. Both measures show the same pattern, with the highest similarity being found between the FDM and SEM1 predictions. However, the phase misfit seems to be more helpful in tracking differences between predictions. For example, the amplitude misfit between DGM and SEM1 is roughly identical to the one between SEM1 and SEM2, but larger phase misfits are seen between SEM1 and SEM2. Note also that the increase of the total TF misfit between FDM and SEM1 predictions with distance only appears in the amplitude (envelope) misfit, the difference in phase being roughly constant for all 40 receivers.

To better understand the differences between numerical predictions for the S1-FLAT case, we plot in Figure 19 the amplitude and phase misfits computed in three frequency bands: low-frequency (LF) 0.2,0.5 Hz; intermediate frequency (IF) 0.5,1.0 Hz; and high-frequency (HF) 1.0,2.0 Hz. Note that the LF band is roughly centered at the fundamental frequency of the Grenoble Valley (around 0.3 Hz); the energy radiated by the source in the S1-FLAT case decreases significantly in the HF band, suggesting that the weight of the HF misfit in the total TF misfit is weak. There is a global trend for the TF misfits (amplitude and phase) to increase with frequency. Therefore, it becomes more difficult at higher frequencies to assume a linear dependence on the source-receiver distance. This can be mainly explained by the fact that intrinsic errors of each numerical method (in particular numerical dispersion) increase with frequency.

We finally remark that there is a strong dependence of the amplitude misfit between DGM and SEM1 with frequency, which results in large differences in the HF band. The TF misfits computed for the W1-FLAT case (see Fig. 13) suggest that these discrepancies become dominant when the high-frequency content of the source is larger.

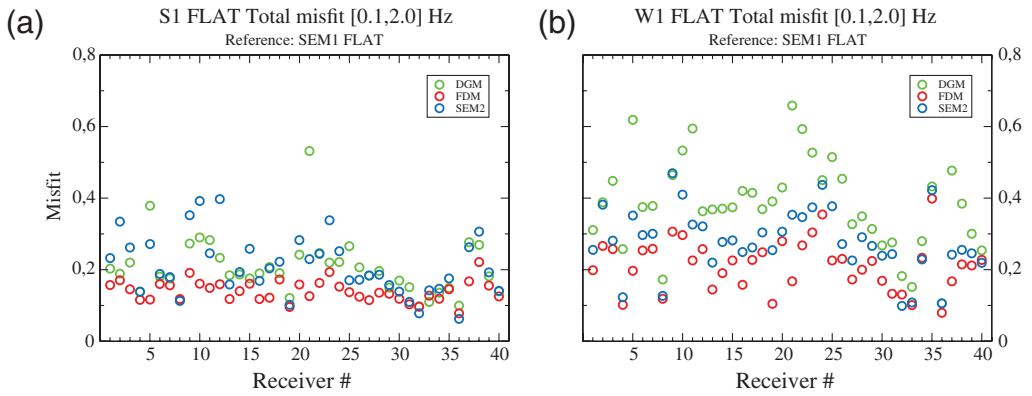

Figure 13. (a) TF misfits computed for the S1-FLAT case and (b) for the W1-FLAT case, taking the SEM1 prediction as reference. Each dot corresponds to the average of the 3 components of total misfit (average of envelope and phase) measured on the predictions of ground acceleration at each receiver in the frequency band 0.1,2.0 Hz. Receivers R01, R04, R08, and R33–R40 are located on rock sites.

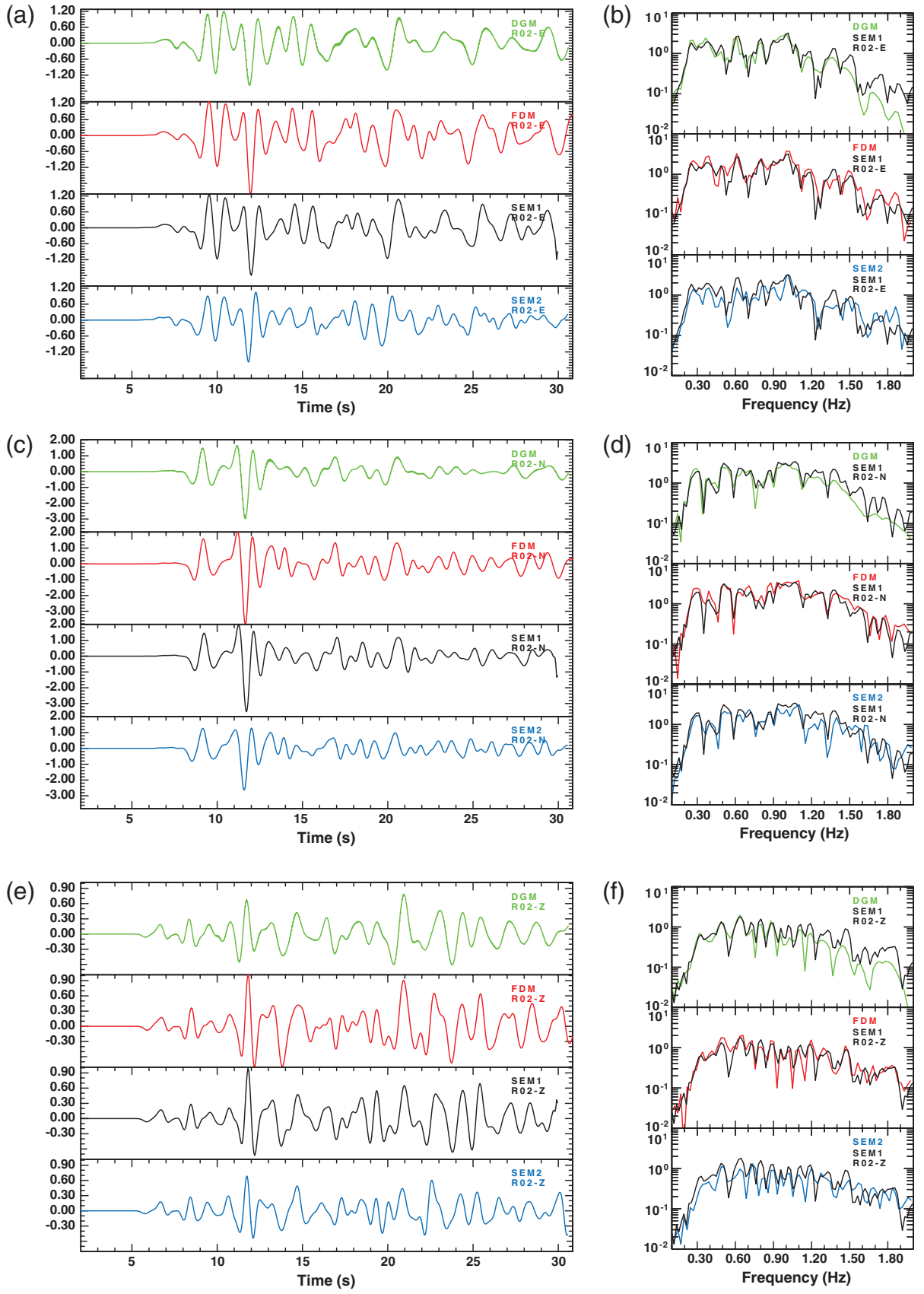

Figure 14. (a),(c),(e) Time series and (b),(d),(f) amplitude spectra of ground acceleration (EW, NS, UD) computed at receiver R02 by the four different codes for the strong motion case S1-FLAT.

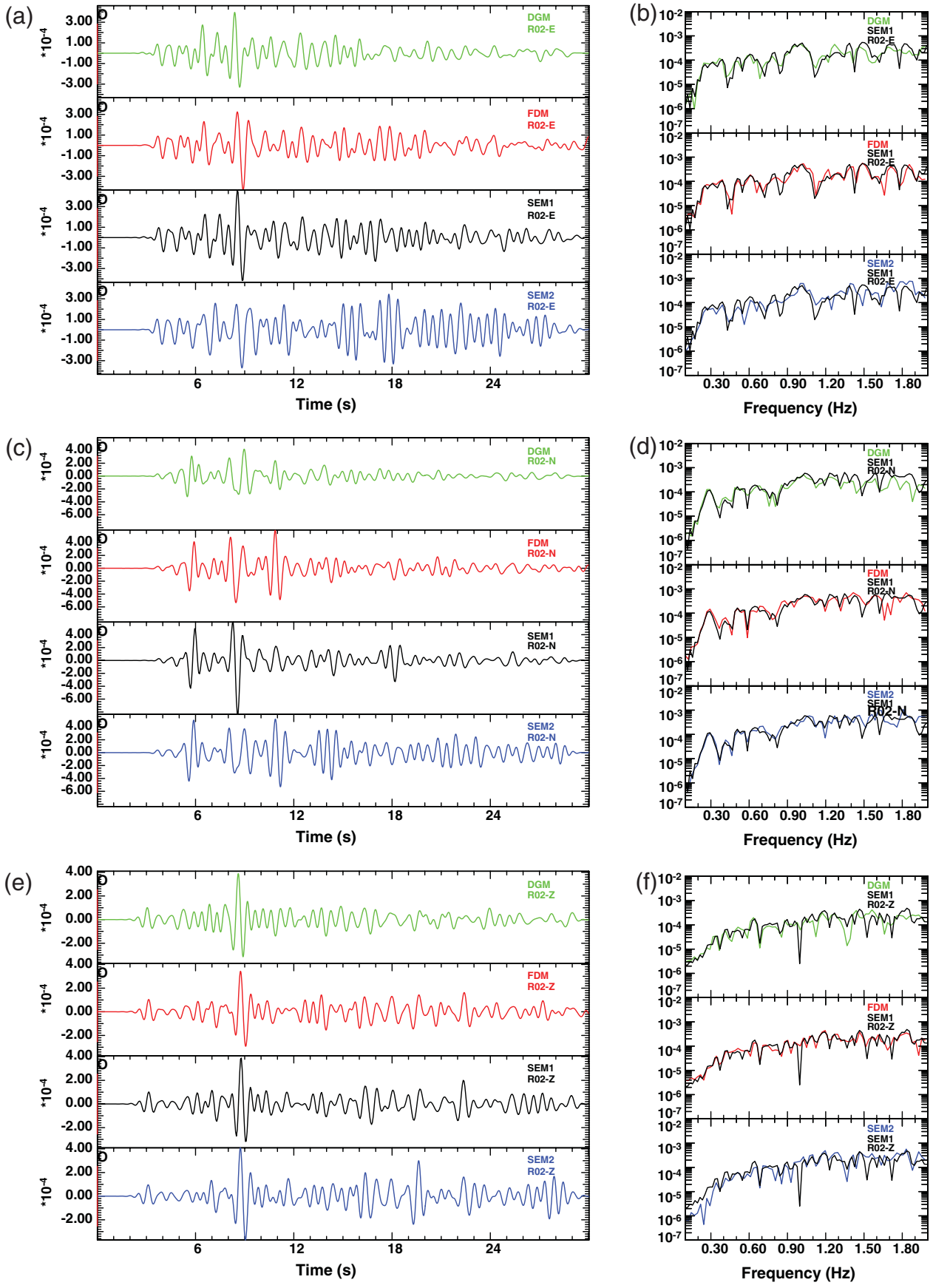

Figure 15. Same as Figure 14 for the weak motion case W1-FLAT.

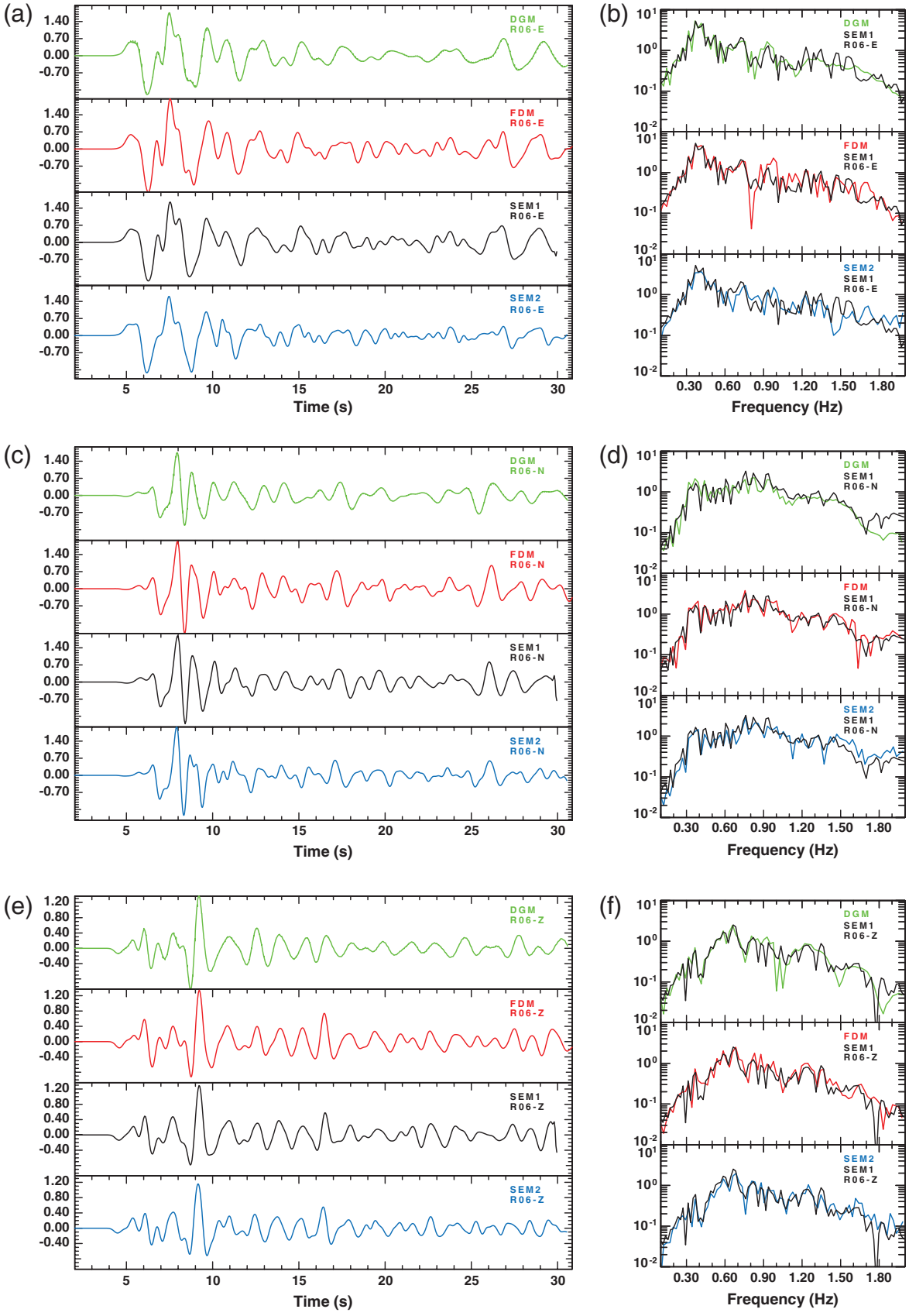

Figure 16. (a),(c),(e) Time series and (b),(d),(f) amplitude spectra of ground acceleration (EW, NS, UD) computed at receiver R06 by the four different codes (DGM, FDM, SEM1, and SEM2) for the strong motion case S1-FLAT.

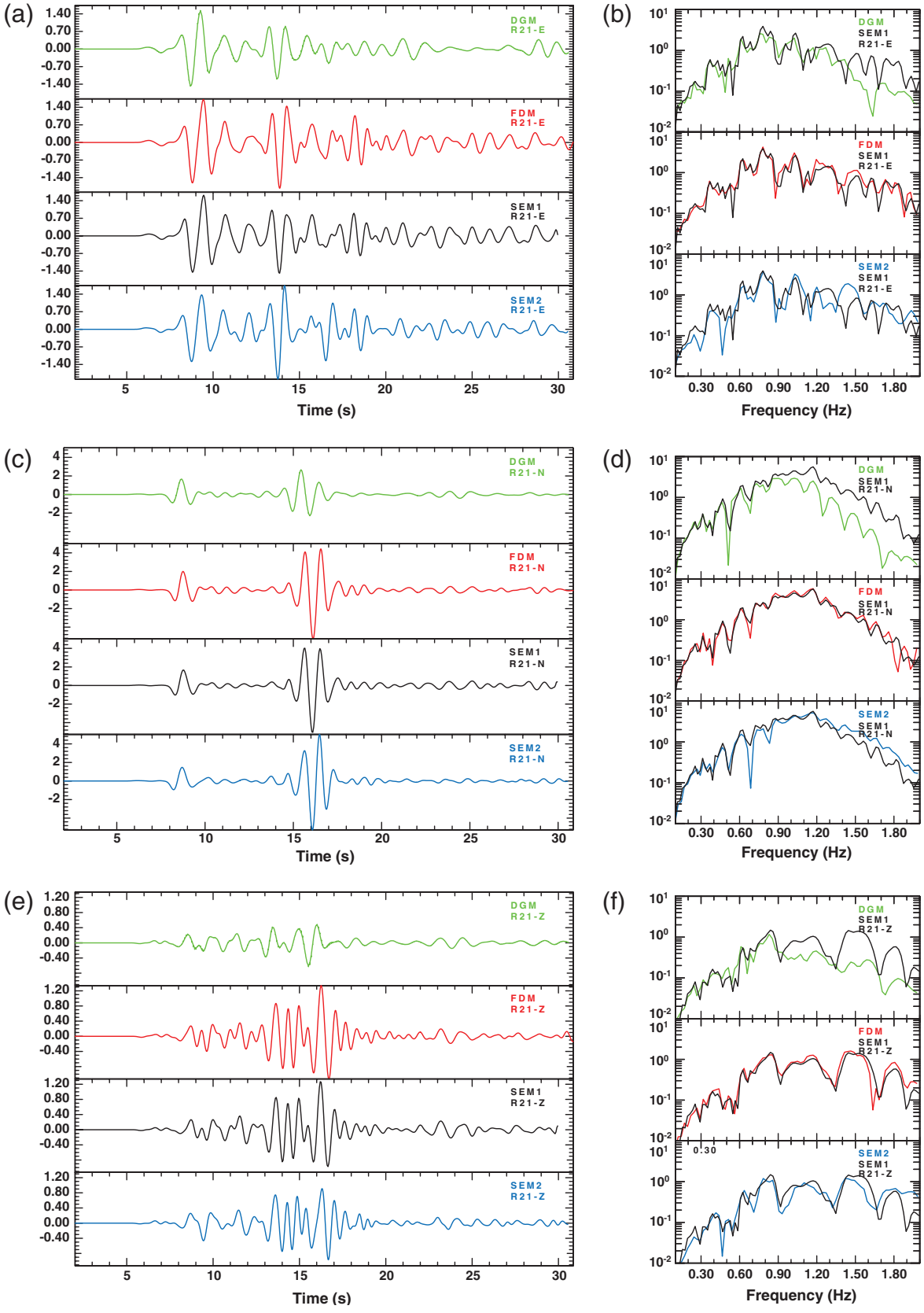

Figure 17. (a),(c),(e) Time series and (b),(d),(f) amplitude spectra of ground acceleration (EW, NS, UD) computed at receiver R21 by the four different codes for the strong motion case S1-FLAT. Note the low similarity between the DGM and SEM1 predictions on the vertical component.

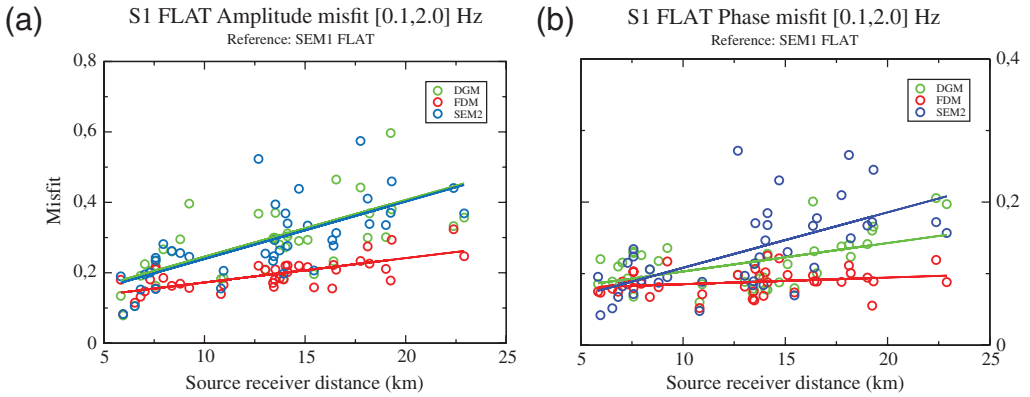

Figure 18. (a) Envelope and (b) phase misfits computed for the S1-FLAT case and plotted against source-receiver distance. Solid lines indicate linear regressions through the sets of points.

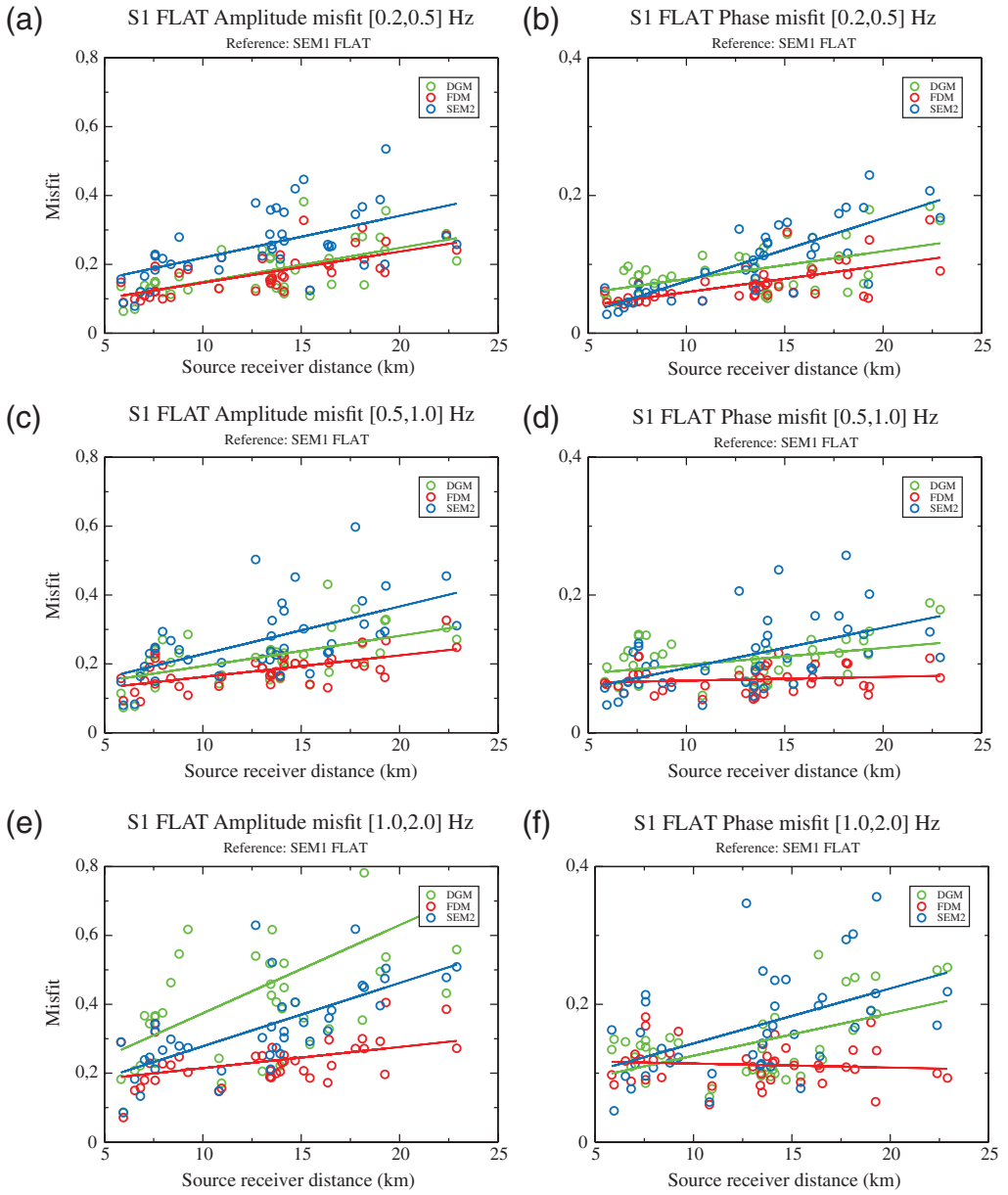

Figure 19. Same as Figure 18 for different frequency bands: (a),(b) 0.2,0.5 Hz; (c),(d) 0.5,1.0 Hz; and (e),(f) 1.0,2.0 Hz.

Effect of Surface Topography

Three codes (DGM, SEM1, and SEM2) computed the strong motion case S1-TOPO, which includes the effect of surface topography. The PGV maps obtained for the S1-TOPO case are shown in Figure 20. Note the deformation of the predicted patterns (compare with Fig. 9) close to the source due to the presence of surface topography on top of the fault plane. The overall distributions of peak values look quite similar inside the valley, suggesting that the main differences with respect to the S1-FLAT case occur on the rock sites. This is only partly confirmed by Figure 21, which shows the maps obtained by dividing the PGV by those obtained in the S1-FLAT case. Noticeable differences are indeed observed in the southwestern part of the valley, a region where strong variations of the sediment thickness occur. The patterns observed on the three maps of PGV ratios are quite consistent outside of the valley: systematic amplification is found on the mountain peaks (see, for example, receivers R33 and R34 in the eastern Belledonne chain and receivers R39 and R40 in the northern Chartreuse massif), whereas deamplification is found in valleys (see receiver R35). Seismic motion on slopes is more complex because amplification or deamplification can occur depending on the slope orientation with respect to the seismic event (see the two flanks bordering the Romanche Valley around receiver R35 at coordinates $X = 880$ km, $Y = 2015$ km). Extreme and mean values of amplification and deamplification are given in Table 3.

The average effect of surface topography inside the valley, as measured by the ratio of the PGV, is found to be negligible, but large differences in extreme values occur: the maximal predicted amplifications vary significantly on

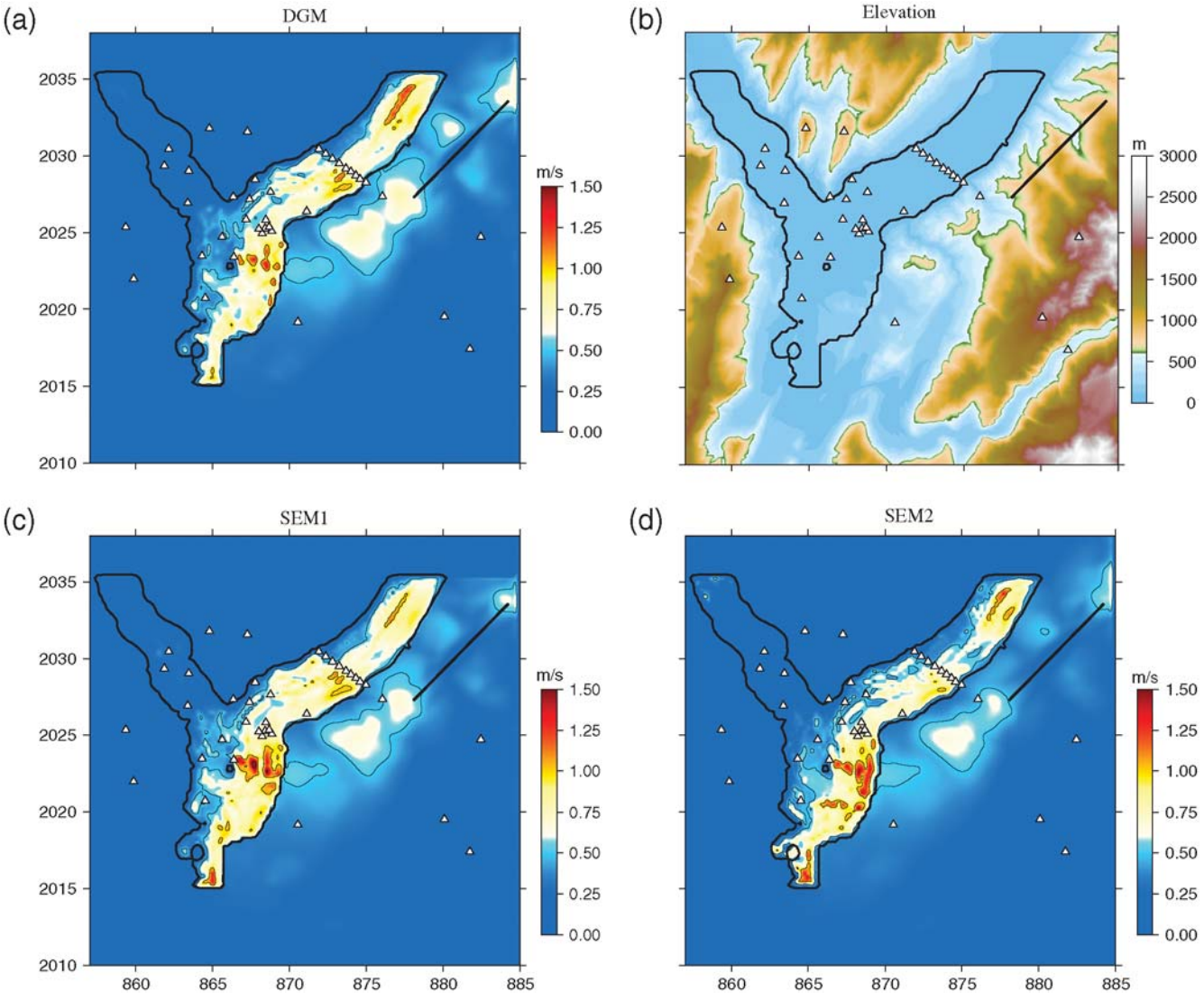

Figure 20. PGV maps obtained by three codes: (a) DGM, (c) SEM1, (d) SEM2 for the strong motion case S1-TOPO. (b) The map of surface elevation is shown. Receiver locations are indicated by the triangles; the X and Y labels denote distances (in km) in the local Lambert coordinate system. The bold curve indicates the 50 m contour line in the sediment thickness map; the bold straight line shows the surface projection of the fault for the S1 event.

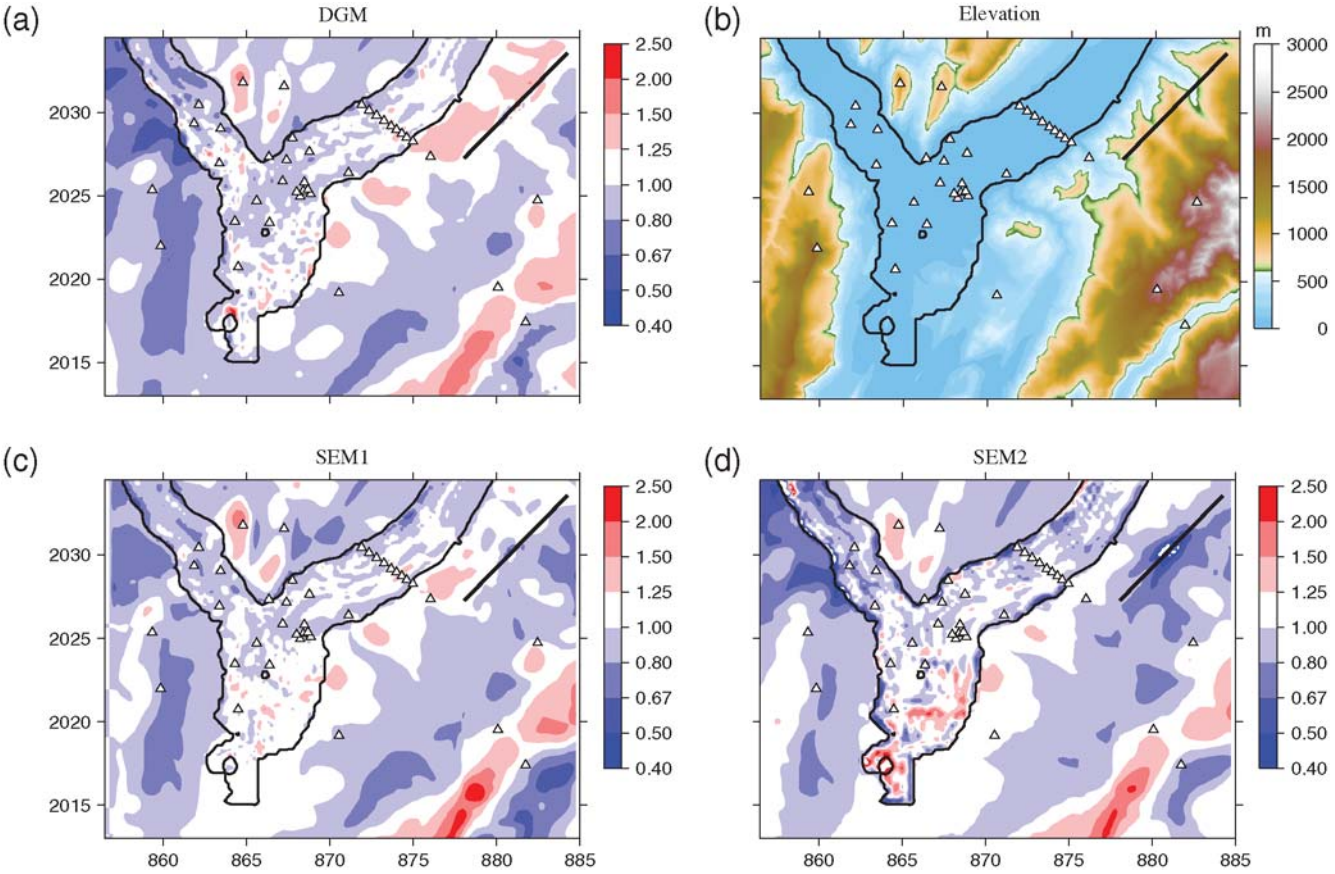

Figure 21. Maps of ratios between the PGV obtained with the surface topography and PGV obtained for the flat free surface by the three codes: (a) DGM, (c) SEM1, and (d) SEM2. (b) The map of surface elevation is shown. Receiver locations are indicated by the triangles and the *X* and *Y* labels denote distances (in km) in the local Lambert coordinate system. The bold curve indicates the 50 m contour line in the sediment thickness map and the bold straight line shows the surface projection of the fault for the S1 event.

rock sites and, more surprisingly, within the valley. This could result from differences in the implementation of surface topography, in the representation of velocity contrasts near the valley edges, and in the design of the meshes for the S1-FLAT and S1-TOPO cases.

Conclusions

The third international symposium on the effects of surface geology in Grenoble, France (ESG 2006), provided an excellent opportunity to focus the traditional blind prediction experiment on numerical modeling of earthquake motion in a typical deep Alpine sediment-filled structure, the Grenoble Valley.

The Grenoble urban area gathers a significant population of around 500,000, a number of high-tech and sensitive industrial facilities, and educational and research institutions. This and observed broadband site effects imply that the moderate regional seismic activity poses a concern about the seismic risk in the area. Moreover, similar conditions are also met in other areas within the European Alps and in other mountainous areas with embanked valleys filled with young, postglacial lacustrine sediments. This specific area also presents a further interest in relation to its relatively small extent, which allows performing deterministic numerical simulation up to higher frequencies than is usually considered in much wider areas such as the Los Angeles basin.

The present article reports partial results from this simulation exercise for four structure wave-field configurations that were specified for voluntary participants: W1-FLAT, S1-FLAT, W1-TOPO, S1-TOPO, with *W* and *S* meaning weak and strong, FLAT and TOPO meaning geometry of the free surface, respectively. The weak configurations comprised

Table 3
Extreme and Average Values of the Ratio of Peak Ground Velocity Computed by the Codes DGM, SEM1, and SEM2*

	DGM	SEM1	SEM2
Minimum ratio (valley)	0.447	0.549	0.133
Maximum ratio (valley)	2.255	1.641	3.599
Mean ratio (valley)	0.996	0.998	0.991
Minimum ratio (rock)	0.543	0.533	0.277
Maximum ratio (rock)	3.222	2.464	2.095

*With and without accounting for the effects of surface topography.

double-couple point sources, the strong ones finite kinematic source models.

Fourteen groups from eight countries contributed to the ESG 2006 comparison with at least one numerical method and possibly different cases, providing a total of 18 prediction sets; seven groups addressed the 3D problem, out of which three could account for the effects of both underground and surface topography. The numerical schemes used for the 3D contributions belong to the finite-difference, spectral-element, and discontinuous-Galerkin finite-element methods. Four participants whose 3D predictions were surprisingly close updated their results after the ESG meeting, after correcting some nonmethodological errors (evidenced by comparing to other predictions) in preparation of the numerical simulations. Only the results from the corrected predictions were considered here.

One of the main lessons of this comparative exercise concerns the present capabilities of numerical simulation and is indeed a lesson of modesty: all the submitted predictions exhibit a very large variability. This variability confirms that the numerical prediction of ground motion in general certainly cannot be considered a mature, push-button approach, and the variability in direct uncorrected numerical predictions can be significantly larger than the variability associated with empirical predictions. This is also because not all applied numerical codes implement the best methodologically possible algorithms; some of the codes are not yet bug free. Much care should be also given to an unambiguous definition of the input solicitation (input signal and/or source kinematics). Not sufficiently elaborated numerical predictions may yield wrong results and therefore will lead to large mistrust from end users.

However, there is also another lesson, which is a lesson of hope: the striking similarity between predictions by completely different numerical methods is a very encouraging result. Despite the structural complexity, that is geometry and relatively large velocity contrast at the sediment-basement interface as well as smooth heterogeneity, and the methodological differences among the simulation methods, we found a surprisingly good level of agreement among four of the submitted predictions obtained by the finite-difference method (FDM), two implementations of the spectral-element method (SEM1 and SEM2), and arbitrary high-order derivative, the discontinuous Galerkin method (ADER-DGM). It clearly shows that, when used with caution, numerical simulation is actually able to handle wave radiation correctly from an extended source and their subsequent propagation in complex 3D media.

The expression good agreement is not simply a matter of subjective feeling. It indeed results from a detailed, quantitative comparison between the four numerical predictions using the misfit criteria proposed by Kristekova *et al.* (2006). These misfit criteria are based on the time-frequency representations of the signals and allow proper quantification and characterization of disagreement between signals. This misfit measurement is found to be consistent with the engineering-oriented similarity score proposed by Anderson (2004). Another instructive comparison was achieved by looking at predicted PGV maps.

The main conclusions from the detailed comparison are explained in the following list:

- The objective quantification of the mismatch between the different predictions proves to be effective and useful. The two different comparison tools used for quantification, although very different, do provide very consistent results. While Anderson's engineering-based criteria are probably enough for validating numerical predictions for end users, more refined comparisons based on time-frequency analysis greatly help in understanding the origin of differences. In particular, the analysis of the phase misfit with the technique of Kristekova *et al.* (2006) proves very instructive in identifying differences in propagation properties from one numerical method to another, and thus in orienting further investigations to refine computational tools.
- The match is found to be good at low frequencies (below 1 Hz) and to gradually deteriorate with increasing frequency, as expected. The reasons for that could not be unambiguously individualized, but may be related both to differences in the numerical methods (numerical dispersion, implementation of damping) and differences in the model implementation.
- An important component to explain the differences is certainly related to the meshing. While the applied finite-difference scheme authorizes a good automatic accounting for the details of the sediment-basement interface, different strategies were used by the three other groups: some used a rather coarse meshing that did not follow details of the valley boundaries, especially at shallow depth, while some others spent much time in refining the mesh. The 2 Hz maximum frequency considered here is still too low to actually clearly identify the effects of the valley boundaries, considering also the rather smooth velocity variation in the sediments and the absence of shallow weathered layers in the bedrock. This issue is presently investigated within the framework of another numerical comparative exercise on the Volvi–Euroseistest site in Greece, where both sediments and bedrock exhibit complex shallow structures with inner interfaces between different units.
- The effects of free-surface topography were found significant in elevated areas in the three surrounding mountain ranges, but less important within the valley. However, while they are negligible in the S1 case, they slightly increase in the W1 case corresponding to higher predominant frequencies. This result cannot therefore be extrapolated to frequencies higher than 2 Hz, and the question is still open.

The comparison of the numerical predictions obtained with the FDM, two implementations of the SEM, and ADER-DGM indicates that each of these methods can be applied to simulation of the earthquake motion in structurally complex sediment-filled valleys with the flat free surface. In addition to being methodologically relatively simpler than the SEM

and ADER-DGM, the presented implementation of the FDM can be computationally more efficient because the volume harmonic averaging of moduli and volume arithmetic averaging of density allows to account for irregular interfaces in regular grids well-suited to parallel implementation, while abrupt changes in the grid size are also allowed at the transition between sediments and much stiffer bedrock. In the case of the presented predictions, the FDM needed approximately 65% of the computational time used by SEM, but obviously the difference may depend on the used computer and on the particular case under study. On the other hand, for the SEM and ADER-DGM the incorporation of the nonplanar free surface poses no methodological problem; thus, the methods can be equally easily applied to both the flat and nonplanar free surface. In general, it is far from easy and natural to implement free-surface condition in the FDM. The applied DSG Velocity-Stress FDM cannot account for the free-surface topography. If the incorporation of the topography is inevitable, for example, at particular sites and at higher frequencies, a hybrid combination with the finite-element method (Galis *et al.*, 2008) might be an alternative to the applied DSG VS FDM.

We would like to stress two main conclusions based on the ESG 2006 simulation exercise and the detailed comparison of the four closest numerical predictions:

1. No single numerical modeling method can be considered as the best for all important medium wave-field configurations in both computational efficiency and accuracy.

2. Reliable predictions of the earthquake ground motion in complex structures should be made using at least two different but comparably accurate methods to enhance reliability of the prediction. Our study indicates that the proper formulations and implementations of the FDM, SEM, and ADER-DGM can be applied.

Data and Resources

All data used in this article came from published sources listed in the references. The Fortran 95 computer code for performing the finite-difference scheme is available at www.nuquake.eu/Computer_Codes/ (last accessed June, 2010). A detailed description of the SEM1 software package can be found at www.geodynamics.org/cig/software/packages/seismo/specfem3d (last accessed June, 2010). A detailed description of the software package adopted for the SEM2 simulation can be found at http://geoelse.stru.polimi.it (last accessed June, 2010). The software CUBIT is available at http://cubit.sandia.gov/ (last accessed June, 2010).

Acknowledgments

This work was supported in part by the Slovak Research and Development Agency under the contract number APVV-0435-07 (project OPTIMODE) and VEGA Project 1/4032/07. All the computations using the SEM1 code were performed at the Service Commun de Calcul Intensif (SCCI) of the Grenoble Observatory. The authors providing the ADER-DG solutions thank the Deutsche Forschungsgemeinschaft (DFG), who supported the work through the Emmy Noether program (KA 2281/2-1). The cooperation of P. Bunge and J. Oeser for allowing the extensive use of the Tethys cluster is also gratefully acknowledged, as well as the support by the Leibniz Rechenzentrum in München. This comparison work was made possible through various financial helps and grants from ILL (Institut Laue-Langevin) and CEA (French Atomic Energy Commission) through the Cashima project, from the INTERREG IIIB Alpine Space Program of the European Commission through the Sismovalp project, and from the French National Research Agency (ANR) through the QSHA project.

References

Aki, K., and P. Richard (2002). *Quantitative Seismology*, Second Ed., University Science Books, Sausalito, California, 700 pp.

Anderson, J. G. (2004). Quantitative measure of the goodness-of-fit of synthetic seismograms, *13th World Conf. on Earthquake Engineering Conference Proc.*, Paper 243.

Canuto, C., M. Y. Hussaini, A. Quarteroni, and T. A. Zang (1988). *Spectral Methods in Fluid Dynamics*, Springer-Verlag, New York.

Chaljub, E. (2009). Spectral element modeling of 3D wave propagation in the Alpine valley of Grenoble, France, in *ESG 2006, Third Intl. Symposium on the Effects of Surface Geology on Seismic Motion*, P.-Y. Bard, E. Chaljub, C. Cornou, F. Cotton, and P. Guéguen (Editors), LCPC Editions, ISSN 1628-4704, Vol. 2**,** 1467–1473.

Chaljub, E., C. Cornou, and P.-Y. Bard (2009). Numerical benchmark of 3D ground motion simulation in the valley of Grenoble, French Alps, in *ESG 2006, Third Intl. Symposium on the Effects of Surface Geology on Seismic Motion*, P.-Y. Bard, E. Chaljub, C. Cornou, F. Cotton, and P. Guéguen (Editors), LCPC Editions, ISSN 1628-4704, Vol. **2,** 1365–1375.

Chaljub, E., D. Komatitsch, J.-P. Vilotte, Y. Capdeville, B. Valette, and G. Festa (2007). Spectral element analysis in seismology, in *Advances in Wave Propagation in Heterogeneous Media*, R.-S. Wu and V. Maupin (Editors), Vol. **365–419,** Elsevier Academic Press, New York.

Chapron, E., M. Dietrich, C. Beck, P. Van Rensbergen, P. Finckh, G. Menard, G. Nicoud, F. Lemeille, F. Anselmetti, and M. De Batist (2009). High-amplitude reflections in proglacial lacustrine basin fills of the NW Alps: Origin and implications, in *ESG 2006, Third Intl. Symposium on the Effects of Surface Geology on Seismic Motion*, P.-Y. Bard, E. Chaljub, C. Cornou, F. Cotton, and P. Guéguen (Editors), LCPC Editions, ISSN 1628-4704, Vol. 2**,** 1587–1596.

Cornou, C. (2002). Traitement d'antenne et imagerie sismique dans l'agglomération grenobloise (Alpes Françaises): Implications pour les effets de site, *Ph.D. Thesis*, (260 pages, www-lgit.obs.ujf-grenoble.fr/~cornouc/PUBLIS_CECILE/These_Version_Finale_Cecile.pdf), Joseph Fourier University, Grenoble (in French).

Cornou, C., P.-Y. Bard, and M. Dietrich (2003a). Contribution of dense array analysis to the identification and quantification of basin-edge-induced waves, part I: Methodology, *Bull. Seismol. Soc. Am.* **93,** 2604–2623.

Cornou, C., P.-Y. Bard, and M. Dietrich (2003b). Contribution of dense array analysis to the identification and quantification of basin-edge-induced waves, part II: Application to Grenoble basin (French Alps), *Bull. Seismol. Soc. Am.* **93,** 2624–2648.

Cornou, C., E. Chaljub, J. Verbeke, J. Converset, C. Voisin, L. Stehly, L. Margerin, S. Tsuno, J.-R. Grasso, P. Guéguen, S. Roussel, P. Roux, S. Hatton, and M. Campillo (2009). Measurement and variability study of site effects in the 3D glacial valley of Grenoble, French Alps, in *ESG 2006, Third Intl. Symposium on the Effects of Surface Geology on Seismic Motion*, P.-Y. Bard, E. Chaljub, C. Cornou, F. Cotton, and P. Guéguen (Editors), LCPC Editions, ISSN 1628-4704, Vol. **2,** 1621–1627.

Davis, P. and P. Rabinowitz (Editors) (1984). *Methods of Numerical Integration*, Academic Press, New York.

Day, S. M., J. Bielak, D. Dreger, R. Graves, S. Larsen, K. Olsen, and A. Pitarka (2003). *Tests of 3D Elastodynamic Codes: Final Report*

for Lifelines Project 1A02, Pacific Earthquake Engineering Research Center, Berkeley, California.

de Basabe, J. D., and M. K. Sen (2007). Grid dispersion and stability criteria of some common finite-element methods for acoustic and elastic wave equations, *Geophysics* **72,** T81–T95.

de la Puente, J., M. Dumbser, M. Käser, and H. Igel (2008). Discontinuous Galerkin methods for wave propagation in poroelastic media, *Geophysics* **73,** T77–T97.

de la Puente, J., M. Käser, M. Dumbser, and H. Igel (2007). An arbitrary high order discontinuous Galerkin method for elastic waves on unstructured meshes IV: Anisotropy, *Geophys. J. Int.* **169,** 1210–1228.

Deville, M. O., P. F. Fischer, and E. H. Mund (2002). *High-Order Methods for Incompressible Fluid Flow*, Cambridge University Press, New York.

Dietrich, M., C. Cornou, G. Ménard, F. Lemeille, F. Guyoton, and R. Guiguet (2009). Seismic profiling and borehole measurements in the Isère Valley near Grenoble, France: 1—Data acquisition and processing, in *ESG 2006, Third Intl. Symposium on the Effects of Surface Geology on Seismic Motion*, P.-Y. Bard, E. Chaljub, C. Cornou, F. Cotton, and P. Guéguen (Editors), LCPC Editions, ISSN 1628-4704, Vol. **2,** p. 1597–1608.

Dumbser, M., and M. Käser (2006). An arbitrary high order discontinuous Galerkin method for elastic waves on unstructured meshes II: The three-dimensional case, *Geophys. J. Int.* **167,** 319–336.

Dumbser, M., M. Käser, and E. Toro (2007). An arbitrary high order discontinuous Galerkin method for elastic waves on unstructured meshes V: Local time stepping and *p*-adaptivity, *Geophys. J. Int.* **171,** 695–717.

Faccioli, E., F. Maggio, R. Paolucci, and A. Quarteroni (1997). 2D and 3D elastic wave propagation by a pseudo-spectral domain decomposition method, *J. Seismol.* **1,** 237–251.

Galis, M., P. Moczo, and J. Kristek (2008). A 3-D hybrid finite-difference–finite-element viscoelastic modelling of seismic wave motion, *Geophys. J. Int.* **175,** 153–184.

Gallovic, F., R. Barsch, J. de la Puente Alvarez, and H. Igel (2007). Digital library for computational seismology, *Eos* **88,** 559.

Gamond, J.-F., J.-P. Gratier, and F. Thouvenot (2009). Seismotectonic frame of the Grenoble Valley, in *ESG 2006, Third Intl. Symposium on the Effects of Surface Geology on Seismic Motion*, P.-Y. Bard, E. Chaljub, C. Cornou, F. Cotton, and P. Guéguen (Editors), LCPC Editions, ISSN 1628-4704, Vol. 2**,** p. 1569–1575.

Guéguen, P., C. Cornou, S. Garambois, and J. Banton (2007). On the limitation of the H/V spectral ratio using seismic noise as an exploration tool: Application to the Grenoble Valley (France), a small apex ratio basin, *Pure Appl. Geophys.* **164,** 115–134.

Guéguen, P., S. Garambois, S. Tadenuma, B. Lebrun, and F. Cotton (2009). Geotechnical, geophysical and seismological data used for the estimate of the highest amplified frequency in the basin of Grenoble, in *ESG 2006, Third Intl. Symposium on the Effects of Surface Geology on Seismic Motion*, P.-Y. Bard, E. Chaljub, C. Cornou, F. Cotton, and P. Guéguen (Editors), LCPC Editions, ISSN 1628-4704, Vol. 2**,** 1629–1637.

Harris, R. A., M. Barall, R. Archuleta, E. Dunham, B. Aagaard, J. P. Ampuero, H. Bhat, V. Cruz-Atienza, L. Dalguer, P. Dawson, S. Day, B. Duan, G. Ely, Y. Kaneko, Y. Kase, N. Lapusta, Y. Liu, S. Ma, D. Oglesby, K. Olsen, A. Pitarka, S. Song, and E. Templeton (2009). The SCEC/USGS dynamic earthquake rupture code verification exercise, *Seism. Res. Lett.* **80,** 119–126.

Jerram, J., P. Foray, S. Labanieh, and E. Flavigny (2009). Characterizing the nonlinearities of the lacustrine clays in the Grenoble basin, in *ESG 2006, Third Intl. Symposium on the Effects of Surface Geology on Seismic Motion*, P.-Y. Bard, E. Chaljub, C. Cornou, F. Cotton, and P. Guéguen (Editors), LCPC Editions, ISSN 1628-4704, Vol. 2**,** 1639–1648.

Käser, M., and M. Dumbser (2006). An arbitrary high order discontinuous Galerkin method for elastic waves on unstructured meshes I: The two-dimensional isotropic case with external source terms, *Geophys. J. Int.* **166,** 855–877.

Käser, M., M. Dumbser, and J. de la Puente Alvarez (2006). An efficient ADER-DG method for 3-dimensional seismic wave propagation in media with complex geometry, in *ESG 2006, Third Intl. Symposium on the Effects of Surface Geology on Seismic Motion*, P.-Y. Bard, E. Chaljub, C. Cornou, F. Cotton, and P. Guéguen (Editors), LCPC EditionsVol. 1**,** pp. 455–464, Grenoble.

Käser, M., M. Dumbser, J. de la Puente, and H. Igel (2007). An arbitrary high order discontinuous Galerkin method for elastic waves on unstructured meshes III: Viscoelastic attenuation, *Geophys. J. Int.* **168,** 224–242.

Komatitsch, D., and J. Tromp (1999). Introduction to the spectral element method for three-dimensional seismic wave propagation, *Geophys. J. Int.* **139,** 806–822.

Komatitsch, D., and J. P. Vilotte (1998). The spectral-element method: an efficient tool to simulate the seismic response of 2D and 3D geological structures, *Bull. Seismol. Soc. Am.* **88,** 368–392.

Komatitsch, D., Q. Y. Liu, J. Tromp, P. Suss, C. Stidham, and J. H. Shaw (2004). Simulations of ground motion in the Los Angeles basin based upon the spectral-element method, *Bull. Seismol. Soc. Am.* **94,** 187–206.

Komatitsch, D., R. Martin, J. Tromp, M. A. Taylor, and B. A. Wingate (2001). Wave propagation in 2-D elastic media using a spectral element method with triangles and quadrangles, *J. Comp. Acoustics* **9,** 703–718.

Komatitsch, D., S. Tsuboi, and J. Tromp (2005). The spectral-element method in seismology, in *Seismic Earth: Array Analysis of Broadband Seismograms*, A. Levander, and G. Nolet (Editors), American Geophysical Union Monograph 157, 205–228.

Kosloff, R., and D. Kosloff (1986). Absorbing boundaries for wave propagation problems, *J. Comp. Physics* **63,** 363–373.

Kristek, J., and P. Moczo (2003). Seismic-wave propagation in viscoelastic media with material discontinuities: A 3D fourth-order staggered-grid finite-difference modeling, *Bull. Seismol. Soc. Am.* **93,** 2273–2280.

Kristek, J., P. Moczo, and R. J. Archuleta (2002). Efficient methods to simulate planar free surface in the 3D 4(th)-order staggered-grid finite-difference schemes, *Stud. Geophys. Geod.* **46,** 355–381.

Kristek, J., P. Moczo, and P. Pazak (2009). Numerical modeling of earthquake motion in Grenoble basin, France, using a 4th-order velocity-stress arbitrary discontinuous staggered-grid FD scheme, in *ESG 2006, Third Intl. Symposium on the Effects of Surface Geology on Seismic Motion*, P.-Y. Bard, E. Chaljub, C. Cornou, F. Cotton, and P. Guéguen (Editors), LCPC Editions, ISSN 1628-4704, Vol. 2**,** p. 1517–1526.

Kristekova, M., J. Kristek, P. Moczo, and S. M. Day (2006). Misfit criteria for quantitative comparison of seismograms, *Bull. Seismol. Soc. Am.* **96,** 1836–1850.

Lebrun, B., D. Hatzfeld, and P. Y. Bard (2001). Site effect study in urban area: Experimental results in Grenoble (France), *Pure Appl. Geophys.* **158,** 2543–2557.

Liu, H. P., D. L. Anderson, and H. Kanamori (1976). Velocity dispersion due to anelasticity: Implications of seismology and mantle composition, *Geophys. J. Roy. Astron. Soc.* **47,** 41–58.

Lysmer, J., and R. L. Kuhlemeyer (1969). Finite dynamic model for infinite media, *J. Eng. Mech. Div. Proc. Amer. Soc. Civil Eng.* **95,** 859–877.

Maggio, F., and A. Quarteroni (1994). Acoustic wave simulation by spectral methods, *East–West J. Num. Math* **2,** 129–150.

Ménard, G., O. Blein, C. Fournier, A. Guyomard, C. Julian, J.-F. Gamond, and A. Paillet (2009). Relations between present vertical movements and sedimentary fill in the Grenoble area, in *ESG 2006, Third Intl. Symposium on the Effects of Surface Geology on Seismic Motion*, P.-Y. Bard, E. Chaljub, C. Cornou, F. Cotton, and P. Guéguen (Editors), LCPC Editions, ISSN 1628-4704, Vol. 2**,** 1577–1585.

Ménard, G., M. Dietrich, M. Vallon, S. Tadenuma, C. Bordes, O. Méric, F. Lemeille, and A. Paillet (2009). Seismic profiling and borehole mea-

surements in the Isère Valley near Grenoble, France: 2—Interpretation, in *ESG 2006, Third Intl. Symposium on the Effects of Surface Geology on Seismic Motion*, P.-Y. Bard, E. Chaljub, C. Cornou, F. Cotton, and P. Guéguen (Editors), LCPC Editions, ISSN 1628-4704, Vol. 2**,** 1609–1620.

Mercerat, E. D., J. P. Vilotte, and F. J. Sanchez-Sesma (2005). Triangular spectral-element simulation of 2D elastic wave propagation using unstructured triangular grids, *Geophys. J. Int.* **166,** 679–698.

Moczo, P., and J. Kristek (2005). On the rheological models used for time-domain methods of seismic wave propagation, *Geophys. Res. Lett.* **32,** L01306.

Moczo, P., J.-P. Ampuero, J. Kristek, S. M. Day, M. Kristekova, P. Pazak, M. Galis, and H. Igel (2006). Comparison of numerical methods for seismic wave propagation and source dynamics—the SPICE Code Validation, in *ESG 2006, Third Intl. Symposium on the Effects of Surface Geology on Seismic Motion*, P.-Y. Bard, E. Chaljub, C. Cornou, F. Cotton, and P. Guéguen (Editors), LCPC Editions, Vol. 1**,** 495–504, Grenoble.

Moczo, P., J. Kristek, and M. Galis (2004). Simulation of the planar free surface with near-surface lateral discontinuities in the finite-difference modeling of seismic motion, *Bull. Seismol. Soc. Am.* **94,** 760–768.

Moczo, P., J. Kristek, M. Galis, P. Pazak, and M. Balazovjech (2007). The finite-difference and finite-element modeling of seismic wave propagation and earthquake motion, *Acta Phys. Slovaca* **57,** 177–406.

Moczo, P., J. Kristek, V. Vavrycuk, R. J. Archuleta, and L. Halada (2002). 3D heterogeneous staggered-grid finite-difference modeling of seismic motion with volume harmonic and arithmetic averaging of elastic moduli and densities, *Bull. Seismol. Soc. Am.* **92,** 3042–3066.

Moczo, P., J. O. A. Robertsson, and L. Eisner (2007). The finite-difference time-domain method for modeling of seismic wave propagation, in *Advances in Wave Propagation in Heterogeneous Media*, R.-S. Wu and V. Maupin (Editors), Vol. **421–516**, Elsevier Academic Press, New York.

Nicoud, G., G. Royer, J. C. Corbin, F. Lemeille, and A. Paillet (2002). Creusement et remplissage de la vallée de l'Isère au Quaternaire récent. Apports nouveaux du forage GMB1 (1999) dans la région de Grenoble (France), *Géologie de la France* **4,** 39–49 (in French).

Oeser, J., H. P. Bunge, and M. Mohr (2006). Cluster design in the Earth Sciences tethys, in *High Performance Computing and Communications—Second Intl. Conf.*, *HPCC 2006*, Munich, Germany, Lecture Notes in Computer Science, vol. 4208**,** M. Gerndt and D. Kranzlmuller Vol. 31–40**,** Springer-Verlag Berlin.

Seriani, G., and S. P. Oliveira (2007). Dispersion analysis of spectral element methods for elastic wave propagation, *Wave Motion* **45,** 729–744.

Seriani, G., and E. Priolo (1991). High-order spectral element method for acoustic wave modeling, *Expanded Abstracts of the Soc. Expl. Geophys.* 1561–1564.

Seriani, G., and E. Priolo (1994). A spectral element method for acoustic wave simulation in heterogeneous media, *Finite Elem. Anal. Des.* **16,** 337–348.

Stacey, R. (1988). Improved transparent boundary formulations for the elastic wave equation, *Bull. Seismol. Soc. Am.* **78,** 2089–2097.

Stupazzini, M. (2009). 3D Ground Motion Simulation of the Grenoble Valley by GeoELSE, in *ESG 2006, Third Intl. Symposium on the Effects of Surface Geology on Seismic Motion*, P.-Y. Bard, E. Chaljub, C. Cornou, F. Cotton, and P. Guéguen (Editors), LCPC Editions, ISSN 1628-4704, Vol. **2,** 1551–1560.

Stupazzini, M., R. Paolucci, and H. Igel (2009). Near-fault earthquake ground motion simulation in the Grenoble Valley by a high-performance spectral element code, *Bull. Seismol. Soc. Am.* **99,** 286–301.

Thouvenot, F., J. Frechet, L. Jenatton, and J. F. Gamond (2003). The Belledonne Border Fault: Identification of an active seismic strike-slip fault in the western Alps, *Geophys. J Int.* **155,** 174–192.

Thouvenot, F., L. Jenatton, and R. Guiguet (2009). Seismicity of the Grenoble area, in *ESG 2006, Third Intl. Symposium on the Effects of Surface Geology on Seismic Motion*, P.-Y. Bard, E. Chaljub, C. Cornou, F. Cotton, and P. Guéguen (Editors), LCPC Editions, ISSN 1628-4704, Vol. 2**,** 1563–1567.

Titarev, V. A., and E. F. Toro (2002). ADER: Arbitrary high order Godunov approach, *J. Sci. Comput.* **17,** 609–618.

Tsuno, S., E. Chaljub, and P. Y. Bard (2009). Grenoble Valley simulation benchmark—comparison of results and main learnings, in *ESG 2006, Third Intl. Symposium on the Effects of Surface Geology on Seismic Motion*, P.-Y. Bard, E. Chaljub, C. Cornou, F. Cotton, and P. Guéguen (Editors), LCPC Editions, ISSN 1628-4704, Vol. 2**,** 1377–1433.

Vallon, M. (1999). Estimation de l'épaisseur d'alluvions et sédiments quaternaires dans la région grenobloise par inversion des anomalies gravimétriques, Unpublished IPSN/CNRS report, 33 pp. (in French).

Laboratoire de Géophysique Interne et Tectonophysique
CNRS
Observatoire de Grenoble, Université J. Fourier, France
Maison des Géosciences
BP 53, 38041 Grenoble
Cedex 9, France
Emmanuel.Chaljub@obs.ujf-grenoble.fr
Seiji.Tsuno@obs.ujf-grenoble.fr
bard@obs.ujf-grenoble.fr
(E.C., S.T., P.-Y.B.)

Faculty of Mathematics
Physics and Informatics
Comenius University Bratislava
Mlynska dolina F1
842 48 Bratislava, Slovakia
Peter.Moczo@fmph.uniba.sk
Jozef.Kristek@fmph.uniba.sk
(P.M., J.K.)

Department für Geo-und Umweltwissenschaften
Ludwig-Maximilians-Universität München
Theresienstrasse 41 80333 München, Germany
martin.kaeser@geophysik.uni-muenchen.de
(M.K.)

Department of Structural Engineering
Politecnico di Milano
Piazza Leonardo da Vinci, 32
20133 Milano, Italy
stupa@stru.polimi.it
(M.S.)

Geophysical Institute
Slovak Academy of Sciences
Dubravska cesta 9
845 28 Bratislava, Slovakia
kristekova@savba.sk
(M.K.)

Manuscript received 23 February 2009

Geophysical Journal International

Geophys. J. Int. (2010) **182,** 250–264 doi: 10.1111/j.1365-246X.2010.04605.x

Seismic waves in heterogeneous material: subcell resolution of the discontinuous Galerkin method

Cristóbal E. Castro,[1] Martin Käser[1] and Gilbert B. Brietzke[2]

[1]*Department of Earth and Environmental Sciences, Geophysics Section, Ludwig-Maximilians-Universität, München, Germany. E-mail: ccastro@uc.cl*
[2]*Helmholtz Centre Potsdam, GFZ German Research Centre for Geosciences, Potsdam, Germany*

Accepted 2010 March 22. Received 2010 March 22; in original form 2009 October 4

SUMMARY

We present an important extension of the arbitrary high-order discontinuous Galerkin (DG) finite-element method to model 2-D elastic wave propagation in highly heterogeneous material. In this new approach we include space-variable coefficients to describe smooth or discontinuous material variations inside each element using the same numerical approximation strategy as for the velocity–stress variables in the formulation of the elastic wave equation. The combination of the DG method with a time integration scheme based on the solution of arbitrary accuracy derivatives Riemann problems still provides an explicit, one-step scheme which achieves arbitrary high-order accuracy in space and time. Compared to previous formulations the new scheme contains two additional terms in the form of volume integrals. We show that the increasing computational cost per element can be overcompensated due to the improved material representation inside each element as coarser meshes can be used which reduces the total number of elements and therefore computational time to reach a desired error level. We confirm the accuracy of the proposed scheme performing convergence tests and several numerical experiments considering smooth and highly heterogeneous material. As the approximation of the velocity and stress variables in the wave equation and of the material properties in the model can be chosen independently, we investigate the influence of the polynomial material representation on the accuracy of the synthetic seismograms with respect to computational cost. Moreover, we study the behaviour of the new method on strong material discontinuities, in the case where the mesh is not aligned with such a material interface. In this case second-order linear material approximation seems to be the best choice, with higher-order intra-cell approximation leading to potential instable behaviour. For all test cases we validate our solution against the well-established standard fourth-order finite difference and spectral element method.

Key words: Numerical solutions; Numerical approximations and analysis; Computational seismology; Wave propagation.

1 INTRODUCTION

The numerical computation of complete and sufficiently accurate wave fields for complex subsurface models is getting increasingly important in seismology, as full wave form inversion techniques become feasible with modern supercomputers. However, there is a large variety of numerical schemes to choose from when computing synthetic seismograms and this choice might be problem-dependent. A method called the discontinuous Galerkin (DG) finite-element method has first been introduced for the solution of hyperbolic partial differential equations (PDE) by Reed & Hill (1973) in the context of the neutron transport equation. Since then, a variety of DG methods have been developed in other research areas and its convergence properties on different mesh types have been analysed by many authors (e.g. Bernard *et al.* 2007; De Basabe *et al.* 2008; Gassner *et al.* 2008). For a comprehensive overview of the history of DG-related developments we refer to chapter 1.1 in (Hesthaven & Warburton 2008) and the book of Cockburn *et al.* (2000). In particular, Hu *et al.* (1999) analysed the dispersion and dissipation properties of the DG method for 2-D wave propagation problems discretized by triangular and regular quadrilateral elements. Later Dumbser & Munz (2006) introduced an arbitrary high-order DG scheme in space and time by applying the Cauchy–Kowalewski procedure that makes extensive and recursive use of the governing equations. The original idea of constructing such explicit one-step time integration schemes that automatically provide the same time accuracy as space accuracy was presented by Toro *et al.* (2001) and Titarev & Toro (2002) based on Arbitrary accuracy DErivatives

Riemann problems (ADER). We remark that this method allows discontinuous solution between two adjacent elements. This discontinuity is then treated by numerical fluxes.

Recently, this approach, now termed ADER-DG, has been introduced in the field of computational seismology in a series of papers (Dumbser & Käser 2006; Käser & Dumbser 2006; de la Puente *et al.* 2007; Käser *et al.* 2007a; de la Puente *et al.* 2008) using a triangular and tetrahedral discretization of the computational domain for the seismic wave equation and different rheologies. Furthermore, the approach allows for p-adaptation (local usage of higher-order elements) as well as local time-steeping (Dumbser *et al.* 2007), enhancing its flexibility and applicability for realistic, large-scale problems.

In this paper, we extend the ADER-DG method for 2-D seismic wave propagation problems incorporating the high-order polynomial approximation of variable material inside each element. In other words, we extend the numerical method to solve linear hyperbolic PDE systems with variable coefficients. The variable material (or variable coefficients) introduces additional terms, compared to the above mentioned papers, in the form of volume integrals and adds further computational complexity to the calculation of flux and stiffness matrices. In order to solve the PDE with the ADER-DG method we discretize the computational domain with a conforming mesh of triangular or quadrilateral elements. The size of the elements provides an initial spatial resolution, which can be further increased by higher-degree polynomials inside each element. The necessary combination of mesh spacing and approximation polynomials for a desired level of accuracy and wave propagation distance is investigated in previous work (Käser *et al.* 2008).

In contrast to previous formulations of the ADER-DG scheme, the incorporation of the variable coefficient enables us to treat also the material variations inside an element and its effect on the seismic wave field more accurately. Therefore, simulations can be carried out with coarser meshes, as subcell information about the material is considered inside each element. Furthermore, the approximation order for the material variation and the wave propagation can be chosen independently to enhance computational efficiency.

The paper is structured as follows. In Section 2, we introduce the governing equations based on the velocity–stress formulation of the 2-D seismic wave equation with variable material. The detailed derivation of the ADER-DG scheme providing subcell resolution for variable coefficients is given in Section 3. Section 4 shows the results of a convergence test to demonstrate the expected order of convergence and accuracy. In Section 5, we perform three numerical experiments that confirm the performance of the proposed method for realistic applications in computational seismology. Finally, we summarize the results in the conclusions in Section 6.

2 ELASTIC WAVE EQUATIONS

The elastic wave equations (see e.g. LeVeque 2002) describe the linear response of solids to deformation and yield the physical background to explain wave propagation phenomena of seismic waves produced by either earthquakes or man-made sources (see e.g. Aki & Richards 2002; Stein & Wysession 2003). In a velocity–stress formulation (Virieux 1984, 1986) the elastic wave equations are a first-order variable-coefficients linear hyperbolic PDE system which, in 2-D, has the form

$$\frac{\partial u_p(\vec{x},t)}{\partial t} + A_{pq}(\vec{x})\frac{\partial u_q(\vec{x},t)}{\partial x} + B_{pq}(\vec{x})\frac{\partial u_q(\vec{x},t)}{\partial y} = S_p(u(\vec{x},t),\vec{x},t)\,, \tag{1}$$

where the Einstein summation convention applies. In eq. (1) we make use of the five-component unknown vector $u_p(\vec{x},t) = (\sigma_{xx},\sigma_{yy},\sigma_{xy},u,v)^T$, where σ_{xx} and σ_{yy} are the normal stresses in x- and y-directions, respectively, σ_{xy} is the shear stress, and u and v are the particle velocities in x- and y-directions, respectively. The space-dependent Jacobian matrices $A_{pq}(\vec{x})$ and $B_{pq}(\vec{x})$ contain the material properties of the elastic medium, that is, density $\rho(\vec{x})$ and *Lamé* constants $\lambda(\vec{x})$ and $\mu(\vec{x})$, and have the explicit form

$$A_{pq}(\vec{x}) = \begin{pmatrix} 0 & 0 & 0 & -(\lambda+2\mu) & 0 \\ 0 & 0 & 0 & -\lambda & 0 \\ 0 & 0 & 0 & 0 & -\mu \\ -\frac{1}{\rho} & 0 & 0 & 0 & 0 \\ 0 & 0 & -\frac{1}{\rho} & 0 & 0 \end{pmatrix},$$

$$B_{pq}(\vec{x}) = \begin{pmatrix} 0 & 0 & 0 & 0 & -\lambda \\ 0 & 0 & 0 & 0 & -(\lambda+2\mu) \\ 0 & 0 & 0 & -\mu & 0 \\ 0 & 0 & -\frac{1}{\rho} & 0 & 0 \\ 0 & -\frac{1}{\rho} & 0 & 0 & 0 \end{pmatrix}. \tag{2}$$

We consider the isotropic elastic material properties to be space-dependent, but for simplicity we omit this dependency in the next sections. The real eigenvalues of matrices A_{pq} and B_{pq} are given by

$$s_1 = -c_\mathrm{p},\ s_2 = -c_\mathrm{s},\ s_3 = 0,\ s_4 = c_\mathrm{s},\ s_5 = c_\mathrm{p}, \tag{3}$$

where c_p and c_s are the P- and S-wave velocities, respectively, and are defined as

$$c_\mathrm{p} = \sqrt{\frac{\lambda+2\mu}{\rho}} \quad \text{and} \quad c_\mathrm{s} = \sqrt{\frac{\mu}{\rho}}.$$

The term $S_p(u(\vec{x},t),\vec{x},t)$ in eq. (1) is a general source term representing different physical phenomena which add or subtract energy from the system, as could be viscoelastic effects (Käser *et al.* 2007a) or external sources (Käser *et al.* 2007b) like forces or seismic moment tensors.

3 NUMERICAL SCHEME

Here we present an extension of the numerical scheme based on the DG method coupled with an ADER high-order time integration procedure to achieve subcell resolution of material variations. We keep the properties of a fully explicit one-step arbitrarily high-order accurate numerical method in space and time known as ADER-DG method. We generate a discretization of the computational domain $\Omega \in \mathbb{R}^2$ into conforming elements $E^{(i)}$, where (i) is the index that uniquely identifies each element. Inside $E^{(i)}$ we approximate the solution $u_p(\vec{x},t)$ with a linear combination of space-dependent basis functions $\Phi_l(\xi,\eta)$ and time-dependent degrees of freedom $\hat{u}^{(i)}_{pl}(t)$. The basis functions are defined using the reference coordinate system (ξ,η). We connect physical and reference coordinate system in each element $E^{(i)}$ using a mapping function $(x,y) = (x(\xi,\eta), y(\xi,\eta))$, see Appendix A. The approximation to the solution $u_p(\vec{x},t)$ inside element $E^{(i)}$ reads

$$u_p(\vec{x},t) \approx \hat{u}^{(i)}_{pl}(t)\Phi_l(\xi,\eta) = \sum_{l=0}^{N-1} \hat{u}^{(i)}_{pl}(t)\Phi_l(\xi,\eta)\,, \tag{4}$$

where N is the number of degrees of freedom in each element given by the highest polynomial degree of the basis functions d via

$N = (d + 1)(d + 2)/2$. Depending on the type of element, that is triangular or quadrilateral, the basis functions $\Phi(\xi, \eta)$ are chosen differently as shown in detail in Appendix B.

The numerical scheme is constructed by integrating in space and time the governing equation (1) over the physical elements $E^{(i)}$ and making use of the approximation of unknowns given in eq. (4).

3.1 Semi-discrete formulation

The semi-discrete form of the scheme is obtained by multiplying eq. (1) by a test function Φ_k, chosen from the same set of basis functions as in the approximation eq. (4), and integrating in space over a physical element $E^{(i)}$:

$$\int_{E^{(i)}} \Phi_k \frac{\partial u_p}{\partial t} \mathrm{d}V + \int_{E^{(i)}} \Phi_k A_{pq} \frac{\partial u_q}{\partial x} \mathrm{d}V + \int_{E^{(i)}} \Phi_k B_{pq} \frac{\partial u_q}{\partial y} \mathrm{d}V = \int_{E^{(i)}} \Phi_k S_p \mathrm{d}V. \tag{5}$$

Note that, in this formulation, the Jacobian matrices A_{pq} and B_{pq} are not assumed to be constant inside element $E^{(i)}$ and therefore cannot be taken out of the integral. This is new compared with previous formulations of the ADER-DG method applied to the seismic wave equation (Dumbser 2003; Dumbser & Käser 2006; Käser & Dumbser 2006).

Using the divergence theorem when integrating the second and third terms of eq. (5) we obtain

$$\int_{E^{(i)}} \Phi_k \frac{\partial u_p}{\partial t} \,\mathrm{d}V + \int_{\partial E^{(i)}} \Phi_k (F_p \cdot \vec{n}) \,\mathrm{d}S - \int_{E^{(i)}} \frac{\partial}{\partial x}(\Phi_k A_{pq}) u_q \,\mathrm{d}V - \int_{E^{(i)}} \frac{\partial}{\partial y}(\Phi_k B_{pq}) u_q \,\mathrm{d}V = \int_{E^{(i)}} \Phi_k S_p \,\mathrm{d}V\,, \tag{6}$$

where $F_p \cdot \vec{n} = (A_{pq} u_q, B_{pq} u_q) \cdot (n_x, n_y)$ is the numerical flux and $\vec{n} = (n_x, n_y)$ is the outward pointing unit normal vector with respect to the edge of element $E^{(i)}$. Vector $\vec{n}$ is uniquely defined edge-wise. In eq. (6), F_p must be evaluated along the edge of the element and is computed from the solution of the Riemann problem considering the data (velocities and stresses) inside the element $E^{(i)}$ and its direct neighbour.

Expanding the derivatives $\frac{\partial}{\partial x}(\Phi_k A_{pq})$ and $\frac{\partial}{\partial y}(\Phi_k B_{pq})$ and applying the coordinate transformation to the reference element we obtain

$$\int_{E^{(i)}} \Phi_k \frac{\partial u_p}{\partial t} \,\mathrm{d}V + \int_{\partial E^{(i)}} \Phi_k (F_p \cdot \vec{n}) \,\mathrm{d}S - \int_{E^{(i)}} \frac{\partial \Phi_k}{\partial \xi} A^*_{pq} u_q \,\mathrm{d}V - \int_{E^{(i)}} \frac{\partial \Phi_k}{\partial \eta} B^*_{pq} u_q \,\mathrm{d}V - \int_{E^{(i)}} \Phi_k \frac{\partial A^*_{pq}}{\partial \xi} u_q \,\mathrm{d}V - \int_{E^{(i)}} \Phi_k \frac{\partial B^*_{pq}}{\partial \eta} u_q \,\mathrm{d}V = \int_{E^{(i)}} \Phi_k S_p \,\mathrm{d}V\,, \tag{7}$$

where we have introduced the star Jacobians A^* and B^* defined as

$$A^*_{pq} = A_{pq} \frac{\partial \xi}{\partial x} + B_{pq} \frac{\partial \xi}{\partial y}\,, \qquad B^*_{pq} = A_{pq} \frac{\partial \eta}{\partial x} + B_{pq} \frac{\partial \eta}{\partial y}\,. \tag{8}$$

Introducing the polynomial approximation $u_p(\vec{x}, t) \approx \hat{u}_{pl}(t)\Phi_l(\xi, \eta)$ and writing the volume integrals in the reference element E_R we obtain

$$\int_{E_R} \Phi_k \frac{\partial \hat{u}_{pl}}{\partial t} \Phi_l \;|J| \,\mathrm{d}\xi \mathrm{d}\eta + \int_{\partial E^{(i)}} \Phi_k (F_p \cdot \vec{n}) \,\mathrm{d}S - \int_{E_R} \frac{\partial \Phi_k}{\partial \xi} A^*_{pq} \hat{u}_{ql} \Phi_l \;|J| \,\mathrm{d}\xi \mathrm{d}\eta - \int_{E_R} \frac{\partial \Phi_k}{\partial \eta} B^*_{pq} \hat{u}_{ql} \Phi_l \;|J| \,\mathrm{d}\xi \mathrm{d}\eta - \int_{E_R} \Phi_k \frac{\partial A^*_{pq}}{\partial \xi} \hat{u}_{ql} \Phi_l \;|J| \,\mathrm{d}\xi \mathrm{d}\eta - \int_{E_R} \Phi_k \frac{\partial B^*_{pq}}{\partial \eta} \hat{u}_{ql} \Phi_l \;|J| \,\mathrm{d}\xi \mathrm{d}\eta = \int_{E_R} \Phi_k S_p \;|J| \,\mathrm{d}\xi \mathrm{d}\eta, \tag{9}$$

where $|J| = |J|^{(i)}$ is the determinant of the Jacobian of the metric for each element $E^{(i)}$, as discussed in Appendix A. The surface integral, which connect the discrete elements of the mesh, is treated in Section 3.2.

As the material is allowed to be non-constant inside each element $E^{(i)}$, we approximate this heterogeneity via an expansion of the entries of the matrices A^* and B^* as given by eq. (4). However, as we assume that the material is not varying in time, the degrees of freedom for the material approximation of the linear combination are evaluated only once at the beginning and then stored for the full duration of the simulation. In particular, we use the same basis functions for the material expansion as for the wave propagation variables and for the test functions in eq. (5). Therefore, we have

$$A^*_{pq} \approx \hat{A}_{pqm} \Phi_m(\xi, \eta) \quad \text{and} \quad B^*_{pq} \approx \hat{B}_{pqm} \Phi_m(\xi, \eta)\,. \tag{10}$$

Introducing this approximation into eq. (9) leads to

$$\frac{\partial \hat{u}_{pl}}{\partial t} |J| \int_{E_R} \Phi_k \Phi_l \,\mathrm{d}\xi \mathrm{d}\eta + \int_{\partial E^{(i)}} \Phi_k (F_p \cdot \vec{n}) \mathrm{d}S - \hat{A}_{pqm} \hat{u}_{ql} \,|J| \int_{E_R} \frac{\partial \Phi_k}{\partial \xi} \Phi_l \Phi_m \,\mathrm{d}\xi \mathrm{d}\eta - \hat{B}_{pqm} \hat{u}_{ql} \,|J| \int_{E_R} \frac{\partial \Phi_k}{\partial \eta} \Phi_l \Phi_m \,\mathrm{d}\xi \mathrm{d}\eta - \hat{A}_{pqm} \hat{u}_{ql} \,|J| \int_{E_R} \Phi_k \Phi_l \frac{\partial \Phi_m}{\partial \xi} \,\mathrm{d}\xi \mathrm{d}\eta - \hat{B}_{pqm} \hat{u}_{ql} \,|J| \int_{E_R} \Phi_k \Phi_l \frac{\partial \Phi_m}{\partial \eta} \,\mathrm{d}\xi \mathrm{d}\eta = |J| \int_{E_R} \Phi_k S_p \mathrm{d}\xi \mathrm{d}\eta\,. \tag{11}$$

Eq. (11) is the semi-discrete form of this ADER-DG scheme including subcell resolution of material variations. Note that the degrees of freedom that describe the material ($\hat{A}_{pqm}$ and $\hat{B}_{pqm}$) remains constant during the entire simulation, whereas the degrees of freedom of the wave propagation variables ($\hat{u}_{ql}$) change in each time step. Furthermore, the spatial integrals on the left-hand side of eq. (11) can be pre-computed in the reference element E_R where we define the element mass matrix M and stiffness matrices K by

$$M_{kl} = \int_{E_R} \Phi_k \Phi_l \mathrm{d}\xi \mathrm{d}\eta\,,$$

$$K^{\xi,k}_{klm} = \int_{E_R} \frac{\partial \Phi_k}{\partial \xi} \Phi_l \Phi_m \,\mathrm{d}\xi \mathrm{d}\eta\,, \qquad K^{\eta,k}_{klm} = \int_{E_R} \frac{\partial \Phi_k}{\partial \eta} \Phi_l \Phi_m \,\mathrm{d}\xi \mathrm{d}\eta\,,$$

$$K^{\xi,m}_{klm} = \int_{E_R} \Phi_k \Phi_l \frac{\partial \Phi_m}{\partial \xi} \,\mathrm{d}\xi \mathrm{d}\eta\,, \qquad K^{\eta,m}_{klm} = \int_{E_R} \Phi_k \Phi_l \frac{\partial \Phi_m}{\partial \eta} \,\mathrm{d}\xi \mathrm{d}\eta\,, \tag{12}$$

where M is an $N \times N$ matrix and K are $N \times N \times N_m$ tensors. Here N is the number of degrees of freedom as introduced in eq. (4). N_m is the number of degrees of freedom used to represent the variable

material depending on the degree d_m of the polynomial for the material approximation via $N_m = (d_m + 1)(d_m + 2)/2$,with $d_m \leq d$. The superscripts stand for the direction of the spatial derivatives, that is, ξ or η, and the particular basis function which is derivated, that is, Φ_k or Φ_m. We call the first two stiffness matrices $K^{\xi,k}_{klm}$ and $K^{\eta,k}_{klm}$ the test stiffness matrices because the spatial derivatives act on the test function Φ_k. The other two, $K^{\xi,m}_{klm}$ and $K^{\eta,m}_{klm}$, are called the material stiffness matrices, as the spatial derivatives act on the material basis function Φ_m. Notice that the test and the material stiffness matrices can be obtained from each other by a component transposition. Moreover, if we assume constant material, the material stiffness matrices vanish and we recover the original formulation presented in previous work, for example, Käser & Dumbser (2006). In the following we discuss the computation of the numerical flux in eq. (11).

3.2 Flux evaluation

The numerical flux $F_p \cdot \vec{n}$ in eq. (11) is a space and time dependent vector, computed along the boundary of the element $E^{(i)}$ and valid during one time step Δt. As we are solving a linear PDE, the structure of the numerical flux is completely determined by the material properties. We refer to Castro (2007) or Toro (2009) for details on Riemann problems and high-order flux computations.

At each position along the edge $\partial E^{(i)}$ the numerical flux can be expressed as

$$F_p \cdot \vec{n} = T_{pq} \left(F^L_{qr} T^{-1}_{rs} u^{(i)}_s + F^R_{qr} T^{-1}_{rs} u^{(i_j)}_s \right) , \tag{13}$$

with

$$F^L_{qr} = \frac{A + |A|}{2} , \quad F^R_{qr} = \frac{A - |A|}{2}$$

and

$$|A| = \begin{pmatrix} c_\mathrm{p} & 0 & 0 & 0 & 0 \\ \frac{\lambda c_\mathrm{p}}{\lambda + 2\mu} & 0 & 0 & 0 & 0 \\ 0 & 0 & c_\mathrm{s} & 0 & 0 \\ 0 & 0 & 0 & c_\mathrm{p} & 0 \\ 0 & 0 & 0 & 0 & c_\mathrm{s} \end{pmatrix} . \tag{14}$$

Recall that the material parameters are space-dependent and therefore also the flux matrices F^L and F^R are space-dependent. Matrices T and its inverse T^{-1} are responsible for rotating the coordinate system from the physical space to an edge-aligned system defined by the outward normal vector $\vec{n}$. The vectors $u^{(i)}_s$ and $u^{(i_j)}_s$ include the velocity and stress data of element $E^{(i)}$ and its direct jth neighbour $E^{(i_j)}$. Writing the space-dependent matrices $F^L_{qr} \approx \hat{F}^L_{qrm} \Phi_m$ and $F^R_{qr} \approx \hat{F}^R_{qrm} \Phi_m$ as linear combinations of basis functions like in eq. (4) we can write the boundary integral in eq. (11) as

$$\begin{aligned} \int_{\partial E^{(i)}} \Phi_k (F_p \cdot \vec{n}) \mathrm{d}S = & \sum_{j=1}^{n_j} T^j_{pq} \hat{F}^L_{qrm} \left(T^j_{rs}\right)^{-1} \hat{u}^{(i)}_{sl} |S_j| \, F^{j,0}_{klm} \\ & + \sum_{j=1}^{n_j} T^j_{pq} \hat{F}^R_{qrm} \left(T^j_{rs}\right)^{-1} \hat{u}^{(i_j)}_{sl} |S_j| \, F^{j,i}_{klm} , \end{aligned} \tag{15}$$

where the index j refers to the direct neighbours of the element $E^{(i)}$ with $n_j = 3$ for triangular elements and $n_j = 4$ for quadrilateral elements. The length of the element edge is given by $|S_j|$. Matrices $F^{j,0}_{klm}$ and $F^{j,i}_{klm}$ are normalized boundary integrals over the interval $0 \leq \chi_j \leq 1$ with χ_j a parameter describing the jth edge. These matrices are pre-computed once and stored at the beginning of a simulation and have the explicit form

$$\begin{aligned} F^{j,0}_{klm} &= \int_0^1 \Phi^{(i)}_k(\chi_j) \Phi^{(i)}_m(\chi_j) \Phi^{(i)}_l(\chi_j) \, \mathrm{d}\chi_j , \\ F^{j,i}_{klm} &= \int_0^1 \Phi^{(i)}_k(\chi_j) \Phi^{(i)}_m(\chi_j) \Phi^{(i_j)}_l(\chi_j) \, \mathrm{d}\chi_j . \end{aligned} \tag{16}$$

Note that in contrast to previous formulations of the ADER-DG scheme, these integrals consist of a product of three basis functions Φ_k, Φ_m and Φ_l coming from the test function, the material, and the wave approximation, respectively.

3.3 Time integration

In order to complete the numerical scheme and to update the numerical solution $u_p(x, t^n)$ from time level t^n to time level t^{n+1} we integrate eq. (11) in time with the same order of accuracy as the spatial integrations. This is done by following the ADER approach, where the time evolution of the solution $u_p(x, t)$ inside the time interval $\Delta t = t^{n+1} - t^n$ is approximated by a Taylor time-series expansion using the governing equation, in this case eq. (1) (see Castro & Toro 2008, and references therein for more details).

The governing eq. (1) written in the reference element's coordinates reads

$$\begin{aligned} & \frac{\partial u_p(\vec{\xi}, t)}{\partial t} + A^*_{pq}(\vec{\xi}) \frac{\partial u_q(\vec{\xi}, t)}{\partial \xi} + B^*_{pq}(\vec{\xi}) \frac{\partial u_q(\vec{\xi}, t)}{\partial \eta} \\ & \quad = S_p[u(\vec{\xi}, t), \vec{\xi}, t] , \end{aligned} \tag{17}$$

with $\vec{\xi} = (\xi, \eta)$ and A^*_{pq} and B^*_{pq} defined in eq. (8). Multiplying eq. (17) by the test function Φ_k, integrating over the reference element and introducing the polynomial approximation of eq. (4) we obtain

$$\begin{aligned} \frac{\partial \hat{u}_{pl}(t)}{\partial t} \int_{E_R} \Phi_k \Phi_l \mathrm{d}\xi \mathrm{d}\eta = & -\hat{A}_{pqm} \hat{u}_{ql}(t) \int_{E_R} \Phi_k \frac{\partial \Phi_l}{\partial \xi} \Phi_m \mathrm{d}\xi \mathrm{d}\eta \\ & - \hat{B}_{pqm} \hat{u}_{ql}(t) \int_{E_R} \Phi_k \frac{\partial \Phi_l}{\partial \eta} \Phi_m \mathrm{d}\xi \mathrm{d}\eta \\ & + \hat{S}_{pl}(t) \int_{E_R} \Phi_k \Phi_l \mathrm{d}\xi \mathrm{d}\eta . \end{aligned} \tag{18}$$

Note that in eq. (18) only the degrees of freedom $\hat{u}_{ql}(t)$ are time dependent. At this point we can use the mass matrix and the test stiffness matrices defined in eq. (12) and thus simplify eq. (18) to

$$\frac{\partial \hat{u}_{pl}(t)}{\partial t} = - \frac{\left(\hat{A}_{pqm} K^{l,\xi}_{klm} + \hat{B}_{pqm} K^{l,\eta}_{klm} \right)}{M_{kl}} \hat{u}_{ql}(t) + \hat{S}_{pl}(t) , \tag{19}$$

providing the first time derivative of the solution $\hat{u}_{pl}(t)$. The nth time derivative can be written in the recursive form

$$\frac{\partial^n \hat{u}_{pl}(t)}{\partial t^n} = - \frac{\left(\hat{A}_{pqm} K^{l,\xi}_{klm} + \hat{B}_{pqm} K^{l,\eta}_{klm} \right)}{M_{kl}} \frac{\partial^{n-1} \hat{u}_{ql}(t)}{\partial t^{n-1}} + \frac{\partial^{n-1} \hat{S}_{pl}(t)}{\partial t^{n-1}} . \tag{20}$$

With these time derivatives of the degrees of freedom we can now express the Taylor time-series expansion within the time interval $[t^n, t^{n+1}]$ via

$$\hat{u}_{pl}(t^n + \tau) = \sum_{k=0}^{N_t - 1} \left[\frac{\partial^k \hat{u}_{pl}(t^n)}{\partial t^k} \right] \frac{\tau^k}{k!} , \tag{21}$$

with $\tau \in [0\,,\Delta t]$, where Δt is the explicit time step, and N_t is the order of the Taylor series expansion. Eq. (21) can be integrated analytically in time from time level t^n to t^{n+1} resulting in

$$\int_0^{\Delta t} \hat{u}_{pl}(t^n+\tau)\mathrm{d}\tau = \sum_{k=0}^{N_t-1}\left[\frac{\partial^k \hat{u}_{pl}(t^n)}{\partial t^k}\right]\frac{\Delta t^{k+1}}{(k+1)!}\,. \tag{22}$$

Finally we use eq. (22) to integrate in time the degrees of freedom in the semi-discrete form of the scheme in eq. (11) and the flux contribution in eq. (15) to obtain

$$\begin{aligned}
&\left[\hat{u}_{pl}^{n+1}-\hat{u}_{pl}^{n}\right]M_{kl}\,|J| \\
&\quad+\sum_{j=1}^{n_j} T_{pq}^{j}\,\hat{F}_{qrm}^{L}\,\left(T_{rs}^{j}\right)^{-1}\,|S_j|\,F_{klm}^{j,0}\int_{t^n}^{t^{n+1}}\hat{u}_{sl}^{(i)}(\tau)\,\mathrm{d}\tau \\
&\quad+\sum_{j=1}^{n_j} T_{pq}^{j}\,\hat{F}_{qrm}^{R}\,\left(T_{rs}^{j}\right)^{-1}\,|S_j|\,F_{klm}^{j,i}\int_{t^n}^{t^{n+1}}\hat{u}_{sl}^{(mj)}(\tau)\,\mathrm{d}\tau \\
&\quad-\hat{A}_{pqm}\,K_{klm}^{\xi,k}\,|J|\int_{t^n}^{t^{n+1}}\hat{u}_{ql}^{(i)}(\tau)\,\mathrm{d}\tau \\
&\quad-\hat{B}_{pqm}\,K_{klm}^{\eta,k}\,|J|\int_{t^n}^{t^{n+1}}\hat{u}_{ql}^{(i)}(\tau)\,\mathrm{d}\tau \\
&\quad-\hat{A}_{pqm}\,K_{klm}^{\xi,m}\,|J|\int_{t^n}^{t^{n+1}}\hat{u}_{ql}^{(i)}(\tau)\,\mathrm{d}\tau \\
&\quad-\hat{B}_{pqm}\,K_{klm}^{\eta,m}\,|J|\int_{t^n}^{t^{n+1}}\hat{u}_{ql}^{(i)}(\tau)\,\mathrm{d}\tau \\
&=|J|\int_{t^n}^{t^{n+1}}\int_{E_R}\Phi_k S_p\,\mathrm{d}\xi\,\mathrm{d}\eta\,.
\end{aligned} \tag{23}$$

The expression in eq. (23) shows the fully discrete form of this ADER-DG method. The operation to obtain the updated solution $\hat{u}_{pl}^{n+1}$ from $\hat{u}_{pl}^{n}$ provides the same high-order approximations in space and time including also the high-order material approximation necessary for subcell resolution of variable material. We emphasize that the volume and surface integrals are pre-computed and stored as the mass matrix, stiffness tensors from eq. (12) and boundary integral tensors from eq. (16). Note that the source term S_p has to be taken into account in the update formula eq. (23) as well as in the time evolution of the degrees of freedom in eq. (20) as shown in the previous work of Käser & Dumbser (2006).

The time-dependent degrees of freedom $\hat{u}_{pl}^{(i)}(t)$ at time $t=0$ are obtained from a given initial condition $u_p(\vec{x},0)$ using an L2 projection (see Appendix C) onto the $N+1$ basis functions $\Phi_l(\xi,\eta), l=0,\ldots,N$. We remind that the approximation order of the proposed ADER-DG scheme depends on the chosen polynomial degree d of the basis functions for the velocity and stress approximation. The material approximation with polynomial degree d_m, however, can be chosen independently such that wave and material approximation can be treated separately. In this way, the internal material representation automatically adapt to the local complexity of the medium.

In the following section, we will analyse the accuracy of our numerical method and confirm its correct implementation by performing a numerical convergence test before applying the scheme to numerical experiments of relevance to computational seismology.

4 NUMERICAL CONVERGENCE STUDIES

Here, we validate the theoretical and technical correctness of the proposed numerical scheme by performing a numerical convergence study. The convergence test consists of the measurement of the numerical errors with respect to an analytic reference solution on a series of refined meshes discretizing the computational domain as shown in Fig. 1. Comparing these errors for different mesh spacings h gives us the order of convergence of the numerical scheme via the expression

$$\mathcal{O}=\frac{\log(E_{i+1}/E_i)}{\log(h_{i+1}/h_i)}\,, \tag{24}$$

with h_i and h_{i+1} indicating the mesh characteristic sizes of two successively refined meshes and E_i and E_{i+1} denoting the corresponding errors.

The computational domain is $\Omega=[-1,1]\times[-1,1]\in\mathbb{R}^2$ with periodic boundary conditions. The numerical convergence test uses a plane P- and S-wave propagating through spatially varying material leading to space-dependent Jacobian matrices in eq. (2) for each element. In order to compare the numerical result with an analytic reference solution we use the following approach. We assume an exact solution of the wave propagation problem to be given in space and time as $u_p(\vec{x},t)$. Inserting this solution into the wave eq. (1) allows us to derive the source term $S_p(\vec{x},t)$ which ensures that $u_p(\vec{x},t)$ is the exact solution of eq. (1). Therefore we define the smooth exact solution as

$$u_p(\vec{x},t)=R_{p2}^{\vec{n}}\,\sin(\vec{k}\cdot\vec{x}-\omega_2 t)+R_{p5}^{\vec{n}}\,\sin(\vec{k}\cdot\vec{x}-\omega_5 t)\,, \tag{25}$$

with the wavenumber vector $\vec{k}=(2\pi,2\pi)^T$. The vectors $R_{p2}^{\vec{n}}$ and $R_{p5}^{\vec{n}}$ are the eigenvectors of matrix A rotated in the direction $\vec{n}=(1,\,1)$ and $\omega_2=-c_\mathrm{s}\,|\vec{k}|$ and $\omega_5=+c_\mathrm{p}\,|\vec{k}|$ are defined in terms of the eigenvalues of matrix A. The variable material is described by a spatially periodic function in Ω perturbing the constant entries

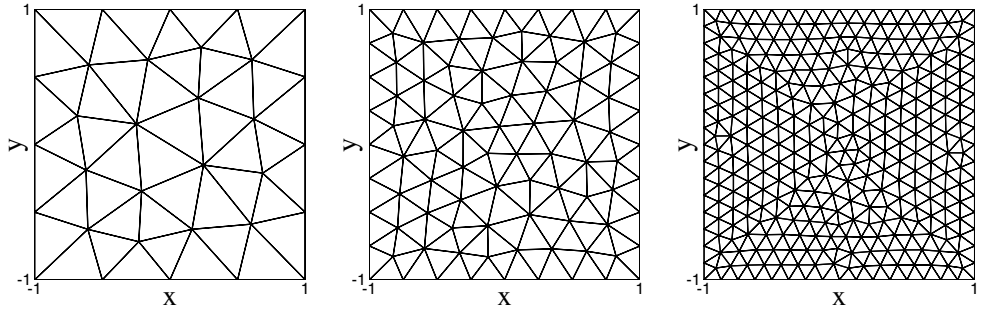

Figure 1. Refinement of triangular meshes: (left-hand panel) $h=2/4=0.5$, (middle panel) $h=2/8=0.25$, and (right-hand panel) $h=2/16=0.125$.

$\rho^o = 1.0$, $\mu^o = 1.0$, and $\lambda^o = 2.0$ of the matrix A by

$$\rho(\vec{x}) = \rho^o + \frac{1}{2}\sin(\vec{k}\cdot\vec{x})$$
$$\mu(\vec{x}) = \mu^o + \frac{1}{2}\sin(\vec{k}\cdot\vec{x})$$
$$\lambda(\vec{x}) = \lambda^o + \frac{1}{2}\sin(\vec{k}\cdot\vec{x}). \quad (26)$$

The simulation time can now be chosen arbitrarily as we know the exact solution at any point in space and time via eq. (25). We set the final simulation time to $t_{\text{end}} = 2\sqrt{2}$ such that the P wave travelled one and the S wave two wavelength. The Courant number for numerical stability is kept constant. The initial condition of the wave propagation problem is defined by evaluating eq. (25) for $t = 0$.

In Table 1, we show the resulting errors in the different norms and the corresponding convergence orders obtained for the final time t_{end} for a 5th and 8th order ADER-DG scheme on triangular meshes. We obtain analogous results using quadrangular meshes. The results confirm that the expected orders of convergence are reached. Furthermore, Fig. 2 (left-hand panel) shows the complete results for convergence tests of the ADER-DG schemes from order 2 using linear P1-elements to order 8 using P7-elements for the wave propagation and material approximations. In contrast, Fig. 2 (right-hand panel) shows the dependency of the schemes accuracy on the material approximation. To this end, we show the results of an ADER-DG scheme using polynomials of degree 4 (P4) for the wave propagation and polynomials of degree 1 (M1) to 4 (M4) for the material representation. We clearly observe how the error decreases with improved material approximation. In fact, using a ADER-DG scheme P4M2 reduces the accuracy of the scheme to a pure P3M3 scheme, while the results of a P4M1 scheme is comparable to a pure P2M2 scheme. Therefore, the correct convergence order $\mathcal{O}$, that is, the slope of the error lines in Fig. 2, is only reached, if the polynomial degree d for the wave propagation approximation and the degree d_m for the material approximation are the same, that is, if the scheme is a PdMd_m scheme with $d = d_m = \mathcal{O} - 1$.

5 NUMERICAL EXPERIMENTS

In the following we apply the new extended ADER-DG scheme, with subcell resolution, to more realistic cases that typically occur in seismic wave propagation problems. The first experiment consists of a heterogeneous velocity model with smooth variations as provided by seismic tomography. The second experiment represents a problem typically encountered on a smaller scale, like the shallow upper crust or sedimentary environments, with strong material heterogeneities with short spatial wavelength. There we study the performance of the new method by varying the mesh spacing, the wave propagation order, and the material approximation order to assess their influence on the computational cost. In the third experiment we investigate the effects of the polynomial subcell resolution approach on the accuracy of the synthetic seismograms, if the material shows a sharp discontinuity that is not respected in the mesh generation process, that is, an intracell discontinuity where the element goes across the material jump. For each experiment, we compare our results with those obtained from other independent codes, for example, the standard fourth-order staggered finite differences (FD) method (Levander 1988) or the spectral element method (SEM). We remark, that better methods, such as the improved FD scheme of Moczo *et al.* (2002) have been developed, however, we overcame the weakness of the standard FD-scheme by massive oversampling. Note that the aim here is not to accomplish

Table 1. Numerical convergence results for the velocity component u by the ADER-DG scheme of order 5 using polynomials P4M4 and order 8 using polynomials P7M7 on irregular triangular elements for variable material.

$1/h$	L^∞	$\mathcal{O}_{L^\infty}$	L^2	$\mathcal{O}_{L^2}$	L^1	$\mathcal{O}_{L^1}$
2.0	8.755×10^{-4}	–	6.122×10^{-4}	–	1.848×10^{-3}	–
3.0	1.391×10^{-4}	4.54	9.725×10^{-5}	4.54	5.367×10^{-4}	3.05
4.0	3.629×10^{-5}	4.67	2.532×10^{-5}	4.68	1.358×10^{-4}	4.78
5.0	1.189×10^{-5}	5.00	8.614×10^{-6}	4.83	8.513×10^{-5}	2.09
2.0	4.154×10^{-6}	–	3.560×10^{-6}	–	1.814×10^{-5}	–
3.0	1.310×10^{-7}	8.53	1.353×10^{-7}	8.06	2.296×10^{-6}	5.10
4.0	1.556×10^{-8}	7.41	2.016×10^{-8}	6.62	2.688×10^{-7}	7.46
5.0	2.596×10^{-9}	8.03	1.945×10^{-9}	10.48	1.967×10^{-8}	11.72

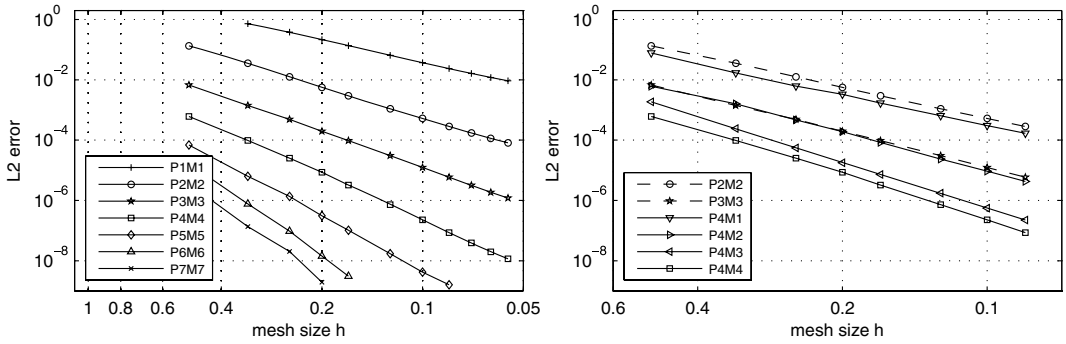

Figure 2. Left-hand panel: convergence results for ADER-DG schemes from order $\mathcal{O} = 2$ to $\mathcal{O} = 8$ using P1M1 to P7M7 elements for the wave propagation and material approximation, respectively. Right-hand panel: comparison of results with reduced accuracy due to wave propagation polynomials P4 but lower-order material approximation polynomials P4–P1.

a competitive benchmark of the FD or the SEM method against the ADER-DG scheme. The goal of the comparison is to validate the new extended ADER-DG scheme in the more realistic cases presented in the following. A detailed theoretical study comparing the efficiency of each numerical method in comparison is beyond the scope of this paper.

5.1 Smoothly variable material with strong velocity gradients

This numerical experiment consists of a smoothly variable velocity model typically encountered in seismic tomography with perturbations of only a few percent. However, we create velocity perturbations with unrealistically high variations (see Fig. 3) in order to produce strong velocity gradients that emphasize the effect of material heterogeneity. The computational domain is $\Omega = [-2500\,\mathrm{m}, 2500\,\mathrm{m}] \times [-2000\,\mathrm{m}, 0\,\mathrm{m}]$ with a free surface boundary condition at $y = 0$ and absorbing boundaries otherwise. The velocity model is defined by P- and S-wave velocities described by

$$c_\mathrm{p} = 2000 + 1200 \sin\left(\frac{x\pi}{3000}\right) \cos\left(\frac{(y-1000)\pi}{1500}\right),$$
$$c_\mathrm{s} = \frac{c_\mathrm{p}}{\sqrt{(2)}} - (350 + 0.12x). \qquad (27)$$

The density is kept constant at $\rho = 2200\,\mathrm{kg\,m^{-3}}$. The maximum and minimum for P-wave velocities are 3200 and 800 m s^{-1}, respectively, while for the S-wave velocities they are 2100 and 27 m s^{-1}.

We place an explosive point source at position $\vec{x}_s = (25, -1025)$ m with a Ricker source time function $S(t) = a_1[0.5 + a_2(t-t_D)^2]\exp^{a_2(t-t_D)^2}$, with delay time $t_D = 115$ ms, $a_1 = 2\times10^{11}$, and $a_2 = -(\pi f_c)^2$, where the central frequency of the wavelet is $f_c = 10$ Hz. We place 41 equidistant receivers every 100 m along the free surface from $x = -1975$ to 2025 m to record synthetic seismograms in a 1.6 s window.

We discretize the computational domain with regular quadrilateral elements with an edge size of 16.67 m. For this mesh the maximum percentile change within one element of the P-wave velocity is 2 per cent. The order of accuracy for the wave propagation and material approximation is 5, that is, we apply an ADER-DG P4M4 scheme. In Fig. 4, we show a series of snapshots of the wave field for the horizontal velocity component u. The initially generated compressional wave propagates away from the source following a non-radial symmetry pattern due to the heterogeneous velocity model. Note that in low-velocity zones the wavelengths are shorter than in high-velocity zones and the amplitudes increase and decrease accordingly. Note also the clear reflection of the incident P wave at the free surface producing also a converted P–S wave. In Fig. 5, we compare our solution at each receiver with two independent numerical solutions from the FD and the SEM

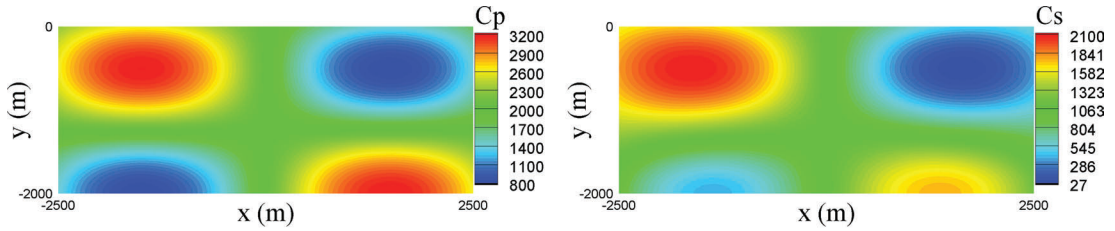

(a) P-wave velocity model (b) S-wave velocity model

Figure 3. Smooth velocity models for (a) P waves and (b) S waves with strong velocity gradients between minimum and maximum values.

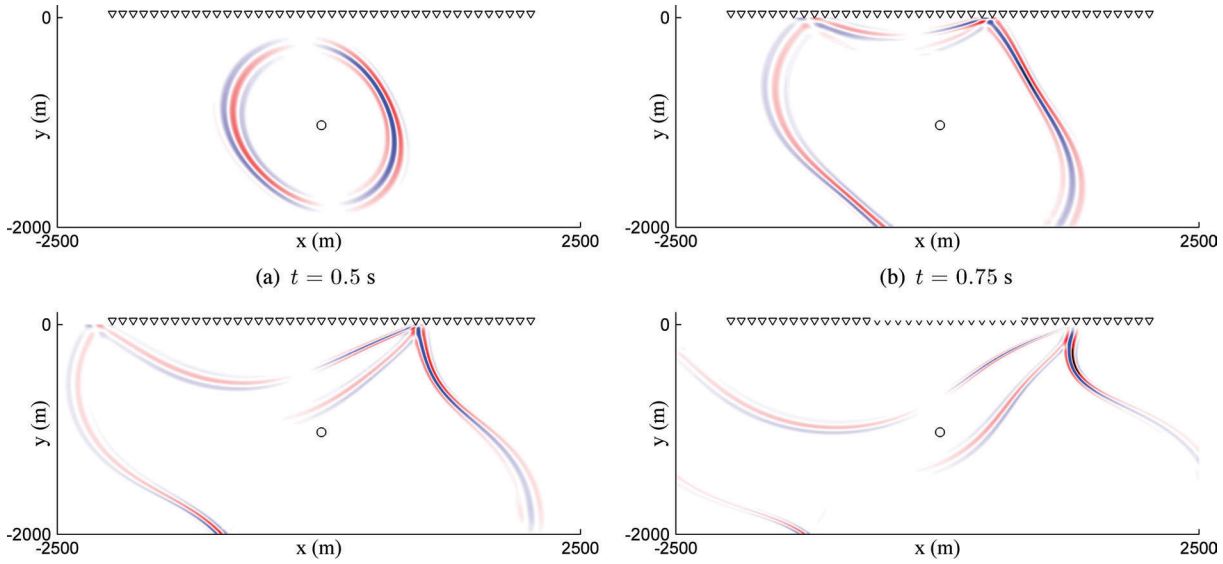

(a) $t = 0.5$ s (b) $t = 0.75$ s

(c) $t = 1.0$ s (d) $t = 1.25$ s

Figure 4. Snapshots of the horizontal velocity wave field u in the smooth model at four different times. The circle represents the location of the explosive source while the triangles are receivers in the free surface.

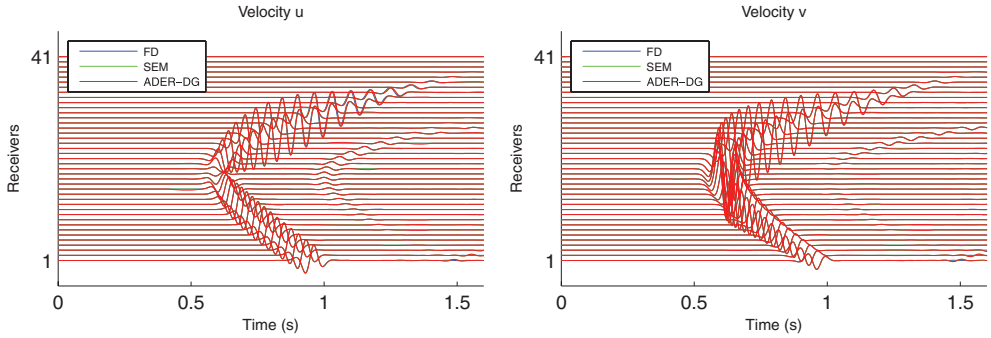

Figure 5. Comparison of the numerical solution of the particle velocity u (left-hand panel) and v (right-hand panel) on each of the 41 receivers placed on the free surface for the smoothly variable material test case.

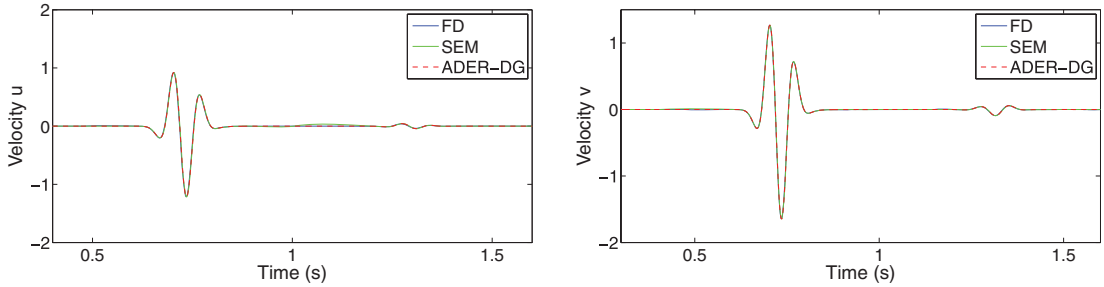

Figure 6. Seismic signals of the horizontal velocity component u (left-hand panel) and vertical velocity component v (right-hand panel) recorded at receiver 25 at $x = 425$ m.

simulations and observe an excellent agreement between all three numerical solutions. Furthermore, the seismograms show a weak S wave occurring after about 1 s and propagation along the receiver line, which is caused by the material heterogeneity. The SEM solution is obtained on exactly the same mesh using the same order of accuracy, whereas the standard FD solution required a mesh spacing of $h = 2.5$ m in order to obtain results that are compatible with the SEM solution.

In Fig. 6, we show a detailed comparison of the numerical solutions of the three methods for the receiver 25 at $x = 425$ m to demonstrate their visually perfect fit, where the amplitude differences are smaller than 1.0 per cent. Thus, the test validates the accurate treatment of strong gradients inside each element for smoothly variable material and also confirms the correct implementation of this new functionality of the ADER-DG scheme.

5.2 Strong material heterogeneity of short spatial wavelength

Here, we apply the proposed ADER-DG scheme to a more challenging problem, where seismic waves propagate through a highly heterogeneous medium. The computational domain $\Omega = [-2500\,\text{m}, 2500\,\text{m}] \times [-2000\,\text{m}, 0\,\text{m}]$ contains a random perturbation of the mean material properties $\rho = 2200\,\text{kg}\,\text{m}^{-3}$, $\mu = 2.295$ GPa and $\lambda = 2.295$ GPa. The perturbation is created using a random field generator based on high-cut filtering in the spatial Fourier domain (e.g. see Klimeš 2002; Gallovič. & Brokešová 2004). We chose the correlation length of the material variation to be much shorter in the vertical y-direction than in the horizontal x-direction to produce a layered material variation typically encountered in sedimentary environments. The resulting heterogeneity of the P-wave speed is shown in Fig. 7 where a number of thin, lens-shaped high- and low-velocity zones are visible. The top boundary represents the free surface while the other boundaries are absorbing. An explosive source is located at $\vec{x}_s = (0, -1000)$ m with the same Ricker wavelet as specified in Section 5.1 generating a wave field of 10 Hz dominant frequency. The wave propagation is recorded at the same 41 equidistant receivers at the free surface ($y = 0$ m) as in the previous Section 5.1. Therefore, the dominant wavelength is in the length scale as the vertical velocity variations. We use the FD method on a very fine regular grid discretizing Ω with 25.6×10^6 gridpoints of grid spacing $h = 0.625$ m to obtain a reference solution. To check the reliability of the reference solution we compute a further SEM solution using a square mesh with a regular element edge length of 16 m and fifth order of accuracy. Finally, we solve the problem on the same 16 m mesh with the new ADER-DG scheme of order 5 using P4M4 approximation polynomials. Snapshots of the obtained horizontal velocity field u are shown in Fig. 8, which displays strong scattering of the seismic waves and deformation of the wave fronts due to the highly heterogeneous material. The comparison of recorded seismograms at the free surface is plotted in Fig. 9. The visual fit between all three solutions is again almost perfect even for the late arrivals of signals in the coda. We also show a more detailed comparison of the seismic signals at receiver 15 in Fig. 10 which clearly demonstrates that all methods produce visually the same solution. In the following we choose the oversampled FD solution (295 gridpoints per dominant wavelength) as a reference.

We solve the strongly heterogeneous material problem with the new ADER-DG scheme on four different meshes with mesh spacings $h = [50, 30, 20, 16]$ m. On each mesh we simulate the wave propagation with a series of schemes where the approximation order of the wave propagation and the material representation is systematically varied. To this end, we use polynomials P3, P4 and P5 for the wave propagation approximation on each mesh and increase

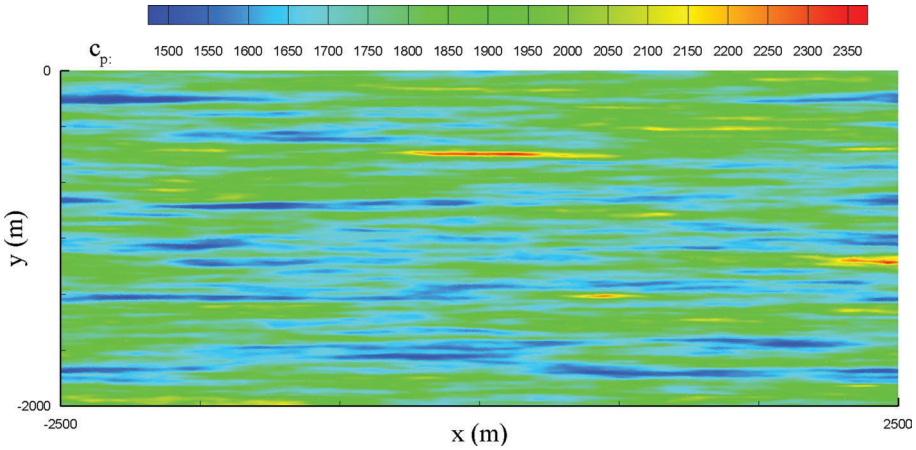

Figure 7. Spatial variation of the *P*-wave velocity with extreme values ranging from 1450 to 2400 m s^{-1}. The *S*-wave velocity has an identical spatial distribution, however, with extreme values ranging from 830 to 1370 m s^{-1}.

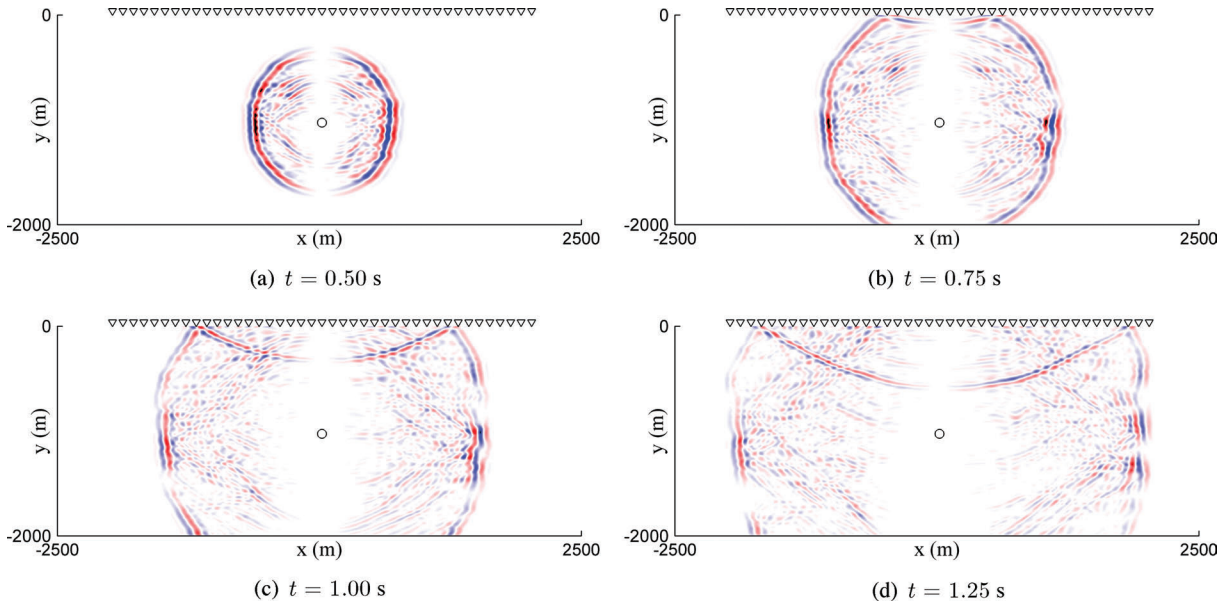

Figure 8. Snapshots of the horizontal velocity wave field u in the randomly heterogeneous model at four different times. The circle represents the location of the explosive source while the triangles are receivers at the free surface.

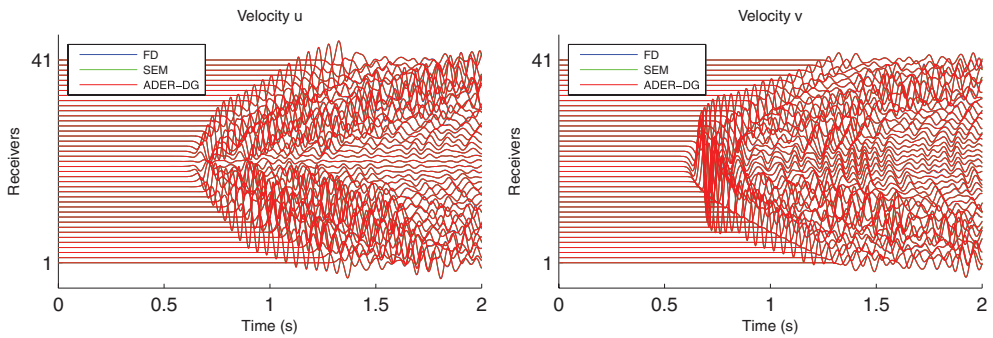

Figure 9. Comparison of the numerical solution of the particle velocity u (left-hand panel) and v (right-hand panel) on each of the 41 receivers placed on the free surface for the randomly heterogeneous material test case.

the degree of the material approximation successively from M0 to M3, M4 or M5 depending on the wave approximation polynomial P used. Therefore, the degree of the material approximation is always lower or equal to that of the wave propagation approximation. In total this leads to $(4 + 5 + 6) \times 4 = 60$ simulations providing different solutions. The error of each solution is measured against the FD reference solution by calculating the rms error $E_{L_2} = (\sum_i (u_i^{\text{num}} - u_i^{\text{ref}})^2)^{1/2} / (\sum_i (u_i^{\text{ref}})^2)^{1/2}$ of the wave field

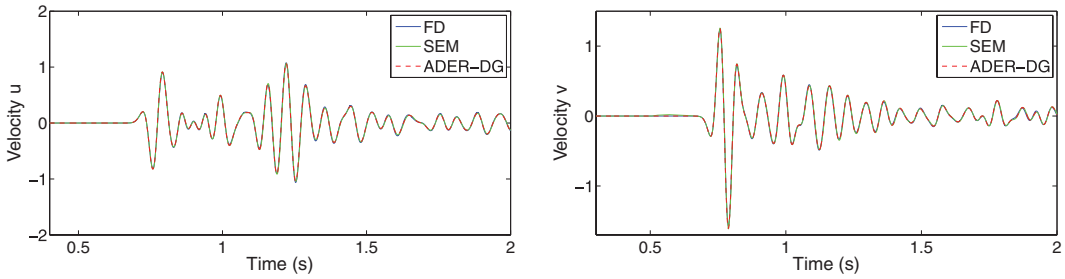

Figure 10. Seismic signals of the horizontal velocity component u (left-hand panel) and vertical velocity component v (right-hand panel) recorded at receiver 15 at $x = -575$ m.

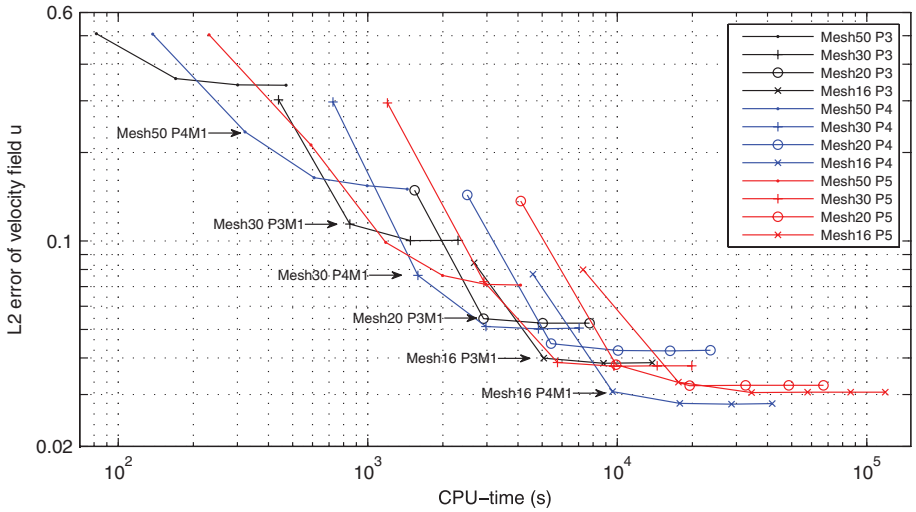

Figure 11. Error plot of the accuracy study versus CPU-time for the series of 60 different wave propagation simulations. Four meshes of different mesh spacings (50, 30, 20 and 16 m) are used and indicated by different symbols. Different colours denote the degrees of the wave propagation approximations in space and time (P3), (P4) and (P5). Each line graph shows results for an increasing degree of the material approximation from M0 to it maximum value Md determined by Pd.

component u at time $t = 0.5$s over all FD gridpoints i, which ensures that no possible boundary effects are influencing the measurement.

The results of this accuracy study are plotted in Fig. 11 versus the CPU-time required for each simulation. Here, the symbols indicate the used mesh and the colours indicate the degree P of the wave propagation approximation. Each graph is then obtained by computing the errors resulting from increasing degrees of the material approximation, that is, from M0 to the corresponding maximum Md determined by Pd, $d = 3, 4, 5$. Therefore, the three graphs for each mesh consist of an increasing number of data points for an increasing degree of the wave approximation P.

Starting from the top left-hand side of each graph we observe that improved material approximation decreases the error. However, most graphs show a similar behaviour in the sense that they flatten out and asymptotically seem to reach a limit where improved material approximation by higher M does reduce the error only slightly. Significantly smaller errors can then only be obtained by mesh refinement or increase of the wave propagation approximation P. The only exception to this rule appears when comparing the graph of the finest mesh (Mesh16) with highest wave approximation P5 in the lower right part of the figure. Here the obtained errors are slightly larger than those obtained from the P4 approximation. We explain this effect by considering that the standard fourth-order FD reference solution is not exact but seems to produce small errors that are comparable to the one that we try to measure.

The general and expected observation is that refining the mesh and increasing the approximation degree of the wave propagation P or the material representation M reduces the error while increasing the computational time. However, we recognize that increasing P alone cannot always reduce the error significantly. This clearly shows that a highly accurate wave propagation approximation alone might not be sufficient, if the velocity model is not represented well enough. In order to improve the representation of the elastic model we can refine the mesh or increase the degree of the material approximation. Which strategy is more efficient in terms of CPU-time is answered by Fig. 11. In fact, we observe that for coarse meshes (Mesh50 and Mesh30), the improved material approximation can still reduce the error significantly if the wave propagation order is sufficiently high (e.g. for P5). Otherwise, an efficient combination of mesh size, wave and material approximation mainly involves the linear representation (M1) of the material inside each element as indicated by arrows to the corresponding data points in Fig. 11.

In order to have a better understanding of the error level presented in Fig. 11, we show seismograms comparisons for the signals recorded at receiver 15 in Fig. 12. We plot four numerical solutions, from the 60 used to construct Fig. 11, and compare them with the reference FD solution. The maximum amplitude difference for Mesh16 P4M4 is 6.2 per cent and 4.6 per cent for the velocity components u and v, respectively. In Table 2, we also give the envelope and phase mitfits (Kristeková *et al.* 2006) for the seismograms of Fig. 12 showing a consistent error behaviour with the one of the

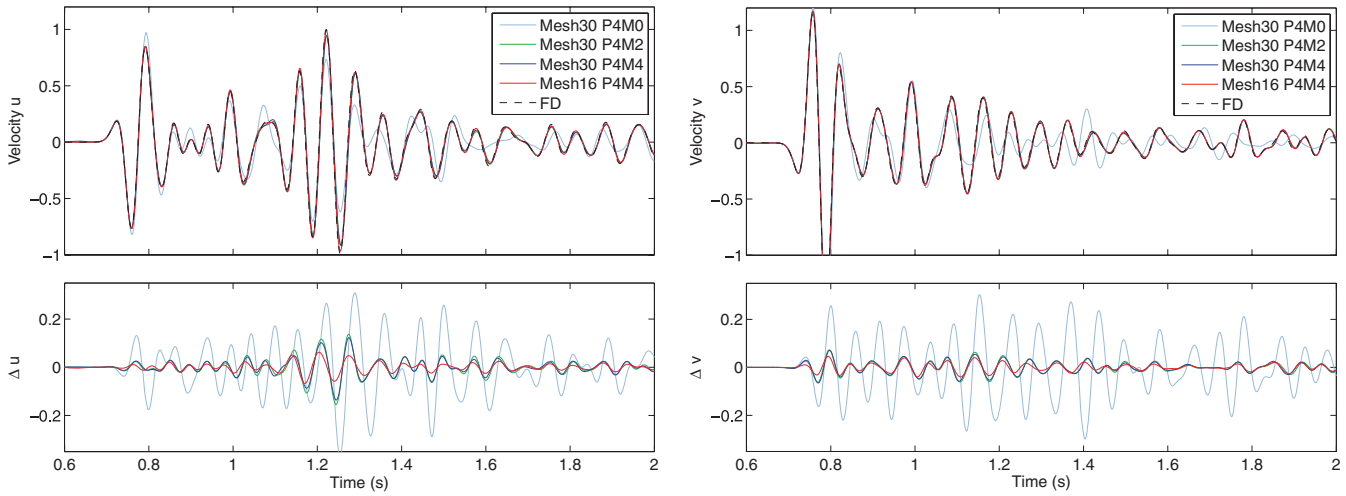

Figure 12. Seismic signals of the horizontal velocity component u (left-hand panel) and vertical velocity component v (right-hand panel) recorded at receiver 15 for wave propagation order 5 (P4) for 4 of the 60 numerical simulations. We plot the direct (top panel) comparison and the difference Δu and Δv (bottom panel) with the FD reference solution.

Table 2. Time–frequency misfit errors (envelope and phase) for the seismograms presented in Fig. 12.

Mesh	Order	Envelope	Phase
Mesh30	P4M0	0.299	0.098
Mesh30	P4M2	0.045	0.034
Mesh30	P4M4	0.038	0.031
Mesh16	P4M4	0.022	0.017

entire wave field shown in Fig. 11 in the sense that refining the mesh and/or increasing the order reduce the numerical error.

We conclude that in this case it is computationally most efficient to keep the material approximation at M1 (or maximum M2) and the wave propagation approximation at P3 or P4, and then further reduce the numerical error by refining the mesh.

There is, of course, the issue of discrete velocity models that needs to be considered when solving seismic wave propagation in heterogeneous velocity models. When dealing with discrete velocity models, as the one presented in this test problem, their numerical representations used by different computational codes can vary and therefore will lead to slightly different discrete physical problems. Therefore, we explain the fact, that the ADER-DG and the FD results differ even on the finest discretization, by these slight differences in the discrete velocity models. We believe that with further improvements in numerical techniques and the reduction of numerical errors in the simulation of the wave propagation process these discrepancies of discrete velocity models might became even more evident. Alternatively, homogenization techniques (Capdeville & Marigo 2007, 2008) could be applied in order to build smooth *effective* media which average small-scale heterogeneities in the original models without losing the accuracy for wave field computations.

5.3 Intracell material discontinuity

This experiment considers an important issue often encountered during the mesh generation process, when complex geometries of material interfaces or very thin material layers cannot be honoured, that is, elements cannot be edge-aligned with the interface's geometry but extend across the material discontinuity. We are interested in the influence of this issue on the accuracy of the synthetic seismograms and investigate the behaviour of the new high-order polynomial material approximation of such discontinuities.

To this end, we define a computational domain $\Omega = [-2000\,\text{m}, 2000\,\text{m}] \times [-2000\,\text{m}, 2000\,\text{m}]$ with absorbing boundary conditions on all sides. We subdivide Ω into two zones of different material properties with a single discontinuity at $y = 0$ m. The high-velocity zone ($y > 0$) has the material properties $\rho = 2500\,\text{m s}^{-1}$, $\mu = 5$ GPa and $\lambda = 5$ GPa, while the low-velocity zone ($y < 0$) is characterized by $\rho = 2000\,\text{m s}^{-1}$, $\mu = 0.5$ GPa and $\lambda = 0.5$ GPa leading to a strong velocity contrast of a factor of 2.8. We place a point force as source acting equally on the velocity components u and v at position $\vec{x}_s = (0, -400)$ m. The source time function is a Ricker wavelet as defined in Section 5.1 with delay time $t_D = 250$ ms, $a_1 = 1 \times 10^5$ and $a_2 = -(\pi f_c)^2$, where the central frequency is set to $f_c = 5$ Hz. We place 11 receivers equidistantly from $x = -1000$ to 1000 m in each zone, that is $y = 1000$ and -1000 m, to record the synthetic seismograms as shown in Fig. 13. Furthermore, Fig. 13 visualizes snapshots of the reference solution with the material discontinuity indicated by the black line. The low amplitudes of the transmitted waves into the high-velocity zone are hardly visible, while the direct P and S waves as well as the reflected waves due to the impedance contrast appear clearly in the low-velocity zone.

In order to isolate the errors generated by the intracell discontinuity and to avoid any other numerical effects, we split the computational domain Ω into $\Omega_1 = [-2000\,\text{m}, 2000\,\text{m}] \times [-37.5\,\text{m}, 37.5\,\text{m}]$ around the material discontinuity and the remaining $\Omega_2 = \Omega \setminus \Omega_1$. We discretize Ω_2 with a regular square mesh of $h = 25$ m and keep it fixed for all tests. For Ω_1 is discretized with the same fixed mesh spacing in x-direction, however, we generate four different spacings in y-direction with $h_1 = 25$ m, $h_2 = 15$ m, $h_3 = 10.71$ m and $h_4 = 8.33$ m, respectively, leading to the meshes denoted by Mesh 1, Mesh 2, Mesh 3 and Mesh 4. Therefore, we get a set of meshes successively refined only around the material interface without respecting it properly by element edges to always keep the intracell discontinuity.

We run two simulations for each of the four meshes applying an ADER-DG scheme of wave propagation approximation P4, one

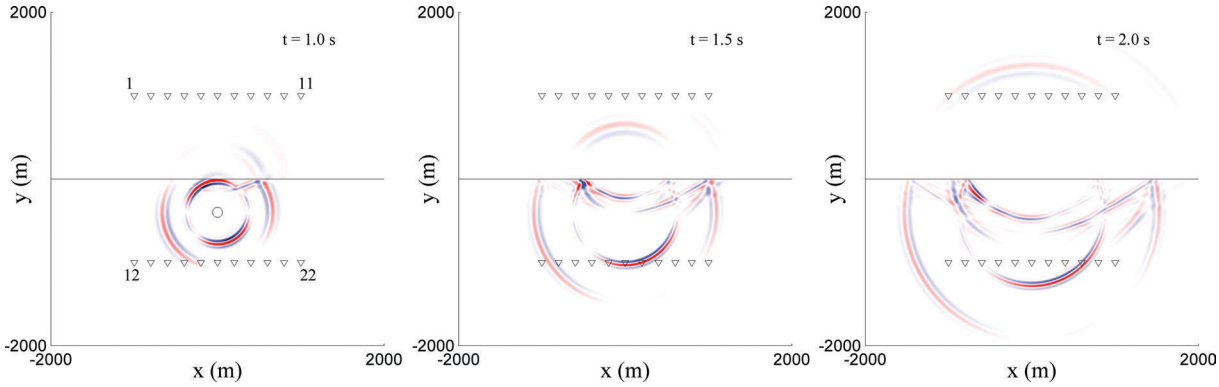

Figure 13. Snapshots of the reference solution for the material discontinuity test problem at three time levels. The black line represents the position of the material discontinuity, the black circle the location of the source, and the black triangles the locations of the receivers. We mainly observe the direct waves as well as the reflected and refracted waves due to the impedance contrast at the discontinuity.

with constant (M0) and one with linear (M1) material approximation polynomials. For each of these eight simulations we record the signals at all 22 receivers and perform a time–frequency misfit analysis as suggested by Kristeková *et al.* (2006). The reference solution is computed by the SEM on a regular 25 m mesh respecting the discontinuity which agrees excellently with our ADER-DG solution, if we respect the discontinuity. In Figs 14 and 15, we present the Envelope Misfits (EM) and Phase Misfits (PM) at all receivers. The top rows of these figures show the results on receivers 1–11 in the high-velocity zone, whereas the bottom rows show the results for receivers 12–22 in the low-velocity zone. The plots in the left- and right-hand columns are obtained by the constant (M0) and linear (M1) material representations, respectively. The asymmetry of the EM and PM curves is due to the oblique orientation of the point source with respect to the interface. Obviously, the EM and PM decrease with mesh refinement as expected. However, increasing the material approximation from M0 to M1 generally decreases the misfits even more, in particular, in the low-velocity zone (bottom rows). We believe that the explanation is the clear improvement of the representation of the material interface that affects the accuracy of the reflected and especially the refracted wave that travels along the discontinuity.

To understand this improvement more clearly, Fig. 16 shows the results obtained at the receivers 6 (left-hand column) and 15 (right-hand column) in the high- and low-velocity zone, respectively. The top row displays the best solutions obtained with the ADER-DG P4M1 scheme on Mesh 4 together with the reference solutions. The visual fit is perfect. Note also the amplitude differences of the horizontal velocity component u in the two zones. The middle row shows the error in form of the difference between the reference and the numerical solutions for all four meshes with constant material representation M0. We observe that the intracell discontinuity introduces a significant error in comparison to the reference solution computed on a mesh that respects the material discontinuity. Clearly, the amplitudes of these difference seismograms decrease with mesh refinement. Note also that for the first two wave arrivals of the direct P and direct S wave on receiver 15 there is no difference amplitude visible as these direct waves are not affected by the interface. Finally, the bottom row is similar to the middle row, just that here the linear material approximation M1 was used. Again the differences decrease systematically with mesh refinement. However, the absolute amplitude of the error is much smaller, that is, the accuracy using the M1 material representation for the intracell discontinuity is significantly higher than that of the M0 representation.

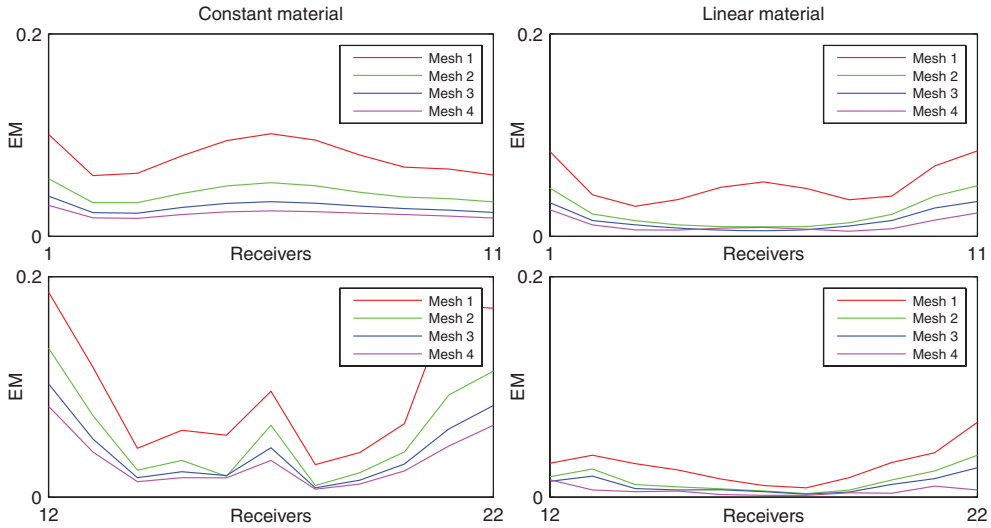

Figure 14. Envelope misfits for the intracell discontinuity problem. Results obtained for constant (left-hand panel) and linear (right-hand panel) material approximations are compared for receivers 1-11 in the high-velocity (top panel) and for receivers 12-22 in the low-velocity (bottom panel) zone.

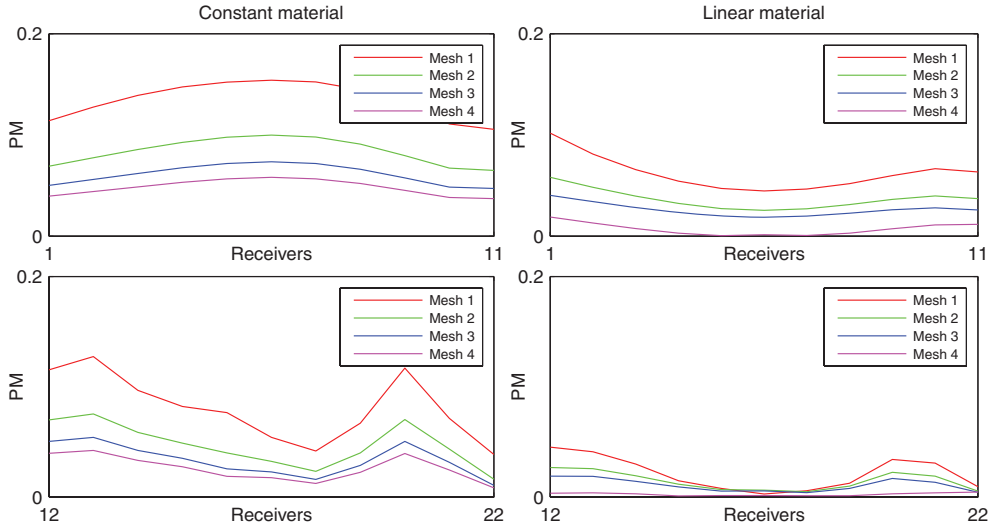

Figure 15. Phase misfits for the intracell discontinuity problem. Results obtained for constant (left-hand panel) and linear (right-hand panel) material approximations are compared for receivers 1-11 in the high-velocity (top panel) and for receivers 12-22 in the low-velocity (bottom panel) zone.

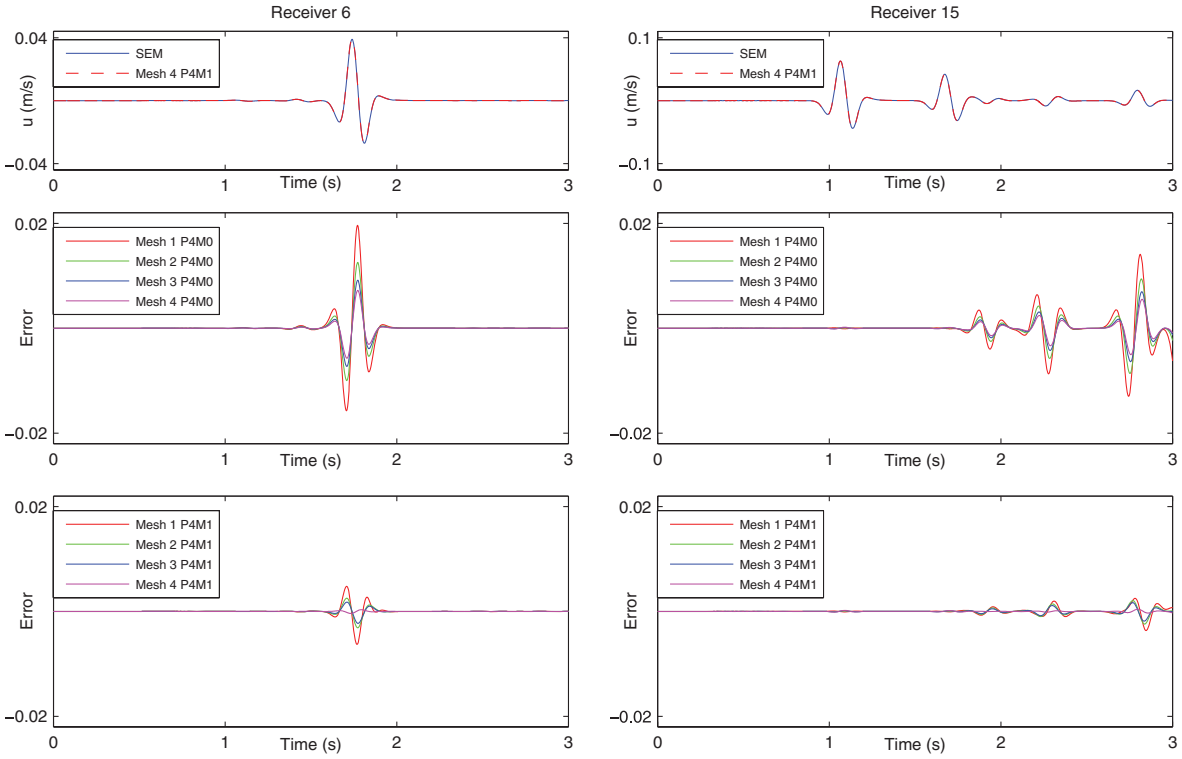

Figure 16. Comparison of results obtained at receivers 6 (left-hand panel) and 15 (right-hand panel). Top row: fit between the best numerical solution by the ADER-DG P4M1 scheme on Mesh 4 and the reference solution. Middle row: errors as difference seismograms between numerical and reference solutions for different meshes using constant material representation M0. Bottom row: errors as difference seismograms between numerical and reference solutions for different meshes using linear material representation M1. Note the clear improvement due to the better material approximation.

An important aspect to mention is that test using higher-degree material representations than M1 to approximate the intracell discontinuity did generally lead to larger errors or even caused numerical instabilities. This is due to the well-known problem of high-order polynomial approximation of a discontinuity leading to strong oscillations. Therefore, we suggest to limit the polynomial degree for subcell resolution to M1 in the case of intracell material discontinuities.

6 CONCLUSIONS

We have presented an important extension of the ADER-DG scheme for 2-D elastic wave propagation problems including the high-order approximation of variable material inside each element. Furthermore, we prove numerically the expected order of convergence for smoothly varying material properties. Through different numerical examples we test and compare our new method with other

independent numerical methods, the FD and SEM, finding excellent agreement of the synthetic seismograms. We conclude that the best performance of the ADER-DG method, when simulating seismic waves in heterogeneous material depends on the combination of the mesh spacing and the degree of the approximation polynomials for the wave propagation and elastic material properties. In the investigated example, the highest efficiency is reached for rather low, that is, linear or quadratic, material approximation as increased accuracy is rather obtained by mesh refinement. We also observed that for very small error levels in the numerical solution, slight discrepancies in the discrete representation of the velocity model could lead to different solutions obtained by different numerical methods. Finally, we considered the case of sharp material discontinuities which are not respected by the mesh. We find that in such cases the linear approximation of the material across such interfaces also seems to be a good choice to reduce the numerical error. Moreover, higher-order polynomial representations of a sharp material discontinuity inside an element often cause problems possibly due to their oscillatory behaviour in the presence of the discontinuity. A further investigation is necessary to find a possible regularization of the instable behaviour at intracell discontinuities. Future work will focus on the extension of the proposed approach to anisotropic and viscoelastic material properties as well as unstructured 3-D meshes of tetrahedral and hexahedral elements.

ACKNOWLEDGMENTS

The authors thank the Deutsche Forschungsgemeinschaft (DFG), as the work was supported through the Emmy Noether-Program (KA 2281/2-1). Furthermore, we thank the Leibniz-Rechenzentrum in München for using their computational resources within the DEISA Consortium (www.deisa.eu), co-funded through EU FP6 projects RI-508830 and RI-031513, and for their support within the DEISA Extreme Computing Initiative. The help of our system administrator Jens Oeser when using the local Cluster TETHYS (Oeser *et al.* 2006) is also appreciated.

REFERENCES

Aki, K. & Richards, P.G., 2002. *Quantitative Seismology*, University Science Books, Sausalito, California.

Bernard, P.-E., Chevaugeon, N., Legat, V., Deleersnijder, E. & Remacle, J.-F., 2007. High-order h-adaptive discontinuous Galerkin methods for ocean modelling, *Ocean Dyn.,* **57,** 109–121.

Castro C.E., 2007. *High order ADER FV/DG Numerical Methods for Hyperbolic Equations,* Monographs of the School of Doctoral Studies in Environmental Engineering, University of Trento.

Capdeville, Y. & Marigo, J.-J., 2007. Second order homogenization of the elastic wave equation for non-periodic layered media, *Geophys. J. Int.,* **170**(2), 823–838.

Capdeville, Y. & Marigo, J.-J., 2008. Shallow layer correction for Spectral Element like methods, *Geophys. J. Int.,* **172**(3), 1135–1150.

Castro, C.E. & Toro, E.F., 2008. Solvers for the high-order Riemann problem for hyperbolic balance laws, *J. Comput. Phys.,* **227**(4), 2481–2513.

Cockburn, B., Karniadakis, G.E. & Shu, C.W., 2000. *Discontinuous Galerkin Methods,* Lecture Notes in Computational Science and Engineering. Springer, Berlin.

De Basabe, J.D., Sen, M.K. & Wheeler, M.F., 2008. The interior penalty discontinuous Galerkin method for elastic wave propagation: grid dispersion, *Geophys. J. Int.,* **175**(1), 83–93.

de la Puente, J., Käser, M., Dumbser, M. & Igel, H., 2007. An arbitrary high order discontinuous Galerkin method for elastic waves on unstructured meshes IV: anisotropy, *Geophys. J. Int.,* **169**(3), 1210–1228.

de la Puente, J., Dumbser, M., Käser, M. & Igel, H., 2008. Discontinuous Galerkin methods for wave propagation in poroelastic media, *Geophysics,* **73**(5), T77–T97.

Dumbser, M., 2003. On the improvement of efficiency and storage requirements of the discontinuous Galerkin method for aeroacoustics, *PAMM,* **3,** 426–427.

Dumbser, M. & Käser, M., 2006. An arbitrary high order discontinuous Galerkin method for elastic waves on unstructured meshes II: the three-dimensional case, *Geophys. J. Int.,* **167**(1), 319–336.

Dumbser, M. & Munz, C., 2006. Building blocks for arbitrary high order discontinuous Galerkin schemes, *J. Sci. Comput.,* **27,** 215–230.

Dumbser, M., Käser, M. & Toro, E.F., 2007. An arbitrary high order discontinuous Galerkin method for elastic waves on unstructured meshes V: local time stepping and p-adaptivity, *Geophys. J. Int.,* **171**(2), 695–717.

Gallovič, F.G. & Brokešová, J.B., 2004. On strong ground motion synthesis with k^{-2} slip distributions, *Journal of Seismology,* **8,** 211–224.

Gassner, G., Lörcher, F. & Munz, C.-D., 2008. A discontinuous Galerkin scheme based on a space-time expansion II. Viscous flow equations in multi dimensions, *J. Sci. Comput.,* **34,** 260–286.

Hesthaven, J. & Warburton, T., 2008. *Nodal Discontinuous Galerkin Methods: Algorithms, Analysis, and Applications,* Springer, New York.

Hu, F., Hussaini, M. & Rasetarinera, P., 1999. An analysis of the discontinuous Galerkin method for wave propagation problems, *JCP,* **151,** 921–946.

Käser, M. & Dumbser, M., 2006. An arbitrary high order discontinuous Galerkin method for elastic waves on unstructured meshes I: the two-dimensional isotropic case with external source terms, *Geophys. J. Int.,* **166**(2), 855–877.

Käser, M., Dumbser, M., de la Puente, J. & Igel, H., 2007a. An arbitrary high order discontinuous Galerkin method for elastic waves on unstructured meshes III: viscoelastic attenuation, *Geophys. J. Int.,* **168**(1), 224–242.

Käser, M., Mai, P. & Dumbser, M., 2007b. On the accurate treatment of finite source rupture models using ADER-DG on tetrahedral meshes, *Bull. seism. Soc. Am.,* **97**(5), 1570–1586.

Käser, M., Hermann, V. & de la Puente, J., 2008. Quantitative accuracy analysis of the discontinuous Galerkin method for seismic wave propagation, *Geophys. J. Int.,* **173**(3), 990–999.

Klimeš, L., 2002. Correlation functions of random media, *Pure appl. geophys.,* **159,** 1811–1831.

Kristeková, M., Kristek, J., Moczo, P. & Day, S., 2006. Misfit criteria for quantitative comparison of seismograms, *Bull. seism. Soc. Am.,* **96**(5), 1836–1850.

Levander, A.R., 1988. Fourth-order finite difference P-SV seismograms, *Geophysics,* **53,** 1425–1436.

LeVeque, R., 2002. *Finite Volume Methods for Hyperbolic Problems,* Cambridge University Press, Cambridge.

Moczo, P., Kristek, J., Vavrycuk, V., Archuleta, R.J. & Halada, L., 2002. 3D Heterogeneous staggered-grid finite-difference modeling of seismic motion with volume harmonic and arithmetic averaging of elastic moduli and densities, *Bull. seism. Soc. Am.,* **92**(8), 3042–3066.

Oeser, J., Bunge, H.-P. & Mohr, M., 2006. High performance computing and communications—Second International Conference, HPCC 2006, Munich, Germany, eds. Michael Gerndt and Dieter Kranzlmüller, *Lecture Notes in Computer Science,* **4208,** 31–40.

Stein, S. & Wysession, M., 2003. *An Introduction to Seismology, Earthquakes, and Earth Structure,* Blackwell Publishing, Oxford.

Reed, W.H. & Hill, T.R., 1973. Triangular mesh methods for the neutron transport equation., Tech. Rep. LA-UR-73-479, Los Alamos Scientic Laboratory.

Titarev, V.A. & Toro, E.F., 2002. ADER: arbitrary high order Godunov approach., *J. Sci. Comput.,* **17,** 609–618.

Toro, E.F., 2009. *Riemann Solvers and Numerical Methods for Fluid Dynamics,* 3rd edn, Springer, Berlin.

Toro, E.F., Millington, R.C. & Nejad, L.A.M., 2001. Towards very high order godunov schemes., in *Godunov Methods; Theory and Applications,* pp. 907–940, Kluwer Academic Plenum Publishers, Oxford, International Conference.

Virieux, J., 1984. SH-wave propagation in heterogeneous media: velocity-stress finite-difference method, *Geophysics,* **49,** 1933–1942.

Virieux, J., 1986. P-SV wave propagation in heterogeneous media: velocity-stress finite-difference method, *Geophysics,* **51,** 889–901.

APPENDIX A: REFERENCE ELEMENTS AND MAPPING FUNCTIONS

For triangular meshes we define the reference element E_R as $0 \leq \xi \leq 1, 0 \leq \eta \leq 1-\xi$. The mapping function from the reference element to the physical element $E^{(i)}$ with vertexes $\vec{x}_i = (x_i, y_i)$ with $i = 1 \ldots 3$ is written as follows:

$$x(\xi,\eta) = x_1 + (x_2 - x_1)\xi + (x_3 - x_1)\eta\,,$$
$$y(\xi,\eta) = y_1 + (y_2 - y_1)\xi + (y_3 - y_1)\eta\,, \tag{A1}$$

where the inverse functions $\xi = \xi(x, y)$ and $\eta = \eta(x, y)$ can be obtained explicitly.

For quadrangular meshes we define the reference element E_R as $0 \leq \xi \leq 1, 0 \leq \eta \leq 1$. The mapping function from the reference element to the physical element $E^{(i)}$ with vertexes $\vec{x}_i = (x_i, y_i)$ with $i = 1 \ldots 4$ is written as follows:

$$x(\xi,\eta) = (1-\xi)(1-\eta)x_1 + \xi(1-\eta)x_2 + \xi\eta x_3 + (1-\xi)\eta x_4\,,$$
$$y(\xi,\eta) = (1-\xi)(1-\eta)y_1 + \xi(1-\eta)y_2 + \xi\eta y_3 + (1-\xi)\eta y_4\,. \tag{A2}$$

In this case, the inverse functions can be obtained explicitly only for parallelograms as physical elements.

We enumerate the vertices of elements in counter-clock wise direction. The Jacobian matrix $J = \partial(x, y)/\partial(\xi, \eta)$ of the mapping and its inverse are

$$J = \begin{bmatrix} x_\xi & x_\eta \\ y_\xi & y_\eta \end{bmatrix}, \quad J^{-1} = \begin{bmatrix} \xi_x & \xi_y \\ \eta_x & \eta_y \end{bmatrix}. \tag{A3}$$

Useful relations are

$$\int_{E^{(i)}} u_p(\vec{x}, t)\,\mathrm{d}\vec{x} = \int_{E_R} |J|\, u_p(\vec{\xi}, t)\,\mathrm{d}\vec{\xi}\,, \tag{A4}$$

and

$$\begin{bmatrix} \dfrac{\partial u_p(\vec{x},t)}{\partial x} \\ \dfrac{\partial u_p(\vec{x},t)}{\partial y} \end{bmatrix} = J^{-1^T} \begin{bmatrix} \dfrac{\partial u_p(\vec{\xi},t)}{\partial \xi} \\ \dfrac{\partial u_p(\vec{\xi},t)}{\partial \eta} \end{bmatrix}. \tag{A5}$$

APPENDIX B: BASIS FUNCTIONS

We use orthogonal hierarchical basis functions given in terms of the Jacobi polynomials as given in Cockburn *et al.* (2000). Here we show the first six basis functions for the third-order numerical method using triangular or square meshes.

Basis functions up to third order for triangular elements.

$$\Phi_0 = 1\,,$$
$$\Phi_1 = -1 + 2\,\xi + \eta\,,$$
$$\Phi_2 = -1 + 3\,\eta\,,$$
$$\Phi_3 = 1 - 6\,\xi - 2\,\eta + 6\,\xi^2 + 6\,\xi\eta + \eta^2\,,$$
$$\Phi_4 = 1 - 2\,\xi - 6\,\eta + 10\,\xi\eta + 5\,\eta^2\,,$$
$$\Phi_5 = 1 - 8\,\eta + 10\,\eta^2\,. \tag{B1}$$

Basis functions up to third order for square elements.

$$\Phi_0 = 1\,,$$
$$\Phi_1 = -1 + 2\,\xi\,,$$
$$\Phi_2 = -1 + 2\,\eta\,,$$
$$\Phi_3 = 1 - 6\,\xi + 6\,\xi^2\,,$$
$$\Phi_4 = 1 - 2\,\xi - 2\,\eta + 4\,\xi\eta\,,$$
$$\Phi_5 = 1 - 6\,\eta + 6\,\eta^2\,. \tag{B2}$$

APPENDIX C: L2 PROJECTION

The L2 projection of a continuous function $u_p(\vec{x}(\xi, \eta), t)$ that allow us to obtain the time-dependent degrees of freedom $\hat{u}_{pl}(t)$ reads

$$\hat{u}_{pl}(t) = \frac{\displaystyle\int_{E_R} u_p(\vec{\xi}, t)\Phi_k(\vec{\xi})\,\mathrm{d}\xi\,\mathrm{d}\eta}{\displaystyle\int_{E_R} \Phi_l(\vec{\xi})\Phi_k(\vec{\xi})\,\mathrm{d}\xi\,\mathrm{d}\eta} = \frac{\displaystyle\int_{E_R} u_p(\vec{\xi}, t)\Phi_l(\vec{\xi})\,\mathrm{d}\xi\,\mathrm{d}\eta}{M_{ll}}\,. \tag{C1}$$

Solid Earth, 2, 95–105, 2011
www.solid-earth.net/2/95/2011/
doi:10.5194/se-2-95-2011

Solid Earth

Exploring the potentials and limitations of the time-reversal imaging of finite seismic sources

S. Kremers[1], **A. Fichtner**[1,*], **G. B. Brietzke**[1,**], **H. Igel**[1], **C. Larmat**[2], **L. Huang**[2], **and M. Käser**[1]

[1]Department of Earth and Environmental Sciences, Ludwig-Maximilians-University, Theresienstr. 41/III, 80333 Munich, Germany
[2]EES-17 Geophysics Group, Los Alamos National Laboratory, Los Alamos, NM 87545, USA
[*]now at: Faculty of Geosciences, Utrecht University, Utrecht, The Netherlands
[**]now at: GFZ German Research Centre for Geosciences, Potsdam, Germany

Received: 28 January 2011 – Published in Solid Earth Discuss.: 17 March 2011
Revised: 30 May 2011 – Accepted: 31 May 2011 – Published: 21 June 2011

Abstract. The characterisation of seismic sources with time-reversed wave fields is developing into a standard technique that has already been successful in numerous applications. While the time-reversal imaging of effective point sources is now well-understood, little work has been done to extend this technique to the study of finite rupture processes. This is despite the pronounced non-uniqueness in classic finite source inversions.

The need to better constrain the details of finite rupture processes motivates the series of synthetic and real-data time reversal experiments described in this paper. We address questions concerning the quality of focussing in the source area, the localisation of the fault plane, the estimation of the slip distribution and the source complexity up to which time-reversal imaging can be applied successfully. The frequency band for the synthetic experiments is chosen such that it is comparable to the band usually employed for finite source inversion.

Contrary to our expectations, we find that time-reversal imaging is useful only for effective point sources, where it yields good estimates of both the source location and the origin time. In the case of finite sources, however, the time-reversed field does not provide meaningful characterisations of the fault location and the rupture process. This result cannot be improved sufficiently with the help of different imaging fields, realistic modifications of the receiver geometry or weights applied to the time-reversed sources.

The reasons for this failure are manifold. They include the choice of the frequency band, the incomplete recording of wave field information at the surface, the excitation of large-amplitude surface waves that deteriorate the depth resolution, the absence of a sink that should absorb energy radiated during the later stages of the rupture process, the invisibility of small slip and the neglect of prior information concerning the fault geometry and the inherent smoothness of seismologically inferred Earth models that prevents the beneficial occurrence of strong multiple-scattering.

The condensed conclusion of our study is that the limitations of time-reversal imaging – at least in the frequency band considered here – start where the seismic source stops being effectively point-localised.

Correspondence to: S. Kremers
(kremers@geophysik.uni-muenchen.de)

1 Introduction

Time reversal (TR) is a universal concept that can be found in numerous physical sciences, including meteorology (e.g. Talagrand and Courtier, 2007), geodynamics (e.g. Bunge et al., 2003), ground water modelling (e.g. Sun, 1994) and seismology. The misfit χ between observed and synthetic data is propagated backwards in time to detect the underlying discrepancies between the real world and its mathematical model. TR can be approached from two closely related directions: (1) the invariance of a non-dissipative physical system with respect to a sign change of the time variable, and (2) the computation of the gradient of χ with the help of the adjoint method.

From a seismological perspective, the time-invariance of perfectly elastic wave propagation provides the intuitive justification for the TR imaging of seismic sources: Seismograms $\boldsymbol{u}_0(\boldsymbol{x}^r,t)$ recorded at positions $\boldsymbol{x}^r$ $(r=1,...,n)$ are reversed in time, re-injected as sources at their respective receiver locations and the resulting wave field $\boldsymbol{u}(\boldsymbol{x},t)$ is then

propagated backwards in time through an appropriate Earth model. When the receiver configuration is sufficiently dense, the time-reversed wave field $\boldsymbol{u}$ approximates the original wave field $\boldsymbol{u}_0$. Focussing of $\boldsymbol{u}$ then occurs at the time and location where $\boldsymbol{u}$ was excited, thus, providing information on the original earthquake source.

While being mathematically more rigorous, the adjoint method (e.g. Tarantola, 1988; Tromp et al., 2004; Fichtner et al., 2006; Fichtner, 2010) leads to a similar result: The gradient of the misfit χ with respect to the source parameters is given in terms of the time-reversed wave field generated by adjoint sources that radiate the misfit from the receiver positions back into the Earth model. In the case of a moment tensor point source, for instance, the derivative of χ, with respect to the moment tensor $\boldsymbol{M}$, is given by

$$\frac{\partial \chi}{\partial M_{ij}} = -\int \epsilon_{ij}(\boldsymbol{x}^s, t)\, dt\,, \tag{1}$$

where ϵ_{ij} and $\boldsymbol{x}^s$ denote the strain tensor computed from the time-reverse field $\boldsymbol{u}$ and the source position, respectively. In this sense, TR can be interpreted as the first step in an iterative gradient-based source inversion (e.g. Tromp et al., 2004; Hjörleifsdóttir, 2007; Fichtner, 2010).

The history of TR imaging is likely to have started in ocean acoustics (e.g. Parvulescu and Clay, 1965; Derode et al., 1995; Edelmann et al., 2002), from where it migrated to medical imaging (e.g. Fink, 1997; Fink and Tanter, 2010), nondestructive testing (e.g. Chakroun et al., 1995; Sutin et al., 2004) and many other fields. One of the earliest seismic applications can be found in the work of McMechan (1982) who introduced TR source imaging as a modified version of migration. The time-reversed wave equation is used to image earthquake sources instead of subsurface structures (Artman et al., 2010). Kennett (1983) pinpointed the advantages of TR as early as 1983: (1) no prior interpretation of the time-series is needed and (2) the full elastic wave field is used to obtain the best image of the source. Early applications were limited to structurally simple or acoustic models (e.g. McMechan et al., 1985; Rietbrock and Scherbaum, 1994; Fink, 1996), but recent advances in numerical modelling enabled applications in more complex scenarios with different types of seismic sources, including the classic double couple point source (Gajewski and Tessmer, 2005), extended faults (Ishii et al., 2005; Larmat et al., 2006; Allmann and Shearer, 2007), micro-seismic tremor (Steiner et al., 2008) and volcanic long-period events (O'Brien et al., 2011). Larmat et al. (2009) demonstrate the need to use specific imaging fields such as divergence or strain to distinguish sources from low velocity zones.

While TR imaging of effective point sources is now well-understood, little has been done to explore its potential to detect the details of finite rupture processes. This is surprising because classical finite-source inversions (e.g. Cotton and Campillo, 1995; Cesca et al., 2010) are known to be highly non-unique (Mai et al., 2007). The urgent need to improve finite-source inversions motivates this study where we attempt to answer several key questions with the help of both synthetic and real-data experiments: (1) How well does the time-reversed field focus in the source area? (2) Does TR imaging provide constraints on the source volume? (3) Can regions with large slip (asperities) be identified? (4) Can the rupture speed be estimated? (5) Up to which level of complexity does TR imaging provide useful information on the rupture process?

This paper is organised as follows: In a first series of synthetic tests, we study TR imaging of single and multiple point sources under nearly ideal conditions. We then extend our experiments to synthetic data computed from a finite-rupture model. To improve the focussing of the time-reversed field, we investigate the influence of the station configuration and the weighting of the adjoint sources. Finally, we provide an application to the strong-motion data recorded during the 2000 Tottori (Japan) earthquake.

2 Numerical method

For our TR experiments, we employ a spectral-element algorithm to model wave propagation in 3-D elastic media (Fichtner and Igel, 2008; Fichtner et al., 2009a,b). The model volume is divided into equal-sized hexahedral elements, and Perfectly Matched Layers (PML) are used to avoid reflections from the nonphysical model boundaries. In the interest of simplicity, we restrict ourselves to isotropic and non-dissipative media.

The model used in our synthetic tests is $160 \times 170 \times 40$ km wide. It comprises $60 \times 60 \times 16$ elements, which corresponds to ~ 3 million grid points when the polynomial degree is 4. This setup allows us to model wave fields with frequencies up to 2 Hz. Both the receiver configuration (Fig. 1, left) and the structural model (Fig. 1, right) in most of our simulations are the same as in the SPICE source inversion benchmark (Mai et al., 2007) that was intended to mimic the circumstances of the 2000 Tottori (Japan) earthquake. For the real data experiment, we use the Japanese KiK-net stations (Fig. 11) and the layered velocity model of Semmane (2005). As we intend to work in the frequency range of kinematic source inversions ($f = 0.1 - 1$ Hz) the velocity models were chosen alike. Even if the models seem dramatically smooth for time-reversal purposes, we argue that no unknown complexity should be added.

To generate the time-reversed wave field, the displacement is recorded at the surface receivers, flipped in time and then re-injected as three-component adjoint sources. For the propagation of the reverse field we use the same algorithm, setup and velocity model as for the forward simulation.

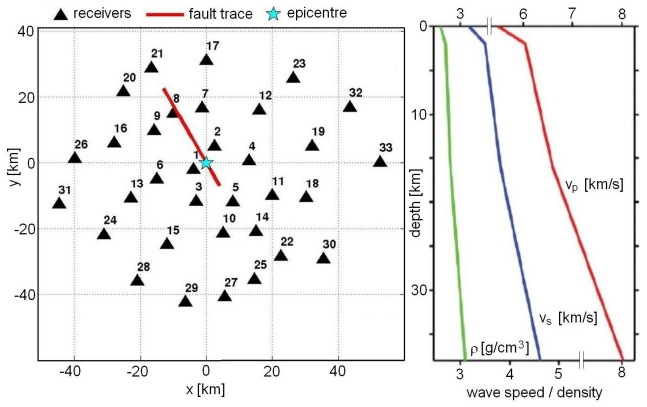

Fig. 1. Left: Geographic model setup. Stations are marked by triangles. The red line and the star mark the fault trace and the epicentre for the finite-fault simulations in Sect. 4. Right: Velocity and density model used in all synthetic simulations.

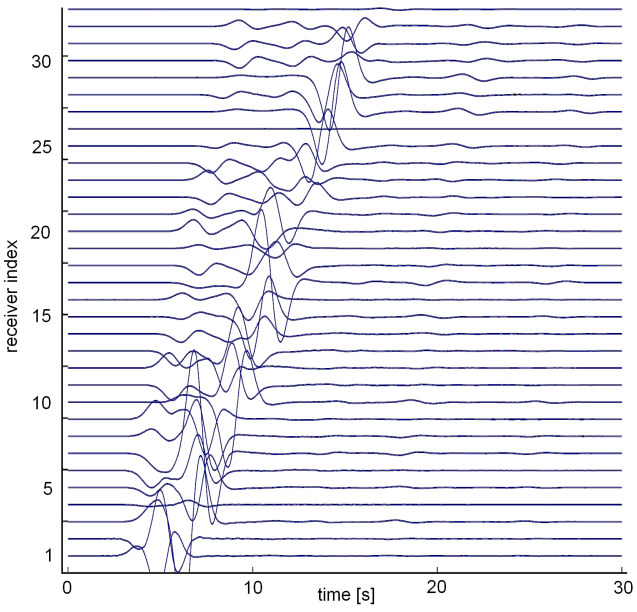

Fig. 2. N–S-component synthetic seismograms recorded at the 33 stations for a moment tensor point source with only $M_{xy} \neq 0$. The stations are sorted by distance to the epicentre and the traces are scaled to the maximum amplitude.

3 Synthetic points source simulations

3.1 Single point source

Our first series of tests with one single double couple point source is deliberately simplistic. It is intended to serve as a reference for TR under near-ideal conditions. The TR method should be able to recover the point source, because otherwise there would be little hope for success in finite-source imaging.

The moment tensor point-source, with only M_{xy} different from zero, is at 12.5 km depth. As source time function, we use a Gaussian wavelet with a dominant frequency of 1 Hz. The wave field is computed for the 33 receivers shown in the left panel of Fig. 1. To illustrate the characteristics of the waveforms, a selection of N–S-component synthetic seismograms is shown in Fig. 2.

As suggested by Eq. (1), we monitor the time-reversed strain component ϵ_{xy}. Snapshots of ϵ_{xy} at different times are shown at the point-source depth (12.5 km) in Fig. 3. The adjoint field starts to propagate from the stations with the largest epicentral distance and then focusses at the hypocentre as t approaches 0. Weaker or no focussing was observed for the other components of the strain tensor, as expected. While the focussing of ϵ_{xy} near the source can clearly be observed, $\epsilon_{xy}|_{t=0}$ is still significantly different from zero in other regions of the model volume that are distant from the source. These "ghost waves" result from the imperfect reconstruction of the forward wave field by a finite number of irregularly spaced adjoint sources located at the surface. Depending on the particular setup, ghost waves may dominate the reverse field, thus, masking the focussing at the source location.

The influence of ghost waves can be reduced by using, for instance, the energy $E = \frac{1}{2}\mathbf{v}^2$ to image the source (Fig. 3, lower right). This leads to the suppression of contributions far from the source, but also to a less optimal focussing directly at the source location. In numerous experiments, a similar trade-off could be observed for other functionals of the time-reversed field, including the different components of the rotation vector $\nabla \times \mathbf{u}$ and the rotation energy $\frac{1}{2}(\nabla \times \mathbf{u})^2$. This suggests that time-reversal imaging always involves a compromise between the focussing at the source and the suppression of ghost waves.

Our test with a point source moment tensor demonstrates that focussing in space and time can indeed be observed, at least under the previously described circumstances. This result motivates the study of more complex scenarios. In the following, we focus our attention on the xy-component of the time-reversed strain field, ϵ_{xy}. This restriction effectively corresponds to the injection of the prior information that the displacement on the infinitesimal or finite faults is a pure strike-slip.

3.2 Multiple point sources

Based on the encouraging results from the previous section, we add complexity to the source model and now consider three double couple point sources (only $M_{xy} \neq 0$) that are positioned along the fault of the SPICE Tottori benchmark (Fig. 1, left). The point sources have different initiation times

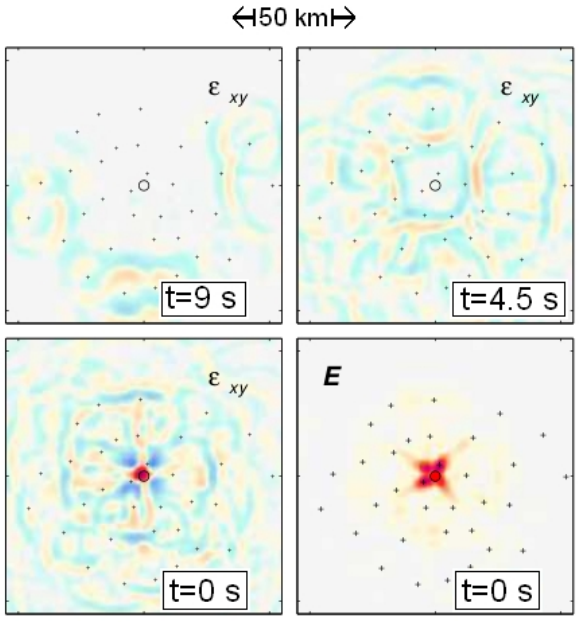

Fig. 3. Snapshots at the point-source depth (12.5 km) of the time-reversed strain field ϵ_{xy} at different times, and the energy $\frac{1}{2}\mathbf{v}^2$ (lower right) at $t = 0$.

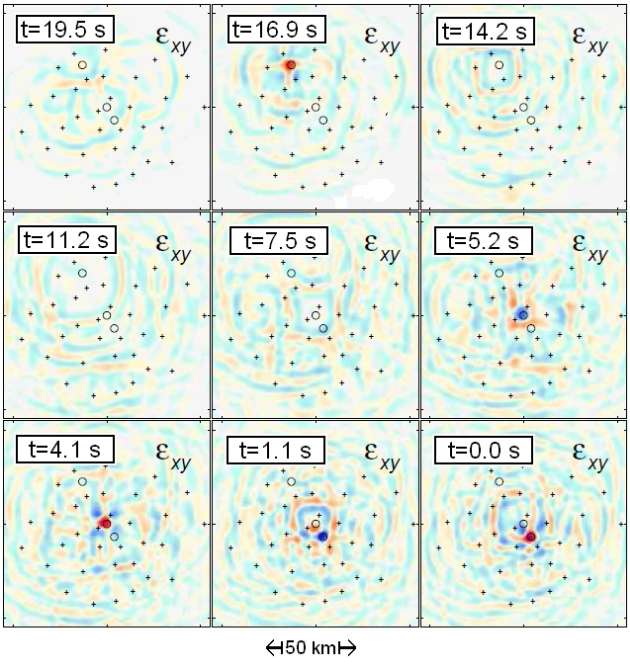

Fig. 4. Snapshots of the time-reversed strain field ϵ_{xy} at 12.5 km depth. Receiver and source locations are indicated by + and ∘, respectively. Focussing at all three source locations can be observed with an uncertainty of ∼ 5 km in space and ∼ 1 s in time. The observed hypothetical rupture velocity is $2 \pm 0.3\,\mathrm{km\,s^{-1}}$, compared to $2\,\mathrm{km\,s^{-1}}$ used to generate the forward wave field.

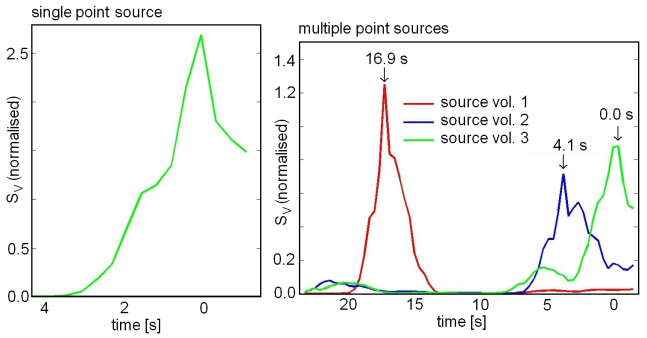

Fig. 5. Left: Time evolution of the normalised $S_V = \int_V \epsilon_{xy}^2 d^3\mathbf{x}$ for the single point source experiment from section 3.1. A pronounced peak occurs at the focal time $t = 0.0$ s. Right: The same as to the left, but for the multiple point source experiment from Sect. 3.2. Peaks can be observed at the focal times of the different point sources.

that correspond to a hypothetical rupture velocity of $2\,\mathrm{km\,s^{-1}}$ along the fault. The objective of this test is to reveal whether each of the three point sources can be resolved individually in both time and space.

Snapshots of the xy-component reverse strain, ϵ_{xy}, are shown in Fig. 4. Circles mark the point source locations. Moving from the upper left to the lower right corner, we observe focussing at each of the three source locations around their respective initiation times of 16.9 s, 4.1 s and 0.0 s, with an uncertainty of ∼ 1 s. The width of the regions where focussing can be observed is ∼ 5 km, which is close to the wavelength of the surface waves (∼ 3 km). From this we infer that the observed hypothetical rupture velocity is $2 \pm 0.3\,\mathrm{km\,s^{-1}}$. We have, thus, obtained a first, and probably optimistic, estimate of the achievable space-time resolution in the subsequent finite-source imaging experiments.

3.3 Quantitative assessment of focussing for point sources

So far, a purely visual analysis of the time-reversed wave fields was sufficient to observe focussing. However, in anticipation of more complex finite-source scenarios, we examine the usefulness of a more quantitative criterion for the focal time within a pre-defined test volume: starting with the point source simulations we determine the quantity $S_V = \int_V \epsilon_{xy}^2 d^3\mathbf{x}$ within a test volume V around the source locations, and then consider the time when the maximum occurs as an estimate of the focal time. Since the wavelengths range between 4 and 20 km, we let V extend 10 km in all directions around the hypocentre location. As we seek a quantitative comparison of the focussing for various setups, we normalise S_V by $S_\otimes = \int_\otimes \epsilon_{xy}^2 d^3\mathbf{x}$, where $\otimes$ denotes the remaining model volume outside V.

Figure 5 shows the normalised S_V for the single and multiple point source scenarios from Sects. 3.1 and 3.2, respectively.

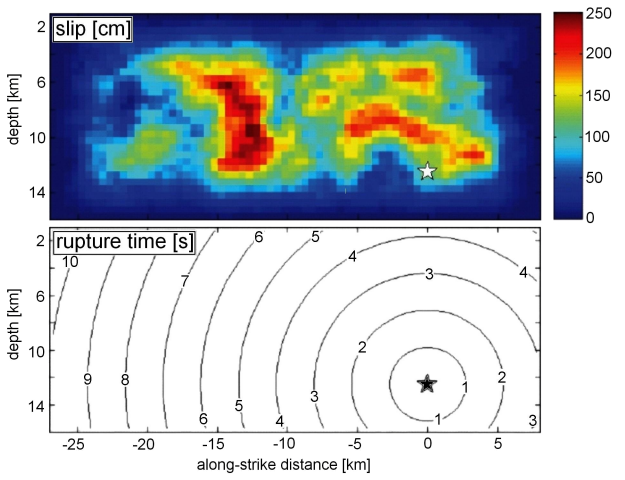

Fig. 6. Synthetic slip (top) and rupture time (bottom) distributions of the SPICE Tottori benchmark (Mai et al., 2007). Both the rupture speed and the rise time are constant at $v_r = 2.7\,\mathrm{km\,s^{-1}}$ and 0.8 s, respectively.

Distinct peaks at the expected source times are clearly visible in both cases. In the multiple point source experiment, we observe that the peaks for the first two sources (at 0.0 s and 4.1 s) are comparatively low, probably due to their spatial proximity and overlapping test volumes.

We conclude that the analysis of S_V is, at least for point sources, a useful diagnostic that allows us to estimate focal times and to compare the quality of focussing for different experimental setups.

Considering the multiple point source test successful, we now increase the complexity and make the transition to finite source models.

4 Synthetic finite source simulations

The SPICE kinematic source inversion blind test offers the opportunity to analyse the performance of TR finite source imaging. The blind test mimics the 2000 Tottori (Japan) earthquake that was recorded by a large number of strong-motion sensors. Figure 1 (left) shows the receiver configuration, the fault trace and the epicentre location. Synthetic seismograms for the 33 receivers are part of the benchmark package. They were generated by pure strike slip motion and with the slip and rupture time distributions shown in Fig. 6. The excited wave field has a maximum frequency of 3 Hz.

Snapshots of the corresponding time-reversed strain component ϵ_{xy} are shown in the top panel of Fig. 4. In reverse time, the rupture propagates in NW–SE direction. However, a clear focus restricted to the fault plane cannot be observed – in contrast to our expectation. The wave field remains diffuse, compared to the previous point source simulations. A robust inference concerning the hypocentre location and the initiation time is not possible.

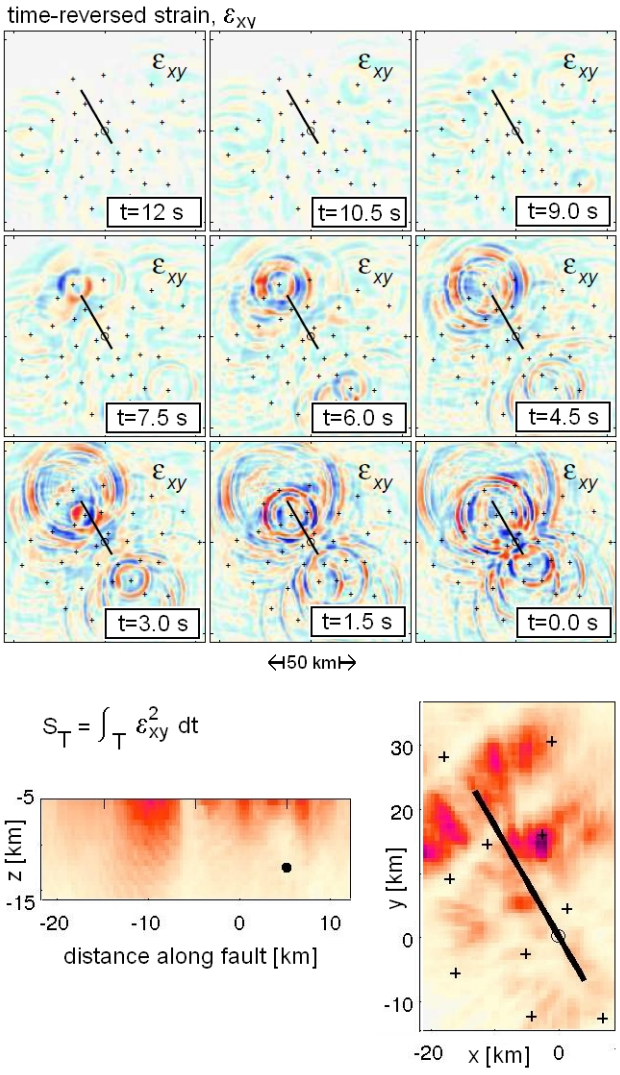

Fig. 7. Top: Snapshots of the time-reversed strain component ϵ_{xy} at 12.5 km depth. The fault trace is indicated by the black line. All snapshots are shown in the same amplitude range. Bottom: Cumulative squared strain $S_T = \int_T \epsilon_{xy}^2 dt$ plotted on the fault plane (left) and integrated over depth (right).

In an attempt to facilitate the visual identification of both the fault and the rupture process, we analyse the cumulative squared strain $S_T = \int_T \epsilon_{xy}^2 dt$. Based on physical intuition one would expect S_T to be large only in those regions where significant strain occurs consistently over a longer period of time, i.e., along the fault. However, neither S_T directly on the fault plane nor S_T integrated over depth allow any meaningful inference concerning the location of the fault or the original slip distribution (see the bottom panels of Fig. 4). In fact, S_T is largest near the surface, which reflects the dominance of surface waves in the time-reversed wave field. Moreover, S_T on the fault plane reaches a local maximum where the original slip distribution (Fig. 6) is close to zero. The depth-integrated S_T is largest far off the fault trace.

Similar efforts to enhance the focussing on the fault by integrating, for instance, ϵ_{xy} or $\frac{1}{2}\mathbf{v}^2$ over time, did not lead to any significant improvements. We are, therefore, led to the early conclusion that no obvious functional of the time-reversed field allows us to identify the fault plane or the slip distribution unambiguously. In what follows, we try to improve our results by (1) modifying the station distribution, and (2) weighting the adjoint sources.

4.1 Modifications of the station distribution

4.1.1 Dense regular grid of stations

The results from the previous section suggest that the number of stations and their spatial distribution provided insufficient information for the reconstruction of the original wave field. This motivates a synthetic test with a larger number of receivers (225 instead of 33) that are regularly spaced. While this scenario may be too optimistic in the near future, it provides valuable insight into TR finite source imaging under idealistic conditions.

For this experiment, we computed synthetic seismograms with the help of a Discontinuous Galerkin method (Käser and Dumbser, 2006) that allows us to model the discontinuous displacement on the fault with high accuracy. Snapshots of the resulting time-reversed strain component ϵ_{xy} are displayed in Fig. 8.

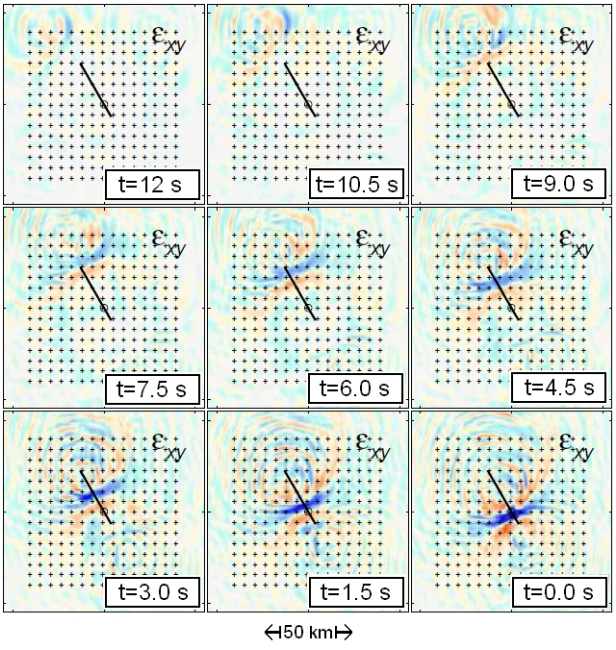

Fig. 8. Snapshots of the time-reversed strain component ϵ_{xy} at 12.5 km depth for the dense array of 225 regularly spaced receivers. The fault trace is indicated by the black line. All snapshots are shown in the same amplitude range.

Compared to Fig. 4 (original station distribution), we observe a sharper peak. Most of the energy propagates along the fault plane and in a direction that is consistent with the rupture time distribution (6, bottom). However, the focus is still elongated perpendicular to the fault, which complicates its unambiguous identification. Any inference on the details of the original slip distribution (Fig. 6) remains clearly impossible.

To obtain more useful results, we again explored a variety of functionals of the time-reversed field, including the time-integrated strain, the kinetic energy and the rotation amplitude. Neither of these functionals provided significant improvements, thus, confirming our earlier conclusion that the overall quality of the focussing is rather independent of the field used for imaging.

4.2 Station arrays

As an alternative to the previous densification of the receiver configuration, we investigate the installation of several small sub-arrays that are composed of four stations that form a 2 km by 2 km quadrangle. This geometry is intended to have a beam-forming effect that hopefully improves the focussing of the time-reversed field.

The corresponding time-reversed strain field ϵ_{xy} is shown in Fig. 9. The use of small sub-arrays clearly results in a more pronounced concentration of energy along the fault than with the original station setup (Figs. 1 and 4). However, the problem of unambiguously identifying the fault itself remains unresolved also with this configuration. Again, the use of various functionals of the time-reversed field does not lead to significantly better results.

The previous experiments seem to imply that modifications of the receiver geometry are unlikely to improve the reconstruction of the original wave field to an extent that is sufficient to infer the slip distribution on the fault or even the fault itself.

4.3 Weighting of adjoint sources

A visual analysis of this failure (see Figs. 4 and 9) reveals that the highly unequal contributions from different receivers may be part of the problem. While receivers close to the fault dominate the time-reversed field due to the high amplitudes of the recorded waveforms, receivers at larger distances make only negligible contributions. This suggests that the reconstruction of the original wave field may be improved by assigning weights to the adjoint sources at position $\mathbf{x}^r$ that compensate for the geometric amplitude reduction with increasing propagation distance. In the following, we examine the effects of two different schemes where the weights are proportional to (1) the squared epicentral distance, and (2) the inverse energy of the recorded waveforms, i.e., $2/\int \mathbf{v}(\mathbf{x}^r)^2 dt$. It is important to note that the weighting scheme based on the distance from the epicentre corresponds to the incorporation

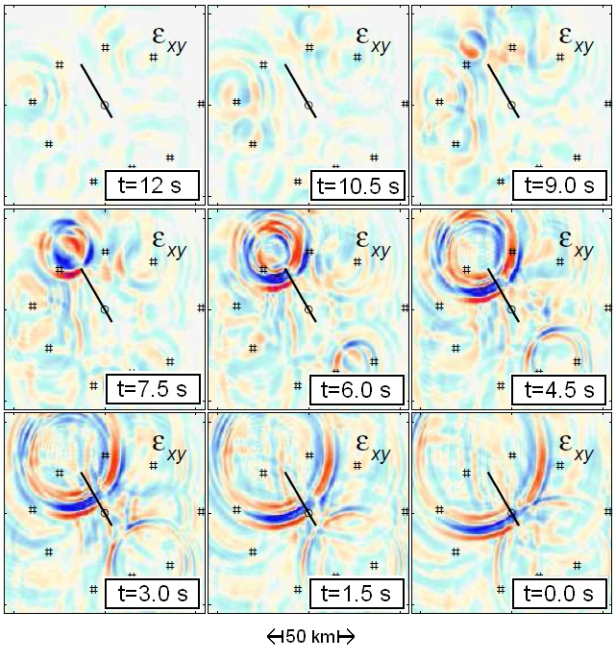

Fig. 9. Snapshots of the time-reversed strain component ϵ_{xy} at 12.5 km depth for the 9 sub-arrays composed of 4 receivers each. The fault trace is indicated by the black line. All snapshots are shown in the same amplitude range.

of prior information that may not be available in applications where the epicentral coordinates are among the unknowns.

Contrary to our expectations, the adjoint source weighting deteriorates the focussing of the time-reversed strain field, as can be seen in Fig. 10. The negative effect is strongest for the inverse energy weight. In both cases, neither the details of the rupture process nor the fault trace can be inferred from the images.

5 Time-reverse imaging of the Tottori earthquake source

One of the original motivations for this study was to use time reversal imaging in order to reveal the rupture details of the 2000 Tottori (Japan) earthquake. However, following the negative results of our finite-source synthetic experiments, we are forced to revise our ambitious goals, and to limit ourselves to the detection of the epicentre and the focal time.

For this real-data experiment, we use 111 surface recordings from the Japanese KiK-net (Fig. 11, http://www.kik.bosai.go.jp/), band-pass filtered between 0.03 and 0.5 Hz which is similar to the frequency range commonly used in kinematic source inversions. The dominant wavelength of the surface wave-dominated field is around 20 km, which is close to the estimated fault length of ~ 30 km (Semmane, 2005). We, therefore, expect to resolve only a point

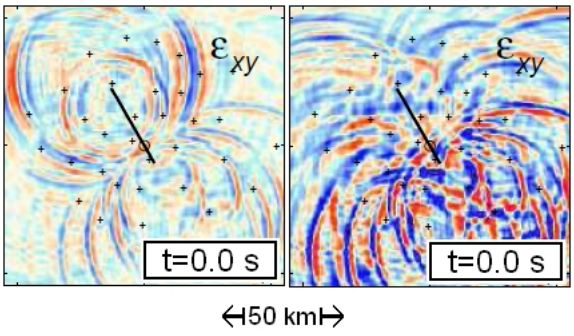

Fig. 10. Snapshots of the time-reversed strain component ϵ_{xy} at 12.5 km depth and $t = 0$ for the weighted adjoint sources. Left: weight proportional to the squared epicentral distance. Right: weight proportional to the inverse energy $2/\int \mathbf{v}(\mathbf{x}^r)^2 dt$.

source. The amplitude at all adjoint sources was set equal to one to remove the strong influence of stations close to the source. For the time-reversed field wave propagation, we use the layered Earth model described in Semmane (2005). All data processing was done using ObsPy, a newly developed python-based toolbox for seismology (Beyreuther et al., 2010).

Figure 12 shows the propagation of the time-reversed strain component ϵ_{xy} from $t = 30$ s to $t = -30$ s. We observe clear focussing around the focal time and epicentre location as estimated by Semmane (2005). The uncertainty in time is ~ 3 s, and the uncertainty in space is around 50 km, which is close to the dominant wavelength. The identification of the focal depth is not possible due to the comparatively long wavelengths and the presence of large-amplitude surface waves that mask the focussing of lower-amplitude body waves at greater depth. For negative times, i.e., prior to the initiation of the rupture, the time-reversed field propagates away from the epicentre, therefore, attesting to the appropriateness of the structural model. A very similar focussing and defocussing could be observed for the other strain components and various functionals of the time-reversed field.

To obtain a more quantitative estimate of the focal time, we proceed as in Sect. 3.3, where we computed the quantity $S_V = \int_V \epsilon_{xy} d^3\mathbf{x}$ for a volume V surrounding the inferred point-source location. The time evolution of S_V, shown in Fig. 13, reveals a pronounced peak that serves as an estimate of the focal time. Our estimate positions the focal time at $+3$ s relative to the initiation time of the rupture as inferred by Semmane (2005). This discrepancy is likely to be related to the inferred location of the Tottori hypocentre within an area of a small amount of final slip (e.g. Semmane, 2005; Piatanesi et al., 2007). Taking the corresponding rise times into account, this may explain a weak detectability by means of TR for the hypocentral parameters of the Tottori event. The peak in Fig. 13 is, therefore, likely to approximate the rupture time of the first large-slip region, or the centroid time

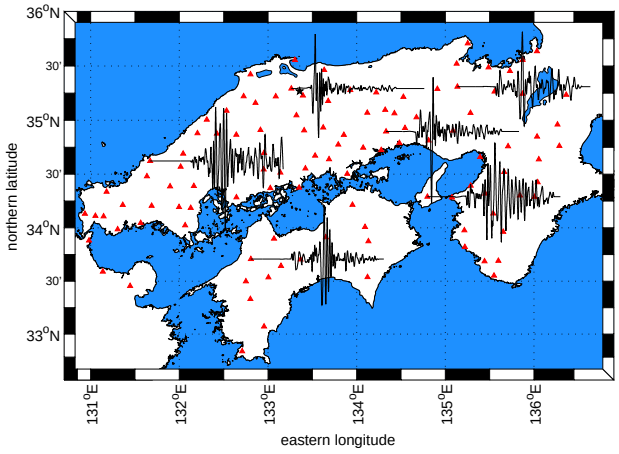

Fig. 11. Source-receiver geometry of the real-data TR experiment for the 2000 Tottori earthquake. Red triangles mark the positions of the 111 stations used in the experiment, and the black star indicates the epicentre as inferred by Semmane (2005). The seismograms shown are vertical component velocities in the chosen frequency band.

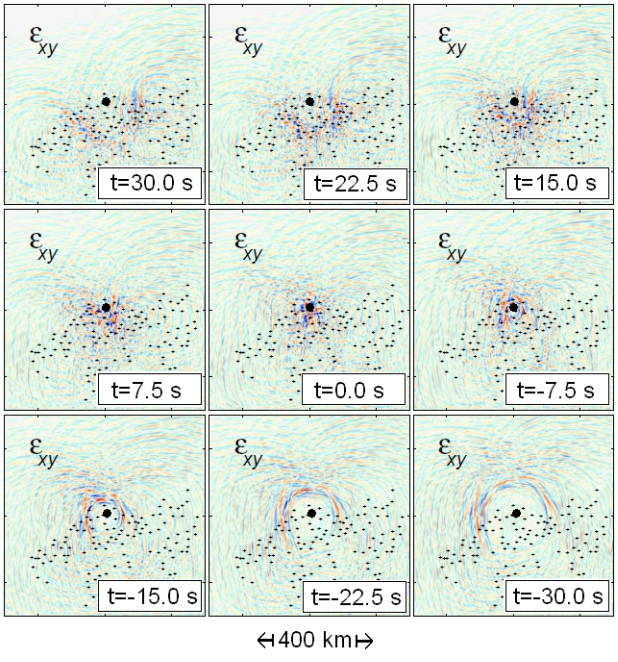

Fig. 12. Snapshots of the time-reversed strain component ϵ_{xy} at the surface for the Tottori data recorded at the 111 stations shown in Fig. 11. The coastlines are omitted to enhance the visibility of the time-reversed field. Estimates of both the focal time ($t = 0$ s) and the epicentre location (black dot) are taken from Semmane (2005).

of the whole event (both at about +4 s, according to Semmane (2005) or Piatanesi et al. (2007) rather than the precise initiation time of the finite-size rupture.

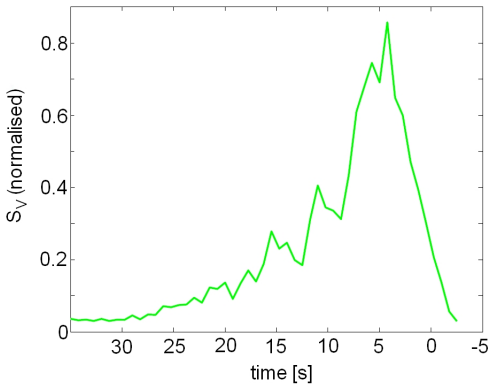

Fig. 13. Time evolution of the normalised $S_V = \int_V \epsilon_{xy}^2 d^3\mathbf{x}$ for a volume V that extends 20 km by 20 km around the epicentre as estimated from the time-reversal images from Fig. 12. The peak occurs at +3 s relative to the focal time estimated by Semmane (2005) ($t = 0$).

6 Discussion

In the previous sections, we explored the potentials and limitations of the TR imaging of seismic sources on regional scales. For this we studied a variety of scenarios with both synthetic and real data.

The potential of the method clearly lies in the estimation of the location and the timing of point sources. In a series of synthetic experiments, we were able to observe the focussing of the time-reversed field in the vicinity of the original point source location and the original focal time. The uncertainties in the source location and time are governed by the frequency content and the receiver configuration. Our point source scenarios provide a proof of principle, but they are idealistic in the sense that we disregarded errors in the data and the assumed Earth model.

Our primary interest was in the detection of finite-rupture processes. Unfortunately, however, neither the rupture details nor the position of the fault itself could be inferred from the properties of the time-reversed wave field. To improve this result, we analysed various functionals of the wave field (strain, energy, rotations), modified the receiver geometry (densification, sub-arrays) and applied weights to the adjoint sources in order to compensate for geometric spreading. None of these strategies can be considered successful.

The reasons for this failure are manifold:

1. Incomplete information: Firstly and most importantly, the information recorded at the surface is plainly insufficient to reconstruct the original wave field with an accuracy that allows for the unambiguous identification of the rupture process. For instance, the body wave energy radiated downwards is entirely disregarded. This distinguishes TR on regional scales from TR on global scales where information is lost only through dissipation.

2. Large-amplitude surface waves: Partly as a consequence of the previous item, the time-reversed field from stations that are distant from the fault is dominated by large-amplitude surface waves. The surface waves tend to mask the focussing of the lower-amplitude body waves that are primarily contributed by the stations closer to the fault. This effect results in a weak depth resolution, which means, in particular, that the focal depth can hardly be constrained.

3. The missing sink: An even more profound and general reason for failure is the incompleteness of the TR procedure. Our interest is in the seismic wave equation

$$\rho \ddot{\boldsymbol{u}}(\boldsymbol{x},t) - \nabla \cdot \boldsymbol{\sigma}(\boldsymbol{x},t) = \boldsymbol{f}(\boldsymbol{x},t) \quad (2)$$

where $\boldsymbol{u}$, σ and $\boldsymbol{f}$ denote the seismic displacement field, the stress tensor and an external force density. A complete time reversal of equation 2 would require the implementation of a sink $\boldsymbol{f}(\boldsymbol{x},-t)$ that acts as the counterpart of the source $\boldsymbol{f}(\boldsymbol{x},t)$ in the forward direction, and that absorbs elastic energy so that the time-reversed field is zero for $t < 0$. The sink, however, is disregarded simply because it is unknown. The missing sink poses a serious problem for finite-source inversions when fault segments are active at different times. The energy from segments that act late in the rupture process is not absorbed by the sink and, therefore, continues to propagate. The unabsorbed energy masks the focussing at the fault segments that act early in the rupture process. The immediate implication is that TR for finite sources is always dominated by those fault segments with large slip near the end of the rupture time.

4. Invisibility of small slip: A corollary of the previous item is that no information can be obtained about the rupture details on segments of the fault with small amount of final slip. This means, in particular, that the hypocentral parameters cannot be detected in those cases where the rupture initiation is associated with small slip.

5. Lack of prior information: The poor performance of TR finite-source imaging as compared to the classical kinematic source inversions is also due to the neglect of an apparently essential piece of prior information: The rupture occurs along a fault and is not diffusely distributed throughout the model volume.

6. Incomplete knowledge of the 3-D Earth structure: While excluded a priori in the synthetic experiments, inaccurate Earth models can prevent focussing in real-data applications. The focussing observed in our experiment with Tottori data suggests that the model is sufficient to explain at least the arrival times of the direct waves. However, the absence of horizontal heterogeneities in the model does not allow for the correct back-propagation of scattered or even multiple-scattered waves. This issue is closely related to

7. The insufficient complexity of 3-D Earth models that results either from the inherent smoothness of the Earth or the limited resolution of seismic tomography. The presence of strong multiple scattering is known to enhance focussing in laboratory experiments, but cannot be exploited in seismology where the knowledge about sub-wavelength heterogeneities is too inaccurate.

7 Conclusions

The principal conclusions to be drawn from our work are as follows: (1) Time-reversal imaging is well-suited to infer both the location and the timing of point sources. (2) Time-reversal imaging in the used frequency range is not able to detect the details of finite rupture processes. Neither modifications of the receiver configuration (within reasonable bounds) nor the weighting of adjoint sources lead to sufficient improvements. (3) The dominant causes for this failure are the incomplete recordings of wave field information at the surface, the presence of large-amplitude surface waves that deteriorate the depth resolution, the missing sink that should absorb energy radiated during the later stages of the rupture process, the invisibility of small slip and the neglect of prior information.

While our experiments are certainly not exhaustive, they nevertheless suggest that the limitations of TR imaging start where the source stops being point-localised.

Acknowledgements. HI and SK gratefully acknowledge support through the Geophysics Group at Los Alamos National Labs for their research visits in 2008. We thank the Leibniz Rechenzentrum Munich for providing access to their supercomputer facilities and the IT support team (Jens Oeser) at the Geophysics Section of the Department of Earth Sciences at LMU Munich. We are also grateful to Martin Mai for giving us access to the SPICE dataset. We are grateful to J.-P. Montagner and B. Artman whose comments improved the manuscript. This work would not have been possible without the support of the European Commission in connection with the Research and Training Network SPICE (spice-rtn.org) and the Initial Training Network QUEST (quest-itn.org).

Edited by: R. Carbonell

References

Allmann, B. P. and Shearer, P. M.: A high-frequency secondary event during the 2004 Parkfield earthquake., Science (New York, N.Y.), 318, 1279–83, doi:10.1126/science.1146537, http://www.ncbi.nlm.nih.gov/pubmed/18033878, 2007.

Artman, B., Podladtchikov, I., and Witten, B.: Source location using time-reverse imaging, Geophys. Prospect., 58, 861–873, doi:10.1111/j.1365-2478.2010.00911.x, 2010.

Beyreuther, M., Barsch, R., Krischer, L., Megies, T., Behr, Y., and Wassermann, J.: ObsPy: A Python Toolbox for Seismology, Seismol. Res. Lett., 81, 530–533, doi:10.1785/gssrl.81.3.530, 2010.

Bunge, H.-P., Hagelberg, C. R., and Travis, B. J.: Mantle circulation models with variational data assimilation: inferring past mantle flow and structure from plate motion histories and seismic tomography, Geophys. J. Int., 152, 280–301, doi:10.1046/j.1365-246X.2003.01823.x, 2003.

Cesca, S., Heimann, S., Stammler, K., and Dahm, T.: Automated procedure for point and kinematic source inversion at regional distances, J. Geophys. Res., 115, B06304, doi:10.1029/2009JB006450, 2010.

Chakroun, N., Fink, M., and Wu, F.: Time reversal processing in ultrasonic nondestructive testing, IEEE T. Ultrason. Ferr., 42, 1087–1098, doi:10.1109/58.476552, 1995.

Cotton, F. and Campillo, M.: Frequency domain inversion of strong motions: Application to the 1992 Landers earthquake, J. Geophys. Res., 100, 3961–3975, 1995.

Derode, A., Roux, P., and Fink, M.: Robust Acoustic Time Reversal with High-Order Multiple Scattering, Phys. Rev. Lett., 75, 4206–4209, doi:10.1103/PhysRevLett.75.4206, 1995.

Edelmann, G., Akal, T., Hodgkiss, W., and Kuperman, W.: An initial demonstration of underwater acoustic communication using time reversal, IEEE Journal of Oceanic Engineering, 27, 602–609, doi:10.1109/JOE.2002.1040942, 2002.

Fichtner, A.: Full seismic waveform modelling and inversion, Springer, Heidelberg, 2010.

Fichtner, A. and Igel, H.: Efficient numerical surface wave propagation through the optimization of discrete crustal models-a technique based on non-linear dispersion curve matching (DCM), Geophys. J. Int., 173, 519–533, doi:10.1111/j.1365-246X.2008.03746.x, 2008.

Fichtner, A., Bunge, H., and Igel, H.: The adjoint method in seismologyI. Theory, Phys. Earth Planet. In., 157, 86–104, doi:10.1016/j.pepi.2006.03.016, 2006.

Fichtner, A., Igel, H., Bunge, H.-P., and Kennett, B. L. N.: Simulation and Inversion of Seismic Wave Propagation on Continental Scales Based on a Spectral-Element Method, Journal of Numerical Analysis, Industrial and Applied Mathematics, 4, 11–22, 2009a.

Fichtner, A., Kennett, B. L. N., Igel, H., and Bunge, H.-P.: Full seismic waveform tomography for upper-mantle structure in the Australasian region using adjoint methods, Geophys. J. Int., 179, 1703–1725, doi:10.1111/j.1365-246X.2009.04368.x, 2009b.

Fink, M.: Time reversal in acoustics, Contemp. Phys., 37, 95–109, 1996.

Fink, M.: Time reversed acoustics, Phys. Today, 50, 34–40, 1997.

Fink, M. and Tanter, M.: Multiwave imaging and super resolution, Physics Today, 63, 28–33, 2010.

Gajewski, D. and Tessmer, E.: Reverse modelling for seismic event characterization, Geophys. J. Int., 163, 276–284 doi:10.1111/j.1365–246X.2005.02,732.x, 2005.

Hjörleifsdóttir, V.: Earthquake source characterization using 3D Numerical Modeling, Ph.D. thesis, California Institute of Technology, Pasadena, California, USA, 2007.

Ishii, M., Shearer, P. M., Houston, H., and Vidale, J. E.: Extent, duration and speed of the 2004 Sumatra-Andaman earthquake imaged by the Hi-Net array., Nature, 435, 933–6, doi:10.1038/nature03675, 2005.

Käser, M. and Dumbser, M.: An arbitrary high-order discontinuous Galerkin method for elastic waves on unstructured meshes – I. The two-dimensional isotropic case with external source terms, Geophys. J. Int., 166(2), 855–877, doi:10.1111/j.1365–246X.2006.03,051.x, 2006.

Kennett, B. L. N.: A new way to estimate seismic source parameters, Nature,f 302, 659–660, 1983.

Larmat, C., Montagner, J.-P., Fink, M., Capdeville, Y., Tourin, A., and Clévédé, E.: Time-reversal imaging of seismic sources and application to the great Sumatra earthquake, Geophys. Res. Lett., 33, L19312, doi:10.1029/2006GL026336, 2006.

Larmat, C. S., Guyer, R. A., and Johnson, P. A.: Tremor source location using time reversal: Selecting the appropriate imaging field, Geophys. Res. Lett., 36, L22304, doi:10.1029/2009GL040099, 2009.

Mai, P., Burjanek, J., Delouis, B., Festa, G., Francois-Holden, C., Monelli, D., Uchide, T., and Zahradnik, J.: Earthquake Source Inversion Blindtest: Initial Results and Further Developments, AGU Fall Meeting San Francisco, 2007.

McMechan, G. A.: Determination of source parameters by wavefield extrapolation, Geophys. J. R. astr. SOC., 71, 613–628, doi:10.1111/j.1365-246X.1982.tb02788.x, 1982.

McMechan, G. A., Luetgert, J. H., and Mooney, W. D.: Imaging of earthquake sources in Long Valley Caldera, California, 1983, Bull. Seismol. Soc. Am., 75, 1005–1020, 1985.

O'Brien, G. S., Lokmer, I., De Barros, L., Bean, C. J., Saccorotti, G., Metaxian, J.-P., and Patane, D.: Time reverse location of seismic long-period events recorded on Mt Etna, Geophys. J. Int., 184, 452–462, doi:10.1111/j.1365-246X.2010.04851.x, 2011.

Parvulescu, A. and Clay, C. S.: Reproducibility of signal transmissions in the ocean, Radio Electron. Eng., 29, 223–228, doi:10.1049/ree.1965.0047, 1965.

Piatanesi, A., Cirella, A., Spudich, P., and Cocco, M.: A global search inversion for earthquake kinematic rupture history: Application to the 2000 western Tottori, Japan earthquake, J. Geophys. Res., 112, B07314, doi:10.1029/2006JB004821, 2007.

Rietbrock, A. and Scherbaum, F.: Acoustic imaging of earthquake sources from the Chalfant Valley, 1986, aftershock series, Geophys. J. Int., 119, 260–268, doi:10.1111/j.1365-246X.1994.tb00926.x, 1994.

Semmane, F.: The 2000 Tottori earthquake: A shallow earthquake with no surface rupture and slip properties controlled by depth, J. Geophys. Res., 110, B03306, doi:10.1029/2004JB003194, 2005.

Steiner, B., Saenger, E. H., and Schmalholz, S. M.: Time-reverse modeling of microtremors: Application to hydrocarbon reservoir localization, Geophys. Res. Lett., 35, L03307, doi:10.1029/2007GL032097, 2008.

Sun, N.-Z.: Inverse problems in ground water modelling, Kluwer Academic Publishers, 1994.

Sutin, A. M., TenCate, J. A., and Johnson, P. A.: Single-channel time reversal in elastic solids, The Journal of the Acoustical Society of America, 116, 2779, doi:10.1121/1.1802676, 2004.

Talagrand, O. and Courtier, P.: Variational Assimilation of Meteorological Observations With the Adjoint Vorticity Equation. I: Theory, Q. J. Roy. Meteor. Soc., 113, 1311–1328, doi:10.1002/qj.49711347812, 2007.

Tarantola, A.: Theoretical background for the inversion of seismic waveforms including elasticity and attenuation, Pure Appl. Geophys., 128, 365–399, doi:10.1007/BF01772605, 1988.

Tromp, J., Tape, C., and Liu, Q.: Seismic tomography, adjoint methods, time reversal and banana-doughnut kernels, Geophys. J. Int., 160, 195–216, doi:10.1111/j.1365-246X.2004.02453.x, 2004.

Geophysical Journal International

Geophys. J. Int. (2011) **184,** 746–758 doi: 10.1111/j.1365-246X.2010.04858.x

Non-conforming hybrid meshes for efficient 2-D wave propagation using the Discontinuous Galerkin Method

Verena Hermann, Martin Käser and Cristóbal E. Castro

Department of Earth and Environmental Sciences, Geophysics Section, Ludwig-Maximilians-Universität, München, Germany.
E-mail: hermann@geophysik.uni-muenchen.de

Accepted 2010 October 16. Received 2010 September 14; in original form 2010 June 7

SUMMARY

We present a Discontinuous Galerkin finite element method using a high-order time integration technique for seismic wave propagation modelling on non-conforming hybrid meshes in two space dimensions. The scheme can be formulated to achieve the same approximation order in space and time and avoids numerical artefacts due to non-conforming mesh transitions or the change of the element type. A point-wise Gaussian integration along partially overlapping edges of adjacent elements is used to preserve the schemes accuracy while providing a higher flexibility in the problem-adapted mesh generation process. We describe the domain decomposition strategy of the parallel implementation and validate the performance of the new scheme by numerical convergence test and experiments with comparisons to independent reference solutions. The advantage of non-conforming hybrid meshes is the possibility to choose the mesh spacing proportional to the seismic velocity structure, which allows for simple refinement or coarsening methods even for regular quadrilateral meshes. For particular problems of strong material contrasts and geometrically thin structures, the scheme reduces the computational cost in the sense of memory and run-time requirements. The presented results promise to achieve a similar behaviour for an extension to three space dimensions where the coupling of tetrahedral and hexahedral elements necessitates non-conforming mesh transitions to avoid linking elements in form of pyramids.

Key words: Numerical solutions; Numerical approximations and analysis; Computational seismology; Wave propagation.

GJI Seismology

1 INTRODUCTION

Current research in seismology often relies upon appropriate computational methods to model particular wave phenomena with sufficient accuracy. In addition, with the increasing computational resources more realistic scenarios can be modelled and investigations can be carried out with higher resolution. Therefore, many different numerical methods have been developed, for example the finite-difference (FD) schemes (Madariaga 1976; Virieux 1984, 1986; Moczo *et al.* 2002; Saenger & Bohlen 2004; Geller & Takeuchi 1998; Kristek & Moczo 2006), the Fourier pseudospectral (PS) methods (Fornberg 1975; Carcione 1994; Fornberg 1996), finite-element (FE) approaches (Marfurt 1984; Bielak *et al.* 2003; Koketsu *et al.* 2004; Moczo *et al.* 2007), boundary integral equation methods (BIEM) and boundary element methods (BEM) (Bouchon & Sánchez-Sesma 2007) and spectral element methods (SEM) (Seriani & Priolo 1994; Komatitsch & Vilotte 1998; Komatitsch *et al.* 2004; Chaljub *et al.* 2003, 2007). Rather recently, the Discontinuous Galerkin Finite-Element method using a time integration based on Arbitrarily high-order DERivatives (ADER-DG) concepts (Titarev & Toro 2002) has been introduced into numerical seismology (Käser & Dumbser 2006; Dumbser & Käser 2006) and extended to viscoelastic (Käser *et al.* 2007) and anisotropic (de la Puente *et al.* 2007) media. Furthermore, important technical improvements concerning adaptive approximation orders and local time stepping have been achieved (Dumbser *et al.* 2007). The DG method has the advantage, that it can be formulated with arbitrary high-orders of accuracy in space and time, while at the same time unstructured meshes can be used to model complex geometries. However, regarding the CPU time, it turns out to be more efficient to compute on regular meshes instead of unstructured ones to reach a desired error level. Therefore, the performance of the ADER-DG method can be increased by combining different mesh types, that is creating hybrid meshes, similarly to certain FE methods (Ichimura *et al.* 2007, 2009) or to the combination of FE and FD methods (Moczo *et al.* 1997).

Furthermore, the mesh spacing—and therefore the stability-constrained maximal time step for explicit time stepping schemes—is usually determined by the shortest wavelength to be propagated. In fact, when waves propagate through different materials, their wavelengths might change and it is suitable to adapt the mesh spacing to the local velocity structure to optimize accuracy with respect to run time. This issue was studied in detail for the 2-D spectral-element method computing spherical-earth seismograms

(Nissen-Meyer *et al.* 2008). In this work, we propose an ADER-DG scheme that achieves high-order approximation properties on hybrid meshes consisting of regular quadrilateral and unstructured triangular elements where appropriate. In this context, we also introduce a straight forward refinement and coarsening strategy for velocity-adapted quadrilateral meshes. However, this procedure leads to non-conforming element interfaces. To this end, the presented ADER-DG scheme is able to treat both, hybrid meshes and non-conforming interfaces, using the same numerical methodology. Furthermore, this work serves as a feasibility study to analyse the correctness and performance of this new ADER-DG approach before extending it to tetrahedral and hexahedral meshes in three space dimensions. In this case, non-conformity of the mesh will be necessary to avoid pyramids as an additional element type that links tetrahedral with hexahedral meshes.

This paper is structured as follows: We first introduce the ADER-DG method focusing on the necessary changes in the flux computation across interfaces between adjacent elements which are needed to handle non-conforming boundaries. Then we present information on the parallelization strategy related to this new type of model discretization based on non-conforming hybrid meshes. In the following, we show results of convergence tests for validation of the parallel implementation of our scheme and present two different numerical examples of seismic wave propagation problems. Finally, we illustrate an application to a realistic scenario in the area of the city of Grenoble.

2 THE NUMERICAL SCHEME

We solve the elastic wave equation in two space dimensions using its velocity–stress formulation leading to the first-order hyperbolic system of partial differential equations (PDE) of the form

$$\frac{\partial Q_p}{\partial t} + A_{pq}\frac{\partial Q_q}{\partial x} + B_{pq}\frac{\partial Q_q}{\partial y} = S_p\,, \tag{1}$$

where $Q = (\sigma_{xx}, \sigma_{yy}, \sigma_{xy}, u, v)^{\mathrm{T}}$ is the vector of unknown stress components (σ_{xx}, σ_{yy}, σ_{xy}) and particle velocities (u, v), A and B are the square Jacobian matrices including the material properties, and S is a source term. Note that the space–time dependency of $Q = Q(\vec{x}, t)$ and $S = S(\vec{x}, t)$ as well as the space dependency of $A = A(\vec{x})$ and $B = B(\vec{x})$ are omitted to simplify the notation, where $\vec{x} = (x, y)$. Furthermore, we use the Einstein summation convention over indices. The pth component of the solution, Q_p, is numerically approximated inside each element (m) by $(Q_h^{(m)})_p$ via a linear combination of only space-dependent orthogonal polynomial basis functions $\theta_l(\xi, \eta)$ of degree N and only time-dependent degrees of freedom $\hat{Q}_{pl}^{(m)}(t)$, that is

$$\left(Q_h^{(m)}\right)_p(\xi, \eta, t) = \hat{Q}_{pl}^{(m)}(t)\,\theta_l(\xi, \eta)\,, \tag{2}$$

where index (ξ, η) denote the coordinates in reference space.

As we are using hybrid meshes, these general basis functions $\theta_l(\xi, \eta)$ defined in reference space can be different depending on the element type of the particular element $E^{(m)}$ (Fig. 1) and we introduce the following notation to distinguish them as

$$\theta_l(\xi, \eta) = \begin{cases} \Phi_l(\xi, \eta) & \text{if } E = E_T \text{ (element type is triangular),} \\ \Psi_l(\xi, \eta) & \text{if } E = E_Q \text{ (element type is quadrilateral).} \end{cases} \tag{3}$$

Explicit expressions for the basis functions $\Phi_l(\xi, \eta)$ on the triangular reference element E_T and for the basis functions $\Psi_l(\xi, \eta)$ on the quadrilateral reference element E_Q are given in Appendix A. For simplification, we will use the general notation E for an element and θ for the basis functions in the following. Therefore, depending on the particular element type the corresponding basis functions have to be substituted.

The derivation of the numerical Discontinuous Galerkin (DG) finite element scheme for the simulation of seismic wave propagation on purely triangular meshes has already been published in previous work (Käser & Dumbser 2006). Therefore, we avoid the repetition of a comprehensive derivation and refer the reader to this work for details. In brief, the multiplication of the eq. (1) by test functions θ_k and integrating over a finite element $E^{(m)}$ gives

$$\int_{E^{(m)}} \theta_k \frac{\partial Q_p}{\partial t}\mathrm{d}V + \int_{E^{(m)}} \theta_k \left(A_{pq}\frac{\partial Q_q}{\partial x} + B_{pq}\frac{\partial Q_q}{\partial y}\right)\mathrm{d}V = \int_{E^{(m)}} \theta_k S_p \mathrm{d}V. \tag{4}$$

Note that in the DG approach the test functions θ_k are chosen from the same space as the basis functions θ_l for the numerical approximation of the vector Q in (2). Then, integration of (4) by parts yields

$$\int_{E^{(m)}} \theta_k \frac{\partial Q_p}{\partial t}\mathrm{d}V + \int_{\partial E^{(m)}} \theta_k F_p\,\mathrm{d}S - \int_{E^{(m)}} \left(\frac{\partial \theta_k}{\partial x}A_{pq}Q_q + \frac{\partial \theta_k}{\partial y}B_{pq}Q_q\right)\mathrm{d}V = \int_{E^{(m)}} \theta_k S_p\,\mathrm{d}V, \tag{5}$$

where a so-called numerical flux F_p has been introduced in the surface integral because Q_q may be discontinuous at an element boundary. The main result of the derivation of the DG method for

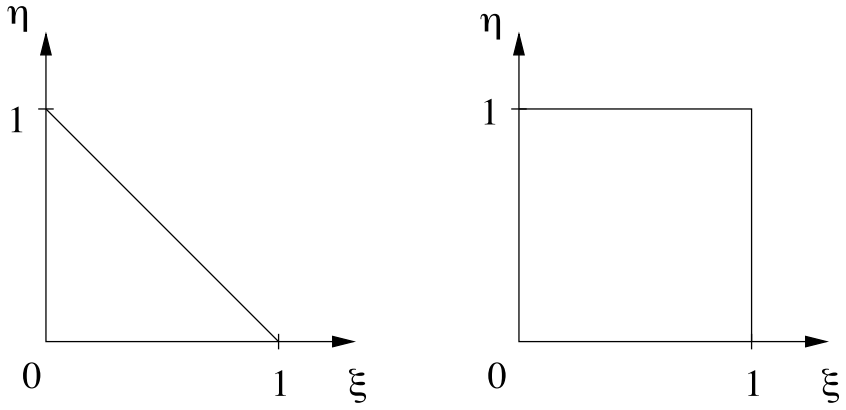

Figure 1. Definition of the triangular reference element E_T (left) and the quadrilateral reference element E_Q (right) in the $\xi\eta$-reference space.

the purpose of our work presented here is the occurrence of the flux term

$$\int_{\partial E^{(m)}} \theta_k F_p \, \mathrm{d}S \, . \tag{6}$$

A key ingredient for the implementation of the DG scheme is the computation of these numerical fluxes that exchange information across element interfaces $\partial E^{(m)}$ to extrapolate the numerical solution of stresses and velocities from one time level to the next one using an explicit time step scheme. In other words, the flux term represents a line integral along the boundary $\partial E^{(m)}$, that is along the edges, of an element $E^{(m)}$ over the product of the test function θ_k and the numerical flux F_p.

The subject of this work is now to construct a DG-scheme that allows for the usage of non-conforming hybrid meshes. Hence, we concentrate on the treatment of the flux term in (6). In fact, all other terms in (5), that is the computation of the volume integrals and the high-order time integration using Arbitrarily high-order DERivatives (ADER) (see Käser & Dumbser 2006), originally introduced in the framework of finite volume methods (Toro *et al.* 2001; Titarev & Toro 2002), remain unchanged. We just have to utilize the correct set of basis and test functions θ corresponding to the particular element type as specified in (3).

Now, considering the flux term in (6) the line integral can be decomposed into a sum of integrals over the element edges such that

$$\int_{\partial E^{(m)}} \theta_k F_p \, \mathrm{d}S = \sum_{j=1}^{n} |S^{(j)}| \int_0^1 \theta_k F_p^{(j)} \, \mathrm{d}\chi \, . \tag{7}$$

Here we integrate over the unit interval $\chi \in [0, 1]$ and therefore introduce the length of the jth edge $|S^{(j)}|$ as a scaling factor due to the interval transformation from the physical into the reference space. The number n of edges depends on the element type, that is $n = 3$ for triangles and $n = 4$ for quadrilaterals. The flux term $F_p^{(j)}$ also depends on the particular edge j and can be decomposed into an outgoing and an incoming part as shown in Chapter 4.14 in (LeVeque 2002) or in (Käser & Dumbser 2006). The explicit form of the flux term at edge j of element (m) can be written as

$$\begin{aligned} F_p^{(j)} = & \frac{1}{2} T_{pq}^{(j)} \left(A_{qr}^{(m)} + \left| A_{qr}^{(m)} \right| \right) \left(T_{rs}^{(j)} \right)^{-1} \hat{Q}_{sl}^{(m)} \theta_l^{(m)} \\ & + \frac{1}{2} T_{pq}^{(j)} \left(A_{qr}^{(m)} - \left| A_{qr}^{(m)} \right| \right) \left(T_{rs}^{(j)} \right)^{-1} \hat{Q}_{sl}^{(m_j)} \theta_l^{(m_j)} \, , \end{aligned} \tag{8}$$

where (m_j) is the index of the adjacent elements, that share edge (j) of element (m). As the flux terms are computed in an edge-aligned coordinate system such that the x-axis is perpendicular to the edge (j) only the local Jacobian matrix A_{qr} responsible for the x-direction is required while the solution vectors of the adjacent element edges (m_j) are needed. The necessary rotation matrices $T_{pq}^{(j)}$ and $(T_{rs}^{(j)})^{-1}$ for the forward and backward transformation of the edge-alignment are given explicitly in B.

Substituting (8) into (7) leads to

$$\begin{aligned} \int_{\partial E^{(m)}} \theta_k F_p \, \mathrm{d}S = & \sum_{j=1}^{n} \frac{1}{2} T_{pq}^{(j)} \left(A_{qr}^{(m)} + \left| A_{qr}^{(m)} \right| \right) (T_{rs}^{(j)})^{-1} \, |S^{(j)}| \, \hat{Q}_{sl}^{(m)} F_{kl}^{(j),0} \\ & + \sum_{j=1}^{n} \frac{1}{2} T_{pq}^{(j)} \left(A_{qr}^{(m)} - \left| A_{qr}^{(m)} \right| \right) (T_{rs}^{(j)})^{-1} \, |S^{(j)}| \, \hat{Q}_{sl}^{(m_j)} F_{kl}^{(j),i} \, , \end{aligned} \tag{9}$$

with the so-called flux matrices

$$F_{kl}^{(j),0} = \int_0^1 \theta_k^{(m)} \theta_l^{(m)} \mathrm{d}\chi \tag{10}$$

and

$$F_{kl}^{(j),i} = \int_0^1 \theta_k^{(m)} \theta_l^{(m_j)} \mathrm{d}\chi \, . \tag{11}$$

Here, the index 0 in (10) denotes that the integral uses test functions $\theta_k^{(m)}$ and basis functions $\theta_l^{(m)}$ from the same element (m) and local edge (j). These integrals can be computed exactly in a pre-processing step and stored in the n different flux matrices $F_{kl}^{(j),0}$, with $j = 1, \ldots, n$, for later flux calculations. So for triangular elements there are $n = 3$, for quadrilaterals $n = 4$ matrices to store, whereas the size of these square matrices depends on the number L of basis functions used and therefore on the order of the DG scheme, that is the degree N of the approximation polynomials. This relation is given by $L = (N + 1)(N + 2)/2$ and therefore $k, l = 0, \ldots, L - 1$. As $F_{kl}^{(j),0}$ only contains information about the element (m) itself, we can compute the outgoing flux given by the first line in (9) for the non-conforming hybrid meshes in exactly the same way as in previous DG approaches. We just have to make sure that the appropriate functions θ are used according to the element type.

If we consider the incoming flux given by the second line in (9) the situation is slightly more complicated. The index i in (11) is the local index of the edge of the adjacent element (m_j). In previous formulations of our ADER-DG schemes, the entire mesh had to consist of one element type and the meshes had to be conforming. In that case, two adjacent elements always shared exactly one entire edge between two element vertices and the matrices given by (11) could be computed exactly via a pre-processing step and stored for later flux calculations. In total there were n^2 matrices of size $L \times L$ to store as each of the n edges of an element (m) can share one of the n edges of the adjacent elements (m_j). Nevertheless, the storage of these few and rather small matrices was negligible compared to the storage requirement of the degrees of freedom $\hat{Q}_{pl}^{(m)}$ for all elements in the computational domain.

Now, in the case of non-conforming boundaries as shown in Fig. 2, two adjacent elements do not have to share exactly one common edge. Therefore, the flux matrices in (11) involving neighbour information have to be computed differently.

In fact, we calculate these integrals numerically by using Gauss–Legendre integration with a sufficiently high number of Gaussian integration points along the edge (j) of element (m) that ensures the exact integration of the product of the two polynomial basis functions θ. This is achieved by

$$\int_0^1 \theta_k^{(m)} \theta_l^{(m_j)} \mathrm{d}\chi = \sum_{c=1}^{N+1} \theta_k^{(m)}(\xi_c, \eta_c) \theta_l^{(m_j)}(\xi_c', \eta_c') w_c \, , \tag{12}$$

with N being the polynomial degree of the used basis functions θ, (ξ_c, η_c) and $(\xi'_c, \eta'_c)$the reference coordinates of the Gaussian integration points in the elements (m) and (m_j), respectively, and w_c the Gaussian weights.

According to (3), there are basically four different combinations of element pairs for such non-conforming hybrid meshes as shown in Fig. 2. Explicitly, this can lead to the following products of basis functions in (12) depending on the element types on either side of the interface: $\Phi_k^{(m)} \Phi_l^{(m_j)}$, $\Psi_k^{(m)} \Psi_l^{(m_j)}$, $\Phi_k^{(m)} \Psi_l^{(m_j)}$ and $\Psi_k^{(m)} \Phi_l^{(m_j)}$. In contrast to conforming meshes, the number of neighbouring elements across non-conforming boundaries can be larger than one. The exact number is determined by the locations of Gaussian integration points. As shown in Fig. 2 each Gaussian point, in general, might fall into a different neighbour or several Gaussian points might fall into the same neighbour. In the special case that a Gaussian

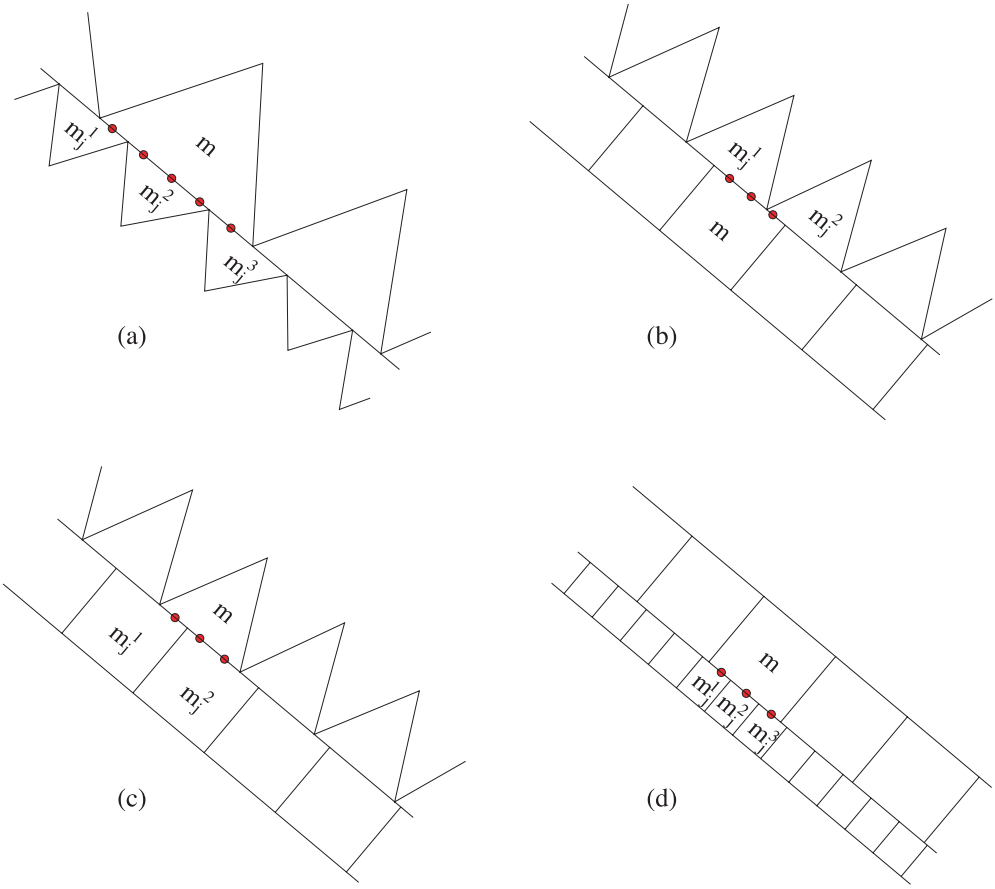

Figure 2. Examples of non-conforming mesh coupling for (a) purely triangular, (b,c) hybrid or (d) purely quadrilateral meshes. In all different cases, the numerical flux entering an element (m) over its edge (j) can be determined by Gauss–Legendre integration. This integration involves all adjacent elements (m_j^v) that include a Gaussian integration point (red dots) along edge (j) of element (m).

integration point falls directly on a vertex belonging to two adjacent neighbour elements, our search algorithm for identifying the neighbours will simply use the one which is found first in the element list. The other one is neglected. Note, that the variation in the number of neighbours also affects the amount of information to be communicated from one processor to another in the case of parallel computing, if the non-conforming interface happens to be a boundary between two partitions of the computational mesh. Therefore, we present a brief description of our parallelization strategy in the following.

3 PARALLELIZATION

Concerning the parallelization of the ADER-DG method it is only the numerical flux that requires information from neighbouring elements. Similar to the ADER-DG scheme working with conforming meshes (Käser & Dumbser 2006), we need the time-integrated degrees of freedom $\hat{Q}_{sl}^{(m_j)}$ and the basis functions $\theta_l^{(m_j)}$ of the neighbour element for computing the flux over an edge (j) according to (9). However, we now might have one or more neighbouring elements across a non-conforming interface and it is possible that some or even all of these neighbours do not belong to the same subdomain due to mesh partitioning. Therefore, the neighbour search carried out in a pre-processing step is based on the location of the Gaussian integration points used for flux integration. In the case of more than one neighbour across one edge the amount of MPI communication increases compared to conforming meshes. However, this increase in communication is negligible with respect to the computation time. Furthermore, in the mesh partitioning process non-conforming meshes have to be treated slightly different from conforming ones. As we are using the Metis software package (Karypis & Kumar 1998) to partition a mesh we have to partition the conforming triangular and quadrilateral parts of the hybrid mesh separately into the desired number of MPI subdomains that are then processed by different CPUs. To reduce the length of internal MPI-boundaries between different subdomains, we try to connect separate subdomains by minimizing the distances of their centres of gravity which we approximate by the sum of all element barycentres of subdomain divided by the corresponding number of elements belonging to this subdomain. We remark that this connection approach only works well for rather small numbers of subdomains. However, it does not significantly affect the efficiency of the scheme if the total number of elements inside a subdomain is large compared to the number of elements at the MPI boundary. For a visual example of the mesh partitioning strategy we refer to the following section of numerical tests. Nevertheless, it might be worth testing other mesh partitioners with respect to their capabilities of partitioning hybrid meshes more efficiently.

4 RESULTS

4.1 Convergence tests

Here, we validate the expected order of approximation and the implementation of our new ADER-DG approach with hybrid non-conforming meshes by performing a numerical convergence test. To this end, we solve the 2-D homogeneous elastic wave eq. (1) for $S = 0$ on a square shaped domain $\Omega = [-1, 1] \times [-1, 1] \in \mathbb{R}^2$ with periodic boundaries. We consider the initial condition

$$Q^0 = Q(\vec{x}, 0) = R_2^{A_n} \sin(k \cdot \vec{x}) + R_5^{A_n} \sin(k \cdot \vec{x}), \tag{13}$$

with the wave number

$$k = (k_x, k_y)^{\mathrm{T}} = \frac{2\pi}{25}(1, 1)^{\mathrm{T}}. \tag{14}$$

The vectors $R_2^{A_n}$ and $R_5^{A_n}$ denote the second and the fifth right eigenvectors of the normal Jacobian A in (1) oriented in direction $n = (1, 1)^{\mathrm{T}}$ normal to the wave front. Therefore, the initial condition (13) creates a plane sinusoidal *P*-wave travelling along the diagonal direction of Ω and a plane sinusoidal *S*-wave travelling into the opposite direction.

We use homogeneous material parameters in the matrices A and B (Käser & Dumbser 2006), that is Lamé constants $\lambda = 2$ and $\mu = 1$, and density $\rho = 1$ throughout the computational domain Ω leading to the constant wave propagation velocities $c_p = 2$ and $c_s = 1$ for the P and S waves, respectively. The final simulation time T is set to $T = 20\sqrt{2}$, such that the exact solution Q_e at simulation time $t = T$ is given by the initial condition, that is $Q_e(\vec{x}, T) = Q^0$. This way, the *P*- and *S*-wave travel 40 and 20 times, respectively, through the computational domain. The computations are performed on a sequence of 12 hybrid meshes (Fig. 3). We use the following notation: MESH M, with $M = 4s$, $s = 1, \ldots,$ 12 contains M quadrilateral elements along each boundary of Ω leading to mesh spacings $h_s = 2/M$. Therefore, the mesh spacings h_s cover a range from $h_1 = 0.5$ to $h_{12} = 0.0417$. The spacing of the triangular mesh scales with the same factors.

We then compute the errors of the numerical solution Q_{h_s} in the L^∞ and in the L^2 norm, given by

$$E^s_{L^\infty} = \max_{\Omega} |Q_{h_s} - Q_e| \tag{15}$$

and

$$E^s_{L^2} = \sqrt{\sum_{\Omega} |Q_{h_s} - Q_e|^2}, \tag{16}$$

where index h_s denotes the numerical solution depending on the mesh spacing.

The numerical convergence orders $\mathbb{O}_{L^\infty}$ and $\mathbb{O}_{L^2}$ can then be determined by two successively refined meshes and the convergence order is computed via

$$\mathbb{O}_{L^\infty} = \log\left(\frac{E^s_{L^\infty}}{E^{s-1}_{L^\infty}}\right) \Big/ \log\left(\frac{h_s}{h_{s-1}}\right). \tag{17}$$

For an arbitrarily chosen component σ_{xx} of the solution vector Q, Table 1 shows the errors measured by (15) and (16) together with the convergence orders, total number N_d of degrees of freedom, and the required CPU time for running the code on four processors of the SGI Altix 4700 (HLRB II) of the Leibniz-Rechenzentrum.

In Fig. 4, we illustrate the results in the L^∞ norm in dependence of the degrees of freedom, the mesh spacing h and the CPU time. It is clear from Table 1 that our implementation of the ADER-DG schemes reaches the expected convergence orders even on non-conforming hybrid meshes. Furthermore, Fig. 4 shows that the errors decrease with refining the mesh or increasing the order of polynomials. Furthermore, it is important to note that for a particular accuracy level the total number of degrees of freedom is always less for higher-order ADER-DG schemes, as typically found in other convergence test (Käser & Dumbser 2006; Dumbser & Käser 2006). This number depends on the amount of elements and the approximation order and is directly proportional to the required computer storage. In addition, we observe that the ADER-DG schemes reach a certain accuracy level faster by using a high-order approximation on coarse meshes.

4.2 Homogeneous material

After validating the convergence properties of the new ADER-DG scheme on non-conforming hybrid meshes we test its accuracy for a typical wave propagation problem using a point force as a source and compare the results to those obtained by the previous ADER-DG method on a conforming mesh as well as to an independent SEM method. For this test case, we take again a square shaped domain $\Omega = [-1, 1] \times [-1, 1] \in \mathbb{R}^2$ and use homogeneous material parameters $\lambda = 1$, $\mu = 1$ and $\rho = 1$ of an ideal Poisson solid.

This way, possibly occurring numerical artefacts can only be caused by the transition of waves through the non-conforming mesh boundaries. As source term we put a single force acting in x-direction at position $(0.31, -0.35)$ with a Ricker-pulse source time function of 8 Hz dominant frequency. Three receivers, located at

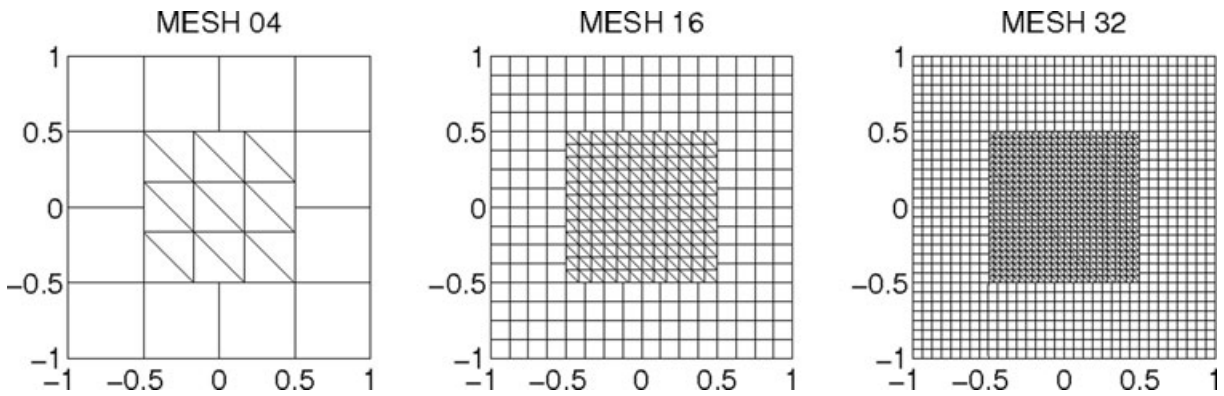

Figure 3. Three of the 12 different meshes for convergence tests showing successive refinements of the triangular and quadrilateral elements. All meshes are hybrid meshes with non-conforming interfaces between two mesh types.

Table 1. Errors and convergence rates of σ_{xx}, degrees of freedom and CPU-times from ADER-DG schemes of order $\mathbb{O}2$ to $\mathbb{O}9$ on non-conforming hybrid meshes.

h	E_{L^∞}	$\mathbb{O}_{L^\infty}$	E_{L^2}	$\mathbb{O}_{L^2}$	N_d	CPU [s]
7.14×10^{-2}	2.6354×10^{0}	–	3.6131×10^{0}	–	4410	2.90×10^{2}
6.25×10^{-2}	2.2751×10^{0}	0.8	3.1501×10^{0}	0.8	5760	3.43×10^{2}
5.00×10^{-2}	1.5622×10^{0}	2.4	2.2096×10^{0}	2.3	9000	7.51×10^{2}
4.17×10^{-2}	1.0490×10^{0}	3.0	1.5245×10^{0}	2.8	12960	1.35×10^{3}
1.00×10^{-1}	2.4524×10^{-1}	–	3.5994×10^{-1}	–	4500	2.11×10^{2}
8.33×10^{-2}	1.2126×10^{-1}	3.9	1.8288×10^{-1}	3.7	6480	3.61×10^{2}
7.14×10^{-2}	6.7487×10^{-2}	3.8	1.0307×10^{-1}	3.7	8820	5.44×10^{2}
6.25×10^{-2}	4.0985×10^{-2}	3.7	6.4898×10^{-2}	3.5	11520	8.44×10^{2}
1.67×10^{-1}	8.0675×10^{-2}	–	1.4083×10^{-1}	–	2700	1.05×10^{2}
1.25×10^{-1}	1.6277×10^{-2}	5.6	3.3277×10^{-2}	5.0	4800	1.86×10^{2}
1.00×10^{-1}	5.0019×10^{-3}	5.3	1.2019×10^{-2}	4.6	7500	3.51×10^{2}
8.33×10^{-2}	2.0084×10^{-3}	5.0	5.4290×10^{-3}	4.4	10800	5.68×10^{2}
7.14×10^{-2}	9.6098×10^{-4}	4.8	2.7815×10^{-3}	4.3	14700	9.19×10^{2}
2.50×10^{-1}	2.9958×10^{-2}	–	7.2238×10^{-2}	–	1800	5.27×10^{1}
1.67×10^{-1}	1.7515×10^{-3}	7.0	6.3241×10^{-3}	6.0	4050	1.63×10^{2}
1.25×10^{-1}	3.5419×10^{-4}	5.6	1.3255×10^{-3}	5.4	7200	3.38×10^{2}
1.00×10^{-1}	1.1372×10^{-4}	5.1	4.2085×10^{-4}	5.1	11250	7.10×10^{2}
2.50×10^{-1}	9.3617×10^{-4}	–	5.0878×10^{-3}	–	2520	1.03×10^{2}
1.67×10^{-1}	1.0519×10^{-4}	5.4	5.4015×10^{-4}	5.5	5670	3.33×10^{2}
1.25×10^{-1}	1.8534×10^{-5}	6.0	1.1989×10^{-4}	5.2	10080	6.84×10^{2}
1.00×10^{-1}	4.1622×10^{-6}	6.7	3.4222×10^{-4}	5.6	15750	2.70×10^{3}
2.50×10^{-1}	6.9493×10^{-5}	–	6.8803×10^{-4}	–	3360	2.74×10^{2}
1.67×10^{-1}	4.3120×10^{-6}	6.9	3.7859×10^{-5}	7.2	7560	8.82×10^{2}
1.25×10^{-1}	5.8470×10^{-7}	6.9	5.0051×10^{-6}	7.0	13440	1.78×10^{3}
1.00×10^{-1}	1.2294×10^{-7}	7.0	1.1322×10^{-6}	6.7	21000	3.61×10^{3}
2.50×10^{-1}	8.4521×10^{-6}	–	6.8741×10^{-5}	–	4320	5.08×10^{2}
1.67×10^{-1}	3.8038×10^{-7}	7.6	3.1907×10^{-6}	7.6	9720	1.67×10^{3}
1.25×10^{-1}	3.8508×10^{-8}	8.0	4.0066×10^{-7}	7.2	17280	3.19×10^{3}
1.00×10^{-1}	6.8260×10^{-9}	7.8	6.6945×10^{-8}	8.0	27000	6.39×10^{3}
2.50×10^{-1}	6.1153×10^{-7}	–	7.0857×10^{-6}	–	5400	8.02×10^{2}
1.67×10^{-1}	1.6421×10^{-8}	8.9	1.8870×10^{-7}	8.9	12150	4.31×10^{3}
1.25×10^{-1}	1.2834×10^{-9}	8.9	1.7835×10^{-8}	8.2	21600	8.49×10^{3}

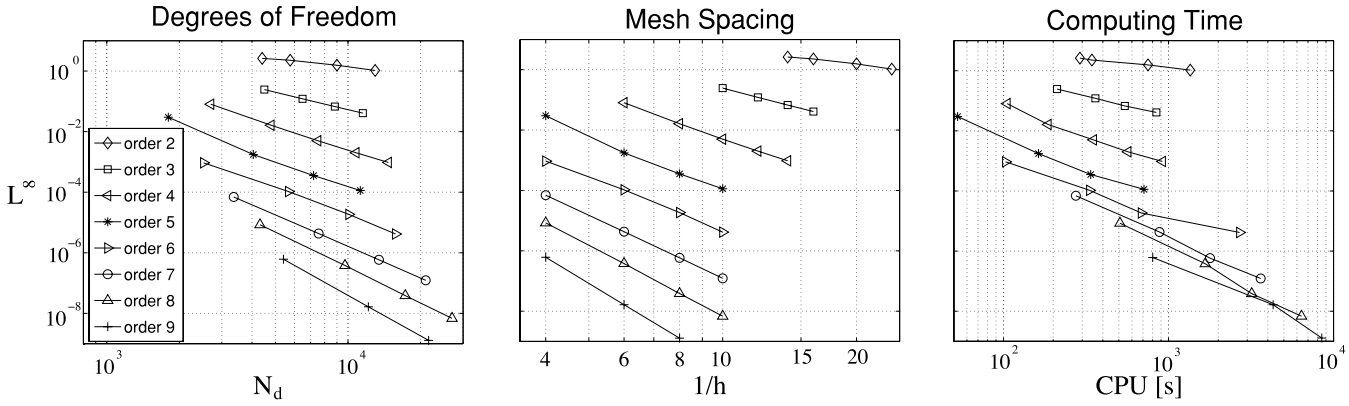

Figure 4. Errors in L_∞ norm in dependence of degrees of freedom, mesh spacing and CPU time on HLRB II.

$(-0.8, 0.0)$, $(-0.9, 0.4)$ and $(-0.9, 0.9)$ register the passing P and S waves during a 3 s simulation. We note that the source or receiver locations can be arbitrary and are also placed on a non-conforming interface. The non-conforming mesh and source and receiver locations are illustrated in Fig. 5(a). The mesh contains boundaries between non-conforming hybrid meshes as well as non-conforming boundaries between equal mesh types. The coarsest mesh spacing of $h = 0.06$ is taken for the innermost area. The conforming mesh used for the ADER-DG reference solution only consists of quadrilaterals of $h = 0.06$ which represents about half the S wavelength. Thus, a simulation with an approximation order 7 provides sufficient accuracy (Käser et al. 2008).

The differently colored elements in Fig. 5(a) show the eight subdomains for the parallel computation. As explained in Section 3 the

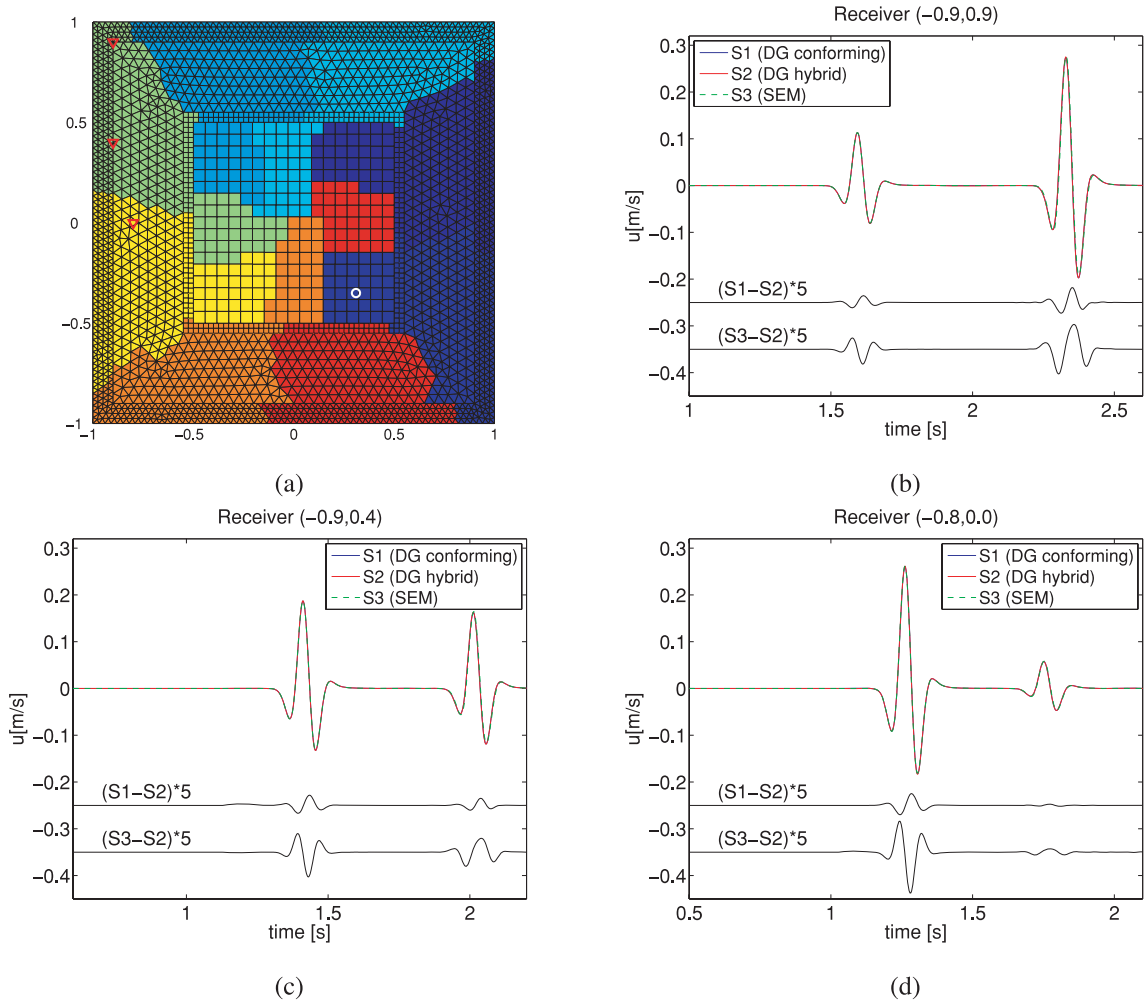

Figure 5. (a) Mesh of non-conforming boundaries with eight colour-coded partitions for parallel computations including the source (white circle) and three receiver locations (red triangles). (b,d) Comparisons of synthetic signals obtained by the DG method using a conforming and the hybrid mesh of (a) together with and independent SEM reference solution at the three different receivers. Difference seismograms between the non-conforming hybrid approach and the conforming or SEM reference amplified by a factor of 5 are shown as black lines.

partitioning routine attempts to assemble neighbouring subdomains of different zones. Starting with the dark blue part of processor 1 it performs well. However, combining the red parts for processor 8 does not permit any more freedom and the residual subdomains of each zone have to be gathered which might lead to non-compact subdomains increasing the number of edges requiring communication.

Figs 5(b)–(d) show time series of the velocity component u in x-direction computed with the ADER-DG method on a non-conforming, hybrid (red) and on a conforming (blue) mesh together with an independent reference solution obtained by the SEM on a regular quadrilateral mesh (dashed green). The comparison shows a visually perfect match between all signals and no numerical artefacts appear due the non-conforming boundaries that the waves propagate across. Seismograms showing the differences between the hybrid DG solution, the conforming DG solution, or the SEM reference are amplified by a factor of 5 and shown for each receiver. The small errors are acceptably small and might be mainly due to the different mesh spacings and time steps for each calculation. However, no spurious oscillations due to the non-conformity of the mesh is observed. This further validates the correctness of our approach and implementation of our new ADER-DG scheme for non-conforming hybrid meshes.

In the following, we treat a more challenging problem of a thin surface layer which is particularly important in computational seismology.

4.3 Thin layer

Here we present the performance of the proposed scheme in comparison to the previous approach with conforming meshes for a more sophisticated test case which considers a strong material contrast between a thin surface layer and an elastic half-space as presented similarly in previous work (Capdeville & Marigo 2008). The thin layer significantly influences the seismic wave field even if its thickness is small compared to the wave length. We use the computational domain $\Omega = [0, 35] \times [-15, 0]$ km^2 and a Ricker pulse of peak frequency 2 Hz as source time function acting as single force in x-direction at (15, −0.2) km. We put one receiver on the free surface at (25, 0) km and the other one into the half-space at (25, −2) km. The elastic parameters of the only 20-m-thick surface layer and

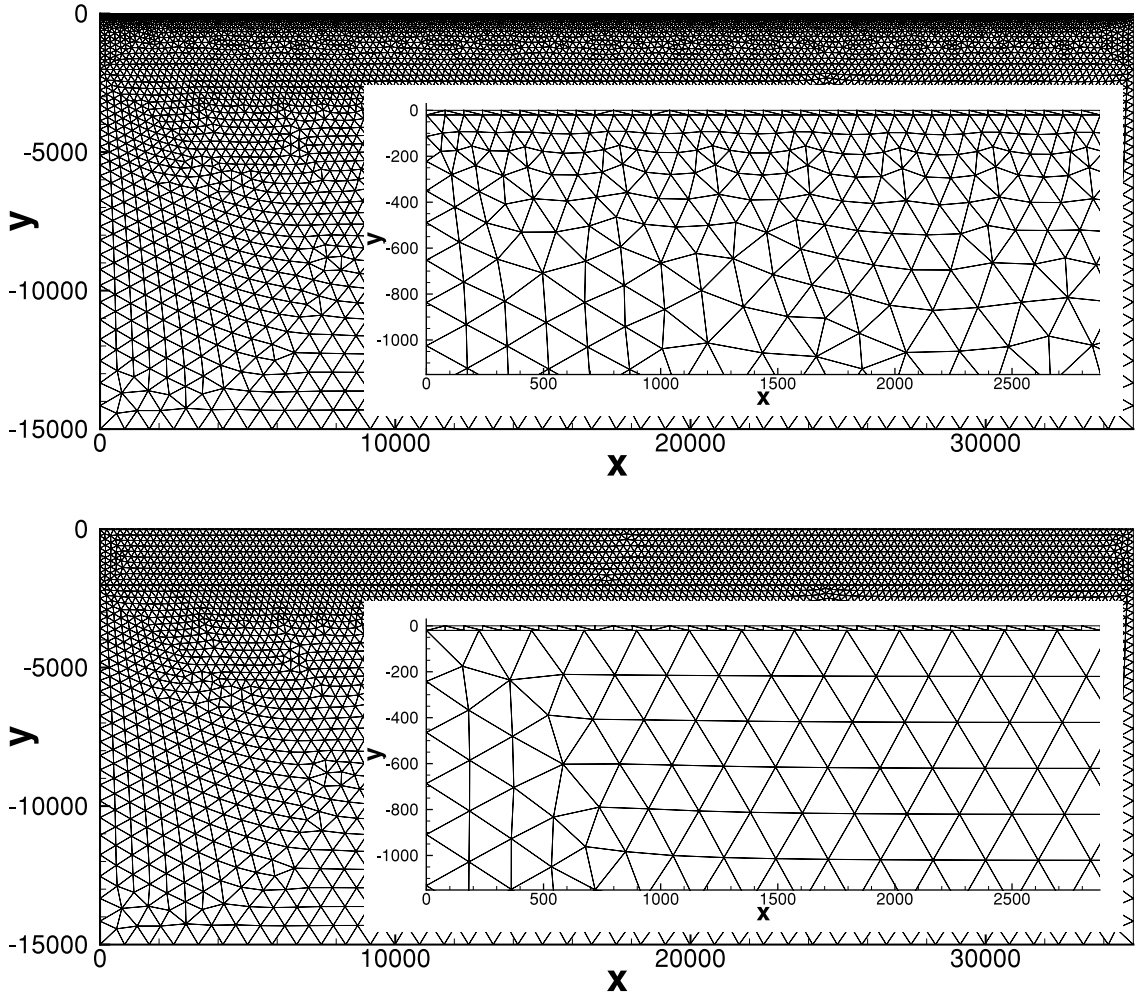

Figure 6. Meshes for thin layer test case with their zoomed sections to visualize the thin layer. Top: the conforming mesh, where the mesh spacing gradually grows from 80 to 225 m. Bottom: the non-conforming mesh with a sudden change in mesh spacing from 80 to 225 m.

Table 2. Definition of the elastic material parameters for the thin layer test case.

Zone	ρ(kg m^{-3})	μ(Pa)	λ(Pa)	c_p(m s^{-1})	c_s(m s^{-1})
Thin layer	2000	5.0e^8	5.0e^8	866	500
Half-space	2500	5.0e^9	5.0e^9	2449	1414

Table 3. Comparison of the conforming (CF) and non-conforming (NC) meshes for the thin layer test case computed on eight processors.

Mesh	Elements	Time step (s)	Restrictive layer	Run-time (s)
CF	13540	4.15×10^{-4}	Half-space	6737
NC	10010	5.52×10^{-4}	Thin layer	4881

the underlying elastic half-space are given in Table 2. The wave velocities in the half-space are 2.8 times faster than in the thin low-velocity surface layer. Note that the dominant *S* wavelength in the half-space is 707 m and therefore about 35 times larger than the layer thickness. To solve the problem with sufficient resolution (Käser et al. 2008) with an ADER-DG scheme of order $\mathbb{O}6$ in space and time, we choose an element edge length of 80 m in the thin layer, corresponding to about three elements per dominant *S* wavelength in this layer. However, due to the thickness of only 20 m of the layer, that has to be respected by the mesh, the triangular elements are slightly elongated as shown in the zoomed parts of Fig. 6. We also see the difference of the two meshes in the connection of the thin layer to the half-space. Although the non-conforming mesh has to adapt its elements in the high velocity half-space to the finely meshed interface, the non-conforming mesh allows for a mesh spacing proportional to the velocity structure immediately below the interface between the two layers. This leads to a reduction of the number of mesh elements, an increase in the critical time step length, and therefore a reduction of 27 per cent in total simulation time as summarized in Table 3. It is interesting that in the conforming mesh the time step is restricted by the high wave velocity and the small elements directly below the material interface in the half-space. The elements could be chosen larger from an accuracy point of view but the mesh conformity forces them to be small at the interface. By contrast, in the non-conforming approach the time step is restricted by the small elements in the thin layer which is due to the physics and geometry of the problem. The domain below 2 km basically serves as an enlargement to avoid any possible effects from the boundaries. Therefore, both the conforming and the non-conforming mesh are gradually coarsened to keep the computational cost low. Furthermore, we compute the same test case with an SEM code of spatial accuracy $\mathbb{O}6$ and time accuracy $\mathbb{O}2$ on a regular quadrilateral mesh with 20 m mesh spacing due to the thin layer.

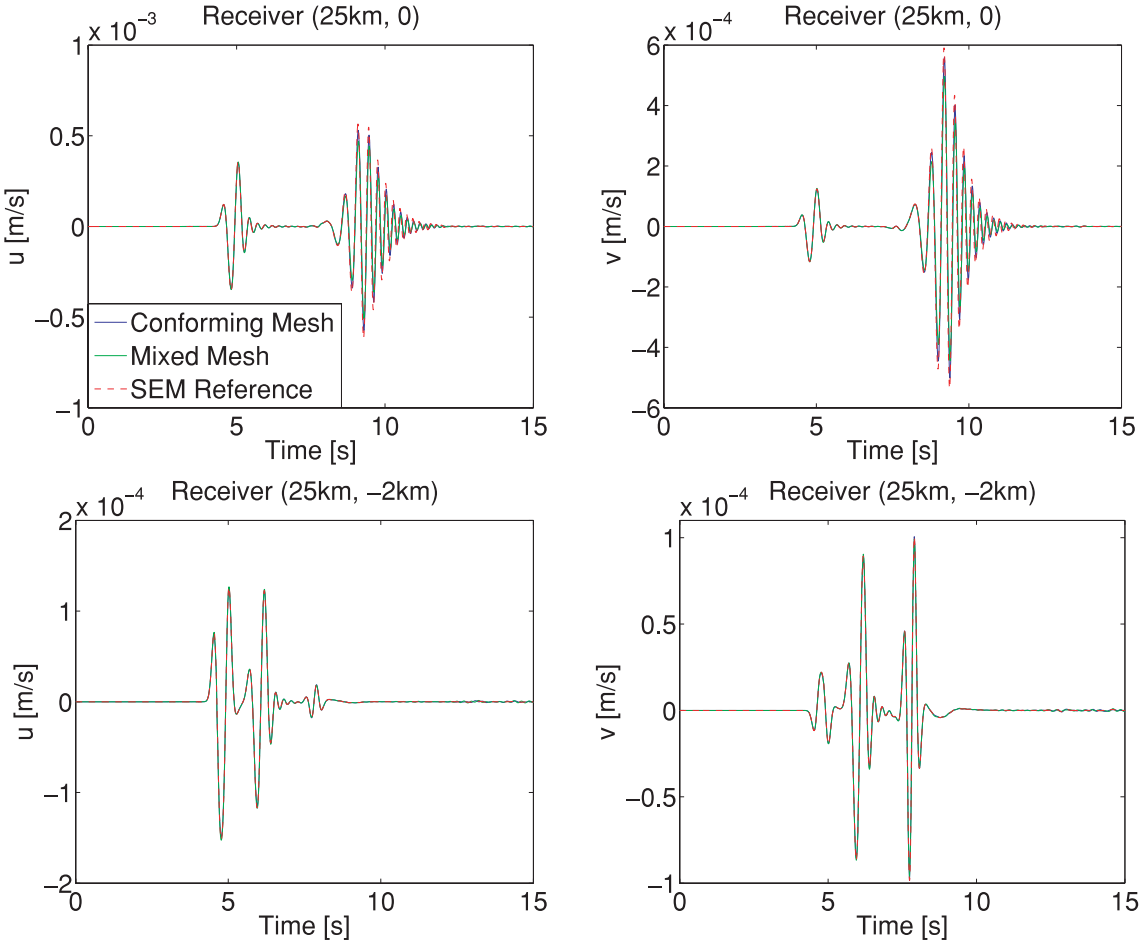

Figure 7. Seismograms of the horizontal and vertical velocity components u and v, respectively, of ground motion at the two receivers. The receiver at the surface (top) shows a clear and highly oscillating Rayleigh wave arriving after the direct wave. The burried receiver (bottom) exhibits the direct P wave and the interference of surface-reflected P and S waves.

The results in form of seismograms at the two receivers are presented in Fig. 7. Visually all three methods provide almost the same solutions except slight amplitude differences in the surface waves. The strong Rayleigh wave at the free surface receiver show some slight differences between the ADER-DG solutions and the independent SEM reference which is due to its extremely high resolution and accuracy using the regular 20 m mesh in the entire computational domain leading to 1 312 500 elements. However, we only detect a small amplitude misfit in this surface wave due to this enormous difference in mesh resolution, whereas the phases and all other waves fit perfectly.

In addition, we computed the same test case with the conforming mesh, but treating the element edges at the material interface as non-conforming to estimate the computational overhead due to the point-wise Gaussian flux integration (12) in comparison to the pre-computed flux matrices (11). The computational overhead seems to be negligible as the computing time due to the non-conforming treatment of the conforming mesh increased only by 0.8 per cent. For truely non-conforming meshes this increase is clearly dominated by the reduction of the computational cost due to a smaller number of elements and the possible increase of the time step. Therefore, the new ADER-DG method for non-conforming meshes seems to be particularly suited for such challenging wave propagation problems and gives additional flexibility as shown in the following more realistic example.

4.4 Grenoble—2-D

In this example we apply the new ADER-DG scheme to a more realistic scenario based on a modified benchmark (Chaljub *et al.* 2010). We are simulating seismic wave propagation in an east–west cross-section north of the city of Grenoble, France, using 50 km width, 27 km depth and 3 km height to include the mountain topography. This 2-D section is shown in Fig. 8 and cuts through two valleys filled with alluvial sediments. The wave speeds in these two basin structures are extremely slow compared to the surrounding solid bedrock as shown by the material parameters in Table 4. To account for the very slow wave speeds in the basin, we apply an extremely fine mesh on them which is visualized in the zoomed section in Fig. 8. Generating the mesh that adapts to the free surface topography and the two basin–bedrock interfaces has been achieved with a triangular mesh of varying mesh spacing. With increasing velocities in the deeper layers we adapt the mesh spacing of the quadrilaterals non-conformingly, but proportionally to the velocity structure to achieve an optimally large time step length. In Fig. 8 we show the colored mesh partition that is applied to the different zones first. Then different subdomains are collected from each zone and gathered on one processor for computation, that is each partition with the same colour is treated by the same processor.

We use an explosive source with a Ricker pulse of 3 Hz dominant frequency just below the Belledonne massif at location (35, −2.5)

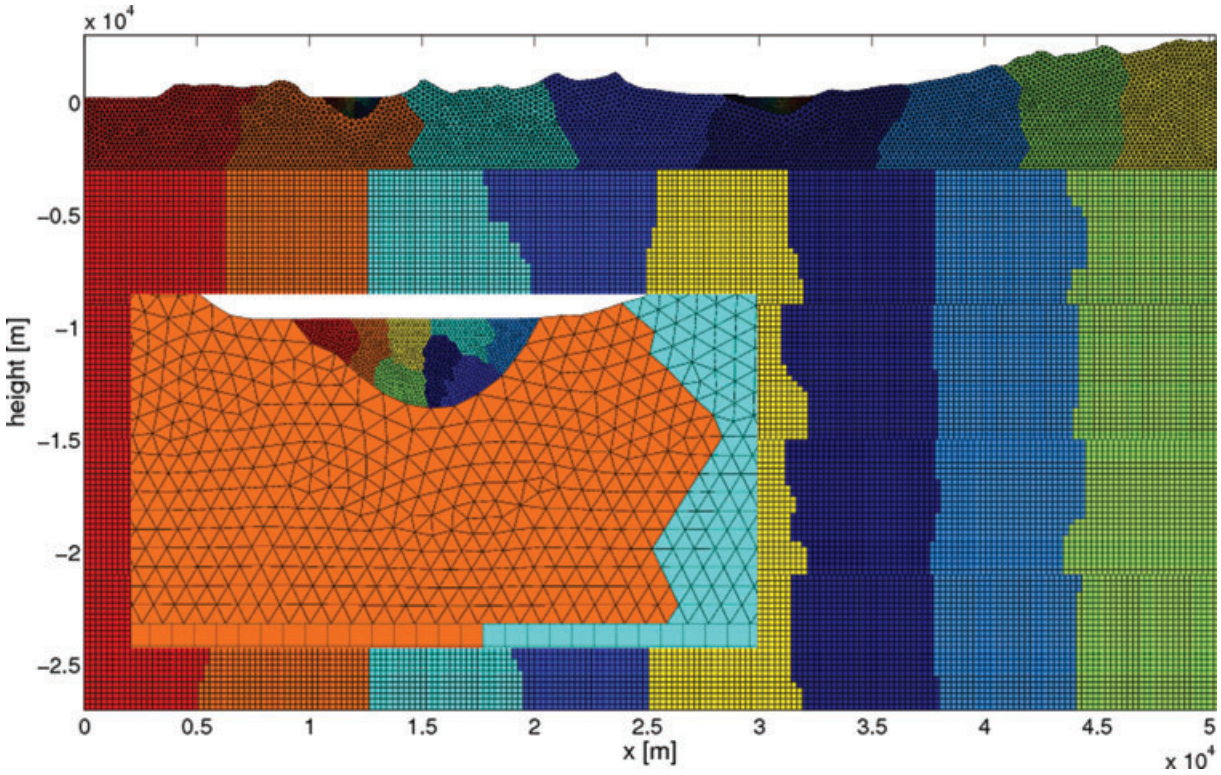

Figure 8. Non-conforming hybrid mesh for the wave propagation scenario of Grenoble with strongly variable material. Each colour indicates the mesh partition handled by one of the eight processors.

Table 4. Material parameters for the east–west cross-section north of Grenoble. The computational domain is divided into seven zones, the two basins and five layers of bedrock.

Zone	$\rho(\mathrm{kg\,m^{-3}})$	μ(Pa)	λ(Pa)	$c_p(\mathrm{m\,s^{-1}})$	$c_s(\mathrm{m\,s^{-1}})$
Basin 1 (west)	2.2×10^3	7.0×10^8	4.8×10^9	1.7×10^3	5.7×10^2
Basin 2 (east)	2.1×10^3	1.9×10^8	4.1×10^9	1.5×10^3	3.0×10^2
Layer 1 (top)	2.7×10^3	3.0×10^{10}	3.0×10^{10}	5.8×10^3	3.3×10^3
Layer 2	2.7×10^3	3.3×10^{10}	3.3×10^{10}	6.0×10^3	3.5×10^3
Layer 3	2.8×10^3	3.6×10^{10}	3.3×10^{10}	6.2×10^3	3.6×10^3
Layer 4	2.8×10^3	3.8×10^{10}	3.8×10^{10}	6.3×10^3	3.7×10^3
Layer 5 (bottom)	2.9×10^3	4.1×10^{10}	4.1×10^{10}	6.5×10^3	3.8×10^3

km. Fig. 9 illustrates snapshots for the horizontal velocity component of the seismic wave field at times 1.5, 3.0, 4.5 and 6.0 s. We observe the strong direct wave as well as reflected and converted waves from the free surface. In particular, there is a remarkable scattering of the seismic wave field due to the rough free surface topography. The maximum amplitude and longest duration of ground motion is obtained inside the basin as expected from the strong impedance contrast between the sediments and the bedrock. Looking especially at the downward propagating waves, no spurious numerical effects due to the non-conforming meshes can be observed in the snapshots, suggesting the use of the proposed ADER-DG with its additional flexibility of non-conforming and hybrid meshes and showing its potential for modelling problems with similar complexity or meshing requirements.

5 DISCUSSION

We have presented an extension of the high-order accurate Discontinuous Galerkin (DG) finite element scheme with ADER-time integration for non-conforming hybrid meshes in two space dimensions. The key issue is the modified computation of the flux integral between adjacent elements that do not need to share a common edge. The applied point-wise Gaussian integration preserves the scheme's high approximation order in space and time as confirmed by numerical convergence tests up to ninth order. Tests on different wave propagation problems show an excellent agreement with reference solutions and can lead to a clear reduction in computational cost due to an optimal adaptation of the mesh spacing to the physical and geometrical properties of the problem. We do not observe numerical artefacts caused by the non-conformity of the mesh and provide a simple mesh refinement or coarsening strategy for regular quadrilateral meshes to use an optimal time step length. Also the parallel implementation of the ADER-DG approach for non-conforming unstructured meshes performs well. The results are encouraging and promise to achieve similar benefits from the mesh coupling of tetrahedral and hexahedral elements in three space dimensions which is subject to our current research and developments.

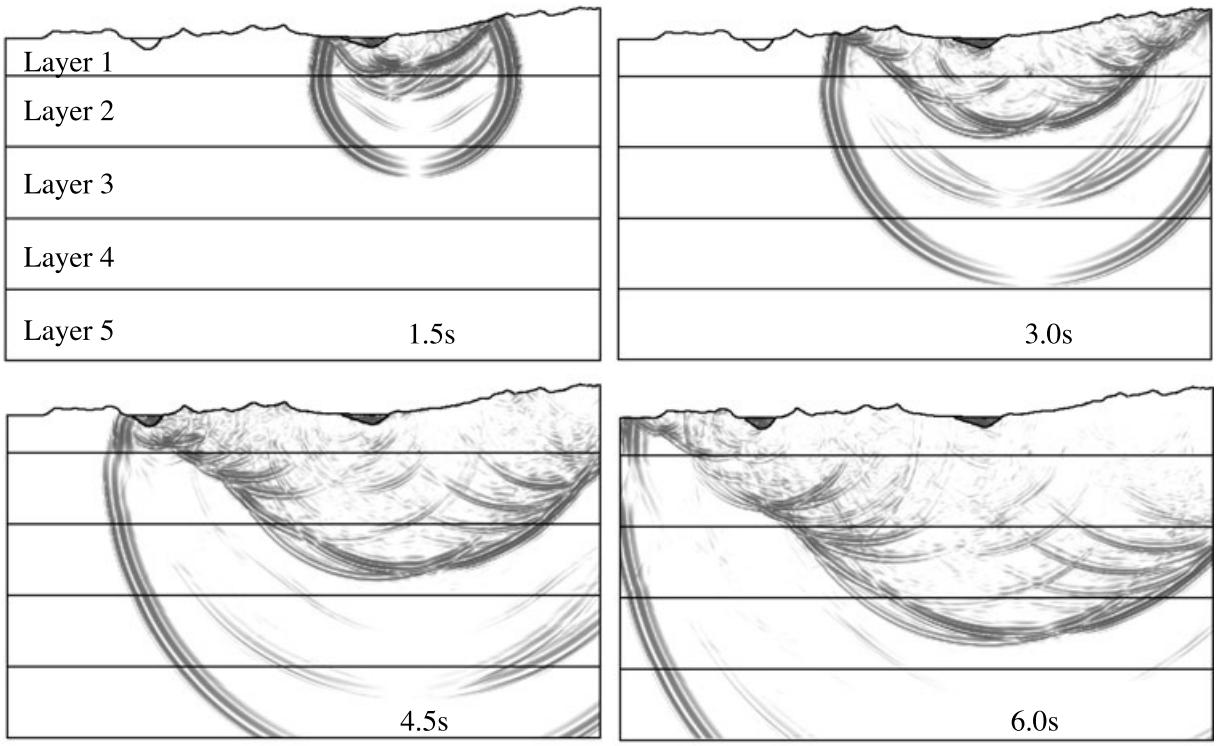

Figure 9. Snapshots of the horizontal seismic velocity component *u* in the 2-D section north of Grenoble for four different times. Note the strong scattering of the wave field due to the rough free surface topography.

ACKNOWLEDGMENTS

The authors thank the DFG (Deutsche Forschungsgemeinschaft) for the support through the Emmy Noether-Program (KA 2281/2-1). Moreover, we want to thank J.P. Ampuero for providing the SEM code to produce the independent reference solutions. The assistance by the local system administrator J. Oeser when using the Linux-Cluster of our department is also appreciated.

REFERENCES

Bielak, J., Loukakis, K., Hisada, Y. & Yoshimura, C., 2003. Domain reduction method for three-dimensional earthquake modeling in localized regions. Part I: Theory, *Bull. seism. Soc. Am.,* **93,** 817–824.

Bouchon, M. & Sánchez-Sesma, F., 2007. Boundary integral equations and boundary elements methods in elastodynamics, in *Advances in Wave Propagation in Heterogeneous Earth,* pp. 157–189, eds Wu, R.-S.& Maupin, V., Elsevier - Academic Press, London.

Capdeville, Y. & Marigo, J., 2008. Shallow layer correction for spectral element like methods, *Geophys. J. Int.,* **172**(3), 1135–1150.

Carcione, J., 1994. The wave equation in generalised coordinates, *Geophysics,* **59,** 1911–1919.

Chaljub, E., Capdeville, Y. & Vilotte, J.-P., 2003. Solving elastodynamics in a fluid-solid heterogeneous sphere: a parallel spectral element approximation on non-conforming grids, *J. Comput. Phys.,* **187**(2), 457–491.

Chaljub, E., Komatitsch, D., Vilotte, J.-P., Capdeville, Y., Valette, B. & Festa, G., 2007. Spectral-element analysis in seismology in advances in wave propagation in heterogeneous earth, *Adv. Geophys.,* **48,** 365–419.

Chaljub, E., Moczo, P., Tsuno, S., Bard, P.-Y., Kristek, J., Käser, M., Stupazzini, M. & Kristekova, M., 2010. Quantitative comparison of four numerical predictions of 3D ground motion in the grenoble valley, France, *Bull. seism. Soc. Am.,* **100**(4), 1427–1455.

Cockburn, B., Karniadakis, G. & Shu, C., 2000. Discontinuous Galerkin Methods, Lecture Notes in Computational Science and Engineering, Springer, Berlin.

de la Puente, J., Käser, M., Dumbser, M. & Igel, H., 2007. An arbitrary high order discontinuous Galerkin method for elastic waves on unstructured meshes IV: Anisotropy, *Geophys. J. Int.,* **169**(3), 1210–1228.

Dumbser, M. & Käser, M., 2006. An arbitrary high order discontinuous Galerkin method for elastic waves on unstructured meshes II: The three-dimensional case, *Geophys. J. Int.,* **167**(1), 319–336.

Dumbser, M., Käser, M. & Toro, E.F., 2007. An arbitvary high order discontinuos Galerkin method for elastic waves on unstructured meshes V: Local time stepping and p-adaptivity, *Geophys. J. Int.,* **171**(2), 695–717.

Fornberg, B., 1975. On a Fourier method for the integration of hyperbolic equations, *Soc. Industr. Appl. Math., J. Num. Anal.,* **12,** 509–528.

Fornberg, B., 1996. *A Practical Guide to Pseudospectral Methods,* Cambridge University Press, Cambridge.

Geller, R. & Takeuchi, N., 1998. Optimally accurate second-order time-domain finite difference scheme for the elastic equation of motion: one-dimensional case, *Geophys. J. Int.,* **135,** 48–62.

Ichimura, T., Hori, M. & Kuwamoto, H., 2007. Earthquake motion simulation with multiscale finite-element analysis on hybrid grid., *Bull. seism. Soc. Am.,* **97,** 1133–1143.

Ichimura, T., Hori, M. & Bielak, J., 2009. A hybrid multiresolution meshing technique for finite element three-dimensional earthquake ground motion modelling in basins including topography., *Geophys. J. Int.,* **177,** 1221–1232.

Karypis, G. & Kumar, V., 1998. Multilevel k-way partitioning scheme for irregular graphs, *J. Parallel Distrib. Comput.,* **48,** 96–129.

Käser, M. & Dumbser, M., 2006. An arbitrary high order discontinuous Galerkin method for elastic waves on unstructured meshes I: The two-dimensional isotropic case with external source terms, *Geophys. J. Int.,* **166**(2), 855–877.

Käser, M., Dumbser, M., de la Puente, J. & Igel, H., 2007. An arbitrary high order discontinuous Galerkin method for elastic waves on unstructured meshes III: Viscoelastic attenuation, *Geophys. J. Int.,* **168**(1), 224–242.

Käser, M., Hermann, V. & de la Puente, J., 2008. Quantitative Accuracy Analysis of the Discontinuous Galerkin Method for Seismic Wave Propagation, *Geophys. J. Int.,* **173**(3), 990–999.

Koketsu, K., Fujiwara, H. & Ikegami, Y., 2004. Finite-element simulation of seismic ground motion with a voxel mesh. *Pure appl. geophys.,* **161,** 2183–2198.

Komatitsch, D. & Vilotte, J., 1998. The spectral-element method: an efficient tool to simulate the seismic response of 2D and 3D geological structures, *Bull. seism. Soc. Am.,* **88,** 368–392.

Komatitsch, D., Liu, Q., Tromp, J., Süss, P., Stidham, C. & Shaw, J.H., 2004. Simulations of ground motion in the Los Angeles basin based upon the spectral element method, *Bull. seism. Soc. Am.,* **94**(1), 187–206.

Kristek, J. & Moczo, P., 2006. On the accuracy of the finite-difference schemes: the 1d elastic problem, *Bull. seism. Soc. Am.,* **96**(6), 2398–2414.

LeVeque, R., 2002. *Finite Volume Methods for Hyperbolic Problems,* Cambridge University Press, Cambridge.

Madariaga, R., 1976. Dynamics of an expanding circular fault, *Bull. seism. Soc. Am.,* **65,** 163–182.

Marfurt, K., 1984. Accuracy of finite-difference and finite-element modeling of the scalar and elastic wave equations, *Geophysics,* **49,** 533–549.

Moczo, P., Bystricky, E., Kristek, J., Carcione, J. & Bouchon. M., 1997, Hybrid modeling of P-SV seismic motion at inhomogeneous viscoelastic topographic structures, *Bull. seism. Soc. Am.,* **87,** 1305–1323.

Moczo, P., Kristek, J., Vavrycuk, V., Archuleta, R. & Halada, L., 2002. 3D heterogeneous staggered-grid finite-difference modeling of seismic motion with volume harmonic and arithmetic averaging of elastic moduli and densities, *Bull. seism. Soc. Am.,* **92**(8), 3042–3066.

Moczo, P., Kristek, J., Galis, M., Pazak, P. & Balazovjech, M., 2007. The finite-difference and finite-element modeling of seismic wave propagation and earthquake motion, *Acta physica slovaca,* **57**(2), 177–406.

Nissen-Meyer, T., Fournier, A. & Dahlen, F., 2008. A 2-d spectral-element method for computing spherical-earth seismograms-II. waves in solid-fluid media, *Geophys. J. Int.,* **174,** 873–888.

Saenger, E. & Bohlen, T., 2004. Finite-difference modeling of viscoelastic and anisotropic wave propagation using the rotated staggered grid, *Geophysics,* **69,** 583–591.

Seriani, G. & Priolo, E., 1994. Spectral element method for acoustic wave simulation in heterogeneous media, *Finite Element Anal. Design,* **16,** 337–348.

Titarev, V. & Toro, E., 2002. ADER: arbitrary high order Godunov approach, *J. Sci. Comput.,* **17,** 609–618.

Toro, E., Millington, R. & Nejad, L., 2001. Towards very high order Godunov schemes. Towards very high order Godunov schemes., *Godunov Methods; Theory and Applications,* Kluwer Academic Plenum Publishers, pp. 907–940.

Virieux, J., 1984. SH-wave propagation in heterogeneous media: velocity-stress finite-difference method, *Geophysics,* **49,** 1933–1942.

Virieux, J., 1986. P-SV wave propagation in heterogeneous media: velocity-stress finite-difference method, *Geophysics,* **51,** 889–901.

APPENDIX A: ORTHOGONAL BASIS FUNCTIONS

We use orthogonal hierarchical basis functions as given in (Cockburn *et al.* 2000). The basis functions are given in terms of the Jacobi polynomials $P_n^{\alpha,\beta}(x)$ which are solutions of the Jacobi differential equation:

$$\left(1-x^2\right)y'' + \left[\beta-\alpha-(\alpha+\beta+2)\,x\right]y' + n\,(n+\alpha+\beta+1)\,y = 0\,. \tag{A1}$$

They are given on the interval $[-1;1]$ by

$$P_n^{\alpha,\beta}(x) = \frac{(-1)^n}{2^n n!}\,(1-x)^{-\alpha}\,(1+x)^{-\beta} \times \frac{\mathrm{d}^n}{\mathrm{d}x^n}\left[(1-x)^{\alpha+n}\,(1+x)^{\beta+n}\right]\,. \tag{A2}$$

For $\alpha=\beta=0$ the Jacobi polynomials $P_n^{0,0}(x)$ reduce to the Legendre polynomials. The Discontinuous Galerkin basis functions are then constructed using the primal functions

$$\Theta_i^a(x) = P_i^{0,0}(x)\,, \tag{A3}$$

$$\Theta_{ij}^b(x) = \left(\frac{1-x}{2}\right)^i P_j^{2i+1,0}(x)\,, \tag{A4}$$

$$\Theta_{ijk}^c(x) = \left(\frac{1-x}{2}\right)^{i+j} P_k^{2i+2j+2,0}(x)\,. \tag{A5}$$

The sets of basis functions θ_l used in eq. (3) constitute orthogonal basis systems with respect to the inner product on the respective reference elements E_T or E_Q.

A1 Triangular elements

For triangles the reference element E_T is defined as

$$E_T = \left\{(\xi,\eta)\in\mathbb{R}^2 \mid 0\le\xi\le 1 \;\wedge\; 0\le\eta\le 1-\xi\right\}\,. \tag{A6}$$

The basis functions $\Phi_l(\xi,\eta)$ are defined on this reference element as the following product of the primal functions:

$$\Phi_{l(p,q)}(\xi,\eta) = \Theta_p^a(\alpha)\times\Theta_{pq}^b(\beta)\,, \tag{A7}$$

with

$$\alpha = \frac{2\,\xi}{1-\eta} - 1\,, \quad \beta = 2\,\eta - 1\,. \tag{A8}$$

The mono-index $l=l(p,q)$ is again a function of the index couple (p,q).

The two-dimensional basis functions up to degree three for a fourth order scheme are:

$$\begin{aligned}
\Phi_0 &= 1\,,\\
\Phi_1 &= -1+2\,\xi+\eta\,,\\
\Phi_2 &= -1+3\,\eta\,,\\
\Phi_3 &= 1-6\,\xi+6\,\xi^2-2\,\eta+6\,\xi\eta+\eta^2\,,\\
\Phi_4 &= 1-2\,\xi-6\,\eta+10\,\xi\eta+5\,\eta^2\,,\\
\Phi_5 &= 1-8\,\eta+10\,\eta^2\,,\\
\Phi_6 &= -1+12\,\xi-30\,\xi^2+20\,\xi^3+3\,\eta-24\,\xi\eta+30\,\xi^2\eta\\
&\quad -3\,\eta^2+12\,\xi\eta^2+\eta^3\,,\\
\Phi_7 &= -1+6\,\xi-6\,\xi^2+9\,\eta-48\,\xi\eta+42\,\xi^2\eta-15\,\eta^2\\
&\quad +42\,\xi\eta^2+7\,\eta^3\,,\\
\Phi_8 &= -1+2\,\xi+13\,\eta-24\,\xi\eta-33\,\eta^2+42\,\xi\eta^2+21\eta^3\,,\\
\Phi_9 &= -1+15\,\eta-45\,\eta^2+35\,\eta^3\,.
\end{aligned} \tag{A9}$$

A2 Quadrilateral elements

For quadrilaterals the reference element E_Q is defined as

$$E_Q = \left\{(\xi,\eta)\in\mathbb{R}^2 \mid 0\le\xi\le 1 \;\wedge\; 0\le\eta\le 1\right\}\,. \tag{A10}$$

The basis functions $\Psi_l(\xi,\eta)$ are defined on this reference element as the following product of the primal functions:

$$\Psi_{l(p,q)}(\xi,\eta) = \Theta_p^a(\alpha)\times\Theta_q^b(\beta)\,, \tag{A11}$$

with

$$\alpha = 2\,\xi - 1, \quad \beta = 2\,\eta - 1\,. \tag{A12}$$

The mono-index $l=l(p,q)$ is again a function of the index couple (p,q).

The two-dimensional basis functions up to degree three for a fourth-order scheme are:

$$\Psi_0 = 1\,,$$

$$\Psi_1 = -1 + 2\,\xi\,,$$

$$\Psi_2 = -1 + 2\,\eta\,,$$

$$\Psi_3 = 1 - 6\,\xi + 6\,\xi^2\,,$$

$$\Psi_4 = 1 - 2\,\xi - 2\,\eta + 4\,\xi\,\eta\,,$$

$$\Psi_5 = 1 - 6\,\eta + 6\,\eta^2\,,$$

$$\Psi_6 = -1 + 12\,\xi - 30\,\xi^2 + 20\,\xi^3\,,$$

$$\Psi_7 = -1 + 6\,\xi - 6\,\xi^2 + 2\,\eta - 12\,\xi\,\eta + 12\,\xi^2\,\eta\,,$$

$$\Psi_8 = -1 + 2\,\xi + 6\,\eta - 12\,\xi\,\eta - 6\,\eta^2 + 12\,\xi\,\eta^2\,,$$

$$\Psi_9 = -1 + 12\,\eta - 30\,\eta^2 + 20\,\eta^3\,. \tag{A13}$$

APPENDIX B: ROTATION MATRICES FOR EDGE-ALIGNED FLUXES

The flux can be derived for a coordinate system which is aligned with the outward pointing unit normal vector $\vec{n}^{(j)} = (n_x^{(j)}, n_y^{(j)})^{\mathrm{T}}$ of the jth edge of an element E. Omitting the edge index j for the 2-D elastic wave equations the transformation matrices T_{pq} and $(T_{pq})^{-1}$ used in eq. (8) read as

$$T_{pq} = \begin{pmatrix} n_x^2 & n_y^2 & -2n_xn_y & 0 & 0 \\ n_y^2 & n_x^2 & 2n_xn_y & 0 & 0 \\ n_xn_y & -n_xn_y & n_x^2 - n_y^2 & 0 & 0 \\ 0 & 0 & 0 & n_x & -n_y \\ 0 & 0 & 0 & n_y & n_x \end{pmatrix},$$

$$(T_{pq})^{-1} = \begin{pmatrix} n_x^2 & n_y^2 & 2n_xn_y & 0 & 0 \\ n_y^2 & n_x^2 & -2n_xn_y & 0 & 0 \\ -n_xn_y & n_xn_y & n_x^2 - n_y^2 & 0 & 0 \\ 0 & 0 & 0 & n_x & n_y \\ 0 & 0 & 0 & -n_y & n_x \end{pmatrix}. \tag{B1}$$

Three-Dimensional Dynamic Rupture Simulation with a High-order Discontinuous Galerkin Method on Unstructured Tetrahedral Meshes

Christian Pelties

Department of Earth and Environmental Sciences, Geophysics Section, Ludwig-Maximilians-University, München, Germany.

Josep de la Puente

Department of Computer Applications in Science and Engineering, Barcelona Supercomputing Center, Barcelona, Spain.

Jean-Paul Ampuero

Seismological Laboratory, California Institute of Technology, Pasadena, USA.

Gilbert B. Brietzke

Department of Physics of the Earth, German Research Centre for Geosciences, Helmholtzstraße 7, 14467 Potsdam, Germany.

Martin Käser

Geo Risks - Münchener Rückversicherungs-Gesellschaft, Königinstrasse 107, 80802 München, Germany.

Abstract. Accurate and efficient numerical methods to simulate dynamic earthquake rupture and wave propagation in complex media and complex fault geometries are needed to address fundamental questions in earthquake dynamics, to assimilate seismic and geodetic data in emerging approaches for dynamic source inversion and to generate realistic physics-based earthquake scenarios for hazard assessment. Modeling of spontaneous earthquake rupture and seismic wave propagation by a high-order discontinuous Galerkin (DG) method combined with an Arbitrarily high-order DERivatives (ADER) time integration method was introduced in 2D by *de la Puente et al.* [2009]. The ADER-DG method enables high accuracy in space and time and discretization by unstructured meshes. Here we extend this method to three-dimensional dynamic rupture problems. In the resulting discrete formulation of the elastic wave equations the physical variables are naturally discontinuous at the interfaces between elements. A Riemann solver provides well defined values of the variables at the discontinuity itself. This holds in particular for dynamic fault interfaces at which non-linear friction relations between traction and slip have to be evaluated. The high geometrical flexibility provided by the usage of tetrahedral elements and the lack of spurious mesh reflections in ADER-DG allows to refine the mesh close to the fault, to model the rupture dynamics adequately while concentrating computational resources only where needed. Moreover, ADER-DG does not generate spurious high-frequency perturbations on the fault and hence does not require artificial damping. We verify our three-dimensional implementation by comparing results of the SCEC TPV3 test problem with two well established numerical methods, Finite Differences and Spectral Boundary Integral. The superior accuracy of the ADER-DG scheme is exemplified by the enabled identification of subtle effects of the friction law in the resulting slip rate time series. Furthermore, a convergence study is presented to demonstrate the systematic consistency of the method. To illustrate the capabilities of the high-order accurate ADER-DG scheme on unstructured meshes we simulate an earthquake scenario, inspired by the 1992 Landers earthquake, that includes curved faults, fault branches and surface topography.

1. Introduction

Strong ground motion simulations of earthquakes require, in order to describe natural phenomena, the proper description and modeling of several features, e.g. seismic source representation, geometry of fault systems, material properties of the bedrock and sediment, topography. A highly accurate solution of the

0148-0227/11/$9.00

resulting wave field is also essential. The seismic source can be described through a prescribed evolution of slip along the fault or by prescribing physical criteria for earthquake rupture and letting the fault slip be a spontaneous consequence of the state of the fault. The two approaches are called kinematic and dynamic fault representation, respectively. The advantage of dynamic source modeling is that one can investigate how the fault interacts with the surrounding conditions such as confining stress, free-surface or transient wavefields. As a drawback, dynamic rupture modeling is much more challenging computationally and results in more uncertainties than kinematic source modeling, due to the non-linear nature and large uncertainties of the underlying physics.

Many numerical algorithms have been tested in the past to model dynamic earthquake rupture, such as finite differences (FD) [*Andrews*, 1973; *Day*, 1982; *Madariaga et al.*, 1998; *Andrews*, 1999; *Day et al.*, 2005; *Dalguer and Day*, 2007; *Moczo et al.*, 2007], boundary integral (BI) [*Das*, 1980; *Andrews*, 1985; *Cochard and Madariaga*, 1994; *Geubelle and Rice*, 1995; *Lapusta et al.*, 2000; *Tada and Madariaga*, 2001], finite volume (FV) [*Benjemaa et al.*, 2007, 2009], finite element (FE) [*Oglesby et al.*, 1998, 2000; *Aagaard et al.*, 2001; *Galis et al.*, 2008] or spectral element (SE) [*Ampuero*, 2002; *Vilotte et al.*, 2006; *Kaneko et al.*, 2008; *Galvez et al.*, 2011] methods. All these methods provide certain advantages, but have also disadvantages. For instance, FD schemes can be implemented efficiently to solve very large problems but have difficulties in modeling non-planar faults and strong material contrasts, like in sedimentary basins with extremely low wave velocities, which require grid adaptivity. The BI method is one of the most accurate and computationally efficient methods but is impractical in heterogeneous media and non-linear materials. FV and FE methods can be implemented on unstructured meshes, which gives flexibility to describe realistic fault and crustal model geometries. However, they are usually formulated as low-order accurate operators that are very dispersive, which affects the small-scale resolution in the near-field and in turn the rupture front evolution. In contrast, SE methods are high-order accurate for seismic wave propagation, but are limited to hexahedral elements, which penalizes geometrical flexibility: it remains challenging to generate hexahedral meshes for complex three dimensional branched fault systems with smooth element refinement or coarsening that adapts to material properties. Furthermore, all approaches suffer from spurious high-frequency oscillations, most notably in the slip-rate time series. Several approaches have been proposed in order to reduce these oscillations, e.g. spatial low-pass filtering [*Ampuero*, 2002], adding an ad-hoc Kelvin-Voigt damping term to the solution [*Day et al.*, 2005] or adaptive smoothing algorithms [*Galis et al.*, 2010]. None of these solutions is completely satisfactory and high-frequency oscillations remain an unsolved nuisance in the numerical modeling of dynamic rupture.

A new approach to overcome these issues was first presented by *de la Puente et al.* [2009]. They incorporated the earthquake source physics into a discontinuous Galerkin (DG) scheme linked to an arbitrary high-order derivatives (ADER) time integration [*Titarev and Toro*, 2002; *Käser and Iske*, 2005; *Dumbser and Käser*, 2006]. The DG method combines ideas from high-order FV and FE methods, where a polynomial basis approximates the physical variables of the elastic wave equations inside each element. This formulation enables the use of fully unstructured meshes, i.e. triangles (2D) or tetrahedrons (3D), to better represent the geometrical constrains of a given geological setting and in particular the fault. The fault is honored by the mesh and can be sampled with small elements in order to capture small-scale rupture phenomena. Fast mesh coarsening with increasing distance from the fault reduces the computational cost without introducing significant spurious grid reflections. Between any two elements the approximated vari-

ables of the elastic wave equation are discontinuous in a DG discretization. In our case, fluxes are defined by the exact solution of the elastic wave equations at a discontinuity (Godunov state) to exchange information between elements. Such kind of problem is known as the Riemann problem [*Toro*, 1999; *LeVeque*, 2002]. At a fault, *de la Puente, Ampuero, and Käser* [2009] showed how the exact solution of the Godunov state has to be modified to take the frictional boundary conditions into account. An important result of their study was that the ADER-DG solution is very smooth and free of spurious high-frequency oscillations. Therefore, it does not require artificial damping or filtering. The superior numerical dispersion properties of the DG method [*Käser et al.*, 2008], the possibility of using unstructured meshes [*Pelties et al.*, 2010], and the natural representation of variables' discontinuities with Godunov fluxes [*de la Puente et al.*, 2009] might be key features for accurate and efficient dynamic rupture simulations in very complex scenarios.

The main goal of this paper is the extension of the ADER-DG rupture modeling scheme to three-dimensional problems on tetrahedral meshes. We present the Riemann problem for the three-dimensional case and show how its solution is used to compute high-order accurate numerical fluxes. We further use these fluxes together with a DG discretization of the elastodynamic system to build up a highly accurate fault modeling and wave propagation algorithm. The accuracy and convergence properties of the method are shown in convergence tests. Further verification is obtained by comparing the results of our novel 3D DG dynamic rupture scheme with other well established numerical solutions in a standard community test problem of fault rupture. Finally, a large earthquake simulation including complex fault systems, inspired from the 1992 Landers earthquake, shows the potential of the method in dealing with complicated geometrical constrains both in the rupture process and in the wave propagation itself.

2. Dynamics of Fault Rupture

In the classical three-dimensional dynamic rupture models considered here a fault is represented by a 2D plane of arbitrary shape (or a set of planes in a fault system with branches) across which fault coplanar displacements can be discontinuous. The kinematics of the sliding process are described by the spatio-temporal distribution of the slip vector $\Delta\mathbf{d} = \mathbf{d}^+ - \mathbf{d}^-$, or the slip rate vector $\Delta\mathbf{v} = \Delta\dot{\mathbf{d}}$, where $\mathbf{d}^\pm$ are the displacements on each side of the fault, in the directions tangential to the fault plane (see Fig. 1a). Earthquakes may involve small-scale fault opening, especially at shallow depth but, for simplicity, here we consider only examples in which both sides of the fault remain in contact. On any point of the fault surface, $\sigma_n > 0$ represents the compressive normal stress and $\boldsymbol{\tau}$ the shear traction vector resolved on the $+$ side of the fault. The dynamics of the sliding process are governed by friction relations between traction and slip [*Andrews*, 1976a, b; *Day et al.*, 2005]. The shear traction is bounded by the fault strength $\mu_f\sigma_n$, which is proportional to the normal stress via the friction coefficient μ_f. Active slip requires the shear traction to reach and remain at the fault strength level, with a direction anti-parallel to the slip rate. These conditions are encapsulated in the following equations for Coulomb friction:

$$\begin{aligned} |\boldsymbol{\tau}| &\leq \mu_f\sigma_n\,, \\ (|\boldsymbol{\tau}| - \mu_f\sigma_n)\,|\Delta\mathbf{v}| &= 0\,, \\ \Delta\mathbf{v}|\boldsymbol{\tau}| + |\Delta\mathbf{v}|\boldsymbol{\tau} &= 0\,. \end{aligned} \tag{1}$$

The evolution of the friction coefficient with ongoing slip is

described by the following linear slip weakening friction law:

$$\mu_f = \begin{cases} \mu_s - \dfrac{\mu_s - \mu_d}{D_c}\delta & \text{if } \delta < D_c\,, \\ \mu_d & \text{if } \delta \geq D_c\,. \end{cases} \tag{2}$$

where $\delta = \int_0^t |\Delta \mathbf{v}| dt'$ is the slip path length. With increasing δ the friction coefficient μ_f drops linearly from the static value μ_s to the dynamic value μ_d over the critical slip distance D_c, as shown in Fig. 1b. The linear slip weakening friction law is capable of modeling initial rupture, arrest of sliding and reactivation of slip. Since it is very simple and easy to implement, it is well suited to verifying numerical methods with dynamic rupture boundary condition. More advanced, realistic friction laws, incorporate rate-and-state effects [*Dieterich*, 1979; *Ruina*, 1983] and thermal phenomena such as flash heating and pore pressure evolution [*Lachenbruch*, 1980; *Mase and Smith*, 1985, 1987; *Rice*, 1999]. We do not expect any fundamental issue in the implementation of other friction laws in the ADER-DG method and leave that for future work.

3. Fault Dynamics within the Discontinuous Galerkin Framework

In contrast to other numerical dynamic rupture implementations, like the traction-at-split-node (TSN) approach [*Andrews*, 1973, 1999; *Day*, 1982], *de la Puente et al.* [2009] followed a new idea employing the concept of fluxes. A detailed description of the adopted DG scheme can be found in *Dumbser and Käser* [2006]. The mathematical and technical analysis of dynamic rupture boundary conditions in a high-order DG formulation was presented by *de la Puente et al.* [2009] in 2D. Therefore, in this section we will explain only the basic ideas and show the extension to three-dimensional spontaneous rupture problems.

3.1. Discretization of the Linear Elastic Wave Equation

The three-dimensional elastodynamic equations for an isotropic medium are written in velocity-stress form as the linear hyperbolic system

$$\begin{aligned}
\frac{\partial}{\partial t}\sigma_{xx} - (\lambda+2\mu)\frac{\partial}{\partial x}u - \lambda\frac{\partial}{\partial y}v - \lambda\frac{\partial}{\partial z}w &= 0\,, \\
\frac{\partial}{\partial t}\sigma_{yy} - \lambda\frac{\partial}{\partial x}u - (\lambda+2\mu)\frac{\partial}{\partial y}v - \lambda\frac{\partial}{\partial z}w &= 0\,, \\
\frac{\partial}{\partial t}\sigma_{zz} - \lambda\frac{\partial}{\partial x}u - \lambda\frac{\partial}{\partial y}v - (\lambda+2\mu)\frac{\partial}{\partial z}w &= 0\,, \\
\frac{\partial}{\partial t}\sigma_{xy} - \mu(\frac{\partial}{\partial x}v + \frac{\partial}{\partial y}u) &= 0\,, \\
\frac{\partial}{\partial t}\sigma_{yz} - \mu(\frac{\partial}{\partial z}v + \frac{\partial}{\partial y}w) &= 0\,, \\
\frac{\partial}{\partial t}\sigma_{xz} - \mu(\frac{\partial}{\partial z}u + \frac{\partial}{\partial x}w) &= 0\,, \\
\rho\frac{\partial}{\partial t}u - \frac{\partial}{\partial x}\sigma_{xx} - \frac{\partial}{\partial y}\sigma_{xy} - \frac{\partial}{\partial z}\sigma_{xz} &= 0\,, \\
\rho\frac{\partial}{\partial t}v - \frac{\partial}{\partial x}\sigma_{xy} - \frac{\partial}{\partial y}\sigma_{yy} - \frac{\partial}{\partial z}\sigma_{yz} &= 0\,, \\
\rho\frac{\partial}{\partial t}w - \frac{\partial}{\partial x}\sigma_{xz} - \frac{\partial}{\partial y}\sigma_{yz} - \frac{\partial}{\partial z}\sigma_{zz} &= 0\,,
\end{aligned} \tag{3}$$

where λ is the first Lamé constant, μ is the shear modulus, ρ is the density, σ_{ij} are the components of the stress tensor and u,

v and w are the components of the particle velocity in the x, y, and z directions, respectively. Grouping stresses and velocities into a vector $\boldsymbol{Q} = (\sigma_{xx}, \sigma_{yy}, \sigma_{zz}, \sigma_{xy}, \sigma_{yz}, \sigma_{xz}, u, v, w)^T$, we write the system of equations (3) in a more compact form:

$$\frac{\partial Q_p}{\partial t} + A_{pq}\frac{\partial Q_q}{\partial x} + B_{pq}\frac{\partial Q_q}{\partial y} + C_{pq}\frac{\partial Q_q}{\partial z} = 0\,, \qquad (4)$$

where the space-dependent Jacobian matrices A, B and C include the material properties. Classical tensor notation and Einstein's summation convention are assumed.

The computational domain Ω is divided into conforming tetrahedral elements $T^{(m)}$ identified by an index m. The physical variables $\boldsymbol{Q}$ are approximated within each tetrahedral element $T^{(m)}$ by high-order polynomials

$$Q_p^m(\boldsymbol{\xi}, t) = \hat{Q}_{pl}^m(t)\Phi_l(\boldsymbol{\xi})\,, \qquad (5)$$

where Φ_l are orthogonal basis functions and $\boldsymbol{\xi} = (\xi, \eta, \zeta)$ are the local coordinates in a canonical reference element T_E, where all the computations are done. The physical variables are expressed by a linear combination of these basis functions with time-dependent coefficients $\hat{Q}_{pl}^m(t)$. The index p is associated with the unknowns in the vector $\boldsymbol{Q}$. The index l indicates the l-th basis function and ranges from 0 to $L-1$, where $L = (N+1)(N+2)(N+3)/6$ is the number of required basis functions for a polynomial degree N. The numerical approximation order is $\mathcal{O} = N+1$.

The elastic wave equation is solved in the weak form. We multiply equation (4) by a test function Φ_k and integrate over an element $T^{(m)}$ and over a time increment of size Δt:

$$\int_t^{t+\Delta t}\int_{T^{(m)}} \Phi_k \frac{\partial Q_p}{\partial t} dV\, dt + \int_t^{t+\Delta t}\int_{T^{(m)}} \Phi_k \left(A_{pq}\frac{\partial Q_q}{\partial x} + B_{pq}\frac{\partial Q_q}{\partial y} + C_{pq}\frac{\partial Q_q}{\partial z}\right) dV\, dt = 0. \qquad (6)$$

Integration by parts of equation (6) yields

$$\int_t^{t+\Delta t}\int_{T^{(m)}} \Phi_k \frac{\partial Q_p}{\partial t}\, dV\, dt + \sum_{j=1}^{4}\mathcal{F}_{pk}^j - \int_t^{t+\Delta t}\int_{T^{(m)}} \left(\frac{\partial \Phi_k}{\partial x}A_{pq} + \frac{\partial \Phi_k}{\partial y}B_{pq} + \frac{\partial \Phi_k}{\partial z}C_{pq}\right) Q_q\, dV\, dt = 0\,. \qquad (7)$$

Equation (7) provides the values of Q_p at time $t+\Delta t$, following the procedures explained by *Käser and Dumbser* [2006] and *Dumbser and Käser* [2006]. In those papers the integration of the first and third terms in equation (7) are fully elaborated. The second term is the sum of numerical fluxes $\mathcal{F}_{pk}^j$ across the four faces, $j = 1, 2, 3, 4$, of a tetrahedral element, accounting for the discontinuity of $\boldsymbol{Q}$. The incorporation of dynamic rupture boundary conditions is based on a modification of these flux terms. Thus, we will have a closer look at them in the next section.

3.2. Flux computation

For simplicity, we consider a single tetrahedral face with its normal aligned with the x axis. The flux term in (7) can then be written as

$$\mathcal{F}_{pk} \;=\; A_{pr}\int_t^{t+\Delta t}\int_S \Phi_k \tilde{Q}_r\, dS\, dt, \qquad (8)$$

where $\tilde{\boldsymbol{Q}}$ stands for a suitable approximation of the unknowns on the fault and the integral covers the face S and a time interval of size Δt. In order to solve the integrals numerically, we evaluate $\boldsymbol{Q}$ at a set of space-time Gaussian integration points on the tetrahedral face at space locations $\boldsymbol{\xi}_i = (\xi_i, \eta_i, \zeta_i)$, with $i = 1, \ldots, (N+2)^2$, and along the time axis at time levels $\tau_l \in [t, t+\Delta t]$, with $l = 1, \ldots, N+1$. We define $Q_{p,il} = Q_p(\boldsymbol{\xi}_i, \tau_l)$. We solve the flux locally at each space-time integration point while ensuring causality by updating the time levels in a sequential way. At special boundaries, such as the free-surface or faults, the values of $\tilde{\boldsymbol{Q}}$ in (8) might be imposed in order to satisfy the physical boundary conditions. In the particular case of dynamic faults, we impose values derived from the Coulomb friction model (1).

A suitable temporal expansion of the variables at a given tetrahedral element is obtained via a Taylor expansion near time t. At time $t+\Delta t$ the expansion of order $O = N+1$ is

$$Q_p(\boldsymbol{\xi}, t+\Delta t) \approx \sum_{k=0}^{N} \frac{\Delta t^k}{k!} \frac{\partial^k Q_q(\boldsymbol{\xi}, t)}{\partial t^k} \,. \tag{9}$$

The high-order time derivatives in (9) are substituted by spatial derivatives using the expression (4) in an iterative way

$$\frac{\partial^k Q_p(\boldsymbol{\xi}, t)}{\partial t^k} = (-1)^k \left(A_{pq} \frac{\partial}{\partial x} + B_{pq} \frac{\partial}{\partial y} + C_{pq} \frac{\partial}{\partial z} \right)^k Q_q(\boldsymbol{\xi}, t). \tag{10}$$

This yields

$$Q_p(\boldsymbol{\xi}, t+\Delta t) \approx$$

$$\sum_{k=0}^{N} \frac{\Delta t^k}{k!} (-1)^k \left(A_{pq} \frac{\partial}{\partial x} + B_{pq} \frac{\partial}{\partial y} + C_{pq} \frac{\partial}{\partial z} \right)^k Q_q(\boldsymbol{\xi}, t) \,. \tag{11}$$

The expansion (11) is performed separately for the states $\boldsymbol{Q}^+(\boldsymbol{\xi}, t)$ and $\boldsymbol{Q}^-(\boldsymbol{\xi}, t)$ of the two elements on the $+$ and the $-$ side of the face across which the flux is evaluated (see Fig. 1a). As mentioned above, between any two elements the variables of the elastic wave equations are in general discontinuous. Such partial differential equation problem with discontinuous initial conditions is called the Riemann problem. The solution of the Riemann problem at an element interface is the Godunov state and can be written in terms of explicit values as [*Toro*, 1999; *LeVeque*, 2002; *de la Puente et al.*, 2009]

$$\begin{aligned}
2\sigma^G_{xx,il} &= (\sigma^+_{xx,il} + \sigma^-_{xx,il}) + c_p \rho (u^-_{il} - u^+_{il}) \,, \\
2\sigma^G_{xy,il} &= (\sigma^+_{xy,il} + \sigma^-_{xy,il}) + \tfrac{\mu}{c_s} (v^-_{il} - v^+_{il}) \,, \\
2\sigma^G_{xz,il} &= (\sigma^+_{xz,il} + \sigma^-_{xz,il}) + \tfrac{\mu}{c_s} (w^-_{il} - w^+_{il}) \,, \\
2u^G_{il} &= (u^+_{il} + u^-_{il}) + \tfrac{1}{c_p \rho} (\sigma^-_{xx,il} - \sigma^+_{xx,il}) \,, \\
2v^G_{il} &= (v^+_{il} + v^-_{il}) + \tfrac{c_s}{\mu} (\sigma^-_{xy,il} - \sigma^+_{xy,il}) \,, \\
2w^G_{il} &= (w^+_{il} + w^-_{il}) + \tfrac{c_S}{\mu} (\sigma^-_{xz,il} - \sigma^+_{xz,il}) \,.
\end{aligned} \tag{12}$$

The variables $\sigma_{yy}, \sigma_{zz}, \sigma_{yz}$ are associated to the so-called zero wave speeds and do not contribute to the Godunov state. The equations (12) together with the flux (8) are used to exchange information between elements, similar to FV methods. A major

advantage of the flux concept, besides its numerical properties, is that it favors data locality: the temporal update of the solution inside one element depends only on its direct neighbors. Therefore, the method is well suited for massively parallel high-performance facilities, in addition to providing a high-order accurate approximation of the physical variables.

The equations (12) are used for wave propagation simulations. In order to honor the Coulomb friction model (1), we have to impose the shear stresses $\sigma_{xy,il}$ and $\sigma_{xz,il}$ at the fault accordingly to obtain new traction values $\tilde{\sigma}_{xy,il}$ and $\tilde{\sigma}_{xz,il}$, which are different from $\sigma^G_{xy,il}$ and $\sigma^G_{xz,il}$ when there is active slip. In turn, this provides boundary conditions for the fault parallel-velocities. Multiplying the second and third equations of (12) by c_s/μ and subtracting the fifth and sixth equations, respectively, leads to

$$\begin{aligned}
\tilde{v}^+_{il} &= v^+_{il} + \frac{c_s}{\mu}\left(\tilde{\sigma}_{xy,il} - \sigma^+_{xy,il}\right) \quad \text{and} \quad \tilde{v}^-_{il} = v^-_{il} - \frac{c_s}{\mu}\left(\tilde{\sigma}_{xy,il} - \sigma^-_{xy,il}\right) , \\
\tilde{w}^+_{il} &= w^+_{il} + \frac{c_s}{\mu}\left(\tilde{\sigma}_{xz,il} - \sigma^+_{xz,il}\right) \quad \text{and} \quad \tilde{w}^-_{il} = w^-_{il} - \frac{c_s}{\mu}\left(\tilde{\sigma}_{xz,il} - \sigma^-_{xz,il}\right) ,
\end{aligned} \tag{13}$$

when we substitute $\sigma^G_{xy,il}$ and $\sigma^G_{xz,il}$ with their imposed values $\tilde{\sigma}_{xy,il}$ and $\tilde{\sigma}_{xz,il}$. $\tilde{v}^-_{il}$ and $\tilde{w}^-_{il}$ are obtained by summing the equations instead of subtracting them.

These expressions are crucial for the understanding of fault dynamics using fluxes, as they state that an imposed traction instantly and locally generates an imposed velocity parallel to the fault. By subtracting them, the slip rates for each possible slip direction are obtained:

$$\begin{aligned}
\Delta\tilde{v}_{il} &= \frac{2c_s}{\mu}\left(\tilde{\sigma}_{xy,il} - \sigma^G_{xy,il}\right) , \\
\Delta\tilde{w}_{il} &= \frac{2c_s}{\mu}\left(\tilde{\sigma}_{xz,il} - \sigma^G_{xz,il}\right) .
\end{aligned} \tag{14}$$

These expressions capture explicitly the analytical form of the immediate slip velocity response to changes in fault tractions, also known as radiation damping [*Cochard and Madariaga*, 1994; *Geubelle and Rice*, 1995]. A consequence of the equations in (14) is that slip (non zero $\Delta\tilde{v}_{il}$ or $\Delta\tilde{w}_{il}$) occurs only if $\tilde{\sigma}_{xy,il} \neq \sigma^G_{xy,il}$ or $\tilde{\sigma}_{xz,il} \neq \sigma^G_{xz,il}$. The remaining Godunov's variables, normal velocity and normal stress, can be computed using (12) as they are independent of $\tilde{\sigma}_{xy,il}$ and $\tilde{\sigma}_{xz,il}$. All equations are evolved at each Gaussian integration point in space and time. Using the shear stresses $\tilde{\sigma}_{xy,il}$ and $\tilde{\sigma}_{xz,il}$ and the velocities from (13) all values of $\tilde{\boldsymbol{Q}}$ at the interface are known and the flux (8) can be computed with the discrete expression

$$\mathcal{F}_{pk} \;=\; A_{pr} \sum_{i=1}^{(N+2)^2} \sum_{l=1}^{N+1} \omega^S_i \omega^T_l \Phi_k(\boldsymbol{\xi}_i) \tilde{Q}_{r,il} \, . \tag{15}$$

where ω^S_i and ω^T_l are the weights of the spatial and temporal Gaussian integration, respectively.

Finally, the slip $\Delta\tilde{d}_{il}$ is obtained by integrating (14). In a last step, we apply the linear slip weakening friction law (2) to get the time-updated value of the friction coefficient $\mu_{f,il+1}$ as

$$\mu_{f,il+1} = \max\left\{\mu_d, \mu_s - \frac{\mu_s - \mu_d}{D_c}\Delta\tilde{d}_{il}\right\} . \tag{16}$$

4. Verification

For geophysically relevant dynamic rupture problems no analytical solution exists that could be used as a reference for code verification. Therefore, the Southern California Earthquake Center (SCEC) created the Dynamic Earthquake Rupture Code Verification Exercise, in which different codes and

methodologies are compared on a suite of benchmark problems of increasing complexity [*Harris et al.*, 2004]. Here, we verify our method with the Test Problem Version 3 (TPV3). Additionally, in section 4.2 the convergence of the ADER-DG method is discussed.

4.1. Code verification on the SCEC TPV3

The TPV3 problem involves rupture on a 30 km long by 15 km deep vertical strike-slip fault embedded in a homogeneous elastic full-space. The fault is governed by linear slip weakening friction and bounded by unbreakable barriers. The initial fault stresses are homogeneous except on a nucleation zone of higher initial shear stress (Fig. 2). The friction parameters and background stresses can be found in Table 1. The medium has density $\rho = 2670$ kg/m^3, P-wave velocity $c_p = 6000$ m/s and S-wave velocity $c_s = 3464$ m/s. We use a conservatively large computational domain, a cube of edge length 72 km, to avoid spurious reflections from non-perfectly absorbing boundaries.

We compare our $\mathcal{O}4$ ADER-DG solution with the results of the Spectral Boundary Integral Equation (SBIE) method of *Geubelle and Rice* [1995] and of a second-order staggered-grid Finite Difference method with traction at split nodes [*Day et al.*, 2005]. In particular, we considered two codes that have been verified during the SCEC exercises, the SBIE implementation of E.M. Dunham (MDSBI: Multidimensional spectral boundary integral, version 3.9.10, 2008, available at http://pangea.stanford.edu/~edunham/codes/codes.html) and the Finite Difference code DFM (Dynamic Fault Model) of *Day et al.* [2005]. Both codes were run with a 50 m grid spacing. DFM incorporates artificial Kelvin-Voigt viscosity [*Day and Ely*, 2002].

We discretize the fault plane by a uniform mesh of equilateral triangles with edge length $h = 200$ m, but we allow the size of the tetrahedral elements in the bulk to increase gradually to 3000 m edge length, to reduce the computational effort. No artificial reflections possibly caused by the mesh coarsening are observed. To facilitate a fair comparison between the methods we define an equivalent mesh spacing $\Delta x = h/(N+1)$, which accounts for the sub-cell resolution of our high-order DG scheme. Although Δx is not consensually accepted as an exact measure of the spatial resolution it is often used for comparing different discretization techniques. The relatively large element size of our ADER-DG simulation, $h = 200$ m, corresponds to an equivalent mesh spacing of $\Delta x = 50$ m, the same as in the DFM and MDSBI computations considered here.

Figs. 3a, b, c and d show, for all three schemes, the time series of the shear stress and slip rate at the two fault locations indicated as PI and PA in Fig. 2, which probe the in-plane and anti-plane rupture fronts, respectively, at hypocentral distance 7500 m and 6000 m, respectively. The ADER-DG solution (black) is in excellent agreement with the results produced by MDSBI (blue) and DFM (red). The signal amplitudes, the arrival time of the rupture front and stopping phases and the subsequent stress relaxation are mutually consistent. A closer inspection of these results (Figs. 3e and f) reveals that the rupture front arrives slightly earlier in DFM than in the other two methods, whereas the rupture times of MDSBI and ADER-DG are more similar. These differences could be due to the Kelvin-Voigt damping in DFM or to different implementations of the non-smooth initial stress conditions.

Spurious high-frequency oscillations are visible in the slip rates produced by MDSBI and DFM, especially around the slip rate peak at the PA station. These are identified clearly in the spectra in Figs. 3g and h: the MDSBI slip rates have a significant spectral peak around 25 Hz and DFM has peaks between 10 and 40 Hz, especially at PA. Such spurious peaks are absent from the slip rate spectra of ADER-DG, which are smoother and follow the theoretically expected frequency decay [*Ida*, 1973].

Therefore, no artificial Kelvin-Voigt damping has to be applied in ADER-DG, which would further reduce the time step size and increase the computational cost. Our DG method is based on upwind numerical fluxes, which are intrinsically dissipative. In particular, in our high-order DG approach the amount of numerical dissipation increases very steeply as a function of frequency, beyond an effective high-frequency cutoff that depends on the element size [*Hesthaven and Warburton*, 2008, p.90, Fig. 4.1]. Hence, the very short wavelengths that are poorly resolved by the mesh elements are adaptively damped, without perturbing the longer, physically meaningful wavelengths.

The absence of spurious oscillations in ADER-DG enables the observation of interesting details of the solution. For instance, the ADER-DG solution reveals a slope discontinuity of the slip velocity shortly after the peak (at 3.15 s in Fig. 3c and at 3.07 s in Fig. 3d). This coincides with the time when the slip reaches D_c and is due to the slope discontinuity in the slip weakening friction law. In the other methods this feature is masked by the spurious oscillations.

4.2. Convergence test

In section 4.1 the good agreement between our ADER-DG method and other numerical methods has been shown. However, since there is no analytical solution available, one cannot determine which numerical method solves the proposed test better. A commonly used technique in computational science to verify the performance of a code is a convergence test. Thereby, we measure the error of the method by the root mean square (RMS) difference of rupture time, peak slip rate and final slip between the finest grid solution and the solutions for coarser grids. The particular RMS metrics we use in this chapter are taken from *Day et al.* [2005].

We solved the SCEC TPV3 with five different mesh spacings, $h = 1061$, 707, 530, 424 and 354 m, defined as the longest triangular edge length on the fault plane, and four different orders of accuracy ranging from $\mathcal{O}2$ to $\mathcal{O}5$. Some of the coarsest meshes at low orders lead to unphysical results and are ignored ($h = 707$ and 1061 m for $\mathcal{O}2$ and $h = 1061$ m for $\mathcal{O}3$). We obtained uniform meshes on the fault plane by first generating a regular mesh of quadrilateral elements of edge length $h/\sqrt{2}$, then dividing each quadrilateral into two triangles. We used mesh coarsening by increasing the element edge length by 10% per element with increasing distance from the fault, up to a maximum edge length of $10\,h$. Our reference solution was obtained with $h = 354$ m and $\mathcal{O}6$. We sampled the solution with 400 randomly distributed receivers along the fault plane. The rupture time is defined as the first time sample at which the slip rate exceeds 1 mm/s. The 15 receivers located in the nucleation zone are excluded for the rupture time measurement since their rupture time is exactly the first time step.

The results are summarized in Table 2 and visualized in Fig. 4. The RMS difference in rupture time, final slip and peak slip rate decrease with increasing mesh refinement and increasing order. This implies that a low-order approximation can achieve the accuracy of high-order approximations only when using a much smaller element size. Except for $\mathcal{O}2$, the RMS rupture time difference is low (Fig. 4a) and all chosen resolutions capture the rupture front evolution reasonably well with respect to the reference solution. The difference between the finest test solution and the reference solution is indeed very small, 0.04% (Table 2). The time step size Δt, shown by dashed lines in Fig. 4a, is much smaller than the RMS rupture time differences, hence temporal sampling does not bias our measurement of rupture times. The RMS difference of the final slip is also low, around 1% at best (Fig. 4b). The RMS difference of peak slip rate is larger (Fig. 4c), as usually found for this very sensitive error metrics based on extreme values of a spiky signal. Overall, the error levels are similar to those obtained by methods such as DFM [*Day et al.*, 2005]. The ADER-DG solu-

tions achieve numerical convergence with respect to the applied order and element size reduction.

The convergence of the errors as a function of h is well described by power laws. The small scattering of the error data around their power law regressions (Fig. 4) is expected when using structured mesh refinement strategies, like "red-refinement" (split a triangle into four geometrically similar triangles), but is remarkable given our fully unstructured meshes. The smooth convergence to the reference solution confirms the robustness and reliability of the method. The exponent of the power laws, or convergence rate, is given in Table 3. The $\mathcal{O}2$ simulations achieve the highest convergence rates but they also have the largest errors, as mentioned above. Between $\mathcal{O}3$ and $\mathcal{O}5$ the convergence rate saturates. In general, the convergence rate of a numerical solution improves when increasing the order of the method only if the exact solution is sufficiently smooth [*Godunov*, 1959; *Krivodonova*, 2007; *Hesthaven and Warburton*, 2008, p.87]. Dynamic rupture problems contain non-smooth features. Linear slip weakening friction guarantees continuity of slip velocity and shear stress but slip acceleration remains singular at the leading and trailing edges of the process zone *Ida* [1973]. Moreover, the initial stress conditions and the stopping barriers are not smooth in the TPV3 problem. However, in smoother rupture problems involving rate-and-state friction and smooth initiation conditions improvements of convergence rate with increasing order have not been observed [*Rojas et al.*, 2009], only reduced rupture time errors below the time sampling precision [*Kaneko et al.*, 2008]. In Table 3 the convergence rates of DFM and of a boundary integral method (from *Day et al.* [2005]) are included for comparison. Whereas the convergence rates of the rupture time agree for the different methods, DFM and BI converge slightly faster than ADER-DG with $\mathcal{O} > 2$ for the other error metrics, final slip and peak slip rate.

Fig. 4d shows the convergence of the rupture time misfit as a function of CPU time, the actual duration of the simulation multiplied by the number of processors involved. The number of processors ranges from 256 to 8192 since the problem size varies so much that the smallest simulation will not run efficiently on the maximum number of processors and the largest problem cannot be solved with fewer processors. Although the scalability of our DG code is in general good, it is still not perfect over this range of number of processors, which affects our measurements of CPU time. From Fig. 4d higher order methods are not more efficient for solving the test problem at a given accuracy. For a given h, high-order methods are more computationally demanding as they store and update more unknowns per element, and this cost is not significantly offset by their improved accuracy. However, the smoothness of the slip rate time series (Section 4.1) and the quality of the wave propagation away from the fault are not quantified by the error metrics considered here. Both aspects are an important part of the overall quality and accuracy of the solution. It has been demonstrated that a high-order approximation in a DG scheme is much more efficient for wave propagation problems than a low-order approximation, i.e. it requires lower computational cost to achieve a given error level [*Käser et al.*, 2008]. The flexibility of the ADER-DG method allows the resolution to be optimized (h- and p-adaptivity) independently for the fault and for the surrounding media based on different criteria, the cohesive zone size and the maximum target frequency, respectively. A high-order approximation is advantageous in strong ground motion simulations based on dynamic rupture scenarios because it provides an accurate wave field at lower cost.

5. The Landers 1992 Earthquake

To demonstrate the potential of the introduced ADER-DG method on unstructured meshes for simulations of rupture dy-

namics in complex fault geometries we consider the June 28th 1992 $M_W 7.3$ Landers, California, earthquake as an example. Our purpose here is not to re-examine the dynamics of this event in detail, as in many previous studies [e.g., *Olsen et al.*, 1997; *Aochi and Fukuyama*, 2002; *Aochi et al.*, 2003; *Fliss et al.*, 2005], but rather to illustrate the potential of our method for future studies. We hence follow the simplified setup introduced by *de la Puente et al.* [2009] and extend it to three dimensions, including topography.

The Landers earthquake occured on a 60 km long complex fault system along the western edge of the Eastern California Shear Zone. Its surface rupture involved at least parts of four major right-lateral strike-slip fault segments, breaking successively from south to north the Johnson Valley, Homestead Valley, Emerson and Camp Rock faults [*Hauksson et al.*, 1993]. These sub-parallel main segments are curved, overlapping and connected by shorter faults (e.g. the Kickapoo, or Landers fault, connecting the Johnson Valley and Homestead Valley faults). A fault geometry comprising six non-planar fault segments (Fig. 5) was adopted from [*Aochi and Fukuyama*, 2002]. Studies based on guided waves [*Li et al.*, 1994] and analysis of the aftershock distribution [*Hauksson et al.*, 1993] show that the surface geometry continues to a depth of at least 10 km. Source inversion results indicate a vertical dip of the fault planes [*Wald and Heaton*, 1994; *Cohee and Beroz*, 1994; *Cotton and Campillo*, 1995]. We hence model the three-dimensional fault system geometry by extending the surface fault traces vertically into depth. The fault plane starts below the surface at sea level (thus surface rupture is not allowed) and extends to 15 km below sea level.

The model domain is a polygon of lateral extension of 180 km times 220 km and depth of 50 km. Fig. 5 shows a map of the model area and its topography. The fault system is enclosed in the south by the San Bernardino mountains, with a maximum elevation of 3505 m, and in the north by smaller dissected mountain ranges.

Since our purpose is to focus on the rupture process on a geometrically complex fault system, we assume a homogeneous medium ($v_p = 6200$ m/s, $v_s = 3520$ m/s and $\rho = 2700$ kg/m^3) and a homogeneous initial stress field with horizontal principal stresses $\sigma_1 = 300$ MPa and $\sigma_2 = 100$ MPa. The assumed direction of the largest principal stress, N22°E, is representative of the northern part of the rupture in the model of *Aochi and Fukuyama* [2002] and is indicated by a red double arrow in Figs. 5 and 7. Although the stress field is homogeneous, the varying fault strike generates a heterogeneous stress state along the fault. The nucleation is initiated by a lower principal stress value of $\sigma_2 = 70$ MPa in a square patch of edge length 3 km around the hypocenter, located on the southern portion of the Johnson Valley fault. Table 4 contains the frictional parameters of the fault. We compute the spontaneous rupture for a total duration of 10 s.

Fig. 6 shows the fault discretized by triangles of size $h = 500$ m (edge length). The horizontal plane below the fault shows the mesh coarsening up to $h = 2500$ m in the closer neighborhood of the fault. The surface mesh above the fault has $h = 500$ m to ensure an accurate representation of the topography. This high-resolution area is surrounded by a much coarser mesh consisting mainly of $h = 5$ km elements, but we allow for $h = 10$ km at the outer borders of the domain. The fast mesh coarsening does not affect the rupture propagation, it only damps the high-frequency content of the wave field in areas of larger mesh spacing [*de la Puente et al.*, 2009]. This allows to concentrate the computational effort on the rupture area, where it is needed. The domain boundaries are located far enough away from the fault to avoid the effect of possible artificial reflections.

The resulting mesh contains $587{,}585$ elements. Using an $\mathcal{O}5$ approximation this model size is relatively inexpensive and

can be computed on a small scale cluster of approximately 100 nodes, which can be currently found in many research institutions. We used the BlueGene/P machine *Shaheen* of the King Abdullah University of Science and Technology, Saudi Arabia. Our 10 s long simulation ran for 20 hours on 512 processors. This relatively large number of processors was conditioned by the low frequency of the BlueGene/P CPUs (850 MHz) and, for standard CPUs, it can be reduced by a factor of 4 to 6. The entire discretization process including topography and fault geometry definition, mesh generation, and boundary specifications took less than two days due to the flexibility and robustness of tetrahedral mesh generation. Hence the manual effort and related cost in terms of expert working hours are kept at a minimum.

Fig. 7 shows the amplitude of the particle velocity generated by the earthquake at four different times on a horizontal cross-section of the nucleation area at a depth of 5 km below sea level. Initially, the rupture propagates bilaterally on the Johnson Valley fault (Fig. 7a). At time 1.5 s the northern rupture front approaches the first branching point (Fig. 7b). It then continues into the Kickapoo fault, without breaking the northern portion of the Johnson Valley fault (Fig. 7c). The rupture breaks the complete Kickapoo segment and continues on the Homestead Valley fault where it stops approximately at time 6 s (Fig. 7d). This rupture branching to the extensional side is consistent with the 2D study of *de la Puente et al.* [2009] and with theoretical considerations *Poliakov et al.* [2002]. While some interesting features of the Landers earthquake rupture, like the backward branching to the southern segment of the Homestead Valley fault [*Poliakov et al.*, 2002; *Fliss et al.*, 2005], are not reproduced by our simulation, it achieves our main intention to conceptually illustrate the capabilities of the 3D ADER-DG method.

Fig. 8 shows the surface wave field developing with time from 2.5 s to 4.5 s. There is a clear directivity effect: most of the energy is traveling northwards, like the rupture front. From visual inspection, the topography seems to increase the complexity of the wave field. However, we expect stronger site effects when incorporating a more realistic geological model with low velocity layers in the valley and stiffer material in the mountains.

6. Conclusions

We successfully incorporated 3D earthquake rupture dynamics in the ADER-DG scheme by modifying the Riemann problem according to the Coulomb friction model. Although we considered here linear slip weakening friction, the method allows for the implementation of more advanced friction laws, e.g. rate-and-state friction. Accuracy was verified by comparing results of the SCEC TPV3 benchmark problem for spontaneous rupture to well established methods. The ADER-DG solution is notably free of spurious high-frequency oscillations, most likely owing to the high-order frequency dependence of the intrinsic dissipation of the DG method. Hence, no artificial viscous damping mechanism has to be applied which could potentially affect the rupture process. The robustness and systematic correctness of the ADER-DG method was proved by a convergence test, which showed that mesh refinement or increasing the order leads to smaller errors.

An example of dynamic rupture simulation on a complex fault system, inspired by the surface rupture geometry of the Landers earthquake, demonstrates the the great benefits of the proposed method based on unstructured tetrahedral meshes that can be aligned into merging faults under shallow angles. Areas of interest, here the topography and the fault, can be modeled adequately by small elements while mesh coarsening can be applied elsewhere to reduce the computational cost. This is of interest in particular for dynamic rupture studies which require a fine sampling of the fault in order to capture the cohesive zone

for a correct simulation of the rupture process while adapting the resolution to the dispersion requirements of wave propagation at lower frequencies far from the fault. We do not observe any artificial reflection due to mesh coarsening in ADER-DG. In methods based on structured grids the mesh refinement is instead applied uniformly in the entire computational domain, propagating frequencies much higher than required for strong ground motion investigations, or through grid-doubling techniques, which could generate artificial reflections.

We conclude that the combination of meshing flexibility and high-order accuracy of the ADER-DG method will make it a very useful tool to study earthquake dynamics on complex fault systems. Future steps in the development include the incorporation of bimaterial fault interfaces, more realistic friction laws and non linear bulk rheologies.

Acknowledgments. The authors thank the DFG (Deutsche Forschungsgemeinschaft), as the work was supported through the *Emmy Noether-Programm* (KA 2281/2-1). J.-P. A. was partially funded by NSF (grant EAR-0944288) and by the Southern California Earthquake Center (funded by NSF Cooperative Agreement EAR-0106924 and USGS Cooperative Agreement 02HQAG0008). The DFM data used for comparison was provided by Luis A. Dalguer and the SBIEM solutions where produced with the code of Eric M. Dunham (MDSBI: Multidimensional spectral boundary integral, version 3.9.10, 2008, available at http://pangea.stanford.edu/~edunham/codes/codes.html). Furthermore, we thank Luis A. Dalguer and Alan Schiemenz for very helpful and fruitful discussions. Cristóbal E. Castro gave valuable comments and advice on the solution of the Riemann problem and the parallelization. We also thank M. Mai for providing computational resources as many parallel tests, the convergence test, and the SCEC benchmark have been computed on the BlueGene/P *Shaheen* of the King Abdullah University of Science and Technology, Saudi Arabia. This paper is SCEC contribution number XXXXXX and Caltech Seismolab contribution number XXXXXX.

References

Aagaard, B., T. Heaton, and J. Hall (2001), Dynamic earthquake rupture in the presence of lithostatic normal stresses: Implications for friction models and heat production, *Bull. Seism. Soc. Am.*, *91*, 1765–1796.

Ampuero, J.-P. (2002), Etude physique et numérique de la nucléation des séismes, Ph.D. thesis, Université Paris 7, Denis Diderot.

Andrews, D. (1973), A numerical study of tectonic stress release by underground explosions, *Bull. Seism. Soc. Am.*, *63*, 1375–1391.

Andrews, D. (1976a), Rupture propagation with finite stress in antiplane strain, *J. Geophys. Res.*, *81*, 3575–3582.

Andrews, D. (1976b), Rupture velocity of plane-strain shear cracks, *J. Geophys. Res.*, *81*, 5679–5687.

Andrews, D. (1985), Dynamic plane-strain shear rupture with a slip-weakening friction law calculated by a boundary integral method, *Bull. Seism. Soc. Am.*, *75*, 1–21.

Andrews, D. (1999), Test of two methods for faulting in finite-difference calculations, *Bull. Seism. Soc. Am.*, *89*, 931–937.

Aochi, H., and E. Fukuyama (2002), Three-dimensional nonplanar simulation of the 1992 Landers earthquake, *J. Geophys. Res.-Solid Earth*, *107*(B2, Art.No. 2035).

Aochi, H., R. Madariaga, and E. Fukuyama (2003), Constraint of fault parameters inferred from nonplanar fault modeling, *Geochem. Geophys. Geosyst.*, *4*(2), 1020.

Benjemaa, M., N. Glinsky-Olivier, V. Cruz-Atienza, J. Virieux, and S. Piperno (2007), Dynamic non-planar crack rupture by a finite volume method, *Geophys. J. Int.*, *171*, 271–285.

Benjemaa, M., N. Glinsky-Olivier, V. Cruz-Atienza, and J. Virieux (2009), 3-D dynamic rupture simulations by a finite volume method, *Geophys. J. Int.*, *178*, 541560, doi:10.1111/j.1365-246X.2009.04088.x.

Cochard, A., and R. Madariaga (1994), Dynamic faulting under rate-dependent friction, *Pure and Applied Geophysics*, *105*, 25,891–25,907.

Cohee, B. P., and G. C. Beroz (1994), Slip distribution of the 1992 Landers earthquake and its implications for earthquake source mechanics, *Bull. Seis. Soc. Am.*, *84(3)*, 692–712.

Cotton, F., and M. Campillo (1995), Frequency domain inversion of strong motions: Application to the 1992 Landers earthquake, *J. Geophys. Res.*, *100*, 3961–3975.

Dalguer, L., and S. Day (2007), Staggered-grid split-node method for spontaneous rupture simulation, *J. Geophys. Res.*, *112*, B02,302.

Das, S. (1980), A numerical method for determination of source time functions for general three-dimensional rupture propagation, *Geophys. J. Roy. Astr. Soc.*, *62*, 591–604.

Day, S. (1982), Three-dimensional finite-difference simulation of fault dynamics: rectangular faults with fixed rupture velocity, *Bull. Seism. Soc. Am.*, *72*, 705–727.

Day, S., and G. Ely (2002), Effect of a shallow weak zone on fault rupture: numerical simulation of scale-model experiments, *Bull. Seism. Soc. Am.*, *92*(8), 3022–3041.

Day, S., L. Dalguer, N. Lapusta, and Y. Liu (2005), Comparison of finite difference and boundary integral solutions to three-dimensional spontaneous rupture, *J. Geophys. Res.*, *110*, B12,307, doi:10.1029/2005JB003813.

de la Puente, J., J.-P. Ampuero, and M. Käser (2009), Dynamic rupture modeling on unstructured meshes using a discontinuous Galerkin method, *J. Geophys. Res.*, *114*, B10,302, doi: doi:10.1029/2008JB006271.

Dieterich, J. H. (1979), Modeling of rock friction 1. experimental results and constitutive equations, *J. Geophys. Res.*, *84(B5)*, 2161–2168, doi:doi:10.1029/JB084iB05p02161.

Dumbser, M., and M. Käser (2006), An arbitrary high order discontinuous Galerkin method for elastic waves on unstructured meshes II: The three-dimensional case, *Geophys. J. Int.*, *167*(1), 319–336.

Fliss, S., H. Bhat, R. Dmowska, and J. Rice (2005), Fault branching and rupture directivity, *J. Geophys. Res*, *110*, B06,312.

Galis, M., P. Moczo, and J. Kristek (2008), A 3-D hybrid finite-differencefinite-element viscoelastic modelling of seismic wave motion, *Geophys. J. Int.*, *175*, 153–184.

Galis, M., P. Moczo, J. Kristek, and M. Kristekova (2010), An adaptive smoothing algorithm in the TSN modeling of rupture propagation with the linear slip-weakening friction law, *Geophys. J. Int.*, *180*, 418–432.

Galvez, P., J.-P. Ampuero, L. Dalguer, and T. Nissen-Meyer (2011), Dynamic rupture modelling of the 2011 M9 Tohoku earthquake with unstructured 3D spectral element method, *Eos Trans. AGU*, *1*(1), Fall Meet. Suppl., Abstract S24.

Geubelle, P., and J. Rice (1995), A spectral method for three-dimensional elastodynamic fracture problems, *J. Mech. Phys. Solids*, *43*, 1791–1824.

Godunov, S. (1959), A finite difference method for the computation of discontinuous solutions of the equations of fluid dynamics., *Mat. Sb.*, *47*, 271–306.

Harris, R., et al. (2004), The source physics of large earthquakes: Validating spontaneous rupture methods, *Eos Trans. AGU*, *85*(47), Fall Meet. Suppl., Abstract S12A–05.

Hauksson, E., L. M. Jones, K. Hutton, and D. Eberhart-Phillips (1993), The 1992 Landers Earthquake Sequence: Seismological Observations, *J. Geophys. Res.*, *98*, 19,83519,858, doi:10.1029/93JB02384.

Hesthaven, J., and T. Warburton (2008), *Nodal Discontinuous Galerkin Methods: Algorithms, Analysis, and Applications*, Springer, New York.

Ida, Y. (1973), The maximum acceleration of seismic ground motion, *Bull. Seism. Soc. Am.*, *63*, 959–968.

Kaneko, Y., N. Lapusta, and J.-P. Ampuero (2008), Spectral element modeling of spontaneous earthquake rupture on rate and state faults: Effect of velocity-strengthening friction at shallow depths, *J. Geophys. Res.*, *113*, B09,317.

Käser, M., and M. Dumbser (2006), An arbitrary high order discontinuous Galerkin method for elastic waves on unstructured meshes I: The two-dimensional isotropic case with external source terms, *Geophys. J. Int.*, *166*(2), 855–877.

Käser, M., and A. Iske (2005), ADER schemes on adaptive triangular meshes for scalar conservation laws, *J. Comp. Phys.*, *205*, 486–508.

Käser, M., V. Hermann, and J. de la Puente (2008), Quantitative Accuracy Analysis of the Discontinuous Galerkin Method for Seismic Wave Propagation, *Geophys. J. Int.*, *173*(3), 990–999.

Krivodonova, L. (2007), Limiters for high-order discontinuous galerkin methods, *Journal of Computational Physics*, *226*, 879–896.

Lachenbruch, A. H. (1980), Frictional heating, fluid pressure and the resistance to fault motion, *J. Geophys. Res.*, *85*, 60976112.

Lapusta, N., J. Rice, Y. Ben-Zion, and G. Zheng (2000), Elastodynamic analysis for slow tectonic loading with spontaneous rupture episodes

on faults with rate- and state-dependent friction, *J. Geophys. Res.*, *105*, 23,765–23,789.

LeVeque, R. (2002), *Finite Volume Methods for Hyperbolic Problems*, Cambridge University Press, Cambridge.

Li, Y.-G., K. Aki, D. Adams, A. Hasemi, and W. H. K. Lee (1994), Seismic guided waves trapped in the fault zone of the Landers, California, earthquake of 1992, *J. Geophys. Res.*, *99*, 11,705–11,722, doi:10.1029/94JB00464.

Madariaga, R., K. Olsen, and R. Archuleta (1998), Modeling dynamic rupture in a 3D earthquake fault model, *Bull. Seism. Soc. Am.*, *88*, 1182–1197.

Mase, C., and L. Smith (1985), Pore-fluid pressures and frictional heating on a fault surface, *Pure and Applied Geophysics*, *122*, 583–607.

Mase, C., and L. Smith (1987), Effects of frictional heating on the thermal, hydrologic, and mechanical response of a fault, *J. Geophys. Res.*, *92*, 6249–6272.

Moczo, P., J. Kristek, M. Galis, P. Pazak, and M. Balazovjech (2007), The finite-difference and finite-element modeling of seismic wave propagation and earthquake motion, *Acta physica slovaca*, *57*(2), 177–406.

Oglesby, D., R. Archuleta, and S. Nielsen (1998), The three-dimensional dynamics of dipping faults, *Bull. Seism. Soc. Am.*, *90*, 616–628.

Oglesby, D., R. Archuleta, and S. Nielsen (2000), Earthquakes on dipping faults: the effects of broken symmetry, *Science*, *280*, 1055–1059.

Olsen, K., R. Madariaga, and R. J. Archuleta (1997), Three-dimensional dynamic simulation of the 1992 Landers earthquake, *Science*, *278(5339)*, 834–838.

Pelties, C., M. Käser, V. Hermann, and C. E. Castro (2010), Regular versus irregular meshing for complicated models and their effect on synthetic seismograms, *Geophys. J. Int.*, *183*(2), 1031–1051, doi: 10.1111/j.1365-246X.2010.04777.x.

Poliakov, A., R. Dmowska, and J. Rice (2002), Dynamic shear rupture interactions with fault bends and off-axis secondary faulting, *J. Geophys. Res*, *107*(2295), 6–1.

Rice, J. R. (1999), Flash heating at asperity contacts and rate-dependent friction, *Eos Trans. AGU*, *80*(46), Fall Meet. Suppl., F681.

Rojas, O., E. M. Dunham, S. Day, L. Dalguer, and J. Castillo (2009), Finite difference modelling of rupture propagation with strong velocity-weakening friction, *Geophys. J. Int.*, *179*, 1831–1858.

Ruina, A. L. (1983), Slip instability and state variable friction laws, *J. Geophys. Res.*, *88*, 10,359–10,370.

Tada, T., and R. Madariaga (2001), Dynamic modelling of the flat 2-D crack by a semi-analytic BIEM scheme, *International Journal for Numerical Methods in Engineering*, *50*(1), 227–251, doi:10.1002/1097-0207(20010110)50:1⟨227::AID-NME166⟩3.0.CO;2-5.

Titarev, V., and E. Toro (2002), ADER: Arbitrary high order Godunov approach., *J. Sci. Comput.*, *17*(1-4), 609–618.

Toro, E. (1999), *Riemann Solvers and Numerical Methods for Fluid Dynamics*, Springer, Berlin.

Vilotte, J.-P., G. Festa, and J.-P. Ampuero (2006), Dynamic fault rupture propagation using nonsmooth spectral element method, *Eos Trans. AGU*, *87*(52), Fall Meet. Suppl., Abstract S52B–05.

Wald, D., and T. Heaton (1994), Spatial and temporal distribution of slip for the 1992 Landers, California, earthquake, *Bull. Seis. Soc. Am.*, *84(3)*, 668–691.

Christian Pelties, Department of Earth and Environmental Sciences, Geophysics Section, Ludwig-Maximilians-Universität, München, Germany. (pelties@geophysik.uni-muenchen.de)

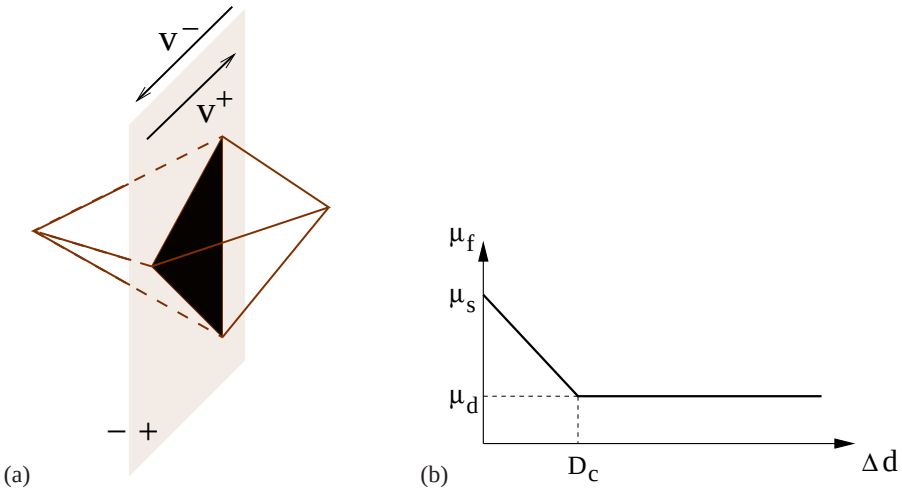

Figure 1. In (a) is depicted a fault segment discretized as the contact surface of two tetrahedral elements. The different fault sides are indicated by plus and minus. In (b) we plot the friction coefficient μ_f vs. the slip Δd for the linear slip weakening friction law.

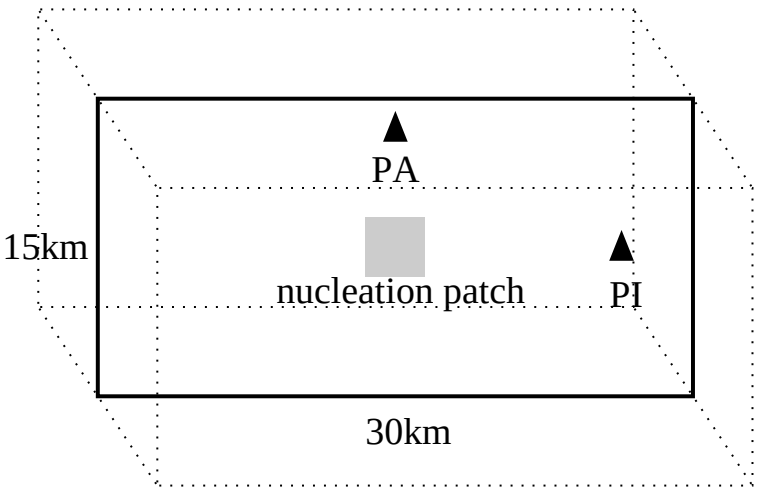

Figure 2. Sketch of the SCEC test case with the nucleation zone (grey shaded). The fault is surrounded by a box with an edge length of 72 km. The black triangles indicate the in-plane receiver (PI) and the anti-plane receiver (PA).

Parameter	Nucleation zone	Outside nucleation zone
Initial shear traction (MPa)	81.6	70.0
Initial normal stress (MPa)	120.0	120.0
Static friction coefficient	0.677	0.677
Dynamic friction coefficient	0.525	0.525
Critical slip distance (m)	0.4	0.4

Table 1. Parameters describing the fault for the SCEC test case.

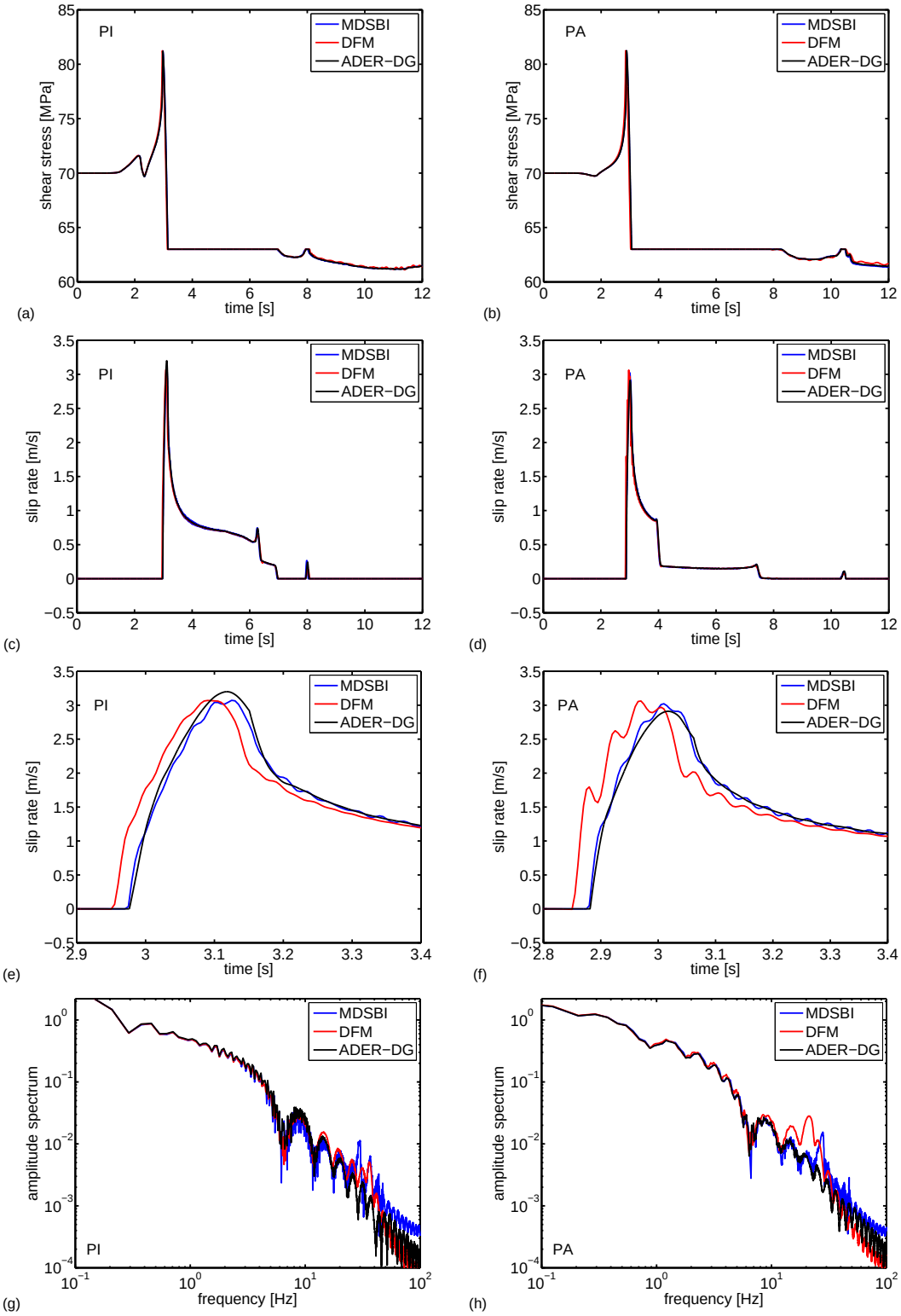

Figure 3. In all subfigures, MDSBI (blue) represents the solution obtained by the boundary integral method with a grid interval of $h = 50$ m and DFM (red) indicates the FD staggered-grid split node method with grid interval $h = 50$ m. All results are in good agreement with the solution produced by our ADER-DG scheme (black) with an equivalent mesh spacing of $\Delta x = 50$ m at the fault. Shown are the shear stresses (a),(b) and the slip rates (c),(d). The panels (e) and (f) provide a clearer image of the slip rate peaks. PI and PA denote the in-plane and the anti-plane receiver as shown in Fig. 2. In the bottom row (g),(h) the spectra of the slip are shown. The ADER-DG solution does not produce spurious high-frequency oscillations.

h (m)	$\mathcal{O}$	RMS rupture time (%)	RMS final slip (%)	RMS peak slip rate (%)	CPU time (s)
1061	4	2.79	2.88	14.52	2288640
	5	0.95	2.35	12.58	7280640
707	3	3.05	2.38	13.48	2764800
	4	0.74	1.85	11.39	8386560
	5	0.31	1.42	8.36	26081280
530	2	37.32	54.31	37.98	1474560
	3	1.44	1.61	10.84	4945920
	4	0.43	1.31	8.00	14991360
	5	0.19	1.22	6.87	49827840
424	2	15.34	39.62	25.84	2580480
	3	0.69	1.35	9.18	8847360
	4	0.20	1.20	6.76	29675520
	5	0.08	1.03	6.20	99901440
354	2	9.99	29.74	21.38	3993600
	3	0.44	1.20	7.65	14499840
	4	0.12	0.98	5.95	45772800
	5	0.04	1.03	5.84	163553280

Table 2. Convergence results for the 3D TPV3 SCEC test case.

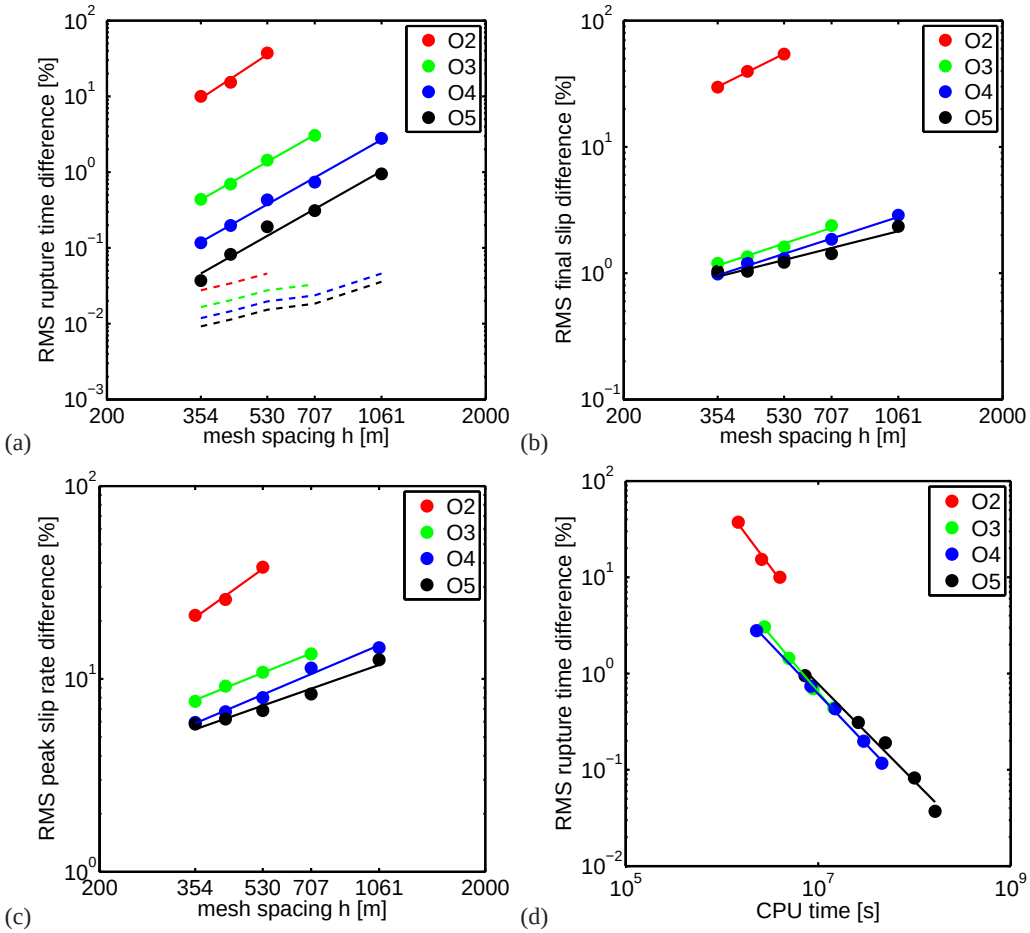

Figure 4. Convergence results for the 3D TPV3 SCEC test case. Dots are the simulation results colored by their order of accuracy. The solid lines represent the regression and the dashed lines denote the levels determined by the timestep Δt. Misfits are shown for the rupture time (a), final slip (b), and peak slip rate (c). Panel (d) shows the convergence of the rupture time misfit as a function of its CPU time.

Method	Rupture time	Final slip	Peak slip rate
ADER-DG $\mathcal{O}2$	3.28	1.48	1.43
ADER-DG $\mathcal{O}3$	2.84	0.99	0.80
ADER-DG $\mathcal{O}4$	2.83	0.97	0.85
ADER-DG $\mathcal{O}5$	2.83	0.75	0.70
DFM[a]	2.96	1.58	1.18
BI[a]	2.74	1.53	1.19

Table 3. Error convergence exponents for ADER-DG schemes of different order. [a]The convergence rates of DFM and BI are from *Day et al.* [2005].

Parameter	Nucleation zone	Outside nucleation zone
Principal stress σ_1 (MPa)	300.0	300.0
Principal stress σ_2 (MPa)	70.0	100.0
Static friction coefficient	0.6	0.6
Dynamic friction coefficient	0.4	0.4
Critical slip distance (m)	0.8	0.8

Table 4. Frictional parameters for the test case of the Landers fault system.

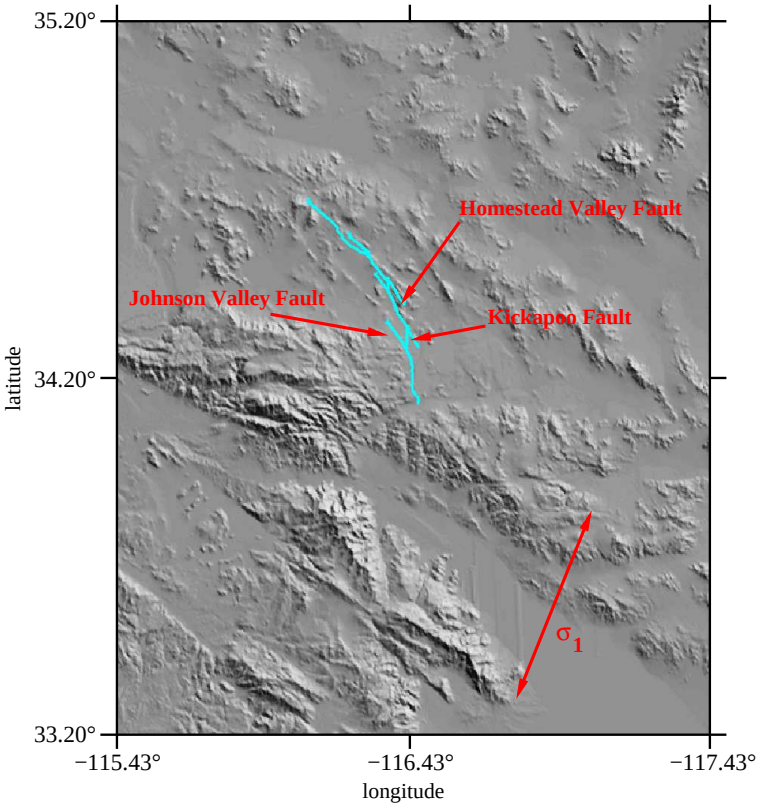

Figure 5. Map view of the 1992 Landers earthquake fault system with topography. The red double arrow indicates the assumed principal stress direction of N22°E. The lateral center of the model domain is the location of the epicenter at $34.20°$N and $116.43°$W.

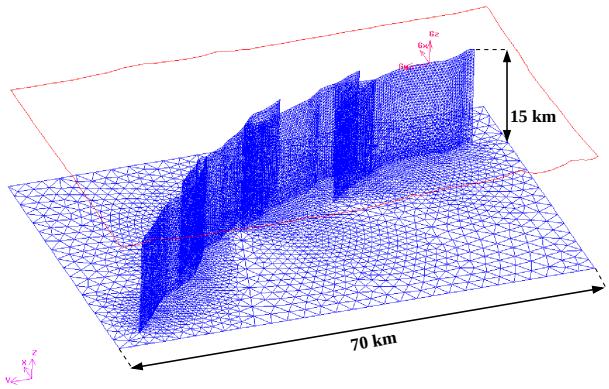

Figure 6. Discretization of the Landers fault system with triangles of 500 m edge length. In the area indicated by a red line the topography is decribed by a fine mesh of 500 m edge length. The box below is filled by 2500 m elements with only moderate mesh coarsening away from the fault.

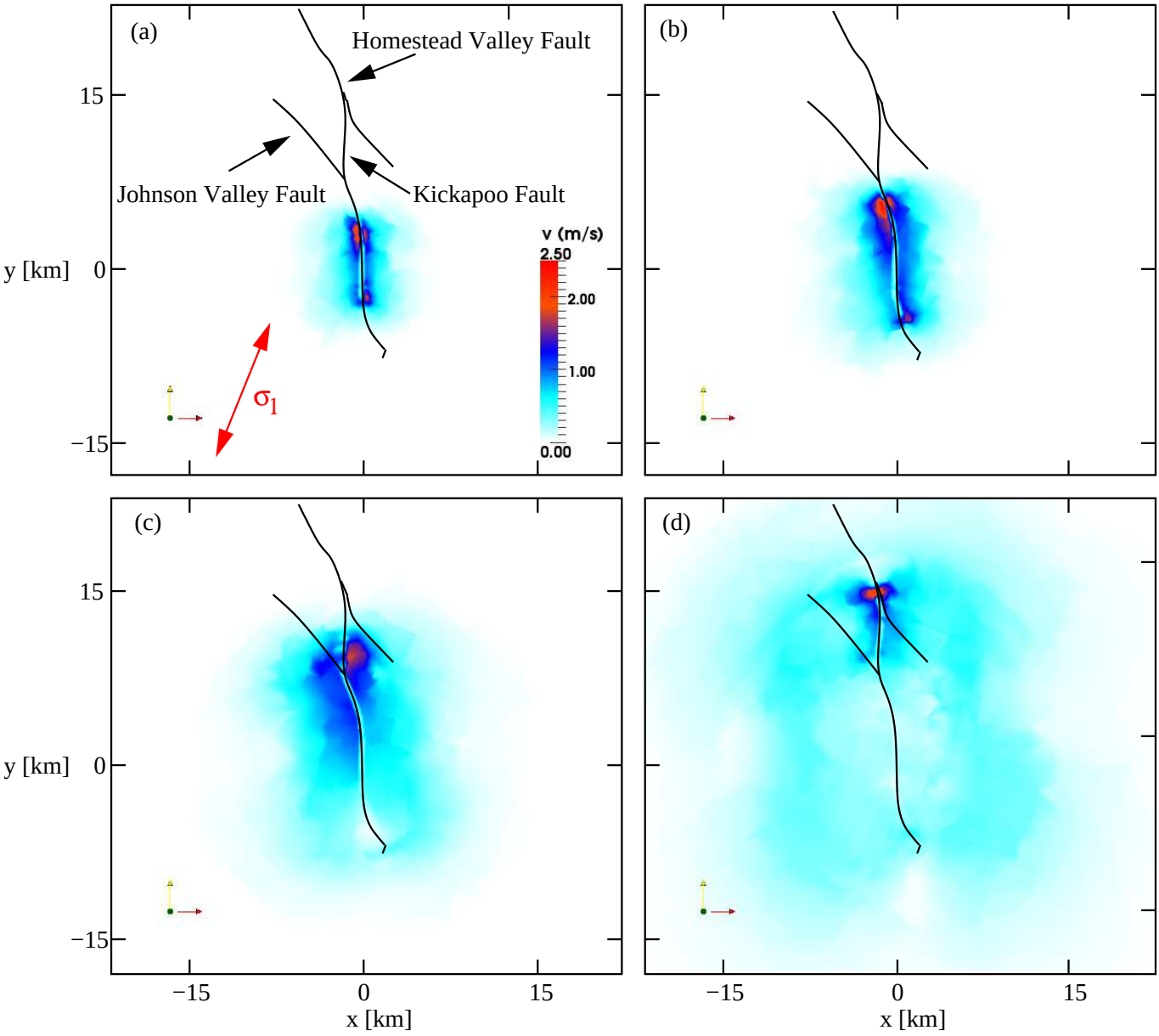

Figure 7. Snapshots of absolute particle velocity at (a) 1, (b) 1.5, (c) 2.5, (d) 4.5 s after rupture initiation on a horizontal cut of the nucleation area at a depth of 5 km below sea level. The red double arrow indicates the assumed principal stress direction.

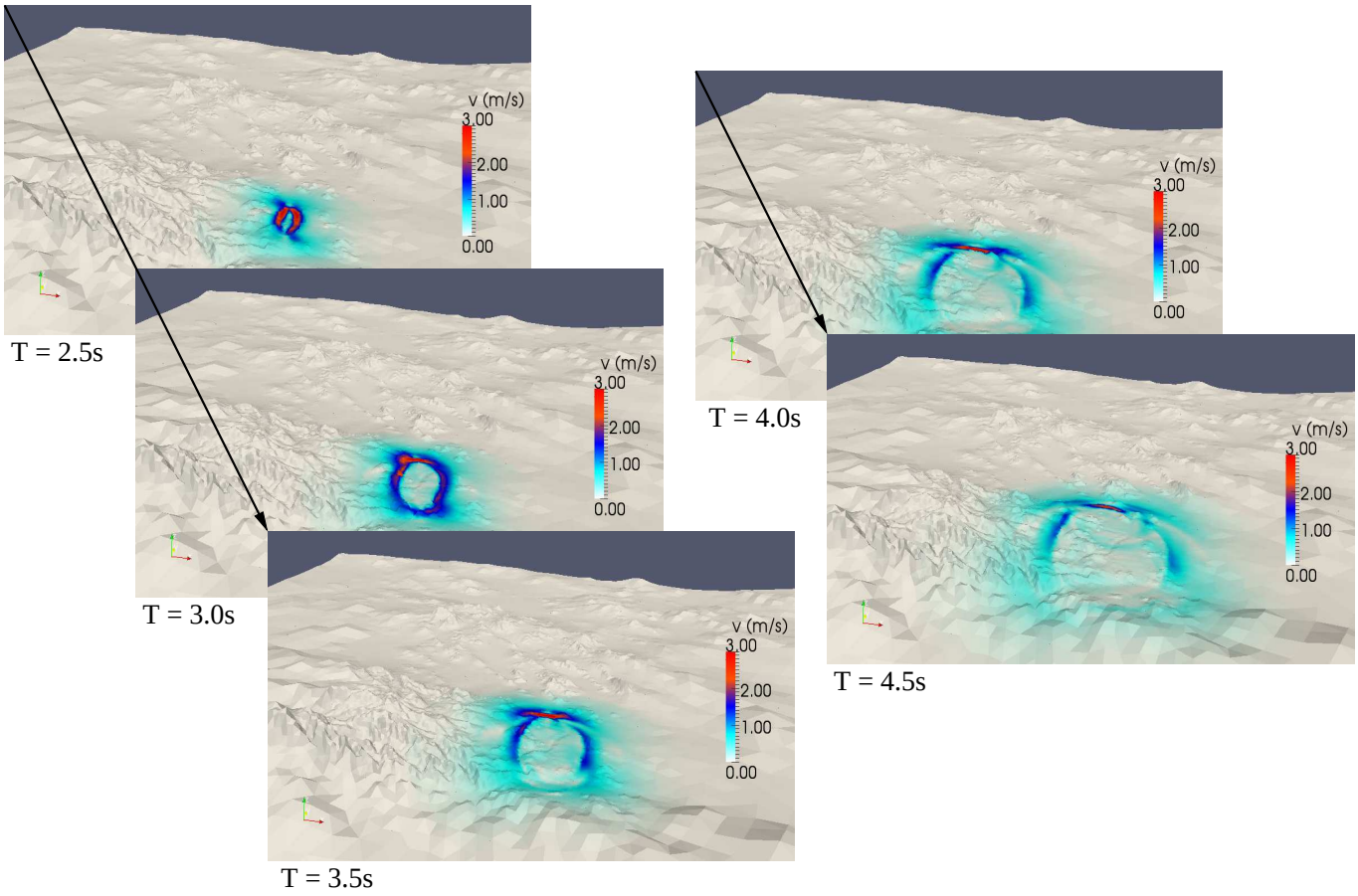

Figure 8. Development of the ground velocity field with time. The topography is scaled by a factor of 3. v represents the absolute particle velocity in m/s. The viewing direction is roughly from southeast to northwest. The directivity effect can be clearly observed.